Université d'Ottawa · University of Ottawa

TURBULENT FLOW IN A POROUS TUBE WITH WALL SUCTION

Manouchehr Heidarpour

A Dissertation
Submitted to School of Graduate Studies
under the supervision of
Dr. E. J. Schiller

in partial fulfillment of the requirements
for the degree of
Doctor of Philosophy in Civil Engineering

Department of Civil Engineering
Faculty of Engineering
University of Ottawa
Ottawa, Canada K1N 6N5
October 1997

The Doctor of philosophy in Civil Engineering is a joint program between Carleton University and the University of Ottawa, which is administered by the Ottawa-Carleton Institute for Civil Engineering

ABSTRACT

This study examines the effects of suction (i.e. lateral flow through the walls) on the structure of a fully developed turbulent pipe flow. Also the effect of suction on pressure gradient and pressure change is examined experimentally. The frictional characteristics of Irrigro®, the porous tubing used in this investigation, is studied by means of a comprehensive experimental program that considered different lengths of porous tubing.

Three aspects of flow in porous pipes are investigated in this study, (i) a computational study of the effects of suction on the flow characteristics, (ii) an experimental study of the frictional characteristics of the porous tubing with no suction condition and (iii) an experimental study of pressure change along a porous tubing with lateral flow.

The numerical study of turbulent pipe flow with wall suction rates ranging from A = 0 to 13 percent showed that in fully developed pipe flow, wall suction results in a more uniform velocity distribution with increased near-wall velocity values and reduced velocities near the centerline. The near-wall component of radial velocity, v, increases with increasing distance from the wall in the zone near the pipe wall. The absolute levels of turbulent kinetic energy decrease with increasing suction rate. Wall suction increases the wall shear stress ,τ_w, along the wall of the tube. The increase in τ_w is significant even for the smallest suction rate (up to 30 percent) while such an increase is much higher for A=13 percent (up to 360 percent).

Analysis of the experimental friction loss data obtained for small diameter porous tubing in this study confirmed that the Colebrook and White (C-W) equation is a very accurate predictor of the friction factor for porous tubing with small diameter size and Reynolds numbers less than 100,000. These results are in agreement with the results of Aggarwal et al (1972). The value of the relative roughness obtained in this study showed that the porous tubing under study is smoother than most of the tubing used as laterals in the traditional trickle irrigation. Also, the fact that the friction factors agreed with the Colebrook-White law indicates that the physical roughness in the porous tubing under study corresponds very nearly to the equivalent sand roughness with a relative roughness of about e/D=0.002. A relationship was established as a convenient and accurate head loss prediction equation (within 5% error) by combining a power function with the Darcy-Weisbach equation. The combination equation is correctable for viscosity changes and accurate for the porous pipe tubing under study.

A pressure change and a pressure gradient prediction relationship were established in the transition zone of the Moody diagram for high suction rates, assuming a uniform radial flow rate along the suction region. The relationships presented herein are based on a control volume approach analysis and incorporated the data obtained from laboratory studies on the porous tubing under study.

In the name of God

ACKNOWLEDGMENTS

The author wishes to express his sincere appreciation to his supervisor, Dr. E. J. Schiller, for his guidance, advice, and encouragements during the course of this research.

The scholarship provided by the Ministry of Culture and Higher Education of the I.R. of Iran is gratefully acknowledged.

Appreciation is extended to the committee members: Dr. C. A. Madramootoo (University of McGill), Dr. H. Tanaka, Dr. K. Kennedy, and R. L. Droste (University of Ottawa).

Particular thanks are due to Louis G. Trembley, technician of the Chemical Engineering Department, for providing me with some experimental devices and tools. Without his help the experimental set-up would not be possible.

Particular thanks and sincere appreciation are extended to my parents, parents in-law, sisters and brothers for their companion, continuous support, and warm encouragement.

Last but not least, thanks to my family, my wife Gity, for her love, perseverance, and patience, as well as to my daughter, Anahita, for her friendly understanding. Their support made this work possible.

TABLE OF CONTENTS

LIST OF SYMBOLS

A = cross-sectional area

A = suction rate (A = Q_A/Q_R)

B = blockage factor

C = Hazen-Williams coefficient of relative roughness of the pipe

D = inside diameter of tubing

e/D = relative roughness of the pipe

e = surface roughness

f = friction factor coefficient

$f_{Blasius}$ = friction factor coefficient in Blasius equation

f = skin friction coefficient (fanning friction factor) in Mellis (1992) study (Figure 3.4)

g =gravitational acceleration

$H_{L(1-2)}$ = drop in elevation of the energy line due to friction between sections 1 and 2

H_L = friction head loss

ΔH = pressure head loss in the pipe

K = constant in equation 3.22

k = Kinetic energy of turbulent fluctuations per unit mass

k = turbulent kinetic energy

k_1 = 5.35 in metric units in Hazen-Williams equation

l = Turbulent length scale; characteristic eddy size

L = Characteristic length scale

L = pipe length

$\hat{p}$ = instantaneous static pressure

P_i = static pressure at the inlet of tubing

P_o = static pressure at the outlet of tubing

P_w = gage pressure

P = mean static pressure

Q_A = extracted mass flow

Q_R = inlet mass flow

Q = flow rate in the pipe

R = radius of pipe

r = radial co-ordinate

Re_{xx} = axial Reynolds number

Re_D = axial Renolds number in Aggarwal (1971) study (Figure 3.3)

Re_w = radial Reynolds number (wall Reynolds number)

Re = Reynolds Number

s_{ij} = instantaneous strain-rate tensor

S_{ij} = mean strain-rate tensor

t = time

t_{ij} = viscous stress tensor

u' = x component of fluctuating velocity

$\hat{u}$ = x component of instantaneous velocity

u = x component of time average velocity

U_1 = area average velocity at the inlet of porous section

U_2 = area average velocity at the outlet of porous section

U = area mean velocity

U_c = centerline velocity

$\hat{u}_i$ = instantaneous velocity in tensor notation

u_i = time average velocity in tensor notation

u_t = turbulent scale ($u_t \propto \sqrt{k}$)

U_τ =friction velocity ($\sqrt{\tau_w/\rho}$)

$\hat{v}$ = y component of instantaneous velocity

v = y component of time average velocity

v' = y component of fluctuating velocity

V_w = transverse velocity at the wall

$\hat{w}$ = z component of instantaneous velocity

w = z component of time average velocity

w' = z component of fluctuating velocity

x = axial co-ordinate

x = axial distance from entry of porous tubing

x_i = position vector in tensor notation

y^+ = Dimensionless, sublayer-scaled, distance, $u_\tau y/\upsilon$

z = potential energy or gravity head in Bernoulli equation

β = momentum correction factor

β_1 = suction coefficient ($\beta = V_w/U$)

η = ratio between characteristic time scales of turbulence and the mean flow fields

ρ = density of water

μ = dynamic viscosity of fluid

γ = specific weight of fluid

τ_w = wall shear stress with suction

δ_{lax} = axisymmetric displacement thickness

τ_{w_0} = wall shear stress without suction

υ = kinematic viscosity of fluid

μ_t = turbulent viscosity (eddy viscosity)

δ_{ltwo} = two-dimensionally defined displacement thickness

δ_{lax} = axisymmetric displacement thickness

Δ = height of the first node above the wall

τ_{app} = apparent stress in turbulent flow

ω = turbulent frequency

LIST OF ABBREVIATIONS

EL = energy line

HGL = hydraulic grade line

RNG = Renormalization Group

EVM = eddy- viscosity models

FIDAP = Fluid Dynamics Analysis Package

FEM= Finite Element Method

FDI = Fluid Dynamics International, Inc.

SAS = Statistical Analysis System

LIST OF FIGURES

LIST OF PLATES

LIST OF TABLES

Chapter 1

1. Introduction

1.1 Statement of the Problem

The flow of fluids through passages with porous walls has been of interest in the last three decades. This kind of flow is encountered in a variety of engineering applications. The filtration of air, water, and sewage, the use of heat pipes, the separation of isotopes by gaseous diffusion, the manufacture of paper, water desalination by reverse osmosis, boundary layer stabilization and most recently microirrigation are some of the engineering applications. Since porous tubing is extensively used as laterals for surface and

subsurface irrigation system, this research study was mainly motivated by a need to find more information about the hydraulic characteristics of these porous tubes.

The distinct difference between a solid boundary and a porous boundary was clearly demonstrated by experiments conducted by Minton and Francis (1958). Their measurements were concerned with the drag force on a set of flat plates consisting of two thin perforated plates with and without a sheet of paper between the plates. They observed a much larger drag on the plates when the sheet of paper was removed from between plates and perforations were continuous through the plates. This experiment can be thought of as an extreme case of permeable boundary layer flows and indicates the importance of flow interactions through the perforations.

Permeable boundaries not only permit flow to pass through the porous media whenever a pressure gradient is applied, but also provide the exchange of mass, momentum and energy between the main turbulent stream and the seepage flow. It can be expected that some of the universal characteristics observed in boundary flows with impervious walls may be preserved in permeable boundary flows. However, the fundamental mechanisms involved in various transfer process may be modified by the boundary permeability.

For fully developed tube flows without surface mass transfer, the friction factor and the axial pressure gradient, normalized by the dynamic pressure, are essentially equivalent quantities. On the other hand, in the presence of surface mass transfer, the axial pressure

gradient is affected by changes in axial momentum flux as well as by the wall shear stress. In particular, when there is mass transfer at the wall, the momentum change of the flow tends to cause an increase in pressure in the flow direction, while the wall shear tends to decrease the pressure.

The development of the heat pipe has intensified interest of the study of the fluid in the porous tubing since the vapor flow in a heat pipe can be modeled by the flow of a fluid in a pipe with porous walls. Heat pipes are devices which remove heat from the source in a two-phase process. The heat pipe is a vacuum-tight pipe that is evacuated and partially filled with a minute amount of water or other working fluid. As heat is directed into the heat pipe, the fluid is vaporized creating a pressure gradient in the pipe. The pressure gradient forces the vapor to flow along the pipe to the cooler section where it condenses, giving up its latent heat of vaporization. The working fluid is then returned to the evaporator by capillary forces developed in the heat pipe's porous section, or by gravity. A schematic presentation of a heat pipe is shown in Figure 1.1*. The evaporation and condensation of the fluid at the porous surface in a heat pipe are modeled by the injection and removal of the fluid through the porous wall.

The most widely used application of fluid in porous tubes occurs in various pressure-driven membrane processes such as hyperfiltration, ultrafiltration and

---

* Figures and Tables are found at the end of each chapter

microfiltration. An important limitation in the performance of pressure-driven membrane process is concentration polarization. In general, the transmembrane flux is adversely effected by the transient build-up of retained solutes (ions, macromolecules and suspended colloids). It has been realized that moving the suspension tangential to the membrane surface results in much higher permeation fluxes (Sieveka, 1966). Reentrainment of polarized and deposited solutes by wall shear stresses have been used to explain this improved performance. Thus, crossflow filtration is widely used in nearly all commercial large-scale pressure-driven membrane plants. The most common designs include flat sheet, spiral wound, tubular (with internal diameters greater than 0.635 cm), capillary (with internal diameters between 0.1 and 0.635 cm), and hollow fiber (with internal diameters between 0.025 and 0.1 cm).

Membrane processes are operated in both laminar and turbulent regimes. Since turbulence prevents a fast build-up of the fouling layer this regime is the preferred operational regime.

The uniformity of application in a microirrigation system using porous tubing as laterals depends completely on the uniformity of the emission rate along the porous tubing. A variation of emission rate can be caused by the pressure change along the porous tubing resulting from friction losses, elevation changes, clogging, or from tolerances in the manufacturing. In order to obtain a good uniformity of application, the pressure difference along porous tubing has to be kept within certain limits to insure a reasonably uniform emission rate.

Friction head loss is one of the main causes of pressure differences resulting in nonuniform emission rate. Therefore, it is important that the designer be able to calculate the friction losses in the system accurately.

1.2 Research Needs

The research efforts concerning the turbulent flow of fluid confined by boundaries in the past mostly dealt with smooth or rough impervious boundaries. Universal characteristics associated with this particular category of boundary layer flow have been found and well documented (Hinze, 1975, and Townsend, 1956). On the other hand, the information concerned with turbulent flow restricted by permeable boundaries is quite limited.

The fluid dynamics of the flow in a porous duct are surprisingly complex even when geometries and boundary conditions are quite simple. Most attempts at theoretical analysis have begun with the simplification of the problem to a steady, incompressible, laminar, and fully developed flow in a uniformly porous duct of simple geometry. These simpler models were expected to provide at least qualitative information on pressure variations, velocity profiles, wall friction characteristics and other properties of more complex and more practical flows. This has not been the case, however, since the difficulties encountered in the solution of even these simple problems have led to much different interpretations among investigators.

The amount of information available concerning the mechanisms of flow in a porous medium exposed to a turbulent shear flow is limited, the primary reason being that direct measurement of velocities in a porous medium is difficult to achieve. Instruments and techniques necessary to provide satisfactory results have not been perfected. Without adequate measurements in a porous medium, the assumptions regarding the interaction of the mechanisms involved in the porous boundary can be checked only through measurements of main stream flow characteristics such as velocity profile and head loss.

Very few experimental studies have been conducted for flow in porous tubing. Most of the earlier experimental studies have been directed for the laminar flow of air in porous tubes. Owing to difficulties in using liquids, even less measurements have been made with liquids. Up to now all the experiments using liquids have been conducted for laminar flows.

Unfortunately the experimental investigations of turbulent flow reported in the literature are mainly concerned with the influence of mass flow transfer of air on the macroscopic properties of turbulent flows for a particular value of axial Reynolds number, Re_{∞} . These experimental studies have shown that mass transfer has a significant effect on mass, momentum and heat transfer rates. Also, it has been realized that mass transfer, even at low rates, affects considerably the near-wall mean velocities and causes an alternation of the universal logarithmic law of the wall. In addition, it increases the wall shear stress in the mass transfer region and reduces the turbulence levels across the pipe

radius. Except for the study of Aggarwal et al. (1972), no data have been taken for pressure drop or pressure gradient along porous tubing.

Due to difficulty in inserting pressure taps in porous walls, particularly in thin-walled porous tubing, it has been impossible to obtain significant experimental data for pressure gradients along the porous tubing. The difficulty in obtaining precise measurements of the pressure along the porous tubing with high extraction, or suction rate, has resulted in a lack of the experimental data in porous tubing. In the flow in a porous tubing at high suction rate, since the pressure drop across the porous wall is much higher than the pressure difference along the tubing, any small pressure change due to the flow along the porous wall close to a pressure tap has an amplified effect on the measurement. The drilling operation in a porous wall in order to insert pressure taps usually does not give a clean hole in the porous wall. This problem combined with the slight change of shape around the hole results in disturbance of the flow and error in pressure measurements. As a result of all these problem no significant data can be found in the literature about the nature of the pressure variation along porous tubes with a high suction rate.

The application of flows through porous-walled tubing to industrial processes requires some knowledge of the pressure drop and pressure gradient values and mass transfer rates involved. For instance, although heat pipes are structures of very high thermal conductance, this conductance exists only up to a certain maximum heat flux, which depends on several factors, one of which is the axial pressure variation in the

vapour flow. Furthermore, these values will be required for assessing the power requirement for this form of porous tubing. In pressure-driven membrane processes, since pressure is mainly used to drive the various feed components through membranes, any quantitative description of the behavior of porous tubing requires spatial and temporal variations of the pressure along the tubing.

In microirrigation applications, a knowledge of the factors causing pressure differences along porous tubing is required before designing an efficient microirrigation system. Friction head loss is one of the main causes of pressure differences resulting in nonuniform emission rate. Therefore, it is important that the designer be able to calculate the friction losses in the system accurately.

To the author's knowledge at the present time no information is available on the friction head loss characteristics of small diameter porous tubing used for microirrigation. Also, no experimental data are available on pressure drop and pressure gradient along porous tubing using liquid in high range of the suction rates and in the transition region. This present research attempts to produce information that has been previously lacking in this field.

1.3 Objective and Scope of Study

The main objectives of the present research work are following:

1- To investigate the effects of wall mass transfer on the structure of fully developed turbulent pipe flow using the FIDAP finite element package and to evaluate the performance of two turbulent models in predicting the structure of fully developed turbulent pipe flow in the presence of the wall mass transfer.

2- To investigate experimentally, the effect of the wall mass transfer on the pressure drop coefficient (dimensionless pressure drop or pressure gain) of a fully developed turbulent pipe flow and also to develop an equation for dimensionless pressure drop in a fully developed turbulent flow in porous tubing with wall mass transfer.

3- To investigate experimentally, the effect of the wall mass transfer on pressure gradient of a fully developed turbulent flow and also to develop equations for pressure gradient of a fully developed turbulent flow of a porous tubing with wall mass transfer.

4- To evaluate the frictional characteristics and relative roughness of porous tubing under study in the "no net wall flux" condition. Also to recommend a simple, precise and convenient head loss prediction equation for small diameter porous tubing under investigation. A comparison of the frictional characteristics of this kind of tubing with the traditional trickle irrigation laterals is another objective of present research.

1.4 Study Program

The experiments covered an inlet axial Reynolds number (defined as $Re_{ax} = \frac{\rho UD}{\mu}$, where ρ= density of fluid, U = axial bulk velocity, D = diameter of tube, μ = dynamic viscosity of fluid) between 3000 and 40000 and wall Reynolds number (defined as $Re_w = \frac{\rho V_w D}{\mu}$, where V_w = transverse velocity at the wall) between 0 and 100.

In all experiments distilled water was used to prevent the porous test section from clogging. It is admitted that the influence of water quality is very important in many practical applications. However in this thesis the study will be limited to the use of pure, distilled water.

The following measurements were carried out:

- The pressure difference between the inlet and outlet of the test section
- The axial inlet flow rate
- The axial outlet flow rate
-The wall flow rate
- The temperature of the distilled water before and after the test section and in the tank

1.5 Experimental Equipment

The experimental apparatus was a closed-circuit system permitting the use of distilled water during the course of the experiments. This system consisted of a 0.1 m^3 plastic tank, a plastic container (for collecting distilled water from test section), four

pumps (one for delivering distilled water from the main reservoir to the test section and for recycling the distilled water back to the main reservoir), a porous tubing made from Tyvec, inlet and outlet stainless steel tubing, collector, heat exchanger, manometer and support stand made of perforated angles.

The porous tubing employed in experiment, known by commercial name of Irrigro® was made from Tyvec®. The mean pore size and the thickness of the porous wall were given by the manufacturer as 0.5 μm and 15 μm, respectively. A long inlet and a long outlet region were added to make sure that the flow was stable and that fully developed flow was present at the inlet of test section. The ratio of the non-porous inlet length to the inside tube diameter was 100. This was adequate to insure fully developed flow at the entrance.

Inlet axial flow rate was measured by a calibrated rotameter. The pressure difference between the entrance and exit of the porous tubing was measured by a manometer. The permeate (wall) flow rate was measured by catching a particular amount of water within a particular time. The temperature of water was measured by three thermocouples installed before and after porous section and in the main reservoir. A heat exchanger was placed after the test section to maintain the temperature at 24 °C. The heat exchanger used tap water for cooling.

1.6 Thesis Description

Chapter 2 of the thesis deals with contributions and advancements relating to the field of fluid flow through a porous boundary and more specifically porous tubing. A review of the following is included: (1) theoretical work in laminar flow conditions, including the entrance flow region and fully developed laminar flow, (2) experimental studies including laminar flow and turbulent flow conditions.

The numerical results of the effects of the wall mass transfer on the structure of a fully developed turbulent pipe flow are discussed in *Chapter* 3.

Chapter 4 is devoted to theoretical considerations and presents a control volume approach to obtain a formula for calculating pressure drop or pressure gain along porous tubing incorporating the friction factor of the porous tubing at the non-suction condition.

In *Chapter* 5, The experimental set-up used in the laboratory program is described in detail.

In *Chapter* 6 the frictional characteristics of the porous tubing in the non-suction condition are investigated. Based on experimental data in a non-suction condition, a simple, precise and convenient head loss prediction equation is suggested for the small diameter porous tubing under investigation for microirrigation applications. Also a comparison is made between the frictional characteristics of this kind of tubing and the

traditional trickle irrigation laterals. The relative roughness of the porous tubing is obtained and compared with the other laterals used in traditional microirrigation.

In *Chapter* 7 the relation obtained in chapter 3 was tested in the transition region of the Moody diagram by analyzing experimental data obtained in this research. Relations for pressure drop or pressure gain and pressure gradient in the transition region of the Moody diagram are presented in this chapter.

Chapter 8 is devoted to conclusions and recommendations for future research. Finally, references and appendices are included at the end of the thesis.

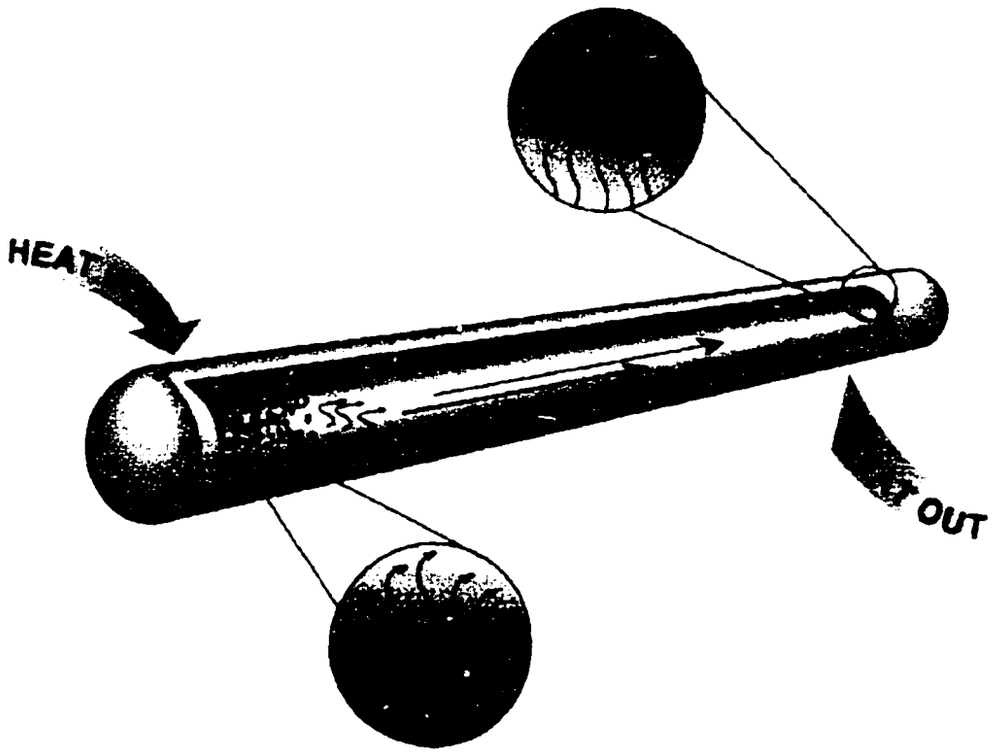

Figure 1.1- Flow of vapour along a heat pipe

Chapter 2

2. Literature Review

2.1 Laminar Flow Studies

2.1.1 Theoretical Studies

The literature describing the flow of pure fluids in porous-walled tubes includes studies of entrance region flows, characterized by changing magnitudes and shapes of both the axial and radial velocity profiles (for example, Weissberg, 1959; Hornbeck et al, 1963; Friedman and Gillis, 1967; Galowin and Desantis, 1971; Galowin et al., 1974; Quale and Levy, 1975; Ku and Leidenfrost, 1981; and Terrill, 1982, 1983, 1984, 1986), and fully-

developed region flows, characterized by changing magnitudes but unchanging shapes of the axial and radial velocity profiles (for example, Yuan and Finkelstein, 1956; Eckert et al., 1957; Berman, 1958; Regirer, 1960; White,1962; Kinny, 1968; Terrill and Thomas, 1969; Raithby, 1971 and Singh and Laurence, 1979).

2.1.1.1 Entrance-Region Flow

An effort to explain the unexpected absence of suction solutions for fully developed flow with suction for certain wall Reynolds numbers led Weisberg (1959) to study of the flow in the entrance region of a porous pipe. Weissberg used an extension of the method-of-averages approximation of Morduchow (1967). The equations for flow in the entrance region were simplified by assuming that the inlet axial Reynolds number was large compared to the wall Reynolds number (defined as $Re_w = \rho V_w D/\mu$, where ρ = density of fluid, V_w = transverse velocity at the wall, D = diameter of tube, μ = dynamic viscosity of fluid). Weissberg found that, for injection and for small suction, the entrance region flow approached fully developed flow far downstream from the inlet of the porous pipe. But in the gap region, the velocity profiles did not approach any asymptotic form far downstream from the pipe inlet. Thus, the absence of similarity solutions for fully developed flow was explained by the fact that the entrance region filled the entire pipe. This condition was calculated for wall Reynolds numbers from 2.41 to 7.63 compared to the region from 2.3 to 9.0 for which Berman (1958) could find no numerical similarity solutions, which are more accurate than those given by the method of averages.

Hornbeck et al. (1963) used a finite-difference marching technique with the axial velocity, the radial velocity, and the pressure as the dependent variables to obtain numerical solutions to the flow equations after making essentially the same high axial Reynolds number approximation as Weissberg (1959). Parabolic and uniform inlet velocity profiles were studied for uniform suction or injection and for wall velocities proportional to the local pressure. Their results for constant wall velocities and a parabolic inlet velocity profile are in good agreement with those of Weissberg (1959).

Friedman and Gillis (1967) solved the complete Navier-Stokes equations for a porous pipe without making any approximate assumptions for inlet axial Reynolds numbers ranging from 0 to 500 using a relaxation technique. The Stokes stream function and the vorticity were the dependent variables. Two conditions were studied: (a) wall suction was permitted over all of the pipe length and (b) over only a finite length, of the pipe wall. A uniform inlet velocity profile was assumed, but a parabolic velocity profile could be obtained at the inlet of the porous section of pipe by placing that section far downstream from the inlet to the pipe and treating the portion of the pipe upstream of the porous section as having a solid wall. Results for flow far downstream of the inlet of the porous section of pipe were generally in good agreement with the results for fully developed flow previously reported by the investigators.

2.1.1.2 Fully Developed Flow

Berman (1953) solved the complete Navier-Stokes equations for the flow in a flat channel with porous walls. His solution gave a nondimensional velocity profile, which did

not change along the axial tube axis (i.e., remains similar). He neglected the velocity profile at the entrance of the porous tube section. In the case of uniform suction, the solution was restricted to Re_w less than 2.3 and to Re_w greater than 9.1. In contrast to the suction case, solutions were found for all values of Re_w for flow with uniform injection. He used a similarity transformation involving a dimensionless stream function to reduce the equations of motion to a single third-order, nonlinear ordinary differential equation. Both viscous and inertial effects were considered to be important. Berman's equation is appropriate for fully developed laminar flow in a porous pipe subject to the following assumptions:

1. The flow is laminar, steady, axisymmetric, and isothermal.

2. The fluid is incompressible.

3. The velocity of the fluid being withdrawn through the wall is in the radial direction and independent of position along the wall. These assumptions, in conjunction with the similarity transformation using a dimensionless stream function, also imply that the axial velocity profile has the same shape at all cross sections in the pipe.

Yuan and Finkelstein (1956) independently reduced the flow equation to a single ordinary differential equation using a similarity transformation. Furthermore, they used a dimensionless radial coordinate, $\eta=(r/a)^2$, which is more convenient than the one that Berman (1952,1958) used.

Berman (1958) used numerical integration to obtain a solution for fully developed flow over the full range of suction and injection wall flows. His numerical solutions, which are presumably accurate, showed Yuan and Finkelstein's (1956) second-order perturbation technique to be valid for large injections, but not for large suctions. In his paper, Berman also developed a third-order perturbation solution, which gave useful results for both suction and injection. He used Morduchow's method (1967) to obtain suction solutions and summarized the work that had been done up to 1958. Berman observed that no similarity solutions for fully developed flow could be obtained by any method for a certain range of suction wall Reynolds numbers. This gap in the suction solutions extended from wall Reynolds numbers of 2.3 to 9.0 for Berman's numerical solutions. This region in which no suction solutions for fully developed flow could be obtained continued to be a feature of later studies as well. These later studies included the work of White (1962) , who obtained power-series solutions that were applicable for fully developed flow over a large range of suction and injection wall velocities.

Terril and Thomas (1969) summarized the solution of previous authors for laminar flow in a uniformly porous circular pipe with constant injection or suction through the wall and combined these with new solutions of their own to present a unified treatment of the numerical and analytical solutions to this problem. They showed that two solutions exist for all values of injection in addition to the dual solutions already noted by previous investigators for suction.

2.1.2 Experimental Studies

The limited amount of experimental results that is available for flow through porous pipes is at such high radial Reynolds numbers that inertial effects would completely dominate the flow. Taylor (1956) measured the discharge coefficient and the velocity profile for the flow of water through a 3.33 cm inner diameter, 45 cm long porous tube formed by three layers of copper wire gauze. The velocity profile was measured at the exit of the porous tube with a pitot probe. The data were taken at a wall Reynolds number, Re_w, ranging from 440 to 600 with all of the fluid being introduced into the pipe through the wall (i.e. injection). Taylor obtained good comparisons between his experimental results and his theoretical results, which were based on the Bernoulli equation.

Wageman and Guevara (1960) tried to observe flow reversals to verify their solution, which gave axial velocity profile having the shape of $\cos\frac{(2n+1)\pi\eta}{2}$, for $n \geq 0$. They calculated the shape of the stream function, machined a plug to fit this function, and inserted it into the gas stream. However, these experiments failed to produce the flow reversals.

Aihara's unpublished velocity-profile measurements are cited by Williams (1968) and compared with results of his linearized theory. Aihara measured the velocity profile at a distance eight tube diameters downstream of the inlet of a porous pipe using a hot-wire anemometer for the flow of air at three different inlet velocities and a wall Reynolds number of $Re_w = 68$. Aihara's measurements are in good agreement with the second-order

perturbation theory of Yuan and Finklestein (1956) for fully developed flow at an infinitely large wall Reynolds number, but not with the linearized theory of Williams.

Even though the data just cited agrees with the results of at least some of the theories for viscous laminar flow in porous tubes (for example, the theory of Yuan and Finkelstein), the data do not provide an adequate test of these theories. As has already been noted, all the data were taken under conditions at which the inertial effects completely dominated the flow. Since the theory for flow through porous pipes was formulated for conditions such that inertial and viscous effects are both important, this theory can, of course, only be verified adequately under such conditions.

Beavers and Joseph (1967) reported experiments on laminar flow in a rectangular conduit with one permeable wall. Their results indicated a reduction of flow resistance due to porous boundary since experiments were conducted with laminar flow conditions.

2.2 Turbulent Flow Studies

A series of studies was carried by Goma and Gelhar (1968), and Chu and Gelhar (1972) for flow through pipes lined with porous walls. It is observed from their results that boundary permeability caused an increase in the resistance to the flow.

Zangni and Smith (1976) carried out experiments involving open channel flow over permeable beds of spherical particles made of lead shots and steel balls with the flow

leaving out the bottom. Their results indicated that the boundary resistance of a permeable boundary is higher than that of impermeable boundaries having identical rugosity.

Plate and Quraishi (1965) observed wind velocity distribution inside and above tall crops using model forests which may be taken as analogous to the permeable bed. The logarithmic law to the flow above the crop led to the transition of the vertical coordinate by an amount which is called the zero plane displacement.The velocity distribution inside the plant cover was not defined through a logarithmic law.

In an analysis of flow resistance data for flat bed stream and laboratory flumes, Loverna and Kennedy (1969) indicated that the resistance characteristics of alluvial streams do not follow the observation made on tough impervious boundary layer flows. For flow of constant depth with a movable bed, they found that the friction factor increased continuously with the flow Reynolds number.

Ruff and Gelhar (1970) developed velocity distribution models analytically for the case of a pipe with a porous lining. By using a shielded hot-wire and supplementary tracer technique, they measured velocity inside the porous wall. The seepage velocity was found to reduce sharply as the distance away from the porous bed surface increased and asymptotically approached the pressure gradient seepage velocity.

Weissberg and Bergman (1955) studied the influence of suction on turbulent velocity situations. Applying uniform suction to a fully established turbulent pipe flow for a range of exit Reynolds numbers from 27,000 to 79,000, they found that the effect of suction was to reduce the streamwise velocity fluctuation, normalized with the local mean velocity, at all radial locations.

In the experiments of Aggarwal et al. (1972), uniform wall suction was applied to a fully established turbulent pipe flow for a length of 10 pipe diameters. It was found in this investigation that turbulent intensities, normalized with the local mean velocity, decreased in the central core at very low suction rates but increased at higher suction rates; however, the absolute level of turbulent fluctuation was always found to be reduced by suction.

Favre (1966) reported some fluctuation measurements for flow in a turbulent boundary layer over a flat plate with uniform suction. Direct measurement of turbulent fluctuations and the Reynolds shear stress demonstrated decreasing values of these quantities with increasing suction rates and increasing distances from the leading edge of the porous wall.

The first experimental investigation into the velocity and pressure distribution in turbulent pipe flow with uniform suction was carried out by Weissberg and Berman (1955). Axial pressure distribution and profiles of temporal-mean axial velocity and axial

turbulent velocity fluctuation were measured with air flowing in a 7.31 m long porous pipe of 76 mm dia. Immediately before entering the test section the air underwent an area reduction of just over 11:1 from a settling chamber, so that the entry velocity profile was virtually flat. The Reynolds number was varied from about 25,000 to 80,000, and the entrance suction coefficient β_1, defined as the ratio of the transverse velocity at the wall to the inlet mean axial velocity, was varied from zero to about 0.005. Turbulence levels over the entire pipe cross-section were found to be lowered by suction. At a given location and at the same Reynolds number, velocity profiles were flatter and friction factors higher with suction than without. However, the changes in the velocity profile resulting from suction were small enough for the velocity profile parameter δ, defined as the ratio $\overline{u^2} / \overline{u}^2$, to have an almost constant value close to 1.02 for all rates of suction tested.

Wallis (1965-6) performed experiments with air flowing in canvas hoses of about 25 mm diameter and of lengths up to 2.3 m, with entry velocity profile undeveloped. An axial Reynolds number range of 25,000-121,000 was covered and in this range the friction factor without suction for the rough canvas hose was constant. The entrance suction coefficient β_1 was varied from zero to 0.02. The suction rate along the tube was fairly uniform, although no attempt was made to control it. Wallis presented his results in terms of pressure changes and did not compute friction factors, but his data suggest that these factors, for a given value of β_1 and x/D (x= axial distance from entry of porous tubing, D= inside diameter of porous tubing), were independent of the inlet Reynolds number

Re_{∞} , perhaps owning to the considerable surface roughness. Wallis, when using total extraction, took a single velocity profile roughly half-way down the 2.3 m long tube and observed a more peaky profile than at inlet, in contrast to the flatter profiles found by Weissberg and Berman. No turbulence measurements were taken.

Aureille (1967) studied the effect of uniform suction on an initially fully-developed turbulent flow of air in a 75 mm diameter sintered nickel tube. The inlet Reynolds number was fixed at 40,800 for all tests while β_1 was varied from zero to 0.00308. At such low rates of suction the static pressure gradient was found to be constant for $x/D > 6$. Aureille found, unlike Wallis, that the axial velocity profile became flatter with suction. Friction factors increased both with β_1 and with x/D. He noted no change, however, in the distribution of radial velocity with x/D. Aureille also deduced from his experimental data, that turbulence was partially destroyed by suction.

The effect of wall suction on the structure of turbulence in a fully established turbulent pipe flow was measured by Schildknecht et al. (1979). Uniform suction was introduced into the test section over a length of 13.5 cm by means of a porous nickel tube 5 cm in diameter. Inlet Reynolds number was 17,250. The values of the mean and turbulence characteristics was measured at the selected stations x/D = 0, 0.503, 1.358 and 2.213 along the suction region for suction rates A (A= Q_A/Q_R , where Q_A = extracted mass flow and Q_R = inlet mass flow) equal to 1.6, 3.3, 6.5, and 13.0 percent. The profiles of the mean axial velocity (u), radial velocity (v) and fluctuating velocity components

(u', v', w') were measured along the pipe radius at selected stations. No measurements were made for wall shear stress (τ_w), friction factor (f) and pressure (p) along the suction region. Schildknecht concluded that with increasing wall suction a more uniform axial velocity profile is obtained. Also with increasing wall suction the absolute level of fluctuation intensity decreases. His measurements showed that a high rate of fluid extraction prevails close to the entrance plane and relax to a fully developed state at about $x/D = 1.3$.

In summary, most of the earlier studies have been theoretical investigations of laminar flow in porous tubes. Most of the industrial processes using porous tubing are operated in turbulent regimes. Since turbulence reduces a build-up of the fouling layer, this is the preferred operational regime. In microirrigation applications a small part of the lateral at the end is operated in the laminar regime but most of the lateral is operated in the turbulent regime.

Very few experimental investigations of turbulent flow are reported in the literature, and they are mainly concerned with the influence of mass flow transfer of air on the structure of turbulent flows for a particular value of inlet axial Reynolds number, Re_{∞}. The application of flows through porous-walled tubing to industrial processes requires some knowledge of the pressure drop and pressure gradient values and the mass transfer rates involved. Due to difficulties in inserting pressure taps in porous walls, particularly in thin-walled porous tubing, it has been extremely difficult to obtain significant experimental

data for pressure gradients along the porous tubing. Owing to difficulties in using liquids, even less measurements have been made with liquids. Up to now all the experiments using liquids have been conducted for laminar flows.

Most of the industrial processes using porous tubing are operated in the transition zone of the Moody diagram. Experimental data are necessary to investigate the pressure gradient behavior along porous tubing with wall suction for flow in the transition zone.

The capability of the existing turbulent flow models in predicting the structure of fully developed turbulent pipe flow with wall suction is not described in the literature. This study will indicate the capability of existing turbulent models to predict the structure of fully developed turbulent flow with wall suction.

A knowledge of the factors causing pressure differences along porous tubing is required before designing an efficient microirrigation system. Friction characteristics of the solid pipe have been thoroughly investigated. For porous tubing, however, more research is necessary to investigate the behavior of the friction head loss.

Table 2.1- Flow in porous ducts: A literature summary

Geometry	Wall flow	Assumptions[a]	Solution method	Conclusions	Reference
Slit	Suction (2 porous walls)	2D, SS, IC, L, P, US, NF	Perturbation for Re_w <1	Velocity, Pressure expressions	Berman (1953)
	Suction/injection (2 porous walls)	2D, SS, IC, L, P, US/I, NF	Perturbation and power series Re_w, small , large	Velocity f'(y)and wall skin function (-f''(y)). Yuan's work only correct for injection Re_w <0	Terrill (1964)
	Suction/injection (2 porous walls); also for tube	2D, SS, IC, L, P, US/I, NF, ignore $(\nabla.\nabla u)$ inertial terms	Fourier analysis for Re_w <0	Limiting and arbitrary seepage rate	Kozinski et al. (1970)
	Suction/injection (2 porous walls)	2D, IC, L, US/I, NF	Finite difference (Patanker and Spalding method)	Friction and velocity equation in developing entrance region	Dougherty and Perkins (1970)
	Suction (2 porous walls)	2D, IC, L, P, US, NF	Finite difference for double parabolic entrance flow	Obtain skewed Raithby profiles	Doughty (1974)
	Suction (One porous wall)	2D, IC, L, P, US, NF	Perturbation for Re_w <1	Velocity, pressure expressions	Green (1980)

Table 2.1 (*continued*)

Geometry	Wall flow	Assumptions[a]	Solution method	Conclusions	Reference
Tube	Suction/injection	AS, SS, IC, L, P, US/I, NF	Perturbation for $Re_w<1$	Velocity, Pressure, wall skin friction expressions	Yuan and Finkelstein (1956)
	Suction/injection	AS, SS, IC, L, P, US/I, NF	Power series	Instabilities appear with wall suction for $0<Re_w<2.3$ (backflow); double solutions for $9.1<Re_w<\infty$ (backflow)	White (1962)
	Suction/Injection	AS, SS, IC, L, P, US/I, NF	Power series	Double solution for all values of Re_w for injection and suction except $2.3<Re_w<9.1$ where no solutions exist	Terrill and Thomas (1969)
	Suction	AS, SS, IC, L, P, US, NF, for suction equals total inlet flow	Finite difference	Subtle differences from Berman's solution	Friedman and Gillis (1967)
	Suction/Injection	AS, SS, IC, L, P, US, NF, wall velocity not independently set but dependent on Darcy's Law	Karman-Pohlhausen integral momentum and 4th order Runge-Kutta	Velocity, pressure, shear and friction factor	Galowin and DeSantis (1971)
	Suction	Same as above but with close-end tube	Same as above	Same as above	Galowin et al. (1974)
	Suction	AS, SS, IC, L, P, US, NF, for suction equals total flow , closed-end tube	Perturbation and power series	Confirms Terrill and Thomas (1969) and theory matches experiments $Re_w<3$	Quaile and Levy (1975)
	Suction/injection	AS, SS, IC, L, P, NF	Analytical, potential flow superimposed on Poisuille flow	Variable velocity suction, axial pressure drop	Terrill (1983)

Table 2.1 (*continued*)

Geometry	Wall flow	Assumptions[a]	Solution method	Conclusions	Reference
Annulus	Suction and injection at each face	2D, SS, L, US/I, IC, NF	Perturbation	Velocity and pressure profiles	Berman (1958)
	Suction/injection	AS, 2D, SS, L, US/I, IC, NF	Perturbation and power series	Velocity for various cases	Terrill (1966)
	Suction/injection	AS, SS, IC, L, US, NF, for suction only through inner wall with closed-end duct	Perturbation and power series	Injection pressure drop with theory (simultaneously) but suction data only agree for low Re<1.0	Gupta and Levy (1974)

[a] The following code is used: AS-axisymmetric; 2D- 2-dimensional; SS- steady state; L- laminar; P-parabolic; US/I-uniform suction/Injection; IC-incompressible; NF-no external forces. Re_w may be defined differently in various papers.

Chapter 3

3. Computational Study

3.1 Introduction

In this chapter the effects of wall mass transfer on the structure of the fully developed turbulent pipe flow are studied numerically by solving the Reynolds-averaged Navier-Stokes equations in conjunction with Renormalization Group (RNG) k-ε and k-ω eddy-viscosity models (EVM) of turbulence of the low-Re type. Detailed results of the most complete experimental study reported in the literature performed by Schilknecht et al. (1979) are used in the present study for comparison with the results of the two models

mentioned above. The effects of wall suction on the mean and turbulence characteristics will be examined at the selected stations in the suction region where detailed experimental measurements are available for suction rates A (A= Q_A/Q_R , where Q_A = extracted mass flow and Q_R = inlet mass flow) equal to 1.6, 3.3, 6.5, and 13.0 percent. The comparisons entail profiles of the mean axial velocity (u) and radial velocity (v) and turbulent kinetic energy (k) along the pipe radius at selected stations. The distribution of the wall shear stress (τ_w) and friction factor (f) in the suction region will be examined. The material in this chapter is not intended as an exhaustive survey of the numerous turbulent models in the field of computational fluid dynamics. Rather, it is intended to illustrate how wall mass transfer affects the structure of a fully developed turbulent pipe flow.

The computer program used in this study was the Fluid Dynamics Analysis Pachage (FIDAP 7.6) which was developed by Fluid Dynamics International, Inc (FDI.). It was available on the University of Ottawa TESLA machine which is located in the Computer Centre in the Vanier Building. FIDAP is a very extensive computer program that is capable of simulating a wide variety of fluid flow situations. The capabilities of this program were first analyzed and then it was applied to the problem of flow through a pipe with a porous wall, which was the subject of this study.

Since the primary emphasis in the computational part of this study is based on the Reynolds-averaged Navier-Stokes equation it is worthwhile to discuss briefly how this equation is obtained from the instantaneous Navier-Stokes equation. This issue will be

discussed in sections 3.1.2 and 3.1.3. Some description of the physics of turbulence in section 3.1.1 will help to better understand sections 3.1.2 and 3.1.3. In order to show how this study fits in the computational fluid dynamics studies a brief history of turbulent models is discussed in section 3.1.4.

3.1.1 Comments on the Physics of Turbulence

Before discussing the mathematics of turbulence, it is worthwhile to first consider physical aspects of turbulence. The following discussion is not intended as a complete description of this complex phenomenon. Rather, it focuses upon a few features of interest in engineering applications, and upon the construction of a mathematical model for the research being considered in this study.

In 1937, Taylor and von Karman (see Goldstein, 1938) proposed the following definition of turbulence: "Turbulence is an irregular motion which in general makes its appearance in fluids, gaseous or liquid, when they flow past solid surfaces or even when neighbouring streams of the same fluid flow past or over one another".

Perhaps the most important feature of turbulence from an engineering point of view is its enhanced diffusivity. Turbulent diffusion greatly enhances the transfer of mass, momentum and energy. Apparent stresses often develop in turbulent flows that are several orders of magnitude larger than in corresponding laminar flows.

As noted by Tennekes and Lumley (1983), "Even the smallest scales occurring in a turbulent flow are ordinarily far larger than any molecular length scale." Nevertheless, the smallest scales of turbulence are still extremely small. They are generally many orders of magnitude smaller than the largest scales of turbulence, the latter being of the same order of magnitude as the dimension of the object about which the fluid is flowing. Furthermore, the ratio of smallest to largest scales decreases rapidly as the Reynolds number increases.

Turbulence consists of a continuous spectrum of sizes ranging from largest to smallest, as opposed to a discrete set of turbulent eddy sizes. In order to visualize a turbulent flow with a spectrum of scales, one often refers to turbulent eddies. A turbulent eddy can be thought of as a local swirling motion whose characteristic dimension is the local turbulence scale. Eddies overlap in space with large ones carrying smaller ones. Turbulence features a cascading process whereby, as the turbulence decays, its kinetic energy transfers from larger eddies to smaller eddies. Ultimately, the smallest eddies dissipate into heat through the action of molecular viscosity. Thus, we observe that turbulent flows are always dissipative

An especially striking feature of a turbulent shear flow is the way large bodies of fluid migrate across the flow, carrying smaller-scale disturbances with them. The arrival of these large eddies near the interface between the turbulent region and nonturbulent fluid distorts the interface into a highly convoluted shape (Figure 3.1). In addition to migrating across the flow, they have a lifetime so long that they persist for distances as much as 30

times the width of the flow (Bradshaw,1972). Hence, the turbulent stresses at a given position depend upon upstream history and cannot be uniquely specified in terms of the local strain-rate tensor as in laminar flow.

3.1.2 The Closure Problem

The instantaneous Navier-Stokes equations are limited in a practical sense to laminar flow. In laminar flow, even an unsteady one, the fluid moves along smooth streamlines, and the velocity at any point is either fixed in time or varies in a regular manner. In turbulent flow, the fluid particles are violently mixed and the fluid velocity at a point varies randomly with time, as shown in Figure 3.2.

In fact the instantaneous property values in a turbulent flow vary to such a degree that little information can be obtained by a direct application of the basic equation, and thus some modification is necessary. It is necessary to use a statistical average and a measure of the deviation from that average.

3.1.2.1 Reynolds Averaging

The solution of the Navier-Stokes equation to capture the random fluctuations of turbulence is practically impossible. Instead, engineers use a statistical approach and work with time averages in turbulent flow. Time averaging is appropriate for a stationary turbulent flow, i.e., a turbulent flow that, on the average, does not vary with time. For

such a flow, an instantaneous flow variable is expressed as $f(x,t)$. Its time average F (x), is defined by

$$F(x) = \lim_{T \to \infty} \frac{1}{T} \int_{t}^{t+T} f(x,t)dt \tag{3.1}$$

and the instantaneous velocity components are expressed as the sum of a time-averaged and a fluctuating part

$$\hat{u} = u + u' \tag{3.2}$$

$$\hat{v} = v + v' \tag{3.3}$$

$$\hat{w} = w + w' \tag{3.4}$$

As in equation (3.1), the quantities u,v, and w are time-average velocities defined by

$$u(x) = \lim_{T \to \infty} \frac{1}{T} \int_{t}^{t+T} \hat{u}(x,t)dt \tag{3.5}$$

$$v(x) = \lim_{T \to \infty} \frac{1}{T} \int_{t}^{t+T} \hat{v}(x,t)dt \tag{3.6}$$

$$w(x) = \lim_{T \to \infty} \frac{1}{T} \int_{t}^{t+T} \hat{w}(x,t)dt \tag{3.7}$$

3.1.2.2 Reynolds Rules of Averaging

If any fluctuating quantity (e.g. u') is time-averaged, that average must be zero as a consequence of its definition (Eq. 3.2). However, if any quantity such as u' is squared before it is averaged (e.g. $\overline{u'^2}$), that average will be non-zero because each value of u'^2 is never less than zero. Also if the product of two fluctuating components is averaged (e.g., $\overline{u'v'}$), that average can be non-zero.

Because these averages are so important in turbulent theory, Reynolds formulated certain rules of approximation in the calculation of averages. The rules are:

1. Quantities which have already been averaged may be considered as constants in subsequent averaging:

$$\overline{\overline{A}} = \overline{A} \tag{3.8}$$

$$\overline{\overline{A}B} = \overline{A}\,\overline{B} \tag{3.9}$$

2. Averaging obeys the distributive law:

$$\overline{A + B} = \overline{A} + \overline{B} \tag{3.10}$$

3. Derivatives of quantities obey the averaging law:

$$\overline{\partial A / \partial x} = \partial \overline{A} / \partial x \tag{3.11}$$

An important consequence of these rules is evident from the following treatment of the average of the product AB, where A and B are instantaneous quantities, each composed as the sum of a mean and a fluctuating value.

$$\begin{aligned} \overline{AB} &= \overline{(\overline{A} + A')(\overline{B} + B')} \\ &= \overline{\overline{A}\,\overline{B}} + \overline{A'\overline{B}} + \overline{\overline{A}B'} + \overline{A'B'} \\ &= \overline{A}\,\overline{B} + \overline{A'B'} \end{aligned} \tag{3.12}$$

3.1.2.3 Reynolds-averaged Navier-Stokes Equations

The equation for conservation of mass and momentum for an incompressible flow are:

$$\frac{\partial \hat{u}_i}{\partial x_i} = 0 \tag{3.13}$$

$$\rho \frac{\partial \hat{u}_i}{\partial t} + \rho \hat{u}_j \frac{\partial \hat{u}_i}{\partial x_j} = -\frac{\partial \hat{p}}{\partial x_i} + \frac{\partial t_{ji}}{\partial x_j} \tag{3.14}$$

The vectors $\hat{u}_i$ and x_i are velocity and position, t is time, $\hat{p}$ is pressure, ρ is density and t_{ij} is the viscous stress tensor defined by

$$t_{ij} = 2\mu s_{ij} \tag{3.15}$$

where μ is molecular viscosity and s_{ij} is the strain rate tensor defined by

$$s_{ij} = \frac{1}{2}\left(\frac{\partial \hat{u}_i}{\partial x_j} + \frac{\partial \hat{u}_j}{\partial x_i}\right) \tag{3.16}$$

To simplify the time-averaging process, the convective term can be rewritten in conservation form, i.e.,

$$\hat{u}_j \frac{\partial \hat{u}_i}{\partial x_j} = \frac{\partial}{\partial x_j}(\hat{u}_j \hat{u}_i) - \hat{u}_i \frac{\partial \hat{u}_j}{\partial x_j} = \frac{\partial}{\partial x_j}(\hat{u}_j \hat{u}_i) \tag{3.17}$$

Combining equations (3.14) through (3.17) yields the Navier-Stokes equation in conservation form.

$$\rho \frac{\partial \hat{u}_i}{\partial t} + \rho \frac{\partial}{\partial x_j}(\hat{u}_j \hat{u}_i) = -\frac{\partial \hat{p}}{\partial x_i} + \frac{\partial}{\partial x_j}(2\mu s_{ji}) \tag{3.18}$$

Time averaging Equations (3.13) and (3.18) using Reynolds rules of averaging mentioned in section (3-1-4) yields the Reynolds averaged equation of motion in conservation form. For the sake of brevity the details of this lengthy manipulation are omitted.

$$\frac{\partial u_i}{\partial x_i} = 0 \tag{3.19}$$

$$\rho\frac{\partial u_i}{\partial t}+\rho\frac{\partial}{\partial x_j}(u_j u_i+\overline{u_j' u_i'})= \\ -\frac{\partial p}{\partial x_i}+\frac{\partial}{\partial x_j}(2\mu S_{ji}) \tag{3.20}$$

Aside from replacement of instantaneous variables by mean values, the only difference between the time-averaged and instantaneous Navier-Stokes equation is the appearance of the correlation $\overline{u_i' u_j'}$.

Herein lies the fundamental problem of turbulence for the engineer. In order to compute all mean-flow properties of the turbulent flow under consideration, a prescription for computing $\overline{u_i' u_j'}$ is needed. Equation (3.20) can be written in its most recognizable form by using Equation (3.17) in reverse. There follows:

$$\rho\frac{\partial u_i}{\partial t}+\rho u_j\frac{\partial u_i}{\partial x_j}= \\ -\frac{\partial p}{\partial x_i}+\frac{\partial}{\partial x_j}(2\mu S_{ji}-\overline{\rho u_i' u_j'}) \tag{3.21}$$

Equation (3.21) is usually referred to as the **Reynolds-averaged Navier-Stokes** equation. The quantity $-\overline{\rho u_i' u_j'}$ is known as the apparent stress tensor or Reynolds-stress tensor and it is denoted by τ_{ij}. Thus,

$$\tau_{ij}=-\overline{\rho u_i' u_j'} \tag{3.22}$$

By inspection, $\tau_{ij}=\tau_{ji}$ so that this is a symmetric tensor, and thus has six independent components. As a result of Reynolds averaging six unknown quantities have been produced. For general three-dimensional flows, there are four unknown mean-flow

properties, viz., pressure and three velocity components. Along with the six Reynolds-stress components, there are ten unknowns. The equations are mass conservation [Equation (3.19)] and three components of Equation (3.21) for a grand total of four. This means the system is not yet **closed**. To close the system there must be enough equations to solve for all of the unknowns.

The function of turbulence modeling is to devise approximations for the unknowns so that a sufficient number of equations exists. Upon making such approximations, the system will be **closed**.

3.1.3 Physical Interpretation of Reynolds-stress

The existence of apparent stresses in turbulent flow can be demonstrated by simple physical arguments. In turbulent flow, macroscopic "lumps" of fluid are thrown about by the turbulent motion. Figure 3.3 illustrates two typical fluid lumps in a turbulent flow. The time-average flow is one-directional (u) and one-dimensional (y). The turbulent fluctuation velocities are two-directional (u, v). The time average velocities of the two lumps are u and $u+\delta u$.

Suppose that two lumps exchange places because of turbulent mixing. The slower lumps arrives at its new location with velocity u, and faster lumps arrives at new location with velocity $u+\delta u$. Now neither lump has the velocity appropriate for its location. At $y+\delta y$, the velocity perturbation is $u' \approx -\delta u$, and at y, the velocity perturbation is $u' \approx +\delta u$. The time averages of velocities at y and $y+\delta y$ are still u and $u+\delta u$. The

interchange of the two lumps has resulted in increase of momentum at location y and decrease of momentum at $y+\delta y$. As this type of interchange occurs in turbulent flow, there is a net rate of momentum transfer between y and $y+\delta y$ because of the velocity fluctuations. From the time-average point of view, this momentum transfer is equivalent to a force or, on a per unit area basis, a stress. The momentum represented by u is transported between y and $y+\delta y$ by the velocity perturbation v'. The momentum flux (per unit area) is $\rho u'v'$. If we treat this momentum flux as a stress, according to d'Alembert's principle, its instantaneous value is:

$$\tau_{app} = -\rho u'v' \tag{3.23}$$

where τ_{app} is the instantaneous apparent stress resulting from turbulent momentum transport.

3.1.4 A Brief History of Turbulence Modeling

The primary emphasis in the computational part of this study is upon the time-averaged Navier-Stokes equation. The origin of this approach dates back to the end of the nineteenth century when Reynolds (1895) published the results of his research on turbulence. His pioneering work proved to have such a profound importance for all future developments that the standard time-averaging process is referred to as a type of Reynolds averaging.

The earliest attempts at developing a mathematical description of turbulent stresses sought to mimic the molecular gradient-diffusion process. In this spirit, Boussinesq (1877) introduced the concept of eddy-viscosity. Neither Reynolds nor Boussinesq attempted a solution of the Reynolds-averaged Navier-Stokes equation in any systematic manner.

Prandtl (1925) introduced the mixing length and a straightforward prescription for computing the eddy viscosity in terms of mixing length. The mixing length hypothesis, closely related to the eddy viscosity concept, formed the basis of all turbulence modeling research for the next twenty years. In modern terminology, the mixing-length model is referred to as an **algebraic model or a zero-equation model of turbulence**.

To improve the ability to predict properties of turbulent flows and to develop a more realistic mathematical description of the turbulent stresses, Prandtl (1945) postulated a model in which the eddy viscosity depends upon the kinetic energy of the turbulent fluctuations, k. He proposed a differential equation which approximated the exact equation for k. This improvement, on a conceptual level, takes account of the fact that the eddy viscosity is affected by where the flow has been, i.e., upon flow history. Thus was born the concept of the so-called **one-equation model of turbulence**.

Kolmogorov (1942) introduced the first complete model of turbulence. In addition to having a modeled equation for k, he introduced a second parameter ω that he referred to as "the rate of dissipation of energy in unit volume and time." The reciprocal of ω

serves as a turbulence time scale, while $k^{1/2}/\omega$ serves as the analog of the mixing length. In this model, known as a k-ω model, ω satisfies a differential equation similar to the equation for k. The model is thus termed a **two-equation model of turbulence.**

3.2 Governing Equations and Theoretical Considerations

The equation governing the steady, incompressible, two dimensional turbulent pipe flow are the Reynolds-averaged Navier-Stokes equations which can be written in cylindrical coordinates as follows:

continuity eqn.

$$\frac{\partial}{\partial x}(ru)+\frac{\partial}{\partial r}(rv)=0 \tag{3.24}$$

x-momentum eqn.

$$\begin{aligned}&\frac{\partial}{\partial x}(ru^2)+\frac{\partial}{\partial r}(rvu)\\&=-r\frac{\partial P}{\partial x}+r\frac{\partial}{\partial x}\left[\upsilon\left(\frac{\partial u}{\partial x}+\frac{\partial u}{\partial x}\right)-\overline{u'^2}\right]\\&+\frac{\partial}{\partial r}\left\{r\left[\upsilon\left(\frac{\partial u}{\partial r}+\frac{\partial v}{\partial x}\right)-\overline{u'v'}\right]\right\}\end{aligned} \tag{3.25}$$

r-momentum eqn.

$$\begin{aligned}&\frac{\partial}{\partial x}(ruv)+\frac{\partial}{\partial r}(rv^2)\\&=-r\frac{\partial P}{\partial r}+r\frac{\partial}{\partial x}\left[\upsilon\left(\frac{\partial v}{\partial x}+\frac{\partial u}{\partial r}\right)-\overline{u'v'}\right]\\&+\frac{\partial}{\partial r}\left\{r\left[\upsilon\left(\frac{\partial v}{\partial r}+\frac{\partial v}{\partial r}\right)-\overline{v'^2}\right]\right\}-\frac{2\upsilon v}{r}-\overline{w'^2}\end{aligned} \tag{3.26}$$

where x, r = axial and radial co-ordinate; u, v = corresponding mean velocity components, P = mean pressure, υ = kinetic viscosity of the fluid and $\overline{u'^2}, \overline{v'^2}, \overline{w'^2}$ and $\overline{u'v'}$ = Reynolds stresses.

3.3 Turbulence Models

3.3.1 Wilcox's Low-Re k-ω Turbulence Model

k-ω model belongs to the so-called two equation group of turbulent models. The particular version of the k-ω model employed in this study was developed by David Wilcox (1993) and for this reason it will be referred to it as Wilcox's k-ω model.

In this model the turbulent scales u_t and δ_t are related to k and a turbulent frequency ω through the following expressions resulting from dimensional arguments:

$$u_t \propto \sqrt{k} \tag{3.27}$$

$$\delta_t \propto \frac{k^{1/2}}{\omega} \tag{3.28}$$

The turbulent frequency ω is itself related to k and ε via the simple expression:

$$\varepsilon = \omega k \tag{3.29}$$

The turbulent viscosity is obtained from:

$$\mu_t = c_\mu \rho \frac{k}{\omega} \tag{3.30}$$

The model transport equations for k and ω in Wilcox's model are as follows:

$$\rho\frac{\partial k}{\partial t}+\rho u_j\frac{\partial k}{\partial x_j}$$
$$=\frac{\partial}{\partial x_j}\left[\left(\mu+\frac{\mu_t}{\sigma_k}\right)\frac{\partial k}{\partial x_j}\right]+G-\rho\omega k \tag{3.31}$$

$$\rho\frac{\partial \omega}{\partial t}+\rho u_j\frac{\partial \omega}{\partial x_j}$$
$$=\frac{\partial}{\partial x_j}\left[\left(\mu+\frac{\mu_t}{\sigma_\omega}\right)\frac{\partial \omega}{\partial x_j}\right]+c_1\frac{\omega}{k}G-c_2\rho\omega^2 \tag{3.32}$$

In the above equations:

$$G=\mu_t\left(\frac{\partial u_i}{\partial x_j}+\frac{\partial u_j}{\partial x_i}\right)\frac{\partial u_i}{\partial x_j} \tag{3.33}$$

The values of Wilcox's model constants are :

c_1	c_2	c_μ	σ_k	σ_ω
0.555	0.8333	0.09	2	2

An important advantage of Wilcox's *k*-ω model is that it can be used to directly predict low-Re effects on the turbulence field in the near-wall regions. These effects are typically predicted through the use of a single layer of specialized near-wall elements. These elements fully contain the viscous sublayers and provide a bridge between the wall and the fully turbulent flow regions a short distance from the wall.

The *k*-ω model can be used in conjunction with a fine near-wall mesh to model both the mean flow variables and the turbulence variables down to the wall and resolve

any geometric feature which may be present in the viscous sublayers. For best results the first grid point away from the wall should be in the vicinity of $y^+ \leq 1$.

3.3.2 The RNG *k*-ε Turbulence model

The RNG *k*-ε turbulence model employed in this study is that developed by Yakhot et al. (1992). This model is very similar in form to the standard and extended *k*-ε turbulence models. Like the extended *k*-ε turbulence model, the RNG *k*-ε turbulence model employs an additional source/sink term in the ε equation and employs different values for the various model coefficients. The form of the *k* and ε equations of the RNG *k*-ε model is as follows:

$$\rho\frac{\partial k}{\partial t}+\rho u_j\frac{\partial k}{\partial x_j} = \frac{\partial}{\partial x_j}\left[\left(\mu+\frac{\mu_t}{\sigma_k}\right)\frac{\partial k}{\partial x_j}\right]+G-\rho\varepsilon \tag{3.34}$$

$$\rho\frac{\partial \varepsilon}{\partial t}+\rho u_j\frac{\partial \varepsilon}{\partial x_j} = \frac{\partial}{\partial x_j}\left[\left(\mu+\frac{\mu_t}{\sigma_\varepsilon}\right)\frac{\partial \varepsilon}{\partial x_j}\right] +c_1\frac{\varepsilon}{k}G-\frac{c_\mu\eta^3(1-\eta/\eta_0)}{1+\beta\eta^3}\frac{\varepsilon^2}{k}-c_2\rho\frac{\varepsilon^2}{k} \tag{3.35}$$

3.4 Computational Aspects and Solution Procedure

3.4.1 Flow Geometry

The flow geometry used in the computations is shown in Figure 3.4. Although at the domain inlet, initial profiles corresponding to the fully developed turbulent pipe flow for all the variables (i.e., U, k, and ε) were inserted, a significant upstream length was also included. The reason was to eliminate errors resulting from the interpolation of these profiles to the grid arrangement used in the solution. Finally, the length from the suction outlet to the domain outlet was proven long enough to allow a fully developed state to be reached again (i.e., uniform streamwise pressure gradient across the pipe radius). This was neccessary for convenient boundary conditions to be imposed at the domain outlet.

3.4.2 Initial profiles

As was mentioned in the previous section, at the domain inlet, initial profiles corresponding to the fully developed turbulent pipe flow for all the variables (i.e., U, k, and ε) were inserted. These fully developed profiles were taken from the solution of the developing turbulent pipe flow with no suction with uniform profiles at the domain inlet. The procedure was that constant values (uniform profiles) for all the variables (i.e., U, k, and ε) were inserted at the domain inlet and development of the profiles from uniform to fully developed were observed along the axial pipe. Profiles for all variables were then taken from fully developed portion of the pipe and were inserted as the initial profiles at the domain inlet.

The measure of flow development used in this study was Sovran and Klop's (1967) blockage factor which is defined by the ratio of the axisymmetric displacement thickness δ_{lax} to pipe radius R or of the ratio of the centerline velocity U_c to the spatial mean velocity U (the bulk velocity)

$$B = \frac{2\delta_{lax}}{R} = 1 - \frac{U}{U_c} \tag{3.36}$$

where

$$\frac{\delta_{lax}}{R} = \int_0^1 \left(1 - \frac{U}{U_c}\right) \frac{r}{R} d\left(\frac{r}{R}\right) \tag{3.37}$$

Some researchers used a two-dimensionally defined displacement thickness

$$\frac{\delta_{lnwo}}{R} = \int_0^1 \left(1 - \frac{U}{U_c}\right) d\left(\frac{r}{R}\right) \tag{3.38}$$

In these cases the blockage factor was calculated from

$$B = \frac{2\delta_{lnwo}}{R} - \left(\frac{2\delta_{lnwo}}{R}\right)^2 \tag{3.39}$$

Based on experiments conducted by Pozzorini (1976), and Klein (1981) concluded that determination of the blockage from U/U_c (where U is derived from the flow rate) will generally be more accurate than from δ_{lax} /D, especially if the latter is calculated from measurements in a single plane only.

Figure 3.5 indicates the development of the velocity profile with nondimensional distance from inlent domain. One can see that at about 50 diameters from the inlent domain a fully developed flow is obtained. Figure 3.6 shows the axial velocity (U) profile at x/D =50 corresponding to fully developed profile applied as initial profile at the domain inlet. Also Figures 3.7 and 3.8 indicate kinetic (k) and dissipation (ε) profiles

3.4.3 Grid Arrangement

An orthogonal, nonuniform grid of 190×128, in the axial and radial directions respectively, was used to carry out the calculations. The grid was particularly fine at the suction inlet and outlet planes. It employed 51 grid nodes upstream of the suction region, 116 nodes covered the suction region and finally 23 nodes were used downstream up to the domain outlet. Computations with both models and for suction rates up to A= 13 percent proved that y^+ is less than one and therefore the condition involved in the low-Re k-ω model was satisfied. Figure 3.9 indicates the values of y^+ for different suction rates along the suction region. With the above grid arrangement, the results are considered to be grid independent since subsequent calculations with increasing the grid by 20 percent did not produce considerable changes. For the sake of brevity no results are presented from the grid independence checks.

3.4.4 Numerical Methods

The solution algorithms used for solving the nonlinear system of matrix equations arising from the FEM discretization of the flow equations is segregated. In the segregated

solution algorithm the global system matrix is decomposed into smaller sub-matrices each governing the nodal unknowns associated with only one conservation equation (i.e, velocity component, pressure, temperature, etc). These smaller sub-matrices are then solved in a sequential manner using either direct Gaussian elimination or conjugate gradient type schemes.

The other solution algorithms for solving the nonlinear system of matrix is a fully coupled solution approach. The fully coupled solution approach requires the formation of the global system matrix which includes all the unknown degrees of freedom associated with the discretized problem. As the storage required for the individual sub-matrices is considerably less than that needed to store the global system matrix, the storage requirements of the segregated approach are substantially less than that of the fully coupled approach. Due to its sequential and uncoupled nature, the segregated solver requires more iterations than the coupled solvers (this may be as few as three times to as many as ten times). On the other hand, as the size of the problem grows (i.e., the number of mesh points) the storage (hard disk space) required for each full iteration of the segregated approach will be increasingly less than that of the coupled approach. Thus there is potentially a trade off between performing a larger number of less expensive iterations with the segregated solver compared to a smaller number of more expensive iterations with fully coupled solver. In this study the hard disk space available dictated the choice of segregated solution algorithm.

3.4.5 Boundary conditions

The boundary conditions inserted along the boundary geometry are as follows: At the domain inlet profiles of U, k, and ε were inserted. On the wall the no-slip condition was employed for u and v. The appropriate boundary conditions for the low-Re k-ω model at a no-slip wall are:

$$k = 0 \tag{3.40}$$

$$\omega = \frac{6\mu}{c_2 \Delta^2} \tag{3.41}$$

The boundary condition of k is applied at the wall whereas that for ω is applied at the first node above the wall. In equation (3.41) Δ is the height of the first node above the wall and c_2 is a constant equal to 0.8333.

3.5 Analysis of Results

The response of the mean axial and radial velocity, turbulent kinetic energy profiles of the fully established pipe flow to wall suction at stations x/D = 0, 0.503, 1.358 and 2.213 along the suction region are examined. Also the effects of wall suction on these profiles are investigated for different suction rates (A = 0, 1.6, 3.3, 6.5, and 13 percent) at the station x/D = 2.213 where detailed experimental measurements were available. Finally the distribution of the wall shear stress along suction region is examined at different suction rates.

3.5.1 Axial velocity profile

Figures 3.10 through 3.14 show the computed and measured axial velocity profiles at a station half a diameter upstream from the exit plane of the porous-walled section, corresponding to x/D = 2.213 for suction rates A= 0, 1.6, 3.3, 6.5, and 13 percent, respectively. The performance of k-ω and RNG k-ε models in predicting these profiles is also compared in these figures. One can see that in all suction rates the RNG k-ε model shows a flatter profile compared to the k-ω model. The RNG k-ε model underestimates velocities in the central region between r/D =0 and 2.5 and close to wall between r/D =0.42 and 0.49 and overestimates these values between r/D =2.5 and 0.42. Discrepancies between measured and computed values particularly close to the center line between r/D = 0 and 2.5 increase for RNG k-ε model as suction rate increases. Computational results are in close agreement with experimental measurements except for a small region between r/D = 0.4 and 0.48 for k-ω model. Disagreement between measured and computed values in this region increases as suction rate increases.

In order to gain an insight into the effects of the suction rate on the axial velocity profiles, both measured and computed values using k-ω model have been plotted in Figure 3.15 related to A, the percentage of mass extracted. Both measured and computed results indicate that increasing mass extraction leads to a more uniform velocity distribution since the flows at the wall layer are accelerated and central flow is decelerated by the increasing radial velocity component. At the largest two extraction rates investigated, an inflection

was produced in the measured mean velocity profile at $r/D \approx 0.4$. This inflection was not observed in the corresponding computed axial velocity profiles.

Figures 3.16 through 3.19 show the measured and computed U-velocity profiles at four axial stations along suction region corresponding to x/D = 0, 0.503, 1.358 and 2.213, respectively for a suction rate A=4 percent. The resulting mass extraction reduces the Reynolds number through the test section by about 4% from a value of 17,250 in the fully developed flow at entrance plane x/D =0 (Figure 3.16) to 16,550 at the exit plane x/D = 2.2. (Figure 3.19). The experimental data at x/D = 0 are included (empty circle) in figures and hence the development of U-velocity profile along the suction region is clearly shown.

One can see that at all stations the RNG k-ε model shows a flatter profile compared to the k-ω model. It can be seen that the RNG k-ε model fails to provide accurate solutions for axial velocity profiles at all stations, whereas the k-ω model more faithfully matches measured U-velocity profiles. Disagreement between measured and calculated profiles for RNG k-ε increases as the distance from inlet test section increases.

The development of a fully established axial velocity profile along the suction region due to wall suction is shown in Figure 3.20 where measured and calculated axial velocity profiles using the k-ω model at all stations has been plotted. Both measured and calculated results show that the velocity profile becomes flat when compared with that at the suction inlet, exhibiting increased velocities near the pipe wall. The increase of near

wall velocities is clearly shown, especially at x/D = 0.503 due to the non-uniformity of the wall suction imposed in the experiments. Such non-uniformity occurs because of difficulties with the construction of the porous material.

3.5.2 Radial velocity profile

A comparison between experimental and computed radial velocity v at stations x/D = 0.503, 1.358, and 2.213 for a suction rate A = 4 percent is shown in Figures 3.21 through 3.23, respectively. It is evident that in all stations the low-Reynolds-number k-ω model perform significantly better than RNG k-ε model. Both models are very close to each other from r/D=0.47 up to the wall at station x/D = 0.503 close to the inlet suction region but the difference between two models increases as x/D increases and r/D decreases. Figure 3.21 shows that for station x/D = 0.503 the k-ω model more faithfully matches measured radial velocity v. Computed and measured radial velocity profiles at this station differ by less than 8% for the low-Reynolds-number k-ω model,. except that close to the wall, computed radial velocities differ from measured values by 20% for RNG k-ε model. Discrepancies between measured and computed values, particularly close to the wall, increase for both models at stations x/D = 1.358 and 2.213.

Figure 3.24 indicates the developement of flow along the suction region for the suction rate A= 4 percent. From this figure it is evident that, due to the construction of the suction region, the suction velocities are much higher in the entrance region while they relax to a "fully developed" state at about x/D=1.3. The computed radial velocity, v/V_w, due to the "numerical" uniformity of the mass transfer takes the value of one (1.0) at the

wall in all stations and increases in the near-wall accelerating flow region. In this region, due to local continuity, the magnitude of v must increase with increasing distance from the wall. This is clearly observed in the computations, as well as in the experimental results.

3.5.3 Turbulent Kinetic Energy

Figure 3.25 through 3.28 show the computed and measured turbulent kinetic profiles at a station half a diameter from the exit plane of the porous-walled section, corresponding to x/D = 2.213 in suction rates A= 0, 1.6, 3.3, and 6.5 percent, respectively. The performance of low-Re k-ω and RNG k-ε models in predicting these profiles is also compared in these figures. The k profile has a sharp spike near the wall and this feature is closely captured in the computations by RNG k-ε model for fully developed turbulent flow (A = 0). Although the low-Re k-ω model fails to predict the peak value of k near the wall the computed k profile differs from measured profile by less than 15% over 80% of the pipe. For pipe flow the standard k-ω model underestimates the sharp peak in turbulence kinetic energy by 25% (Wilcox,1993).The sharp peak in turbulence kinetic energy profile is underestimated by 20% by low-Re k-ω model (Figure 3.25).

A review of the Figures 3.25 through 3.28 shows that at a particular station increasing the wall suction results in decreasing the near-wall turbulent kinetic energy as it is indicated by both the experimental and computed results. For fully developed turbulent pipe flow A = 0 (Figure 3.25) the maximum value of k/U_τ^2 is approximately 4.5, equal to that observed in fully developed pipe flow (Laufer, 1954) while at the suction rates A =1.6. 3.3 and 6.5 percent this value decreases to 4.3, 4.0, and 3.6, respectively.

Figures 3.29 through 3.32 show the development of the turbulent kinetic profile for a suction rate A= 4 percent along the suction region. From these figures it is evident that the near-wall turbulent kinetic energy decreases along the suction region as it is indicated by both the experimental and computed results. Upstream of the suction region $x/D = 0$ the maximum value of k/U_τ^2 is approximately 4.5, equal to that observed in fully developed pipe flow (Laufer, 1954) while at the downstream station x/D=2.213 the maximum value is reduced down to 3.5 (Figure 3.32). For all stations the predictions of the low-Re k-ω model are higher than measured by 20% and that of the RNG k-ε model are lower than measured by 25% from $r/D = 0$ up to the $r/D = 0.4$. However, both models, together with the experimental data, indicate that the effects of suction propagate from the wall to the internal flow and penetrate up to approximately r/D =0.3 at the last station. The absolute reduced levels of turbulent kinetic energy at the suction region indicate that for a considerably long suction region flow laminarization is expected to take place.

3.5.4 Wall Shear Stress

The effects of the wall suction on the wall shear stress, τ_w , are shown in Figures 3.33 through 3.36 for suction rates A= 1.6, 3.3, 6.5, and 13 percent, resectively. Since no measurements are available for wall shear stress with wall suction the computed values are compared to empirical values derived from a simple relation, based on the work of Silver and Wallis (1965) and analytical results of Kinney and Sparrow (1970).

From Figures 3.33 through 3.36 one can see that the difference between predicted values by low-Re k-ω model and RNG k-ε model is significant for all suction rates. Also the increase in wall shear stress is significant even for the smallest suction rate (approximately 30 percent for low-Re k-ω model and 13 percent for RNG k-ε model). For A=13 percent such an increase is much higher and the excess wall shear stress resulting from suction is found to be 3.6 times (low-Re k-ω model) and 2.4 times (RNG k-ε model) the respective one with no suction. In all figures the analytical values of τ_w (Kinney and Sparrow (1970)), are included at the location of the "fully developed" flow. It is shown that for the low suction rate (Figure 3-33) analytical and computed results indicate similar levels of increased τ_w. However, for the high suction rate the analytical results tend to underestimate the computed values. The discrepancy between analytical and computed results in high suction rates demonstrates that owing to the significant axial gradient at high suction rates the boundary layer assumptions made in the analysis are not valid. Such behaviour has also been reported in similar studies of open channels with high suction rates (MacLean, 1991). In the same figures, empirical values derived from a simple relation, based on the work of Silver and Wallis (1965), are presented which indicate a similar increase with that observed in the analytical solution. This is due to the same assumptions involved in both methods for calculating τ_w.

3.5.5 Friction factor

The variation of the friction factor with the relative function velocity, V_w / U, is shown in Figure 3.37. The ordinate variable is the ratio f_0 / f, where f_0 is the friction factor for the case of zero suction, while f includes the effects of suction. The departure of the

curves from unity is a direct measure of the effect of suction. The figure shows that the higher the suction velocity, the greater shear force on the bounding surface in the presence of suction than when suction is absent.

The results of analytical solution [Kinney and Sparrow (1970)] are included in Figure 3.37 for the sake of comparison, since no measurements are available for a friction factor in the presence of suction. From Figure 3.37 it is evident that the RNG k-ε model tends to overestimate the values of f_0 / f at all relative function velocities compared to RNG k-ε model. The results of analytical solutions [Kinney and Sparrow (1970)] are in close agreement with those of the low-Re k-ω model for low values of the relative function velocities (low values of suction rates). However for high suction rates the analytical values tends to underestimate the computed values. In the same figure empirical values based on the work of Silver and Wallis (1965), are shown which indicate similar decrease in f_0 / f with that observed in the analytical solution . This is due to the same assumptions involved in both methods for calculating f.

3.6 Conclusions

The numerical study of the turbulent pipe flow with wall suction rates ranging from A = 0 to 13 percent, in conjunction with experimental measurements of Schilknecht et al. (1979) and analytical solutions indicates the following:

Wall suction effects on fully developed pipe flow leads to more uniform velocity distribution with increased near-wall velocity values and reduced velocities near the centerline. It seems that low-Re k-ω model used in this study is capable of predicting correctly the flow characteristics observed in the experiment whereas the RNG k-ε model fails to predict most of the flow characteristics.

The experimental and computed near-wall component of radial velocity, v, increases with increasing distance from the wall due to the accelerating fluid layers in the longitudinal direction (v component increases to satisfy local continuity)

The absolute levels of turbulent kinetic energy decrease with increasing suction rate. Wall suction effects are evident up to $r/D=0.3$ in both experimental and computational results.

Wall suction increases the wall shear stress ,τ_w, along the suction region. The increase in τ_w is significant even for the smallest suction rate (up to 30 percent) while such an increase is much higher for A=13% (up to 360%). Analytical results and empirical relationships indicate similar levels of increase for the low suction rates but tend to underestimate τ_w for the higher suction rates, where the boundary layer assumption ceases to be valid. There is close agreement between analytical results and empirical relationships and low-Re k-ω model particularly in low suction rate. However due to significant

differences between the RNG k-ε model, the analytical results and empirical relationship, it seems that RNG k-ε model fails to predict wall shear stress in the presence of wall suction.

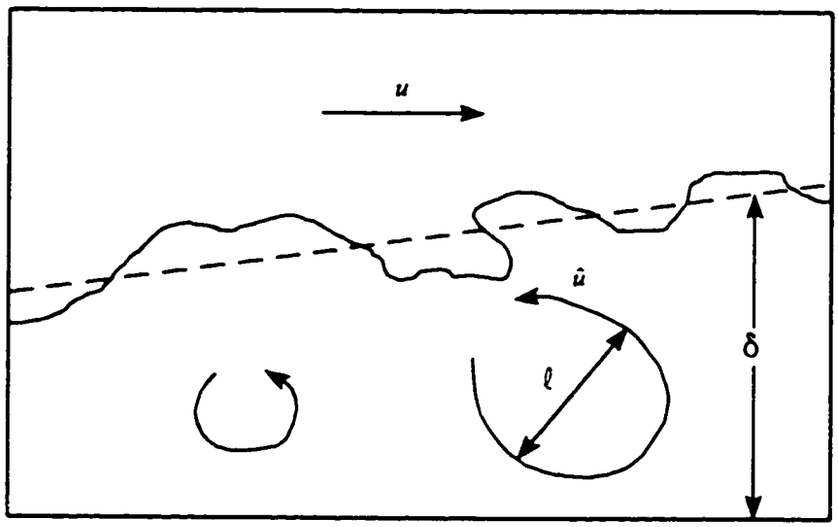

Figure 3.1- Large eddies in a turbulent boundary layer. The flow above the boundary layer has a steady velocity u; the eddies move at randomly-fluctuating velocity of the order of a tenth of u. The largest eddy size ℓ is comparable to the boundary-layer thickness (δ). The interface and the flow above the boundary is quite sharp [Corrsin and Kistler 1954]

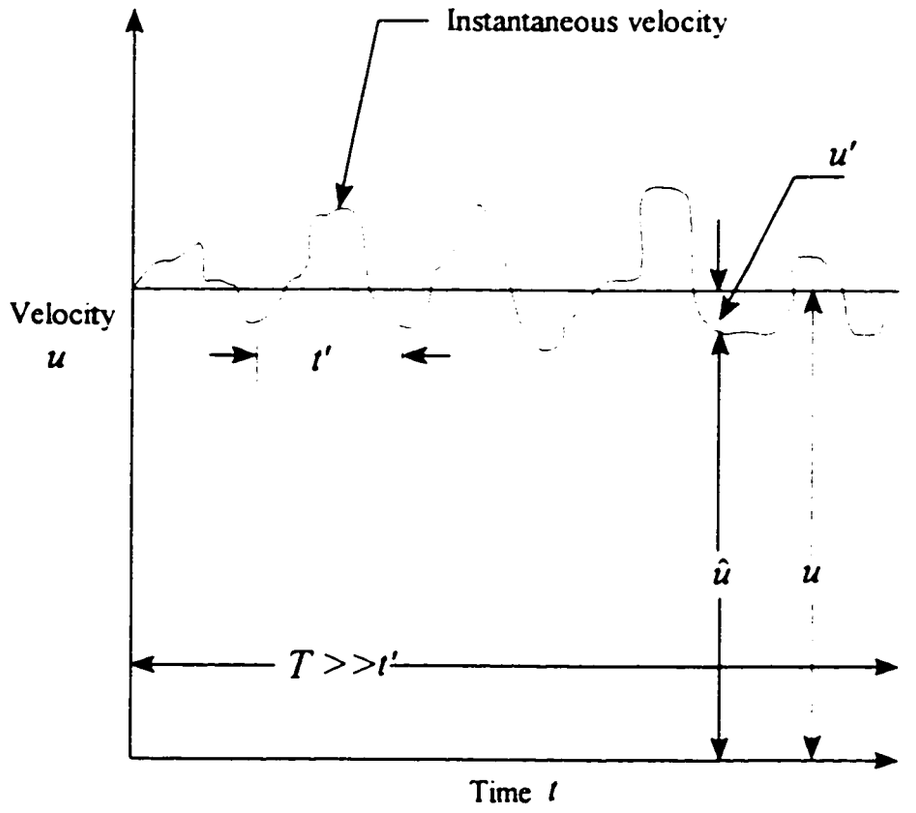

Figure 3.2- Illustration of the definition of time-average velocity in turbulent flow

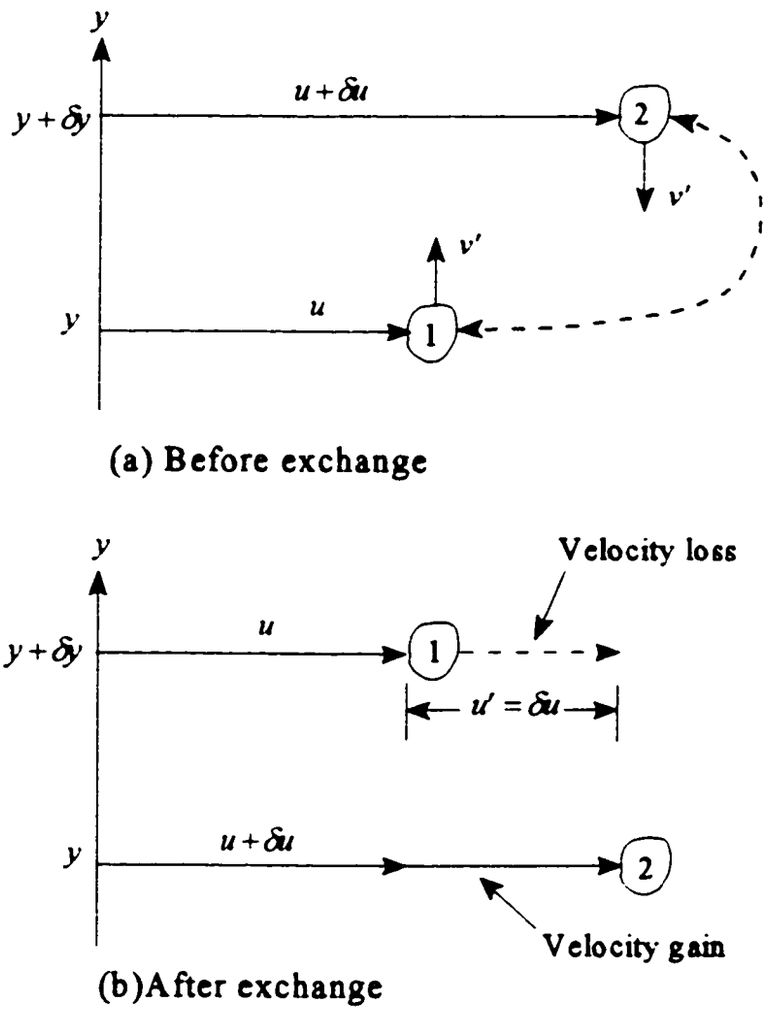

Figure 3.3- Two lumps of fluid with different mean velocities, exchange places in a turbulent flow

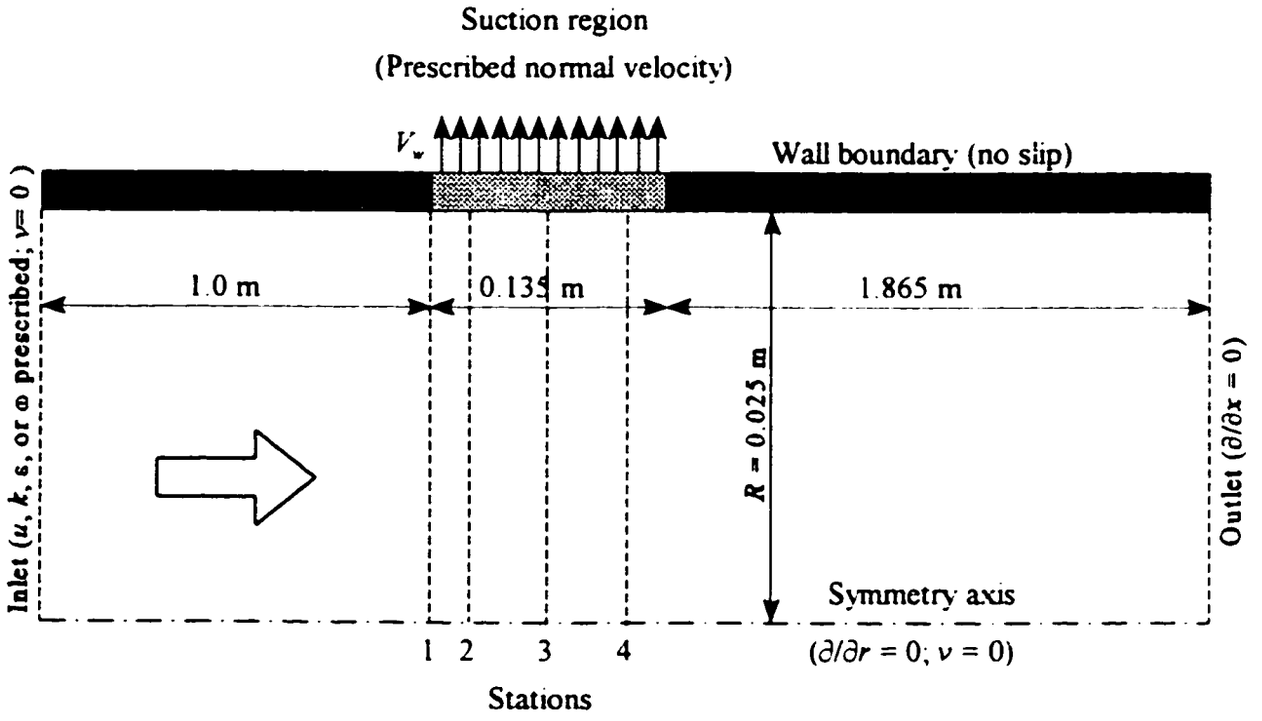

Figure 3.4- Flow geometry and boundary conditions

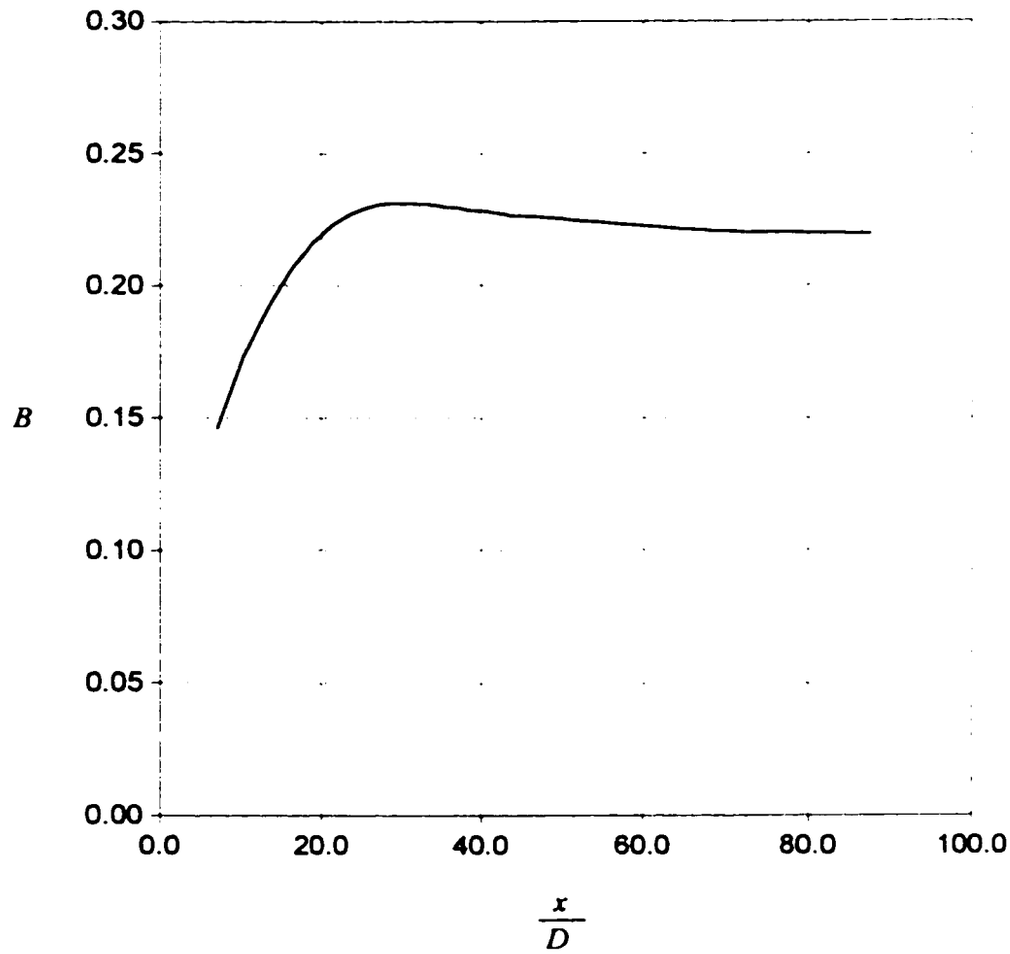

Fig. 3.5- Development of the velocity profile with nondimensional distance from inlet

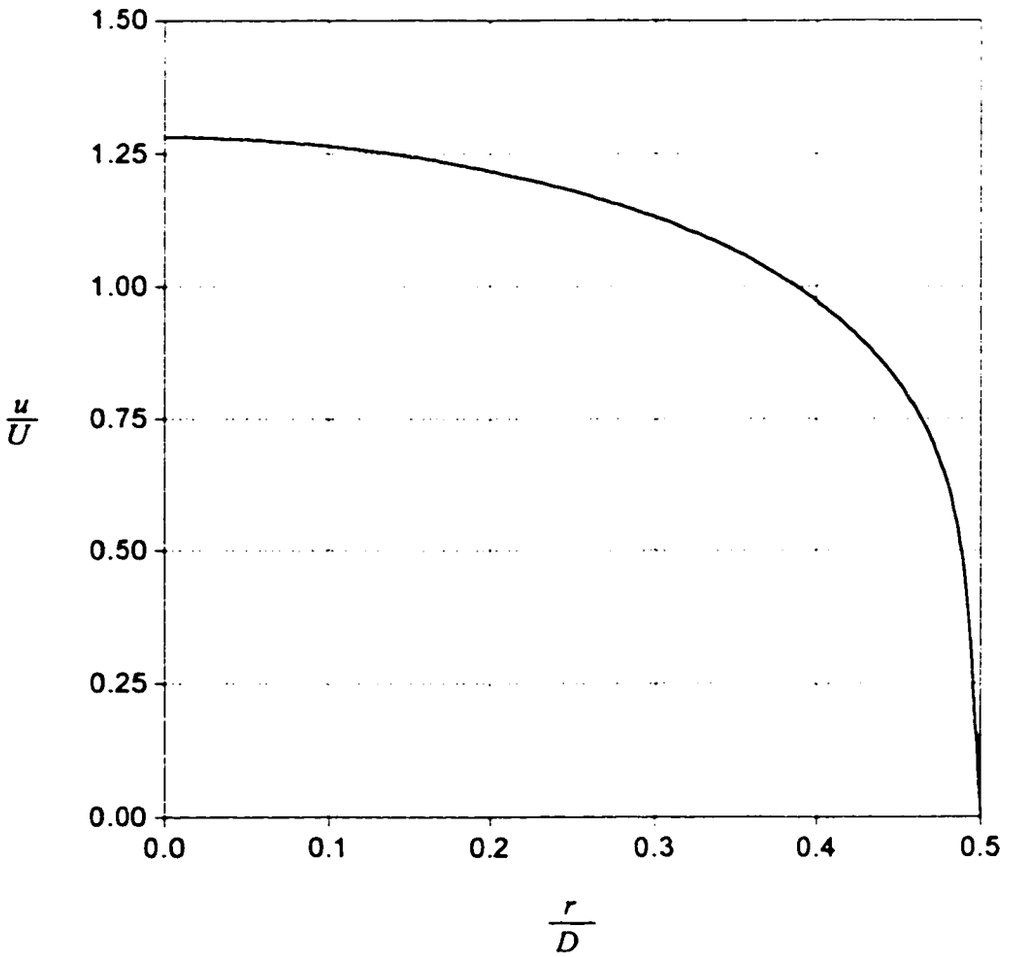

Figure 3.6- Fully developed axial velocity profile applied at the inlet domain

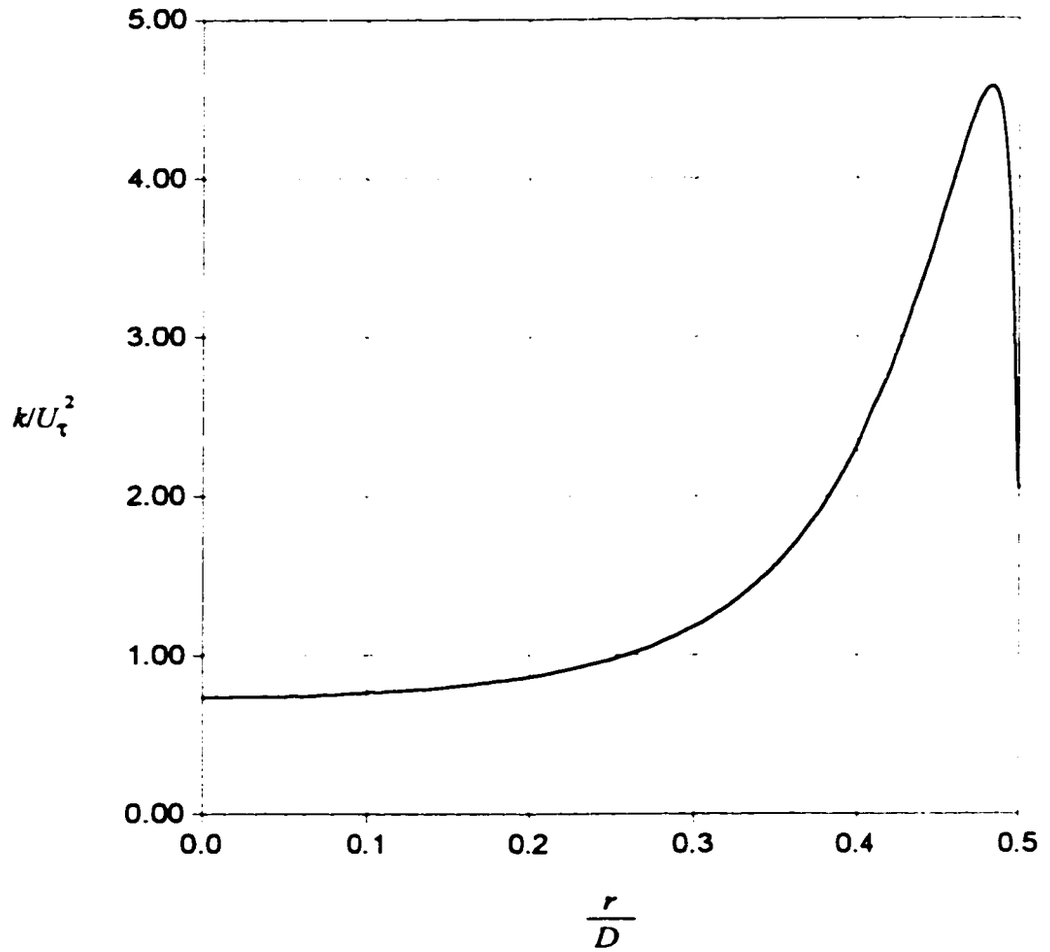

Fig. 3.7- Fully developed turbulent kinetic energy profile, k, applied at the inlet domain

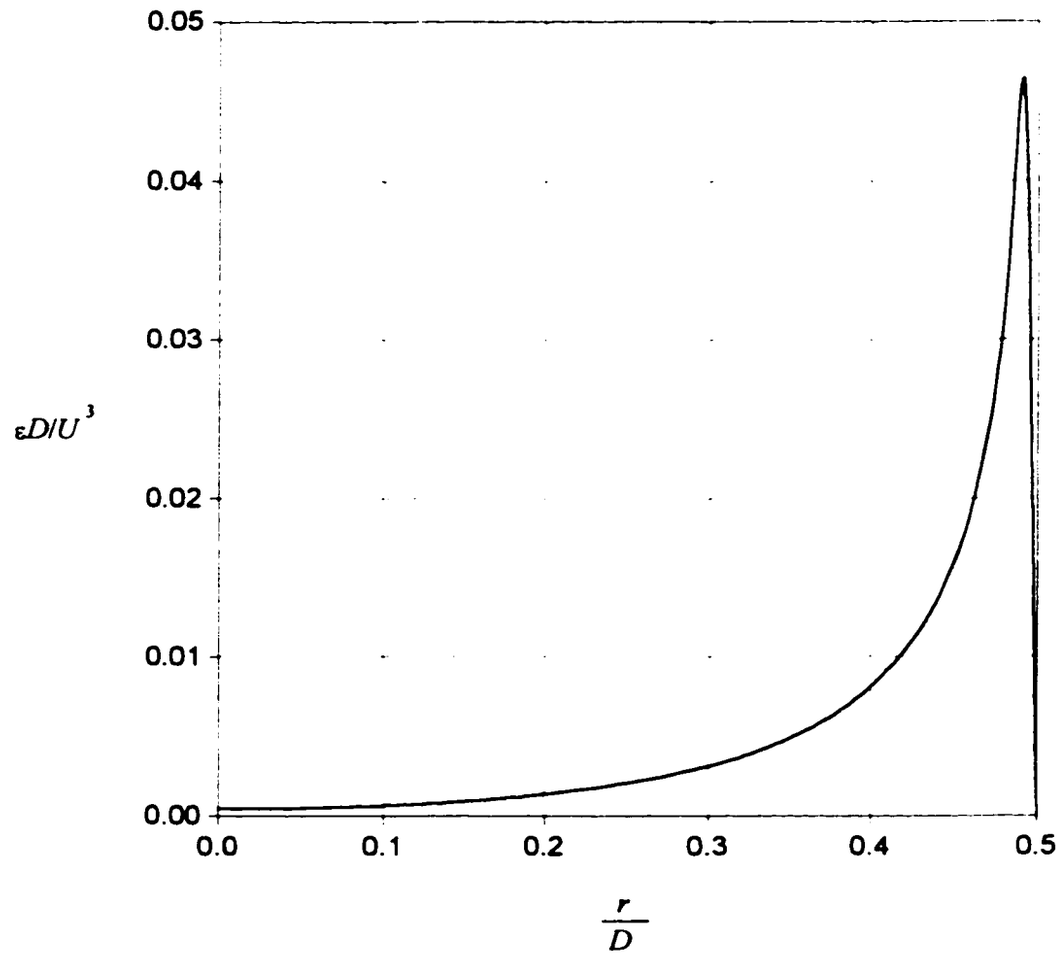

Fig. 3.8- Fully developed dissipation profile applied at the inlet domain

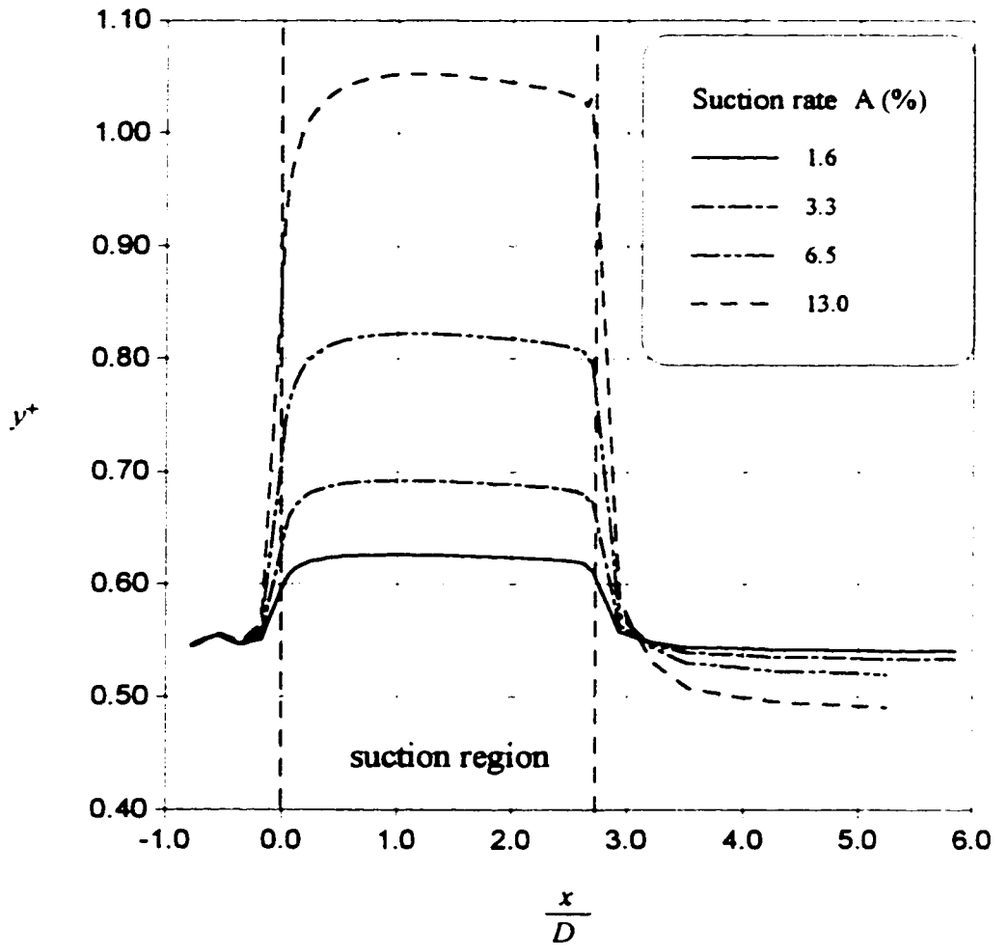

Fig. 3.9- Variation of y^+ along the suction region for different suction rates

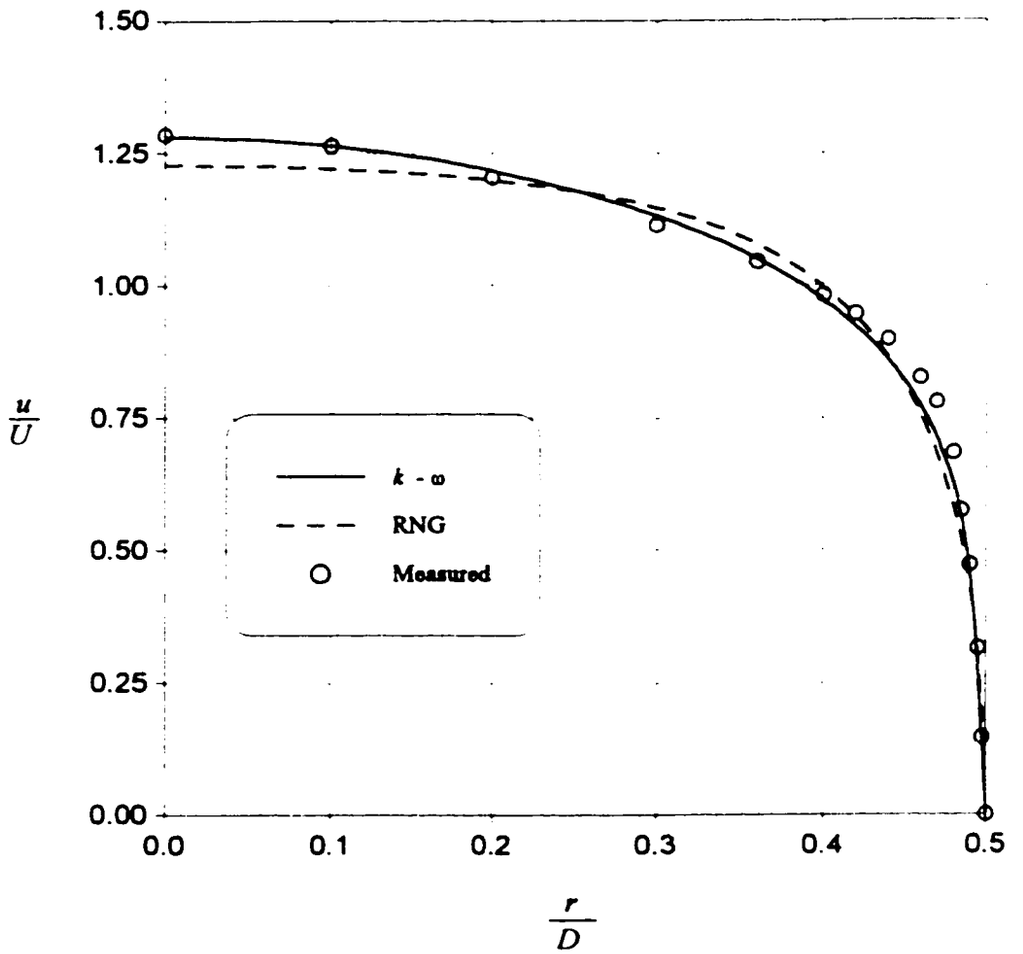

Fig. 3.10- Experimental (Schilknecht et al. 1979) and computed profiles of axial velocity for fully developed pipe flow A = 0 ($V_w = 0$)

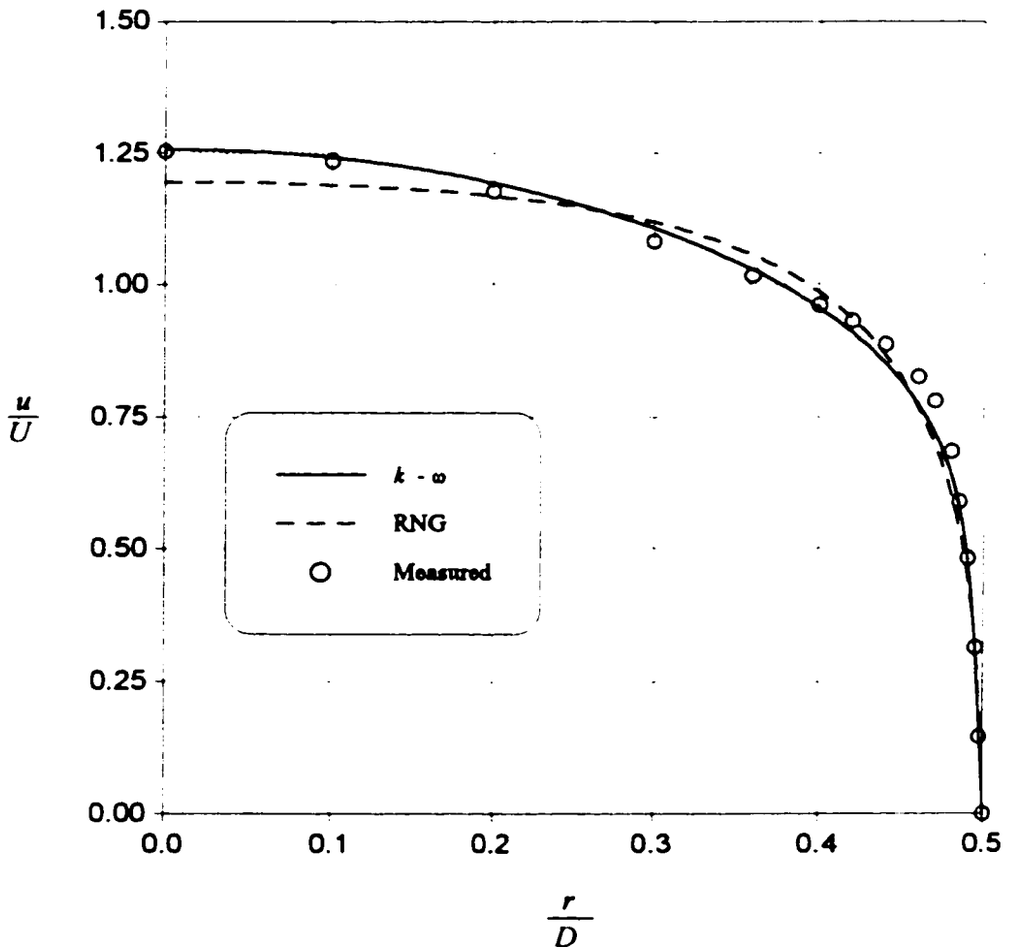

Fig. 3.11- Experimental (Schilknecht et al. 1979) and computed profiles of axial velocity at station x/D=2.212 for A = 1.6% (V_w = 0.732 cm/sec)

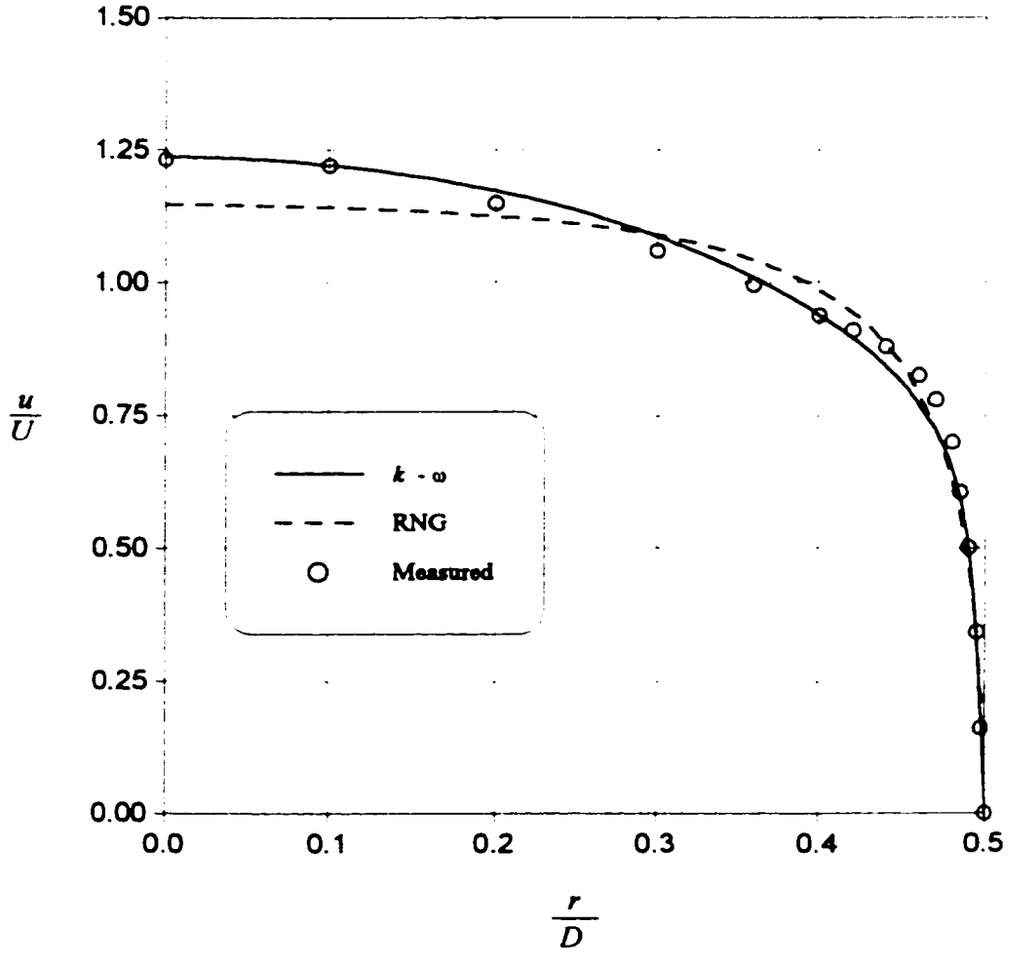

Fig. 3.12- Experimental (Schilknecht et al. 1979) and computed profiles of axial velocity at station x/D=2.212 for A = 3.3% (V_w = 1.511 cm/sec)

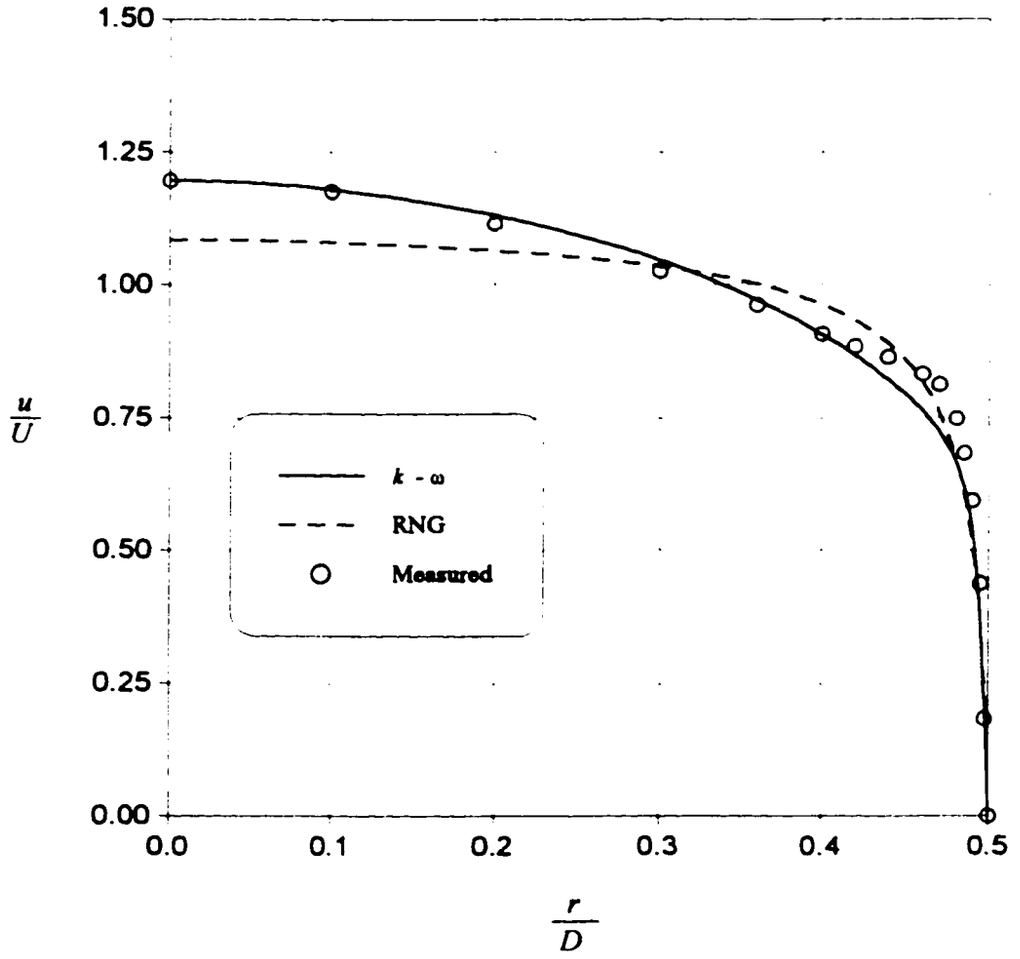

Fig. 3.13- Experimental (Schilknecht et al. 1979) and computed profiles of axial velocity at station x/D=2.212 for A = 6.5% (V_w = 2.977 cm/sec)

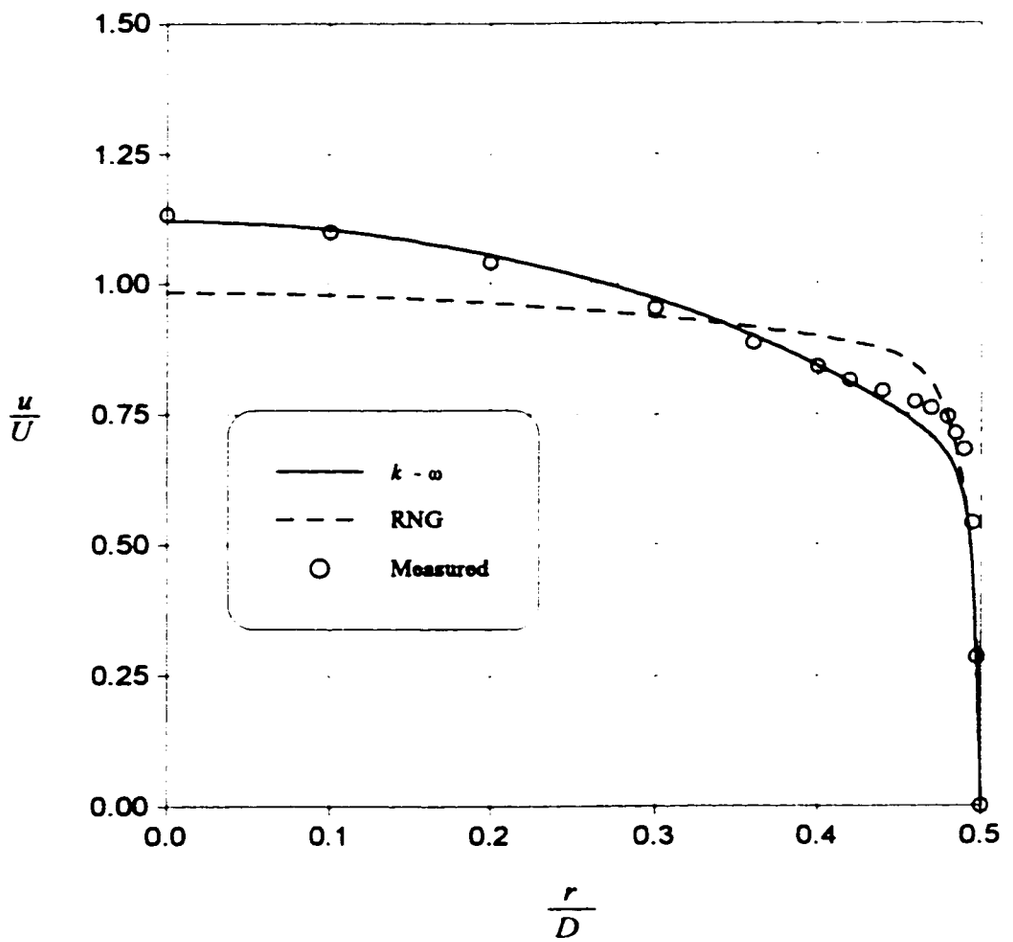

Fig. 3.14- Experimental (Schilknecht et al. 1979) and computed profiles of axial velocity at station x/D=2.212 for A = 13% (V_w =5.954 cm/sec)

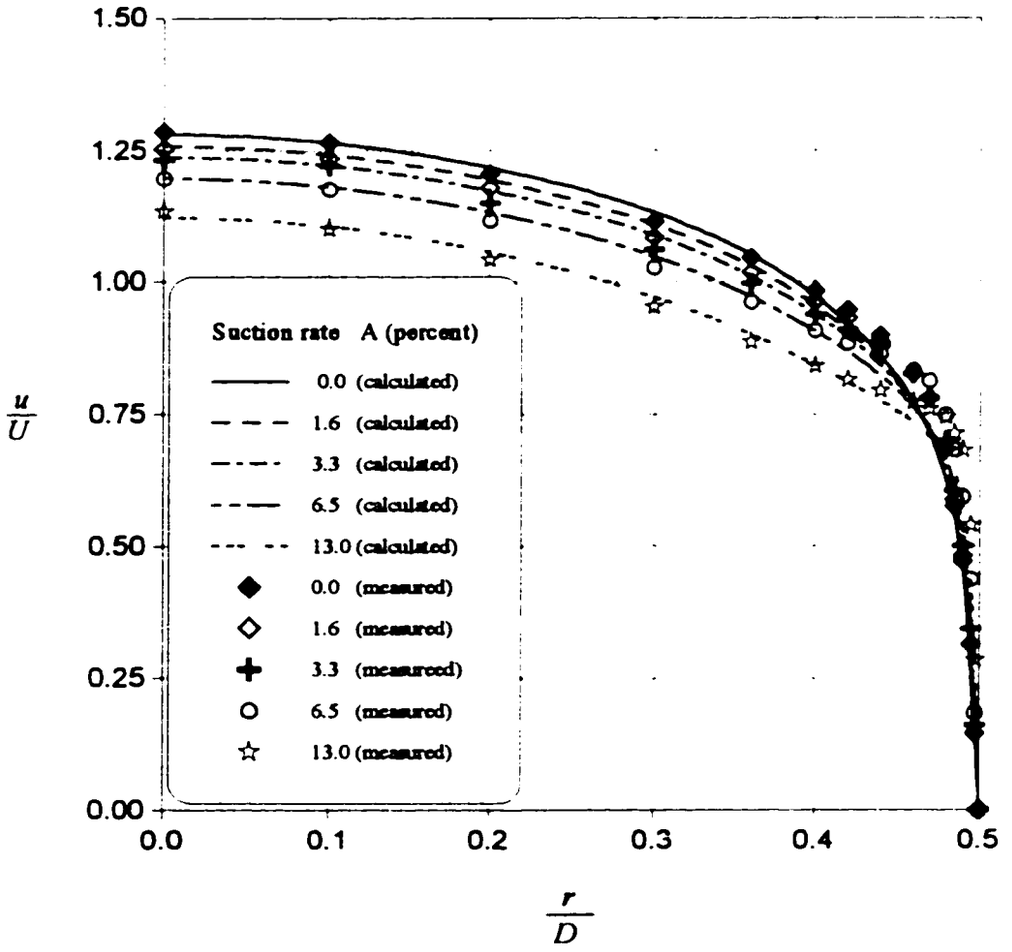

Fig. 3.15- Experimental (Schilknecht et al. 1979) and computed profiles of axial velocity at station x/D=2.212 for different suction rates

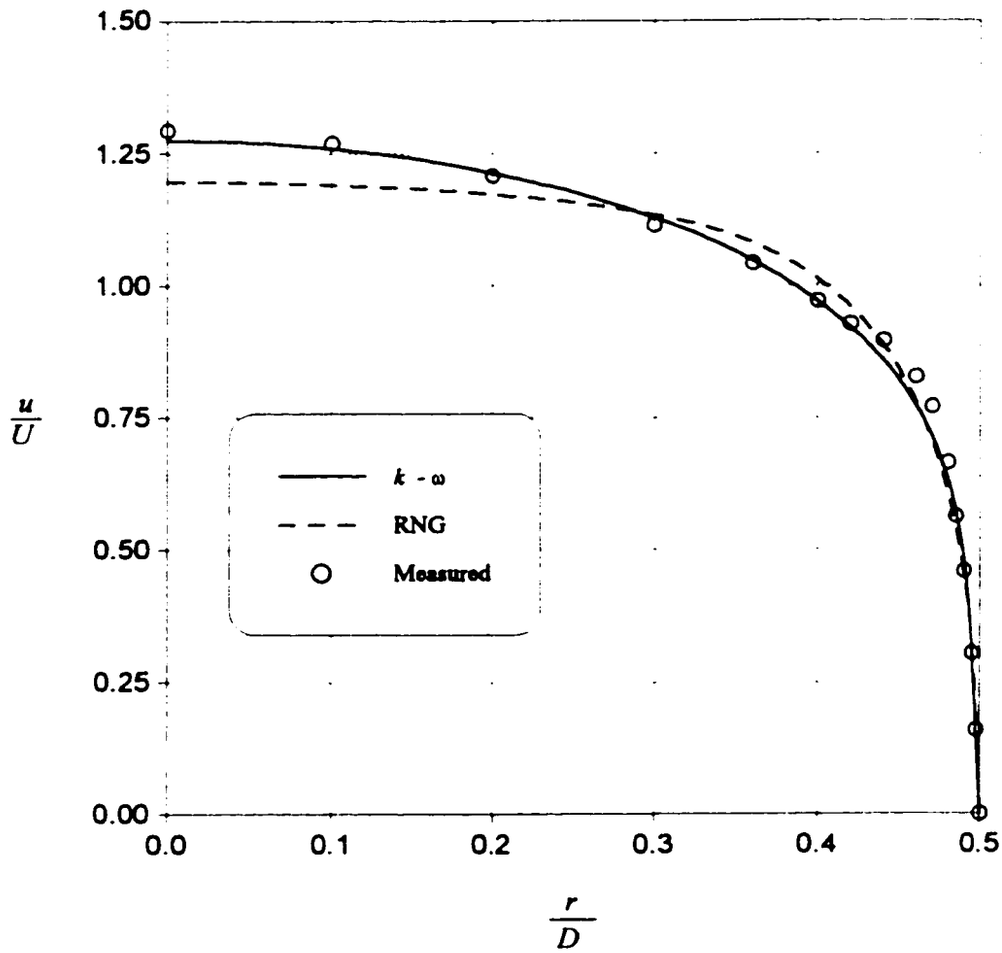

Fig. 3.16- Experimental (Schilknecht et al. 1979) and computed profiles of axial velocity at station $x/D = 0$ for A = 4% ($V_w = 1.832$ cm/sec)

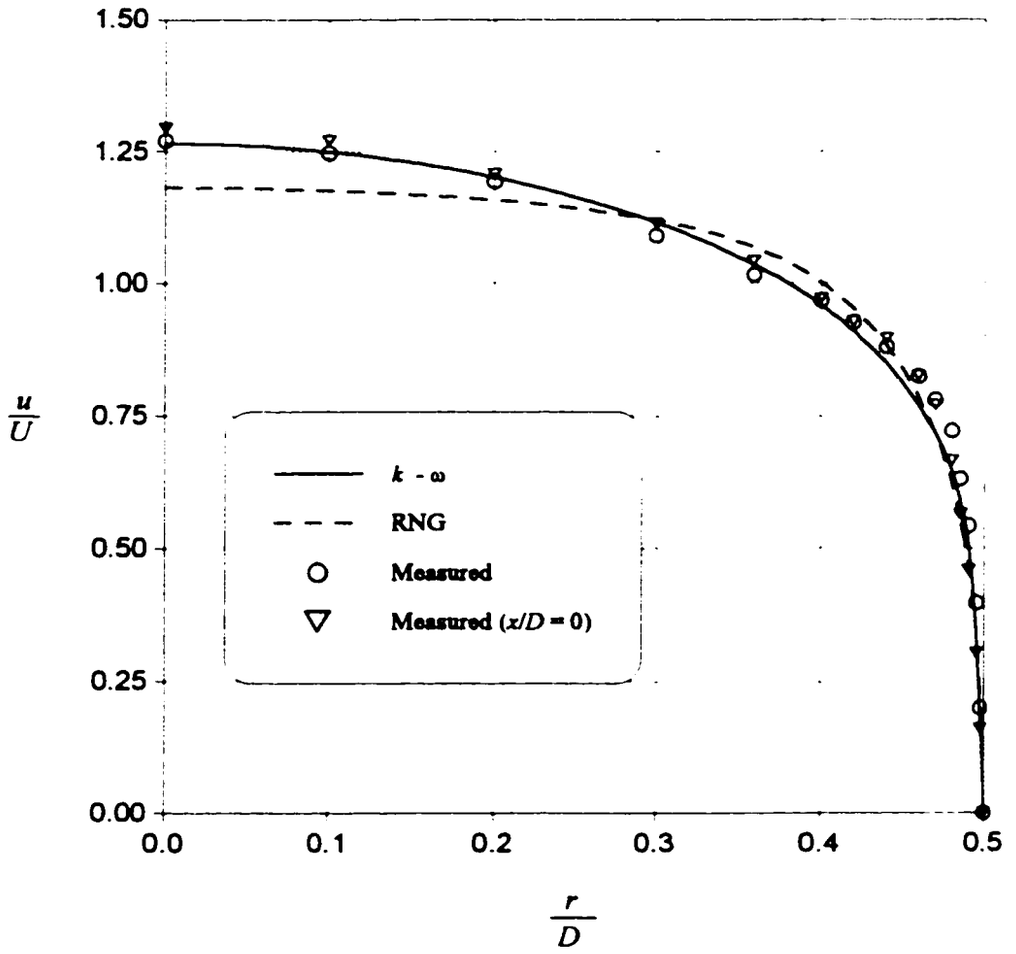

Fig. 3.17- Experimental (Schilknecht et al. 1979) and computed profiles of axial velocity at station $x/D = 0.503$ for A = 4% (V_w = 1.832 cm/sec)

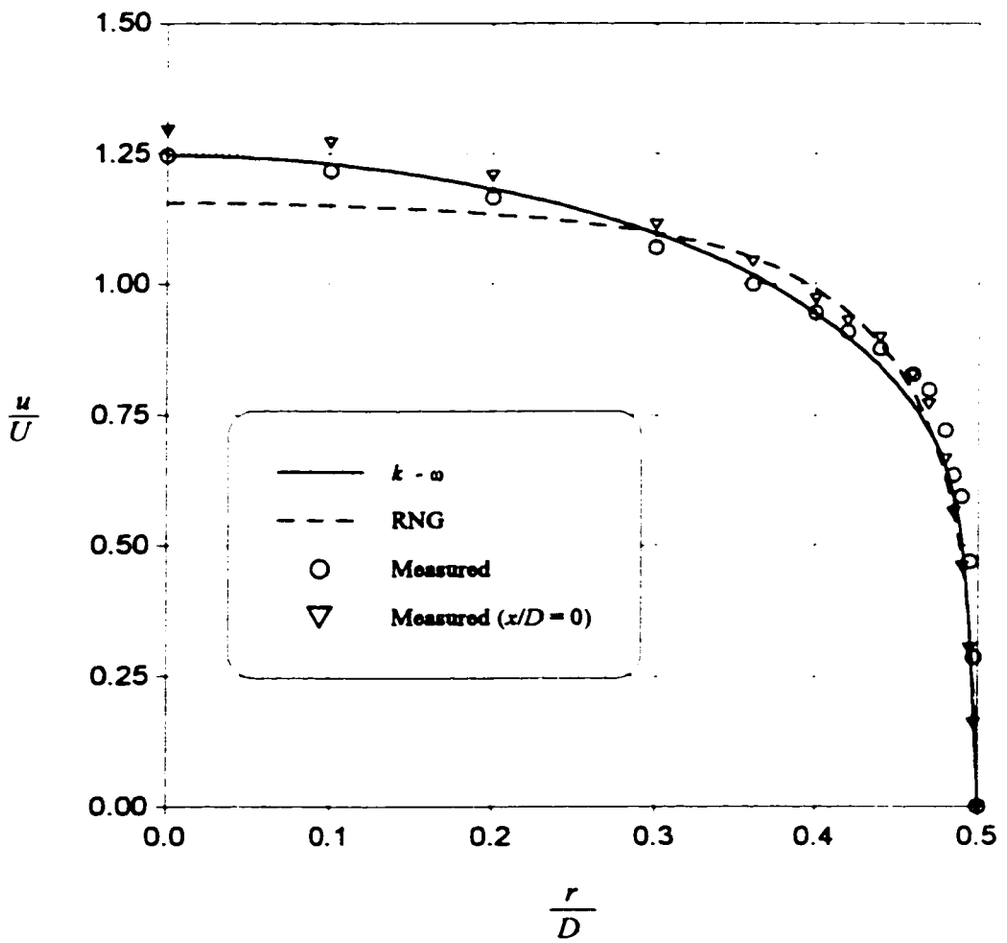

Fig. 3.18- Experimental (Schilknecht et al. 1979) and computed profiles of axial velocity at station $x/D = 1.358$ for A = 4% ($V_w = 1.832$ cm/sec)

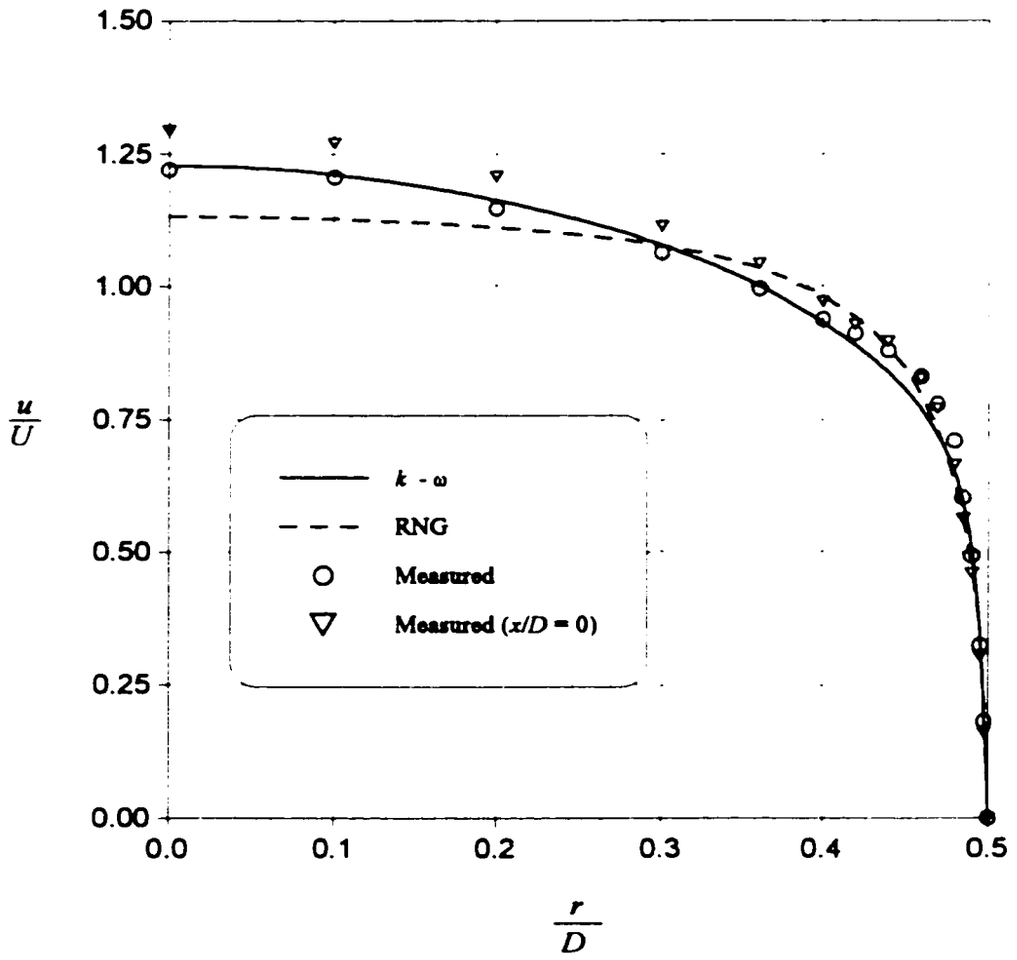

Fig. 3.19- Experimental (Schilknecht et al. 1979) and computed profiles of axial velocity at station $x/D = 2.213$ for A = 4% ($V_w = 1.832$ cm/sec)

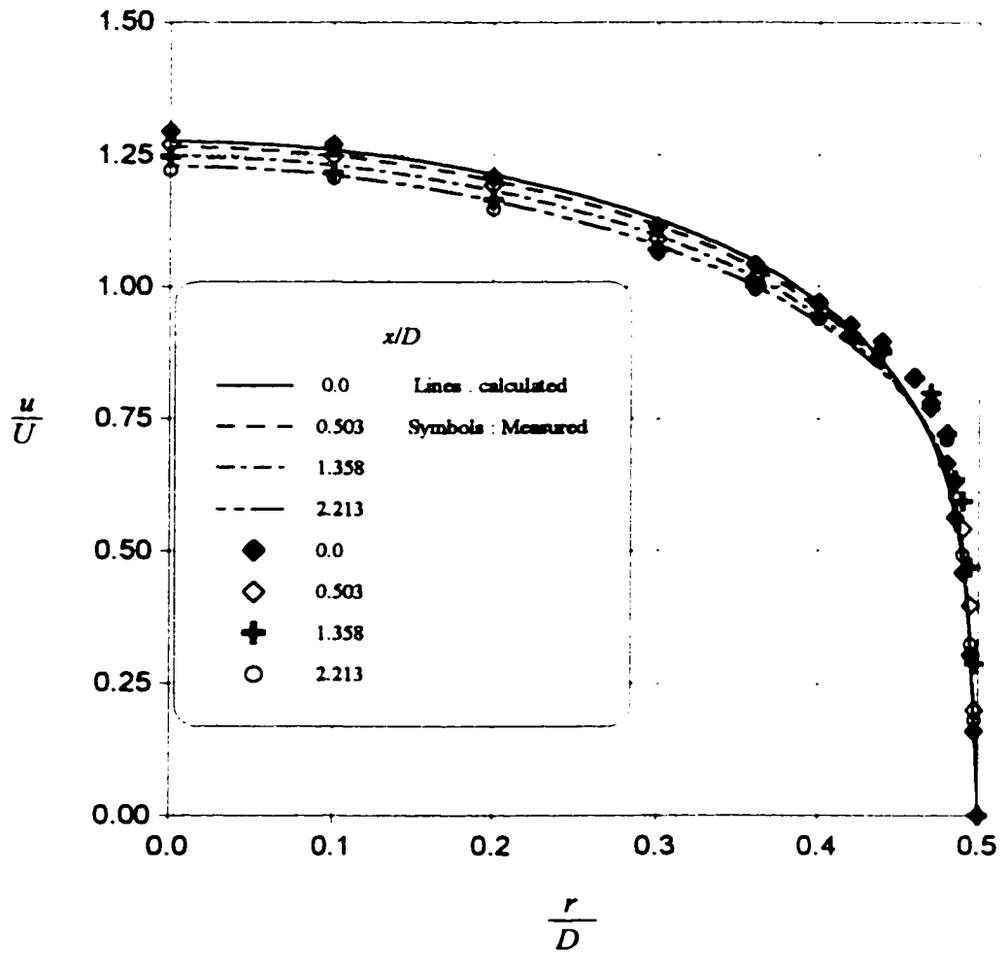

Fig. 3.20- Experimental (Schilknecht et al. 1979) and computed (k-ω model) profiles of axial velocity at different stationas along the suction region

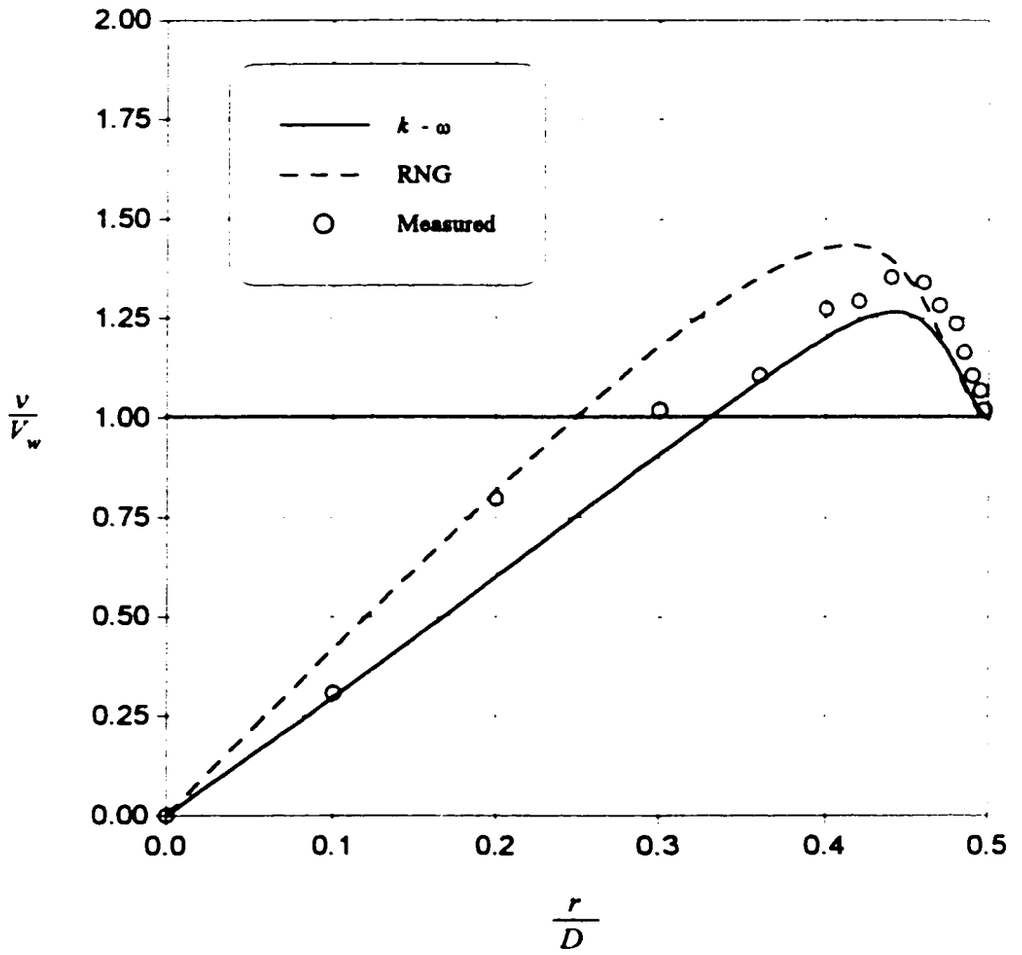

Fig. 3.21- Experimental (Schilknecht et al. 1979) and computed radial velocity distribution at station $x/D = 0.503$ for suction rate A = 4% ($V_w = 1.832$ cm/sec)

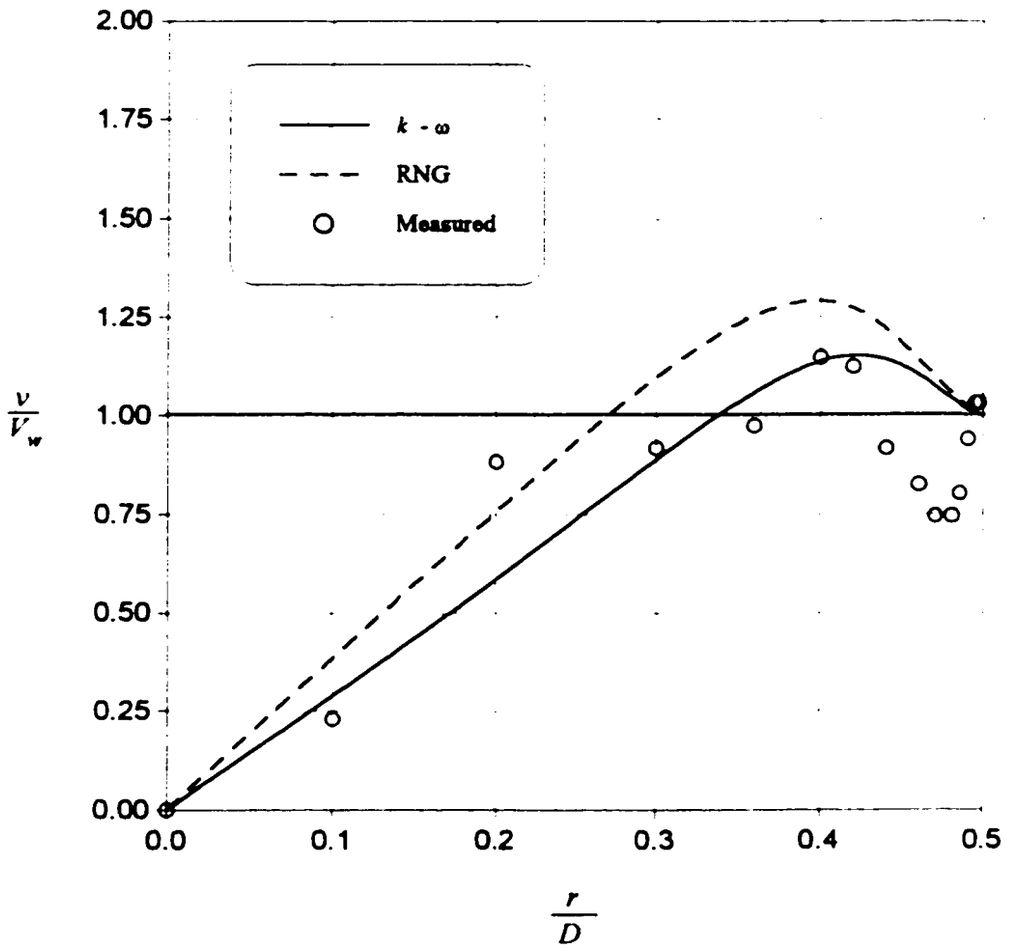

Fig. 3.22- Experimental (Schilknecht et al. 1979) and computed radial velocity distribution at station $x/D = 1.358$ for suction rate A = 4% ($V_w = 1.832$ cm/sec)

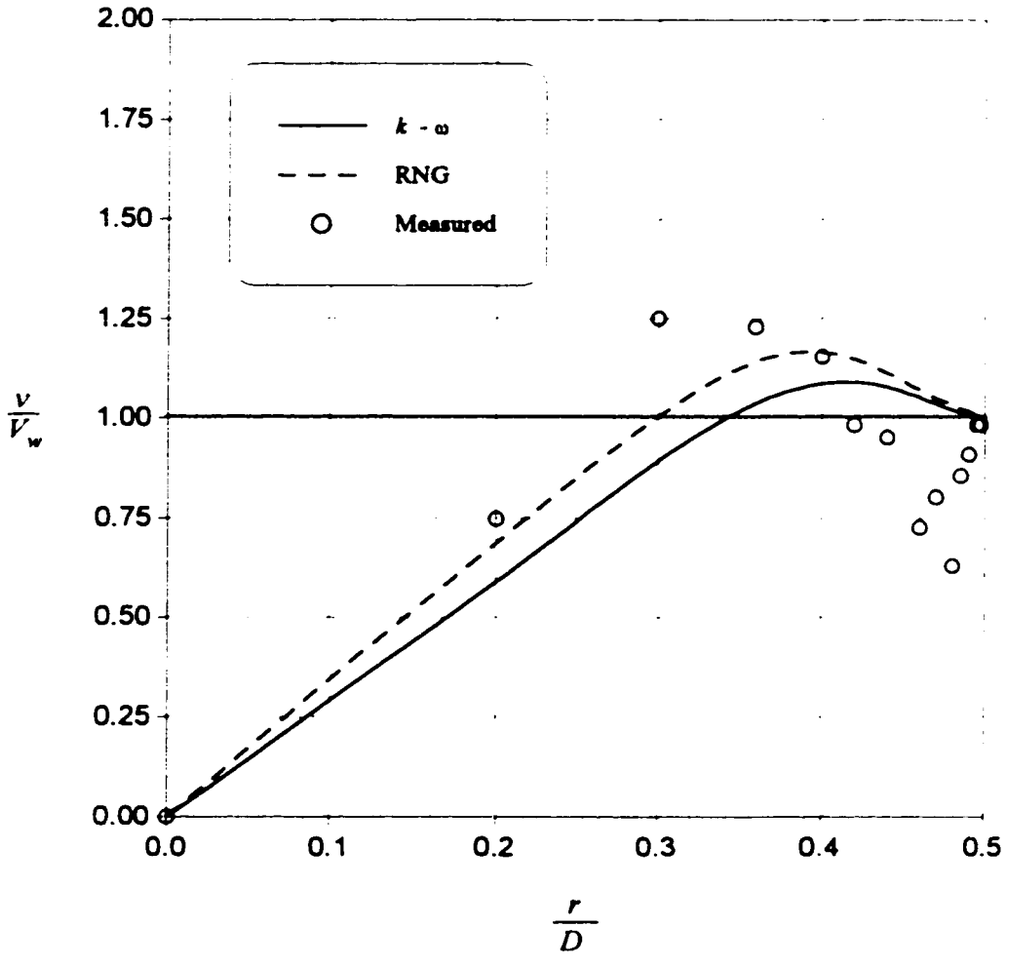

Fig. 3.23- Experimental (Schilknecht et al. 1979) and computed radial velocity distribution at station $x/D = 2.213$ for suction rate A = 4% ($V_w = 1.832$ cm/sec)

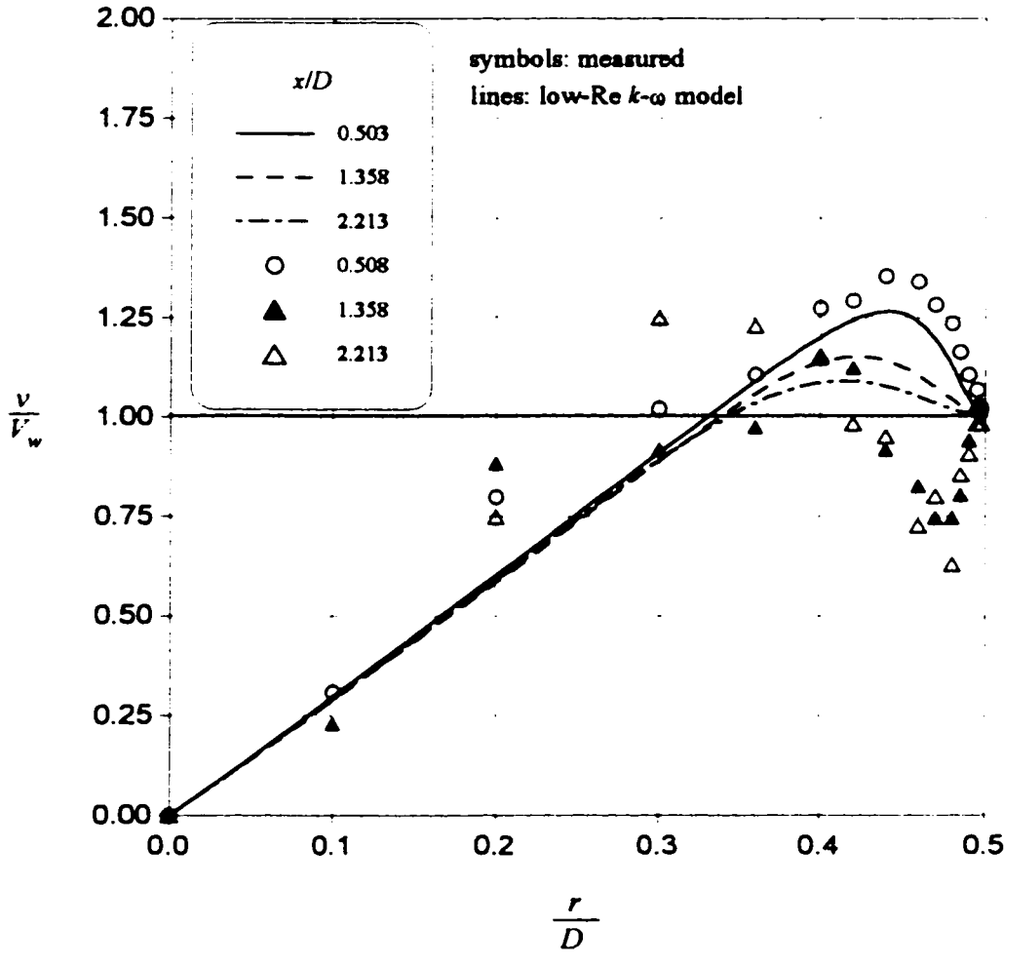

Fig. 3.24- Experimental (Schilknecht et al. 1979) and computed (low-Re k-ω model) radial velocity distribution along the suction region for suction rate A = 4% (V_w = 1.832 cm/sec)

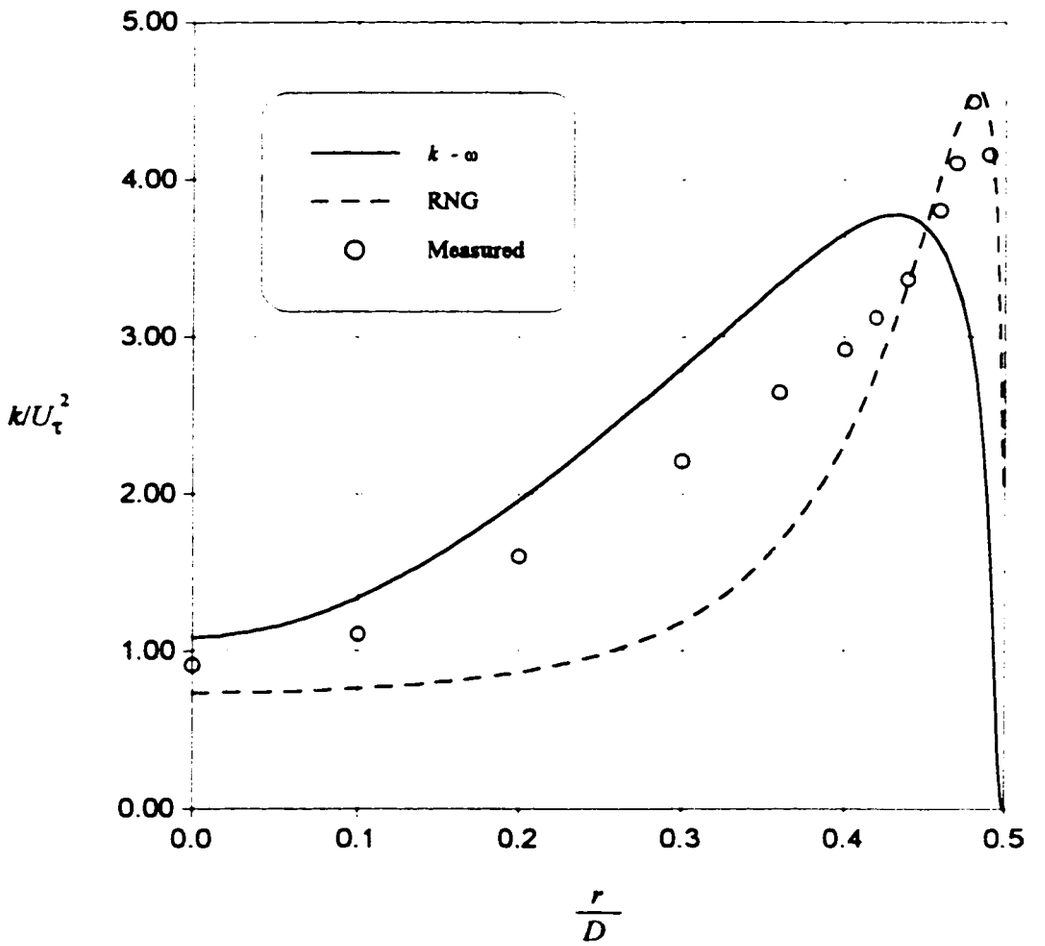

Fig. 3.25- Experimental (Schilknecht et al. 1979) and computed profiles of turbulent kinetic energy, k, at station $x/D = 2.212$ for A = 0 ($V_w = 0$)

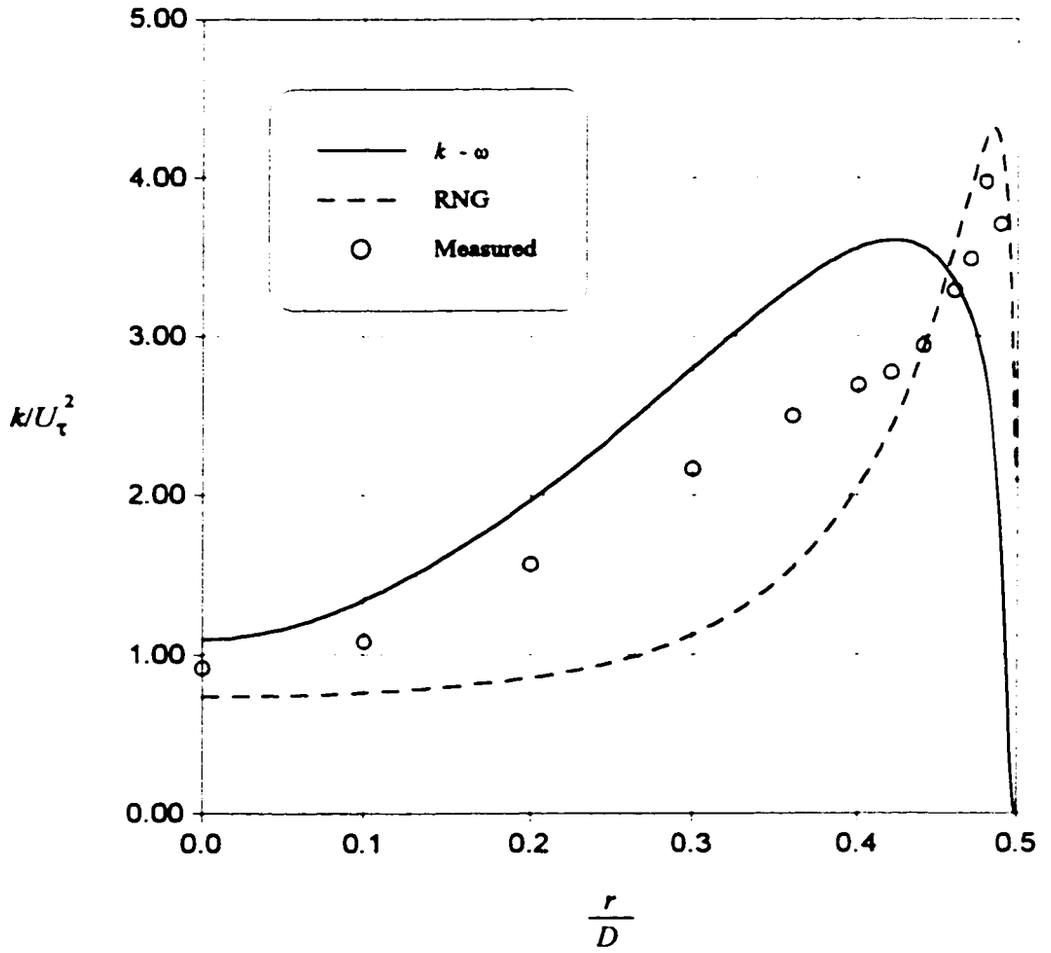

Fig. 3.26- Experimental (Schilknecht et al. 1979) and computed profiles of turbulent kinetic energy, k, at station $x/D = 2.212$ for A = 1.6% ($V_w = 0.792$ cm/sec)

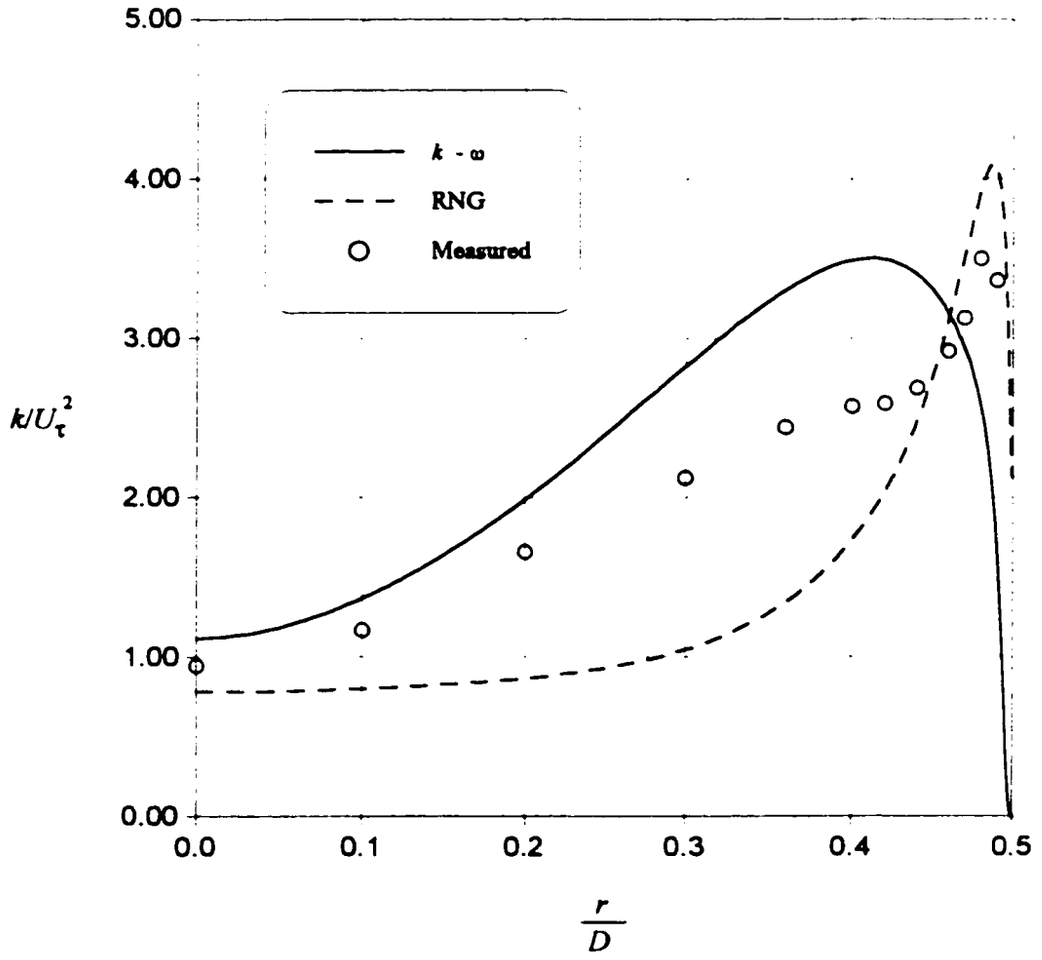

Fig. 3.27- Experimental (Schilknecht et al. 1979) and computed profiles of turbulent kinetic energy, k, at station $x/D = 2.212$ for A = 3.3% (V_w = 1.511 cm/sec)

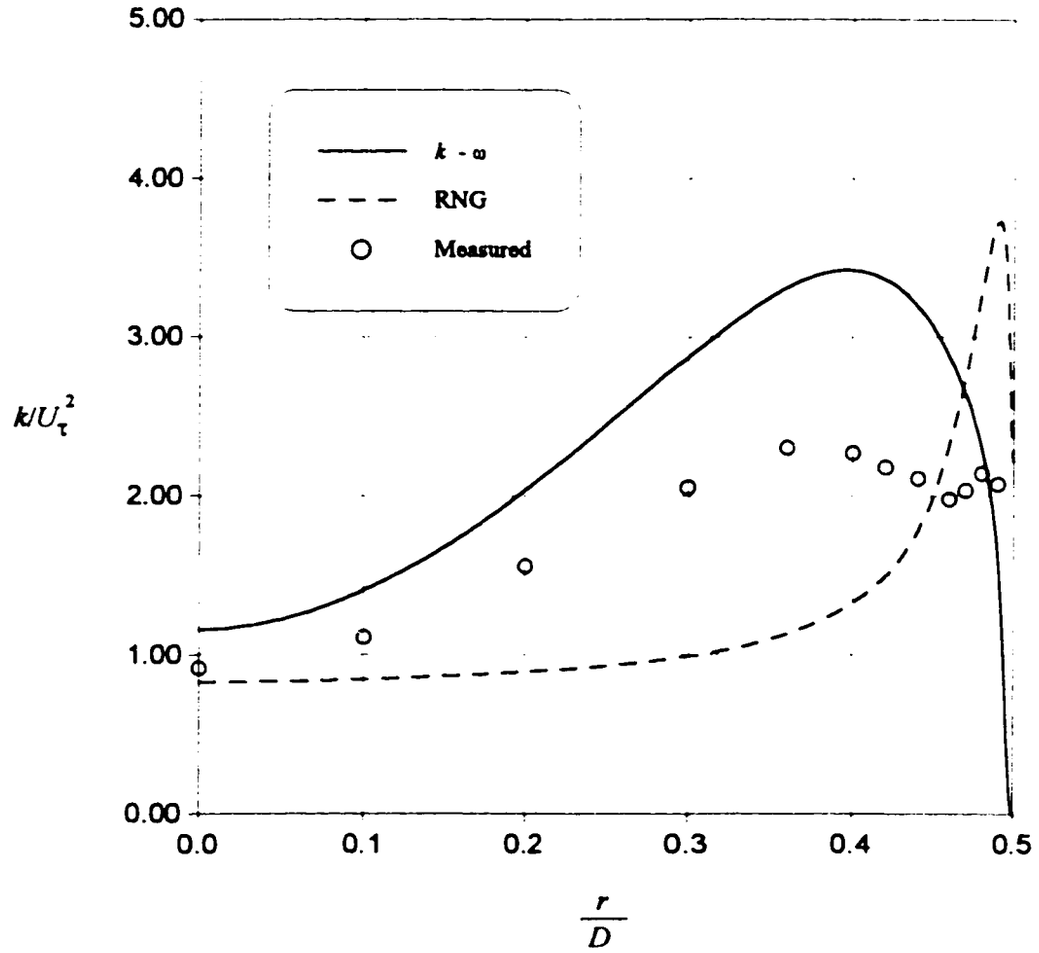

Fig. 3.28- Experimental (Schilknecht et al. 1979) and computed profiles of turbulent kinetic energy, k, at station $x/D = 2.212$ for A = 6.5% ($V_w = 2.977$ cm/sec)

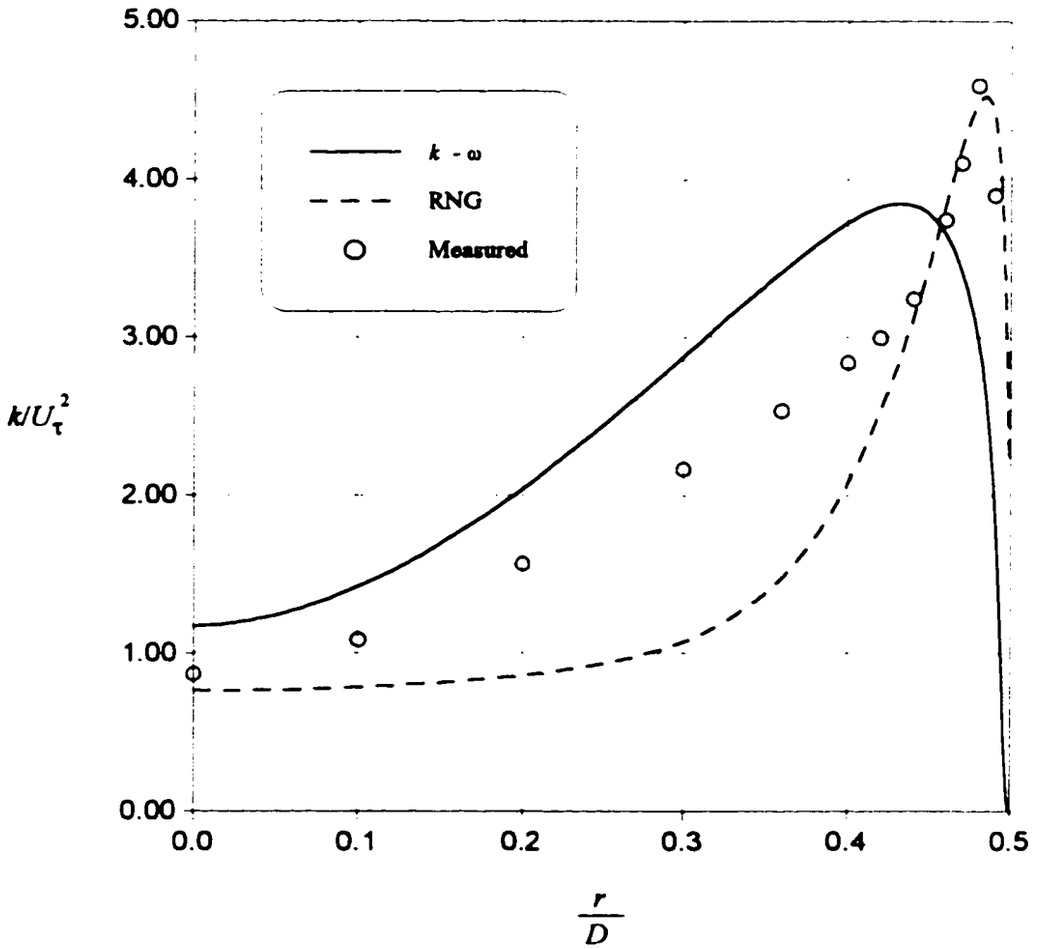

Fig. 3.29- Experimental (Schilknecht et al. 1979) and computed profiles of turbulent kinetic energy, k, at station x/D =0 for A = 4% (V_w = 1.832 cm/sec)

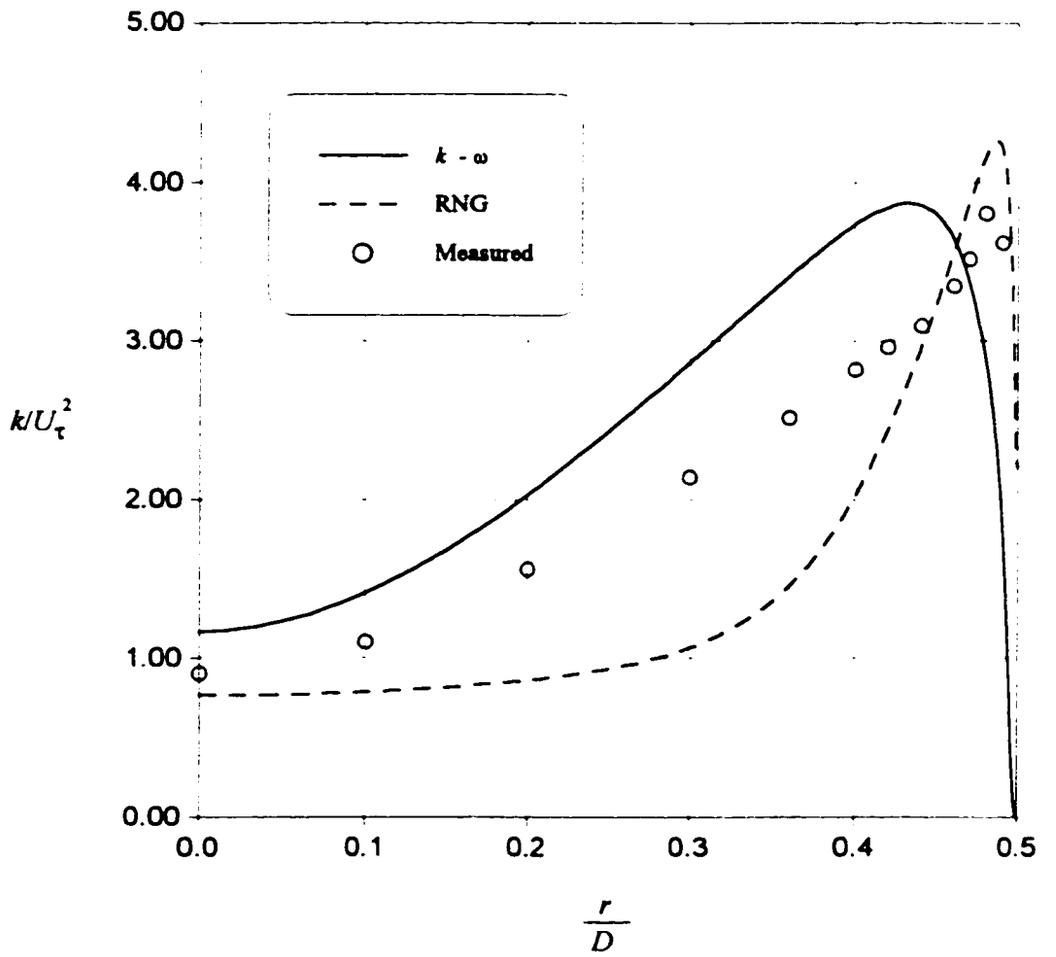

Fig. 3.30- Experimental (Schilknecht et al. 1979) and computed profiles of turbulent kinetic energy, k, at station x/D =0.503 for A = 4% (V_w = 1.832 cm/sec)

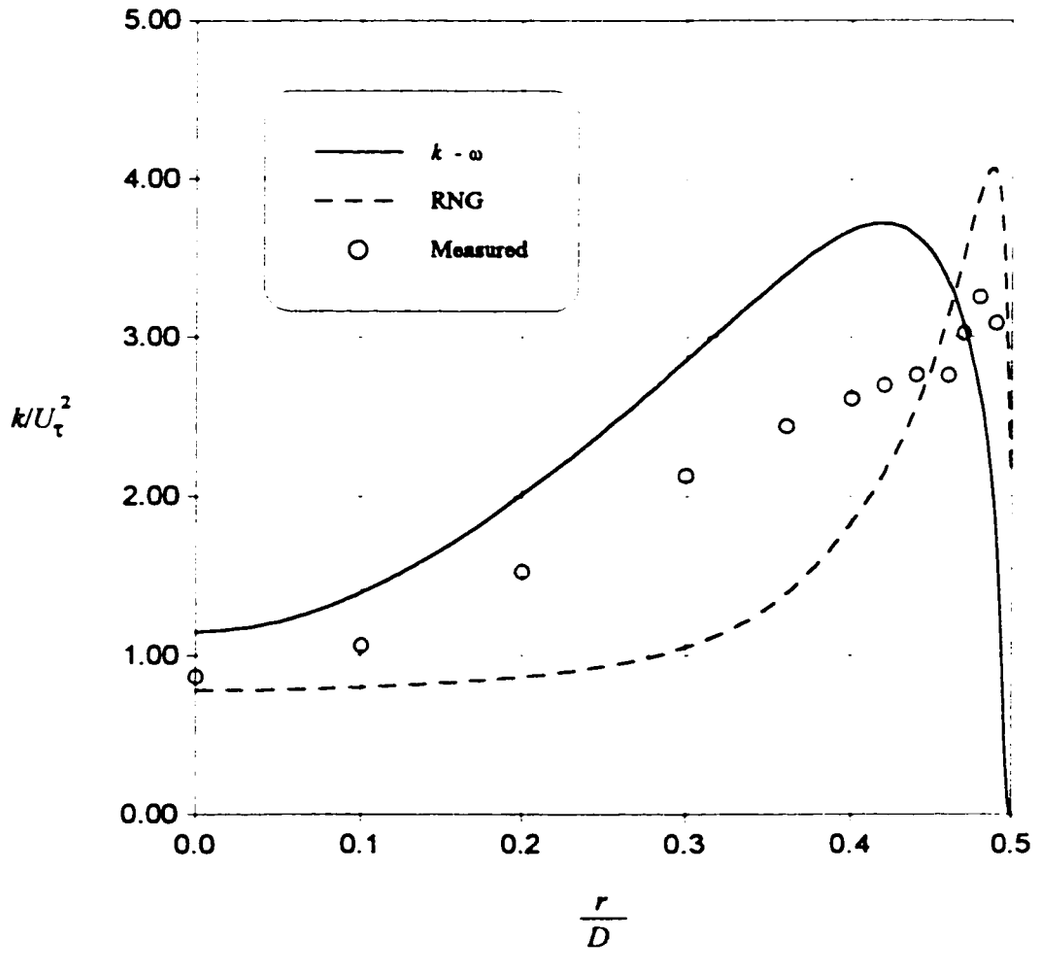

Fig. 3.31- Experimental (Schilknecht et al. 1979) and computed profiles of turbulent kinetic energy, k, at station x/D =1.358 for A = 4% (V_w = 1.832 cm/sec)

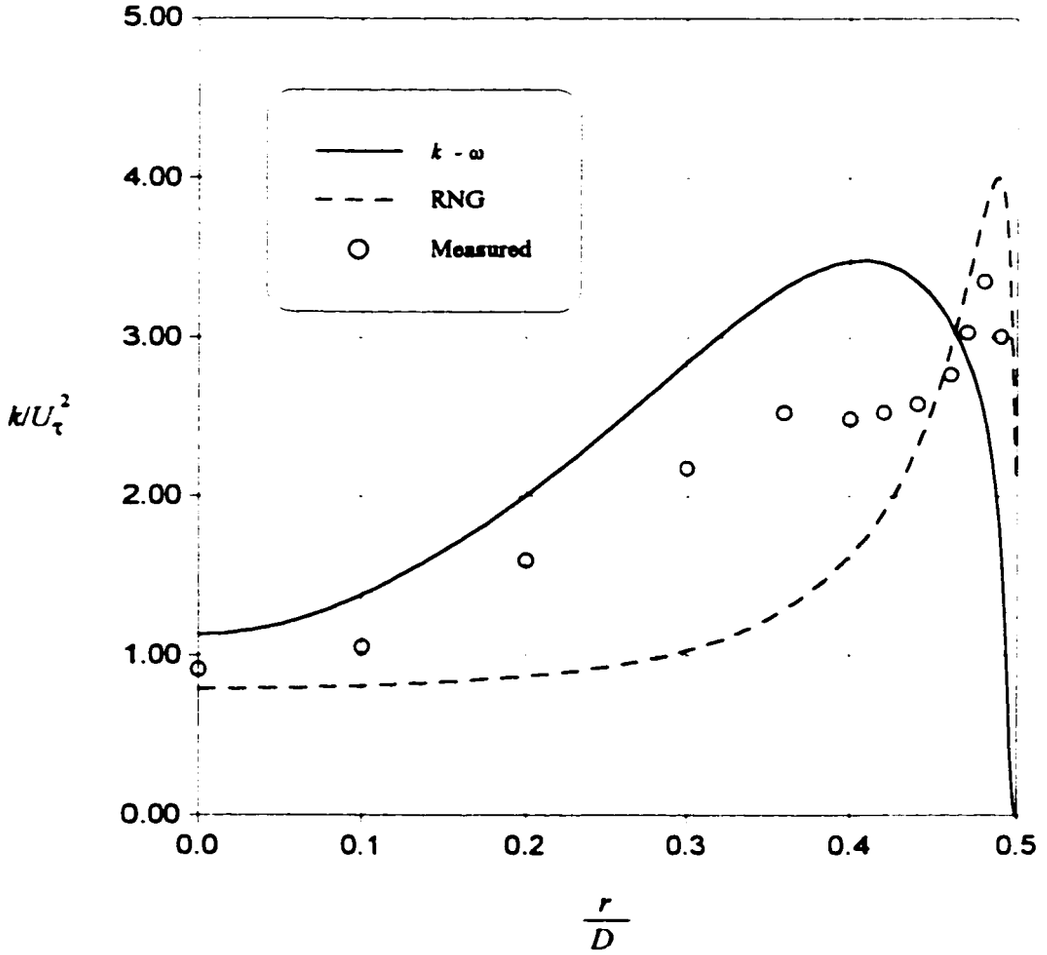

Fig. 3.32- Experimental (Schilknecht et al. 1979) and computed profiles of turbulent kinetic energy, k, at station x/D =2.212 for A = 4% (V_w = 1.832 cm/sec)

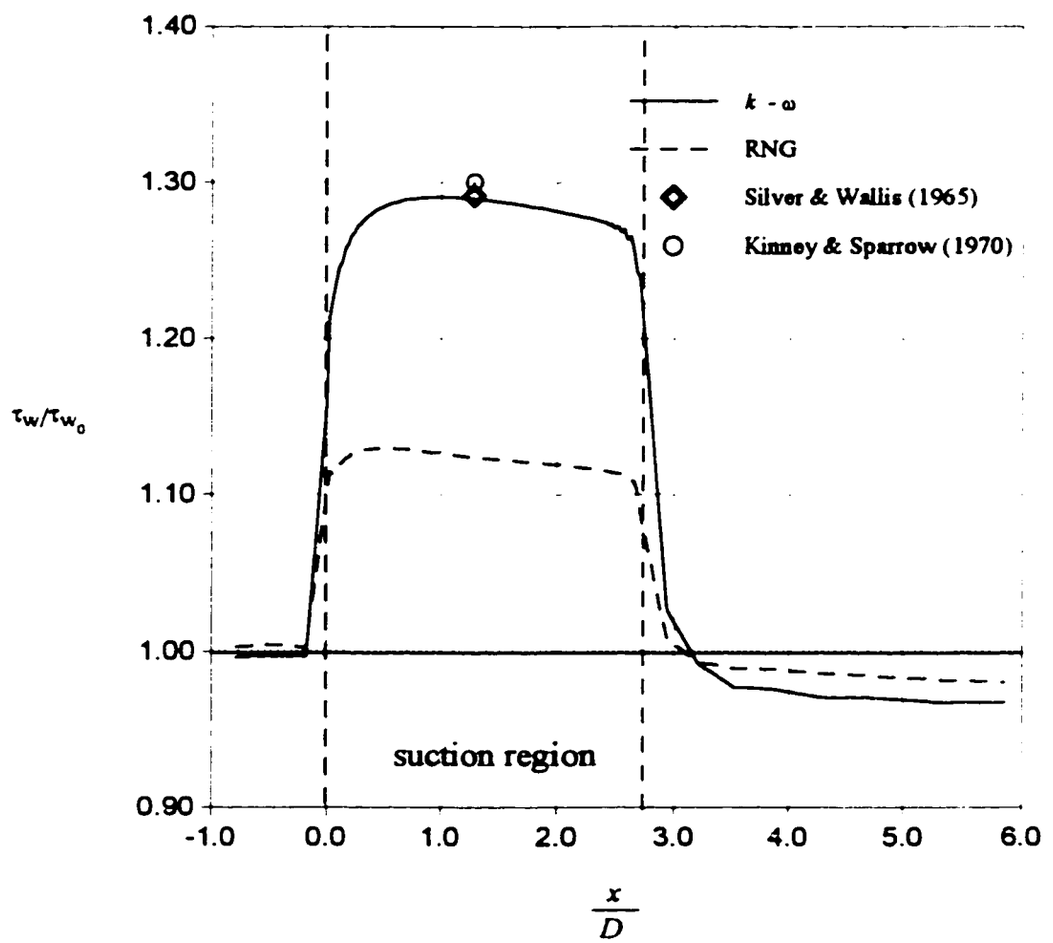

Fig. 3.33- Variation of wall shear stress along the suction region for A = 1.6% (V_w = 0.732 cm/sec)

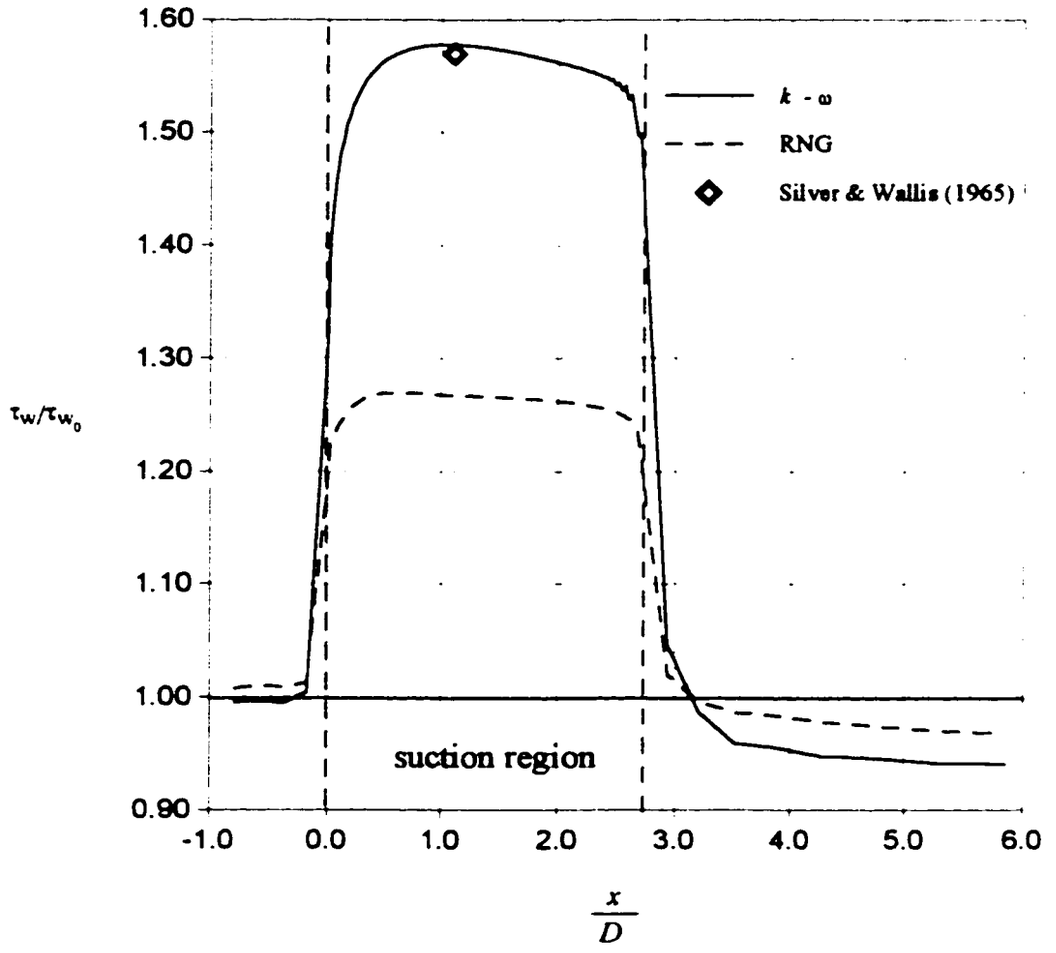

Fig. 3.34- Variation of wall shear stress along the suction region for A = 3.3% (V_w = 1.511 cm/sec)

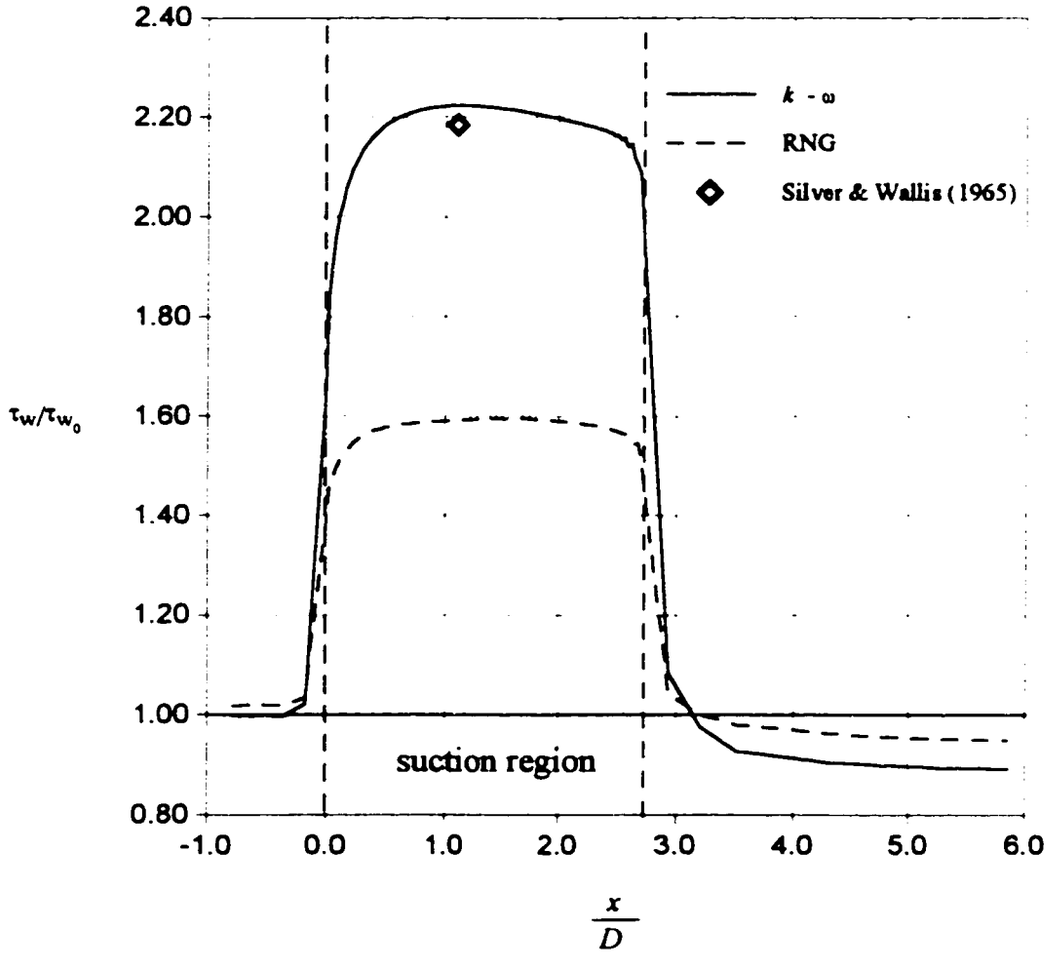

Fig. 3.35- Variation of wall shear stress along the suction region for A = 6.5% (V_w = 2.977 cm/sec)

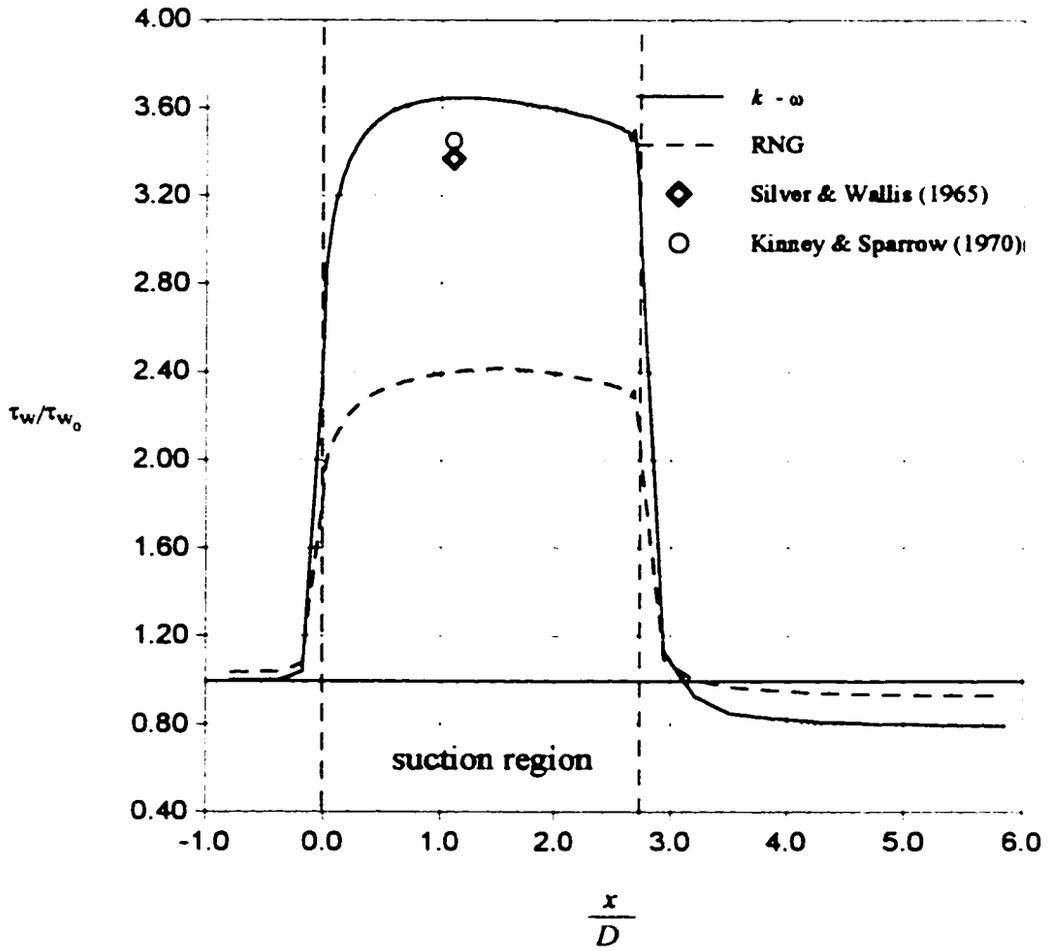

Fig. 3.36- Variation of wall shear stress along the suction region for A = 13.0% (V_w = 5.954 cm/sec)

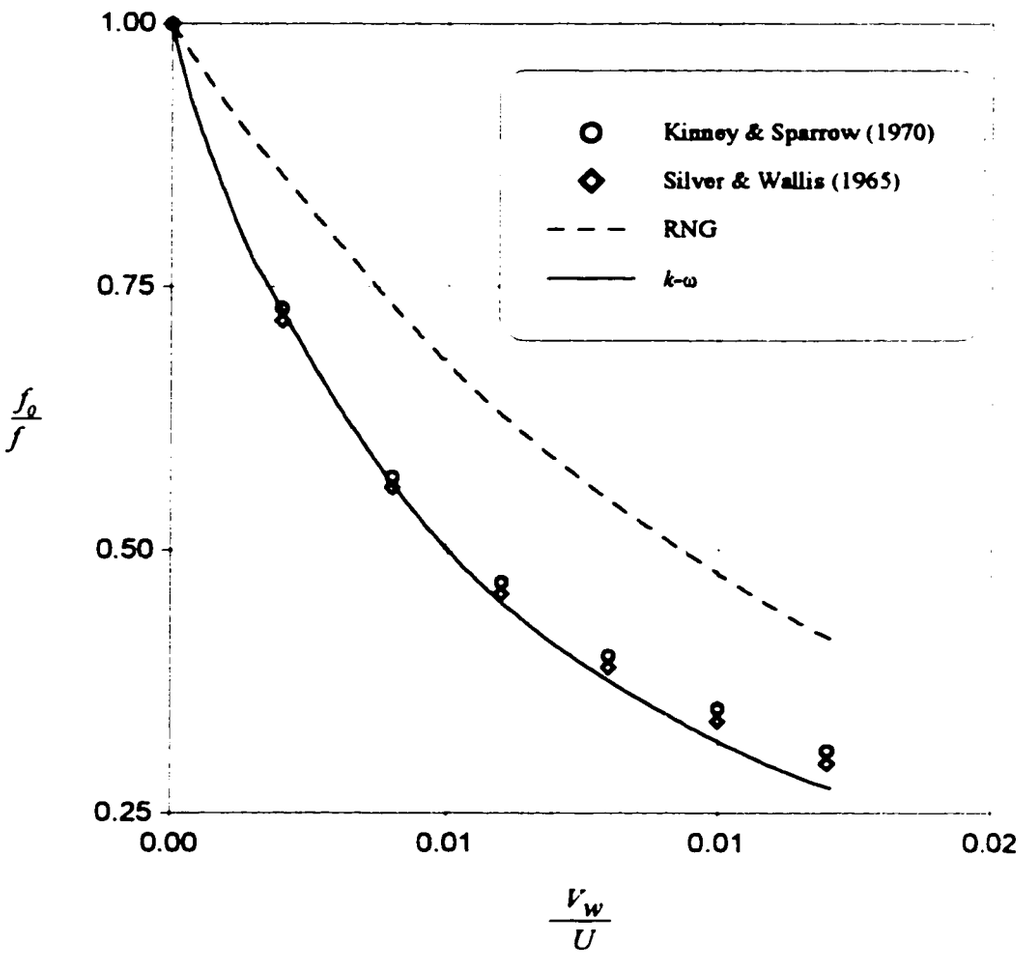

Fig. 3.37- Variation of local friction with relative suction velocity

Chapter 4

4. THEORETICAL CONSIDERATIONS

4.1 Introduction

The flow within a tube without flow through the walls (suction) is fully determined at all points if at the inlet to the tube, the Reynolds number and the velocity distribution are prescribed and in addition the geometric parameter e/D which defines the departure from smoothness at the inner surface is identified. It then follows that the local dimensionless shear stress at the wall can be written as:

$$\frac{\tau_{w0}}{\frac{1}{2}\rho U^2} = f_0 = f_0\left(\frac{\rho UD}{\mu}, \frac{x}{D}, \frac{e}{D}\right) \qquad (4.1)$$

In Equation 4.1 τ_{w0}, ρ, U, f_0, D, μ, x, and e are wall shear stress without suction, fluid density, mean axial velocity over tube cross section, friction factor without suction, inside diameter of tubing, dynamic viscosity of fluid, axial distance from entry of tube and the equivalent sand grain roughness, respectively. When flow occurs through the walls a full description of the suction rate along the entire inner wall surface must, in addition, be given and this must consist of the distribution of the suction velocity from the inlet $x = 0$ to the exit $x = L$ of the porous tube. It is clear that with suction a wide variety of boundary conditions is possible, and it was necessary to limit this study to a very narrow range of possibilities.

Firstly it was decided to position the porous section at the end of a long impervious tube of the same diameter so that fully developed turbulent flow would be achieved prior to the porous section at all Reynolds numbers tested. Secondly, it was decided to study a range of suction when the rate of mass extraction per unit area was uniform over the entire inner surface.

4.2 Methods of Fluid Mechanics Analysis

There are three basic approaches to the analysis of arbitrary flow problems:

1. Control-volume, or large-scale, analysis
2. Differential, or small-scale, analysis
3. Experimental using dimensional analysis

In differential analysis, four basic conservation laws (conservation of mass, conservation of linear momentum, conservation of angular momentum and the energy

equation) are applied to an infinitesimally small control volume or, alternately, to an infinitesimal fluid system. In either case the results yield the basic differential equations of fluid motion. In their basic form, these differential equations of motion are quite difficult to solve. However, for certain conditions the solution of these differential equations is possible analytically by making some simplifying assumptions. Another way to solve these differential equations is the approximating technique known as numerical analysis, whereby the derivatives are simulated by algebraic relations between a finite number of grid points in the flow. This approach was used in chapter four to solve the Reynolds-averaged Navier-Stokes differential equations in order to investigate the effects of wall mass transfer on the structure of the fully developed turbulent pipe flow.

A control volume approach similar to Wallis (1965-66) is used in the analysis. Control volume analysis is the most valuable tool available for flow analysis in fluid mechanics. The bases of this analysis method are some fundamental principles of physics, namely, conservation of mass, Newton's second law of motion, and the first and second laws of thermodynamics. This technique is powerful and applicable to a wide variety of fluid mechanical circumstances that require engineering judgment. A control volume, is a volume in space (a geometric entity, independent of mass) through which fluid may flow. Control volume equations deal with the relations between the fluid properties and the velocity at the control volume boundaries without revealing the details of what is going on inside the volume. Control volume equations deal with a balance between the amount of a quantity that enters the control volume, the amount of the quantity that leaves the control

volume the amount of the quantity stored inside the control volume and the net creation of destruction of the quantity within the control volume.

4.3 Selection of Control Volume

The selection of a control volume is an important matter in fluid analysis. An appropriate control volume can make a problem solution straightforward. The selection of an appropriate control volume in fluid mechanics is very similar to the selction of an appropriate free-body diagram in dynamics or statics. The ease of solving a given fluid mechanics problem is often very dependent upon the choice of the control volume used.

A fixed, nondeforming control volume is selected for analysis of flow in porous pipe. This control volume is shown in Figure 4.1. The pressure loss between inlet and outlet of the porous tubing are expected to be obtained from control volume analysis. Therefore, it is necessary to select these two sections as the boundaries (control surface) of the control volume. The control surface consists of the inside surface of the porous pipe, a section across the inlet of porous tubing, and a section across the outlet of porous tubing. One portion of the control surface is a physical surface (the porous pipe), while the remainder is simply a surface in space.

4.4 Linear Momentum Equation

The linear momentum equation for a fluid flowing through a finite control volume in general form is:

$$\frac{d}{dt}\int_{\forall cv} \rho\vec{V}d\forall + \int_{A out} \rho\vec{V}(V_n)dA - \int_{A in} \rho\vec{V}(V_n)dA = \sum \vec{F} \qquad (4.2)$$

In this equation:

$\frac{d}{dt}\int_{\forall cv} \rho\vec{V}d\forall$: Rate of accumulation of momentum inside the control volume

$\int_{A out} \rho\vec{V}(V_n)dA$: Rate of momentum flux leaving the control volume

$\int_{A in} \rho\vec{V}(V_n)dA$: Rate of momentum flux entering the control volume

$\sum \vec{F}$: Sum of forces acting on the mass inside the control volume

A symbolic form of the linear momentum equation is:

$$\frac{d}{dt}(\vec{M}_{cv}) + \dot{\vec{M}}_{out} - \dot{\vec{M}}_{in} = \sum \vec{F} \qquad (4.3)$$

in which $\dot{\vec{M}}$ represents the momentum flux. The notion of a control volume and system occupying the same region of space at an instant (coincident condition) and the Reynolds transport theorem are key elements in the derivation of this equation.

The momentum equation is a vector equation. As such, it represents three separate component (x, y, z or r, θ, x, etc.) equations. The components of the linear momentum equation along orthogonal coordinate directions are:

$$\frac{d}{dt}(M_{x,cv}) + \dot{M}_{x,out} - \dot{M}_{x,in} = \sum F_x \qquad (4.4)$$

$$\frac{d}{dt}(M_{y,cv}) + \dot{M}_{y,out} - \dot{M}_{x,in} = \sum F_y \qquad (4.5)$$

$$\frac{d}{dt}(M_{z,cv}) + \dot{M}_{x,out} - \dot{M}_{z,in} = \sum F_z \qquad (4.6)$$

Only the axial component of linear momentum equation is considered in this investigation.

4.5 Evaluating the Terms in the Linear Momentum Equation

To apply the linear momentum equation to a particular flow problem, the terms in Equation 4.2 have to be evaluated. This equation takes various forms, depending on the specific application. The primary terms in the equation (the momentum accumulation term, the momentum flux term(s), and the sum-of-forces term) will be separately examined for the porous tubing used in this study.

4.5.1 Momentum Accumulation

The momentum accumulation term,

$$\frac{d}{dt}(\vec{M}_{cv}) = \frac{d}{dt}\int_{\forall cv} \rho \vec{V} d\forall$$

may be important if mass accumulates or depletes in the control volume or if the control volume accelerates. Accelerating control volumes introduce the special problem of noninertial coordinates. If the control volume is fixed and rigid, the accumulation term is:

$$\frac{d}{dt}(\vec{M}_{cv}) = \frac{\partial}{\partial t}\int_{\forall cv} \rho \vec{V} d\forall = \int_{\forall cv} \frac{\partial}{\partial t}(\rho \vec{V}) d\forall$$

If the flow is steady, the momentum accumulation term is:

$$\frac{d}{dt}(\vec{M}_{cv}) = 0$$

In the present study since the flow is steady, the momentum accumulation term vanishes.

4.5.2 Momentum Flux

The momentum flux terms are the two area integrals in Equation 4.2. In these terms V_n is the fluid velocity component perpendicular to the control surface and measured relative to the control surface. Although V_n has no algebraic sign, each portion of the control surface with flow crossing it must be properly identified as "inflow" or "outflow." The velocity $\vec{V}$ is measured relative to an inertial reference.

At the planes inlet and outlet, the flow is one-directional parallel to the pipe axis. Since the flow is fully developed at the beginning of porous tubing, the velocity profile is nonuniform across the inlet and outlet. The momentum flux across the inlet plane is:

$$\dot{M}_{x,in} = \int_{Ain} \rho u^2 dA \tag{4.7}$$

In Equation 4.7, u is temporal-mean axial velocity. The positive x direction of coordinate system is set as being to the right. The velocity in the x direction is positive at the inlet and outlet sections. Replacing the nonuniformly distributed velocity with the average velocity does not give the correct momentum flux, since the real u is nonuniform. The true momentum flux is evaluated by using a momentum correction factor (β), defined by:

$$\beta = \frac{\int \rho u^2 dA}{\rho U^2 A} \tag{4.8}$$

for a constant-density fluid.

Therefore the momentum flux across the inlet and outlet planes would be:

$$\dot{M}_{x,in} = \beta_1 \rho U_1^2 A \tag{4.9}$$

$$\dot{M}_{x,out} = \beta_2 \rho U_2^2 A \qquad (4.10)$$

4.5.3 Sum-of-Forces Terms ($\sum \vec{F}$)

The term $\sum \vec{F}$ represents the sum of all forces acting on the mass inside the control volume. "All forces" means all types of forces and all locations where force may act. Evaluation of $\sum \vec{F}$ is the most common objective of a control volume momentum analysis. Considering the mass within a control volume as a free body, the force can be splited into the three types:

$$\sum \vec{F} = \sum \vec{F}_{gravity} + \sum \vec{F}_{pressure} + \sum \vec{F}_{shear} \qquad (4.11)$$

In this investigation we are concerned with the force in the axial direction, $\sum F_x$. Since the porous tubing is considered to be horizontal the weight of water deos not contribute to the x component of the reaction force and the $\sum \vec{F}_{gravity}$ term vanishes.

The external pressure force on a surface is normal to the surface and inward. Since the unit vector $\hat{n}$ in the control volume calculations is defined as outward, the pressure force can be evaluated by:

$$\sum \vec{F}_{pressure} = -\oint_{Acv} p\hat{n}dA \qquad (4.12)$$

All the *x* and *r* component pressure forces acting on the contents of the control volume are identified in Figure 4.2. The static pressure distribution can be assumed uniform (gravitationl effects can be neglected for such a small diameter porous pipe) and the flow

can be considered one-directional across the inlet cross section, plane 1, and outlet cross section, plane 2. These acceptable assumptions make the evaluation of the pressure integral simple in the pressure force equation. The force term obey the same sign convention as that for the momentum flux. The resulting equation for the $\sum F_{x,pressure}$ term is:

$$\sum F_{x,pressure} = P_i A - P_o A \tag{4.13}$$

The shear forces on the fluid is evaluated by:

$$\sum \vec{F}_{shear} = \oint_{Acv,fluid} \vec{\tau} dA \tag{4.14}$$

where $A_{cv,fluid}$ is the portion of the control surface that is in contact with fluid and $\vec{\tau}$, the stress vector, is defined as the shear force per unit area. For a porous pipe the shear force is the result of shear stress at the walls; that is

$$\sum \vec{F}_{shear} = \int_{Aw} \vec{\tau} dA \tag{4.15}$$

The application of the axial component of Equation 4.15 to the fluid in the control volume results in:

$$\sum F_{x,shear} = \int_{Aw} \tau dA \tag{4.16}$$

The evaluation of the shear force integral in Equation 4.16 requires detailed information on wall shear stress. For fully developed turbulent flow in a horizontal solid pipe the pressure drop and wall shear stress are related by:

$$\tau_w = \Delta P \frac{D}{4L} \tag{4.17}$$

The Darcy-Weisbach equation for fully developed, steady and incompressible pipe flow valid for laminar and turbulent is:

$$\Delta P = f\left(\frac{L}{D}\right)\left(\frac{\rho U^2}{2}\right) \tag{4.18}$$

A desired expression can be obtained for wall shear stress for solid pipes by combining Equations 4.17 and 4.18.

$$\tau_w = f\frac{1}{8}\rho U^2 \tag{4.19}$$

In Equations 4.18 and 4.19 the dimensionless parameter f is called Darcy friction factor. From dimensional analysis it is found:

$$f = f\left(Re, \frac{e}{D}\right) \tag{4.20}$$

where e is the wall-roughness height or equivalent sand grain roughness. From Equations 4.19 and 4.20 it can be found that for a fully developed solid pipe flow at a particular flow rate (or axial Reynolds number), the value of wall shear stress is constant along the wall. In a porous pipe, however, due to radial discharge through the walls, both Darcy friction factor and average velocity vary from the inlet of the porous pipe down to the outlet. Furthermore, the numerical study in chapter 3 showed that even a small suction causes wall shear stress changes.

For the case of a porous pipe, a semi-infinitesimal fluid element is considered in the control volume as is shown in Figure 4.1. It is a circular cylinder of fluid of length dx

centered on the axis of the porous pipe of diameter D. Application of the Equation 4.16 to the contents of semi-infinitesimal fluid element results in:

$$d(\sum F_{x.shear}) = -\pi D \times dx \times \tau_w \tag{4.21}$$

By Integrating Equation 4.21 over the selected control vllume one can get:

$$\sum F_{x.shear} = -\pi D \int_0^L \tau_w dx \tag{4.22}$$

4.6 Linear Momentum Equation for Porous Tube

Substituting all the linear momentum terms (Equations 4.9, 4.10, 4.13, 4.22) obtained for the porous tube in Equation 4.4 gives:

$$\beta_2 \rho U_2^2 A - \beta_1 \rho U_1^2 A = P_i A - P_o A - \pi D \int_0^L \tau_w dx \tag{4.23}$$

Solving this equation for pressure drop (or gain) between inlet and outlet yields:

$$P_o - P_i = \beta_1 \rho U_1^2 - \beta_2^2 \rho U_2^2 - {}^4/_D \int_0^L \tau_w dx \tag{4.24}$$

If it is assumed that the suction rate does not have any effect on wall shear stress, the value of τ_w can be substituted by Equation 4.19.

$$P_o - P_i = \beta_1 \rho U_1^2 - \beta_2 \rho U_2^2 - {}^4/_D \int_0^L f \frac{1}{8} \rho U^2 dx \tag{4.25}$$

Also it is assumed that a uniform extraction exists along the porous tube length. With the assumption of uniform extraction along the porous tube length, the average velocity (U) will change linearly along the porous length. This linear relation can be easily obtained,

$$U = \left(\frac{U_2 - U_1}{L} \times x \right) + U_1 \tag{4.26}$$

Substituting this value in Equation 4.25 one can obtain:

$$P_o - P_i = \beta_1 \rho U_1^2 - \beta_2 \rho U_2^2 - \frac{f\rho}{2D}\int_0^L \left(\left(\frac{U_2 - U_1}{L} \times x\right) + U_1\right)^2 dx \qquad (4.27)$$

$$P_o - P_i = \beta_1 \rho U_1^2 - \beta_2 \rho U_2^2 - \frac{f\rho}{2D} \times \left[\left(\frac{U_2 - U_1}{L}\right)^2 \times \frac{x^3}{3} + \frac{2U_1(U_2 - U_1)}{L} \times \frac{x^2}{2} + U_1^2 \times x\right]_0^L \qquad (4.28)$$

$$P_o - P_i = \beta_1 \rho U_1^2 - \beta_2 \rho U_2^2 - \frac{f\rho}{2} \times \frac{L}{D} \times \left[\frac{(U_2 - U_1)^2}{3} + U_1(U_2 - U_1) + U_1^2\right] \qquad (4.29)$$

$$P_o - P_i = \beta_1 \rho U_1^2 - \beta_2 \rho U_2^2 - \frac{f\rho}{6} \times \frac{L}{D} \times \left(U_2^2 + U_1^2 - 2U_1U_2 + 3U_1U_2 - 3U_1^2 + 3U_1^2\right) \qquad (4.30)$$

Dividing Eq. (4.30) by the inlet dynamic head, $\frac{1}{2}\rho U_1^2$, and rearranging terms one obtains

$$\frac{P_o - P_i}{\frac{1}{2}\rho U_1^2} = 2\left(\beta_1 - \beta_2 \frac{U_2^2}{U_1^2}\right) - \frac{f}{3} \times \frac{L}{D}\left(1 + \frac{U_2}{U_1} + \frac{U_2^2}{U_1^2}\right) \qquad (4.31)$$

Now, if it is assumed that the wall shear stress increases by an amount of $\rho V_w U$ the value of wall shear stress would be:

$$\tau_w = f\,\tfrac{1}{8}\rho U^2 + \rho V_w U \qquad (4.32)$$

It can be easily shown that the value of V_w in terms of U_1 and U_2 for situation where the rate of mass extraction per unit area is uniform over the entire inner surface is

$$V_w = \frac{D(U_1 - U_2)}{4L} \qquad (4.33)$$

By combining Eqs. (4.25),(4.32) and (4.33), one obtains the expression

$$P_o - P_i = \beta_1 \rho U_1^2 - \beta_2 \rho U_2^2 - \frac{f\rho}{2D}\int_0^L \left(\frac{U_2 - U_1}{L} \times x + U_1\right)^2 - \frac{4\rho}{D}\left(\frac{D(U_1 - U_2)}{4L}\right) \times \int_0^L \left(\frac{U_2 - U_1}{L} \times x + U_1\right) dx \tag{4.34}$$

$$P_o - P_i = \beta_1 \rho U_1^2 - \beta_2 \rho U_2^2 - \frac{f\rho}{6} \times \frac{L}{D} \times \left(U_2^2 + U_1^2 + U_1 U_2\right) + \frac{\rho(U_1 - U_2)^2}{2} - \rho U_1 (U_1 - U_2) \tag{4.35}$$

$$P_o - P_i = \beta_1 \rho U_1^2 - \beta_2 \rho U_2^2 - \frac{f\rho}{6} \times \frac{L}{D} \times \left(U_2^2 + U_1^2 + U_1 U_2\right) + \frac{\rho}{2} U_1^2 + \frac{\rho}{2} U_2^2 - \rho U_1 U_2 + \rho U_1 U_2 - \rho U_1^2 \tag{4.36}$$

$$\frac{P_o - P_i}{\frac{1}{2}\rho U_1^2} = (2\beta_1 - 1) - (2\beta_2 - 1)\frac{U_2^2}{U_1^2} - \frac{f}{3} \times \frac{L}{D}\left(1 + \frac{U_2}{U_1} + \frac{U_2^2}{U_1^2}\right) \tag{4.37}$$

From Equations 4.31 and 4.37 one can see that for a particular $\frac{U_2}{U_1}$ there is a linear relation between dimensionless pressure change, $\frac{P_o - P_i}{\frac{1}{2}\rho U_1^2}$, and $\frac{L}{D}$. This hypothesis was tested by experimental study which will be extensively discussed in the chapters six and seven.

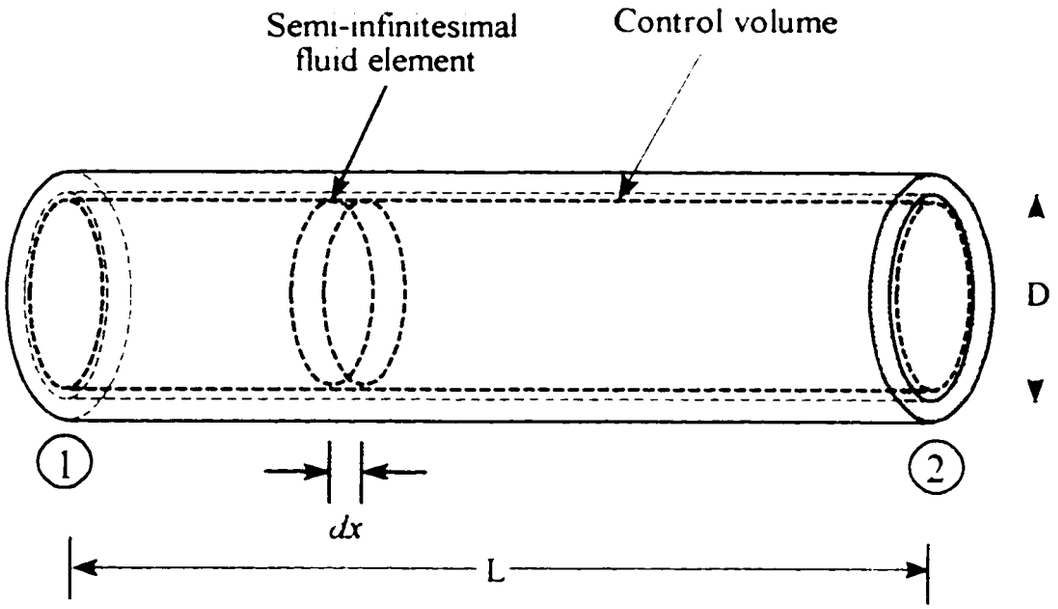

Figure 4.1- Control volume for analysis of flow through porous tubing and semi-infinitesimal fluid element for wall shear calculation

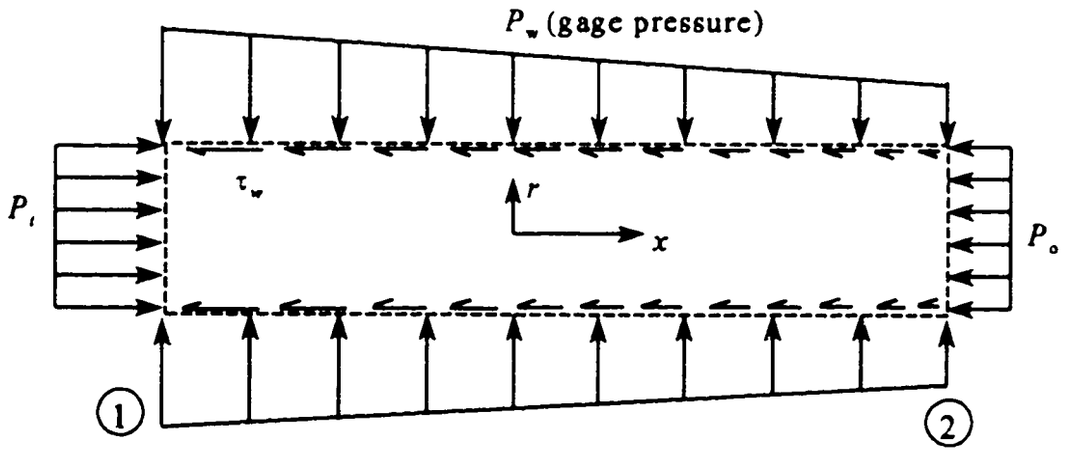

Figure 4.2- Pressure and shear stress on fluid flowing in porous tubing

Chapter 5

5. EXPERIMENTAL APPARATUS AND PROCEDURE

5.1 Introduction

Few publications deal with experiments involving the turbulent flow of pure fluids through porous-walled tubes. Even fewer have been published on the subject of turbulent flow of liquid in porous-walled tubes. The experimental part of the present work attempted to gather data to determine some of the characteristics for flows in porous-walled tubes using distilled water in the turbulent regime for the case of "suction" and "no suction"

conditions. Success in data collection however, requires overcoming the considerable experimental difficulties involved in the measurement of pressure in porous-walled tubes as well as difficulties involved in working with pure water. An experimental apparatus was designed and constructed in the Hydraulic Laboratory of the University of Ottawa to allow measurement of the pressure drop over the porous tubing using distilled water in turbulent conditions.

The experimental apparatus was a closed-circuit system permitting the use of distilled water during the course of the experiments. The components of the system were placed on a series of three stands made from perforated angle iron. Each stand was 1 meter long, 0.25 m wide, and 1 meter high. The support system was made from multiple units to allow for changing the system's length for testing different lengths of porous tubing. Also, more platform can be added to the system to accommodate necessary components, simply by installing additional angle supports.

The system consists of devices for measuring pressure head difference, radial wall flow rate (permeable flow rate), axial flow rate and temperature. Pumps were used to send water from the main reservoir to the test section and for recycling the water back to the main reservoir. There was also a heat exchanger and a collector for the water emitted from the porous tubing which was then led to a small reservoir. The small reservoir is to store the collected water for subsequent pumping to the main reservoir. There was a main reservoir used to collect the recycled water which was then pumped to the test section.

Further components of the system included small stands for holding main reservoir and pump, porous tubing, plastic tubing for transmitting the water, inlet and outlet stainless steel tubing, valves, and connections. The pressure head difference in the system was measured using an air compressor, an air pressure regulator, and a water manometer. The temperature of the system was measured using three thermocouples and a mercury thermometer. A rotameter was used to measure the inlet flow rate. A schematic presentation of the experimental set-up, with all components is shown in Figure 5.1. Also a complete view of the experimental set-up, including the stand can be seen in Plate 5.1.

The porous tubing used in this study is sold commercially as Irrigro® which is distributed by International Irrigation Systems located in St. Catherines, Ontario. The tubing is made of a plastic material called Tyvec®, a fibrous, spun-bonded polyethylene material which was developed by Dupont. Relevant tubing characteristics that were provided by the manufacturer are the following:

Weight: 61.1 gr/m^2

Thickness: 15 μm

Pore size: 0.5 μm

The permeability of the tube was measured and it was found to be 3.38×10^{-16} m^2. To determine the variability in performance due to manufacturing process (manufacturer's variation), tests were conducted on 90 pieces of tubing of length 30 cm selected quite randomly from manufacture's product. Under the same circumstances flow was passed through these lengths of tubing which were closed at the end. Flow through the porous

wall was measured by small flowmeter installed at the beginning of the porous tubing. The coefficient of variation of the flowrate through the porous wall was found to be 3.5%.

In the following sections, the components of the system will be explained separately in detail. Also the construction of some of the components which were designed and constructed in the Hydraulic Laboratory will be discussed. Where appropriate, the method of the calibration and the calibration curves will be given.

5.2 Pressure Head Measurements

The most important measurement in the course of this study was the measurement of pressure. Numerous devices and techniques are used to measure pressure depending on the particular situation. Pressure measurement instruments require the construction of the pressure taps which are necessary to link the pressure inside of the system to the instrument. A very important step in pressure measurement is the proper installation of the pressure taps. A small error in construction of the pressure taps can result in significant errors in pressure measurements.

5.2.1 Pressure Tap Construction

The porous tubing used in the present study was not solid enough to permit the insertion of pressure taps into the wall. Therefore, to measure the pressure drop over the porous tube, two pressure taps were inserted before and after porous section. One pressure tap was located at the end of the stainless steel tubing used as the inlet section and the second was located at the beginning of the stainless steel tubing used as the outlet section, both of

them being placed as close to the porous tubing as possible. The local pressure drop due to the connection of the porous tubing to the stainless steel pipe and the friction head loss due to the small length of stainless steel that extends from the connection to the pressure taps were both considered in the evaluation of the head loss.

The construction details of the pressure taps is shown in Figure 5.2. The procedure for inserting the pressure taps was to first drill a 1.5 mm hole all the way through the wall. The 1.5 mm hole was small enough to prevent flow into the measuring tube once the pressure has adjusted to a steady value. After that a 3 mm hole was drilled half the way through the wall in the same place as the previous 1.5 mm hole to accommodate the nipple connecting the small hole to the small tubing which led to the manometer. Since any slight misalignment in the vicinity of the opening could cause error in measurements, care was taken to drill a hole precisely normal to the surface.

A bronze nipple with inside diameter of 1.5 mm and outside diameter of 3 mm was inserted into the 3 mm hole. The bronze nipple was 3 cm long and was long enough to satisfy the minimum required length of the opening (the length of the opening should be at least twice the diameter). The outside of the nipple bronze was welded to the stainless steel tubing. The burrs at the edges of the opening formed from drilling were completely removed to prevent the formation of eddies in the vicinity of the opening and thus distort the measurement. The surface around the opening was smoothed to prevent any unreliable reading.

Any disturbance in the flow field that might be present, caused by misalignment in the vicinity of opening, by burrs, or by roughness of the surface close to the opening decreases the pressure, since a disturbance of the streamline pattern would increase the local velocity, thus decreasing the pressure according to the Bernoulli equation.

The pressure taps were attached to the manometer with 0.32 cm inner diameter tygon tubing. Plastic three-way stopcocks were attached to the ends of the tygon tubing just before manometer tubing to allow bleeding the pressure-tap lines free of air. Plate 5.2 indicates the three -way stopcocks used for bleeding the pressure-tap lines.

5.2.2 Pressure Measuring Device

There are many devices available for measuring pressure in a moving stream. All take advantage of the fact that pressure applied to a finite area of material causes a force and stress and displacement in the material. These mechanical effects can then be quantified in various ways:

1. A force balance
2. The height of a liquid column (manometer)
3. Direct displacement measurement
4. Indirect (electrical) measurement of displacement

Force balances are commonly used to calibrate pressure instruments rather than as devices for routine measurement. The *fluid manometer* is a widely used device for

measurement of fluid pressure under steady state and laboratory conditions. *Direct displacement* measurement devices make use of the fact that when a pressure acts on an elastic structure the structure will deform, and this deformation can be related to the magnitude of the pressure. The most familiar device of this kind is the Bourdon pressure gage. In *indirect (electrical)* measurement of displacement devices the deformation of an elastic structure is converted into an electrical output.

The manometer is a very accurate device for measuring pressure; however, it is limited in the range of pressure it can measure. For instance a pressure of 340 KN/m^2 (which is the maximum pressure existing in the system of the present study) would require a water column more than 35 m high or a mercury column more than 2.5 m. Another constraint of the manometer is the difficulty of reading the liquid meniscus with high precision.

The two above mentioned problems were overcome by designing a special manometer in the hydraulic laboratory. Since measurement of the difference in pressure head was a very important parameter in this study and the pressure head itself could be measured with less precision, a special manometer was designed to allow measurement of pressure difference in a wide range (from zero up to 180 cm water) with high precision (0.005 cm water) while a high pressure existed in the system. Preliminary investigation showed that no other device could measure pressure difference with such high precision in a wide range of pressure differences, while there was high pressure existing in the system. Investigation in a pressure measurement handbook showed that to achieve this amount of precision, at

least three differential pressure transducers would be needed but there still would be the risk of damaging of the pressure transducer diaphragm because of possible application of instantaneous high pressure on one side of the diaphragm. On the other hand, manometers provide accuracy and precision, but they also require very careful attention in their application.

A schematic presentation of the manometer is indicated in Figure 5.3. The manifold part of the manometer was made from six copper T's connected to each other by small pieces of copper tubing. The small copper tubes were soldered to the T's to make a manifold with six exits. Glass tubes were used as the limbs of the manometers. The inside and outside diameter of the manometer tubes were chosen to be 1.3 and 1.5 cm, respectively. This diameter was large enough for the effect of surface tension to be negligible (Holman, 1983). The connection of the copper tubing to the glass tubing was made by a small piece of thick plastic tubing that had an inside diameter equal to the outside diameter of the copper and glass tubing. The connections were secured from leaking by using two clamps in both sides of the plastic tubing. The use of these connections is to increase the measured pressure range by changing the length of the glass tubing. The same connections were used at the end of the glass tubing to connect glass tubing to the valves.

An air compressor was used to increase the air pressure above the manometer liquid. A highly accurate pressure regulator was used after the air compressor to adjust the air pressure above the manometer liquid close to the pressure of the system. The air pressure

regulator was a Bellofram type 10 regulator, controlling the output pressure with an accuracy of 0.1% and having very low sensitivity to changes in supply pressure.

The manometer was located as close as physically possible to the pressure taps. With water of known density, measuring the pressure drop between two pressure taps attached to the manometer tube merely required measuring the steady-state difference in height between the water in the two tubes of the manometer.

5.2.3 Reading of the Liquid Meniscus

A cathetometer was used to measure the accurate vertical difference between the meniscus in the limbs of the manometer. The cathetometer consists of a tripod stand, a vertical guide bar, and a telescope, horizontally mounted on a carriage. During the course of measurements the cathetometer was placed as close as to the manometer in order to minimize the effect of angular errors. In order to make accurate measurement of vertical differences of the meniscus in the limbs of the manometer, it was necessary to insure that the guide bar was truly vertical. This was accomplished by leveling the base of the frame. The range of measurement of the cathetometer is 100 cm with an accuracy of ± 0.05 mm.

5.3 Flow Rate Measurement

There are many ways flow rate may be measured, e.g., direct, indirect, gravimetric, volumetric, electronic, electromagnetic, and optical. Direct measurement for discharge consists of the determination of the volume or weight of fluid that passes a section in a given time interval. Indirect methods of discharge measurement require the determination

of head, difference in pressure, or velocity at several points in a cross section and, with these, computing the discharge. The most precise methods are the gravimetric or volumetric determinations, in which the weight or volume is measured by weigh scales or by a calibrated tank for a time internal that is measured by a stopwatch. Determining all the flow rates in a porous-walled tube system requires measuring two of the three flow rates : inlet, outlet, and porous section flow rate (filtrate flow rate).

5.3.1 Inlet Flow Rate Measurement

The inlet flow rate was measured by a rotameter with a range of 0.035 to 0.320 l/sec (±2 percent full scale accuracy, ±1/4 percent full scale repeatability, 250 mm scale). Plate 5.3 shows the flow meter being used for the measurement of the flow at the inlet of the test section. Although the calibration of the flow meter was done before installation using tap water, because of the significant difference between temperature of the tap water and that of the system, it was repeated using water flowing in the system. The calibration curve of the flow meter is given in Figure 5.4.

5.3.2 Flow Rate Measurement at the Porous Section

Special collectors were designed to collect the emission flow from porous tubing and conduct it to the small reservoir to be recycled to the main reservoir. These collectors were made from Styrofoam with a triangular cross section. The dimensions of the cross section were selected large enough to collect and convey the porous flow rate at the peak conditions. Collectors with different lengths were made to allow tests at different lengths of porous tubing. For the long collectors, two additional supports were added to prevent

the collector from sagging. A schematic presentation of the collector is indicated in Figure 5.5.

Volumetric determination was used to measure the flow rate through the porous section of the tubing. The time required to collect a certain amount of volume of water was recorded by a stopwatch. The volume measurements were made over long periods to minimize the flow rate errors. The volume of the collected water was then measured and the flow rate calculated. The water was caught by a 5 liter plastic pitcher. The volume of the collected water was measured by the 1,000 cm^3 graduated cylinders with an accuracy of ± 10 cm^3 . The accuracy of the stopwatch was ± 0.01 second. Each measurement was repeated three times and in most cases the difference between measurements (repeatability) was observed to be not more than 0.25 to 0.50 percent.

5.3.3 Outlet Flowrate Measurement

Although the flow rate at the inlet of the test section and at the porous test section were measured and these measurements are sufficient, in the course of the experiments the outlet flow rate at the main reservoir was also measured by the volumetric method to check the measurements at the inlet and porous test sections. For most cases the difference between the flow rate at the inlet, measured by flowmeter, and summation of the flow rates at porous test section and outlet, measured by volumetric method, was not more than 0.5-1.0 percent.

5.4 Water Requirements

In all the experiments, distilled water was used to prevent the porous tubing from clogging. The permeability of the porous section was continuously calculated in the course of the experiment to make certain the clogging of the porous tubing would not occur. There was a slight decrease in the permeability particularly in the experiments with the short porous tubing, but a decrease of more than 1% was not observed in the permeability. Preliminary experiments were conducted using a pump whose impeller and case were cast iron. Very severe corrosion occurred in the pump and after few minutes the porous tubing clogged. It is well known that distilled water is a very corrosive liquid. All the material used in the system were selected either stainless steel or plastic which are resistance to corrosion.

5.5 Temperature Measurements

The fluid temperatures were used in the evaluation of fluid density and viscosity. These properties were then used in the rotameter flow rate calculation and in the calculation of the radial Reynolds number and the axial Reynolds number in the porous tube. Temperatures were measured by means of thermocouples installed before and after the test section, and in the reservoir. The exit temperature of water from the porous tubing was periodically checked with a glass thermometer installed in the water collector under the test section.

A thermocouple was used for temperature measurement and was based on the direct or indirect determination of the resistance of a thermistor (a contraction for "thermally sensitive resistors") immersed in the environment whose temperature is to be measured (Benedict, 1980). The thermocouple used in this study was connected to a LCD digital multimeter to measure the resistance of the thermistor used in the thermocouples. For the thermocouple used in the experiments, the temperature- resistance relationship was obtained using the LCD digital multimeter, and a mercury thermometer with a precision of 0.1 °C. Measurements were taken over a range of water temperatures. Figures 5.6 and 5.7 show the resistance-temperature characteristic of the thermocouples before and after the test section, respectively. The values of the material constant (α) and the temperature coefficient of resistance were -2.19 and 3,395 and -2.05 and 3,350, respectively, for the thermocouple before and after the test section. Plate 5.4 shows the LCD digital multimeter and thermocouple used in this study.

5.6 Inlet and Outlet Region

The porous tube was preceded by a long section of solid wall pipe to insure a stable and fully developed velocity profile at the entrance to the porous tube since the pressure variation in a porous tube is sensitive to the shape of the inlet velocity profile. A long outlet region was also added to make sure that the flow was stable. The ratio of the length of non-porous inlet length to the inside tube diameter was 100. Schlicting (1968) indicated that in laminar flow a length of up to 300 diameters could be necessary to avoid variation, but that in turbulent flow, 100 diameters would be sufficient. The inlet and outlet region were stainless tubing with inside and outside diameter 0.95 cm and 1.27 cm, respectively.

Stainless steel was chosen as inlet and outlet region for two reasons: stainless steel is resistant to corrosion and it is a good conductor to transfer heat from the system to the heat exchanger. The transition between the porous section and the stainless tubings was smooth. Figure 5.8 indicates the construction details of the connection between porous section and stainless steel tubings.

5.7 Heat Exchanger

Due to the viscous dissipation in the pump and in the inlet and exit valves (particularly when the valves were partially closed), the temperature of the system increases. Preliminary tests showed that when the inlet and outlet valves were completely open after half an hour the temperature of water increased from 24 °C to 34 °C and subsequently, this rate of temperature change decreased, but still the temperature was increasing. In cases where the valves were partially closed, it took less time for the changes to occur. The change in temperature from 24 °C to 34 °C caused about 20 percent change in the kinematic viscosity and consequently in the wall Reynolds number and the axial Reynolds number.

A heat exchanger was designed and placed after the test section to maintain the temperature at 24 °C. The advantage of the heat exchanger which was installed was that it did not interfere with the main flow and did not cause any additional head loss in the system. The heat exchanger is a cylindrical unit made of plastic glass with a diameter of 7.5 cm and a length of 30 cm closed at both ends. The inlet and outlet of the heat exchanger were located diagonally opposite each other to allow the flow to circulate and

to cause all of the water inside of the heat exchanger to exit. The stainless steel tubing used as the outlet region of the system passes through the heat exchanger. The inlet of the heat exchanger is connected to tap water and the outlet is attached to a drain. This heat exchanger can maintain the temperature of the water at 24 ± 1 °C by manually changing the flowrate of the cold tap water entering the heat exchanger. As soon as the thermocouples and thermometer showed any increase in temperature above 24 °C the inlet flow was increased by opening the tap. Since the experiments were conducted in the winter time the tap water was cool enough to maintain the temperature at the desired value. Figure 5.9 indicates a schematic presentation of the heat exchanger used in the experimental system. Also Plate 5.5 shows two views of heat exchanger in use and connection to the cold tap water.

5.8 Pumps

There are four pumps in the system to deliver the distilled water from main reservoir to the test section and recycle porous flow back to the main reservoir. A 1/2 HP pump (model 48J2DB11C6, RPM 3450, GRUNDFOS Pump Co.) was used to send the distilled water to the test section. The pressure of the pump in the shut-off condition was 67 psi (4.6 bar or 0.46 MPa) which was enough to give the necessary emission rate from the porous tubing. Three pumps were used to recycle the distilled water back to the main reservoir. A compensated pump (model 3E-NHC, LITTLE GIANT PUMP CO.) was placed inside the small reservoir to pump the low porous flow rate water. With increasing porous flow rates, a second pump (model: AC-2CP-MD # 125-052, HP:1/55, RPM:3500, MARCH MFG., INC., Glenview, ILL) started to pump. For very high flow rates, a third

pump (model: JA2N088N # 135-109-11, MARCH MFG., INC., Glenview, ILL) pumped together with the two other pumps. There was a valve after each pump to control the exit flow rate and prevent the pumps from sucking in air.

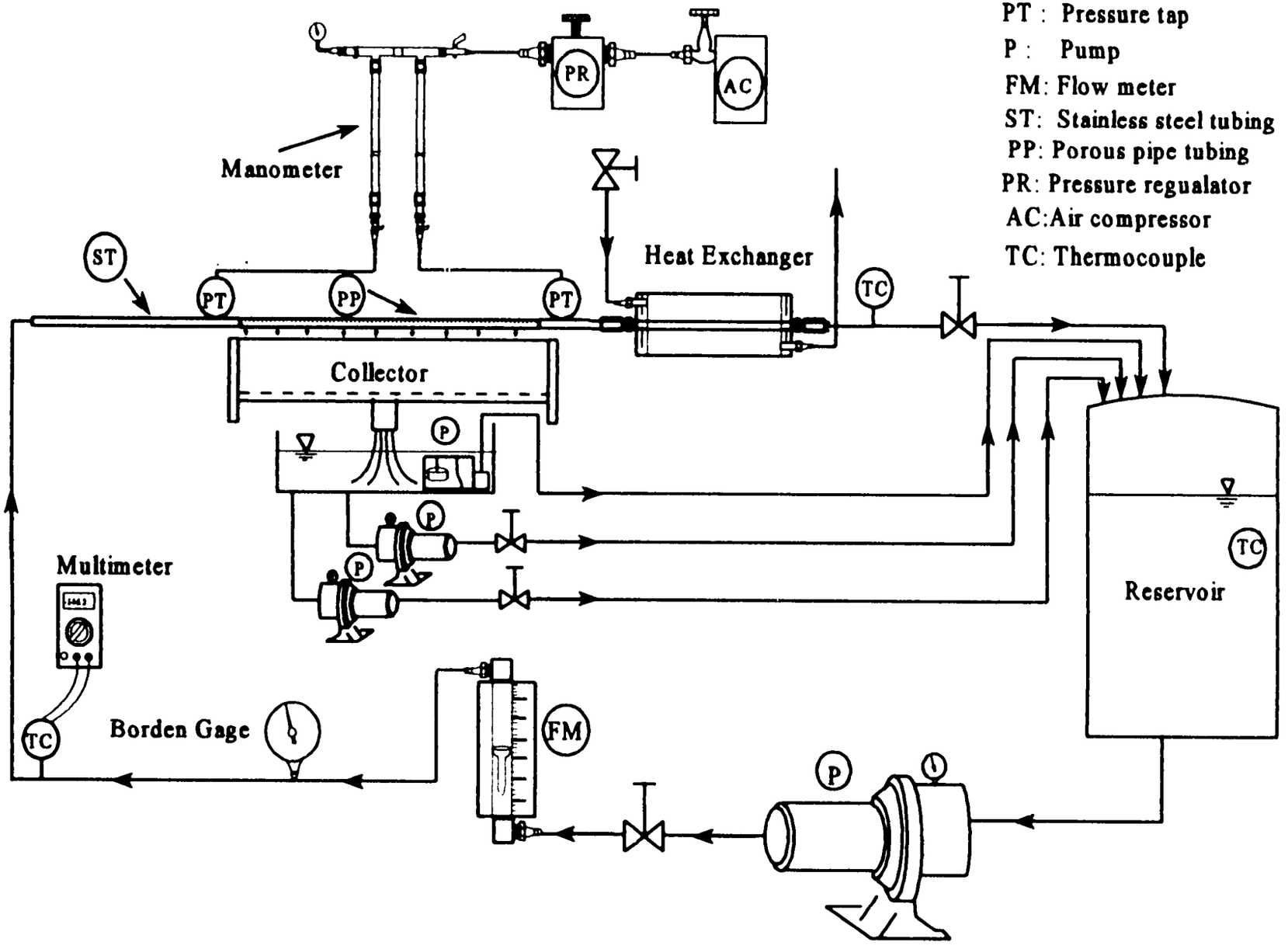

Figure 5.1- Schematic presentation of the experimental set-up

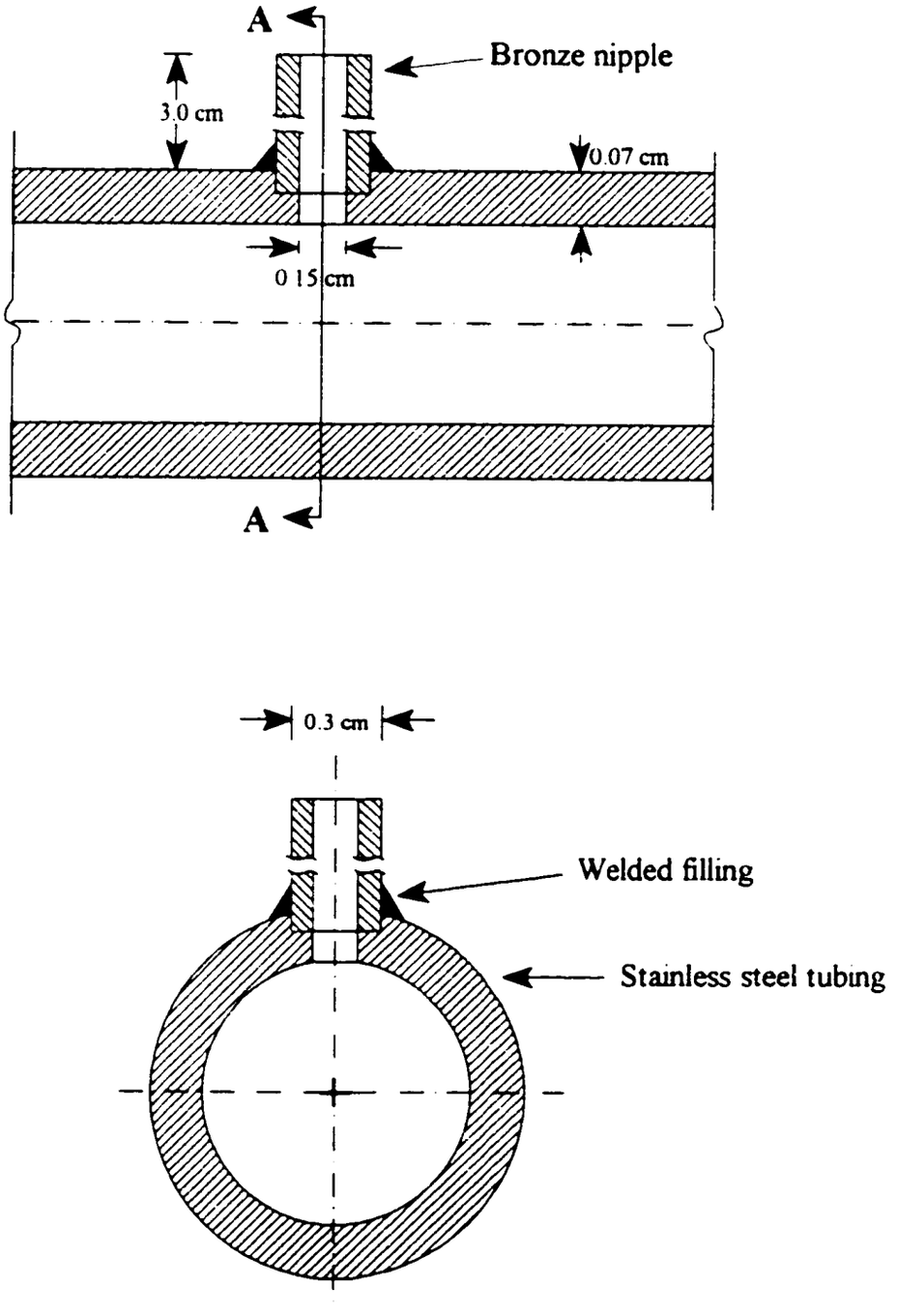

Figure 5.2- Construction details of the pressure taps

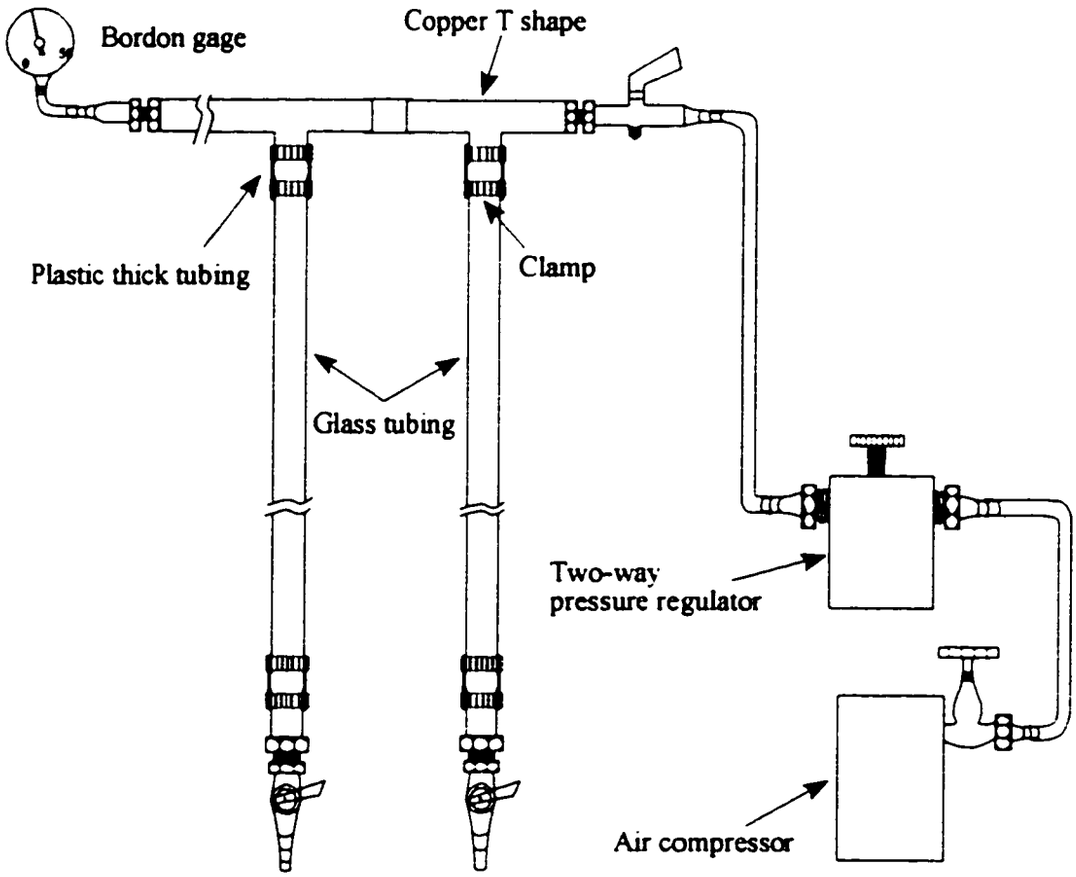

Figure 5.3- Schematic presentation of the manometer and accessories for pressure difference measurement

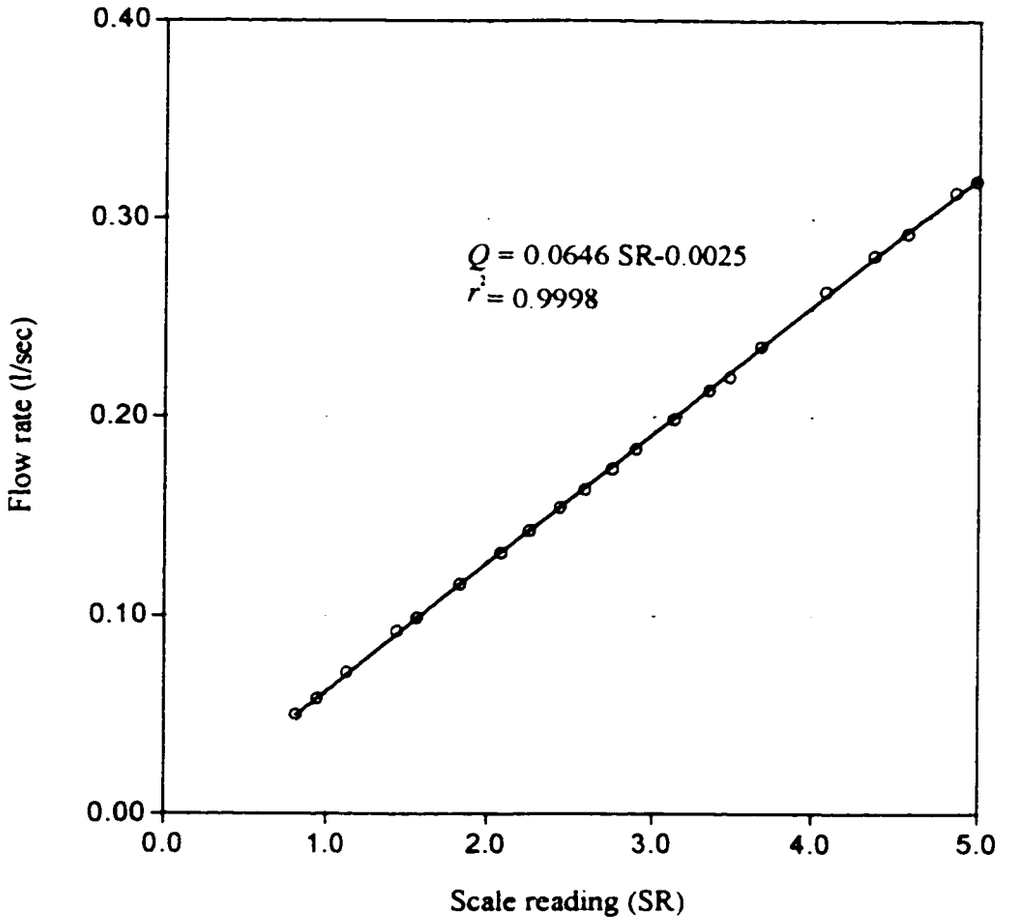

Fig. 5.4- Calibration curve for the flow meter used in the system at 24 °C

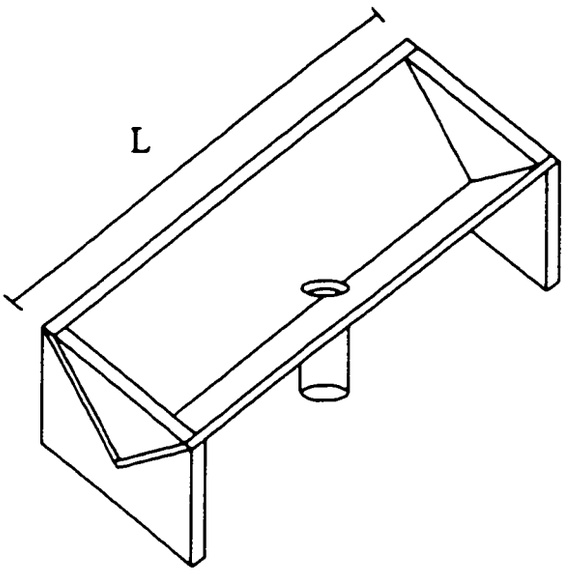

Perspective view

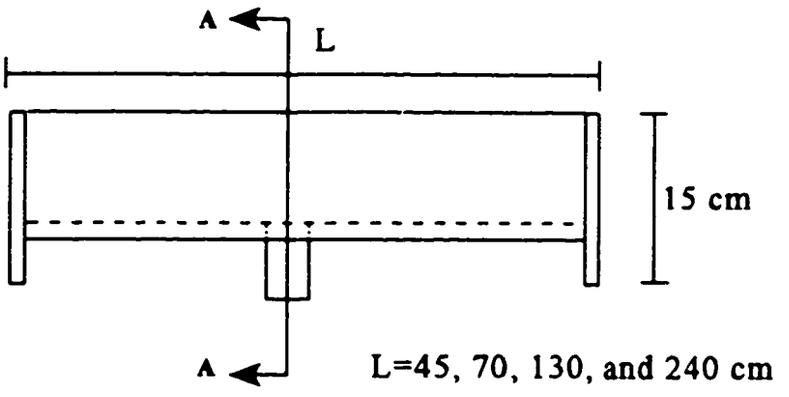

Side view

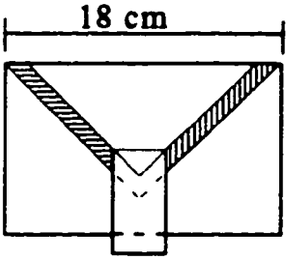

Section A-A

Figure 5.5- Schematic presentation of the collector

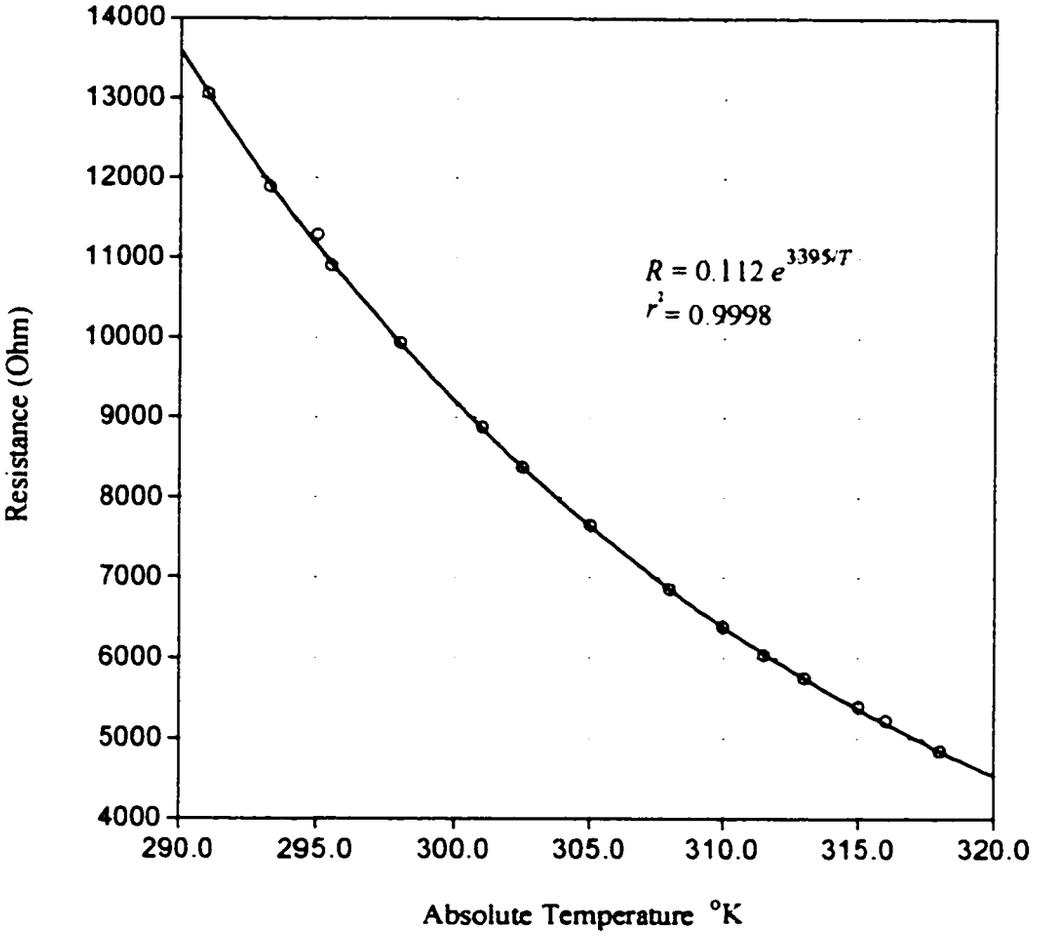

Fig. 5.6- Resistance-temperature characteristics of the thermocouple installed before test section

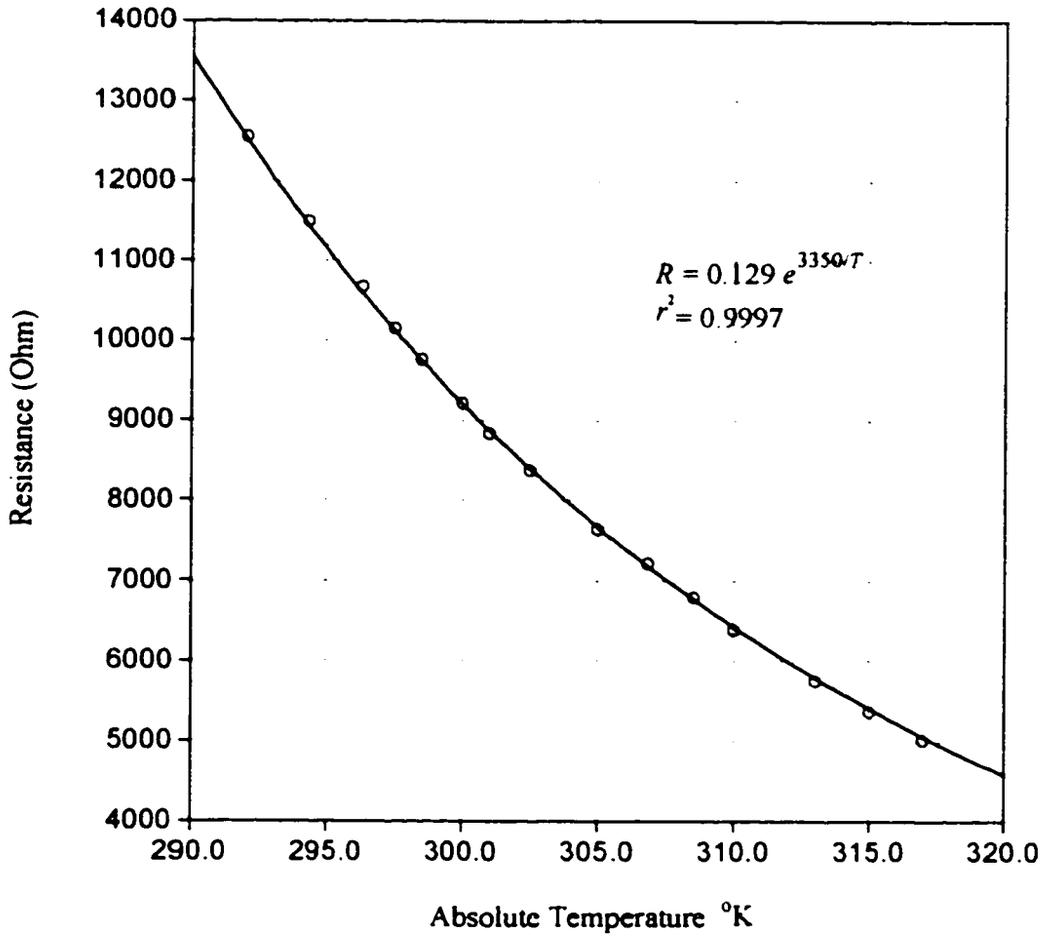

Fig. 5.7- Resistance-temperature characteristics of the thermocouple installed after test section

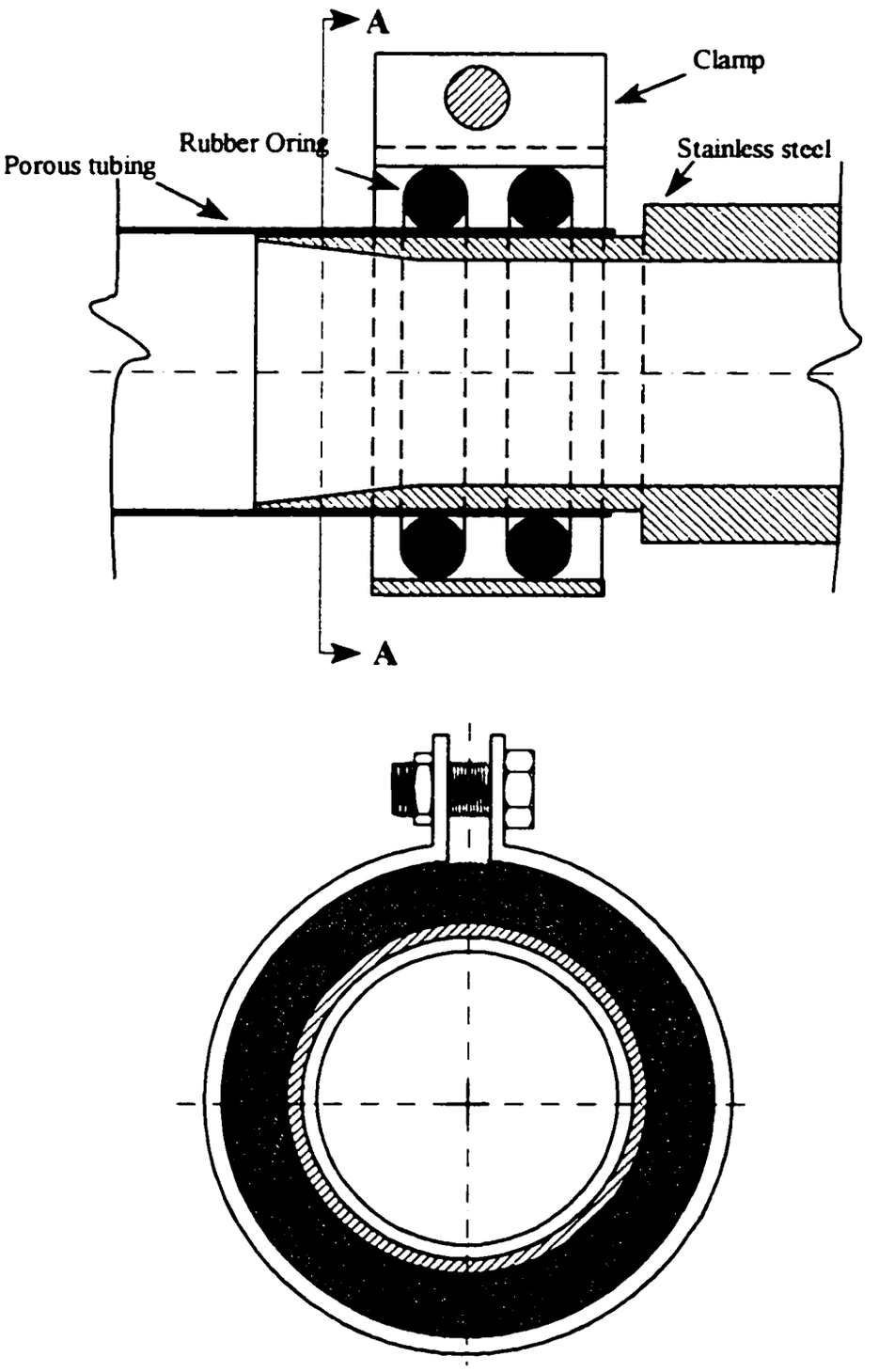

Figure 5.8- Construction details of the connection between porous tubing and stainless steel tubing

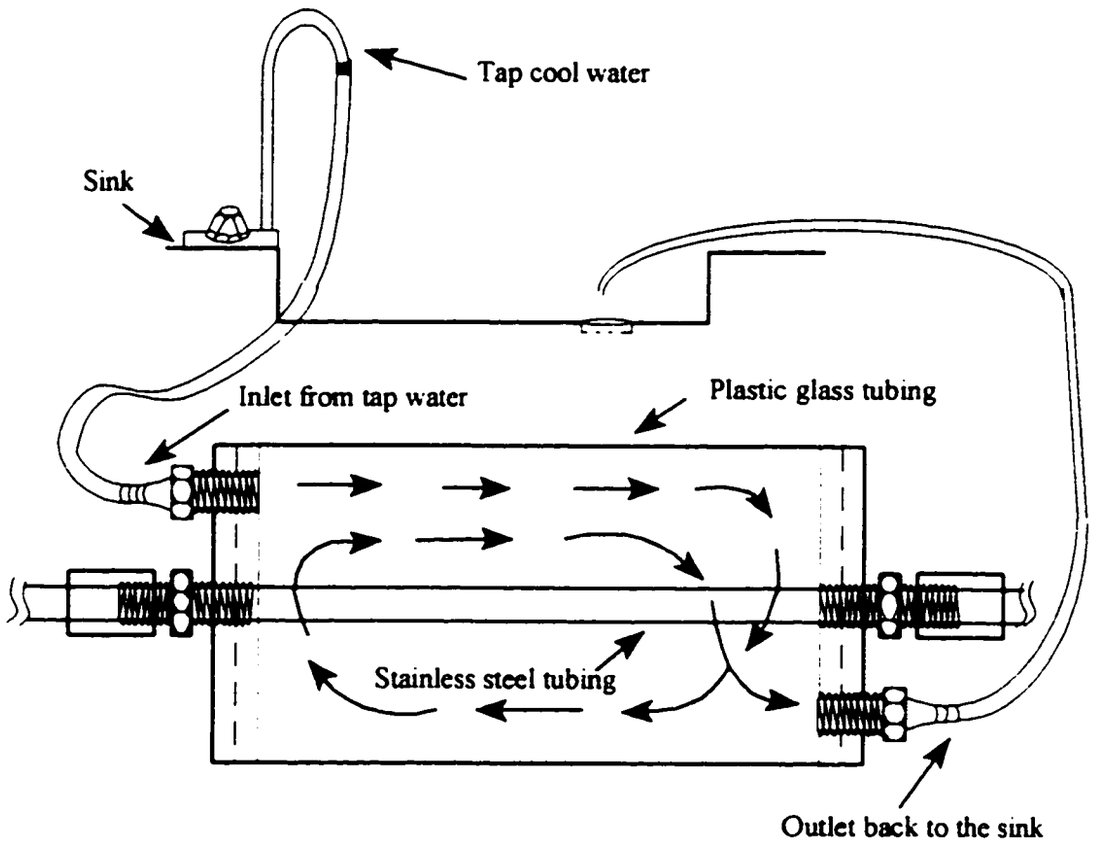

Figure 5.9- Schematic presentation of the heat exchanger used in the experimental system

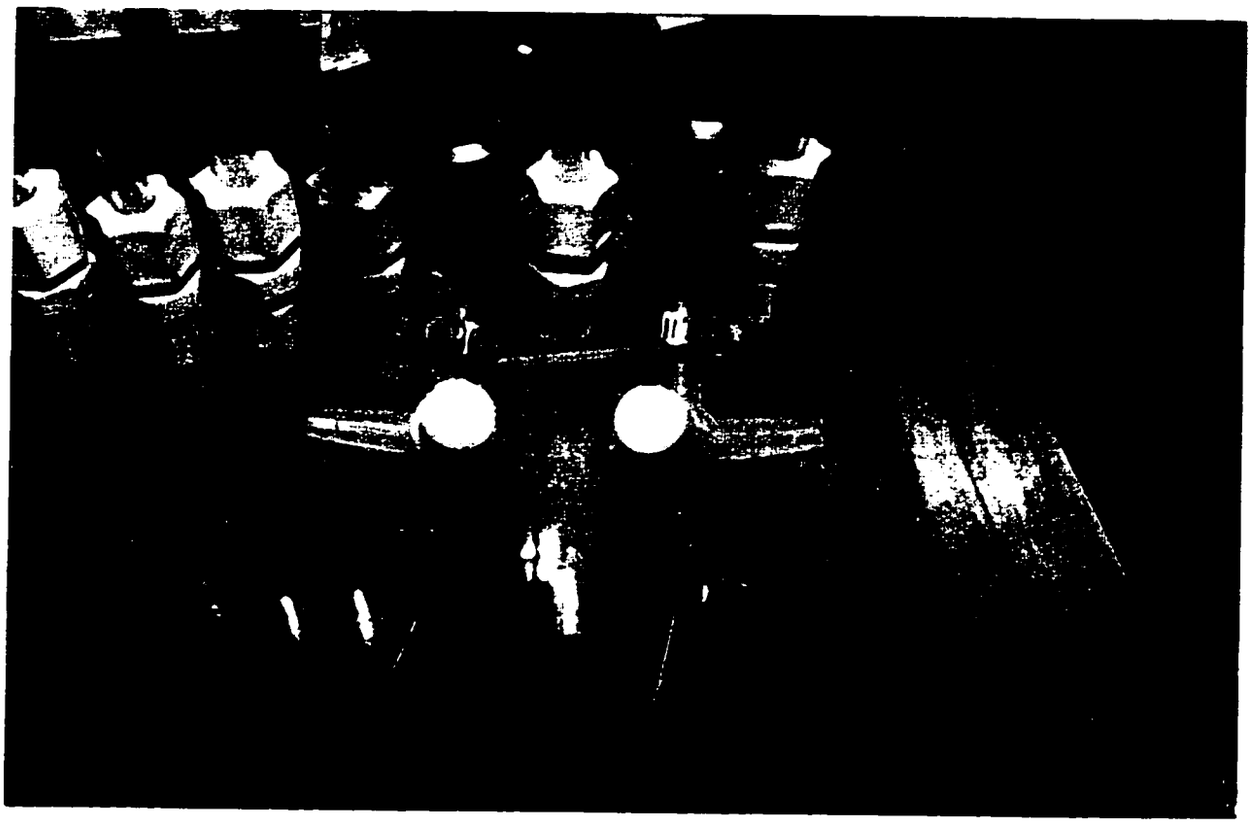

Plate 5.2- The three -way stopcocks used for bleeding the pressure tap lines in the system

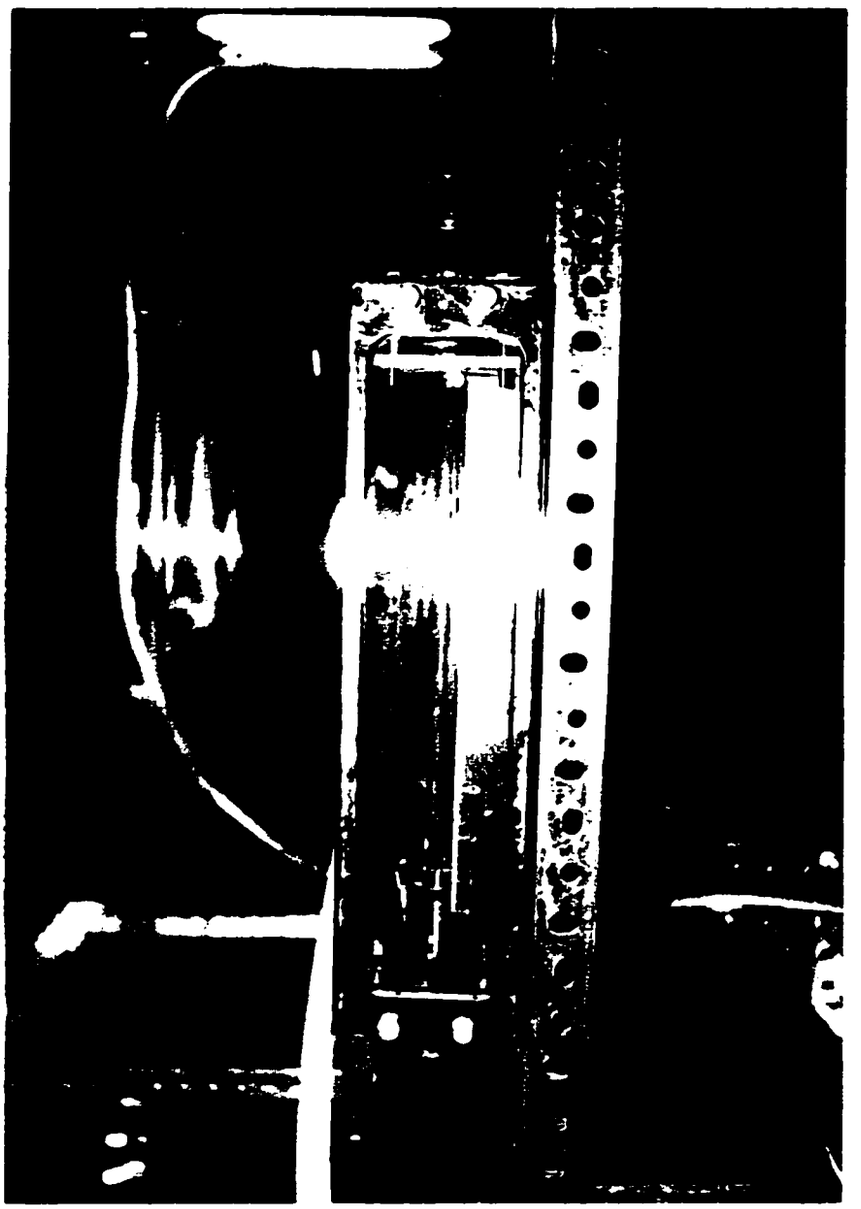

Plate 5.3- The flow meter used for flow rate measurement

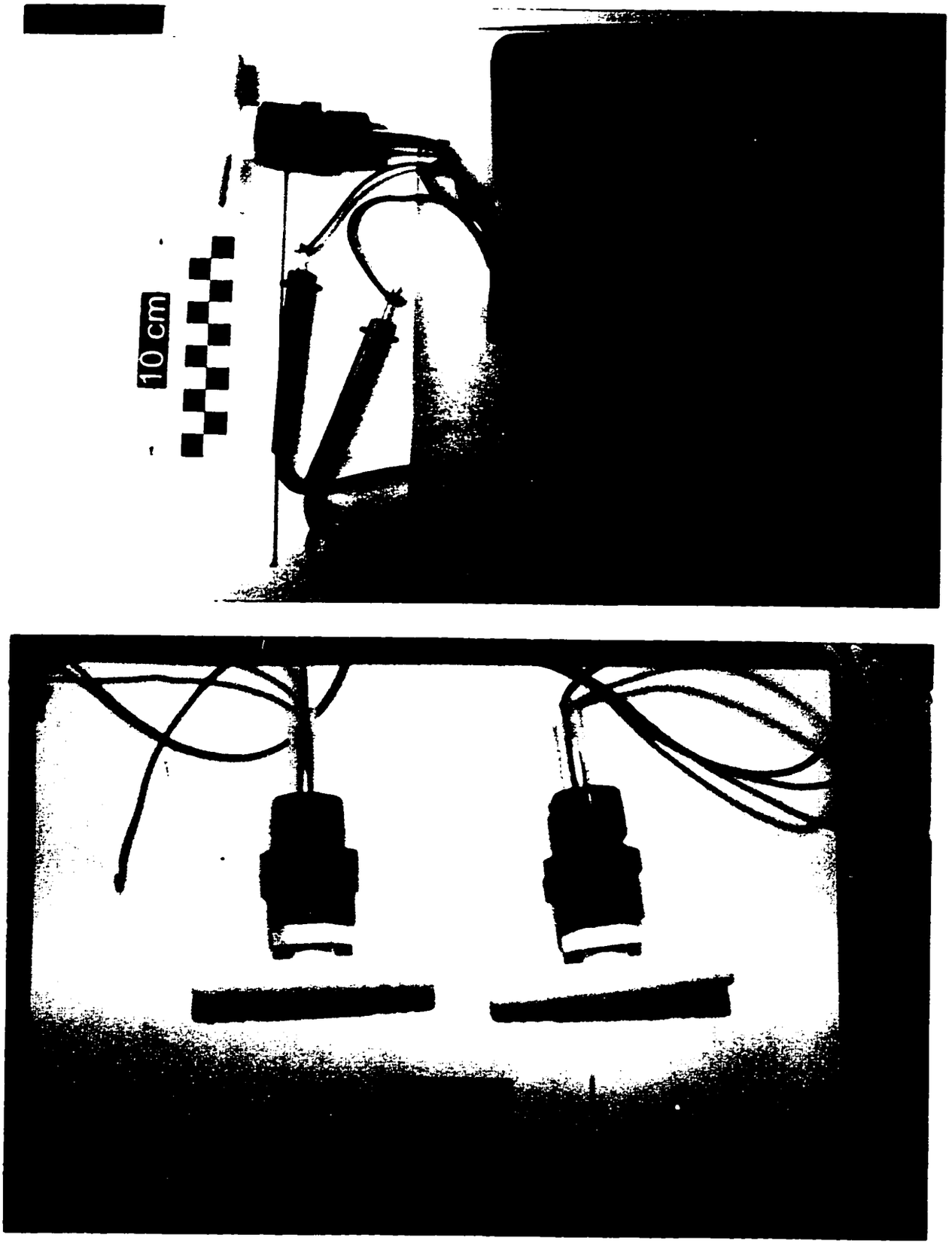

Plate 5.4- LCD digital multimeter and thermocouple used for measurement of the temperature

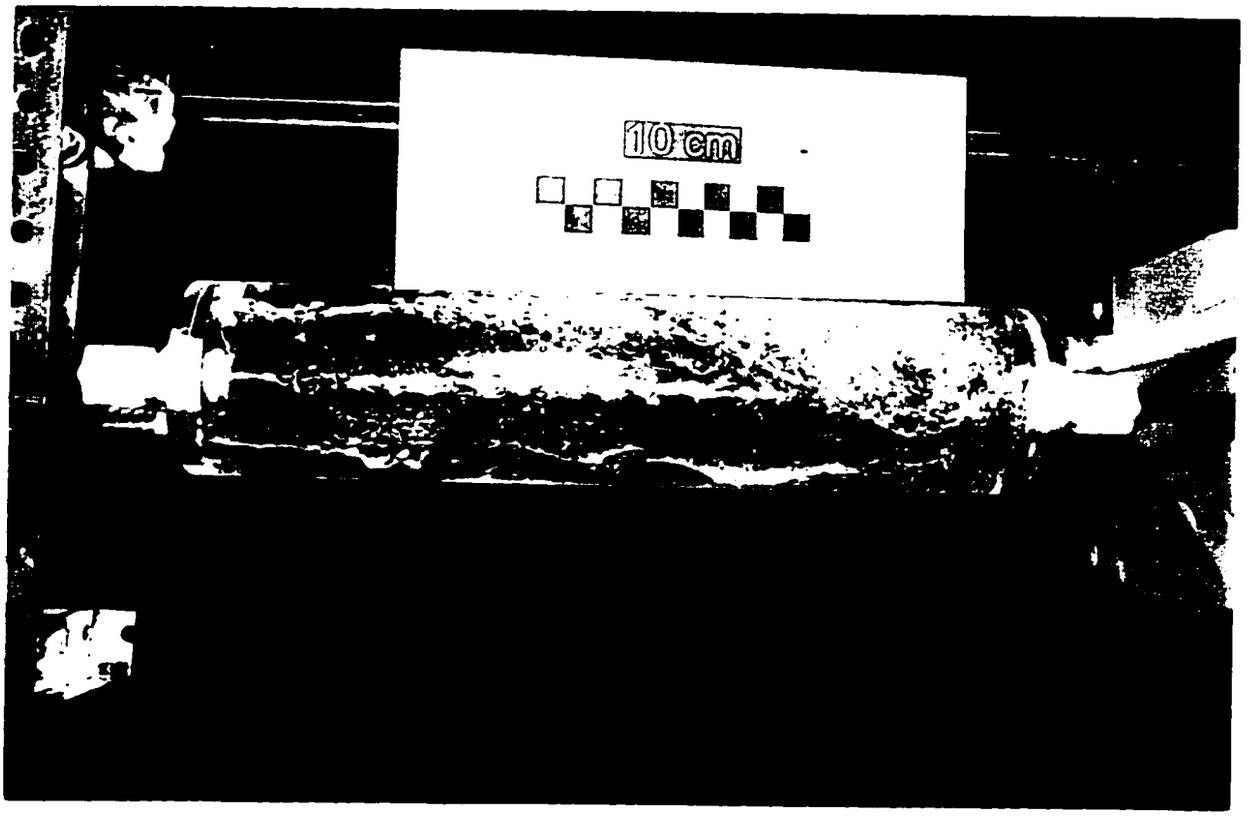

(a)

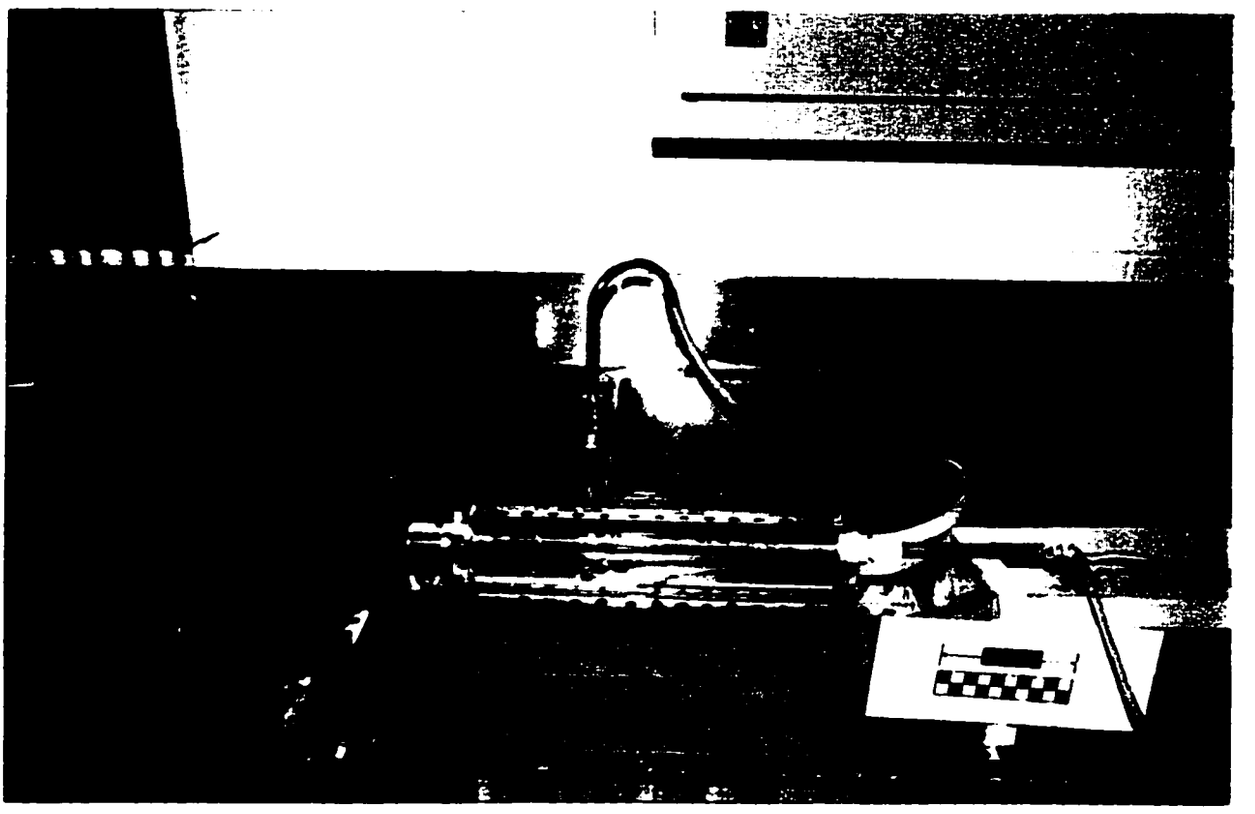

(b)

Plate 5.5- Heat exchanger used in the experimental system:
a) in use b)connection to the cold tap water

Chapter 6

6. Experimental Study

"No Suction" Flow Condition

6.1 Introduction

Porous tubing is being used for surface and subsurface irrigation purposes. The uniformity of application in a microirrigation system using porous tubing as laterals depends completely on the uniformity of the emission rate along the porous tubing. A variation of emission rate can be caused by the pressure change along the porous tubing resulting from friction losses, elevation changes, clogging, or from tolerances in the manufacturing.

In order to obtain a good uniformity of application, the pressure difference along porous tubing has to be kept within certain limits to insure a reasonably uniform emission rate.

A knowledge of the factors causing pressure differences along porous tubing is required before designing an efficient microirrigation system. Friction head loss is one of the main causes of pressure differences resulting in nonuniform emission rate. Therefore, it is important that the designer be able to calculate the friction losses in the system accurately. At the present time no information is available on the friction loss characteristics of porous tubing using for microirrigation.

This chapter deals with the analysis of the experimental data in the non-suction condition (i.e., no flow through the porous walls of the tubing) which in fact could not be directly reproduced with experimental apparatus used in this study and had to be found by extrapolation. The results of the experimental data in the non-suction condition are useful to prove that the apparatus would produce an acceptable result for experiments with suction. The first objective of this chapter is the evaluation of the relative roughness and frictional characteristics of porous tubing under study in the "no net wall flux" condition. A simple, precise and convenient head loss prediction equation will be suggested for use with small diameter porous tubing under investigation. Also a comparison will be made between the frictional characteristics of this kind of tubing and the traditional trickle irrigation laterals.

6.2 Fluid Flow in Solid Pipes

The principle of conservation of mechanical energy states that the energy change of the system is equal to the work done on the system. If there is no friction loss the resulting equation is:

$$\frac{U^2}{2g} + \frac{P}{\gamma} + z = \text{Constant} \qquad (6.1)$$

where U is the average flow velocity; g is the gravitational acceleration; P represents the pressure; γ is the specific weight of the fluid; and z is the elevation with respect to an arbitrary horizontal reference plane.

All the terms in Equation 6.1 have the dimensions of length and in hydraulics they are known as heads. Thus, $\frac{U^2}{2g}$ represents the kinetic energy or velocity head; $\frac{P}{\gamma}$ represents the pressure energy or pressure head; and z is the potential energy or gravity head. This equation is generally known as the Bernoulli equation and can be described as follows; at all points along the streamline of an incompressible fluid in frictionless steady flow, the sum of velocity head, pressure head, and elevation is constant.

In a viscous flow, internal friction converts part of the flow energy into other energy forms (mainly heat) and it is lost from the mechanical processes. Dimensionally, this loss can be considered as the friction head loss, H_L. For a steady flow of real fluids through a conduit, the energy equation is commonly written,

$$\frac{U_1^2}{2g} + \frac{P_1}{\gamma} + z_1 = \frac{U_2^2}{2g} + \frac{P_1}{\gamma} + z_2 + H_{L(1-2)} \qquad (6.2)$$

in which the head loss, $H_{L(1-2)}$, represents the drop in elevation of the energy line between sections 1 and 2. Figure 6.1 shows the energy changes between two sections of a straight pipe where the energy line, EL, represents the total head of the fluid; the hydraulic grade line, HGL, represents the piezometric head $(\frac{P}{\gamma} + z)$. The dissipation of energy by fluid friction results in a fall of piezometric head in the direction of flow, and if the pipe is of uniform cross-section and roughness and the flow has been established, the piezometric head falls uniformly (Massey 1983).

Many experiments on the flow of water in long, straight, cylindrical pipes have been conducted and the relationship among the factors determining head losses has been determined. Darcy and Weisbach proposed an equation of the form:

$$H_L = f \frac{L}{D} \frac{U^2}{2g} \qquad (6.3)$$

where H_L is the head loss (drop in energy line), L the pipe length, D the inside diameter, U the average velocity, and f a dimensionless friction factor coefficient. Many authors have established that the friction factor depends upon the Reynolds Number, Re, of the flow and the relative roughness e/D of the pipe. Dimensional analysis has yielded the following general equation:

$$f = F(Re, e/D) \qquad (6.4)$$

This functional relationship is true for Newtonian fluids flowing through circular pipes.

6.3 Smoothness and Roughness

The radial height of the wall roughness protuberances determines whether a pipe wall is "smooth" or "rough", but the effect of surface roughness on fluid flow depends on the size of the roughness relative to the thickness of the viscous sublayer. Based on this concept, a pipe wall is considered "smooth" if the roughness element height is somewhat less than the thickness of the laminar boundary layer, and "rough" otherwise. Also it has been shown that the laminar film thickness decreases when Reynolds Number increases; therefore, a given pipe wall may perform as a smooth wall at low values of Reynolds number and as a rough wall at higher values.

6.4 Previous Results of Pipe Friction Experiments

For the evaluation of pressure drop for flow through a pipe one needs to know the friction factor f. A great deal of work has been done in order to study the friction factor, f, as a function of the Reynolds Number and the relative roughness. The function represented in Equation 6.4 was studied extensively by Nikuradse (1933) working on artificially roughened pipes. Nikuradse observed, from his experiments based on artificially roughened pipes that there were large deviations if the pressure drop calculations were based on a smooth pipe. However, he gave no formulation to correlate the friction factor data. His results can not be used directly in engineering problems because of the great differences between the artificial roughness used by Nikuradse and that of commercial pipes; however, they provide a suitable basis for quantitative measurement of roughness effects on fluid flow.

Even before Nikuradse's work, it was suspected that the friction factor was not only a function of the projection of the roughness into the path of the fluid, but that it was also a function of the physical characteristics of the roughness. It is accepted that the roughness commonly found in pipes can be classified into two types: granular and wavy. The characteristics for each type of roughness are as follows:

1. Granular Roughness

The irregularities in the pipe wall are sharp and tightly spaced. The wave length of the rugosities is short and the amplitude is long. This type of roughness is characteristic of cast iron pipes, rusted iron pipes, etc.

2. Wavy Roughness

The irregularities in the pipe wall are gentle and their number per unit area is small. The irregularities have long wave length and short amplitude. This roughness is characteristic of asphalt-coated pipes, paint-coated pipes, etc.

The granular roughness corresponds to the relative roughness of sand-roughened pipes.

For wavy roughness, the work of Hopf, as cited by Prandtl and Tietjens (1952), and Jaeger (1957), indicated that if the amplitude of the irregularities is very much less than the wave length, the friction factor decreased with an increase of the Reynolds number along a line above and parallel to the very smooth-wall pipe flow curve. The ratio of the actual friction factor to the theoretical friction factor was reported to be:

1.5-2.0 for wooden pipes

1.2-1.5 for asphalt-coated pipes

1.03-1.1 for bituminous-coated pipes

Powell (1938) reported similar results for smooth pipe lines in oil and gas service. The friction factors that he obtained for this type of service were twenty percent higher than the friction factor predicted by the smooth-wall pipe equation.

Hazen and Williams, in 1920, proposed an equation in which the friction factor was a function of the surface roughness only. This equation, which is restricted to the flow of water at ordinary temperature, is widely used for pipe flow computation. The Hazen-Williams equation can be expressed as:

$$\Delta H = k_1 \frac{Q^{1.852}}{C^{1.852} D^{4.871}} L \qquad (6.5)$$

where ΔH : pressure head loss in the pipe, m

D : inside diameter of the pipe, cm

Q : flow rate in the pipe, L/sec

C : Hazen-Williams coefficient of relative roughness of the pipe, dimensionless

=140 for new steel pipes

=130 for new cast iron pipes

=110 Average cast iron, new riveted steel, vitrified sewer

L : length of the pipe, m

k_1 : 5.35 in SI units

The Hazen-Williams coefficient of relative roughness was found to be directly proportional to the Reynolds number. Therefore, the C-value should be varied with the

flow rate when using the Hazen-Williams equation to calculate head losses, although in engineering practice this is rarely done.

According to Morris and Wiggert (1972), the Hazen-Williams formula is not recommended for calculating head the loss in small-diameter pipes and at low values of Reynolds number. Since the equation is dimensionally non-homogeneous, no account is taken of fluid viscosity. The equation is also based on data obtained at fairly high Reynolds numbers, with a high degree of turbulence.

In the laminar flow regime the friction factor is a function of the Reynolds number only, whereas in the case of turbulent flow the friction factor is a function of Reynolds number and also the relative roughness factor. Blasius showed analytically that the friction factor for turbulent flow in a smooth pipe is a function of Reynolds number only. He examined the experimental data on pressure loss and obtained the following empirical relation

$$f_{Blasius} = 0.3164 Re^{-0.25} \qquad (6.6)$$

Prandtl (1945) using boundary layer theory, mixing length hypothesis and the law of the wall, developed a theoretical law of friction for smooth pipes in turbulent flow as follows

$$\frac{1}{\sqrt{f}} = -2\log\left(\frac{2.51}{Re\sqrt{f}}\right) \qquad (6.7)$$

The best fit of the experimental data points of Nikuradse gives the von Karman-Nikuradse smooth pipe equation

$$\frac{1}{\sqrt{f}} = 2\log(Re\sqrt{f}) - 0.8 \qquad (6.8)$$

It is interesting that some of the newer types of pipes have been found to give friction factors somewhat smaller than specified by the Karman-Nikuradse smooth-pipe equation, indicating that perhaps the smooth-pipe of the earlier investigators may not have been truly smooth after all (Morris and Wiggert, 1972).

In the case of fully developed turbulent flow condition, von Karman first established the following relation for friction in a fully rough pipe

$$\frac{1}{\sqrt{f}} = -2\log\left(\frac{e/D}{3.76}\right) \qquad (6.9)$$

Colebrook developed a mathematical function which, as he claimed, gave a transition curve between smooth and rough pipe and more closely agreed with actual measurements. He simply combined the expressions for the friction factor for smooth and rough pipes, i.e., Prandtl's smooth pipe law of friction and von Karman's fully rough pipe law of friction as

$$\frac{1}{\sqrt{f}} = -2\log\left(\frac{2.51}{Re\sqrt{f}} + \frac{e/D}{3.76}\right) \qquad (6.10)$$

In the above equation , f appears on both sides of the equation and the solution can only be obtained by a trial and error procedure. Because of the inconvenience in solving this equation algebraically, Moody plotted the friction factor as a function of the Reynolds Number with the relative roughness of curves corresponding to various values of e/D. These curves are known as the Moody Diagram which has been widely adopted for the

solution of engineering problems. Figure 6.2 shows the original Moody diagram from which the following points can be noted:

1. In the laminar region (Re <2000), the flow is under the control of viscous forces only; therefore in this region, the friction factor is independent of surface roughness.

2. Between Reynolds numbers of 2000 and 4000, the difference between the laminar and turbulent flow is clearly established by the change in the relationship of f to Re near the critical Reynolds number of 2000.

3. Above a Reynolds number of 4000 two regions are found: the transition zone and the rough-pipe zone. In the transition zone the friction factor is a function of Re and e/D, but at a higher Reynolds number in the rough pipe zone, it depends only upon the relative roughness as indicated by the horizontal lines of constant f .

4. The divergence of the rough pipe curves from the smooth pipe curve indicates that smooth pipes at a low Reynolds Number become rough at high values of Re .

It is one of those amazingly fortuitous happenings in engineering, and a tribute to Colebrook's insight, that this simple addition of the two limiting equations for the friction factor, namely, that for smooth and that for fully rough pipes, also predicts a transition region friction factor which is more realistic concerning the performance of commercial pipe than are Nikuradse's extensive experimental data which led to the two accepted limiting equations. Benedict (1980) states, "Colebrook's entirely empirical arrangement of Prandtl's and von Karman's equations has only one thing in its favour: it works." He points out, as did Colebrook and White, that the values of 2 and 2.51 that appear in the

equation are experimentally-determined coefficients relating to turbulence and boundary conditions, respectively.

Barr (1972) proposed the following equation for friction factor in the transition region,

$$\frac{1}{\sqrt{f}} = -2\log\left[\left(\frac{5.15}{Re^{0.892}}\right) + \left(\frac{e/D}{3.7}\right)\right] \qquad (6.11)$$

Later this equation was modified by Barr (1975) to become,

$$\frac{1}{\sqrt{f}} = -2\log\left[\left(\frac{5.1286}{Re^{0.89}}\right) + \left(\frac{e/D}{3.7}\right)\right] \qquad (6.12)$$

Churchill (1973) proposed the following equation for friction factor in the transition region,

$$\frac{1}{\sqrt{f}} = -2\log\left[\left(\frac{7}{Re}\right)^{0.9} + \left(\frac{e/D}{3.7}\right)\right] \qquad (6.13)$$

Swamee and Jain (1976) proposed a similar type of equation for friction factor in the transition region as

$$\frac{1}{\sqrt{f}} = -2\log\left[\left(\frac{6.97}{Re}\right)^{0.9} + \left(\frac{e/D}{3.7}\right)\right] \qquad (6.14)$$

Haaland (1983) gave the following equation for friction factor in the transition region

$$\frac{1}{\sqrt{f}} = -2\log\left[\left(\frac{6.9}{Re}\right) + \left(\frac{e/D}{3.7}\right)^{1.11}\right] \qquad (6.15)$$

Much experimental and theoretical work has been done on the applicability of the Moody diagram and formulae developed in pipes of different materials and diameters. However, detailled information on low flow in small diameter tubing, such as that used in microirrigation systems, cannot be found in standard hydraulic handbooks and tables.

Aggarwal et al. (1972) performed experiments with air flowing in a porous tube of circular cross- section with fully-developed turbulent profile at the entrance. His experiments covered an inlet Reynolds number range of 11,000-101,000. A porous bronze tube with 26.42 mm inner diameter and length-to-diameter ratio of about 9.3 was employed in his experiments. Friction factors in "no net wall flux" condition were calculated for a range of inlet Reynolds numbers. These are seen plotted against Re_D in Figure 6.3. From his experimental data, he concluded that the Colebrook-White semi-empirical relation is a good relation for predicting friction factors in porous pipe tubing in "no net wall flux."

Mellis et al. (1993) conducted experiments with ultraclean water flowing in a porous tube of circular cross section made from sintered stainless steel powder (SS 316). In his experiments the ultraclean water was produced by exposing tap water to a carbon filter, a reverse osmosis FT-30 membrane module (RO, FilmTec. Corp., MN), ion exchangers and an UV sterilizer (whole system assembled by Megometrics, Syracuse, NY). The inner diameter and the length of the tubing were 1.63×10^{-3} m and 0.301 m, respectively. Mellis et al. noticed that the non-dimensional pressure drop along the porous tubing as a function of axial Reynolds number falls below the Blasius prediction for turbulent flow in a smooth

solid pipe or in a rough pipe (with a roughness factor of $k = 0.004$). The experimental results of Mellis et al. for the "no net wall flux" is shown in Figure 6.4. In this figure the ordinate parameter f is the friction coefficient and Re_{xx} is the axial Reynolds number. The skin friction coefficient (fanning friction factor) f in this figure is 1/4 times the friction factor coefficient f defined in Equation 6.3. The discrepancy between the flow in the porous tube in the "no net wall flux" case and the flow in a solid pipe can be attributed to the set-up used in the experiment. In this set-up the porous tube was encased in a stainless steel tube housing and the wall flow rate was controlled by a valve installed on the stainless steel tube housing. In the "no net wall flux" situation, a portion of the main axial flow inside the porous tube leaks through the porous wall into the shell space close to the entrance due to the high pressure and may then return to the lumen near the end of the porous tube section due to an inverse pressure gradient.

Von Bernuth and Wilson (1989) performed experiments using two commercially available 16 mm and 26 mm inside diameter PVC pipes and a commercially available 14 mm inside diameter polyethylene tubing used in drip irrigation. His experiments covered a Reynolds number range of 4,000-60,000. He found that the Colebroke-White equation is not a good predictor of the Darcy-Weisbach (D-W) friction factor for small diameter plastic pipe and for Reynolds numbers less than 100,000. He proposed a power function relating the friction factor to the Reynolds number (similar to Blasius equation for smooth pipes in turbulent flow, $f = aRe^b$) as an accurate and convenient equation for calculating the Darcy-Weisbach (D-W) friction factor for small diameter tubing. The results of von

Bernuth for 14mm polyethylene tubing, 16 mm PVC and 26 mm PVC pipe are shown in Figures 6.5, 6.6 , and 6.7, respectively.

6.5 Friction Head Loss Measurement Without Suction

The condition of no transverse flow through the tube walls (flow without suction) is characterized as "no net wall flux" in this study. Although this condition does not happen in reality, the information obtained in the "no net wall flux" condition can be considered as a reference for evaluation of flow with suction (which is characterized as "wall flux" condition). Also relative roughness, e/D, of the porous tubing used in this study can be evaluated from information obtained in the "no net wall flux" condition. A comparison of frictional characteristics of porous tubing with other laterals used in trickle irrigation systems is possible with the evaluation of pressure drop in the "no net wall flux" condition. Also the "no net wall flux" can be considered as a control point to check if the apparatus could qualify for experiments with suction.

When there is mass transfer at the wall ("wall flux" condition), the momentum change of the flow tends to cause an increase in pressure in the flow direction, while the friction at the wall tends to decrease the pressure. At the "no net wall flux" condition friction at the wall is responsible for all pressure drop and momentum change does not contribute in pressure drop. Therefore, it is expected that the flow condition within the system is the same as a solid tube.

To generate different values of axial Reynolds number within the porous section in the turbulent regime, depending on the value of axial Reynolds number, different values of pressures at the feed side of the porous section are necessary. These pressures cause radial flow rate and momentum changes along the tubing. Therefore, generation of "no net wall flux" condition in the laboratory is impossible. Measured pressure drop in this condition is a combination of friction pressure loss and momentum changes along the tubing.

Although for the "no net wall flux" condition, direct measurements of the pressure drops at different axial Reynolds number is impossible, these values can be obtained from the relationship between radial Reynolds number (defined as $Re_w = \frac{DV_w}{\upsilon}$ where D: diameter of tubing, V_w: radial velocity at the porous wall, and υ: kinematic viscosity of fluid) and dimensionless pressure drops (normalized with inlet dynamic head) at a particular axial Reynolds number. Figure 6.8 indicates the variation of radial Reynolds number with dimensionless pressure drop for an inlet axial Reynolds number equal to 30,527 and $L/D = 206.4$. As it can be seen from this figure the minimum measurable value of Re_w is 8.1 and this is for the situation where the exit valve is completely open and the inlet valve is open to such a degree that the desired inlet axial Reynolds number can be achieved. The "no flow wall flux" occurs where the radial Reynolds number is zero. By extending the best fit curve up to Re_w=0 the value of dimensionless pressure drop for the "no net wall flux" can be obtained. Many experimental measurements were taken to improve the

confidence in the data for extrapolating up to $Re_{ao} = 0$. The dotted line shows the portion of the curve that has been plotted by extrapolation.

Figures 6.9 through 6.14 indicate the variation of radial Reynolds number with dimensionless pressure drop with the inlet axial Reynolds number as a parameter and $L/D = 206.4, 159.6, 106.4, 79.8, 53.2$, and 26.6, respectively. Since generating high inlet Reynolds number needs a high pressure at the feed side of porous section, the gap in measured data between $Re_w = 0$ and the minimum measurable Re_w increases with increasing inlet axial Reynolds number for a particular L/D. Also for a particular inlet axial Reynolds number the lack of data increases with decreasing L/D.

6.6 Analysis and Discussion

6.6.1 Relative Roughness

This section deals with the investigation of the validity of the Colebrook-White equation in predicting the friction factor in small sizes of the porous tubing. Also the roughness of the porous tubing is determined hydraulically using the Colebrook-White equation. The Colebrook-White equation is an empirical transition function for commercial pipes for the region between smooth pipes and the complete turbulence zone. This equation is the basis for the Moody diagram.

The average velocity of the fluid flowing in a pipe is greatly affected by the pipe roughness (Binder, R. C. 1962; Benedict, R. P. 1980). Therefore, the relative roughness is one of the most important factors for all pipe flow calculations. The relative roughness is defined as e/D, where e is the equivalent sand roughness and D the diameter of the pipe.

The relative roughness of the porous tubing was obtained hydraulically using the Colebrook-White equation. There are two reasons for indirect measurements of relative roughness in porous tubing. The first reason is the lack of a satisfactory and accepted technique for direct measurement of the pipe roughness. Secondly, since the porous tubing is an extruded membrane, its surface does not have uniform roughness and direct measurement of an average of the surface roughness would be extremely difficult.

The values of the dimensionless pressure drop for the "net wall flux" condition at different inlet axial Reynolds numbers and for different L/D were obtained from Figures 6.9 through 6.14. The values of the no-suction friction factors f_0 were then calculated using a modified form of the Darcy-Weisbach equation:

$$f_0 = \frac{P_o - P_i}{1/2\rho U_i^2} \times \frac{D}{L} \qquad (6.16)$$

The result of the calculation has been summarized in Table 6.1. The analyses of the data were performed using SAS (SAS Institute 1985) program. Nonlinear regression procedures and linear regression procedures were used to analyze the data.

There are several approaches that could be taken for calculating the relative roughness factor from the Colebrook-White equation.

1. In the Colebrook-White equation, e is forced to become non-negative and $e\,D$ is then computed. According to Urbina 1976, Paraqueima (1977) and Norum (1984) the maximum value for the second coefficient in the Colebrook-White equation is 1.67 if the non-negativity assumption was retained.

2. The second approach is to assume that the 2.51 coefficient value is correct and remove the nonnegativity constraint.

3. The third approach is to allow both the roughness and the second coefficient to be determined by regression.

Von Bernuth et al. (1989) calculated the roughness factor by the second approach. Venkatesan et al. (1990) used the first approach for the calculation of the roughness. The second approach was used in this study.

The values of the friction factor were plotted versus Reynolds number on a log-log paper. Also plotted on the same graphs are friction factors for hydraulically smooth tube as computed from the Blasius friction law (Eqn. 6.6). Using a nonlinear regression procedure the Colebrook-White equation was fitted to the data with relative roughness as a parameter. The best fit of the data resulting from Colebrook-White equation are indicated in Figures 6.15 through 6.20 for $L/D = 26.6$, 53.2, 79.8, 106.4, 159.6, and 206.4, respectively. Also for each length the value of the relative roughness has been obtained with 95 percent confidence interval. Table 6.2 summarizes the values of relative roughness

and non-linear least squares statistics for different L/D. As can be seen, the lowest coefficient of determination occurs in the shortest porous tube. With increasing length of the porous tubing the coefficient of determination improves. The last row of the table 6.2 indicates the result of the regression when all points are considered in the regression analysis. The value of the relative roughness in this case can be considered a representative of the relative roughness of the porous tubing under study.

Friction factors were predicted by applying the Colebrook-White equation (Eqn. 6.10) with e/D=0.00204 to the various test data, and these were then compared with observed values (Figure 6.21). Figure 6.21 indicates that applying the Colebrook-White equation with a relative roughness of 0.00204 fits the data well and all of the data fall within ±5% error lines.

The absolute roughness value of the porous tubing under study is compared to those of the other tubes used as laterals in trickle irrigation. Table 6.3 shows the absolute roughness values collected from literature as well as that of the present study. The values collected from the literature, except for Venkatesan et al. (1990), were calculated by the first and second approaches. There is no physical explanation for some of the data sets resulting in negative roughness coefficients. The data in column 5 show that the porous tubing under investigation is smoother than many of the tubes used as laterals in trickle irrigation.

In Figure 6.22 the frictional characteristics of the porous tubing under study is compared with frictional characteristics of another porous tubing made of bronze alloy and the frictional characteristics of a plastic tubing. The porous tubing made of bronze alloy had an inner diameter of 26.42 mm and its frictional characteristic was investigated by Aggarwal et al. (1972). The plastic tubing had an inner diameter of 26 mm and its frictional characteristic was investigated by von Bernuth et al. (1989). From this figure it can be seen that the data obtained from the present study and those obtained from the Aggrawal et al. (1972) investigation (both porous tubing) agree with Colebrook-White equation. However, data obtained by von Bernuth et al. shows that the Blasius equation (b=-0.25) is an accurate equation for small diameter plastic tubing when the Reynolds number is less than 100,000.

6.6.2 Blasius Equation

As mentioned earlier several researchers (Von Bernuth et al., 1989; Venkatesan et al., 1990) have reported friction head loss data for small diameter pipe indicating that frictional characteristics of small diameter tubing, with Reynolds number less than 100,000, does not agree with the Colebrook-White equation. Their experiments have shown that for Reynolds numbers less than 100,000, the Blasius equation (b=-0.25) is an accurate predictor of the Darcy-Weisbach friction factor. The validity of the Blasius equation (b=-0.25) in predicting friction factors for the porous tubing under study is shown in Figures 6.23 through 6.28 for L/D = 26.6, 53.2, 79.8, 106.4, 159.6, and 206.4, respectively. As can be seen from these figures, for all lengths of tubing the Colebrook-White equation is a better predictor of the friction factor than to the Blasius equation.

6.6.3 Head Loss Prediction Equation

The second objective of this chapter was to determine a simple and easy to use head loss prediction equation, to be used by designers in designing porous tubing in microirrigation. Although the regression analysis for the coefficient in the Blasius equation ($f = a\,\mathrm{Re}^{b}, b = -0.25$) does not produce an accurate prediction equation for the friction factor in small size diameter in porous tubing, a power function ($f = a\,\mathrm{Re}^{b}$) relating the friction factor to the Reynolds number fits log-log data with an acceptable accuracy.

The power functions were found for different L/D using a generalized least square fit procedure. Figures 6.29 through 6.34 indicate the power functions relating friction factor to the Reynolds number for $L/D = 26.6$, 53.2, 79.8, 106.4, 159.6, and 206.4, respectively. Also in Figure 6.35 the power function can be seen when all points for different L/D are considered in the analysis. From this analysis the following equation was selected which can be considered a representative for all lengths of tubings.

$$f_0 = 0.198 Re^{-0.189} \tag{6.17}$$

A simple, easy to use, and convenient head loss prediction equation results from the combination of the D-W equation (Eq. 6.3) and equation 6.17

$$H_L = 0.198\,\mathrm{Re}^{-0.189}\,\frac{L}{D}\,\frac{U^2}{2g} \tag{6.18}$$

Substituting for $\mathrm{Re} = \dfrac{UD}{\upsilon}$

$$H_L = 0.198\left(\frac{UD}{\upsilon}\right)^{-0.189}\,\frac{L}{D}\,\frac{U^2}{2g} \tag{6.19}$$

Substituting $U = \frac{Q}{A}$ and $A = \frac{\pi D^2}{4}$ one obtains:

$$H_L = 0.198\left(\frac{4Q}{\upsilon\pi D}\right)^{-0.189} \frac{L}{D}\frac{8Q^2}{g\pi^2 D^4} \qquad (6.20)$$

Rearranging the above equation results in:

$$H_L = 0.198\left(\frac{8\times 4^{-0.189}}{g\pi^{1.811}}\right)\upsilon^{0.189}Q^{1.811}D^{-4.811}L \qquad (6.21)$$

where H_l=head loss; υ =kinematic viscosity; Q= flow rate in the pipe; L =pipe length; g = gravitational constant

By substituting K for all of the constants in Equation 6.21 one obtains:

$$H_L = K\upsilon^{0.189}Q^{1.811}D^{-4.811}L \qquad (6.22)$$

The value of $K = 1.564\times 10^{-2}$ for SI (meter, second) units and $K = 4.762\times 10^{-3}$ for English (foot, second) units.

Equation 6.22 has a form similar to Hazen Williams equation (Equation 6.5). One can see that the exponents for Q, D, and L in this study were found 1.811, -4.811 and 1 , respectively. These exponents in the Hazen Williams equation are 1.852, -4.871, and 1, respectively. The advantage of this equation compared to the Hazen Williams equation is that this equation contains a viscosity parameter which is correctable for temperature (viscosity) changes.

Head losses were predicted by applying Equation 6.22 to the various test data, and these were then compared with observed values (Figures 6.36 through 6.38). Since the data

cover a wide range of the head losses, comparison between measured and predicted values has been made in three graphs. Figures 6.36 through 6.38 indicate that this simple and easy to use equation fits the data well and all of the data fall within ±5% error lines.

Although the use of Eq. 6.22 (transition zone friction head loss equation) when the Reynolds number is less than 4,000 will lead to large errors, the frictional head losses are negligible due to the low velocities. It has to be noted that Equation 6.22 applies to new and clean porous pipe. The pipe surface might deteriorate with age and consequently the effective roughness of the porous pipe might vary with time. The rapidity of the roughness variation will depend upon the quality of the water. In addition to the variation in roughness there may be an appreciable change in effective diameter, making an estimate of performance speculative.

6.7 Conclusion

Some researchers (von Bertuth et al.,1989; Venkatesan et al.,1990) found that the Colebrook and White (C-W) equation is not a very good predictor of the friction factor for small diameter plastic pipe for Reynolds numbers less than 100,000. However analysis of the friction loss data obtained for small diameter porous tubing in this study confirmed that the Colebrook and White (C-W) equation is a very accurate predictor of the friction factor for porous tubing with small diameter size and Reynolds number less than 100,000. These results are in agreement with the results of the another researcher (Aggarwal et al, 1972). The equation for computing the friction factor in the Darcy-Weisbach pipe friction loss equation, as presented by Colebrook and White (C-W) has been preferred because of

its presumed superior accuracy and sound theoretical basis. The C-W equation is the basis for the well-known friction factor (Moody) diagram.

The value of the relative roughness obtained in this study showed that the porous tubing under study is smoother than many of the tubing used as lateral in the traditional trickle irrigation. Also, the fact that the friction factors agreed with the Colebrook-White law indicates that the physical roughness in the porous tubing under study corresponds very nearly to the equivalent sand roughness with a relative roughness of about $e/D = 0.002$.

A combination of a power function and Darcy-Weisbach equation was proposed as a convenient and accurate head loss prediction equation (within 5% error). The combination equation is dimensionally homogeneous, correctable for viscosity changes, and accurate for porous pipe tubing under study.

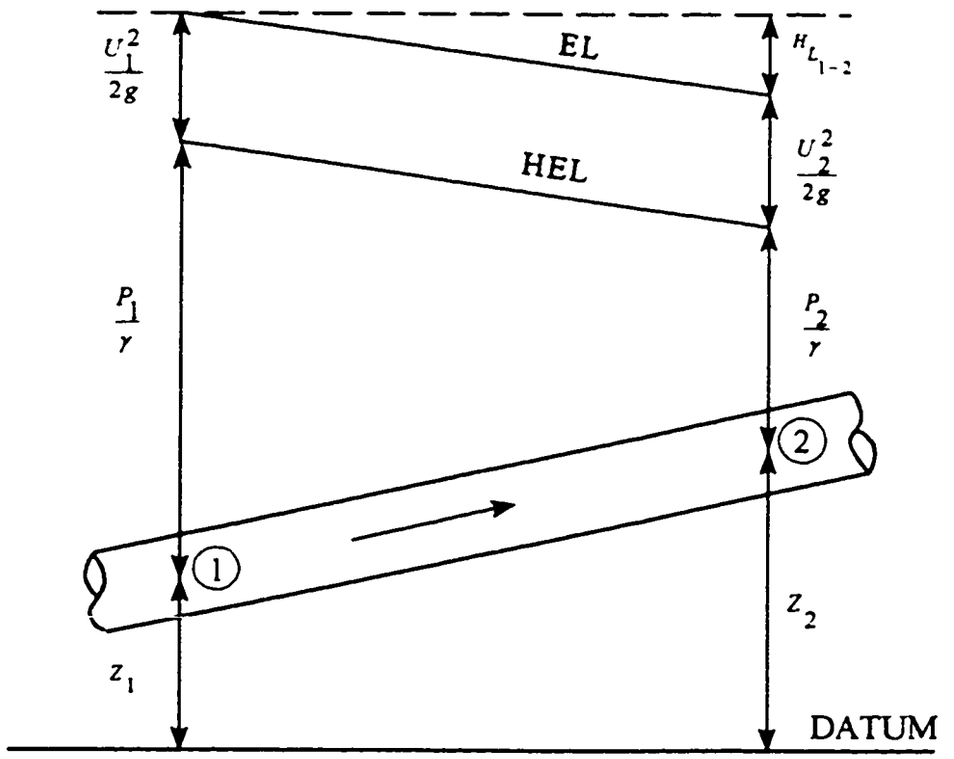

Figure 6.1- Energy changes in fluid flow through a pipe

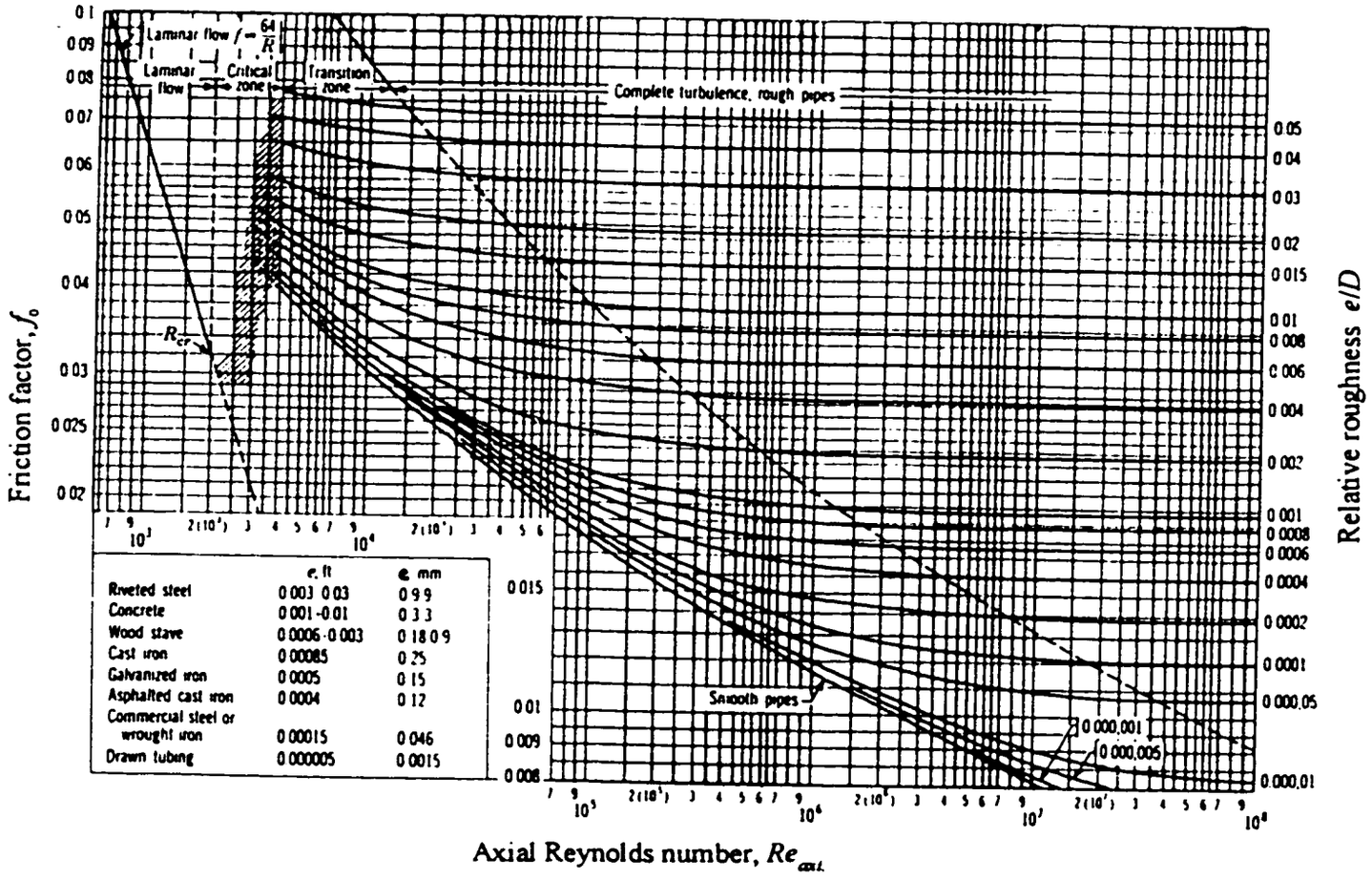

	e, ft	e, mm
Riveted steel	0.003-0.03	0.9-9
Concrete	0.001-0.01	0.3-3
Wood stave	0.0006-0.003	0.18-0.9
Cast iron	0.00085	0.25
Galvanized iron	0.0005	0.15
Asphalted cast iron	0.0004	0.12
Commercial steel or wrought iron	0.00015	0.046
Drawn tubing	0.000005	0.0015

Figure 6.2- The Moody chart for pipe friction with smooth and rough walls

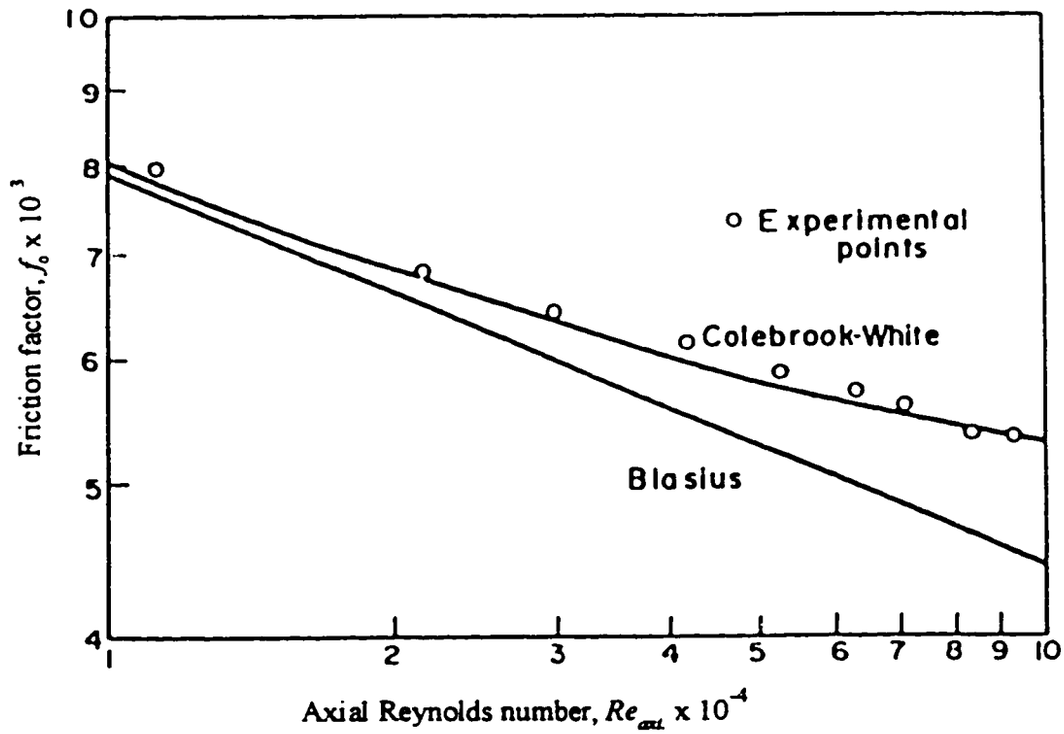

Figure 6.3- Friction factor as a function of axial Reynolds number in the "no net wall flux" case (Aggarwal et al., 1972)

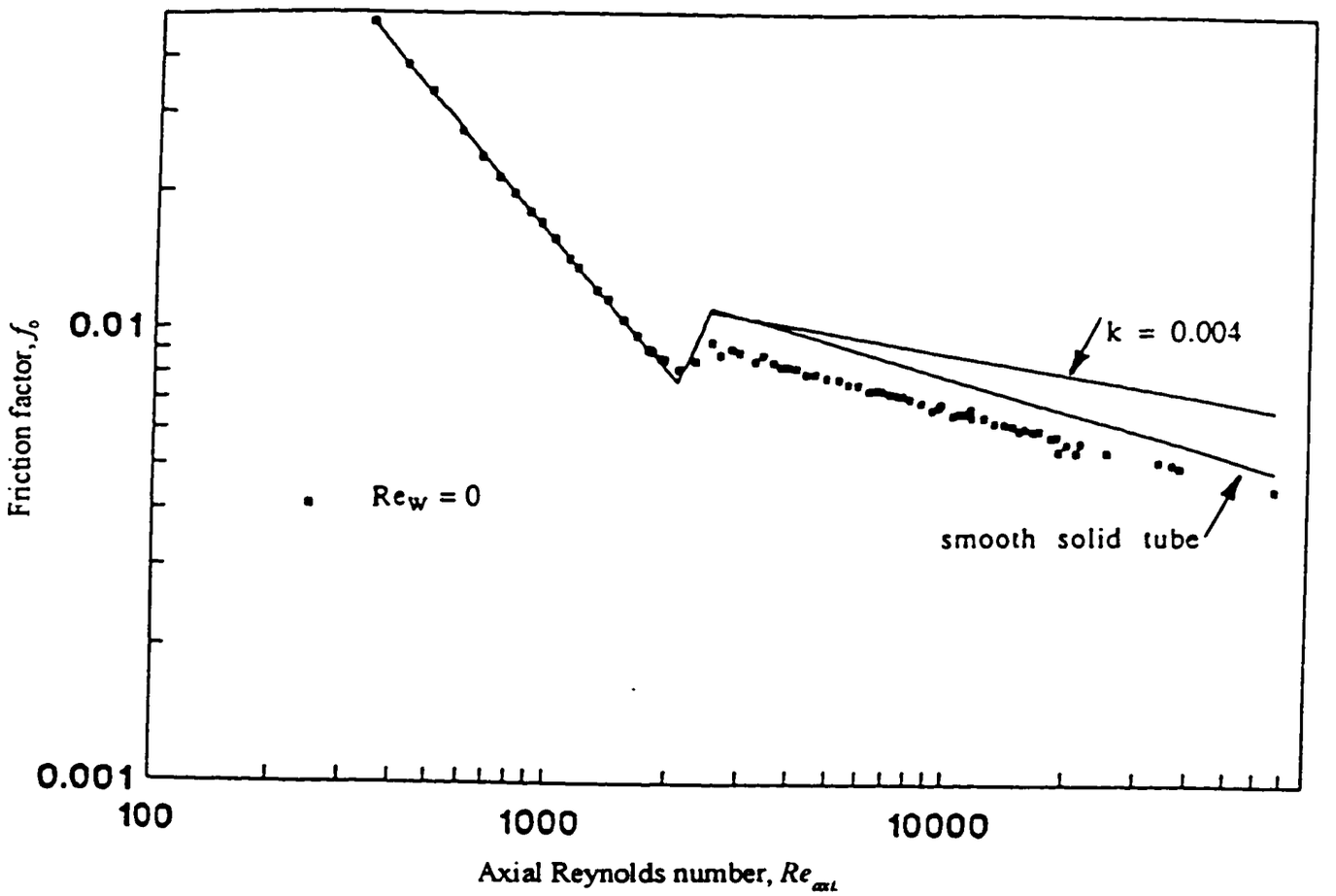

Figure 6.4- Friction coefficient as a function of axial Reynolds number in the "no net wall flux" case (Mellis et al, 1993)

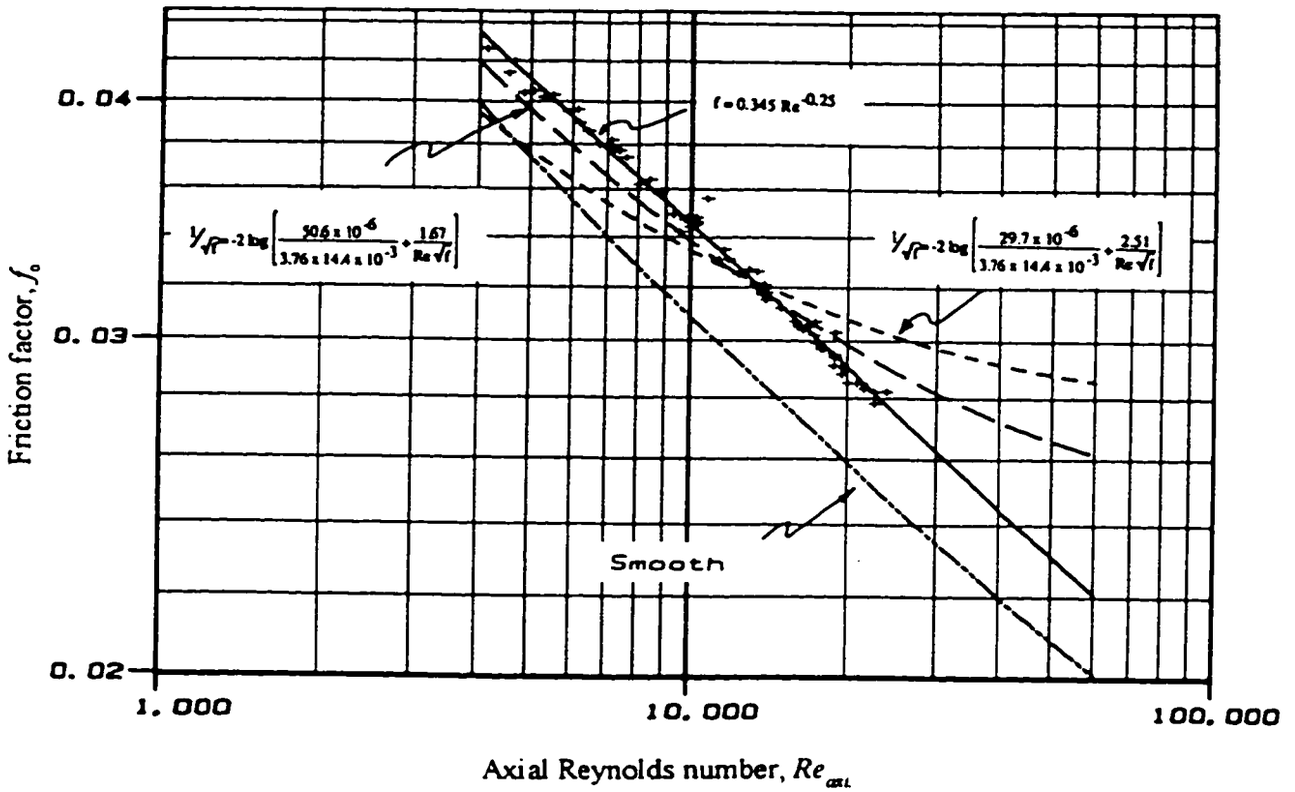

Figure 6.5- Friction factors and prediction curves for 14-mm polyethylene tubing (von Betnuth and Wilson 1989)

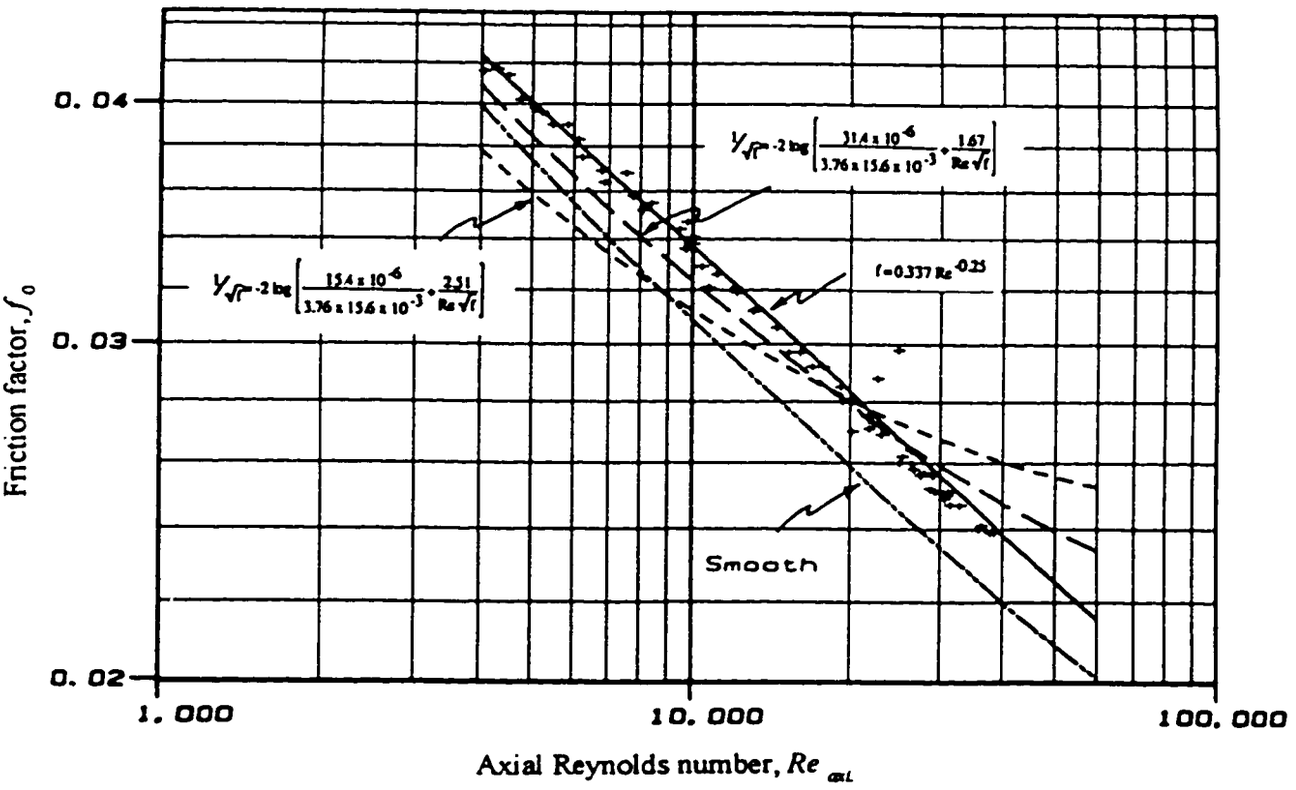

Figure 6.6- Friction factors and prediction curves for 16-mm PVC pipe (von Bernuth and Wilson 1989)

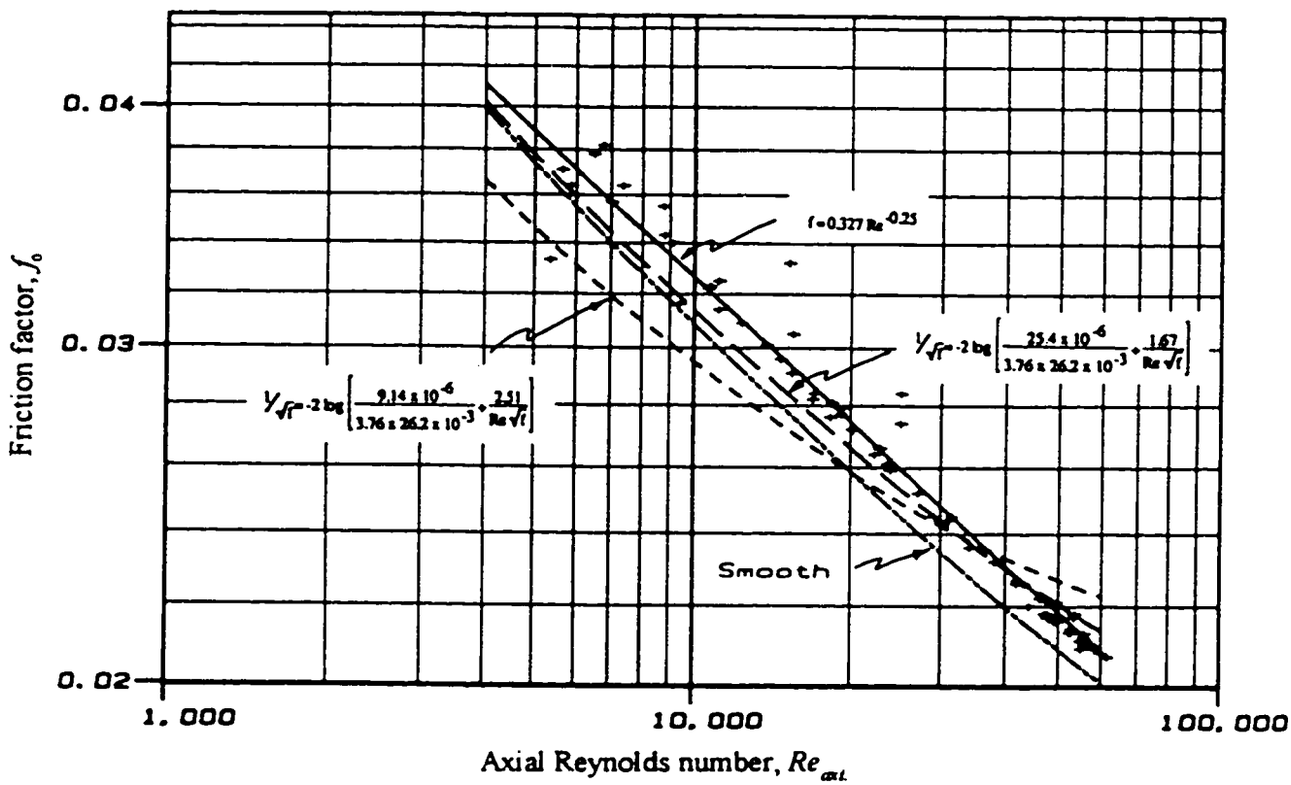

Figure 6.7- Friction factors and prediction curves for 26-mm PVC pipe (von Betnuth and Wilson 1989)

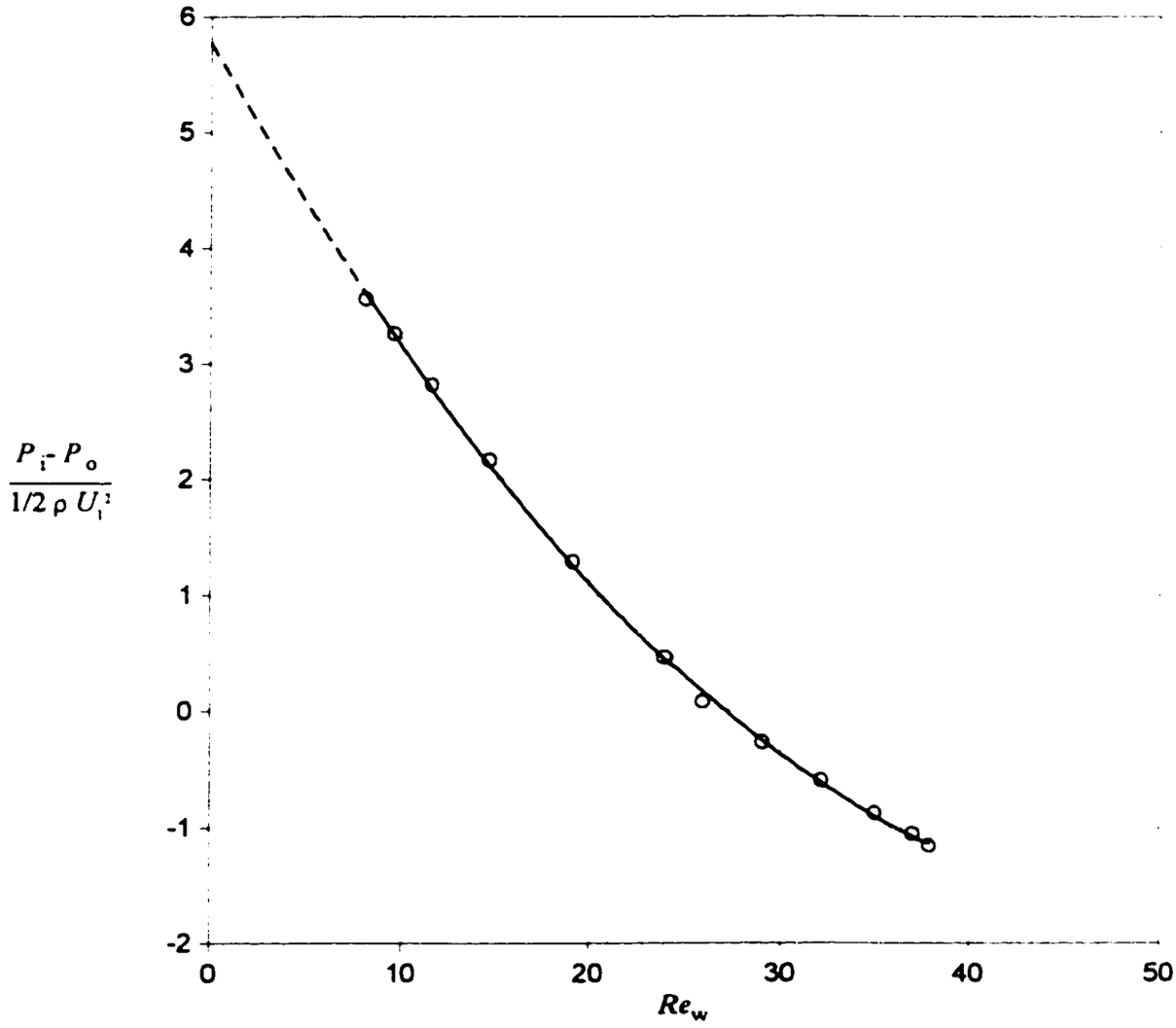

Figure 6.8- Variation of radial Reynolds number with dimensionless pressure drop for $Re_{axi.} = 30527$ and $L/D = 206.4$

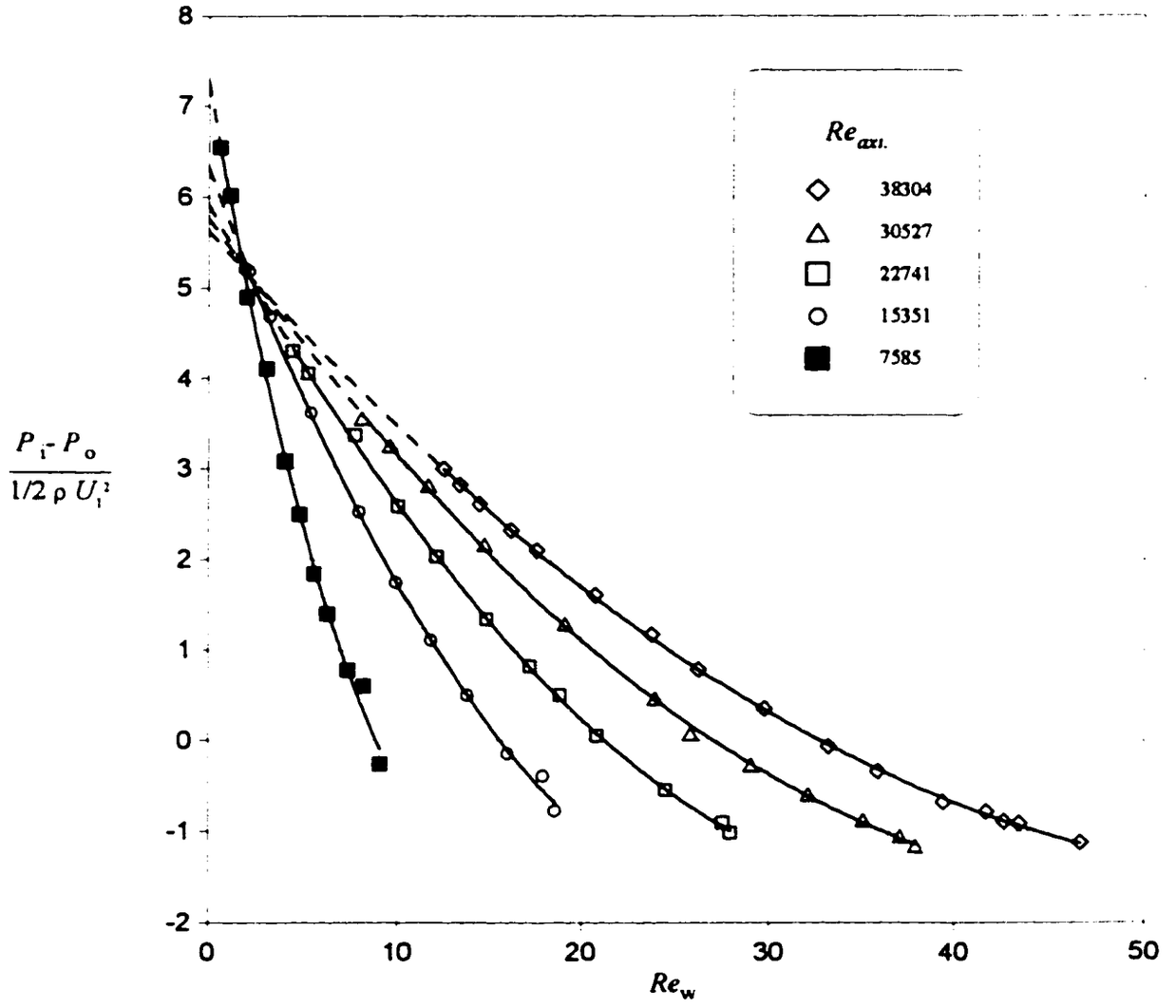

Figure 6.9- Variation of radial Reynolds number with dimensionless pressure drop for different axial Reynolds numbers and L/D = 206.4

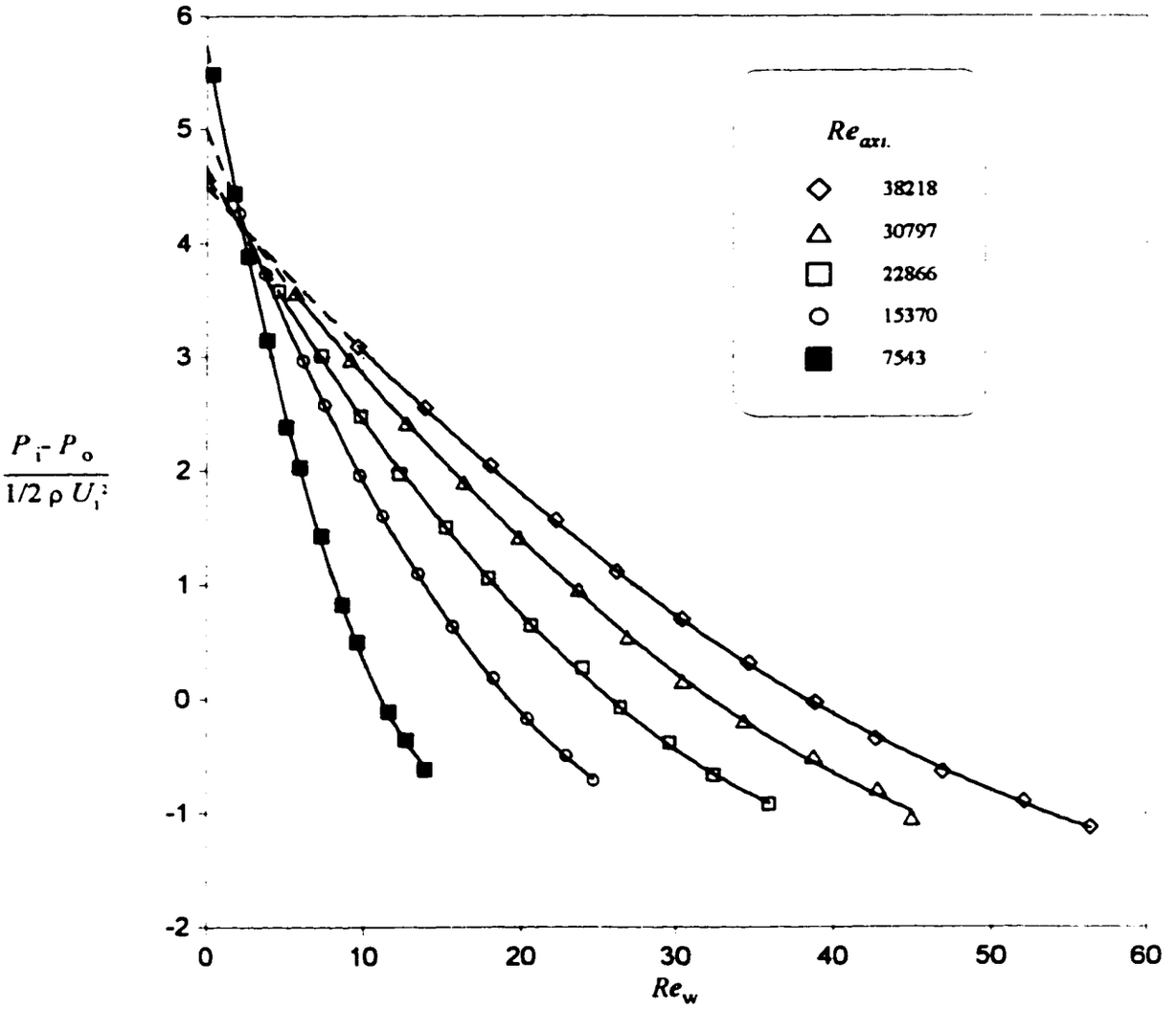

Figure 6.10- Variation of radial Reynolds number with dimensionless pressure drop for different axial Reynolds numbers and L/D = 159.6

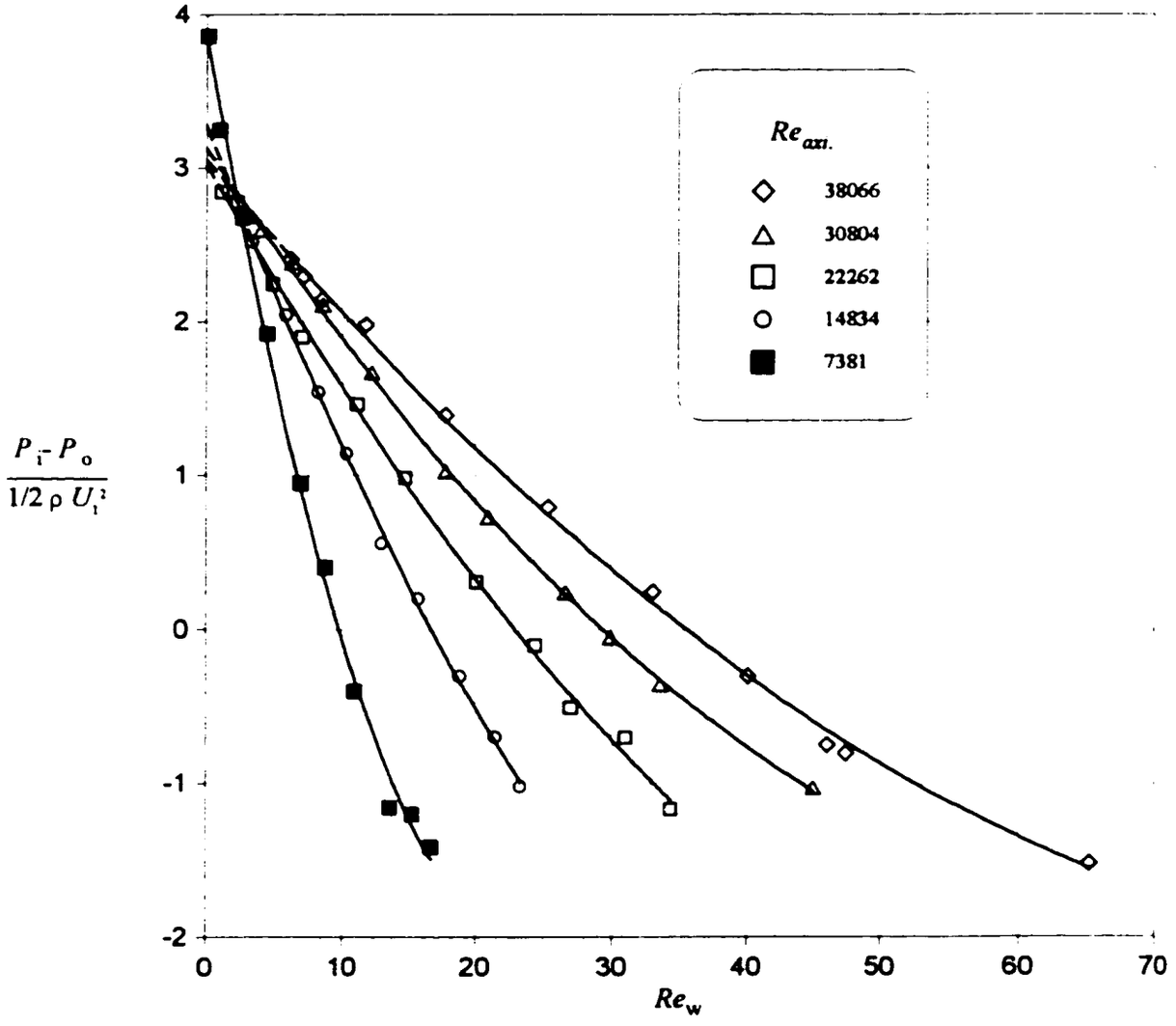

Figure 6.11- Variation of radial Reynolds number with dimensionless pressure drop for different axial Reynolds numbers and L/D =106.4

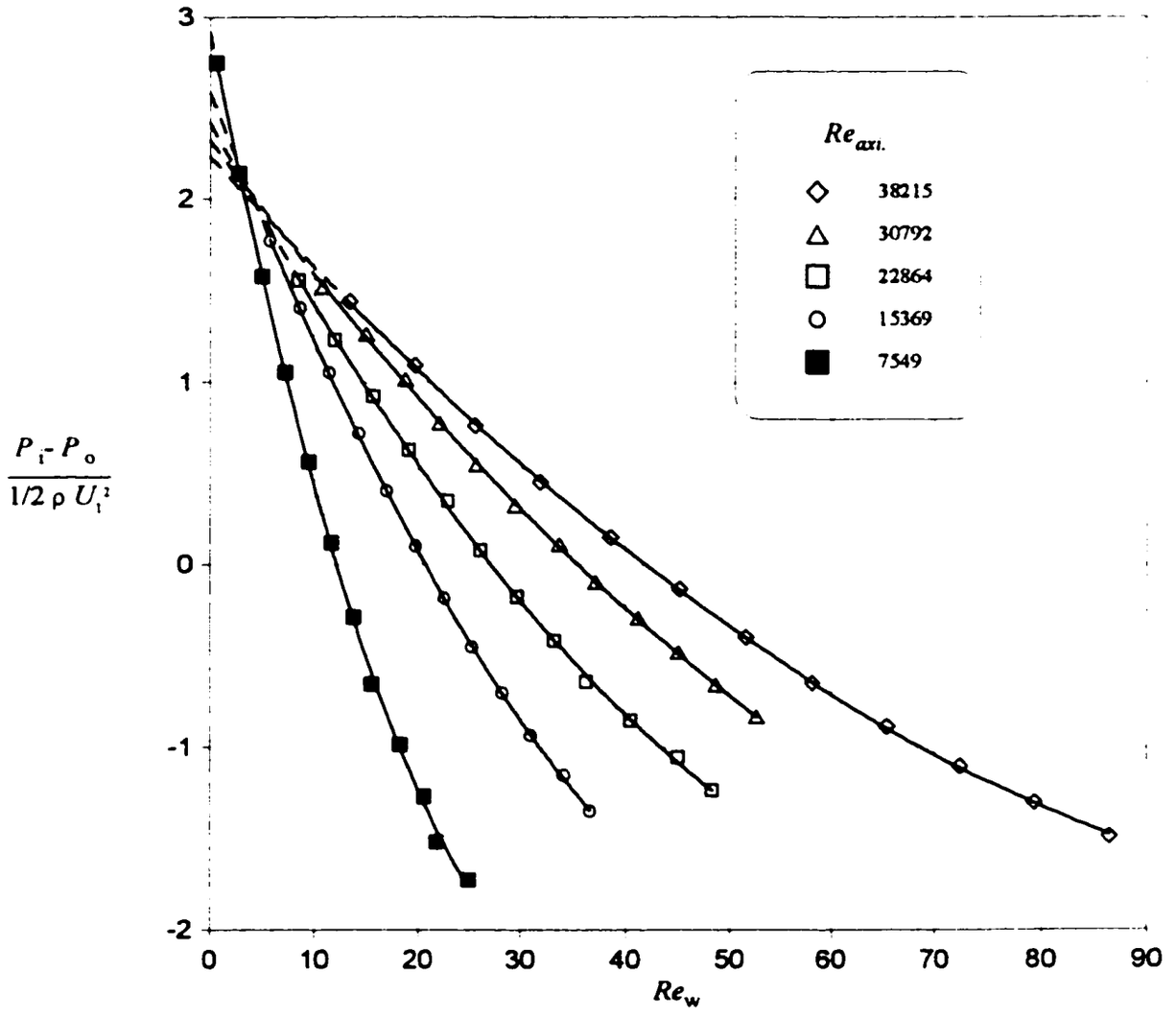

Figure 6.12- Variation of radial Reynolds number with dimensionless pressure drop for different axial Reynolds numbers and $L/D = 79.8$

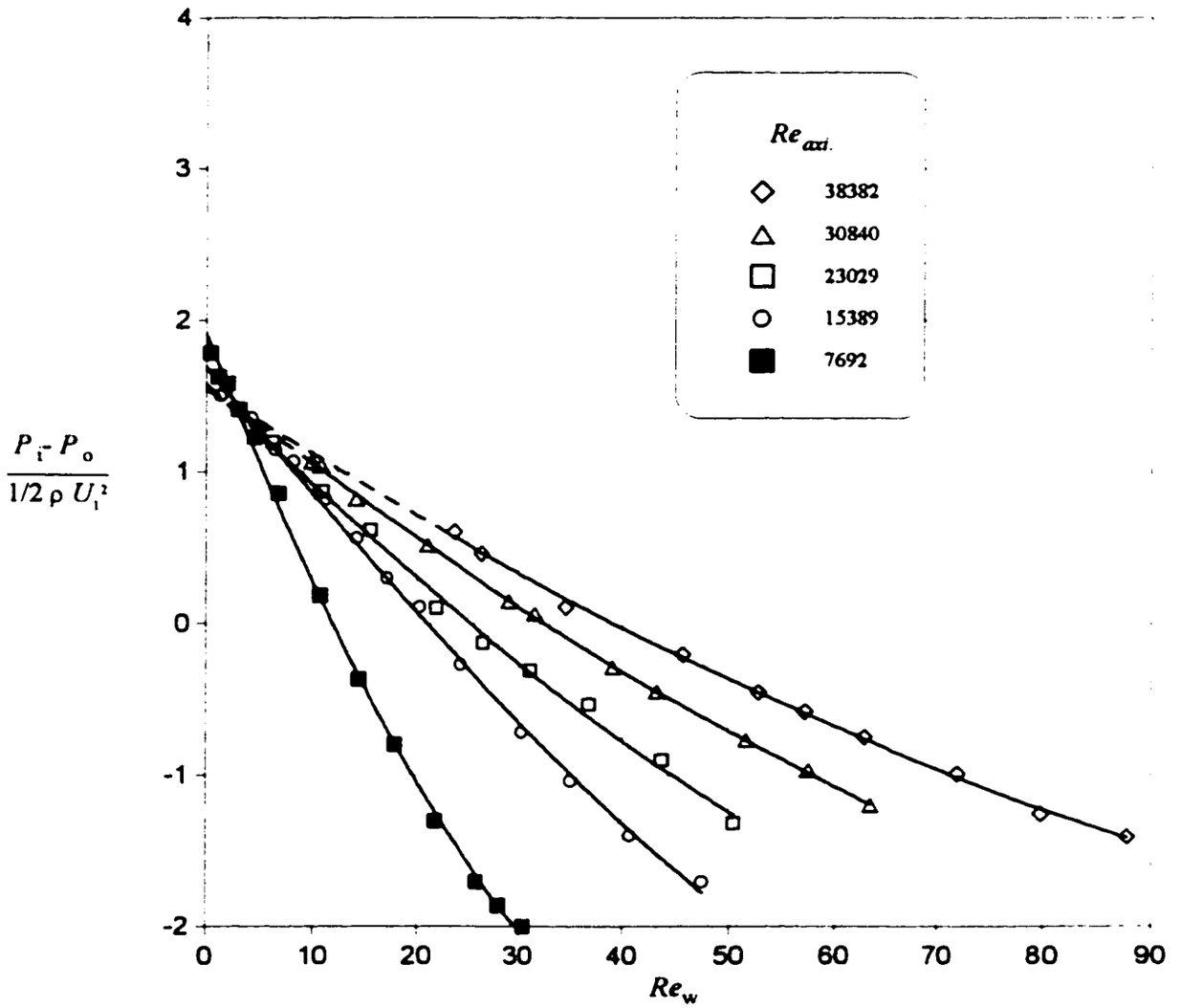

Figure 6.13- Variation of radial Reynolds number with dimensionless pressure drop for different axial Reynolds numbers and L/D =53.2

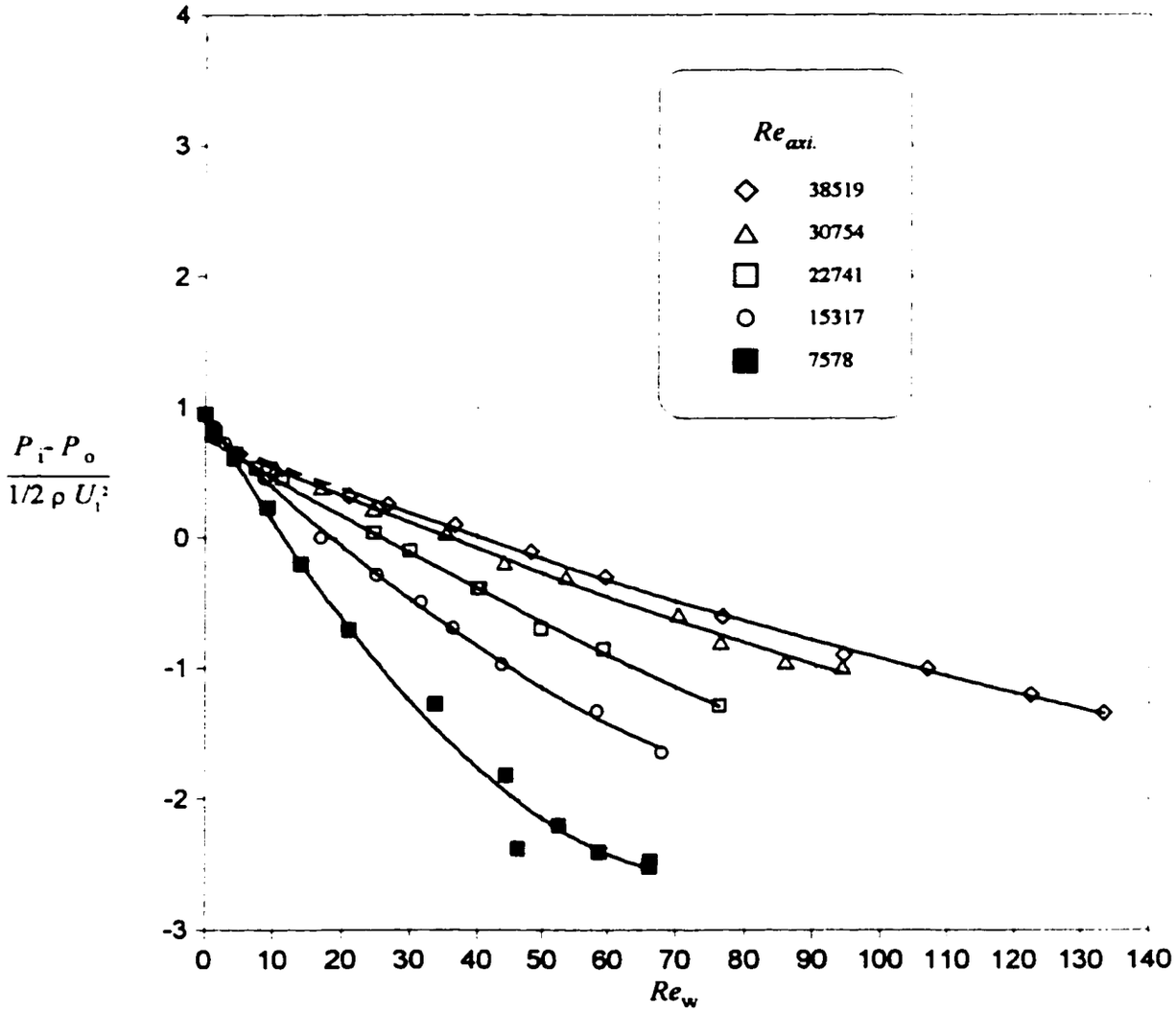

Figure 6.14- Variation of radial Reynolds number with dimensionless pressure drop for different axial Reynolds numbers and L/D =26.6

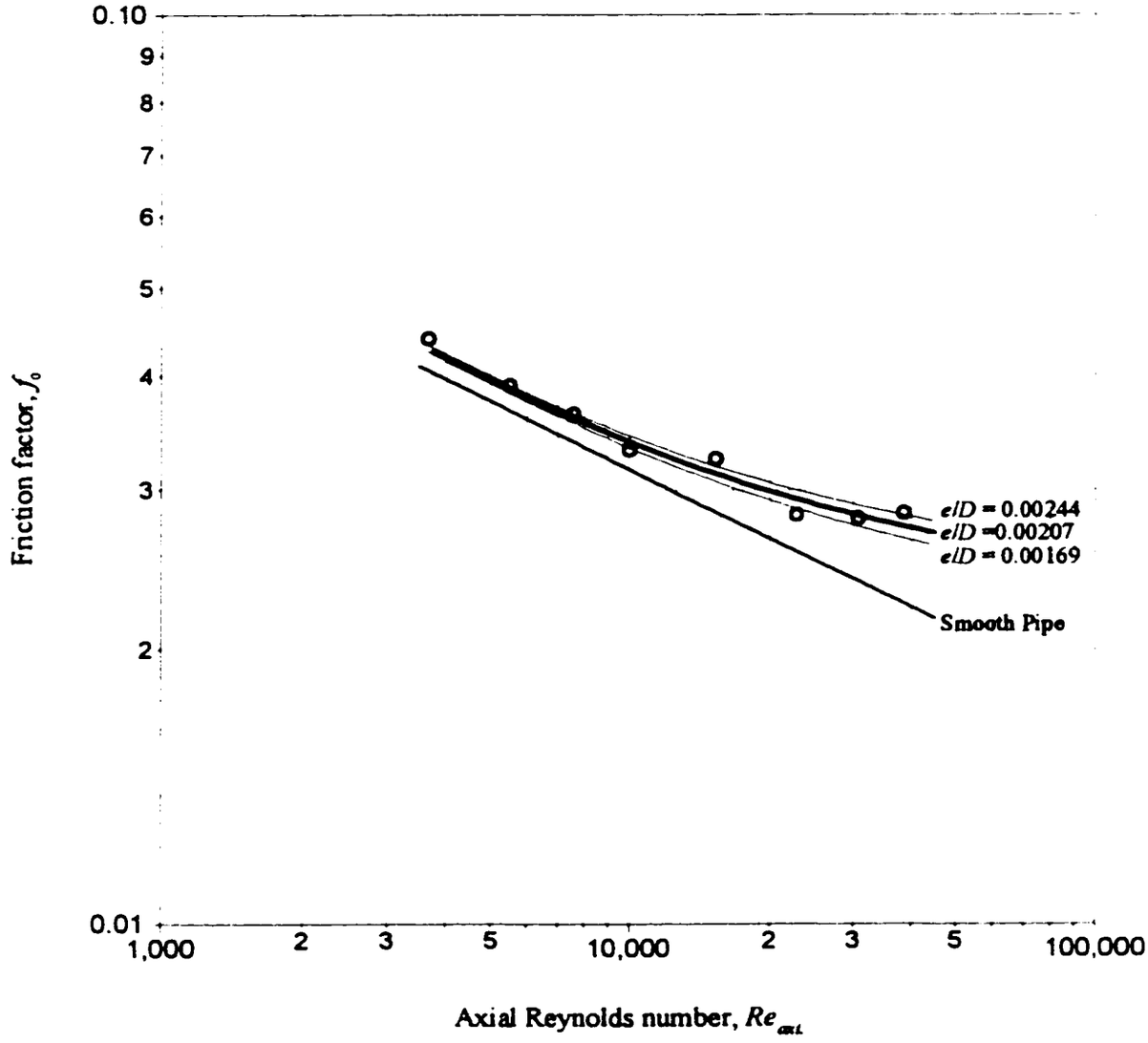

Figure 6.15- No-suction friction factors for $L/D = 26.6$

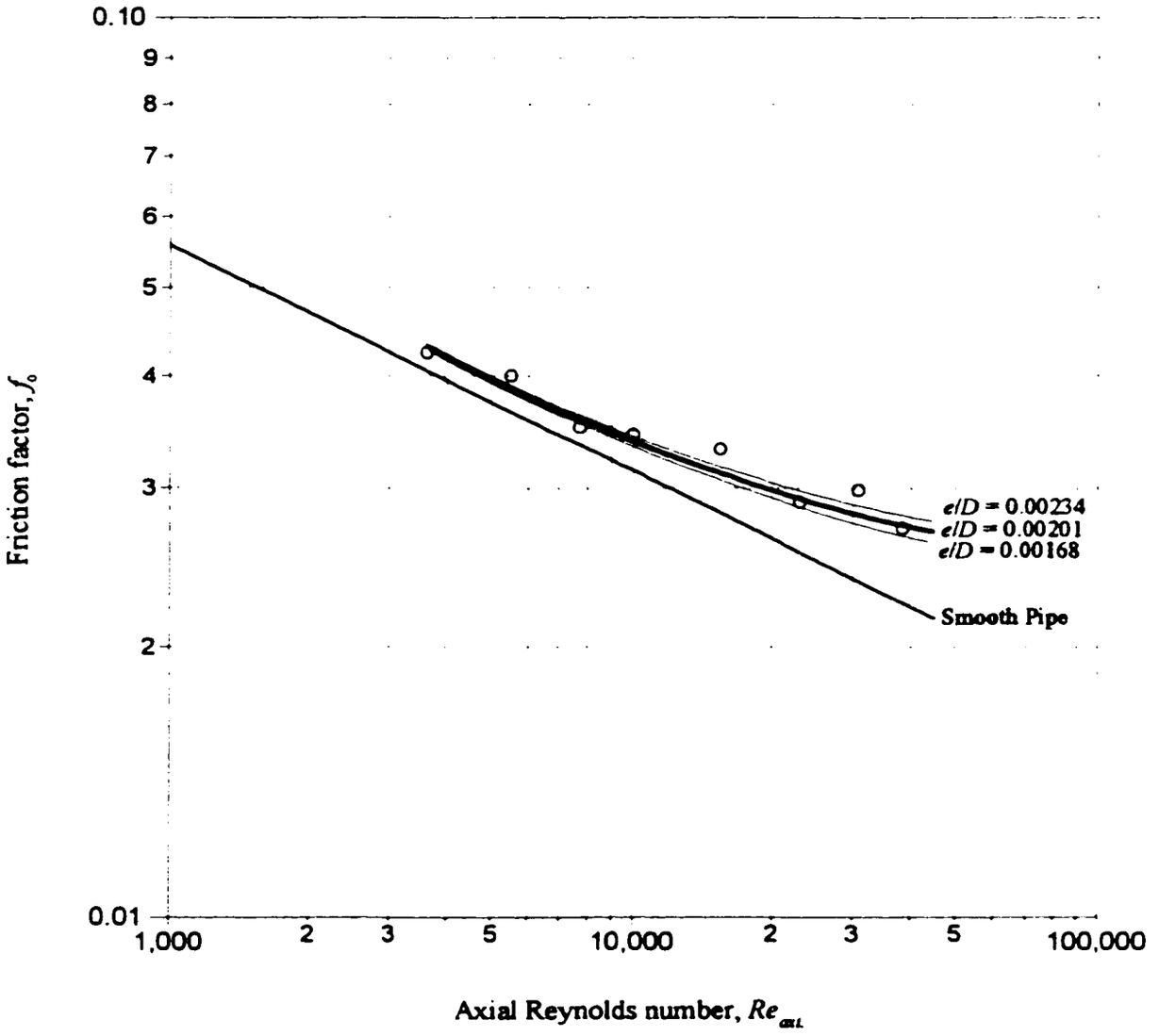

Figure 6.16- No-suction friction factors for $L/D = 53.2$

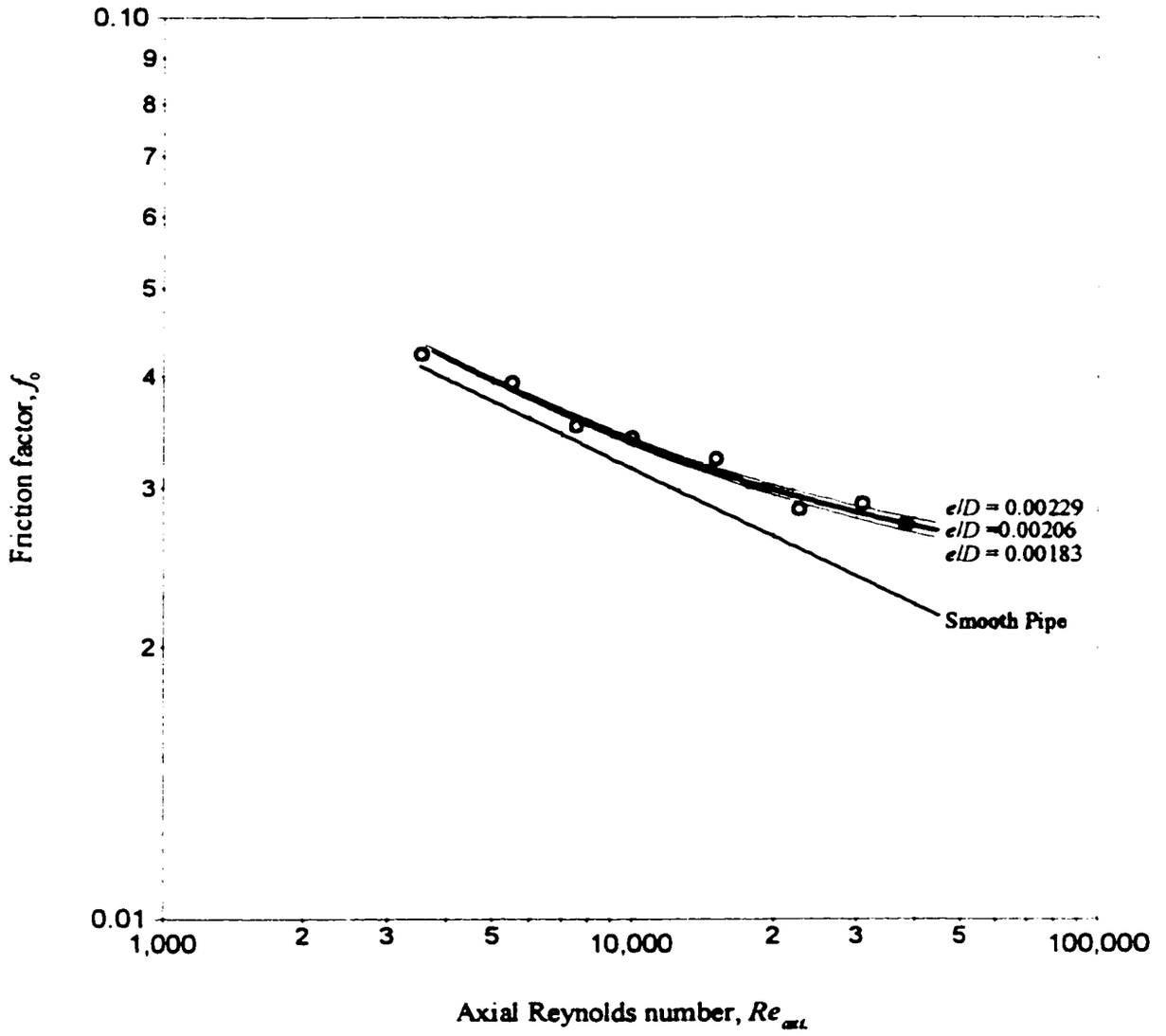

Figure 6.17- No-suction friction factors for $L/D = 79.8$

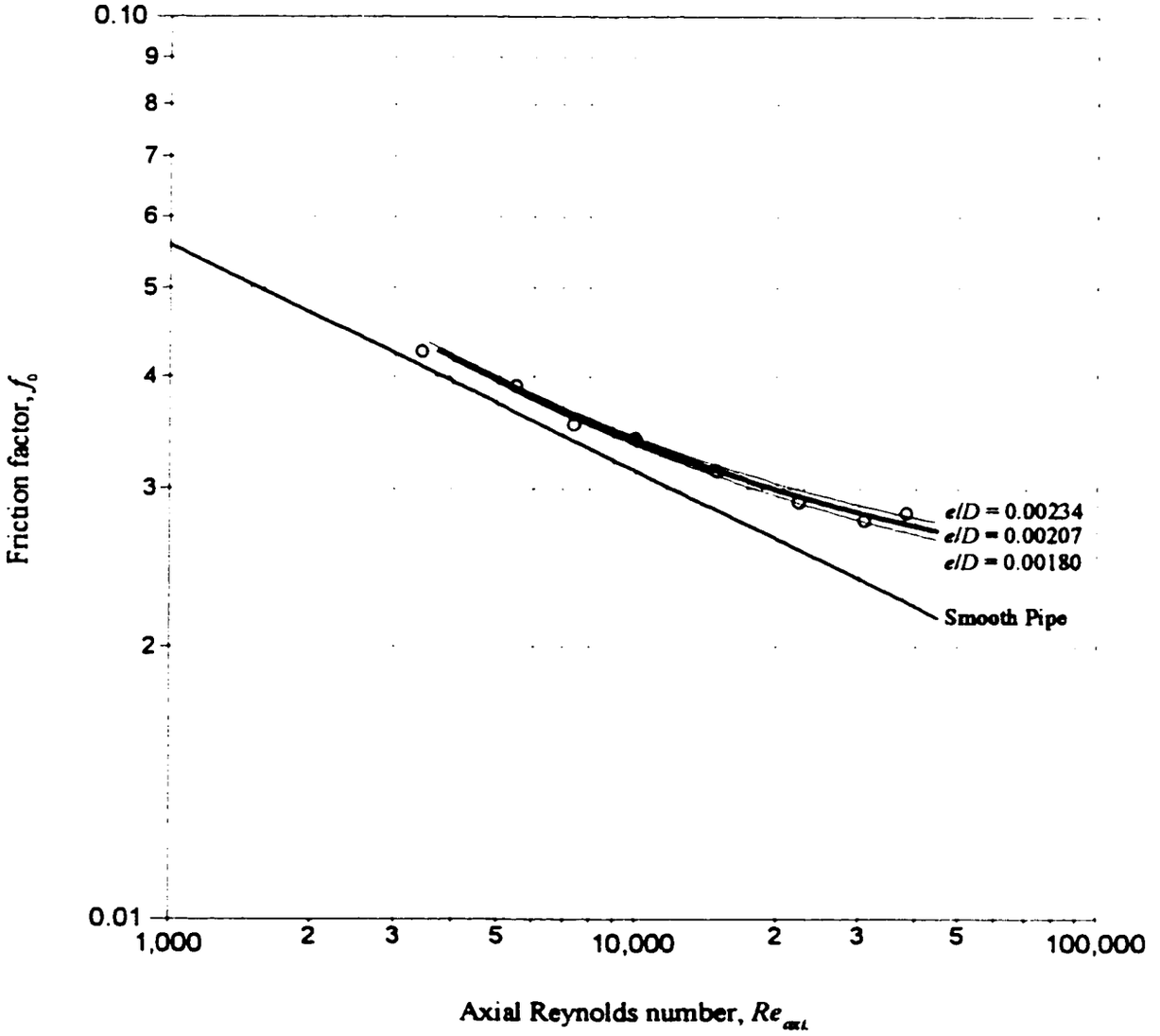

Figure 6.18- No-suction friction factors for $L/D = 106.4$

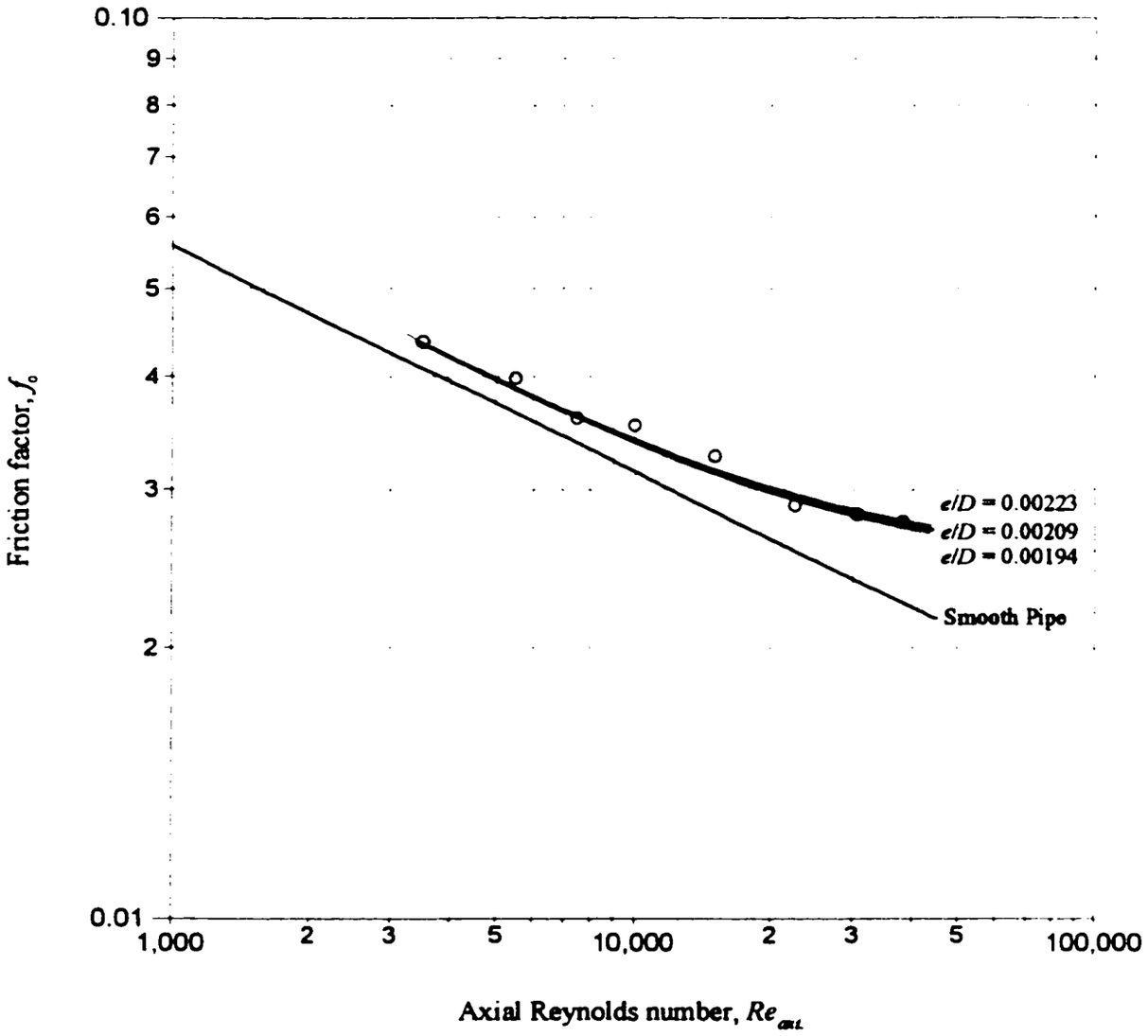

Figure 6.19- No-suction friction factors for $L/D = 159.6$

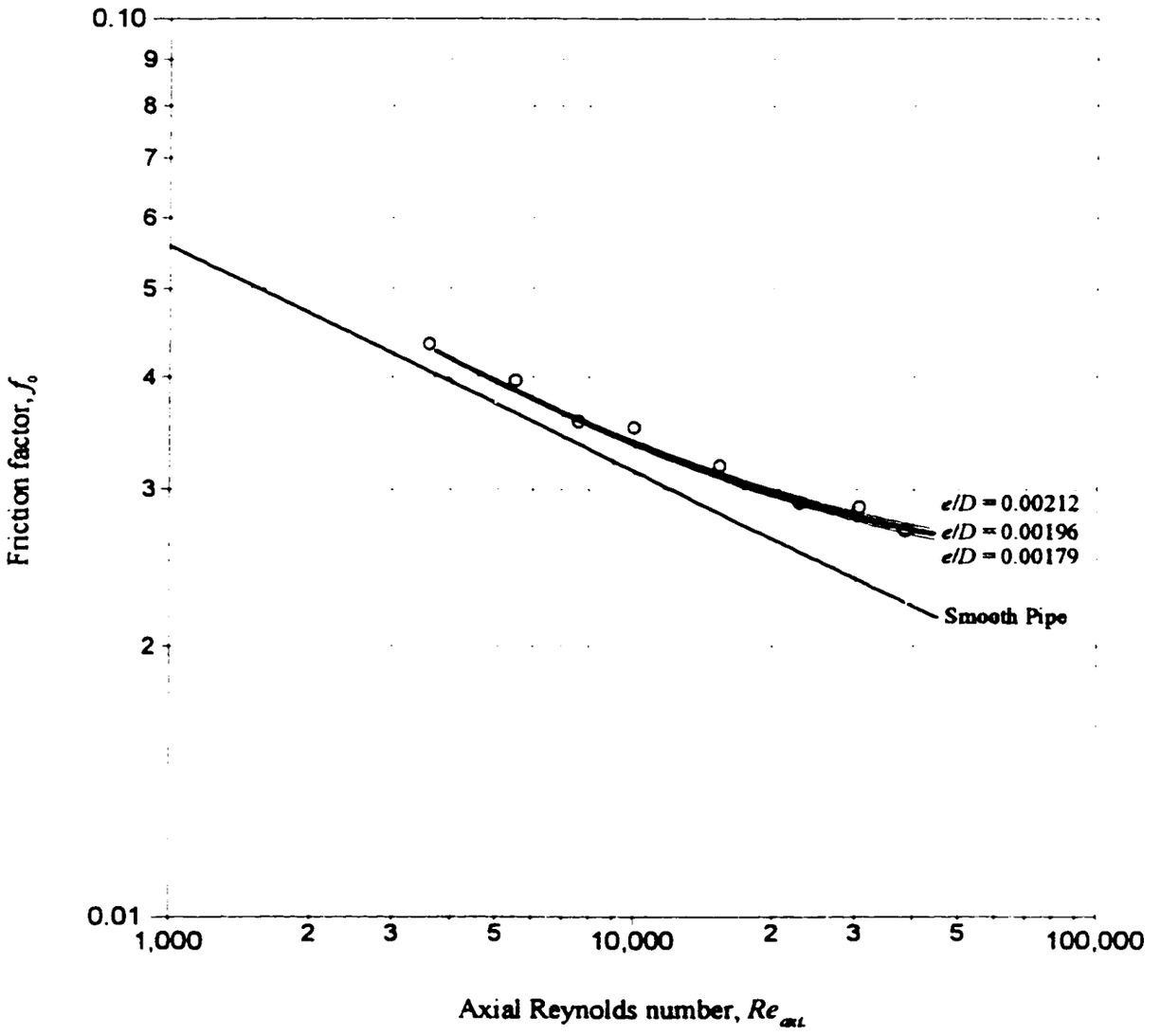

Figure 6.20- No-suction friction factors for $L/D = 206.4$

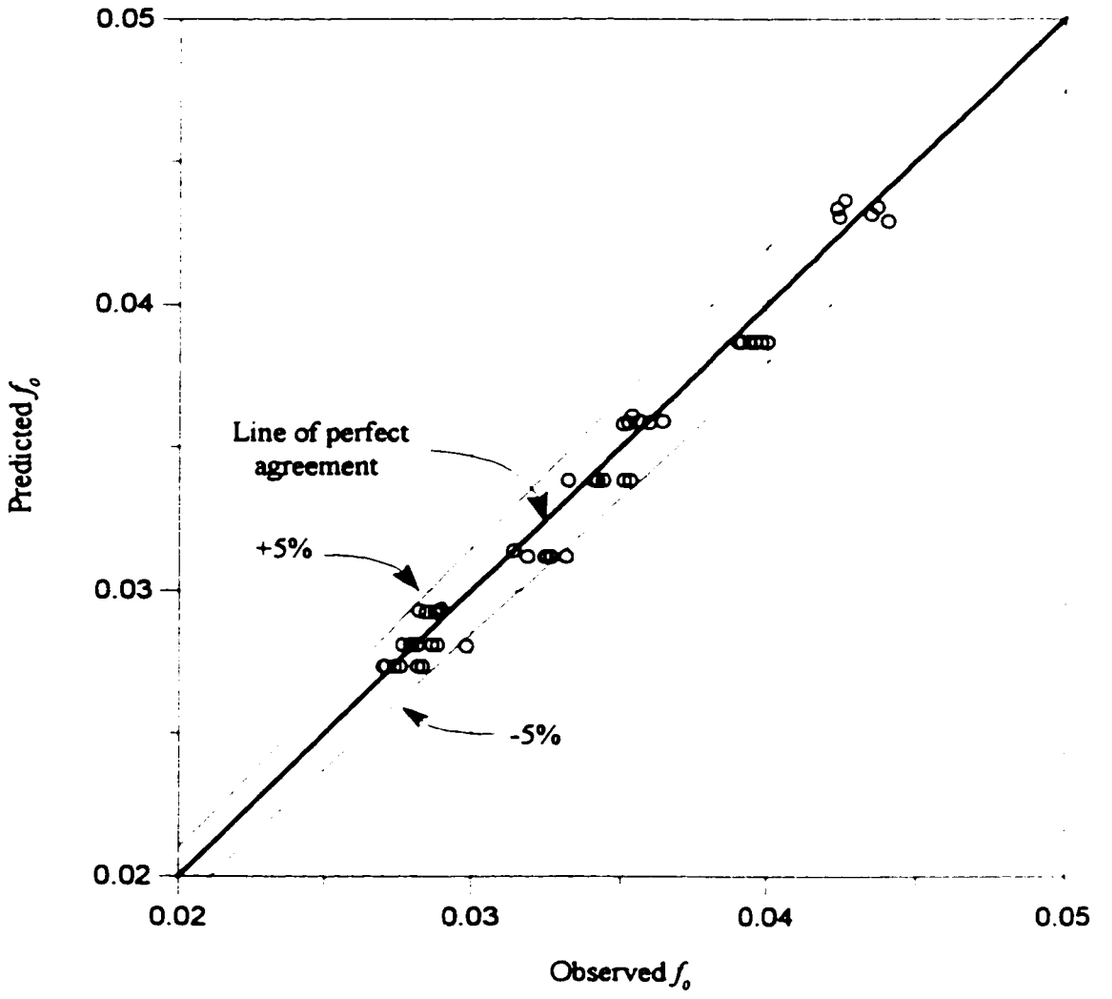

Figure 6.21- Predicted f_o (calculated from Colebrook-White equation with e/D=0.00204) vs. observed f_o

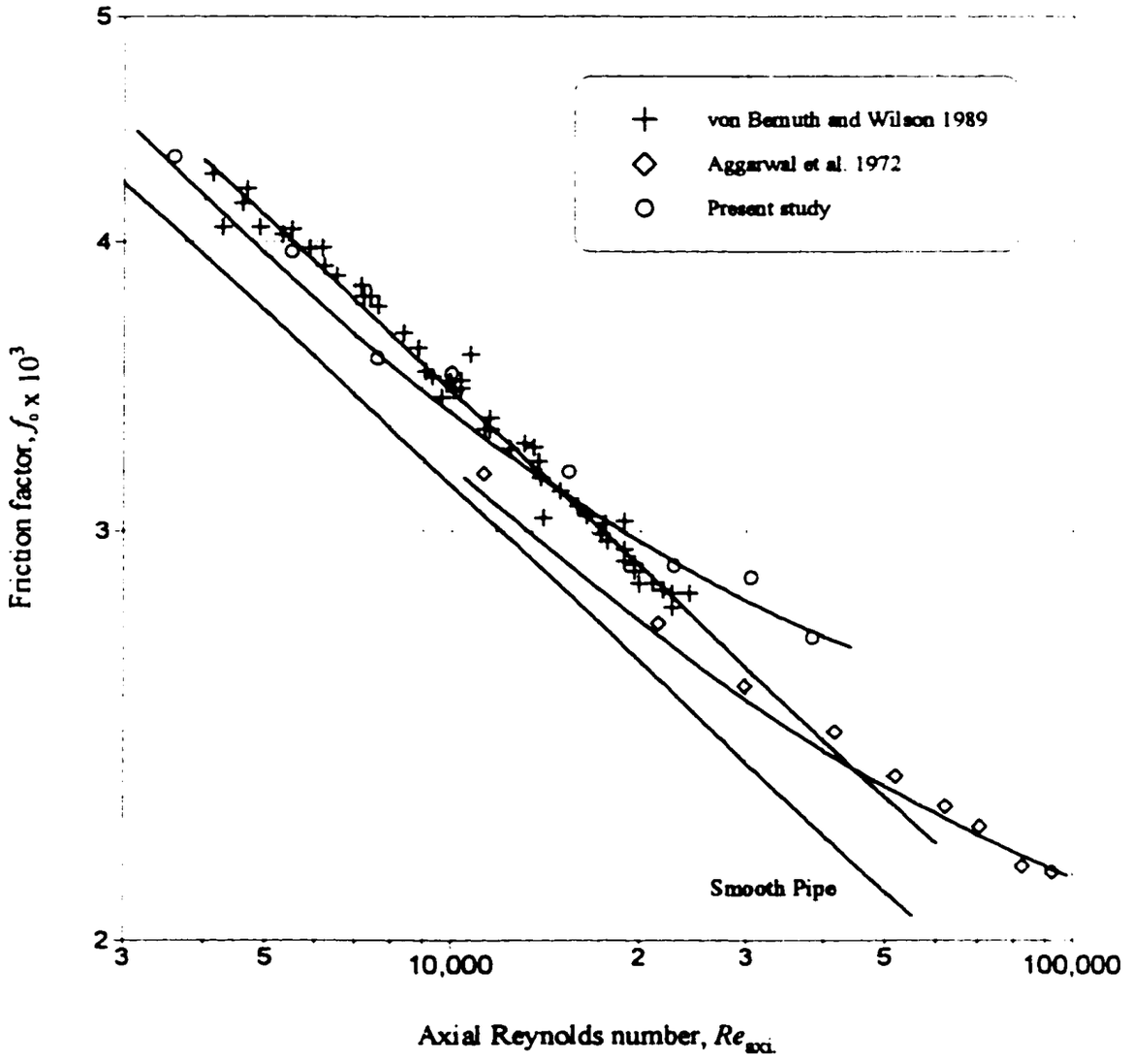

Figure 6.22 - Comparison between the frictional characteristics of the porous tubing used in present study with those of the other investigators

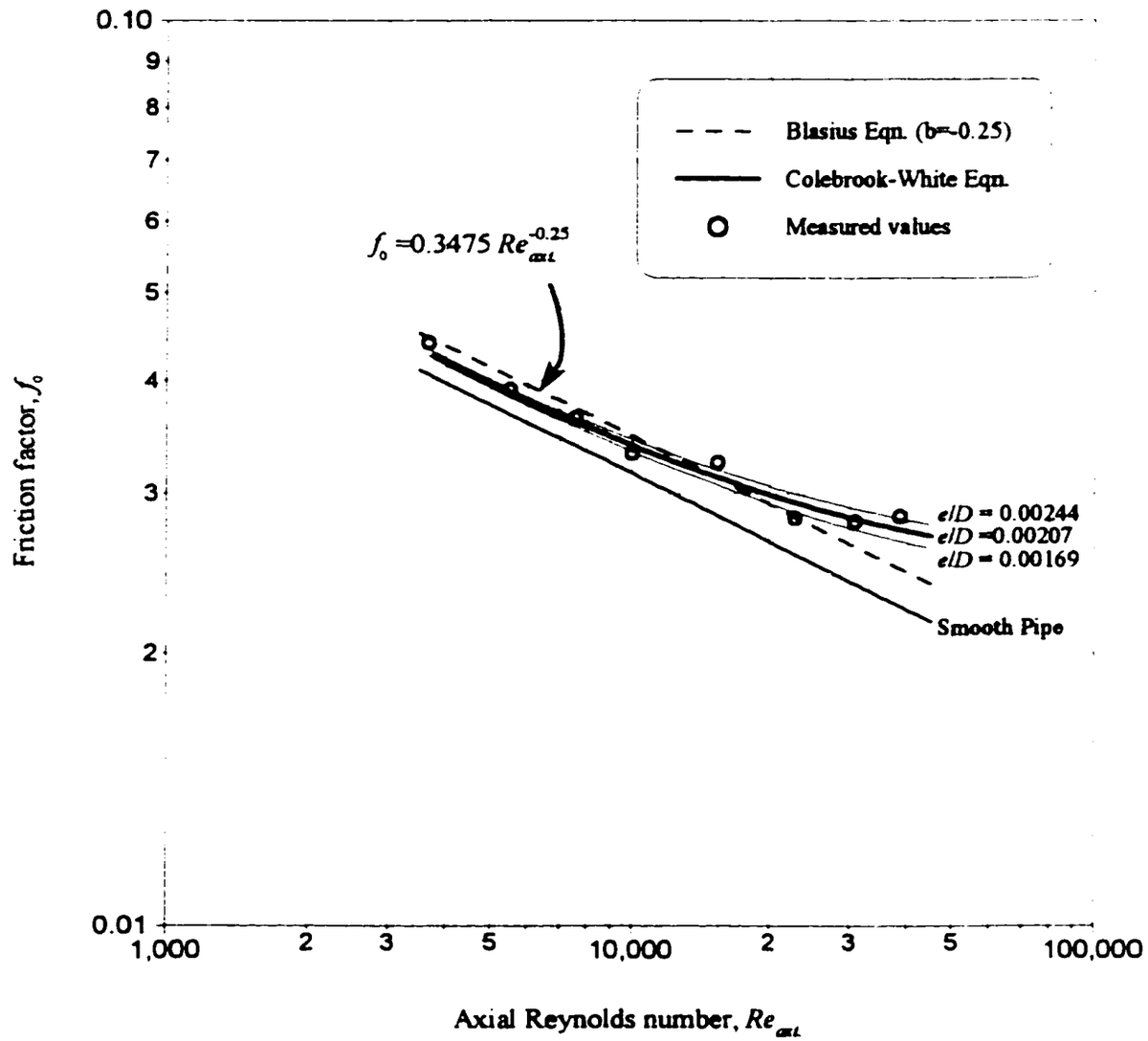

Figure 6.23- Validity of the Blasius equation in predicting friction factor in porous tubing under study for no suction condition and for $L/D = 26.6$

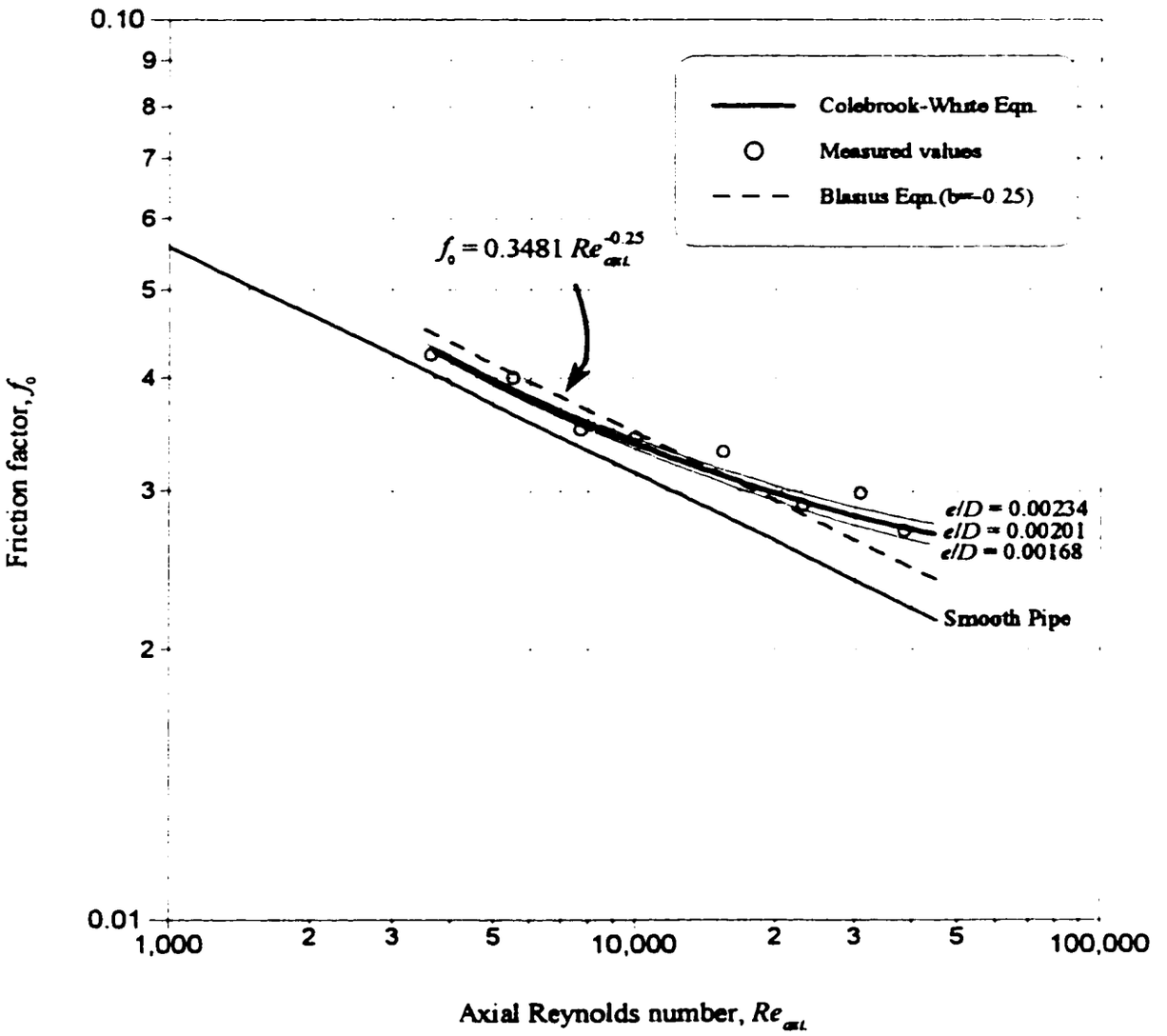

Figure 6.24- Validity of the Blasuis equation in predicting friction factor in porous tubing under study for no suction condition and for $L/D = 53.2$

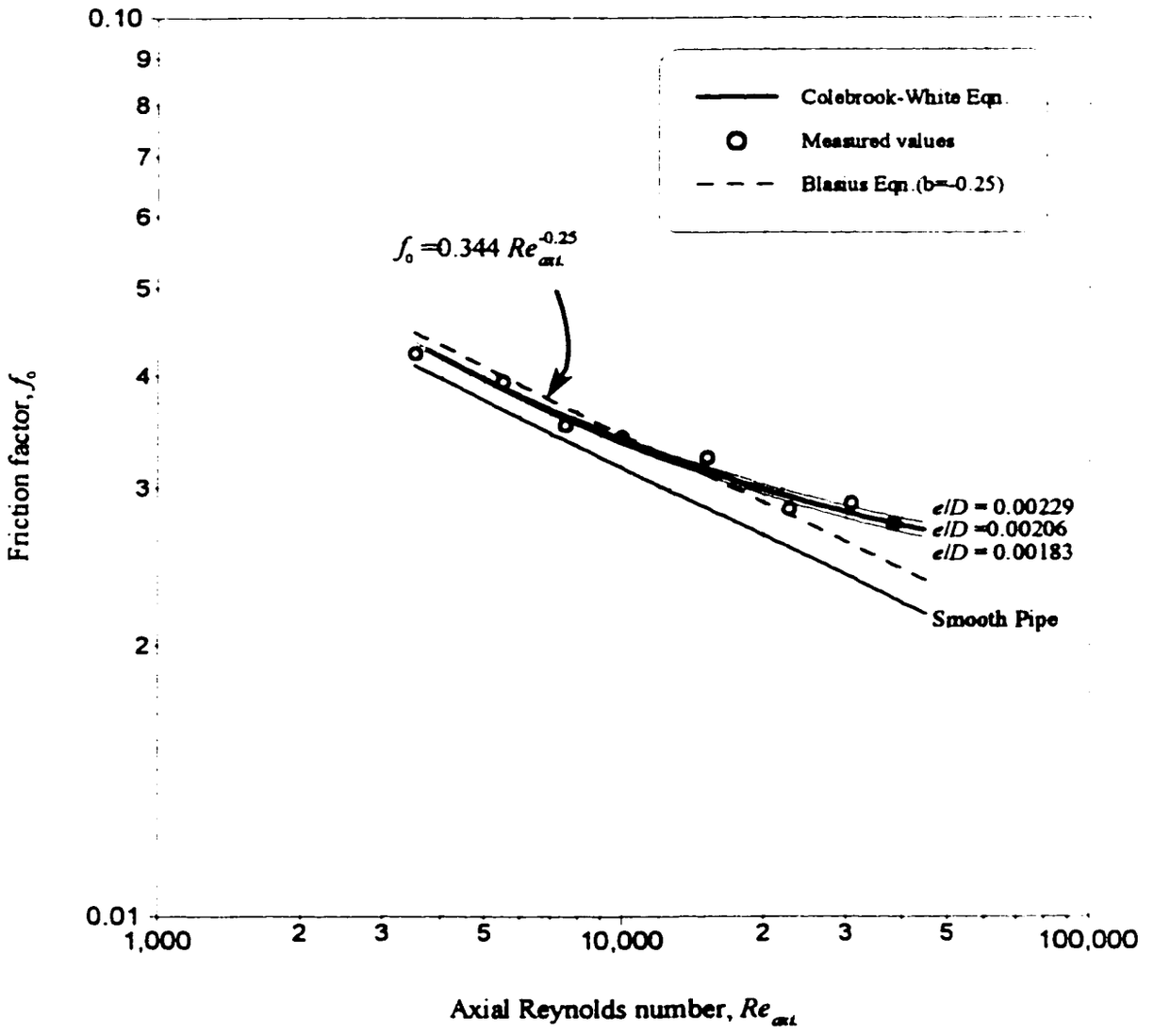

Figure 6.25- Validity of the Blasius equation in predicting friction factor in porous tubing under study for no suction condition and for $L/D = 79.8$

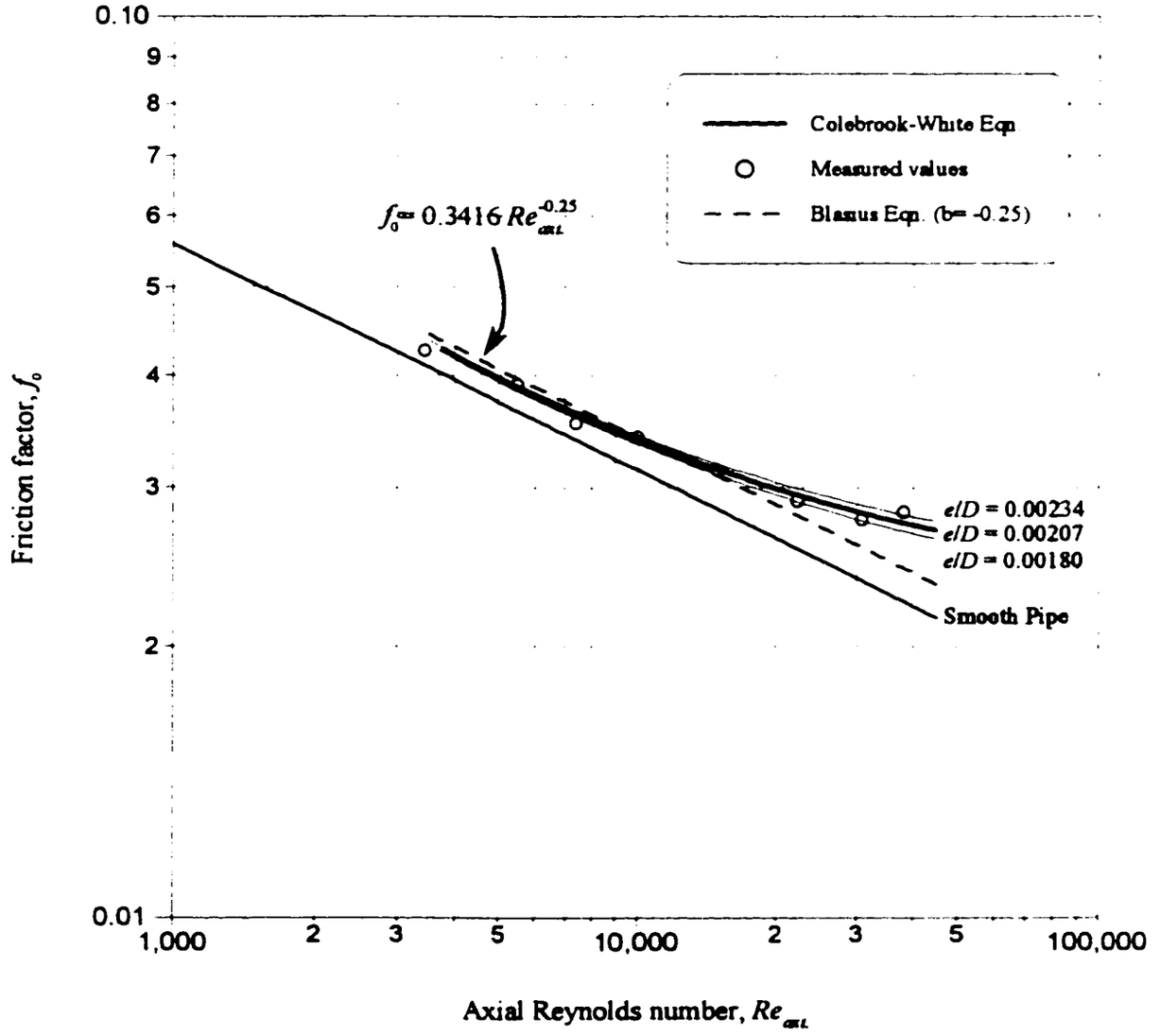

Figure 6.26- Validity of the Blasius equation for predicting friction factor in porous tubing under study for no suction condition and for $L/D = 106.4$

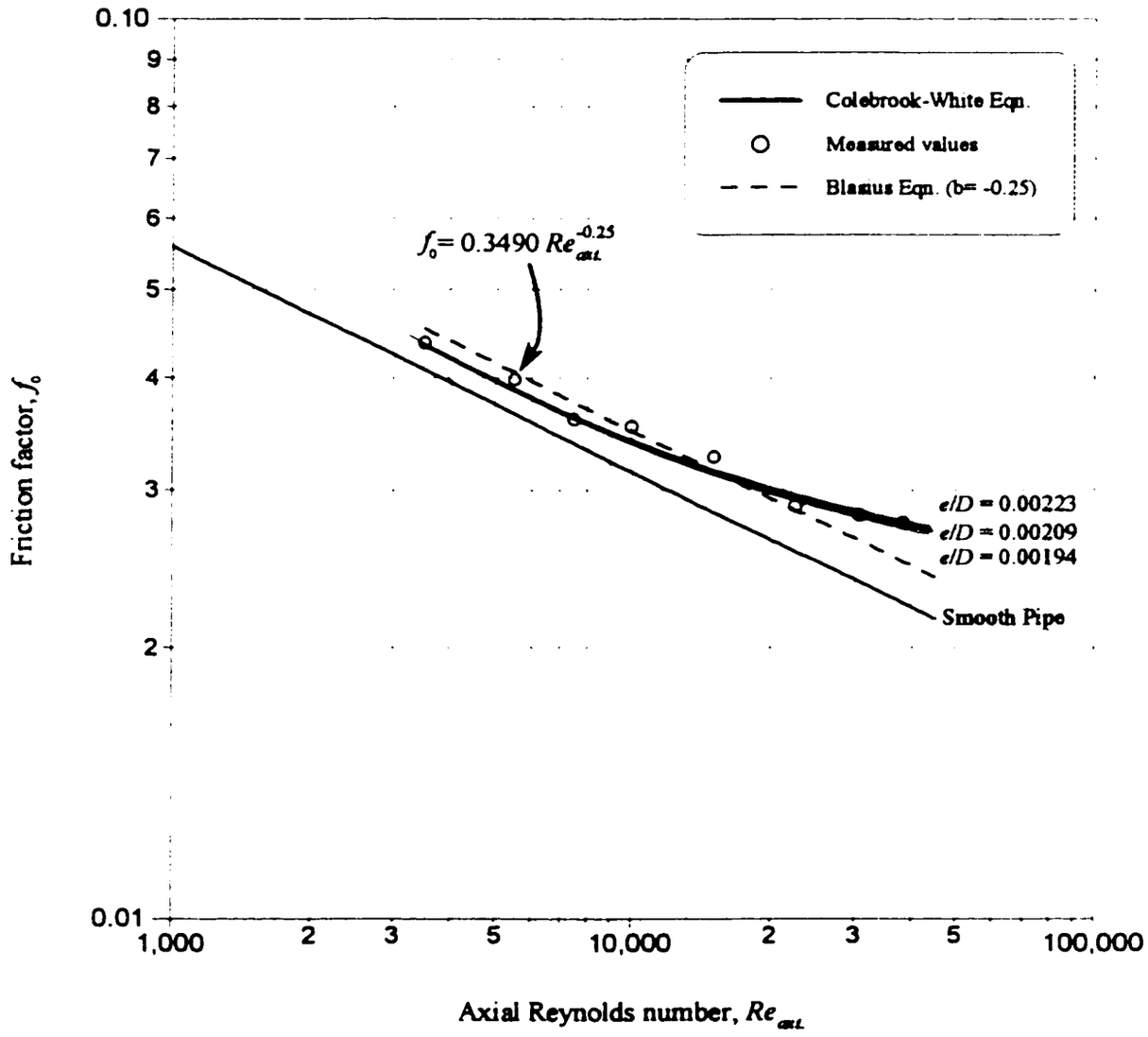

Figure 6.27- Validity of the Blasius equation for predicting friction factor in porous tubing under study for no suction condition and for $L/D = 159.6$

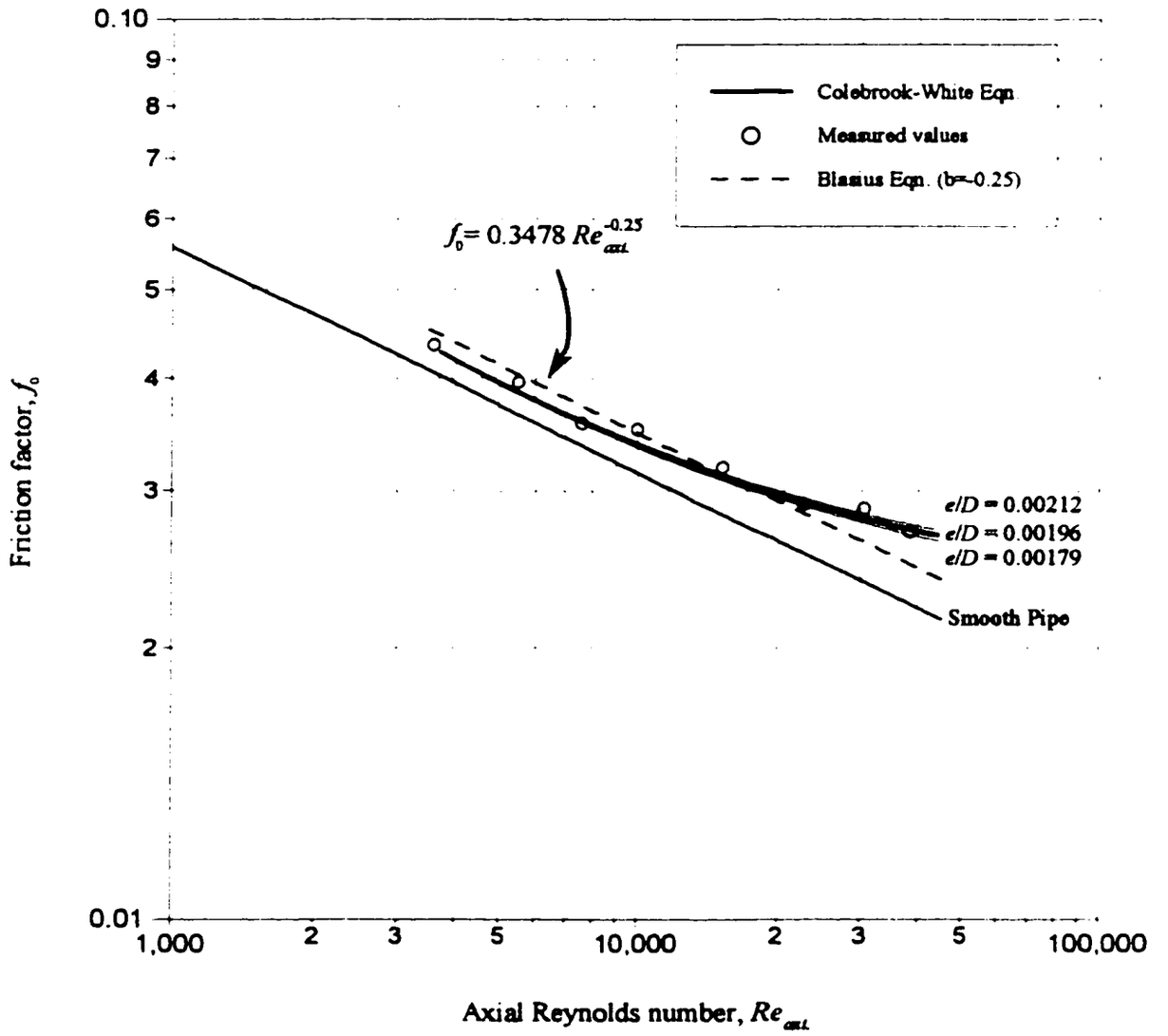

Figure 6.28- Validity of the Blasius equation in predicting friction factor in porous tubing under study for no suction condition and for $L/D = 206.4$

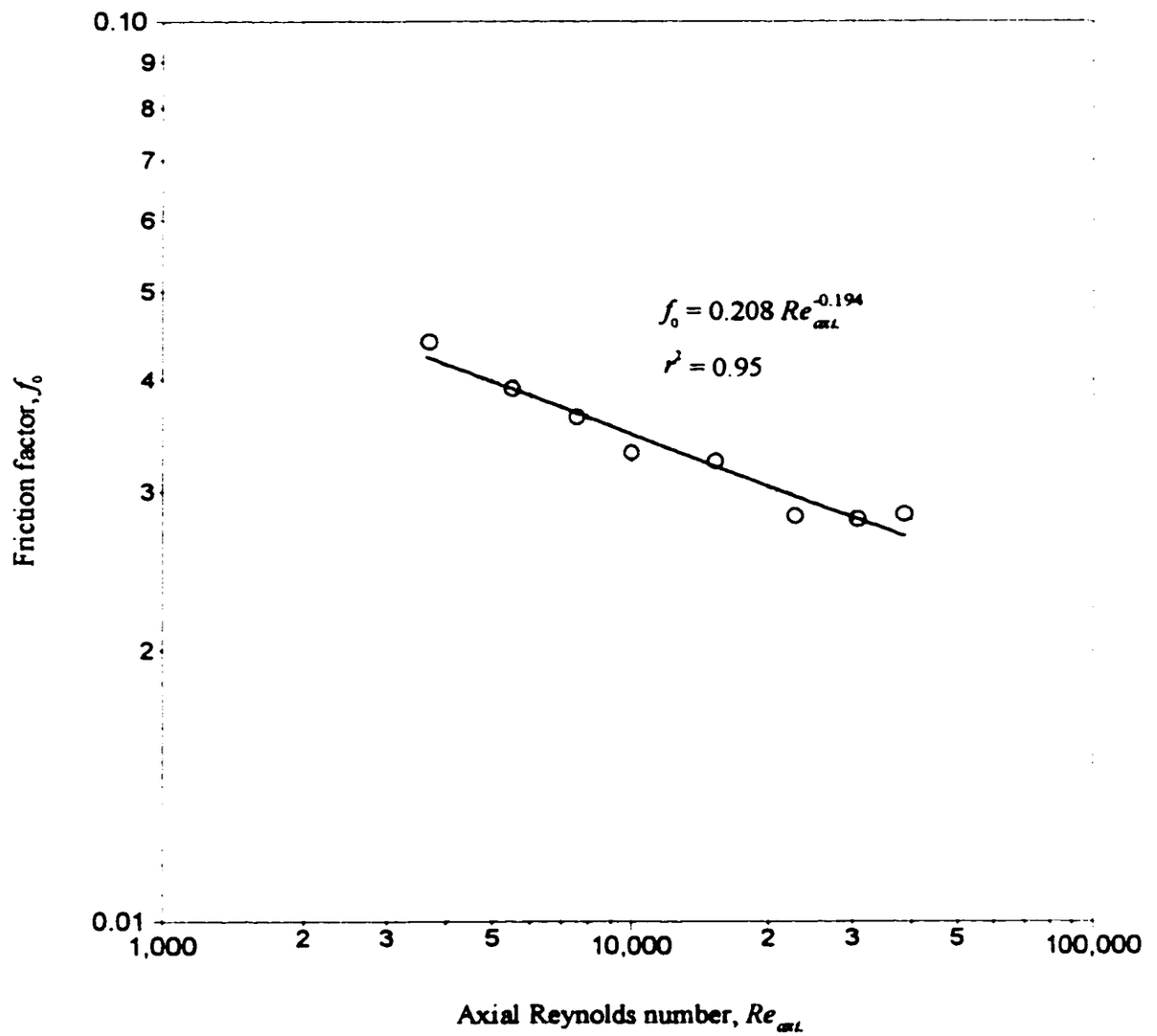

Figure 6.29- Power function relation relating f_0 to the $Re_{axi.}$ for L/D =26.6

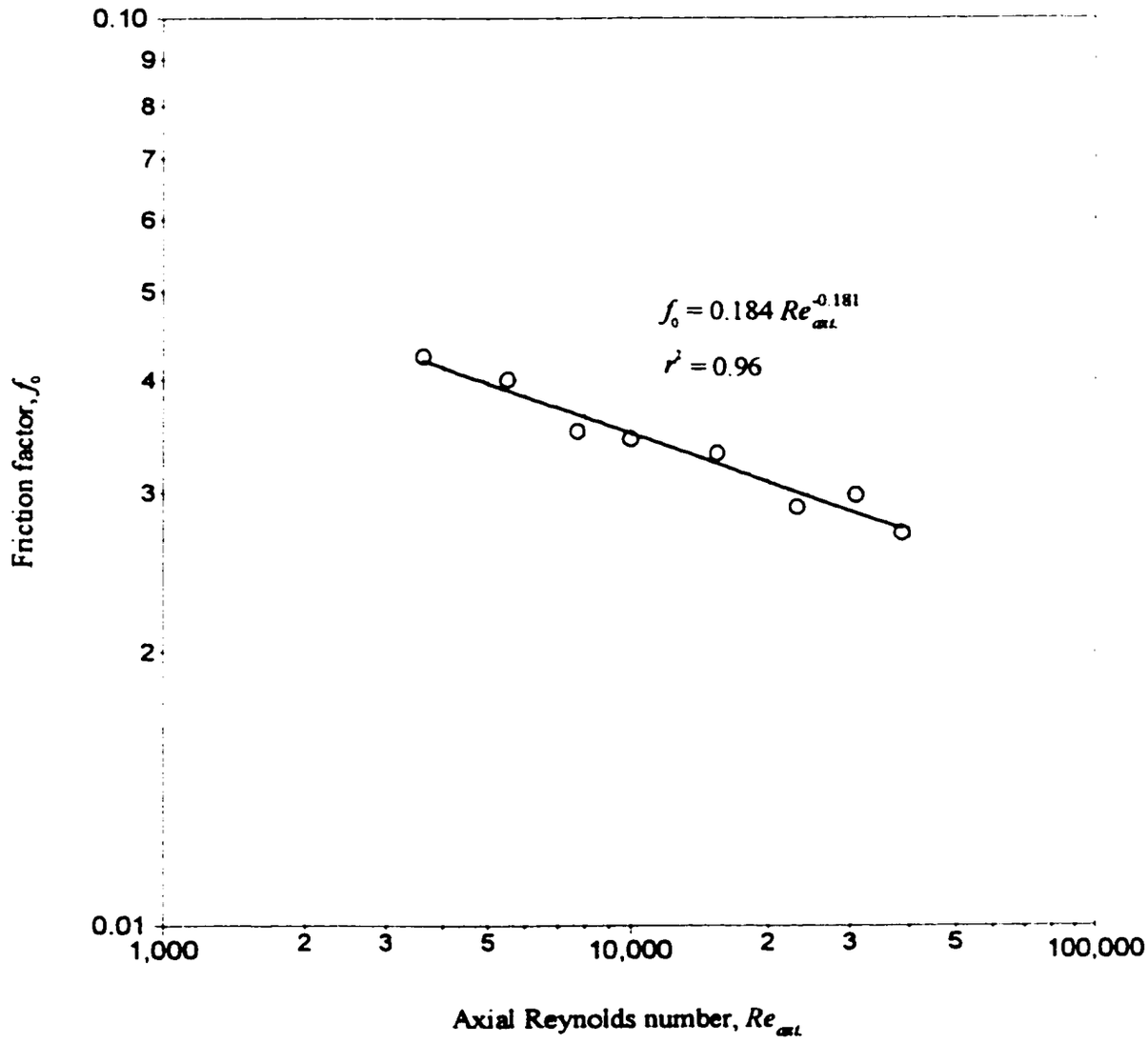

Figure 6.30- Power function relation relating f_0 to the $Re_{axi.}$ for L/D =53.2

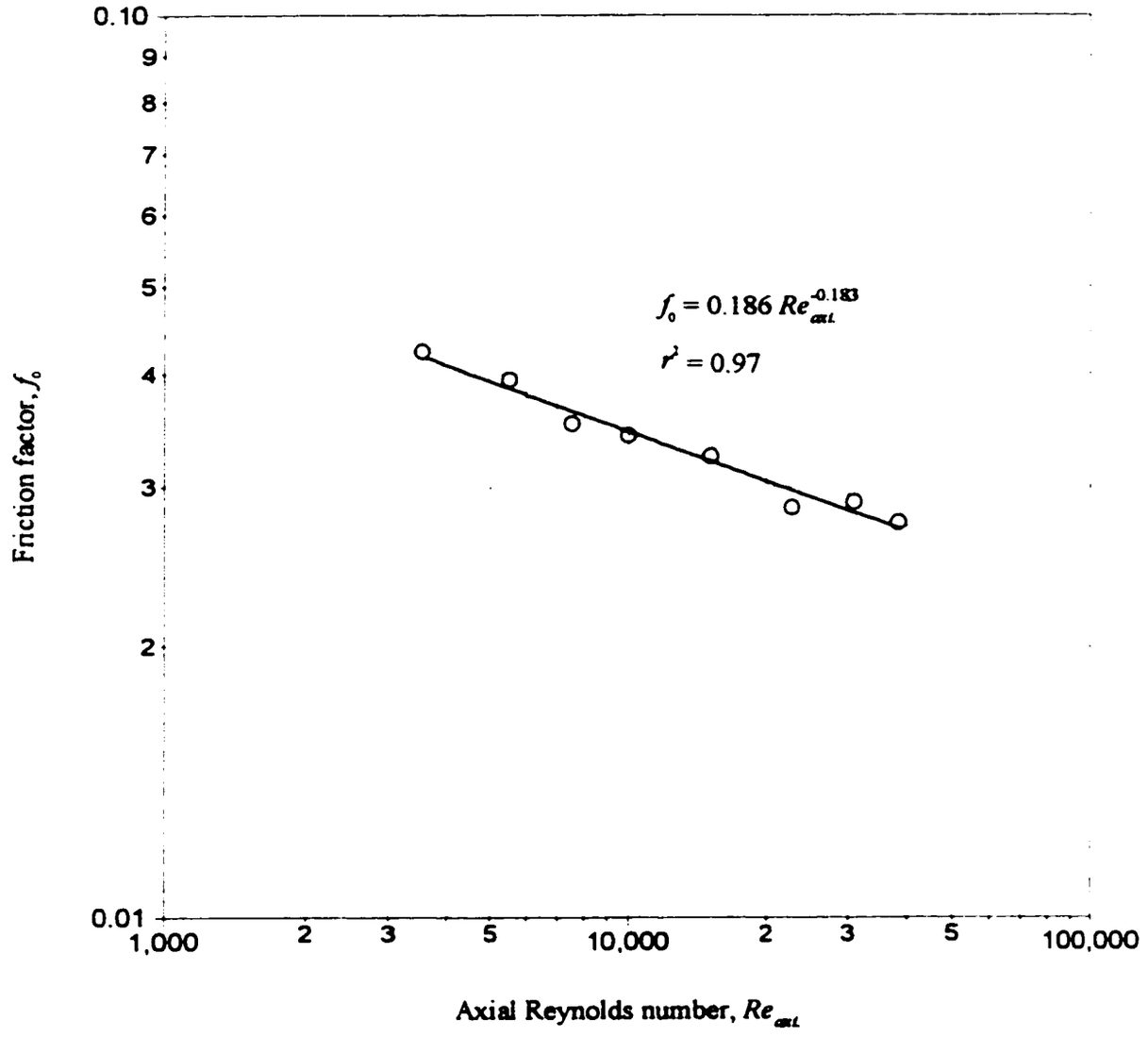

Figure 6.31- Power function relation relating f_0 to the $Re_{axi.}$ for L/D =79.6

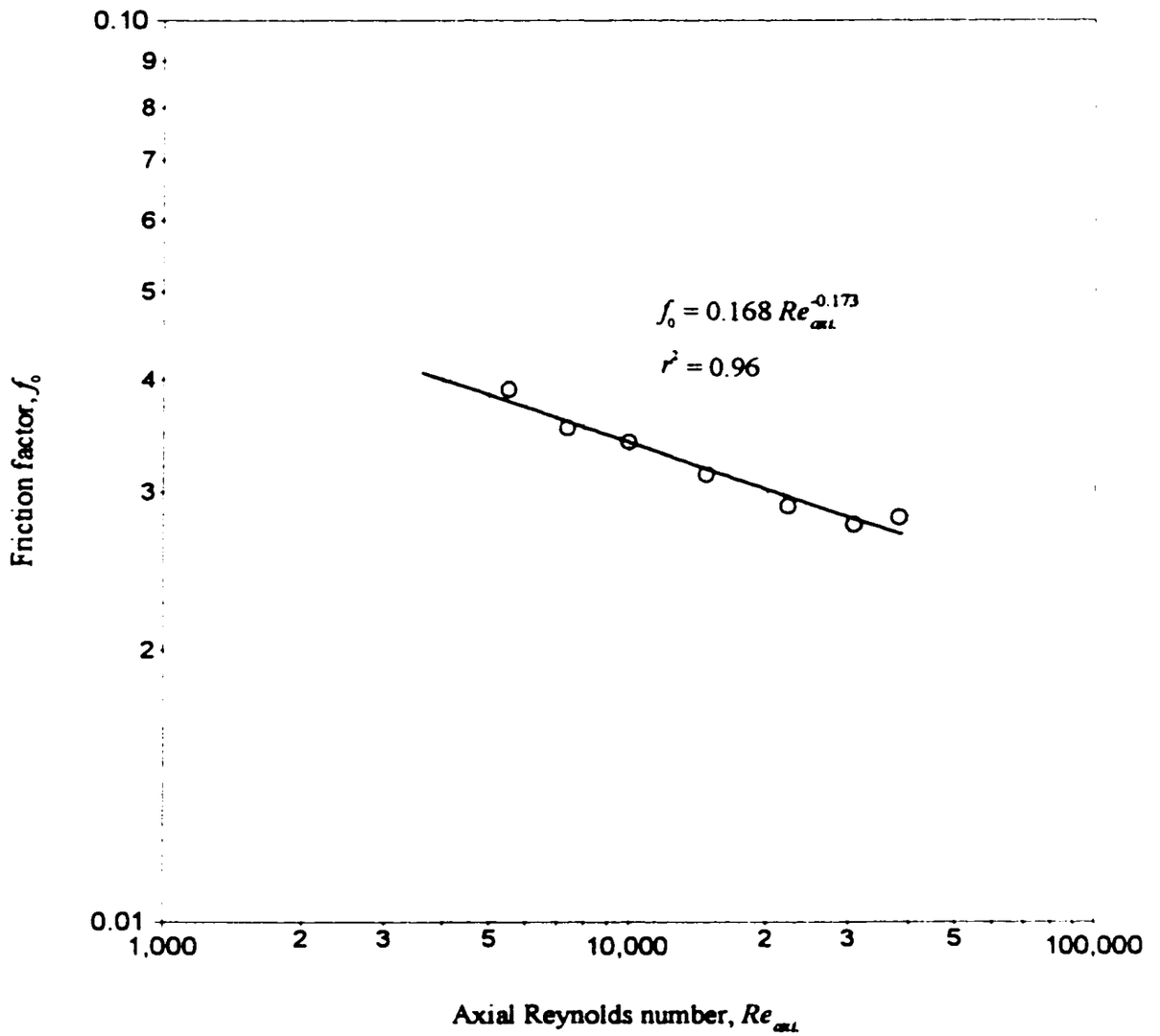

Figure 6.32- Power function relation relating f_0 to the $Re_{axi.}$ for L/D =106.4

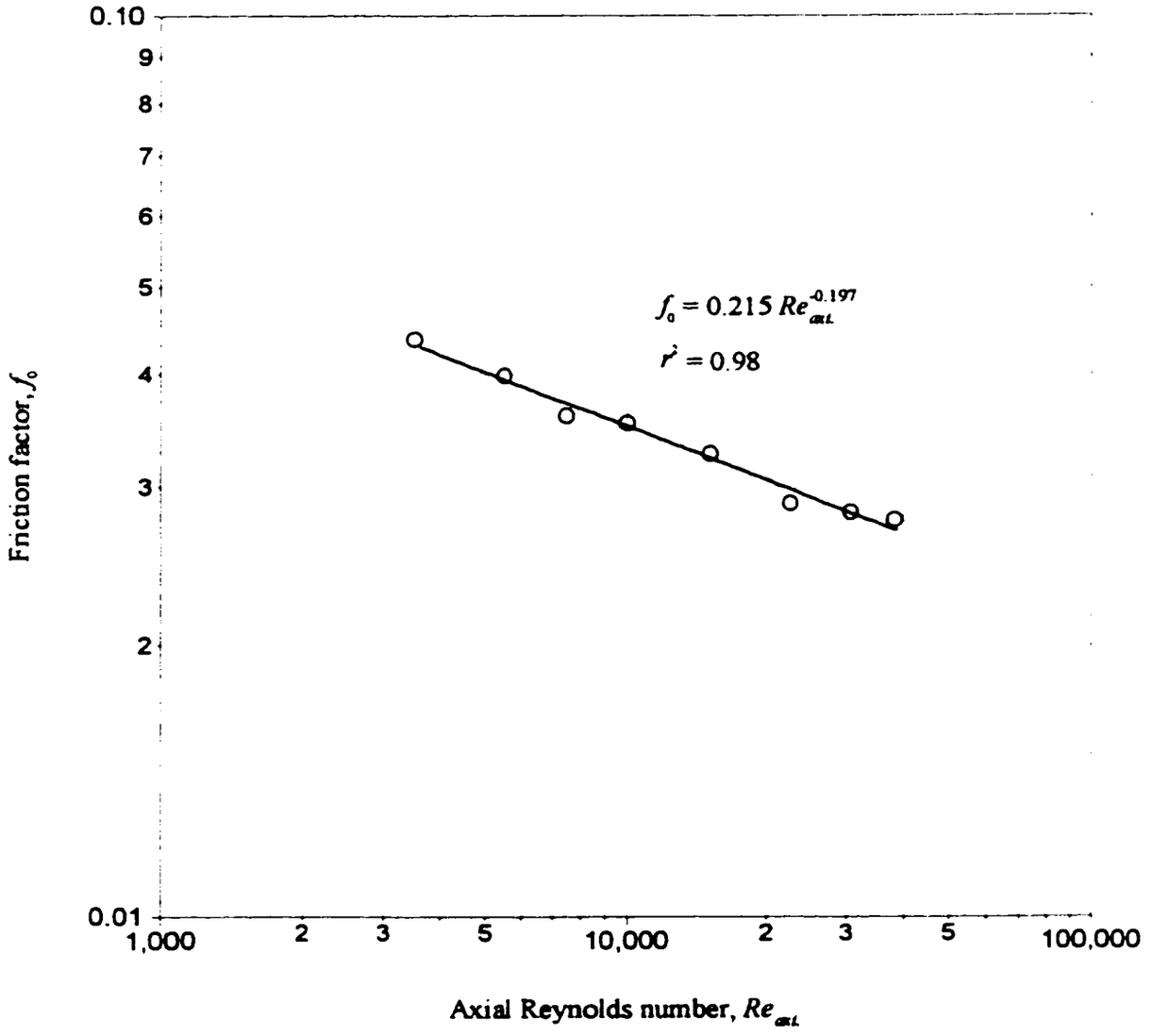

Figure 6.33- Power function relation relating f_0 to the $Re_{axi.}$ for L/D =159.6

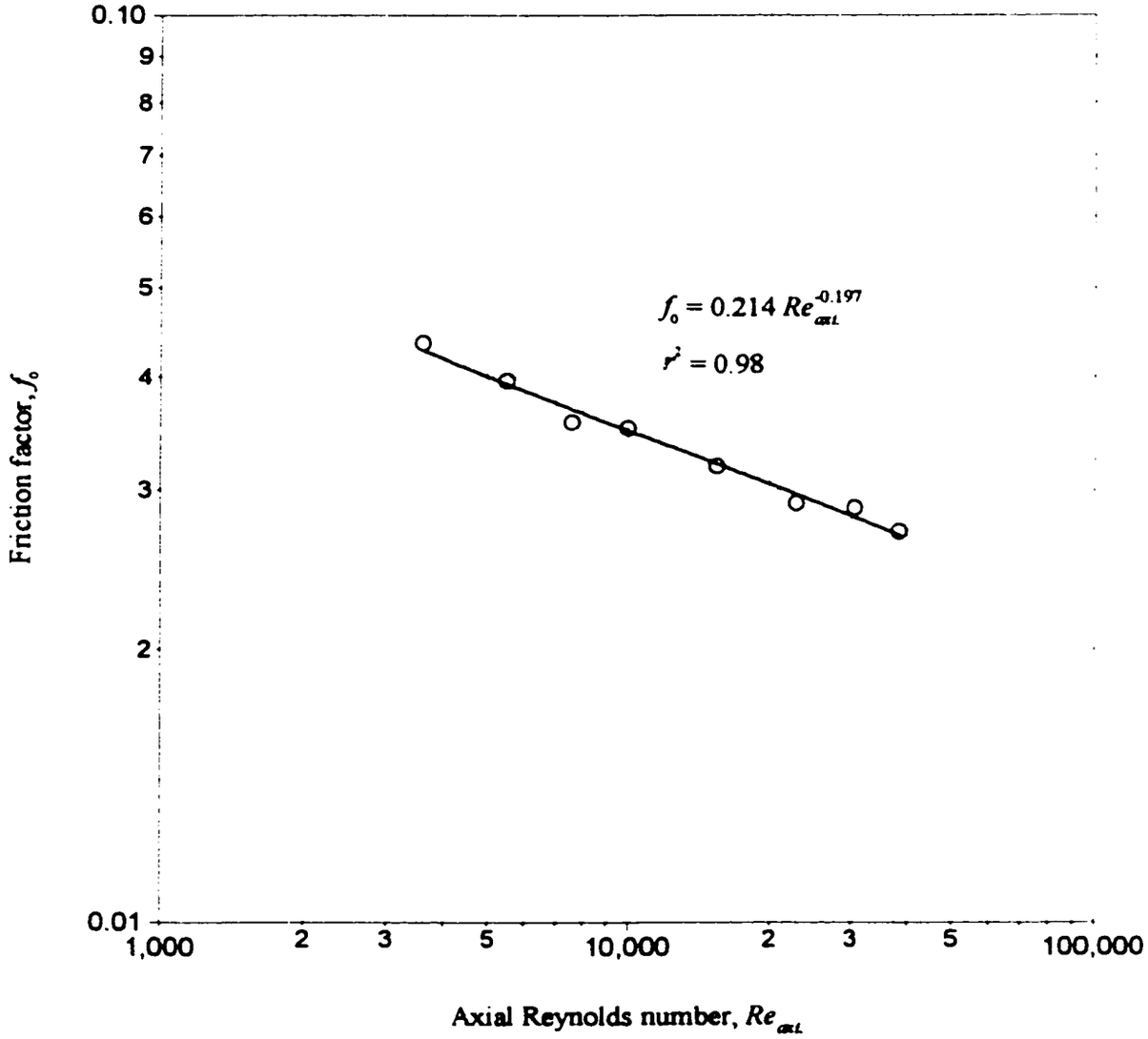

Figure 6.34- Power function relation relating f_0 to the $Re_{axi.}$ for L/D =206.6

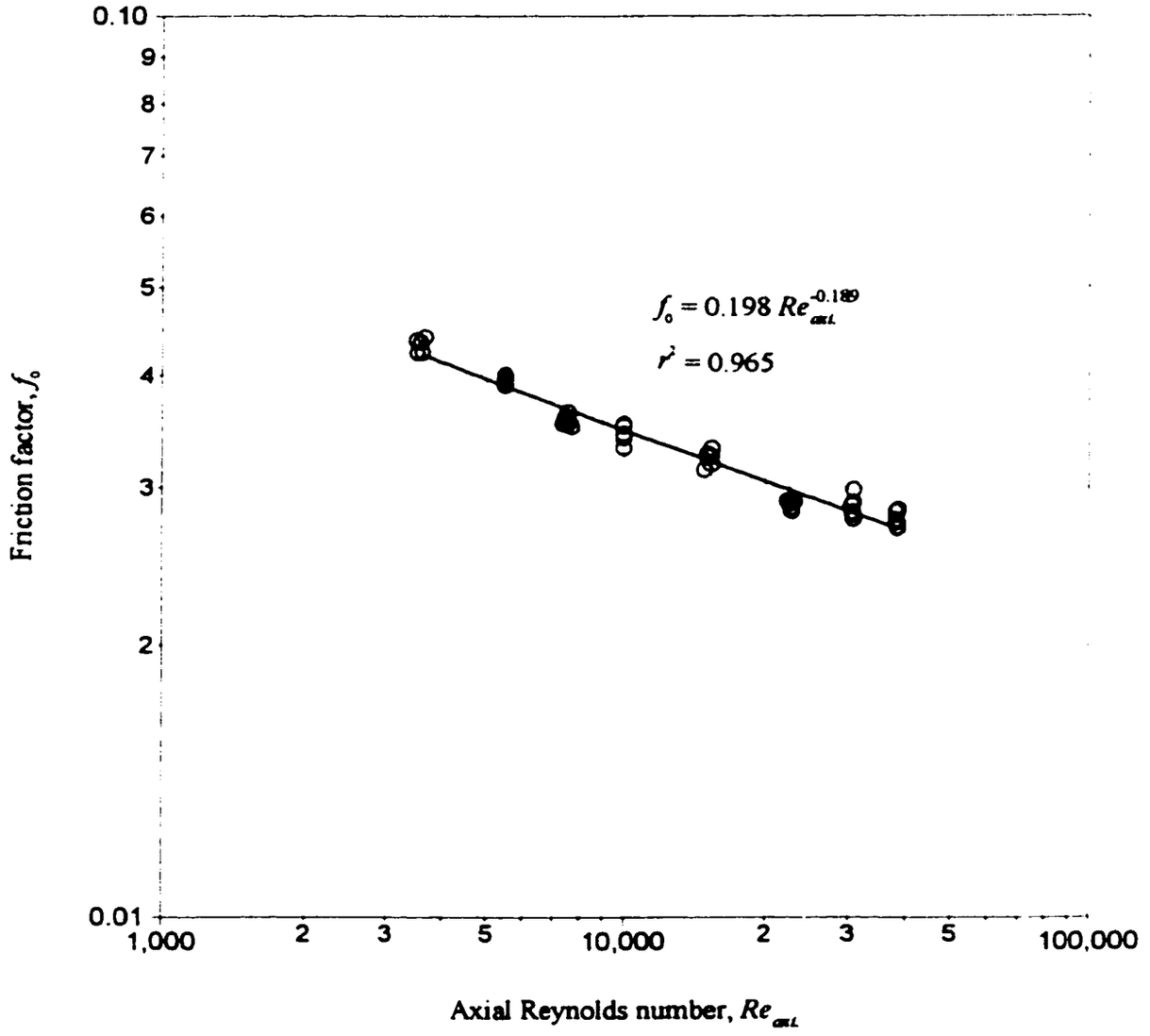

Figure 6.35- Power function relation relating f_0 to the $Re_{axi.}$ for all points

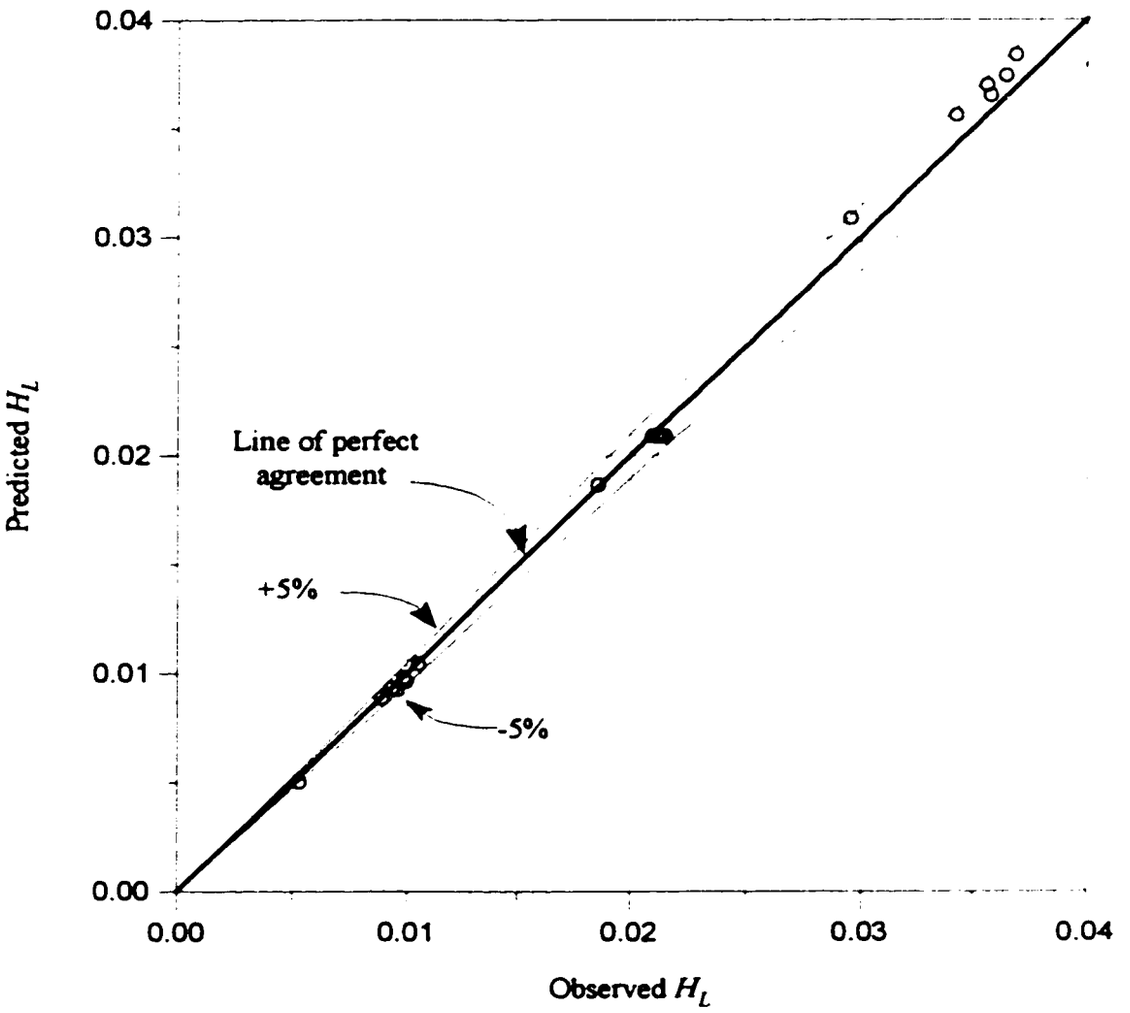

Figure 6.36- Predicted vs. observed H_L values

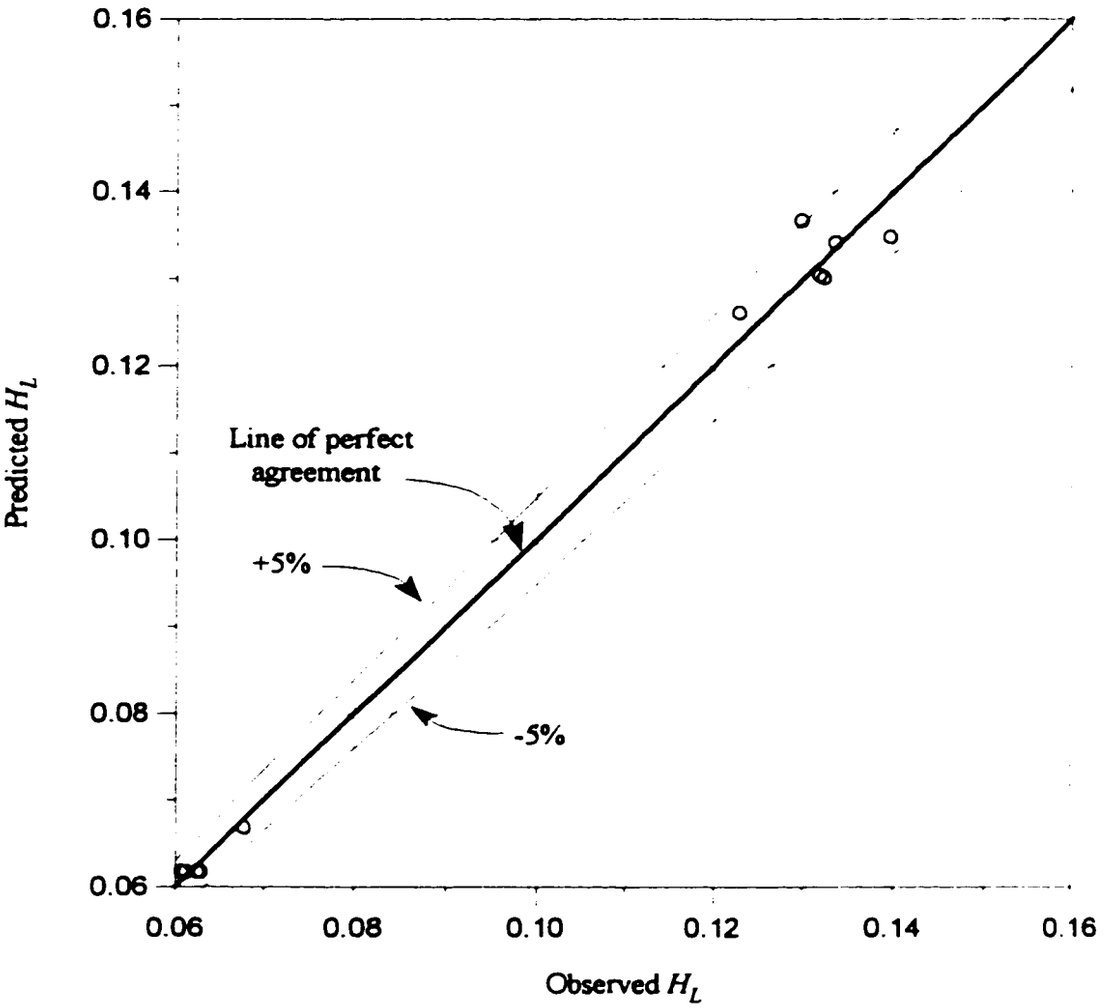

Figure 6.37- Predicted vs. observed H_L values

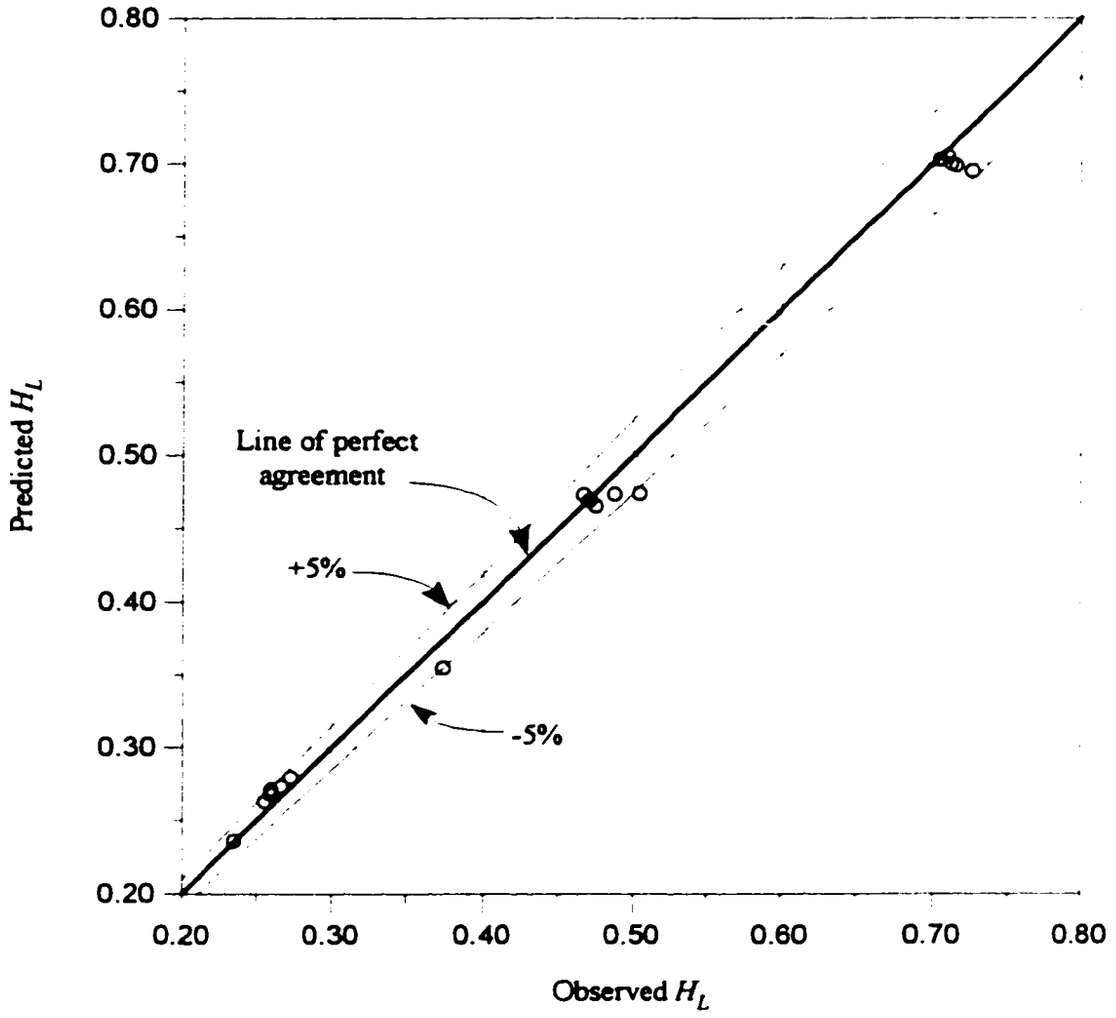

Figure 6.38- Predicted vs. observed H_L values

Table 6.1- No-suction friction factors calculation

L/D	Re_{∞}	$\frac{P_o - P_i}{1/2\rho U_i^2}$	f_o
26.6	38519	0.754	0.02834
	30754	0.744	0.02797
	22741	0.751	0.02822
	15317	0.864	0.03249
	10003	0.883	0.03320
	7578	0.968	0.03638
	5498	1.040	0.03910
	3671	1.172	0.04406
53.2	38382	1.441	0.02709
	30840	1.587	0.02983
	23029	1.540	0.02895
	15389	1.763	0.03314
	10002	1.830	0.03440
	7692	1.866	0.03507
	5494	2.128	0.04000
	3619	2.256	0.04241
79.8	38216	2.187	0.02741
	30792	2.304	0.02887
	22865	2.272	0.02847
	15370	2.588	0.03244
	9998	2.729	0.03420
	7649	2.813	0.03525
	5496	3.144	0.03940
	3524	3.379	0.04235
106.4	38066	2.998	0.02818
	30805	2.944	0.02767
	22262	3.085	0.02899
	14835	3.340	0.03139
	9995	3.628	0.03410
	7381	3.761	0.03535
	5491	4.150	0.03900
	3428	4.532	0.04259
159.6	38218	4.405	0.02760
	30797	4.494	0.02816
	22867	4.596	0.02879
	15370	5.210	0.03264
	9992	5.634	0.03530
	7644	5.734	0.03593
	5500	6.352	0.03980
	3509	6.975	0.04371
206.4	38304	5.573	0.02700
	30527	5.915	0.02866
	22741	5.984	0.02899
	15351	6.572	0.03184
	9992	7.245	0.03510
	7585	7.353	0.03563
	5498	8.173	0.03960
	3589	8.980	0.04351

Table 6.2- The values of e/D and non-linear least squares summary statistics for different L/D values

L/D	e/D	Asymptotic Std. Error	Coefficient of determination (r^2)	Asymtotic 95% Confidence Interval	
				Lower	Upper
26.6	0.00207	0.000159	0.86	0.00169	0.00244
53.2	0.00202	0.000140	0.87	0.00168	0.00234
79.8	0.00206	.000097	0.94	0.00183	0.00229
106.6	0.00207	0.000115	0.92	0.00180	0.00224
159.6	0.00209	0.000062	0.97	0.001942	0.002235
206.6	0.00196	0.000071	0.96	0.00179	0.00212
All points	0.00204	0.000043	0.92	0.00195	0.00212

Table 6.3- Roughness Factors for different tubings used in microirrigation

Data source (1)	Material (2)	Inside diameter		Roughness height			
				1.67		2.51	
		in. (3)	mm (4)	ft×10^{-5} (5)	m×10^{-6} (6)	ft×10^{-5} (7)	m×10^{-6} (8)
Paraqueima (1977)	Polyethylene	0.611	15.5	0.81	2.48	-5.79	-17.6
Paraqueima (1977)	PVC	0.693	17.6	5.94	18.1	-5.70	-17.4
von Bernuth and Wilson (1989)	PVC	0.613	15.6	10.3	31.4	5.06	15.4
von Bernuth and Wilson (1989)	PVC	1.03	16.2	8.34	25.4	3.00	9.14
von Bernuth and Wilson (1989)	Polyethylene	0.568	14.4	16.6	50.6	9.73	29.7
Urbina (1976)	Polyethylene	0.83	21.0	21.0	64.0	9.21	28.1
Urbina (1976)	Polyethylene	0.57	14.0	18.9	57.6	8.90	27.1
Urbina (1976)	Polyethylene	0.35	8.9	0.19	0.58	-8.57	-26.1
Norum (1984)	Polyethylene	0.620	15.7	3.25	9.91	-0.36	-1.09
Venkatesan et al.(1990)	PVC	0.50	12.7	10.4	31.8	----	----
Venkatesan et al.(1990)	PVC	1.00	25.4	13.06	39.8	----	----
Present study	Tyvec (porous)	0.45	11.3	9.45	28.8	7.53	22.9

Chapter 7

7. Experimental Study

"Suction" Flow Condition

7.1 Introduction

The flow of fluids through porous tubing is encountered in a variety of engineering applications in addition to microirrigation. The filtration of air, water, and sewage, transpiration cooling, the separation of isotopes by gaseous diffusion, the manufacture of paper and water desalination by reverse osmosis are some of the engineering applications. In all of these applications, since pressure is mainly used to drive the various feed

components through membranes, any quantitative description of the behaviour of porous tubing requires spatial and temporal variations of pressure along the tubing.

Aggarwall et al. (1972) obtained measurements of pressure gradient with air flowing in a porous tube of circular cross-section with fully-developed turbulent profile at the entrance and with uniform mass extraction through the wall. The inlet Reynolds number was varied in steps of approximately 10,000 from 11,000 to 101,000. Using the method of least squares applied to the experimental data, Aggrawall et al. presented 10 equations. Each equation is valid for a particular inlet Reynolds number and relates the value of the pressure drop (normalized by inlet dynamic head) to x/D (x: axial distance from entry of porous tubing ; D: inside diameter of porous tube) and suction coefficient $\beta = V_w/U$ (V_w: temporal-mean radial velocity, U: area average of axial velocity). Since there is no friction factor incorporated in these equations, they can be used for the particular porous tubing employed in his studies. Also each equation can be applied to a specific inlet Reynolds number. For inlet Reynolds numbers other than those studied, an interpolation procedure should be used.

Due to difficulty in inserting pressure taps in porous walls, particularly in thin-walled porous tubing, it has been impossible to obtain significant experimental data for pressure gradients along the porous tubing. The difficulty in obtaining precise measurements of the pressure along the porous tubing with high suction rate has resulted in a lack of the experimental data in porous tubing. In porous tubing, since the pressure drop across the

porous wall is much higher than the pressure difference along the tubing, any small pressure change due to the flow along the porous wall close to the tap has an amplified effect on the measurement particularly in high suction rates. The drilling operation in a porous wall in order to insert pressure taps usually does not give a clean hole in the porous wall. This problem combined with the slight change of shape around the hole results in disturbance of the flow and error in pressure measurements.

In the discussion on the analytical background in chapter 4 and the experimental work explained in this chapter, a formula is suggested for calculating pressure gradients along porous tubing incorporating a friction factor of the porous tubing in the non-suction condition (f_0) for the transition and rough regions of the Moody diagram. This formula is then compared with measured values obtained by Aggarwall et al. (1972) study, and the results obtained from numerical study .

7.2 Experimental Procedure

7.2.1 Selection of Tubing Length

The analytical work in chapter 4 showed that in a porous tubing with uniform suction for a particular value of U_2/U_1 (U_1:Area average velocity at the inlet, U_2:Area average velocity at the outlet) there is a linear dependence of dimensionless pressure drop or gain (normalized by inlet dynamic head) on the length of tubing (normalized by diameter, L/D). With this hypothesis different lengths of tubing were employed in such a way that both the inertia and friction effects were significant and the ratio of their importance varied

considerably for different suction rates during the course of the experiments. To investigate this relationship porous tubing with length-to-diameter ratios equal to 26.6, 53.2, 79.8, 106.4, 159.6, and 206.4 were selected.

7.2.2 Producing Different U_2/U_1

As mentioned in chapter 4 (experimental apparatus) there were two needle valves, before (inlet needle valve) and after (outlet needle valve) the test section, to control the flow rate at the inlet of the test section and at the porous section. Different values of the U_2/U_1 for each length of tubing at a particular inlet Reynolds number were produced according to the following plan. At the starting point, inlet and outlet valves were completely open. The inlet needle valve was then closed to such a degree, so that the desired inlet Reynolds number was achieved. The reading of the rotameter installed at the beginning of the test section gave the desired inlet Reynolds number. When the outlet valve is completely open for a particular inlet Reynolds number, the minimum possible pressure exists at the feed side of the porous section and at the porous section so that the permeation rate from test section is minimum. Therefore, the maximum value of U_2/U_1 for a particular inlet Reynolds number happens in this situation.

For a given value of the reading on the rotameter installed at the beginning of the test section (or a given value of the inlet Reynolds number) the outlet needle valve was partially closed. Further closing the outlet needle valve causes an increase of the pressure at the test section and thus the permeation rate increases. It has to be noted that partially closing the outlet needle valve causes the inlet flow rate and consequently the inlet

Reynolds number to decrease somewhat. Therefore, it was necessary to adjust (to open more) the inlet needle valve to achieve the desired inlet Reynolds number. The corresponding pressure drop, permeated flow rate, inlet flow rate, outlet flow rate, temperature reading from thermocouples in the system and from thermometer, pressure at the inlet of test section, and pressure of air above the liquid in the manometer were then all recorded.

After all the parameters were recorded, the outlet needle valve was closed more to generate more pressure at the porous section and obtain a new value for U_2/U_1. The inlet needle valve was then adjusted for the same inlet Reynolds number and the necessary parameters were recorded. This procedure continued until the outlet needle valve was completely closed. In this condition the average velocity at the outlet (U_2) and consequently U_2/U_1 were zero and all the water pumped to the system had to go through the porous wall. Although very tedious, uniform and sufficient readings were obtained for U_2/U_1 at a given inlet Reynolds number by adjusting inlet and outlet valves.

The above procedure was then repeated for a new value of the reading on the rotameter installed at the beginning of the test section (a new inlet Reynolds number) by adjusting the inlet needle valve to such a degree so that the desired inlet flow rate is obtained. The experiments were conducted for eight inlet Reynolds numbers, namely: 5,495, 7,552, 9,997, 15,222, 22,693, 30,731, and 38,318 for each length of porous tubing. These values of inlet Reynolds number cover the transition zone of the Moody diagram. As mentioned

earlier six different length of porous tubings (26.6, 53.2, 79.8, 106.4, 159.6, and 206.4) were employed.

As previously noted, when the outlet needle valve is completely closed the average velocity at the outlet (U_2) and consequently U_2/U_1 is zero. This condition was not practically possible for all lengths of tubings, particularly for small lengths with high values of inlet Reynolds number. With the outlet needle valve completely closed, the maximum pressure exists in the system for a particular inlet Reynolds number. The maximum pressure in the case of the outlet closed valve depends on the inlet flow rate (or inlet Reynolds number), the length of the tubing, the permeability of the porous tubing and the fluid employed in the experiment. For high inlet flow rates, higher values of the pressure are needed in the porous section to drive all of the fluid flowing in the system through the porous wall ($U_2/U_1 = 0$) when the three other parameters are constant. Also with an increasing length of the tubing, a lower pressure is required at the outlet closed-valve situation when the rest of the parameters are constant. When the permeability of the porous tubing is high, less pressure is needed to drive all of the fluid flowing in the system through the porous wall for a given value of the other parameters. With an increase in the viscosity of the flow the pressure needed to drive all of the fluid flowing in the system through the porous wall increases. Since the type of fluid and porous tubing were constant in the course of the experiments the maximum pressure in the porous test section depends on the length of the tubing and the inlet flow rate.

The maximum pressure applied in the feed portion of the porous tubing was 45 psi (3.06 bar or 0.306 MegPa). This was the maximum pressure that the porous tubing employed in this study could tolerate. The preliminary tests showed that beyond this pressure the structure of the porous tubing changes and the surface characteristics of the porous tubing is altered. Except for low values of the inlet Reynolds number and long lengths of porous tubing, the condition of a closed outlet needle valve was not possible for most of the lengths of tubing employed and most inlet Reynolds numbers applied, since pressures higher than 45 psi were needed.

7.2.3 Measurement of the Parameters

7.2.3.1 Pressure Drop Measurement

In chapter 4 the experimental device and other accessories for the measurement of the pressure drop along the test section were explained. In this section the procedure for the pressure measurement is discussed. As it was mentioned in section 7.2.2, the pressure in the porous section was increased by closing the outlet needle valve, thus increasing the permeation rate from the porous tubing. Changing the pressure in the system may cause a sudden change in the water level in the manometer limbs thus filling the manometer with water and causing water to flow toward the pressure regulator, or in the case of the decreasing pressure in the system, causing air to flow from the pressure regulator toward the manometer and the system. Therefore, five consecutive steps needed to be taken every time that the pressure is changed to prevent the manometer from filling with water or the system from sucking air: i) before increasing pressure by closing the outlet valve, the

manometer valves were closed. ii) after increasing the pressure, the pressure in the system was read from the Bourdon gage at the inlet of the test section. iii) using an air pressure regulator, the pressure above the manometer liquid was adjusted to be close to that in the system. iv) the valves of the manometer were opened, and v) finally, the overall heights of the water in the manometer were adjusted, to permit easy reading of the meniscuses by the cathetometer. This was achieved by controlling the air pressure above the manometer liquids using the pressure regulator.

7.2.3.2 Temperature, Density and Dynamic Viscosity of the Water

As mentioned in chapter 4, the temperature of water was measured by means of thermocouples installed before and after the test section, and in the reservoir. After changing the pressure in the test section (or changing U_2/U_1 by adjusting the inlet needle valve or the outlet needle valve), the readings of the LCD digital multimeter were recorded for all the thermocouples installed in the system. The temperature-resistance relationship was then used to convert the LCD digital multimeter readings to the temperature. Also at the same time, the exit temperature of water from the porous tubing was recorded with a glass mercury thermometer with a precision of ±0.1 °C installed in the water collector under the test section.

The density and dynamic viscosity of the water were obtained from following relationship for a given temperature of the water (Weast, 1981):

$$\rho_{H20} = (0.99983952 + 0.016945176T - 0.00000798704017T^2) / (1 + 0.01687958T) \qquad (7.1)$$

$$\mu_{H2o} = EXP\left\{0.001998 + 2.30259\left[\begin{matrix}(1.3272(20-T) - 0.001053 \\ (T-20)^2)/(T+105)\end{matrix}\right]\right\} \qquad (7.2)$$

where the ρ_{H2o} is the density of water in gr / cm^3 ; μ_{H2o} is dynamic viscosity of water in poise (dyne-second/cm^2) and T temperature of water in °C.

7.2.3.3 Average Velocity and Reynolds Number at the Inlet

The inlet flow rate was measured by a rotameter with a range of 0.035 to 0.320 l/sec, ±2 percent full scale accuracy, ±1/4 percent full scale repeatability, 250 mm scale. The reading on the rotameter was converted to flow rate using a calibration curve obtained for the rotameter in the system. The inlet average velocity was then obtained by the following relation:

$$U_1 = \frac{4Q_{in}}{\pi D^2} \qquad (7.3)$$

where U_1 is the average velocity at the inlet of the porous section; Q_{in} flow rate at the inlet of the porous section and D diameter of the porous tubing.

The inlet axial Reynolds number was then calculated from:

$$Re_{axi} = \frac{\rho U_1 D}{\mu} \qquad (7.4)$$

where the ρ is the density of water in gr / cm^3 ; μ is dynamic viscosity of water in poise (dyne×second/cm^2).

7.2.3.4 Average Velocity at the Outlet

The outlet flow rate measured by the method explained in chapter 4 was converted to the average velocity at the outlet by the following formula:

$$U_z = \frac{4Q_{out}}{\pi D^2} \tag{7.5}$$

where Q_{out} is the outlet flow rate and D is the diameter of the porous tubing.

7.2.3.5 Radial Velocity and Radial Reynolds Number

As mentioned in chapter 5, a volumetric determination was used to measure the flow rate in the porous section. The flow rate, measured by the procedure explained in chapter 5, was then converted to velocity at the wall assuming a uniform extraction along the wall according to the following relation:

$$V_w = \frac{Q_w}{A_w} = \frac{Q_w}{\pi DL} \tag{7.6}$$

where Q_w is the flow rate in porous section; D the diameter of tubing and L the length of tubing.

The radial Reynolds number (wall Reynolds number) was then calculated from the following formula:

$$Re_w = \frac{\rho V_w D}{\mu} \tag{7.7}$$

where ρ is the density of the water; V_w the radial velocity or velocity at the porous wall; D diameter of tubing and μ dynamic viscosity of the water.

7.3 Analysis and Discussion

7.3.1 Dimensionless Pressure Drop and U_2/U_1 Relation

The analytical work in chapter 4 showed that in a porous tubing with uniform suction, for a particular value of U_2/U_1 (U_1: Average velocity at inlet, U_2: Average velocity at outlet) there is a linear dependence of dimensionlesss pressure change (normalized by the inlet dynamic head) on the length of tubing (L/D). Since obtaining the dimensionless pressure drop or pressure gain against L/D for a specific of the U_2/U_1 is very difficult (if not impossible) for all the lengths employed, the values of the dimensionless pressure drop or pressure gain were plotted against U_2/U_1 and from these curves the values of the dimensionless pressure drop or pressure gain were found for different lengths of tubes at a particular U_2/U_1.

Figure 7.1 indicates the values of the dimensionless pressure drop or pressure gain versus U_2/U_1 for different lengths of tubes (L/D = 26.6, 53.2, 79.8, 106.4, 159.6, and 206.4) at the inlet Reynolds number equal to 5495. In this graph the ordinate parameter (dimensionless pressure change) is the pressure at the outlet minus the pressure at the inlet of the test section normalized by the inlet dynamic head. Therefore, the negative values of the dimensionless pressure change indicate the drop of the pressure and the positive values show the gain of the pressure from inlet to the outlet. As mentioned earlier, in porous tubing the momentum change of the flow due to radial flow rate through the wall tends to cause an increase in pressure in the flow direction, while the wall friction

tends to decrease the pressure. Therefore, the positive values of the dimensionless pressure change indicates that the inertia effect is higher than friction effect and the negative values show that the friction effect dominates the inertia effect in the flow. For all values of the L/D dimensionless pressure change in situation of $U_2/U_1 = 1$ is negative since in this situation the radial flow rate is zero (practically this situation does not occur) and friction force is responsible for all pressure change in the direction of the flow.

The zero point in the ordinate of this graph is a point where the pressure drop resulting from friction is equal the pressure gain due to momentum change. This point is called "pressure recovery". From the graph it is found that for the shortest length of tubing (L/D=26.5) the pressure recovery occurs in U_2/U_1 =0.85. With increasing the length of tubing the value of U_2/U_1 in which the pressure recovery occurs decreases and for the longest tubing this value becomes 0.15.

Figures 7.2 through 7.7 show the dimesionless pressure drop or pressure gain against U_2/U_1 for inlet Reynolds number equal to 7559, 9997, 15222, 22693, 30731, and 38318, respectively. Comparison of the Figures 7.1 through 7.7 indicates that for a given value of length, with increasing inlet Reynolds number, the value of the U_2/U_1 in which the pressure recovery (dimensionless pressure change equal to zero) occurs increases. The reason is that with increasing the inlet Reynolds number friction factor decreases and the inertia effect can overcome the friction effect at higher values of the U_2/U_1. For instance for inlet Reynolds number equal to 5495 the pressure recovery happens at the

U_2/U_1 =0.85 for L/D=26.6 whereas this value for inlet Reynolds number equal 38318 is 0.9.

The dotted lines in Figures 7.1 through 7.7 have been obtained by extrapolation. Taking experimental data in these portions of the curves was not possible. It can be seen with increasing inlet Reynolds numbers, the range of the U_2/U_1 in which the data can be obtained decreases. From these figures one can see that the lack of the experimental data for each length of tubing occurs for low values and high values of the U_2/U_1. The reason for the lack of data for low values of the U_2/U_1 was explained earlier. To obtain different values of axial Reynolds number within the porous section, different values of pressures at the feed side of the porous section are necessary. These pressures cause the radial flow rate and the momentum changes along the porous tubing. Generation of the low values of the U_2/U_1 with the existing set-up was not possible. Increasing the inlet Reynolds number for a particular length of tubing, causes the gap in experimental data for low values of the U_2/U_1 to increase. The reason is that more pressure is needed in the feed portion of the porous tubing to generate higher values of inlet Reynolds number. For a particular inlet Reynolds number with increasing length of tubing the lack of data for low values of the U_2/U_1 increases. For a particular inlet Reynolds number (and therefore for given pressure at the feed portion of the porous tubing) with an increased length of tubing the area within which the radial flow rate can occur increases, and U_2 and consequently U_2/U_1, decreases.

The reason for the lack of experimental data for completely closed outlet needle valve ($U_2/U_1 = 0$) was discussed in detail in section 7.2.2. The same reason can be traced for the lack of the data for low values of the U_2/U_1. From Figures 7.1 through 7.7 one can see that for a given inlet Reynolds number the gap in experimental data increases for a small length of tubing. The reason as discussed in section 7.2.2 is that for small length tubing, a higher pressure is needed to drive flow through the porous wall for a given U_2/U_1, and a given inlet Reynolds number. As was mentioned earlier the maximum allowable pressure at the feed portion of the porous tubing is 45 psi (3.06 bar or 0.306 MegPa). Also the comparison of the figures shows that for a given length of tubing the gap of the experimental data increases with increasing the inlet Reynolds number. The reason is that with a higher inlet Reynolds number, a higher pressure is needed to drive flow through the porous wall for a given value of U_2/U_1 and length of the tubing. Thus the upper limit 45 psi becomes increasingly restrictive at higher inlet Reynolds number.

7.3.2 Dimensionless Pressure Change and L/D Relation

As was mentioned above the values of the dimensionless pressure drop or pressure gain were plotted against U_2/U_1 to obtain the values of the dimensionless pressure drop or pressure gain for different lengths of tubes at a particular U_2/U_1 (Figures 7.1 through 7.7). The values of the dimensionless pressure drop or pressure gain were obtained for eleven values of U_2/U_1 in steps of 0.1 from zero to 1.0 for different values of the inlet Reynolds number (Figures 7.1 through 7.7).

For each inlet Reynolds number, the values of the dimensionless pressure change were then plotted versus L/D for different U_2/U_1. Figures 7.8 through 7.14 indicate the dimensionless pressure drop versus L/D for different U_2/U_1 and for inlet Reynolds numbers of 5,495, 7,559, 9,997, 15,222, 22,693, 30,731, and 38,318 respectively. It can be seen from these figures that the linear dependence of the dimensionless pressure change and L/D for a particular value of the U_2/U_1, as was found by analytical work in chapter 4, (Equation 4.37) is verified. The equation and the coefficient of determination of the each line are indicated in Appendix C. Equation 4.37 obtained in chapter 4 relating dimensionless pressure change and L/D is :

$$\frac{P_o - P_1}{\frac{1}{2}\rho U_1^2} = (2\beta_1 - 1) - (2\beta_2 - 1)\frac{U_2^2}{U_1^2} - \frac{f}{3} \times \frac{L}{D}\left(1 + \frac{U_2}{U_1} + \frac{U_2^2}{U_1^2}\right) \qquad (4.37)$$

According to the equation 4.37 the slope of the each line is:

$$Slope = \frac{f}{3}\left(1 + \frac{U_2}{U_1} + \frac{U_2^2}{U_1^2}\right) \qquad (7.8)$$

The slope of the these line were measured and compared with the values predicted by Equation 7.8. Table 7.1 indicates the comparison between measured and predicted slopes for different inlet Reynolds number and lengths of tubing. As it can be seen from table the values predicted from equation 7.8 and the values obtained by measurements are quite close.

The first term on the right hand side of equation 4.37 is the intercepts of the lines with the ordinates in Figures 7.8 through 7.14 for different inlet Reynolds numbers. From these

figures the values of the intercepts for different values of U_2/U_1 were obtained. The values of the intercepts were then plotted versus U_2/U_1 for different values of the inlet Reynolds number. Figures 7.15 through 7.21 indicate intercepts obtained from Figures 7.8 through 7.14 versus U_2/U_1 for inlet Reynolds number 5,495, 7,559, 9,997, 15,222, 22,693, 30,731, and 38318 respectively.

In Figures 7.15 through 7.21 the curves and the equations fitted to the experimental data have been shown. From these figures one can see that for all inlet Reynolds numbers, the curves can be fitted by a second degree polynomial in the form :

$$z = k(1 - \frac{U_2^2}{U_1^2}) \qquad (7.9)$$

where k is a function of the inlet Reynolds number. The value of the k in Equation (7.9) varies from 2.9 for inlet Reynolds number equal 5495 up to 3.3 for 30731. This value becomes constant after inlet Reynolds number 30731. It can be seen that the equation 6.38 is now a function of U_2/U_1 and f. The final equation for prediction of the pressure change along the porous section is :

$$\frac{P_o - P_i}{\frac{1}{2}\rho U_1^2} = k(1 - \frac{U_2^2}{U_1^2}) - \frac{f}{3} \times \frac{L}{D}\left(1 + \frac{U_2}{U_1} + \frac{U_2^2}{U_1^2}\right) \qquad (7.10)$$

7.3.3 Dimensionless Pressure Drop Prediction

The values of the dimensionless pressure drop or pressure gain along the porous tubing were calculated by Equation 7.10 for different lengths of porous tubing and different inlet Reynolds numbers and were then compared with the measured values. Figures 7.22

through 7.27 indicate these comparisons for inlet Reynolds numbers equal to 22,693. The comparisons for other inlet Reynolds numbers can be found in the Appendix D (Figures D.1 through D.36).

Equation 7.10 was derived based on the assumption of the uniform radial flow rate along the porous tubing. The actual radial flow rates through the tube walls were not exactly constant along the suction region due to the variation of the pressure down the tube axis. In most instances this was quite negligible because the pressure drop down the axis of the porous tubing was not significant compared with the pressure drop through the wall. In this section the validity of the axially constant radial velocity assumption will be investigated and the limits of the Equation 7.10 in predicting of the pressure drop or pressure gain along the porous tubing will be examined.

For all the inlet Reynolds numbers under study and L/D up to 79.8 the prediction of the pressure drop or gain by equation 7.10 is within ±10% accuracy. For the inlet Reynolds numbers equal and higher than 30,731 the pressure drop or pressure gain can be predicted by Equation 7.10 for all lengths of porous tubing under study within ±10% accuracy.

For inlet Reynolds numbers between 5495 and 30731 and for L/D higher than 79.8 the discrepancy between the predicted values using Equation 7.10 and measured values increases, indicating that the assumption of the axially constant radial velocity ceases to be

valid for L/D higher than 79.8 since the pressure drop along the porous tubing is significant compared with pressure drop through the porous tubing.

For a particular inlet Reynolds number with increasing length of tubing the discrepancy between the predicted values and measured values increases. The reason is that with increasing length of tubing, the axial pressure drop between inlet and outlet increases and the pressure drop through the porous wall decreases, so that the assumption of the uniform wall suction ceases to be valid. For a particular length of tubing with increasing inlet Reynolds number the agreement between predicted and measured values improves since although the pressure drop through the porous wall and pressure drop along the porous tubing increases, the rate of increase of the pressure drop through the porous wall is more than that of the along the porous tubing. The pressure drop through the wall is approximately linear with flow rate whereas changes down the axis are scaled by the square of the velocity. Therefore the situation is worse for high velocity flows in long tubes.

To summarize, from the above mentioned figures the following conclusions can be drawn:

1. For all of the inlet Reynolds numbers under study and for L/D= 26.6 excellent agreement exists between observed and predicted dimensionless pressure difference values obtained from Equation 7.10 indicating that the assumption of the uniform radial flow along porous tubing is valid.

2. For inlet Reynolds numbers greater than 30,000 for all lengths of tubing under study there is good agreement between predicted and observed values of the dimensionless pressure change.

3. For a particular inlet Reynolds number with increasing the length of tubing the discrepancy between observed and predicted values increases showing that the assumption of uniform suction along tubing ceases to be valid for this situation.

4. For a particular length of tubing with increasing inlet Reynolds number the agreement between observed and predicted values improves since the assumption of uniform friction factor along tubing is valid.

7.3.4 Pressure Gradient Formula

The Equation 7.10 can be applied to a small length of porous tubing (ΔL). For this small length of porous tubing the different parameters in Equation 7.10 are:

$$P_0 - P_t = \Delta P \tag{7.11}$$

$$U_1 = U \tag{7.12}$$

$$U_2 = U + \Delta U \tag{7.13}$$

$$L = \Delta L \tag{7.14}$$

Substituting Equations 7.11 through 7.14 into Equation 7.10 yields:

$$\Delta P = \tfrac{1}{2}\rho U^2 \left\{ k\left[1 - \left(\frac{U + \Delta U}{U} \right)^2 \right] - \frac{f}{3}\frac{\Delta L}{D}\left[1 + \frac{U + \Delta U}{U} + \left(\frac{U + \Delta U}{U} \right)^2 \right] \right\} \tag{7.15}$$

$$\Delta P = \tfrac{1}{2}\rho U^2 \left\{ \begin{array}{l} k\left[1 - 1 - \dfrac{2\Delta U}{U} - \left(\dfrac{\Delta U}{U}\right)^2\right] - \\ \dfrac{f}{3}\dfrac{\Delta L}{D}\left[1 + 1 + \dfrac{\Delta U}{U} + 1 + \dfrac{2\Delta U}{U} + \left(\dfrac{\Delta U}{U}\right)^2\right] \end{array} \right\} \tag{7.16}$$

$$\frac{\Delta P}{\Delta L} = \tfrac{1}{2}\rho U^2 \left\{ -\frac{k}{U}\frac{\Delta U}{\Delta L} - \frac{k}{U}\left(\frac{\Delta U}{U}\right)\frac{\Delta U}{\Delta L} - \frac{f}{D} - \frac{f}{D}\frac{\Delta U}{U} - \frac{1}{3}\frac{f}{D}\left(\frac{\Delta U}{U}\right)^2 \right\} \tag{7.17}$$

$$\frac{dP}{dL} = Lim_{\Delta L \to 0} \frac{\Delta P}{\Delta L} = \tfrac{1}{2}\rho U^2 \left(-\frac{k}{U}\frac{dU}{dL} - \frac{f}{D} \right) \tag{7.18}$$

For a short length of porous tubing (dL) the continuity equation is:

$$AU - A(U + dU) = V_w \times \pi D \times dL \tag{7.19}$$

where A = cross section of porous tubing; U = velocity at the inlet of porous tubing, $U + dU$ = velocity at the outlet of porous tubing; V_w = velocity at the wall of porous tubing. Substituting $A = \pi D^2/4$ in Equation 7.19 and doing some manipulations gives:

$$\frac{dU}{dL} = -\frac{4V_w}{D} \tag{7.20}$$

Substituting the value of dU/dL from Equation 7.20 in Equation 7.18 yields:

$$\frac{dp}{dL} = \frac{4}{D}\tfrac{1}{2}\rho U^2 \left(\frac{k}{2}\frac{V_w}{U} - f \right) \tag{7.21}$$

7.3.5 Comparison of the Equation 7.21 with Measured Values

As mentioned earlier the porous tubing used in the present study was not rigid enough to permit insertion of the pressure taps into the wall to measure the variation of the pressure along the tubing. Therefore the validity of the Eq. 7.21 in the prediction of the pressure loss or gain along the tubing was tested by the comparison of the predicted values with the

measured values obtained by Aggarwall et al. (1972). Also the prediction of the pressure change along the tubing is compared with that of the numerical study discussed in chapter 3.

Figure 7.28 indicates a comparison between the dimensionless pressure change along tubing predicted by the Equation 7.21 and those measured by Aggrawall et al. (1972) for an inlet Reynolds number equal to 11,260 and radial Reynolds numbers ranging from 18.1 to 108.6. From this figure one can see that for measured and predicted values after Reynolds number greater than about 20, pressure rises rather than falls in the direction of flow (pressure recovery happens). This is because the rate of the loss of momentum of the fluid resulting from suction, for radial Reynolds numbers greater than 20, more than overcomes the wall friction. From this figure it can be also seen that up to a radial Reynolds number of about 72.4, the predicted values of the pressure drop or pressure gain by the Equation 7.21 are in reasonably close agreement with the measured values at the outlet of the porous section. In this range of the radial Reynolds numbers, the Equation 7.21 tends to overestimate the dimensionless pressure change between inlet and outlet of the porous section with the maximum discrepancy at the middle of the porous section. For higher radial Reynolds numbers, the discrepancy between predicted and measured values increases for the all parts of the porous section and it seems that the Equation 7.21 fails to accurately predict the dimensionless pressure gain for radial Reynolds number greater than about 72.4 for inlet Reynolds number 11,260.

Apart from the smaller discrepancy between measured and predicted values between inlet and outlet porous sections and higher pressure recovery with increasing inlet Reynolds number, for inlet Reynolds number equal to 21,710 and 29,980 the agreement between predicted and measured values follows the same trend as for the inlet Reynolds number equal to 11,260. Comparison between measured and predicted values by Equation 7.21 for inlet Reynolds number equal to 21,710 and 29,980 can be seen in Appendix E (Figures E.1 and E.2).

Figure 7.29 indicates the predicted and measured values of the dimensionless pressure change for an inlet Reynolds number equal to 41,840 and radial Reynolds number ranging from 18.1 to 108.6. It can be seen that for measured values the rate of the rise of the dimensionless pressure is slow at the entrance of the porous section, increasing somewhat as the end approached. For predicted values this situation is not observed. Although there is a good agreement between measured and predicted values for the radial Reynolds number equal to 18.1, after Re_w=18.1 the Equation 7.21 tends to overestimate the dimensionless pressure up to x/D=0.6 and underestimate for the rest of the porous section. It can be seen that both Equation 7.21 and measured values show Re_w=72.4 for pressure recovery for this inlet Reynolds number. The same trend with small change can be observed for inlet Reynolds number equal to 52,120, 62,550, 70,670, 83,280 and 91,420 with higher pressure recovery with increasing inlet Reynols number. Comparison between measured and predicted values by Equation 7.21 for inlet Reynolds number equal

to 52,120, 62,550, 70,670, and 83,280 can be seen in Appendix E (Figures E.3 through E.7).

Figure 7.30 shows a comparison between predicted and measured values for inlet Reynolds number equal to 101,160 and radial Reynolds numbers varies from 18.1 to 162.9. One can see that a nearly perfect agreement exists for radial Reynolds number 18.1. There is a small disagreement between predicted and measured values for radial Reynolds number higher than 18.1. The discrepancy between measured and predicted values increases with increasing radial Reynolds numbers. From this figure it is found that for all radial Reynolds number the Equation 7.21 tends to overestimate the pressure drop and underestimate the pressure gain for all parts of the porous section. Both measured and predicted values show a constant pressure gradient for all radial Reynolds number under study along the porous section for this inlet Reynolds number.

7.3.6 Comparison of Equation 7.21 with Numerical Study

In this section the prediction of the pressure drop or gain is compared with the results obtained from numerical study. Boundary conditions, grid arrangement, initial profiles, flow geometry, and governing equations are as discussed in chapter 3. From chapter 3 it was found that the Wilcox's Low-Re k-ω turbulent model is capable of predicting correctly the flow characteristics observed in the experiment. Therefore, this model was used in this section for comparisons.

Four different lengths namely (L/D=13.3, 26.6, 39.9, 53.2) were employed and for each length four inlet Reynolds number namely 10,000, 15,000, 20,000, and 30,000 were selected. For each length and each inlet Reynolds number three radial Reynolds number were selected.

7.3.6.1 Comparison for L/D=26.6

Figure 7.31 indicates a comparison between the dimensionless pressure drop or gain obtained by Equation 7.21 and those obtained by the numerical study for inlet Reynolds number of 10,000. From this figure it is found that the disagreement observed for values of dimensionless pressure drop obtained by two approaches for L/D=13.3 (Figure E.8) does not occur for L/D=26.6. For all values of the radial Reynolds number a good agreement exists between values obtained by two approaches.

Figure 7.32 indicates the axial pressure profile along the porous tubing obtained from Equation 7.21 and numerical study for inlet Reynolds number of 20,000. According to Equation 7.21 the flow experiences a pressure recovery for radial Reynolds numbers greater than about 30. For the numerical study this recovery begins at about a radial Reynolds number of 37. Therefore, the $k-\omega$ model tends to overestimate the pressure recovery in terms of radial Reynolds number.

In Figure 7.33 a comparison between variation of the axial pressure down the tube obtained from Equation 7.21 and numerical study for inlet Reynolds number of 30,000 is shown. From this figure it is found that for an inlet Reynolds number of 30,000 a radial

Reynolds number of 37.0 is not large enough to achieve an axially-increasing pressure. Both approaches show that the shape of the axial profile of the pressure is linear for the range of the radial Reynolds numbers under study.

7.3.6.2 Comparison for L/D=39.9

Figure 7.34 shows a comparison of the axial pressure variation obtained by numerical approach and Equation 7.21 for the inlet Reynolds number of 20,000. The axial pressure variation predicted by the numerical study diverges from the curves obtained by Equation 7.21 by increasing radial Reynolds number. A comparison of this figure with Figure 7.32 indicates that with increasing L/D, the discrepancy between two approaches, particularly for the low radial Reynolds numbers, increases. According to both approaches, the shape of this axial profile of the pressure is approximately linear at radial Reynolds number of 12.3. For higher values of radial Reynolds number a small change can be observed in slope of the pressure gradient along the tube. For radial Reynolds number of 24.7 the rate of decrease of dimensionless pressure is high at the entrance of tube, decreasing somewhat as the end approached. For a radial Reynolds number of 37.0, a reverse trend is observed compared with inlet Reynolds number of 10,000, Figure E.13, i.e., the rate of rise of dimensionless pressure is low at the entrance of tube, increasing as the end approached.

Figure 7.35 shows a comparison of the axial pressure variation along porous section obtained by Equation 7.21 and numerical approach for the inlet Reynolds number of 30,000. Comparison of this figure with Figure 7.33 shows that with increasing the length of tubing the discrepancy between values predicted by two approaches increases. Up to

the radial Reynolds number of 24.7 both approaches show a linear shape for the axial pressure profile. For radial Reynolds numbers 37.0 and higher, a small change can be observed in the rate of the pressure variation along the porous section.

Comparison of the axial pressure variation along porous section obtained by Equation 7.21 and numerical approach for L/D=13.3, 53.2 can be found in Appendix E (Figures E.8 through E.16).

7.4 Conclusion

The equation derived based on uniform suction along a porous tubing can predict the dimensionless pressure change within ±10% in the transition region of Moody diagram for L/D up to 79.8 and for all inlet Reynolds number under study. For inlet Reynolds numbers higher than about 30,000 the dimensionless pressure drop can be predicted by the Equation 7.10 within ±10% for all L/D under study.

Comparison of the pressure gradient changes obtained using Equation 7.21 with measured values show that Equation 7.21 can precisely predict the variations of the pressure along porous tubing for high values of inlet Reynolds number or for low values of inlet Reynolds number and low values of radial Reynolds number.

The best agreement between values obtained by Equation 7.21 and numerical study occurs for an inlet Reynolds number of 10,000 for all lengths and all radial Reynolds numbers

under study. For a particular inlet Reynolds number and length of tubing, the axial pressure variation predicted by the numerical study diverges from the curves obtained by the Equation 7.21 with increasing radial Reynolds number for all inlet Reynolds number and lengths under study. For a particular inlet Reynolds number and radial Reynolds number, the discrepancy between predicted values obtained by the two approaches increases for all values of inlet Reynolds number and radial Reynolds number under study. Both approaches show a linear axial pressure profile for all lengths and inlet Reynolds number under study at the radial Reynolds number of 12.3.

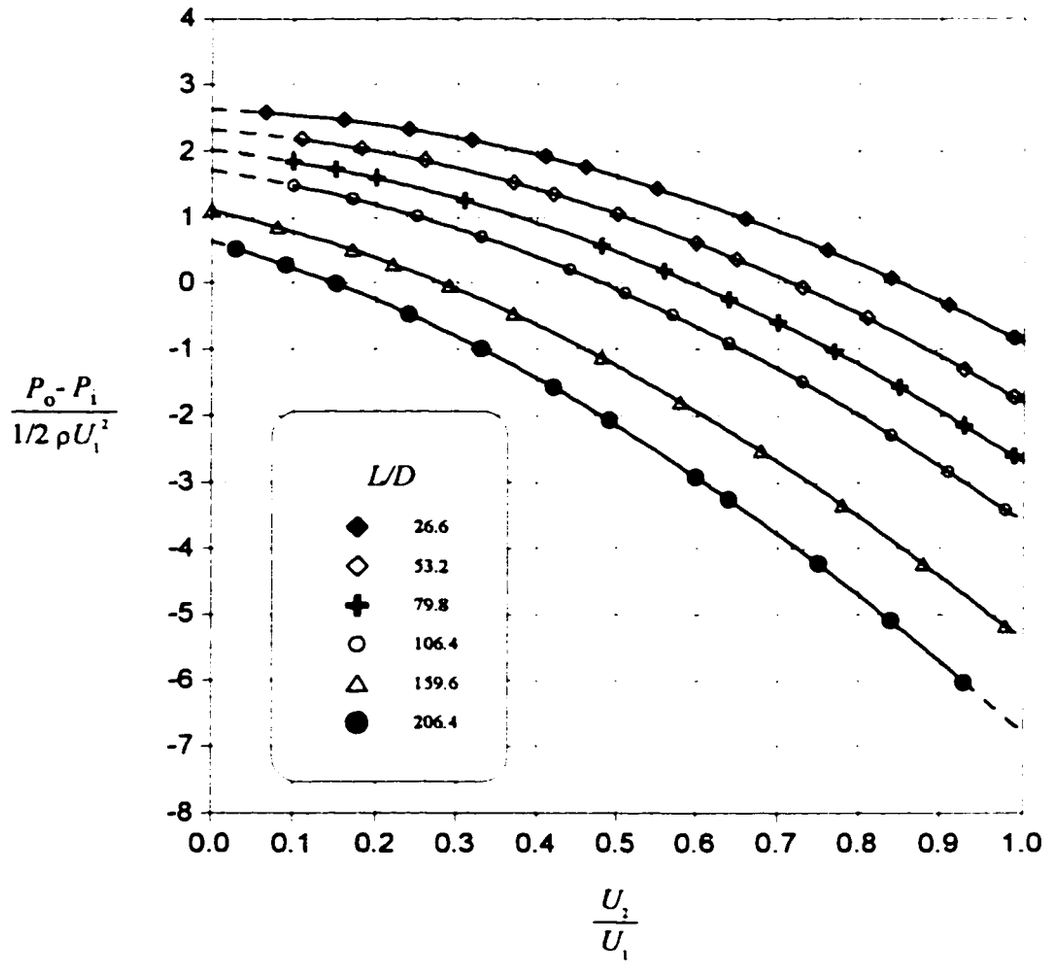

Figure 7.1- Dimensionless pressure change $(P_o - P_i) / \frac{1}{2}\rho U_1^2$ versus $\frac{U_2}{U_1}$ for various tube lengths and $Re_{axi.}$=5495

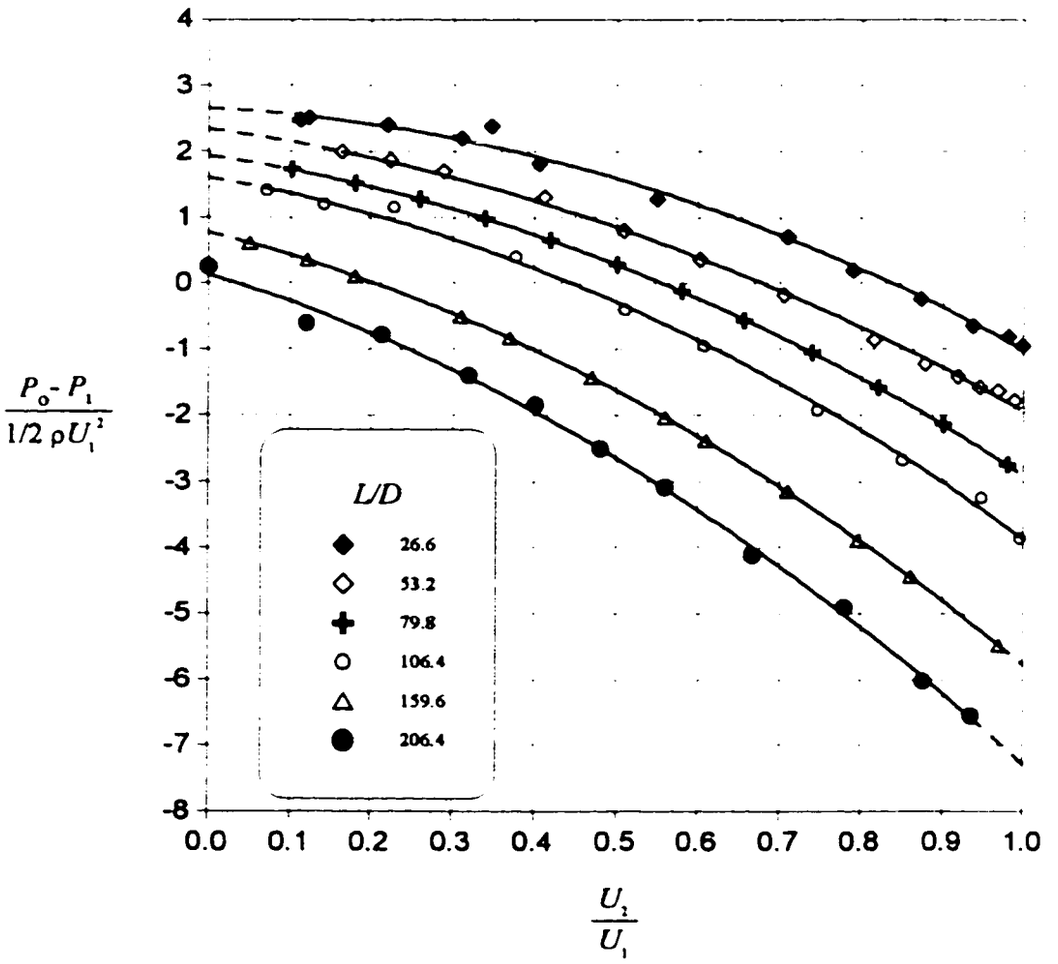

Figure 7.2- Dimensionless pressure change $(P_o - P_i) / \frac{1}{2}\rho U_1^2$ versus $\frac{U_2}{U_1}$ for various tube lengths and $Re_{axi.}$=7559

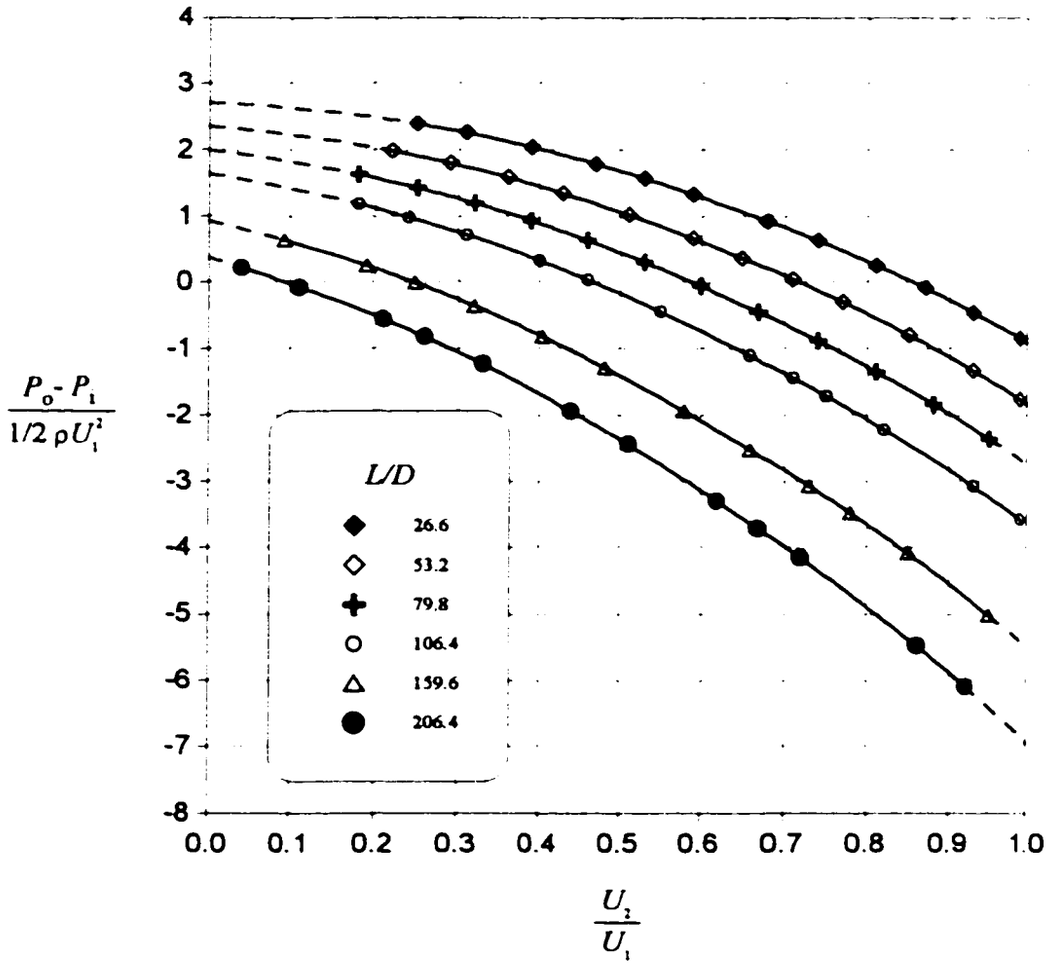

Figure 7.3- Dimensionless pressure change $(P_o - P_i)/\frac{1}{2}\rho U_1^2$ versus $\frac{U_2}{U_1}$ for various tube lengths and $Re_{axi.}$=9997

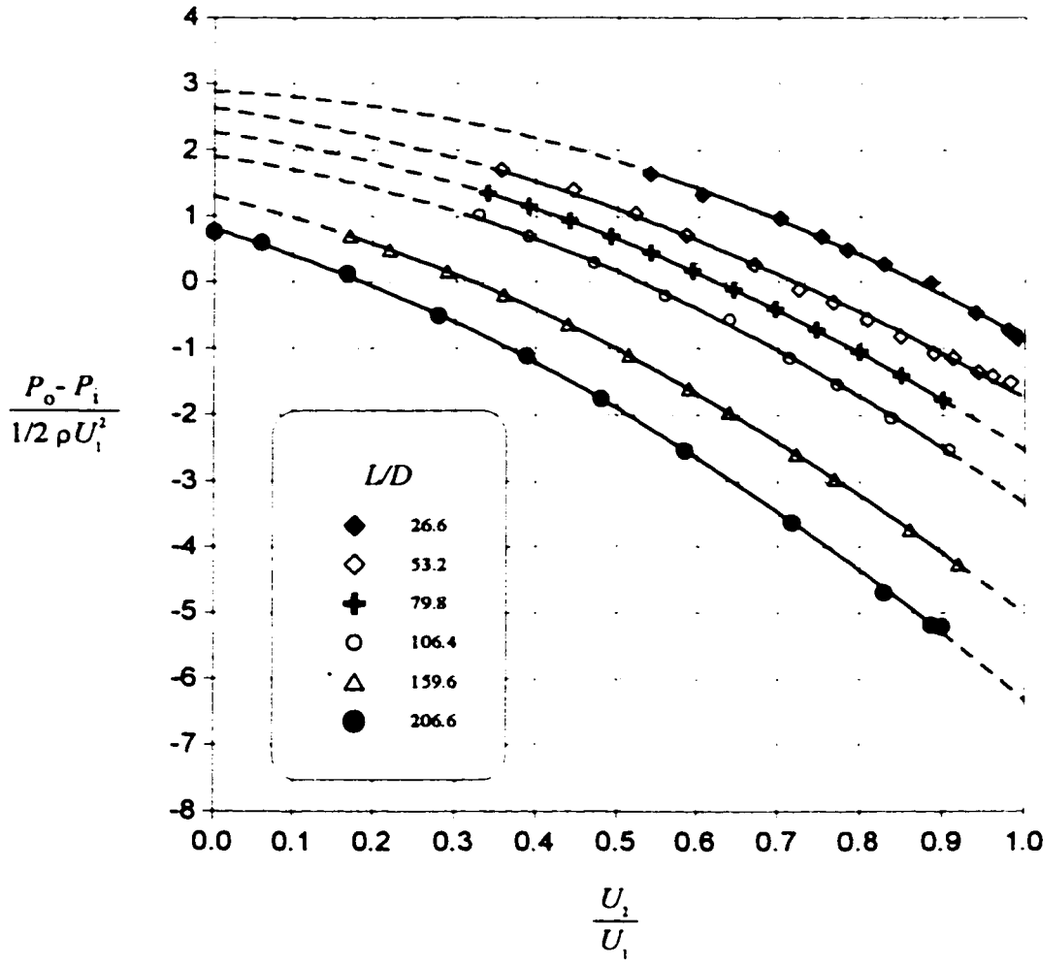

Figure 7.4- Dimensionless pressure change $(P_o - P_i) / \frac{1}{2}\rho U_1^2$ versus $\frac{U_2}{U_1}$ for various tube lengths and $Re_{axi.}$=15222

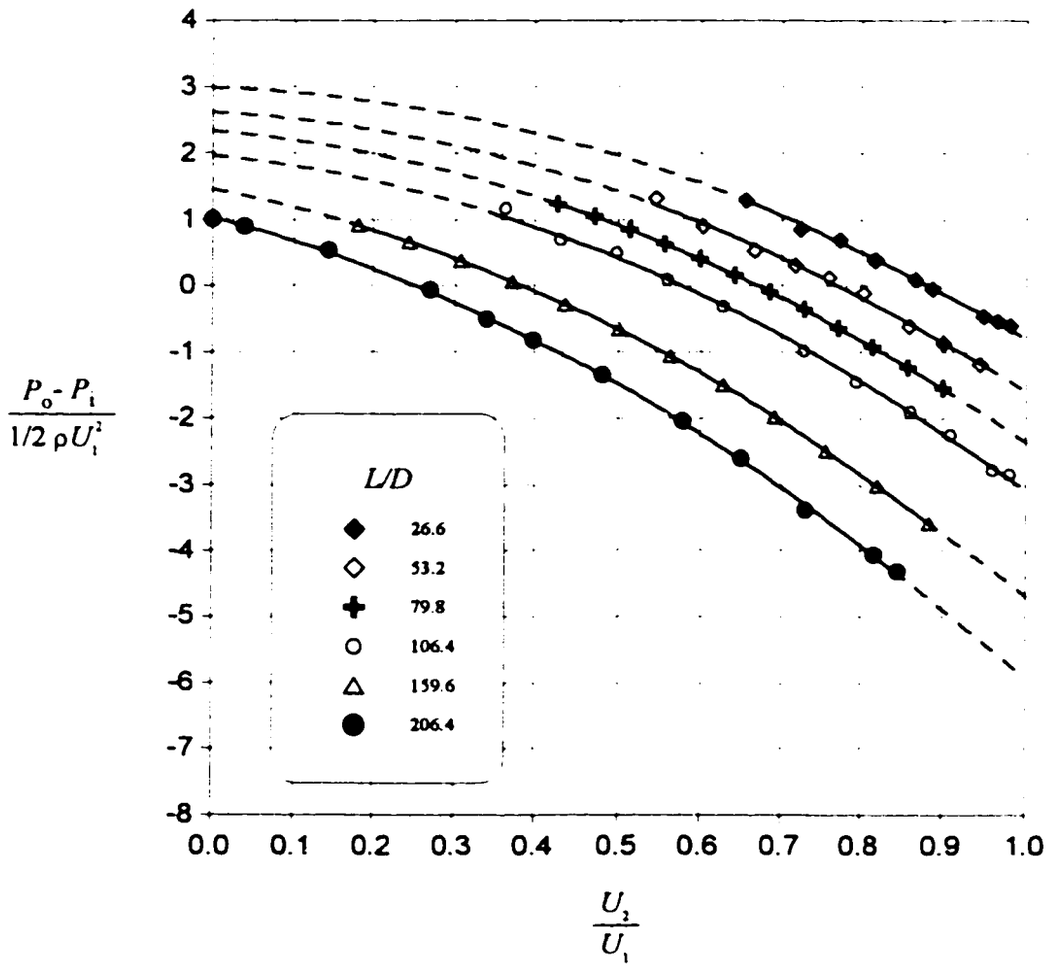

Figure 7.5- Dimensionless pressure change $(P_o - P_i) / \frac{1}{2}\rho U_1^2$ versus $\frac{U_2}{U_1}$ for various tube lengths and $Re_{axi.}$=22693

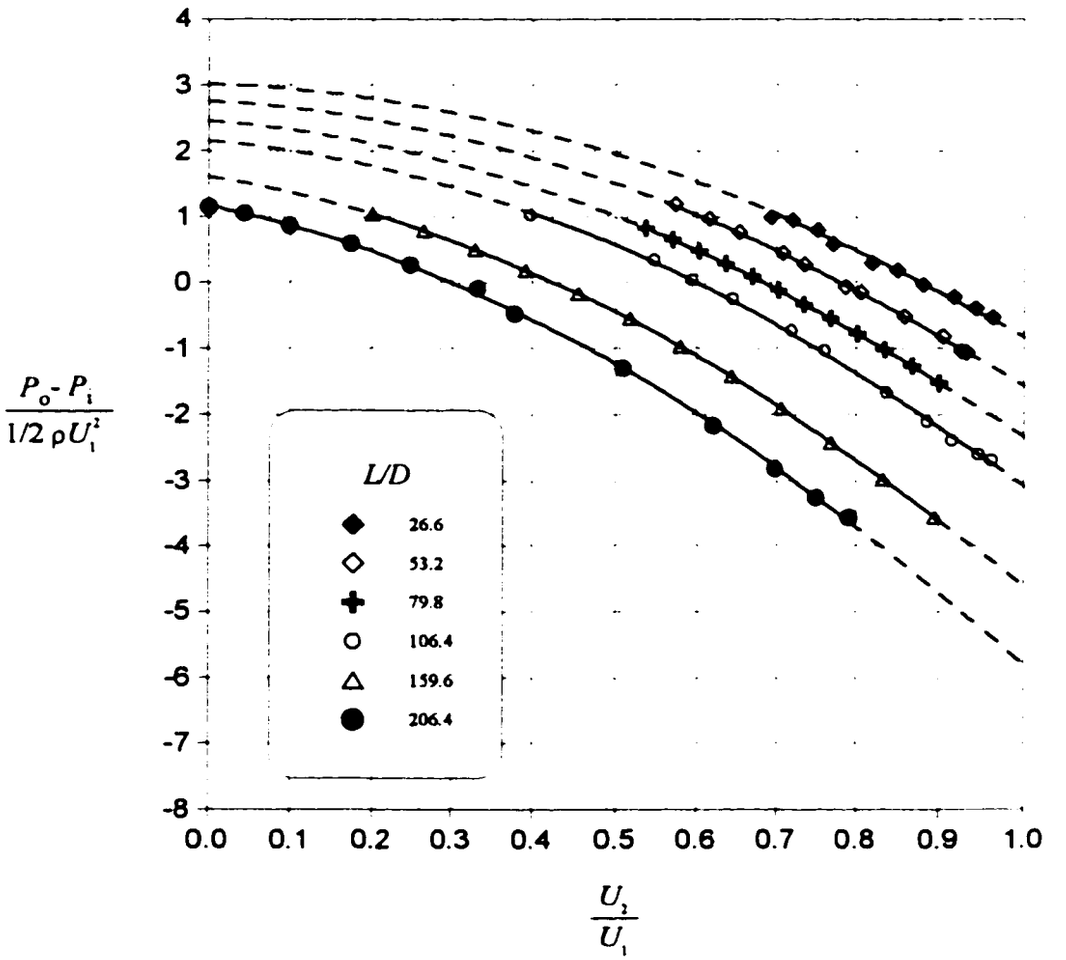

Figure 7.6- Dimensionless pressure change $(P_o - P_i) / \frac{1}{2}\rho U_1^2$ versus $\frac{U_2}{U_1}$ for various tube lengths and $Re_{axi.}$=30731

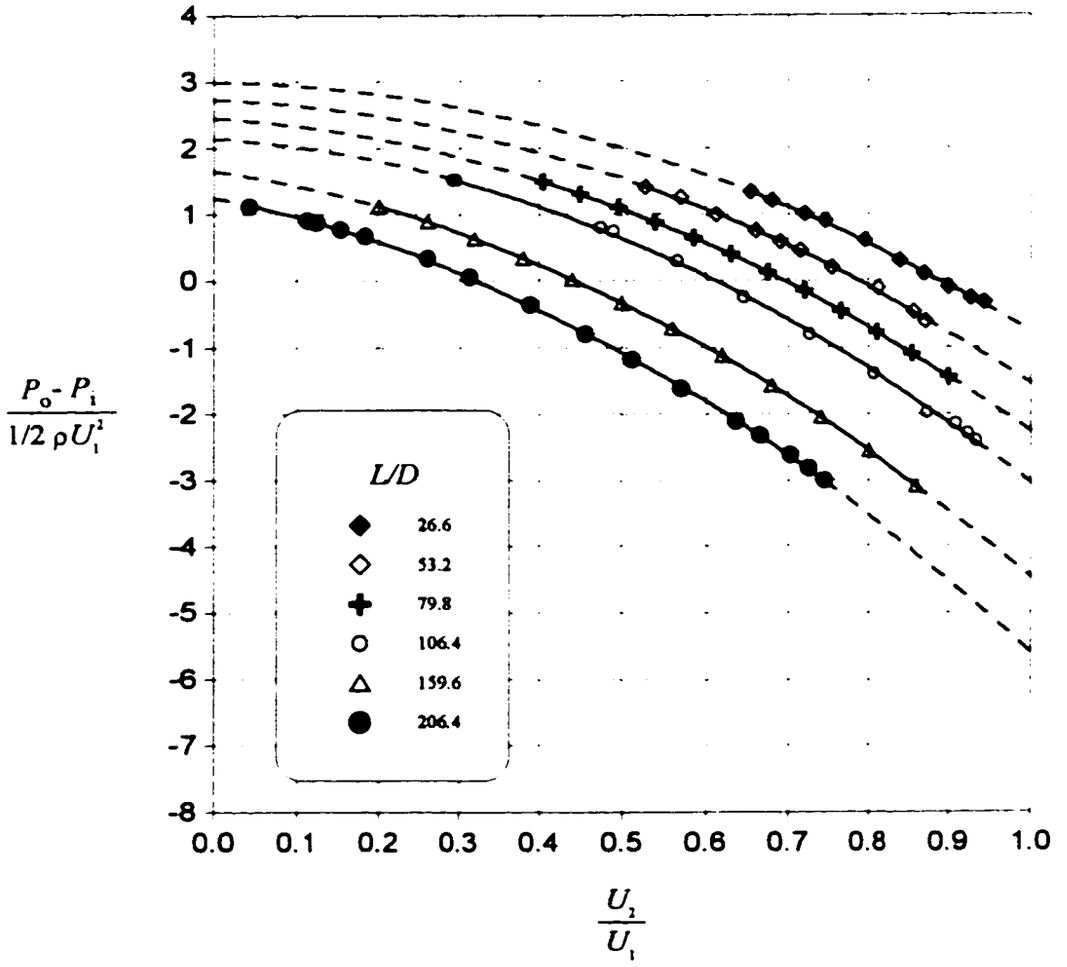

Figure 7.7- Dimensionless pressure change $(P_o - P_i) / \frac{1}{2}\rho U_1^2$ versus $\frac{U_2}{U_1}$ for various tube lengths and $Re_{axi.}$=38318

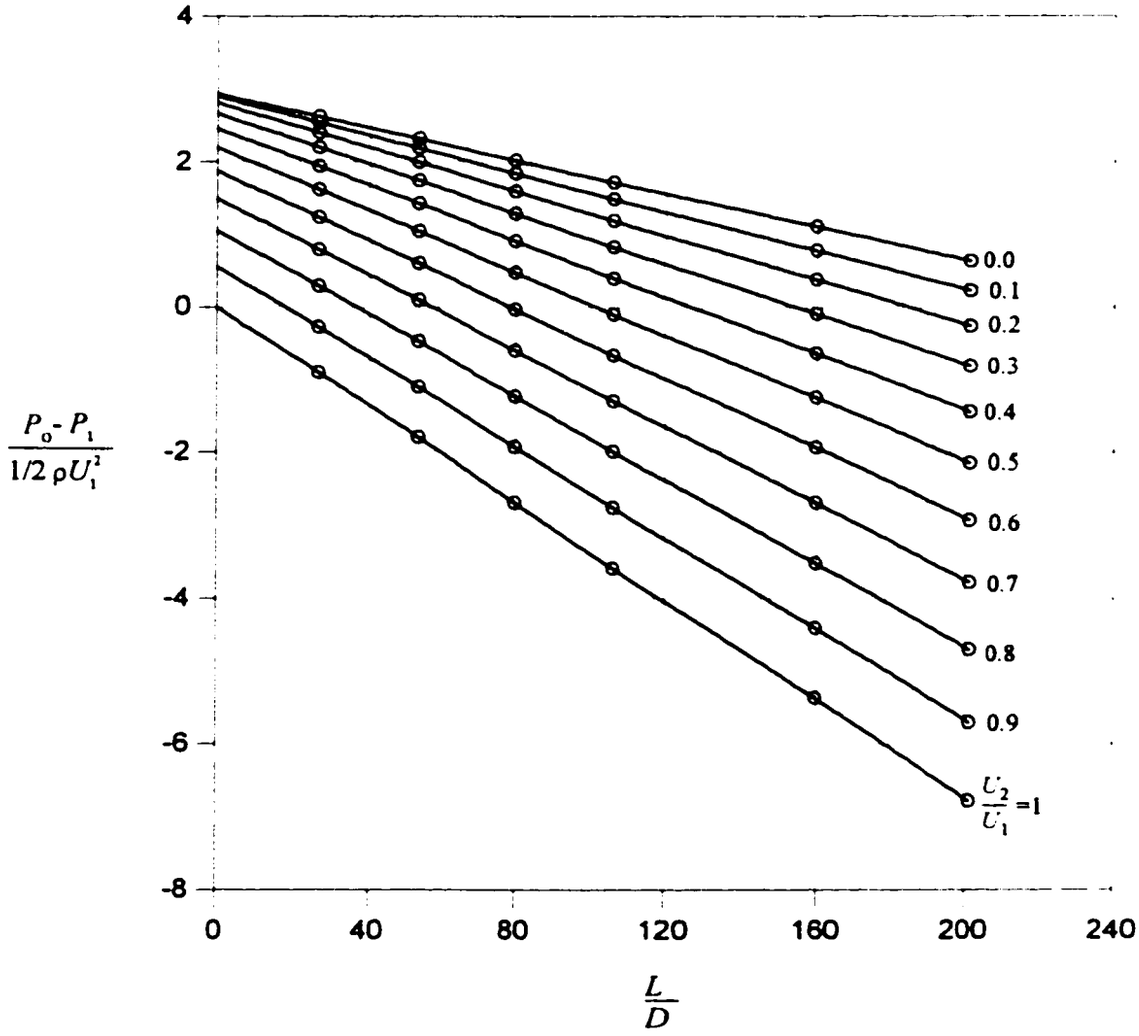

Figure 7.8- Dimensionless pressure change $(P_o - P_i) / \frac{1}{2}\rho U_i^2$ versus L/D for various $\frac{U_2}{U_1}$ and $Re_{axi.}$=5495

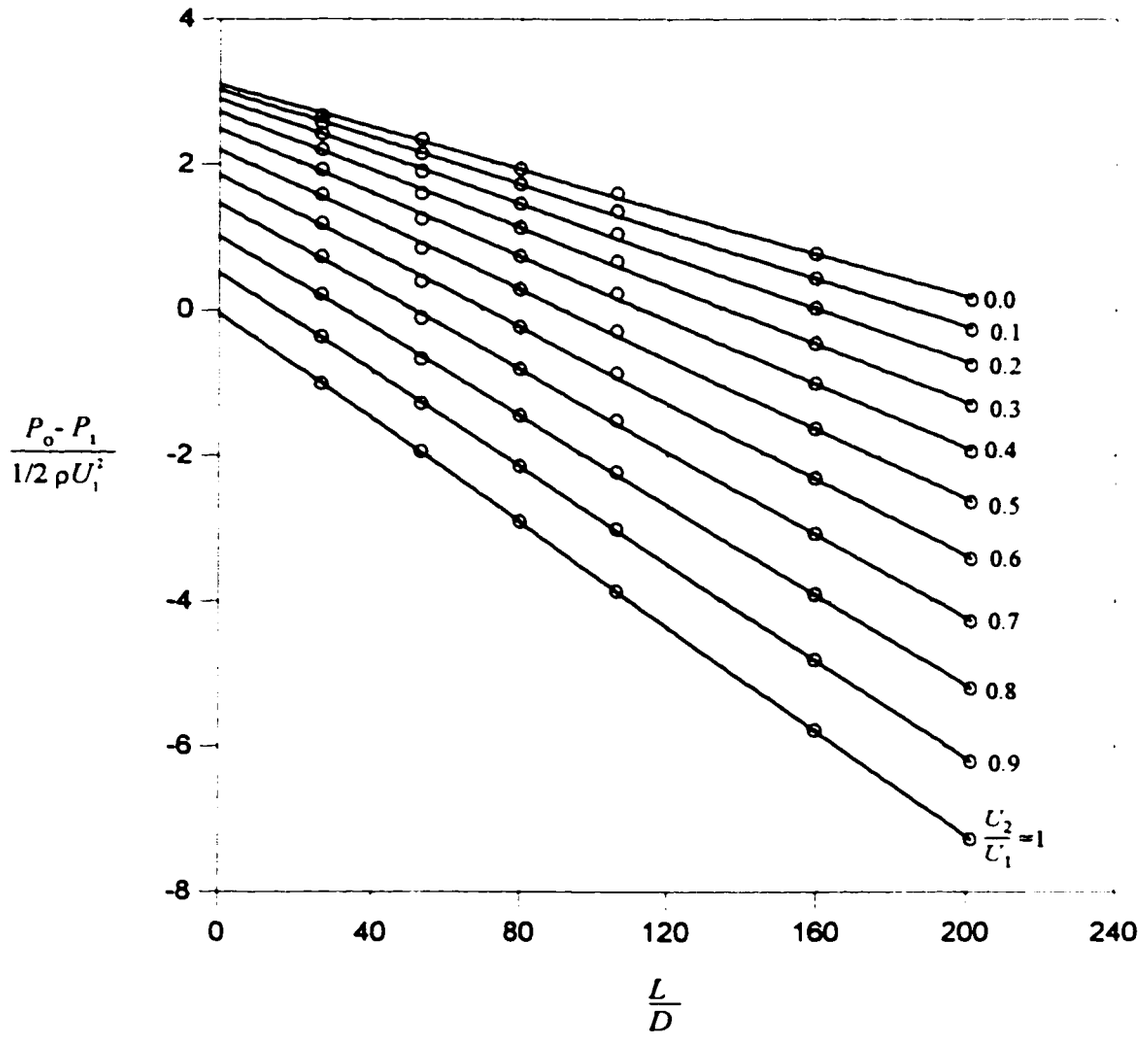

Figure 7.9- Dimensionless pressure change $(P_o - P_i) / \frac{1}{2}\rho U_i^2$ versus L/D for various $\frac{U_2}{U_i}$ and $Re_{axi.}$=7559

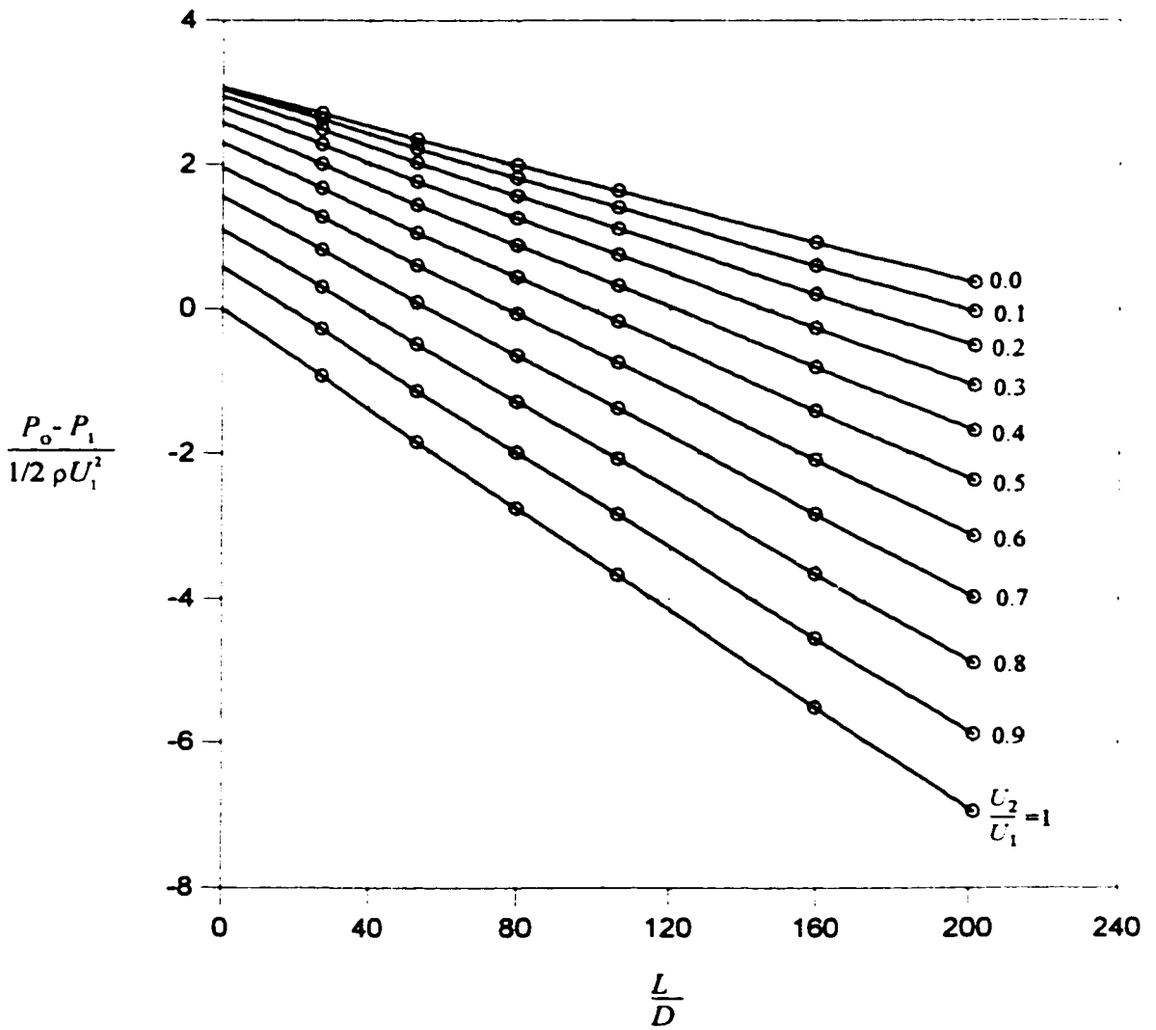

Figure 7.10- Dimensionless pressure change $(P_o - P_i) / \frac{1}{2}\rho U_1^2$ versus L/D for various $\frac{U_2}{U_1}$ and $Re_{axi.}$=9997

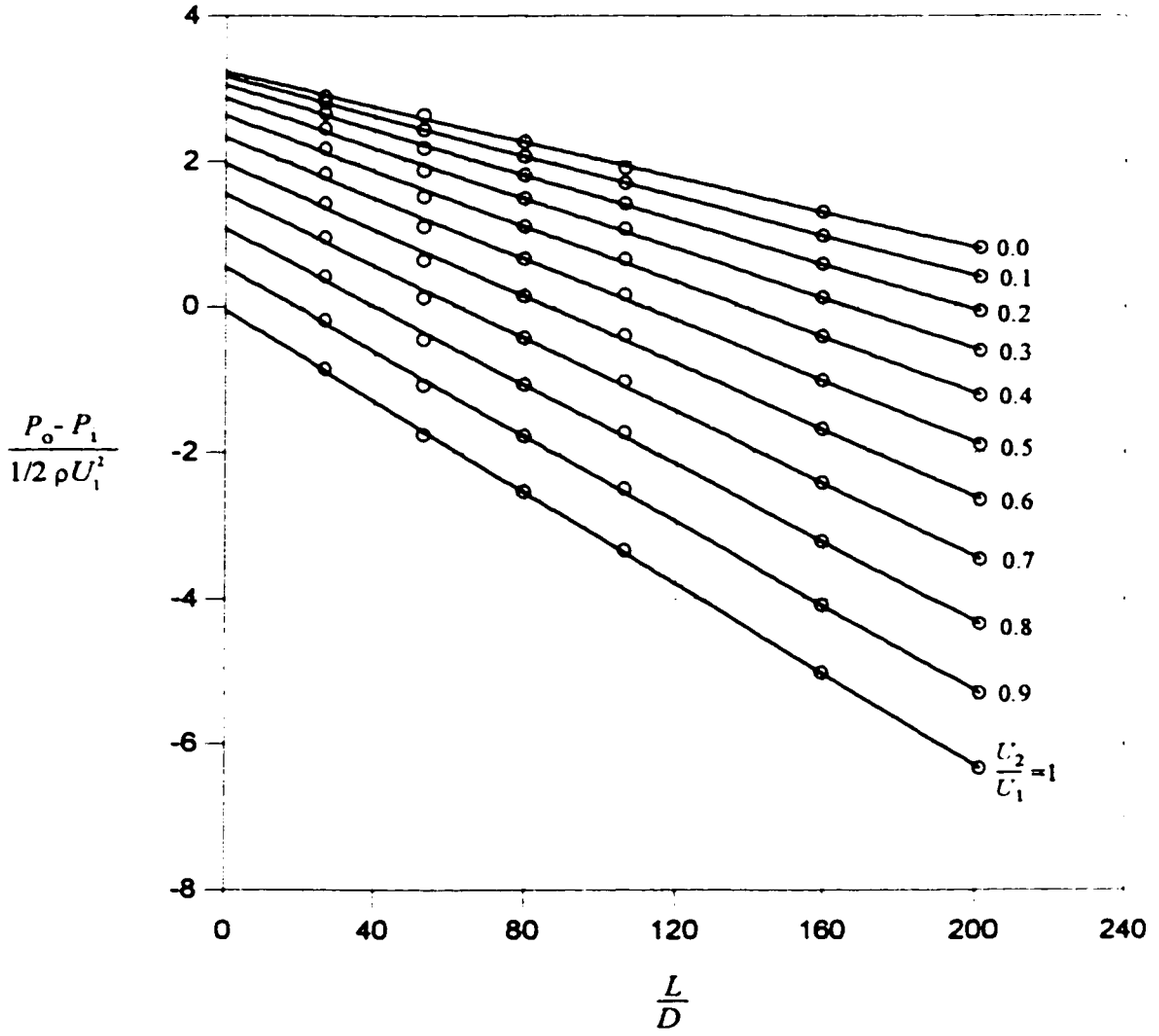

Figure 7.11- Dimensionless pressure change $(P_o - P_i) / \frac{1}{2}\rho U_1^2$ versus L/D for various $\frac{U_2}{U_1}$ and $Re_{axi.}$=15222

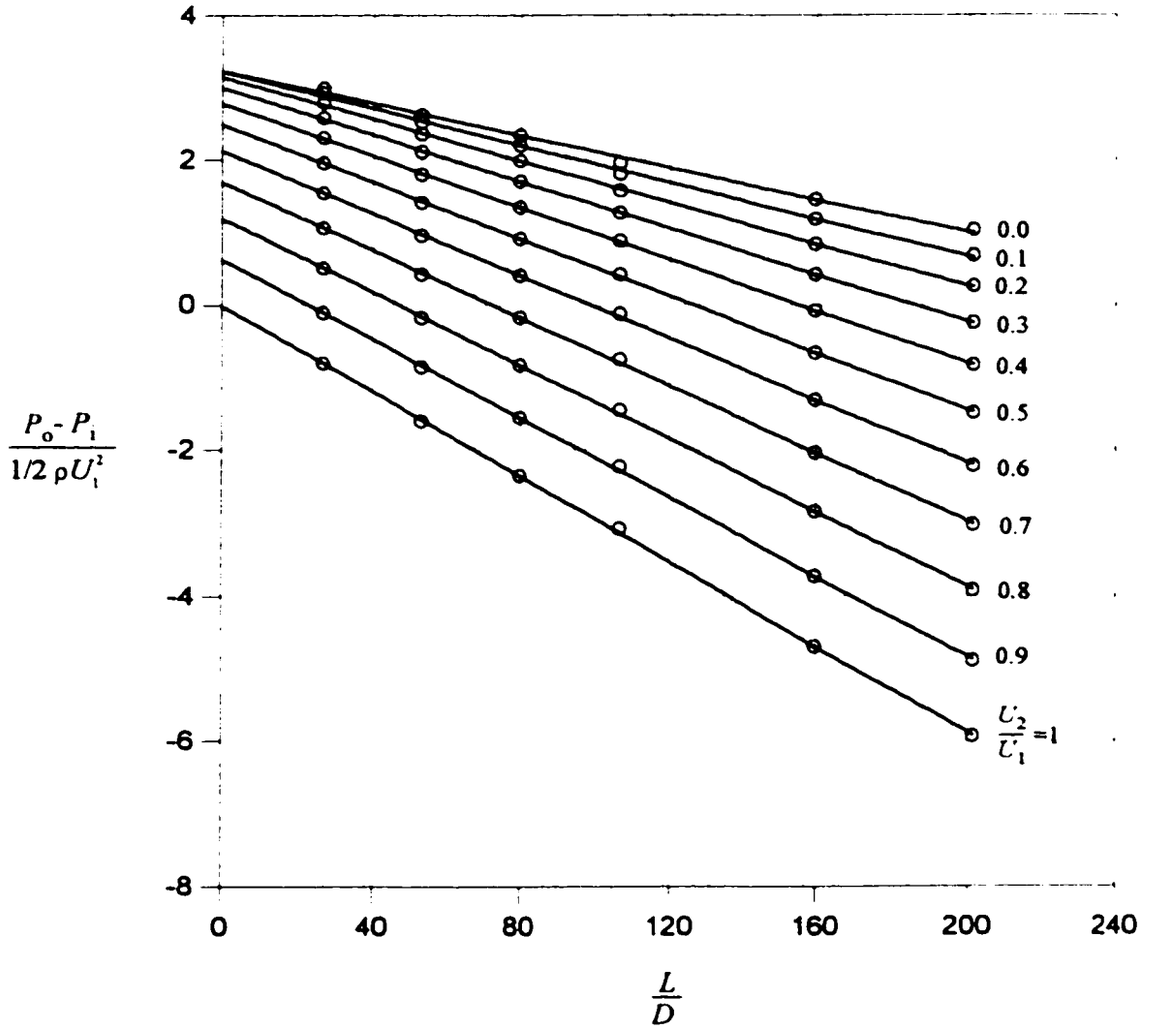

Figure 7.12- Dimensionless pressure change $(P_o - P_i) / \frac{1}{2}\rho U_i^2$ versus L/D for various $\frac{U_2}{U_1}$ and $Re_{axi.}$=22693

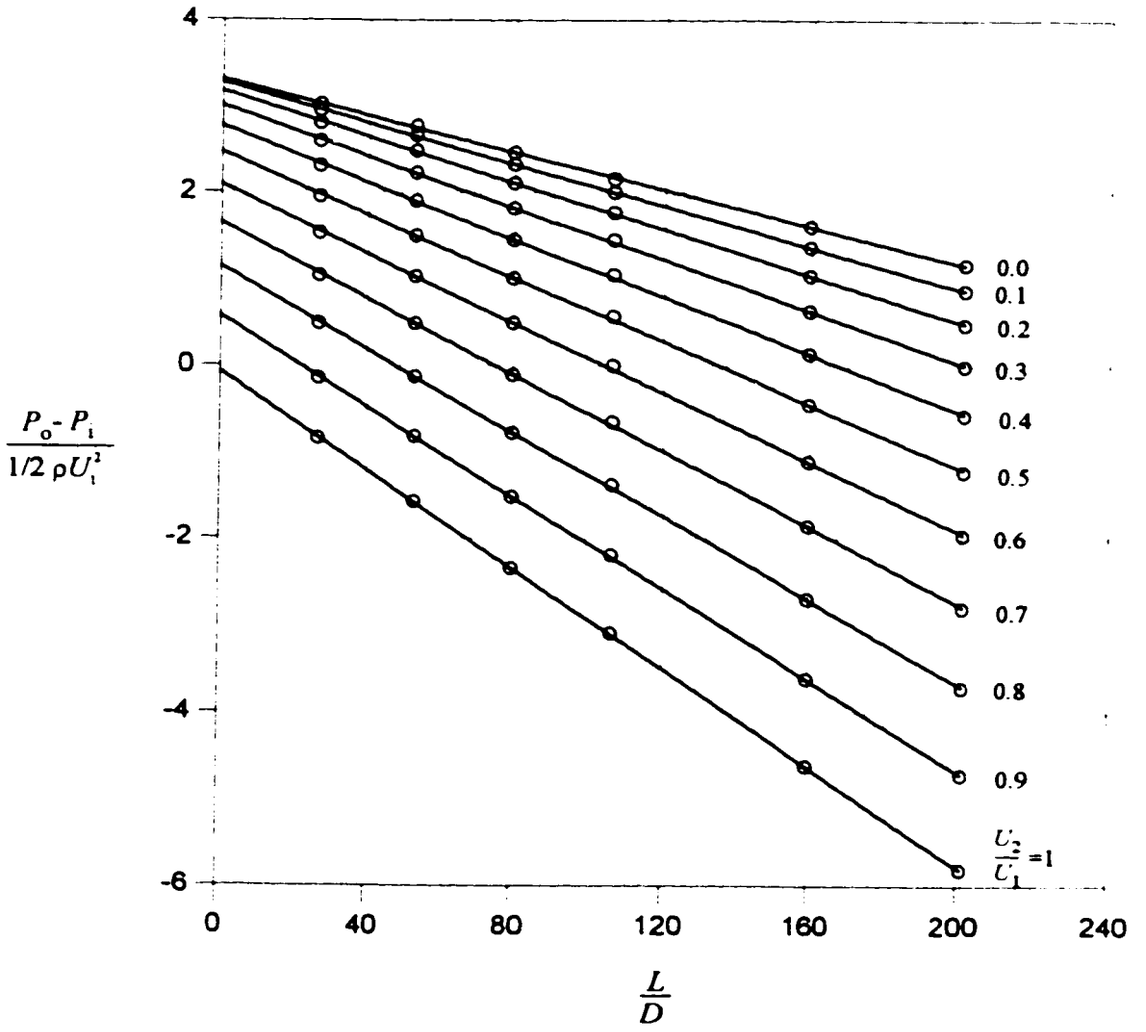

Figure 7.13- Dimensionless pressure change $(P_o - P_i) / \frac{1}{2}\rho U_1^2$ versus L/D for various $\frac{U_2}{U_1}$ and $Re_{axi.}$=30731

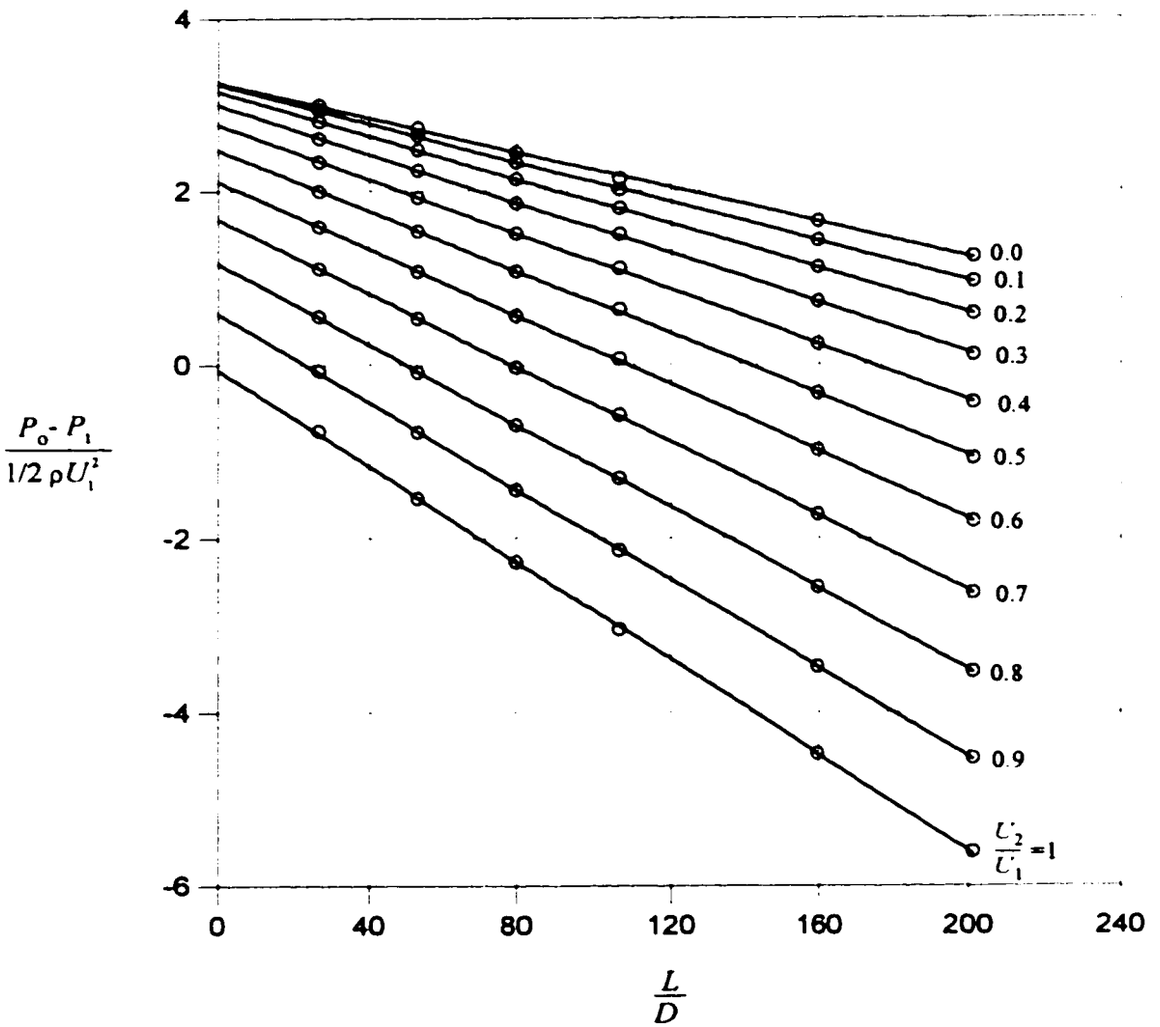

Figure 7.14- Dimensionless pressure change $(P_o - P_i) / \frac{1}{2}\rho U_i^2$ versus L/D for various $\frac{U_2}{U_1}$ and $Re_{axi.}$=38318

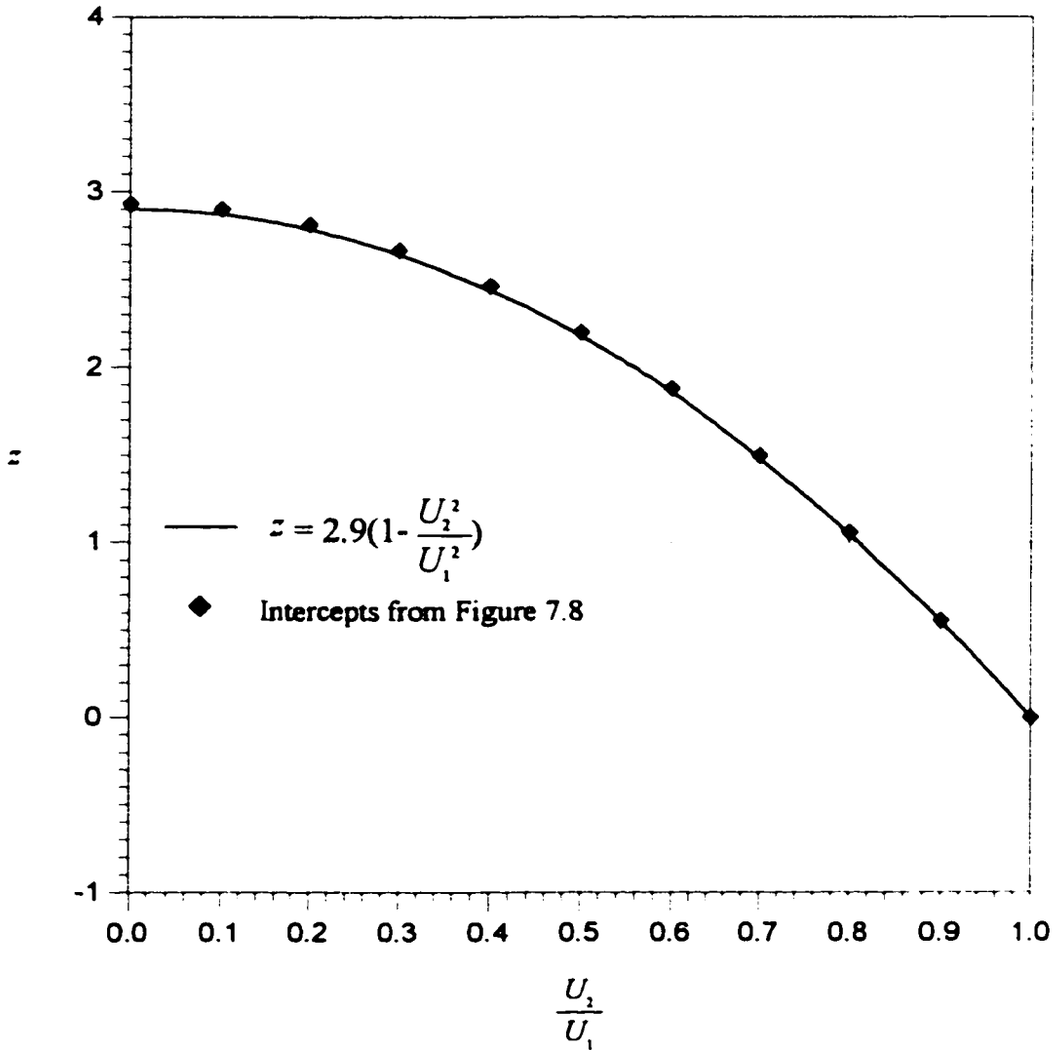

Figure 7.15 - The values of intercepts z versus $\frac{U_2}{U_1}$ for $Re_{axi.}$=5495

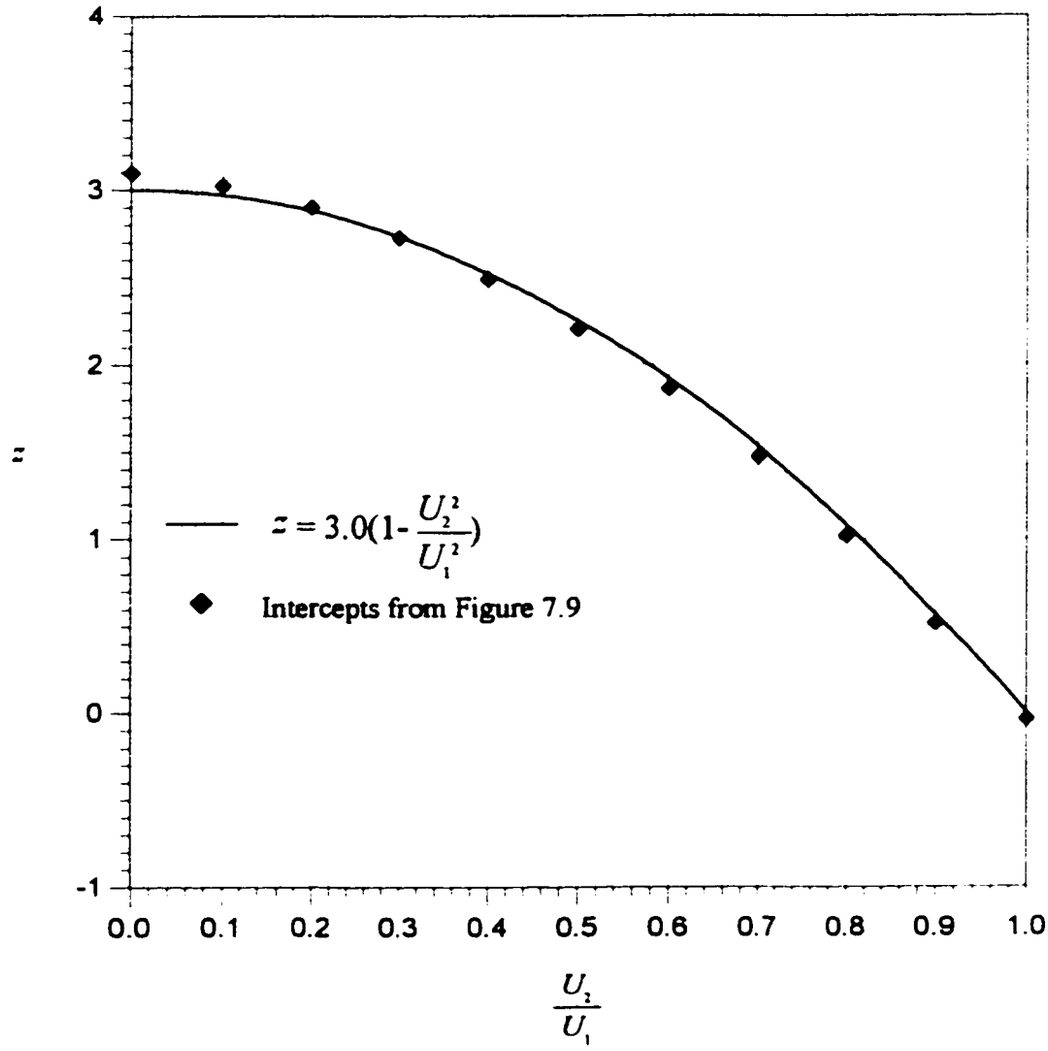

Figure 7.16 - The values of intercepts z versus $\frac{U_2}{U_1}$ for $Re_{axi.}$=7559

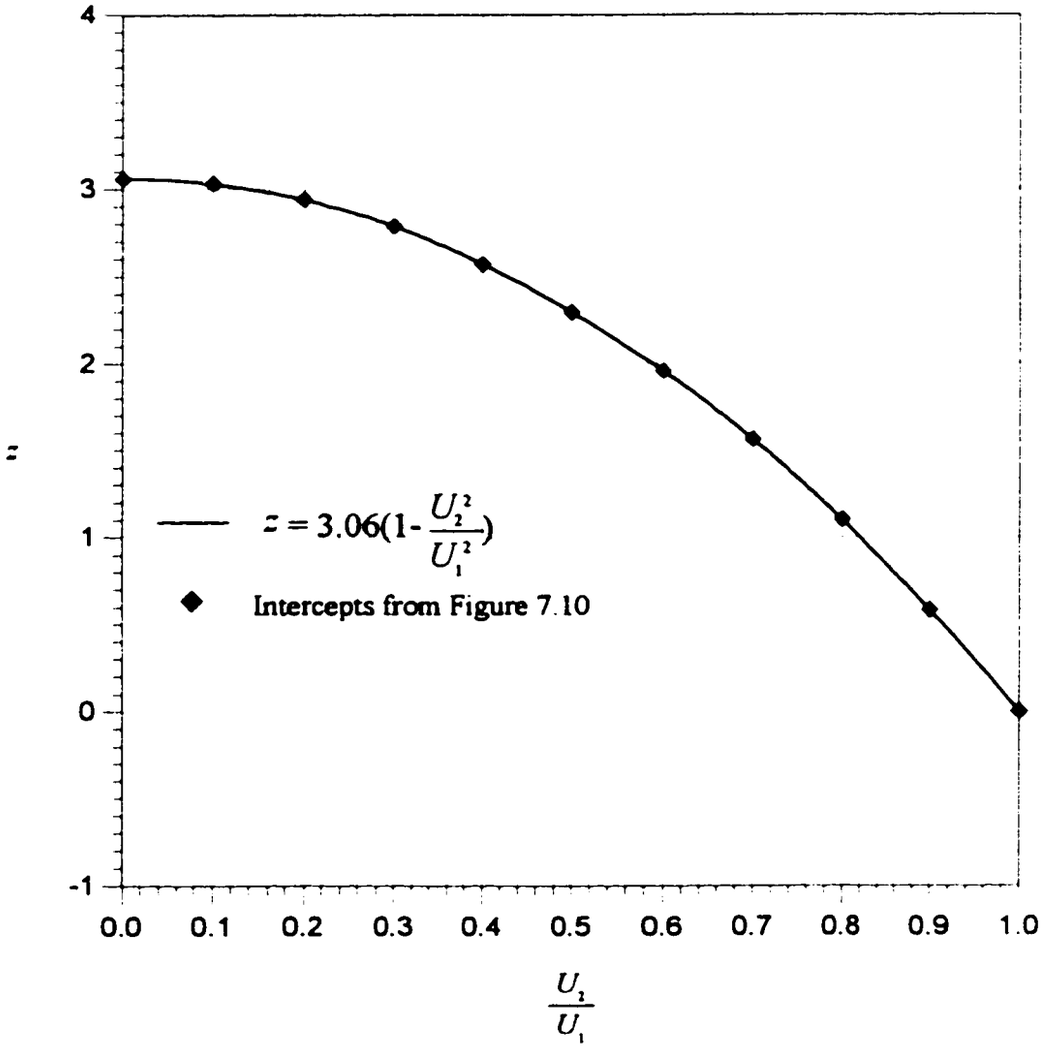

Figure 7.17 - The values of intercepts z versus $\frac{U_2}{U_1}$ for $Re_{axi.}$=9997

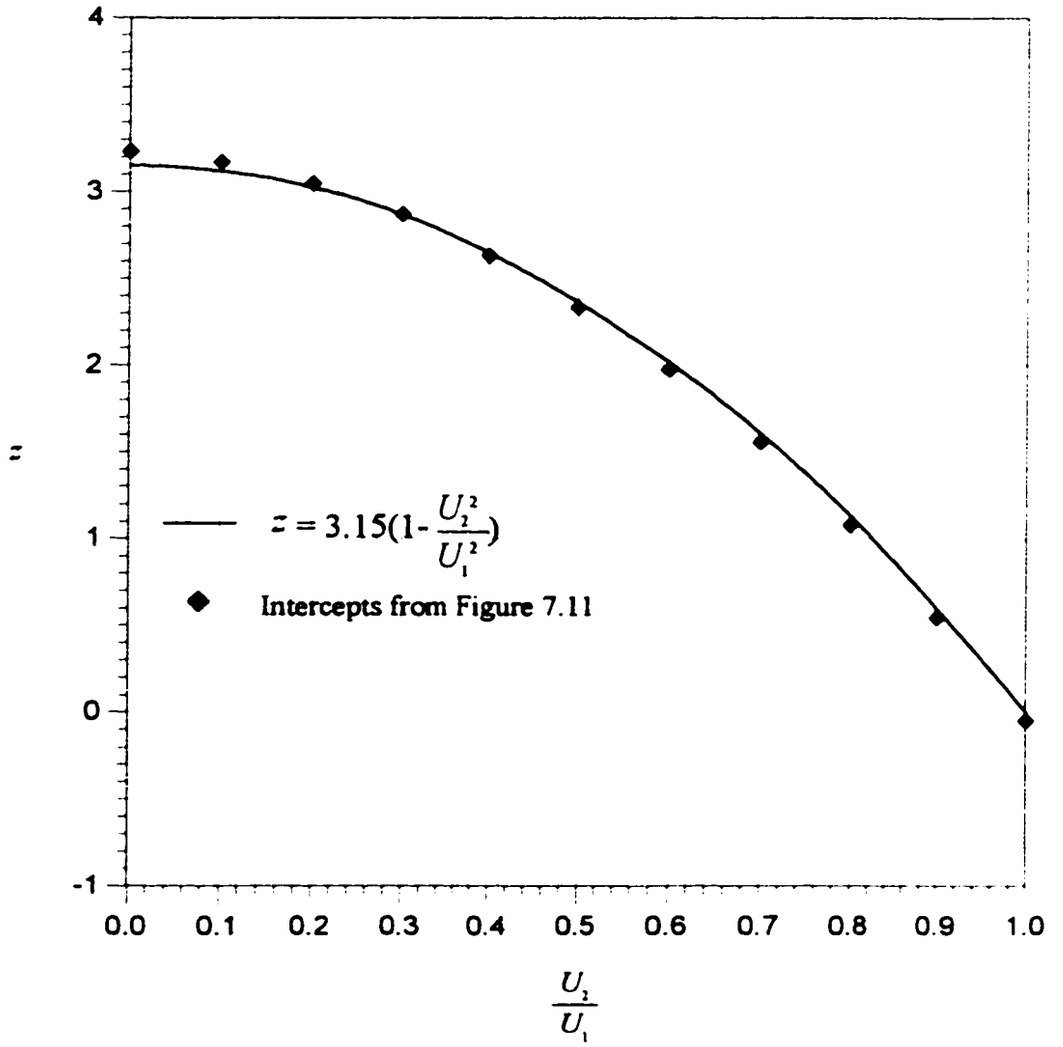

Figure 7.18 - The values of intercepts z versus $\frac{U_2}{U_1}$ for Re_{axi}=15222

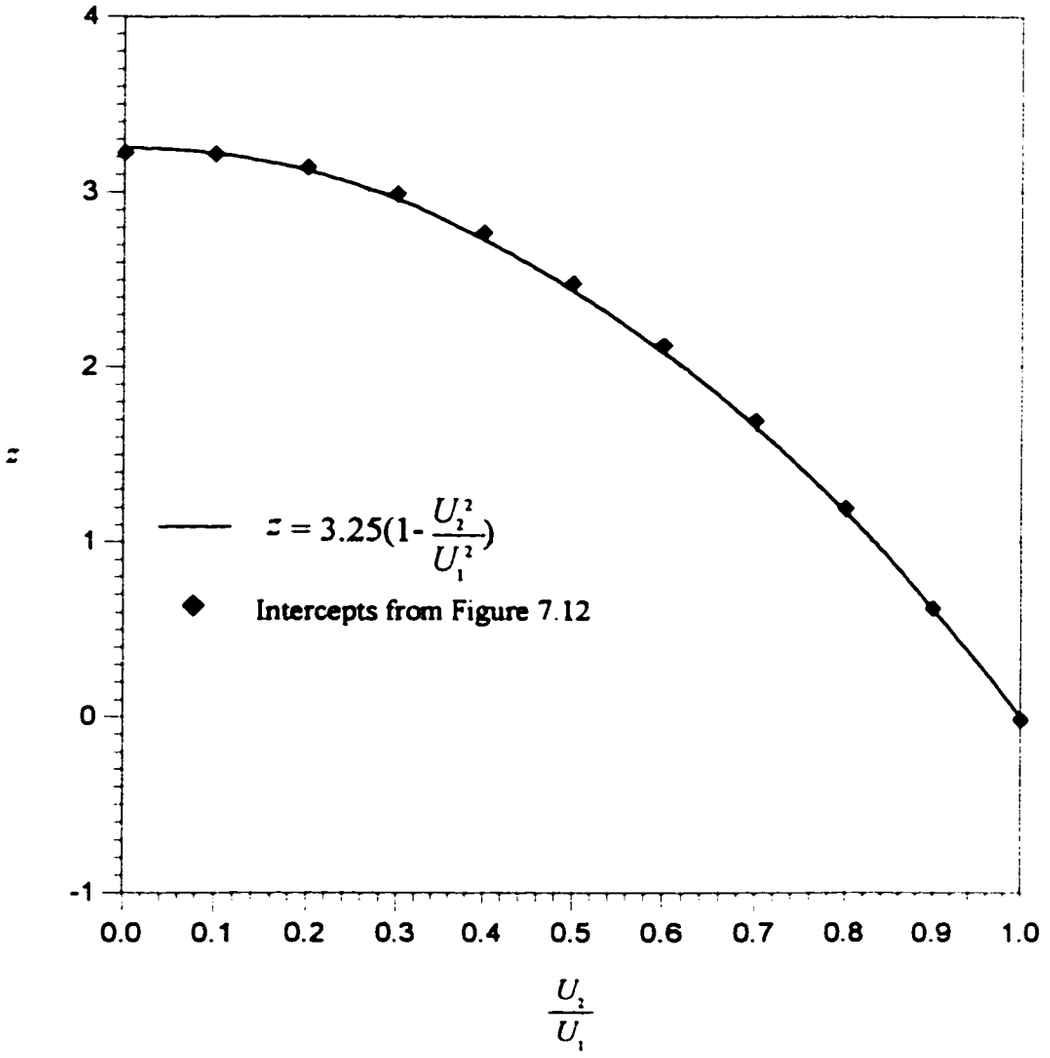

Figure 7.19 - The values of intercepts z versus $\frac{U_2}{U_1}$ for $Re_{axi.}$=22693

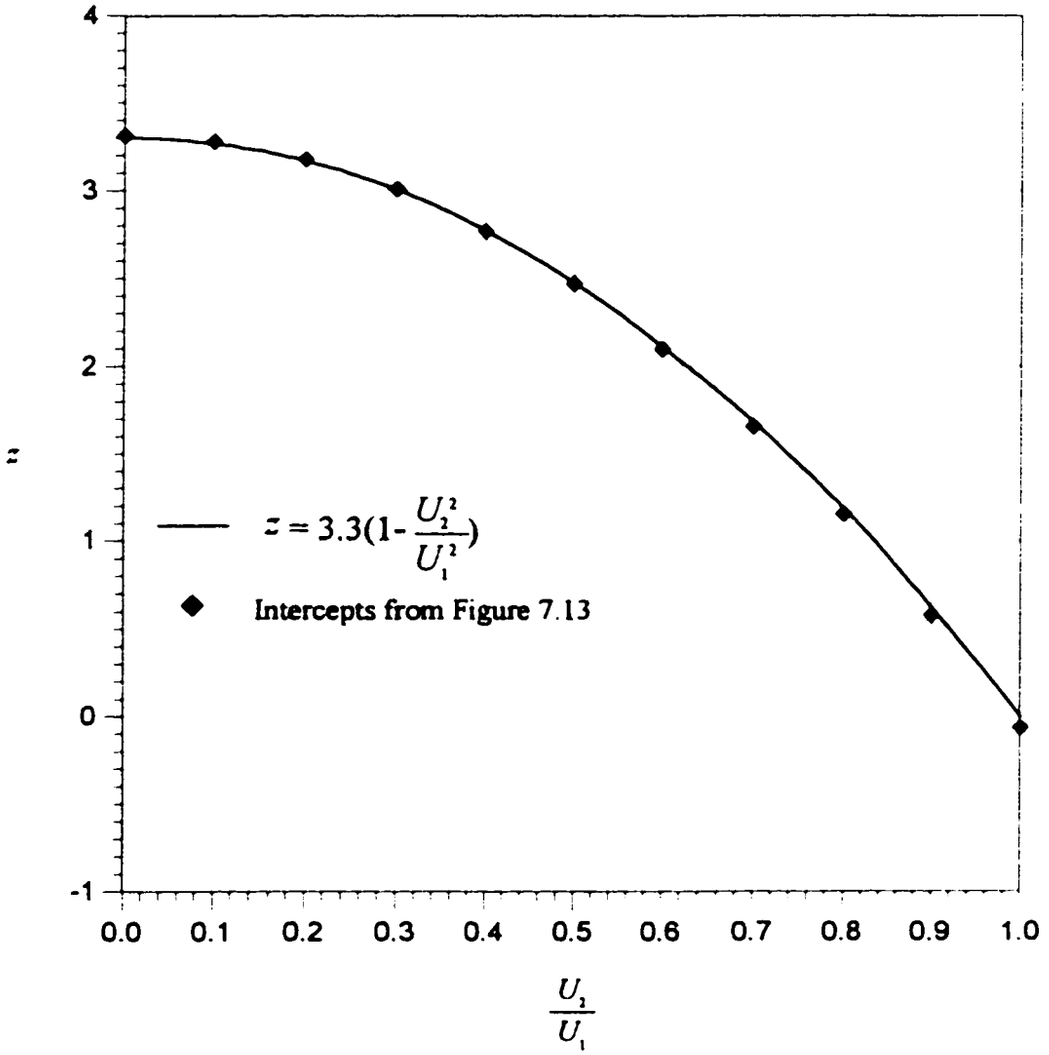

Figure 7.20 - The values of intercepts z versus $\frac{U_2}{U_1}$ for $Re_{axi.}$=30731

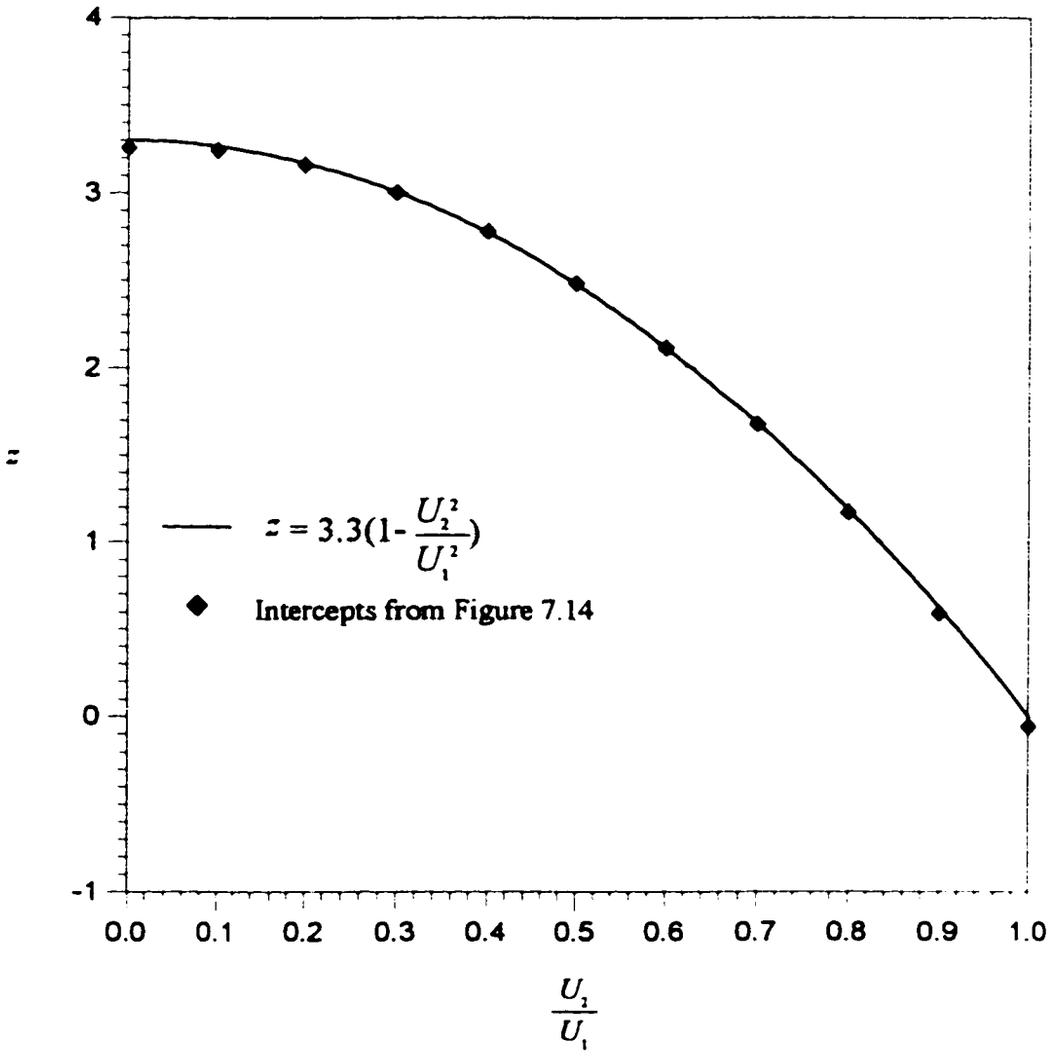

Figure 7.21 - The values of intercepts z versus $\frac{U_2}{U_1}$ for Re_{axi}=38318

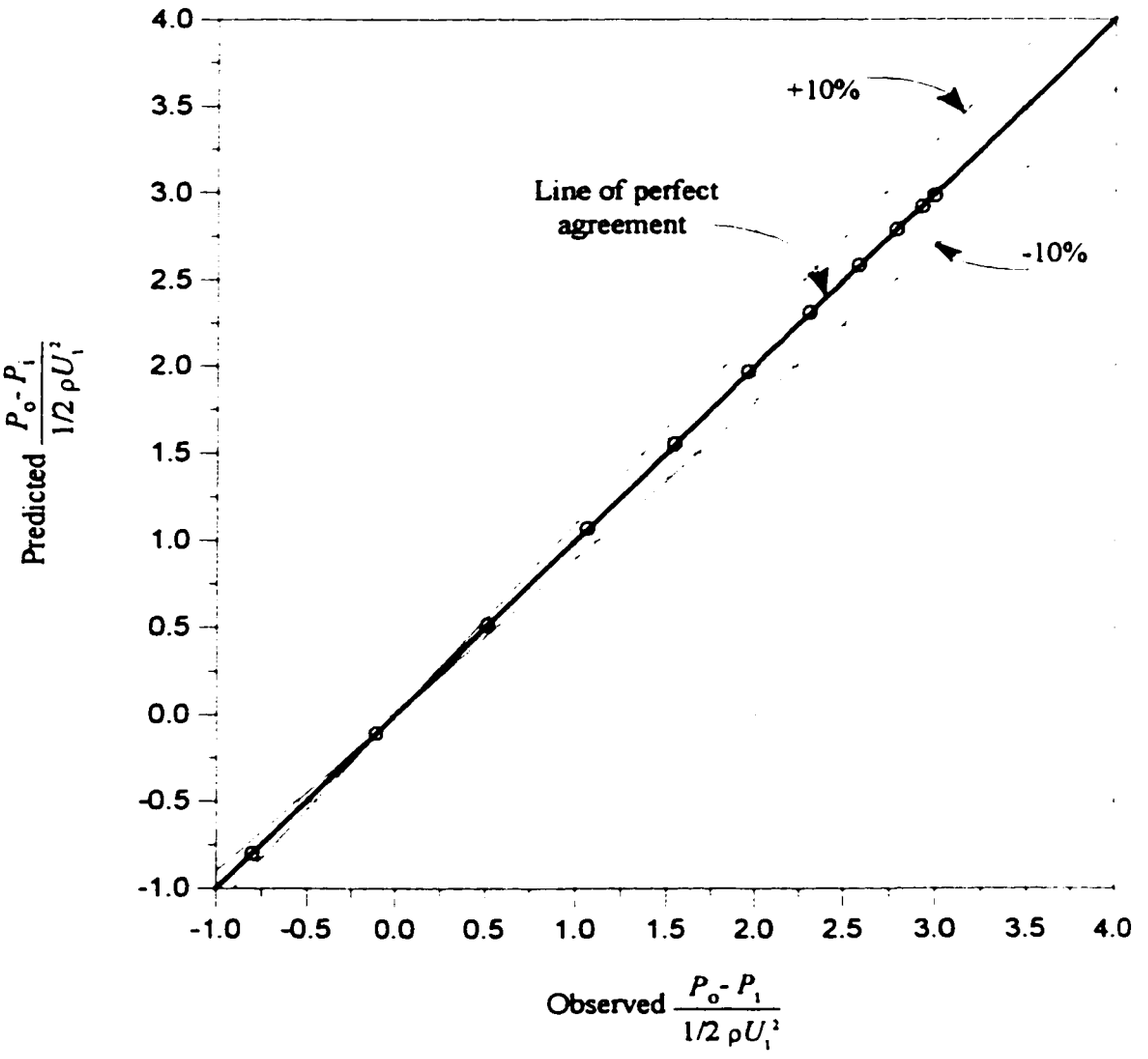

Figure 7.22- Predicted vs. observed $\frac{P_o - P_i}{1/2\,\rho U_1^2}$ for L/D=26.6 and $Re_{axi.}$=22693

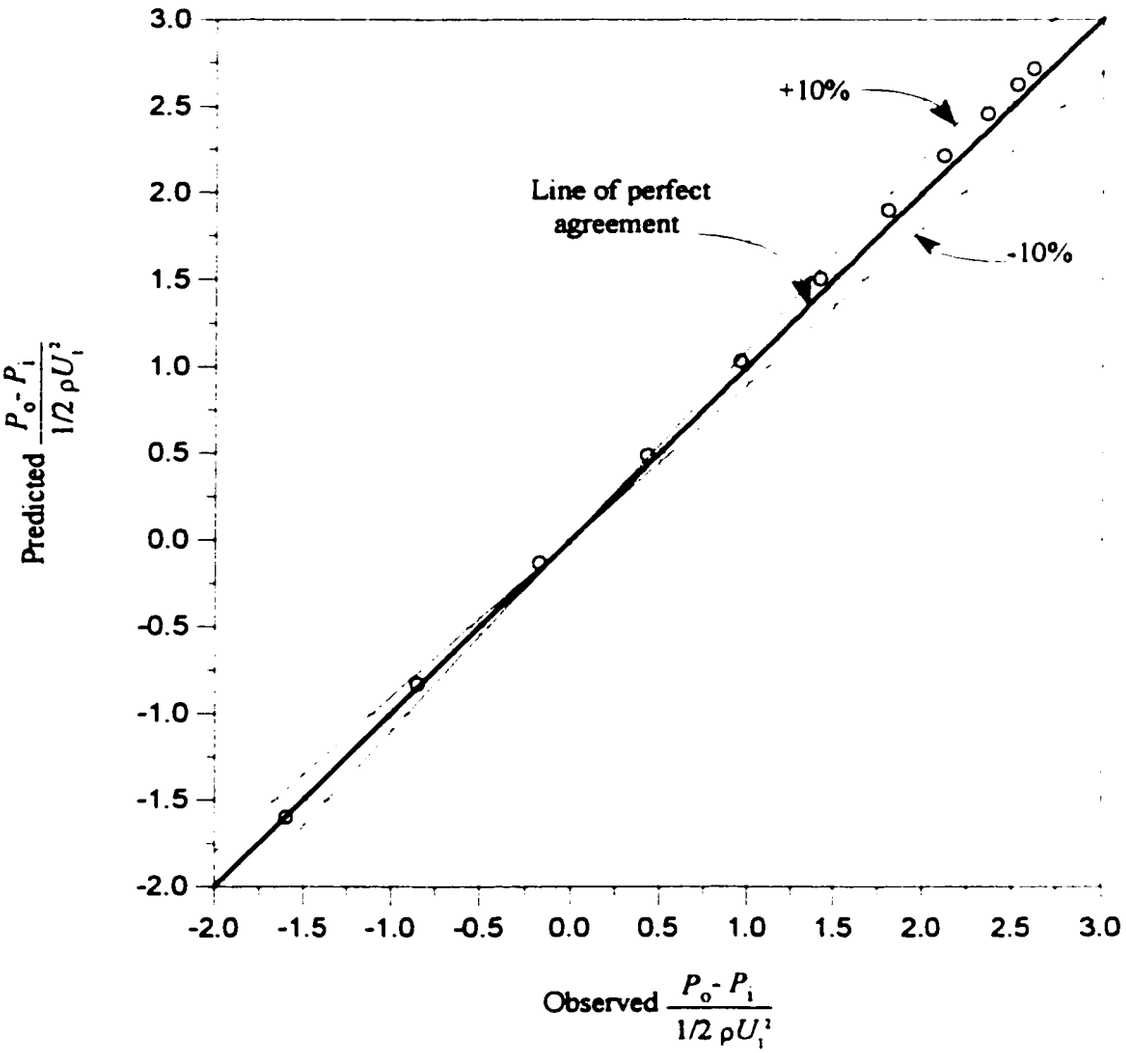

Figure 7.23- Predicted vs. observed $\frac{P_o - P_i}{1/2\,\rho U_1^2}$ for L/D=53.2 and $Re_{axi.}$=22,693

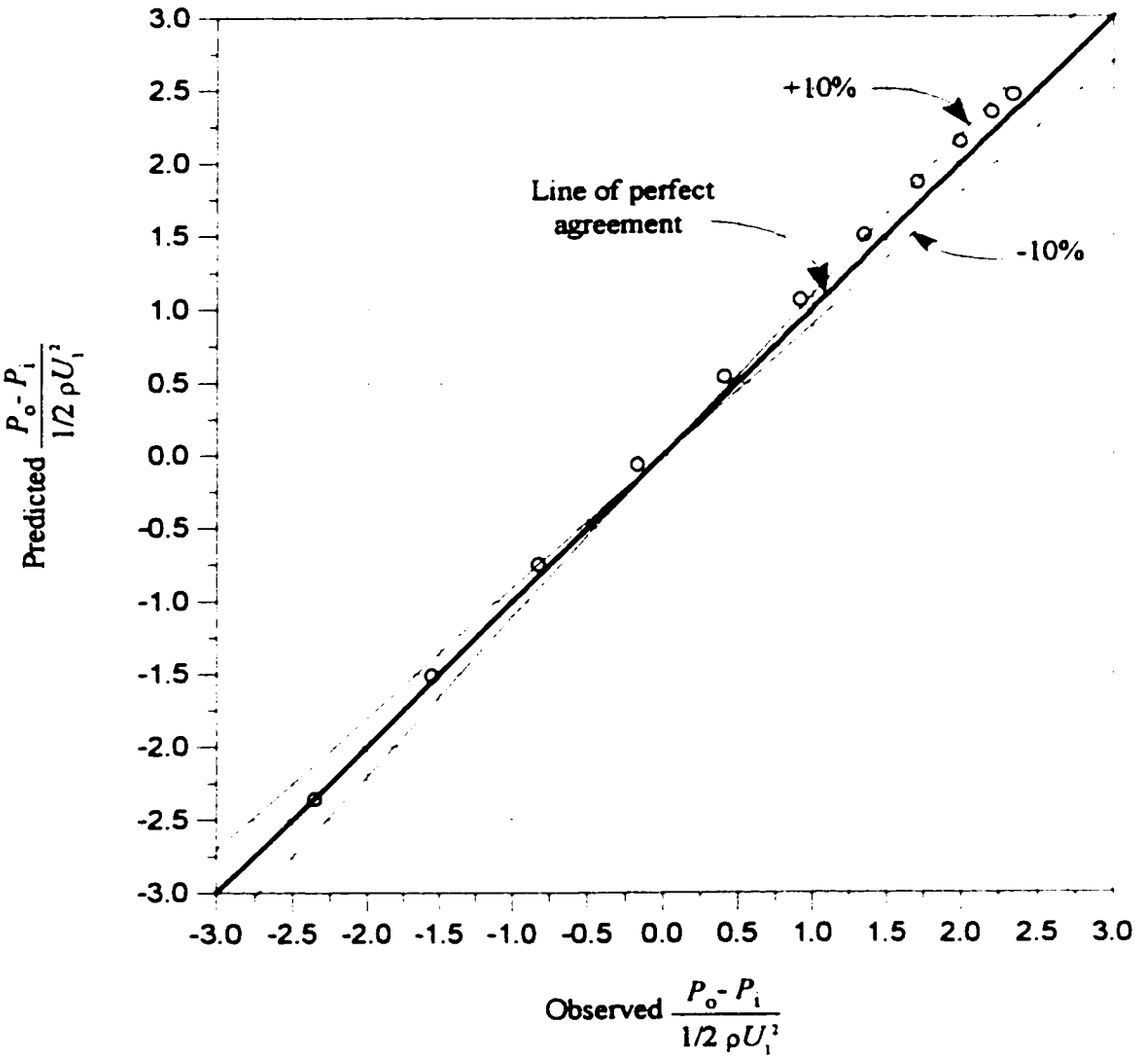

Figure 7.24- Predicted vs. observed $\frac{P_o - P_i}{1/2\,\rho U_i^2}$ for L/D=79.8 and $Re_{axi.}$=22,693

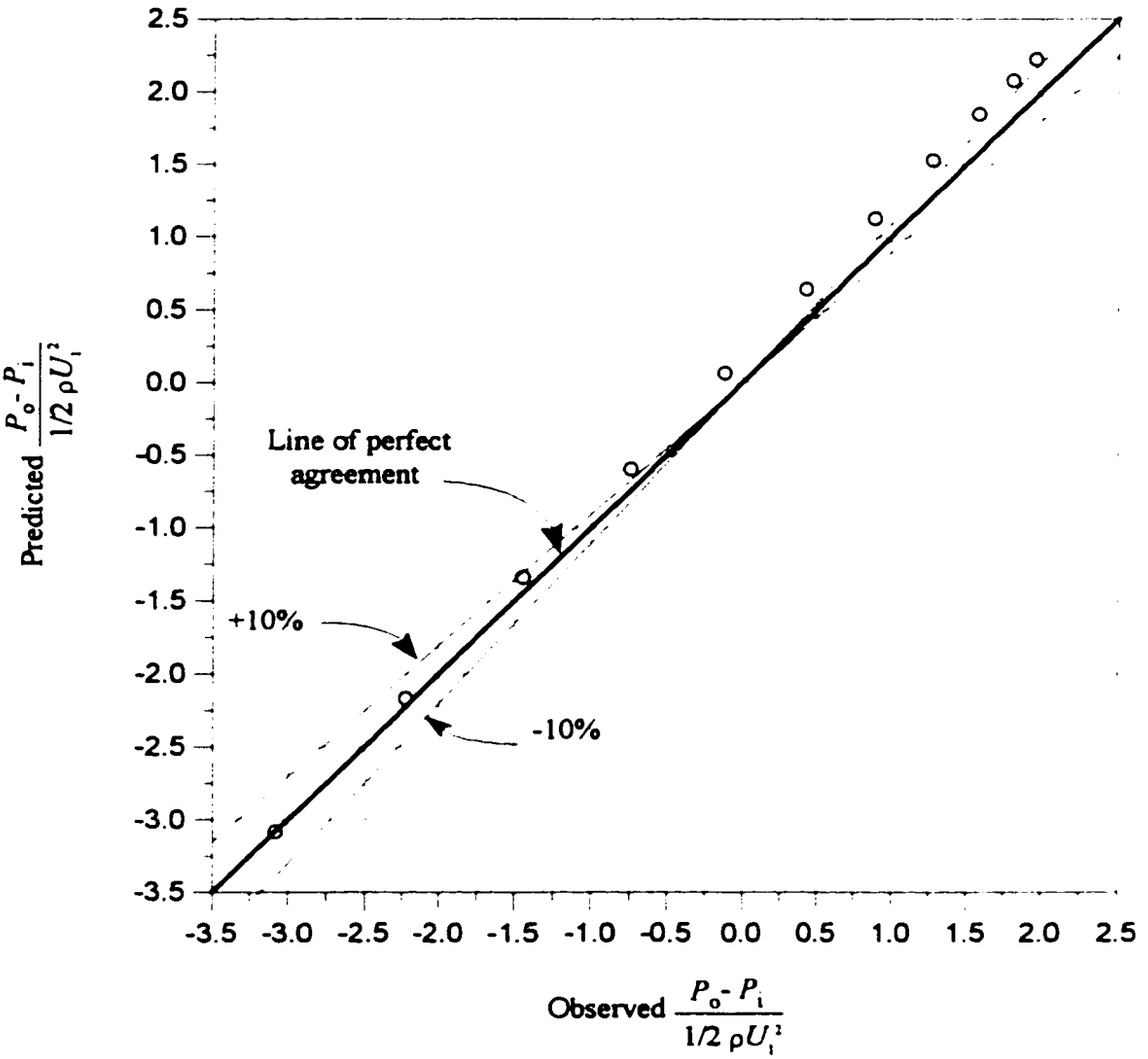

Figure 7.25- Predicted vs. observed $\frac{P_o - P_i}{1/2\,\rho U_i^2}$ for L/D=106.4 and $Re_{axi.}$=22693

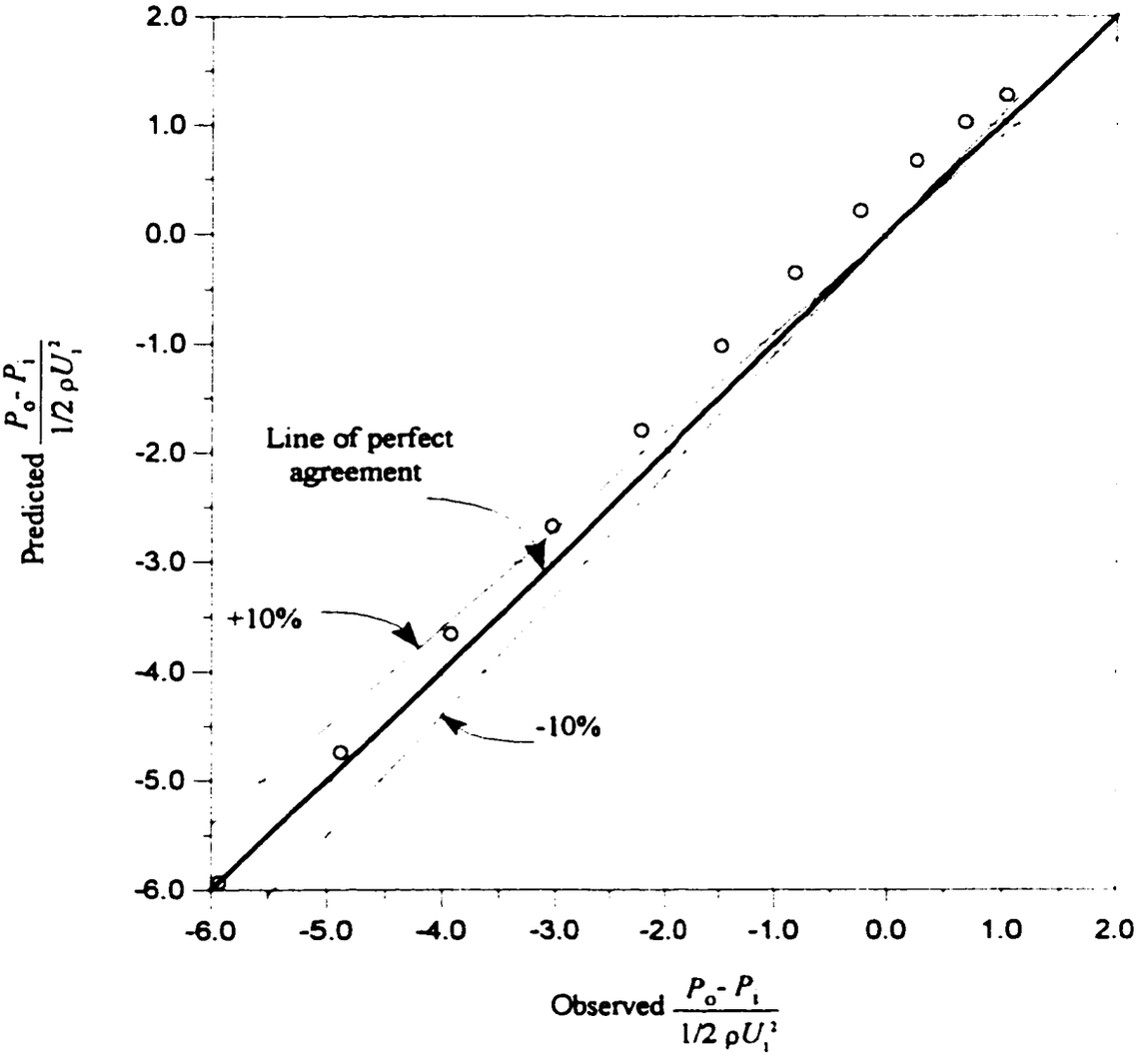

Figure 7.26- Predicted vs. observed $\frac{P_o - P_i}{1/2\,\rho U_i^2}$ for L/D=159.6 and $Re_{axi.}$=22693

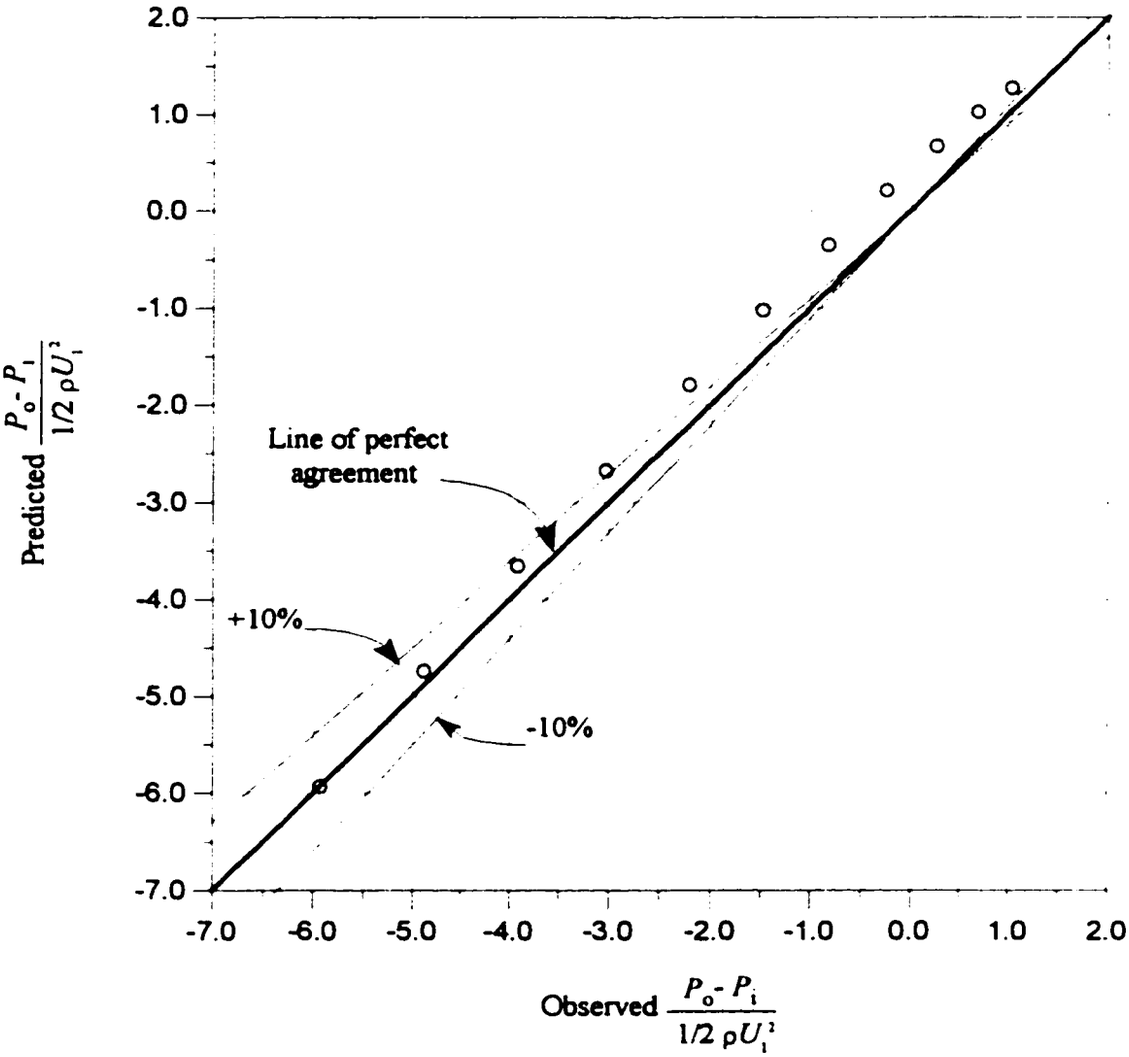

Figure 7.27- Predicted vs. observed $\frac{P_o - P_i}{1/2\,\rho U_i^2}$ for L/D=206.6 and $Re_{axi.}$=22,693

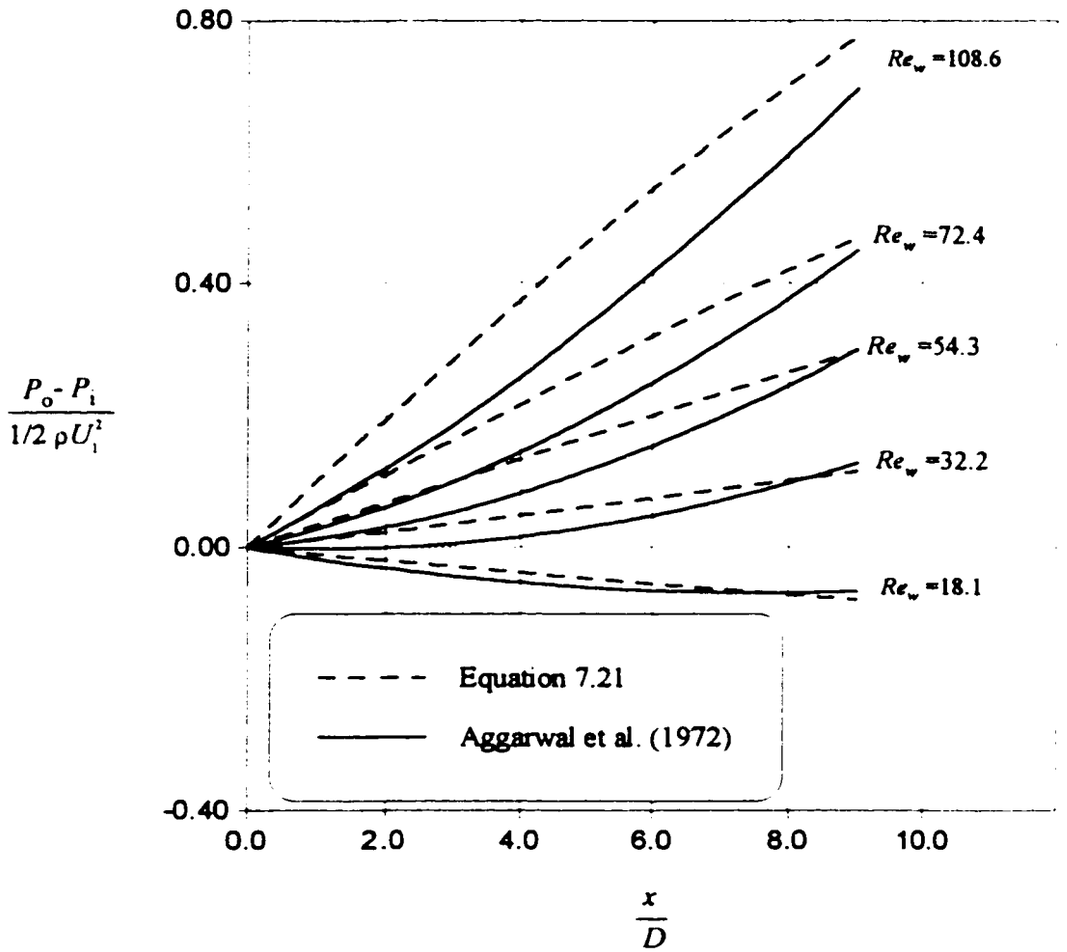

Figure 7.28- Comparison between Equation 7.21 and Aggarwal et al. (1972) study for dimensionless pressure change $(P_o - P_i) / \frac{1}{2}\rho U_i^2$ along tubing for $Re_{axi.}$=11,260

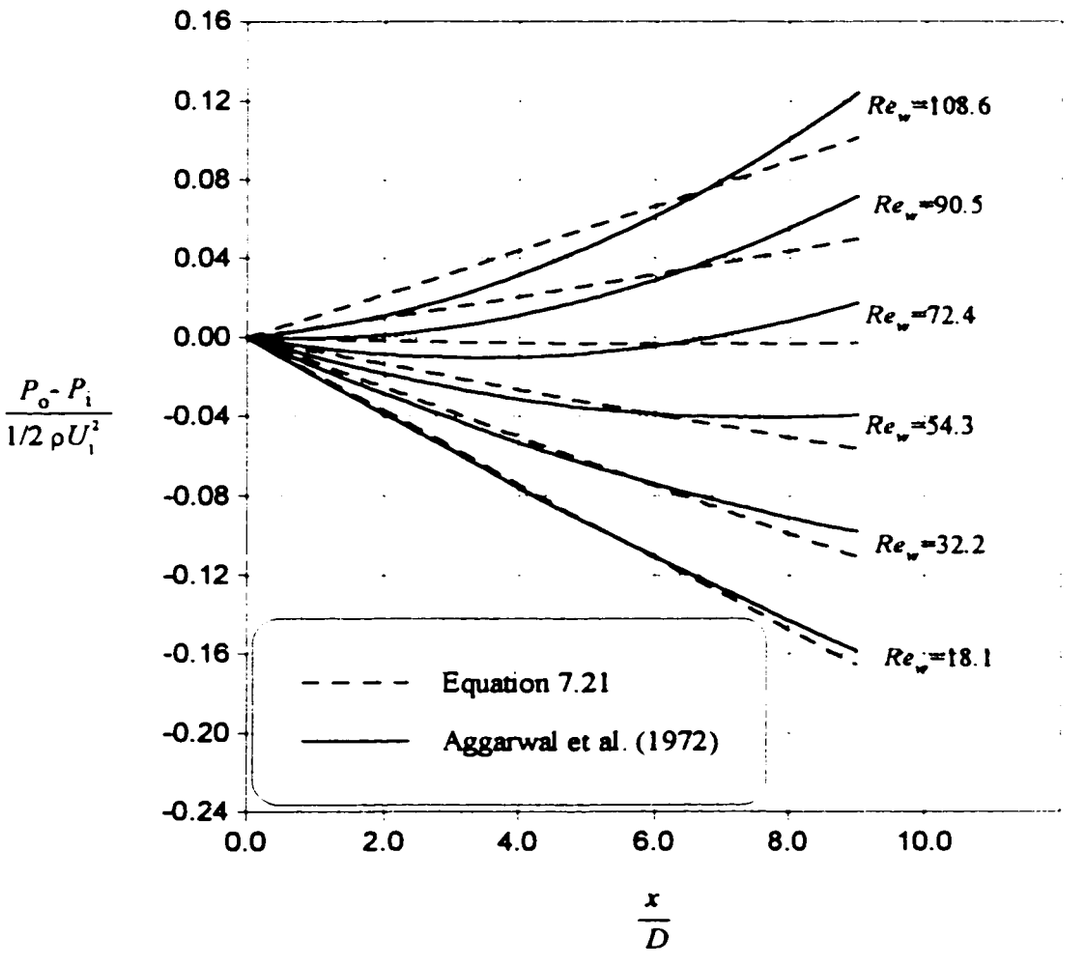

Figure 7.29- Comparison between Equation 7.21 and Aggarwal et al. (1972) study for dimensionless pressure change $(P_o - P_i)/\frac{1}{2}\rho U_i^2$ along tubing for $Re_{axi.}$=41,840

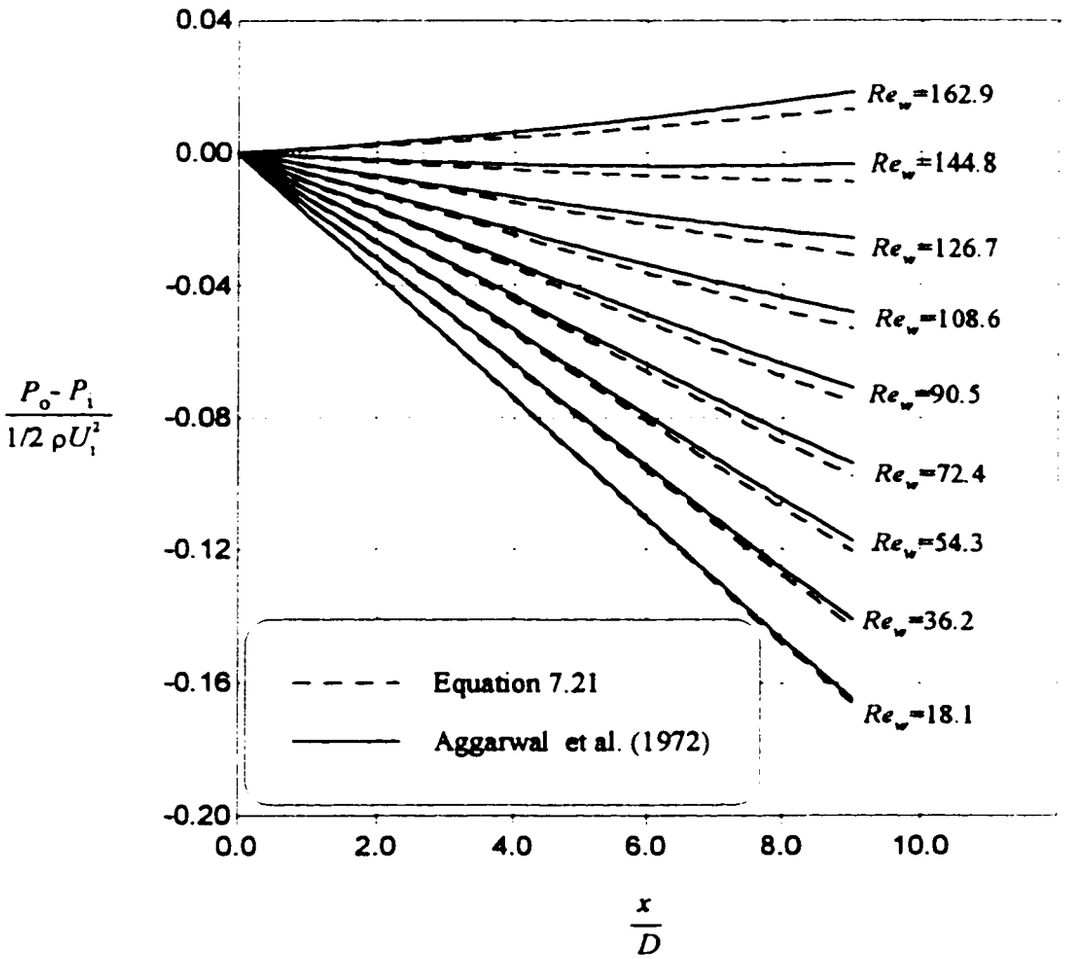

Figure 7.30- Comparison between Equation 7.21 and Aggarwal et al. (1972) study for dimensionless pressure change $(P_o - P_i) / \frac{1}{2}\rho U_i^2$ along tubing for $Re_{axi.}$=101,160

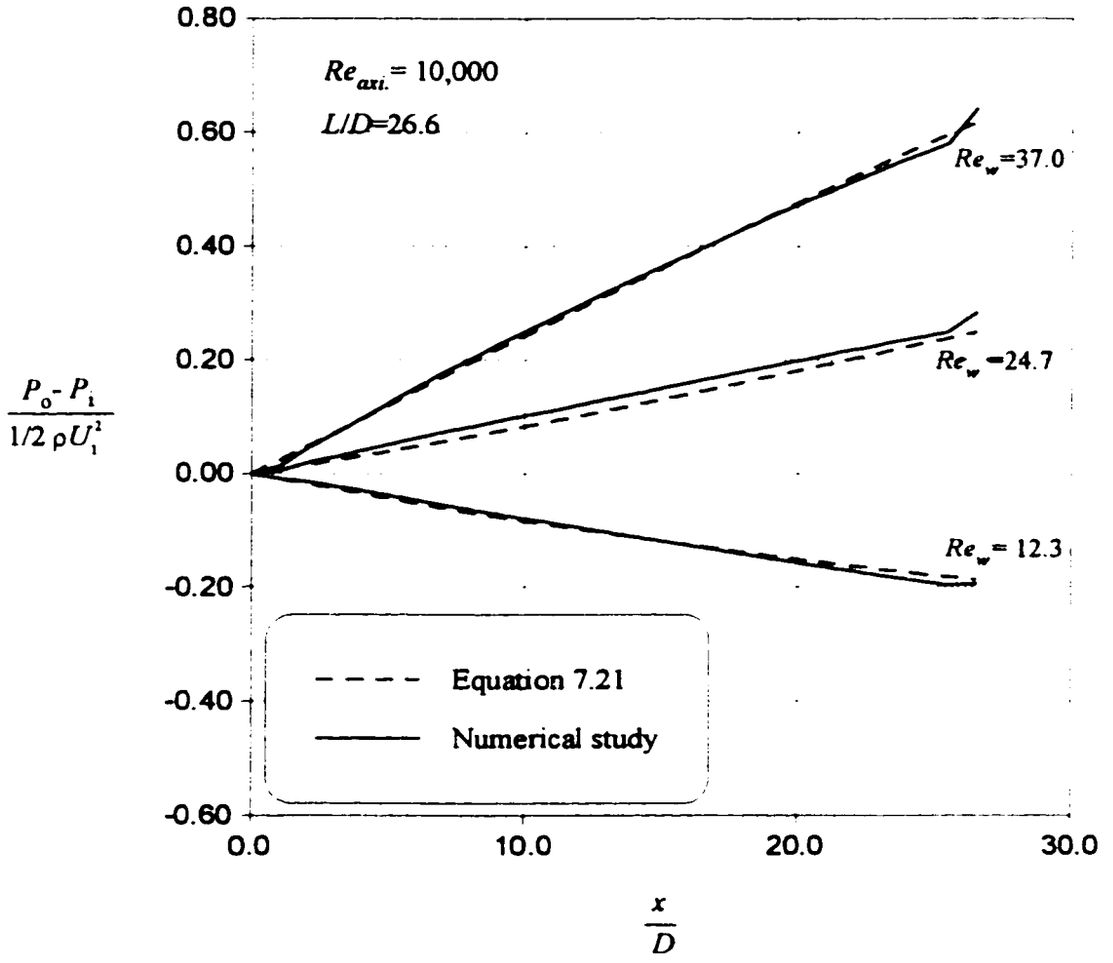

Figure 7.31- Comparison between Equation 7.21 and numerical study for dimensionless axial pressure change $(P_o - P_i)/\frac{1}{2}\rho U_i^2$ along tubing for $Re_{axi.}$=10,000, L/D=26.6

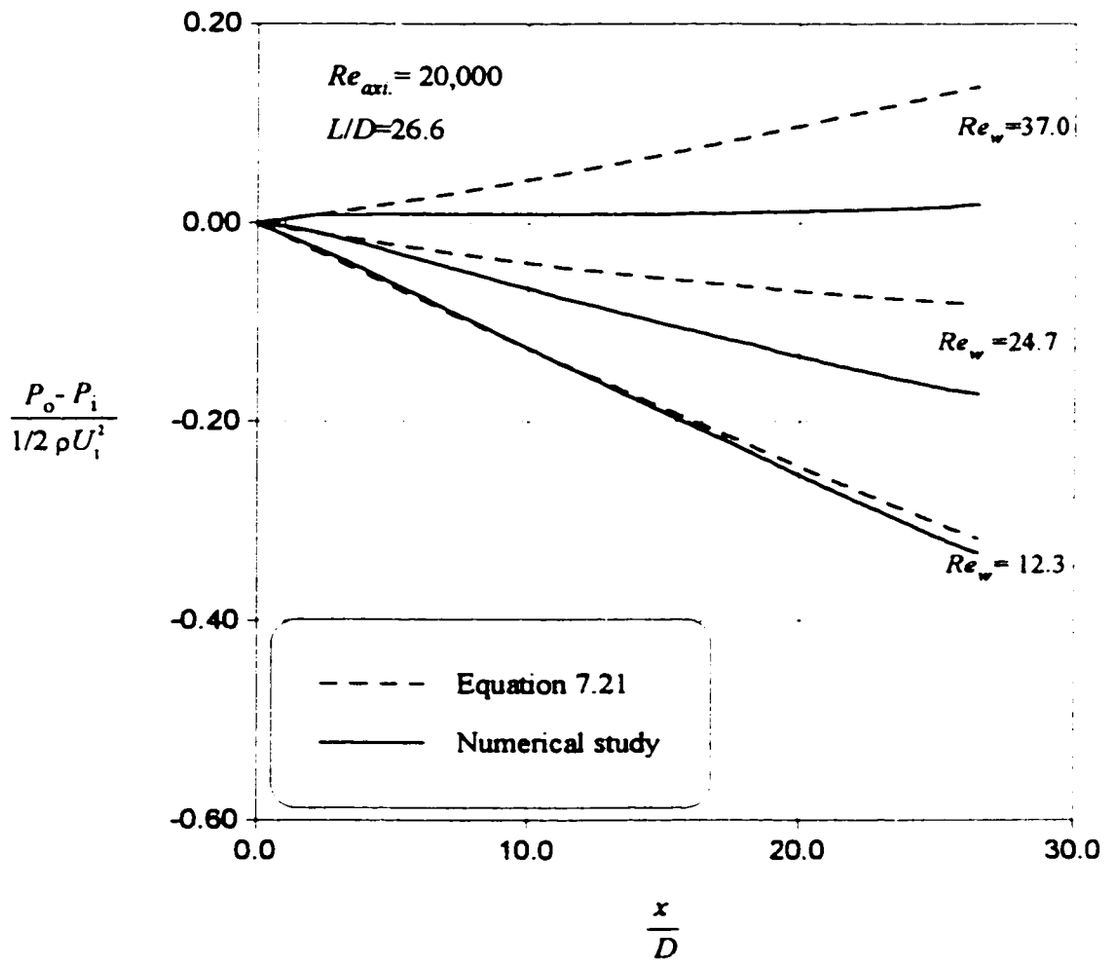

Figure 7.32- Comparison between Equation 7.21 and numerical study for dimensionless axial pressure change $(P_o - P_i) / \frac{1}{2}\rho U_i^2$ along tubing for $Re_{axi.}$=20,000, L/D=26.6

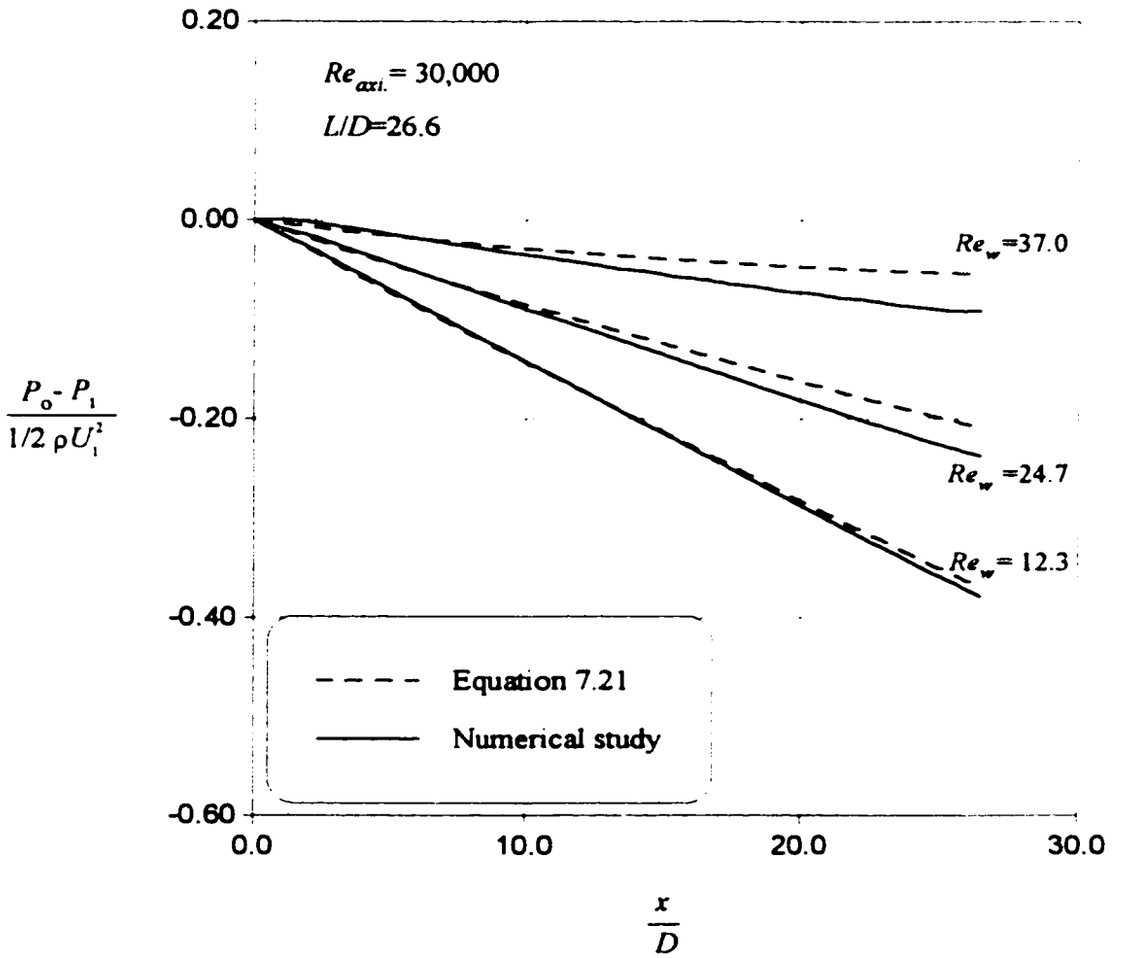

Figure 7.33- Comparison between Equation 7.21 and numerical study for dimensionless axial pressure change $(P_o - P_i) / \frac{1}{2}\rho U_i^2$ along tubing for $Re_{axi.}$=30,000, L/D=26.6

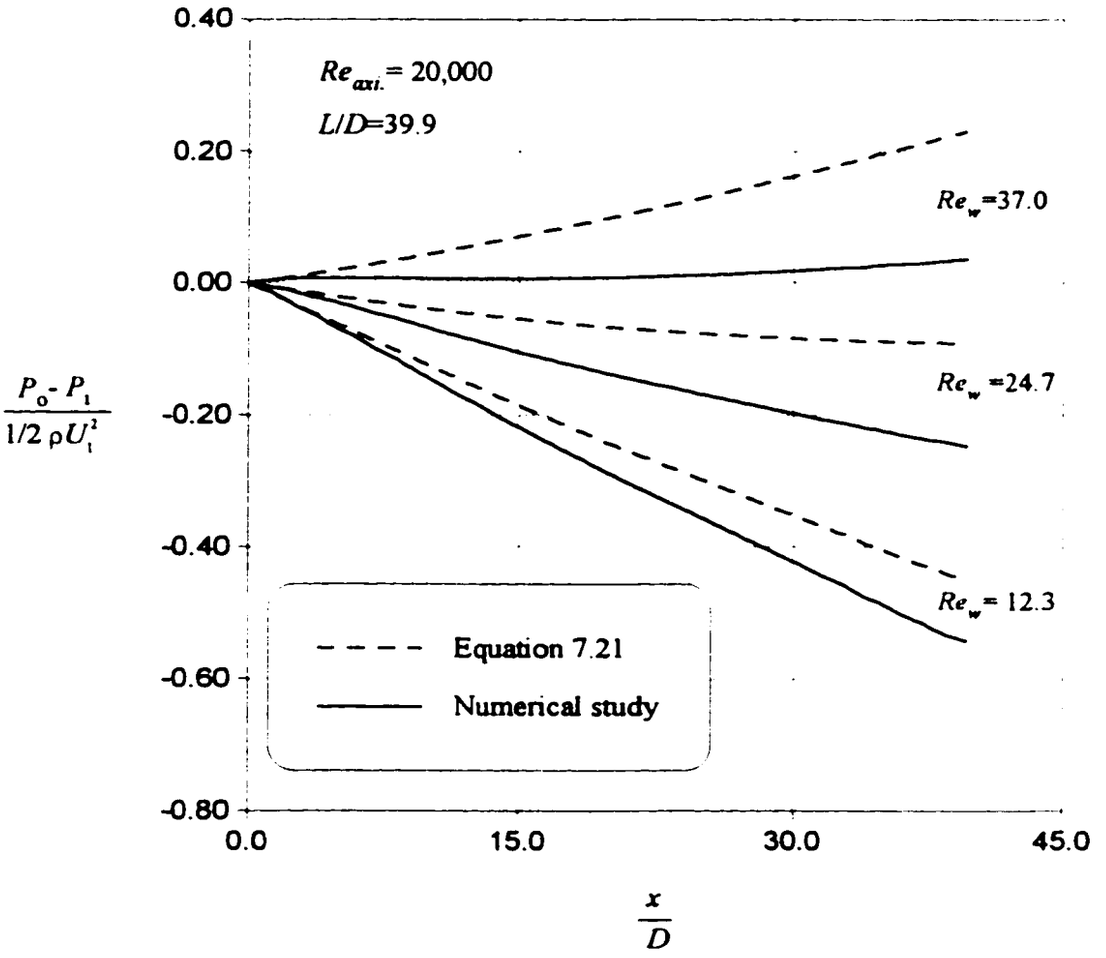

Figure 7.34- Comparison between Equation 7.21 and numerical study for dimensionless axial pressure change $(P_o - P_i) / \frac{1}{2}\rho U_i^2$ along tubing for $Re_{axi.}$=20,000, L/D=39.9

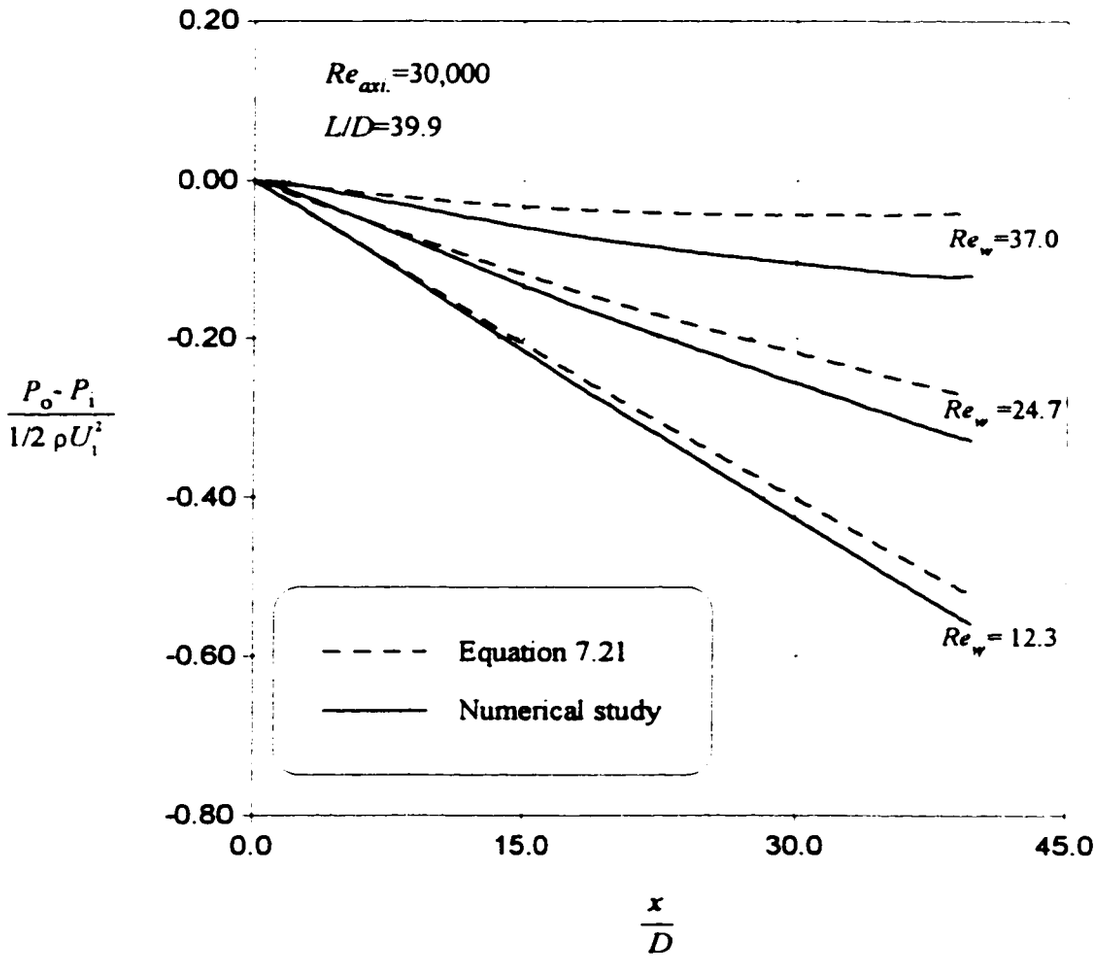

Figure 7.35- Comparison between Equation 7.21 and numerical study for dimensionless axial pressure change $(P_o - P_i) / \frac{1}{2} \rho U_i^2$ along tubing for $Re_{axi.}$=30,000, L/D=39.9

Table 7.1- Measured and calculated slopes for dimensionless pressure change and L/D relation for different inlet Reynolds numbers

	U_2/U_1	1	0.9	0.8	0.7	0.6	0.5	0.4	0.3	0.2	0.1	0
Re_{axi}=38318	Measured slope	0.028	0.025	0.023	0.021	0.019	0.018	0.016	0.014	0.013	0.011	0.010
	Calculated slope	0.027	0.025	0.022	0.020	0.018	0.016	0.014	0.013	0.011	0.010	0.009
Re_{axi}=30731	Measured slope	0.029	0.026	0.024	0.022	0.020	0.018	0.016	0.015	0.013	0.012	0.011
	Calculated slope	0.028	0.025	0.023	0.021	0.018	0.016	0.015	0.013	0.012	0.010	0.009
Re_{axi}=22693	Measured slope	0.029	0.027	0.025	0.023	0.021	0.020	0.018	0.016	0.014	0.013	0.011
	Calculated slope	0.029	0.026	0.024	0.021	0.019	0.017	0.015	0.014	0.012	0.011	0.010
Re_{axi}=15222	Measured slope	0.031	0.029	0.027	0.025	0.023	0.021	0.019	0.017	0.015	0.014	0.012
	Calculated slope	0.031	0.028	0.025	0.023	0.020	0.018	0.016	0.014	0.013	0.012	0.010
Re_{axi}=9997	Measured slope	0.035	0.032	0.030	0.028	0.025	0.023	0.021	0.019	0.017	0.015	0.013
	Calculated slope	0.034	0.031	0.028	0.025	0.022	0.020	0.018	0.016	0.014	0.013	0.011
Re_{axi}=7559	Measured slope	0.036	0.033	0.031	0.028	0.026	0.024	0.022	0.020	0.018	0.016	0.015
	Calculated slope	0.036	0.032	0.029	0.026	0.023	0.021	0.019	0.017	0.015	0.013	0.012
Re_{axi}=5495	Measured slope	0.034	0.031	0.029	0.026	0.024	0.022	0.019	0.017	0.015	0.013	0.011
	Calculated slope	0.039	0.035	0.031	0.028	0.025	0.023	0.020	0.018	0.016	0.014	0.013

Chapter 8

8. SUMMARY, CONCLUSION, AND RESEARCH NEEDS

8.1. SUMMARY

Much literature has been published on flows of pure fluids in porous walled tubes. Most of these studies have dealt with flows of pure fluids in porous walled tubes in the laminar flow regime (Yuan and Finkelstein, 1956; Eckert et al., 1957; Berman, 1958; Weissberg, 1959; Regirer, 1960; White, 1962; Hornbeck et al., 1963; Friedman and Gillis, 1967; Kinney, 1968; Terrill and Thomas. 1969; Raithby, 1971; Galowin and Desantis, 1971;

Galowing et al., 1974; Quaile and Levy, 1975; Singh and Laurence, 1979; Ku and Leidenfrost, 1981; and Terrill, 1982, 1983, 1984, 1986, among others). Studies regarding the effects of wall suction on turbulent pipe flow are rather limited in comparison with those conducted in boundary layers under zero pressure gradient (Antonia et al., 1988; Antonia and Fulachier, 1989; Fulachier et al., 1991, among others). Few publications deal with experiments involving the turbulent flow of pure fluids through porous-walled tubes. Even fewer have been published on the subject of turbulent flow of liquids in porous-walled tubes.

The porous tubing employed in the experimental study is being used as a lateral in microirrigation systems. The average pore size and the thickness of the porous were given by manufacturer as 0.5 μm and 15 μm, respectively. The inner diameter of the porous pipe was 1.128 cm and was made from Tyvec®.

The experimental part of the present work attempted to gather data to determine some of the characteristics of the porous tubing in the case of the non-suction condition for the microirrigation application. Based on these experimental data and the control volume approach explained in chapter 4, relations for the prediction of the pressure drop or pressure gain and pressure gradient along porous tubing in the transition region of the Moody diagram in high suction rate have also been given.

The analysis of data and related discussions were presented in Chapter 6 and 7. In Chapter 6 the frictional characteristics of the porous tubing in the non-suction condition was investigated. The situation of non-suction was obtained by extrapolating the curve relating radial Reynolds number (Re_w) to the dimensionless pressure gain or loss. Based on data for a non-suction condition, a simple, precise and convenient head loss prediction equation was suggested to be used for the small diameter porous tubing under investigation for microirrigation applications. Also a comparison was made between the frictional characteristics of this kind of tubing and the more traditional trickle irrigation laterals. The relative roughness of the porous tubing was obtained and compared with the other laterals used in traditional microirrigation. In this chapter the friction factor of the porous tubing under study in the no suction condition (f_0) at the transition zone were obtained in order to be used in the chapter with suction condition.

In Chapter 4 a control volume approach was used to obtain a formula (Equation 4.37) for calculating pressure drop or pressure gain along porous tubing, incorporating friction factor of the porous tubing at the non-suction condition. According to this formula, with the assumption of the axially uniform radial flow rate along the porous tubing there is a linear relation between dimensionless pressure drop or pressure gain (normalized by inlet dynamic head) and L/D (L : Length of the porous tubing ; D : inside diameter of the porous tubing) at a particular U_2/U_1 (U_1: Area average velocity at the inlet, U_2: Area average velocity at the outlet). This relation was tested in the transition region of the Moody diagram by the experimental program explained in Chapter 7. The intercepts of

these relations were found from experimental data. The pressure gradient relation was then obtained by differentiation of the Equation 4.38 (Equation 7.21). Since there was no experimental data taken for pressure gradient in the present study the validity of the pressure gradient formula was tested by data from Aggarwall et al. (1972) and data obtained from the numerical study.

Chapter 3 of this work deals with a numerical study, investigating the effects of wall mass transfer on the structure of the fully developed turbulent pipe flow. These effects were studied numerically by solving the Reynolds-averaged Navier-Stokes equations in conjunction with the most commonly used turbulence models, i.e, Renormalization Group (RNG) k-ε and k-ω eddy-viscosity models (EVM) of turbulence of the low-Re type. In this chapter the results of the experimental study reported in the literature performed by Schilknecht et al. (1979) were used for comparison purposes. Based on these comparisons the best turbulent model was selected to be used for comparison with Equation 7.10 obtained in chapter seven. In this chapter the effects of wall suction on the mean and turbulence characteristics were determined at the stations in the suction region where detailed experimental measurements were available for suction rates A ($A = Q_A/Q_R$, where Q_A = extracted mass flow and Q_R = inlet mass flow) equal to 1.6, 3.3, 6.5, and 13.0 percent. The profiles of the time-averaged axial velocity (u) and radial velocity (v) obtained from the two turbulence models were compared with measured profiles at the selected stations. The measured profiles of the turbulent kinetic energy (k) along the pipe radius were also compared with the calculated values at the selected stations. The

distribution of the wall shear stress (τ_w) and friction factor (f) in the suction region were examined.

The experimental set-up used in the laboratory program was described in Chapter 5. In preliminary tests two pressure transducers were used for the measurement of the pressure drop or pressure gain. Non of them could provide the necessary accuracy in the desired range of the measurements. A special manometer was designed and constructed in the hydraulic laboratory to allow measurement of the pressure drop or gain providing high accuracy within a wide range of measurement. Preliminary tests showed that distilled water should be used in experiments to prevent the porous tubing from clogging. Based on the analytical work in chapter 6 and preliminary test results, six different lengths of the porous tubing were employed, i.e., $L/D = 26.6$, 53.2, 79.8, 106.4, 159.6, and 206.4. Eight different inlet Reynolds numbers were selected to cover the transition region of the Moody diagram, i.e., 5,495, 7,552, 9,997, 15,222, 22,693, 30,731, and 38,318.

8.2. CONCLUSIONS

From the numerical and experimental investigation of this study the following conclusions may be drawn:

a) The numerical study of the turbulent pipe flow with wall suction rates ranging from A = 0 to 13 percent, in conjunction with experimental measurements and analytical solutions indicates the following:

1- Wall suction effects on fully developed pipe flow lead to more uniform velocity distribution with increased near-wall velocity values and reduced velocities near the centerline.

2- The experimental and computed near-wall component of radial velocity, v, increases with increasing distance from the wall due to the accelerating fluid layers in the longitudinal direction (v component increases to satisfy local continuity)

3- Suction causes the absolute levels of turbulent kinetic energy to increase. Wall suction effects are apparent up to r/D =0.3 in both experimental and computational results.

4- Wall suction increases the wall shear stress ,τ_w, along the suction region. The increase in τ_w is significant even for the smallest suction rate (up to 30 percent) while such an increase is much higher for A = 13 percent (up to 360 percent).

5- Analytical results and empirical relationships indicate similar levels of increase of the shear stress for the low suction rate but tend to underestimate τ_w for the high suction rate, where the boundary layer assumption ceases to be valid.

6- There is close agreement between analytical results, empirical relationships and low-Re k-ω turbulence model particularly for low suction rates in prediction of the wall shear stress in the presence of the wall suction. However, significant differences exist between

the RNG k-ε model, the analytical results and empirical relationship. Therefore, it can be concluded that the low-Re k-ω model can predict wall shear stress in the presence of wall suction better than RNG k-ε model.

7- It seems that the low-Re k-ω model used in this study is capable of predicting correctly the flow characteristics observed in the experiments whereas the RNG k-ε model fails to predict most of the flow characteristics.

8- Analysis of the friction loss data obtained for the small diameter porous tubing in this study confirmed that the Colebrook and White (C-W) equation was a very accurate predictor of the friction factor for porous tubing with small diameter size and Reynolds numbers less than 100,000. These results were in agreement with the results of Aggarwal et al. (1972).

9- The value of the relative roughness obtained in this study showed that the porous tubing under study is smoother than most of the tubing used as lateral in traditional trickle irrigation. Also, the fact that the friction factors agreed with the Colebrook-White law indicates that the physical roughness in the porous tubing under study corresponds very nearly to the equivalent sand roughness with a relative roughness of about e/D =0.002.

10- A combination of a power function and the Darcy-Weisbach equation was proposed as a convenient and accurate head loss prediction equation. The combination equation is

correctable for viscosity changes, and accurate for the porous pipe tubing under study. The equation is given as,

$$H_L = K\upsilon^{0.189} Q^{1.811} D^{-4.811} L \qquad (6.22)$$

The value of $K = 1.564 \times 10^{-2}$ for SI (meter, second) units and $K = 4.762 \times 10^{-3}$ for English (foot, second) units. Equation 6.22 predicted the head loss within ±5% error lines.

11. For all of the inlet Reynolds numbers and for $L/D = 26.6$, excellent agreement existed between observed and predicted dimensionless pressure difference values obtained from Eq. 7.10, indicating that the assumption of the uniform radial flow along porous tubing is valid.

12. For a particular inlet Reynolds number, with increasing length of tubing, the discrepancy between observed and predicted values increases showing that the assumption of uniform suction along tubing ceases to be valid for longer tube lengths.

13. For a particular length of tubing with increasing inlet Reynolds number, the agreement between observed and predicted values improves, indicating that the assumption of uniform radial flow rate along tubing is valid for higher Reynolds numbers.

14. For inlet Reynolds numbers greater than 30,000, for all lengths of tubing under study, there is good agreement between predicted and observed values of the dimensionless pressure head.

15- The best agreement between values obtained by numerical study and Equation 7.21 occurs for an inlet Reynolds number of 10,000 for all lengths and all radial Reynolds numbers under study. For a particular inlet Reynolds number and length of tubing the axial pressure variation predicted by the numerical study diverges from the curves obtained by the suggested formula with increasing radial Reynolds number for all inlet Reynolds number and lengths under study. For a particular inlet Reynolds number and radial Reynolds number the discrepancy between predicted values obtained by two approaches increases for all values of inlet Reynolds number and radial Reynolds number under study. Both approaches show linear axial pressure profile for all lengths and inlet Reynolds number under study at the lower radial Reynolds number of 12.3.

8.3. Future Research Needs

Since this study has only dealt with pure , distilled water, future studies would need to be done to determine the influence of various water quality factors upon the parameters that have been investigated here.

The results of this study has indicated that for small diameter porous tubing at the axial Reynolds number less than 100,000 and for non-suction condition, the Colebrook-White equation can predict the friction factor with a good accuracy. Aggarwall et al. (1972) obtained the same results in his experiments performed with porous tubing in the non-suction condition. However some researchers (von Bernuth,1989; Venkatesan et al.,1990) have shown that the Colebrook and White (C-W) equation is not a very good predictor of

the friction factor for small diameter plastic pipe for Reynolds numbers less than 100,000. More study is needed to confirm that in porous tubing in the non-suction condition the Colebrook-White equation can precisely predict the friction factor.

Whether or not equations of the form of Equation 7.10 and 7.21 have a general validity for different geometry, different surface conditions, fluid properties, etc., remains to be seen and further work is obviously indicated.

REFERENCES

Aggarwal, J. K., Hollingsworth, M. A. and Mayhew, J. R. (1972). Experimental friction factors for turbulent flow with suction in a porous tube. Int. Journal of Heat Mass Transfer 15, 1585-1602

Antonia, R. A., and Fulachier, L., (1989), Topology of a boundary layer with and without wall suction, Journal of Fluid Mechanics, Vol. 198, 429-451.

Antonia, R. A., Fulachier, Krishnamoorthy, L. V., Benabid, T., and Anselmet, F., (1988), Influence of wall suction on the organised Motion in a Turbulent boundary layer, Journal of Fluid Mechanics, Vol. 190, 217-240

Aurelli, A. (1967), Contribution a l'etude de l'ecoulement turbulent dans une conduite cylindrique poreuse avec aspiration., Publ. Sci. Thch. Minist. Air no. 433.

Barr D. I. H. (1972). New forms of equations for the correlation of pipe resistance data. Proc. Instn. Civ. Engrs., Tech Note 72, 53, 383-390.

Barr D., I., H. (1975), Proc Inst Civil Eng., Vol. 59, 375-380.

Beavers, G. S., and Joseph, D. D., (1967), Boundary conditions at a naturally permeable wall., Journal of Fluid Mechanics, Vol 30, Part 1, pp. 197-207.

Beavers, G.S., Sparrow, E.M., and Magnuson, R.A.(1970), "Experiments on Coupled Parallel Flows in a Channel and a Boundary Porous Medium, "Journal of Basic Engineering, ASME, Vol. 92, No. 4, 843-848

Benedict, R. P. (1980). Fundamental of Pipe Flow. Wiley and Sons, New York, N.Y.

Berman, A.S. (1952), Laminar flow in channels with porous walls, Oak Ridge Gaseous Diffusion Plant, USAEC Report K-944, 1952

Berman, A.S. (1958). Effects of porous boundaries on the flow of fluids in systems with various geometries. Proc. 2nd Intern. Congr. Peaceful Rses of Atomic Energy, Paper No. P/720, 351-358

Berman, A.S.(1953), Laminar flow in channels with porous walls. Journal of Applied Physics, Vol 24, .1232-1242

Binder, R. C. (1962), Fluid mechanics, 4th Ed., Prentice Hall, New York, 117-127.

Boussinesq, J. (1877), Theorie de l'Ecoulement Tourbillant, Mem. Presentes par Divers Savants Acad. Sci. Inst. Fr., Vol. 23, pp. 46-50.

Bradshaw, P. (1972), The understanding and prediction of turbulent flow, The Aeronautical Journal, Vol. 76, No. 739, pp. 403-418.

Bruce, R. M., and Donald, F. Y. (1990). Fundamental of fluid mechanics. First ed., John Wiley and Sons, New York, N.Y.

Chen, J. J. J. (1985). Systematic explicit solutions of Prandtle and Colebrook-White equation for pipe flow. Proc, Instn. Civ. Engn., Part 2, Tech. Note 431. 79, 383-389

Chu, Y., and Gelhar, L. W. (1972), "Turbulent pipe flow with granular permeable boundaries, "Report No. 148, Ralph M. Parsons Laboratory for Water Resources and Hydrodynamics, Massachusetts Institute of Technology, Cambridge, MA,

Churchill S.,W. (1973) , AIChE J, 19(2), 375-385.

Colebrook, C. F. (1939), Turbulent flow in pipes, with particular reference to the transition region between smooth and rough pipe laws, Journal Inst. Civil Eng. (London), Vol.. 11, 133-156

Corrsin, S. and Kistler, A. L. (1954), The free-stream boundaries of turbulent flows, NACA TN 3133.

Daugherty and Franzini (1977). Fluid mechanics with engineering applications. Seventh ed., McGraw-Hill, New York, N.Y.

Doughty, J. R., and Perkins, H. C. (1970), Hydrodynamics entry length for laminar flow between parallel porous plates, Journal of Appl. Mech., Vol. 37, pp. 548-550

Doughty, J. R. (1974), Parallel porous plate channel flow characteristics resulting from nonuniform entry velocity profile, Trans. ASME, Journal of Fluid Mech., pp. 1-4

Eckert, E.R.G., Donoughe, P.L., and Moore, B.J. (1957). Velocity and friction characteristics of lamivar viscous boundary-layer and channel flow over surfaces with ejection or suction. National Advisory Committee for Aeronautics, Tech. Note 4102, 1-57.

Favre, A. (1966), Couche limite turbulente sur paroi poreuse avec aspiration. J. Mec. 5.

Fluid Dynamics International Inc. FIDAP Theoretical Manual, Version 7.0, 1993

Fluid Dynamics International Inc. FIDAP Update Manual, Version 7.6, 1996

Friedman, M., and Gillis, J. (1967). Viscous flow in a pipe with absorbing walls. Jornal of Applied Mech. 34(4), 810-822.

Fulachier, L., Anselmet, F., Benabid, T., and Antonia, R. A., (1991), Normalization for a turbulent boundary layer with wall suction, physics of fluids, Vol. A3 (1), 213-235.

Galowin, L.S., and Desantis, M.J. (1971). Theoretical analysis of laminar pipe flow in a porous wall cylinder. Journal Dyn, Sys. NEAS. Control 93(2), 102-108.

Galowin, L.S., and Fletcher, L.S., and Desantis, M.J. (1974) . Investigation of laminar

flow in a porous pipe with variabe wall suction. AIAA J. 12(11), 1585-1589.

Ganna, R. J. m., and Gelgar, L. W. (1972), "Turbulent pipe flow with rough and porous walls," Report No. 109, Ralph M. Parsons Laboratoty for Water Resources and Hydrodynamics, Massachusetts Institute of Technology, Cambridge, MA.

Gerhart, P. M., Gross, R. J., and Hochstein, J. I. (1992). Fundamental of fluid mechanics. Second ed., Addision-Wesley Publishing Copany, New York, N.Y.

Goldstein, S. (1938), Modern Developments in Fluid Dynamics, Vol. 2, p. 331, Oxford University Press, NY.

Goma, R. J. M., and Gelhar, L. W. (1968), "Turbulent pipe flow with rough and porous walls, "Report No. 109, Ralph M. Parsons Laboratory for Water Resources and Hydrodynamics, Massachusetts Institute of Technology, Cambridge, MA,

Green, G. (1980), Experimental study of laminar flow in parallel porous plate, Trans. ASME, pp. 338-342.

Gupta, B. K. and Levy, E. K. (1974). Laminar flow in annuli and flat plate channels with mass transfer at one wall, AIAA paper, no. 74-721.

Haaland S. E. (1983). Simple and explicit formulas for the friction factor in turbulent pipe flow. J. Fluids Eng. Trans. ASME, Vol. 105, 89-90.

Hinze, J. O., (1959). Turbulence, McGraw-Hill

Holman, J. P. (1983), Experimental Methods for Engineers, 4th Ed., McGraw-Hill, New York.

Hornbeck, R.W., Roulear, W.T., and Osterle, F. (1963). Laminar entry probem in porous tubes. Physics of Fluids 6(11), 1649-1654

Jaeger, C.(1957), Engineering fluid mechanics, New York, St. Martin Press Inc.

Kinney, R. B., and Sparrow, E. M., (1970). Turbulent flow, heat transfer and mass transfer in a tube with surface suction, ASME Journal of Heat Transfer, Vol. 92, pp. 117-125.

Kinney, R.B. (1968). Fully developed frictional and heat transfer characteristics of laminar flow in porous tubes. Int. Journal of Heat Nass Transfer 11, 1393-1401.

Klein, A., (1981), Effect of inlet and outlet conditions on conical-diffuser performance, ASME, Journal of Fluid Engineering, pp. 250-257.

Kolmogorov, A. N. (1942), Equations of turbulent motion of an incompressible fluid, Izvestia Academy of Science, USSR; Physics, Vol. 6, Nos. 1 and 2, pp. 56-58.

Kozinski, F. P., Schmidt, F. P., and Lightfoot, E. N. (1970), Velocity profile in porous

walled ducts, Ind. Eng. Chem., Fundam., Vol. 9, pp. 502-505.

Ku, J., and Leidenfrost, W. (1981) Laminar flow in a pouous tube with uniform mass injection. Part 1: Theoretical studies. Ingenieur-Archiv 51, 111-126.

Laufer, J. (1954), The structure of turbulent in fully developed pipe flow, NACA Technical Note no. 2954.

Lovera, F., and Kennedy, J.F. (1969), Friction factors for flat bed flows in sand channels, Journal of the Hydraulics Division, ASCE, Vol. 95, No. HY4, 1227-1234

MacLean, A. G., (1991), Open channel velocity profile over a zone of rapid infiltration, Journal of Hydraulic Research, Vol. 29, 15-27.

Massey, B. S. (1983), "Turbulent Flow in Pipes;"Mechanics of Fluids, 4rd Ed., van Nostrand Reinhold Company, New York, N. Y., 185-210

Mellis, R., Gill, W. N., and Belfort, G. (1993). Fluid dynamics in a tabular membrane: theory and experiment, Chem. Eng. Commun., Vol. 122, 103-125

Minton, P. and Francis, J. R. D. (1958), The aerodynamic drag of perforated plates at zero incidence, Journal of the Royal Aeronautical Society, Vol. 62, pp. 301-303.

Monin, A. S., and Yaglom, A. M. (1971). Statistical fluid mechanics: mechanics of

turbulence. Vol. I (English), MIT press, Cambridge, Mass.

Moody, L. F. (1944), Friction factors for pipe flow, Trans. ASME, Vol. 66, 671-684

Morduchow, M., (1967), On laminar flow through a channel of tube with injection: Application of method of average. Quarterly of applied mathematics, Vol. 14, 1967, pp. 361-368.

Morris, H. M., and Wiggert, J. M. (1972), "Hydraulic of Flow in Closed Conduits," Applied Hydraulics in Engineering, 2nd Ed., The Ronald Press Company, New York, N. Y., 57-83

Nikuradse, J. (1933), Laws of flow in rough pipes, Forsch.-Arb. Ing.-Wesen, No. 361

Nonlinear Regression Modeling A Unified Practical Approach, David A. Ratkowsky, MARCEL DEKKER, INC. , NEW Tork and BASEL, 1983,

Norum, E. M. (1984). "Determining friction loss in polyethylen pipe used for drip irrigation laterals." *Irrig Age*, 17-18, 26K.

Paraqueima, J. R. (1977). Study of some frictional characteristics of small diameter tubing for trickle irrigation laterals, thesis presented to the Utah State University in partial fulfillment of the requirements for the degree of Master of Science.

Plate, E. J., and Quraishi, A. A. (1965), Modeling of Velocity Distribution Inside

above Tall Crops, Journal of Applied Meteorology, Vol. 4, No. 3, 400-408

Powell, R. W. (1938), Mechanics of liquids: New York, The Macmillan Co., 250-254

Pozzorini, R. (1976), Das turbulente stromungsfeld in einem langen kreiskegel-diffusor, PhD dissertation ETH Zurich, 1976. Eduard Truninger AG Zurich.

Prandtl, L. (1925), Uber die ausgebildete Turbulenz, ZAMM, Vol. 5, pp. 136-139

Prandtl, L. (1945), Uber ein neues formelsystem fur die ausgebildete turbulenz, Nacr. Akad. Wiss. Gottingen, Math-Phys. Kl. 1945, pp. 6-19.

Prandtl, L., and Tietjens, O. G. (1952), Applied hydro- and aero-mechanics, New York, Dover Pulishing Co., Chapter 4

Quale, J.P. (1972). Laminar Flow in a pouous Tube with wall suction. J. Heat Transfer, 66-71.

Quale, J. P. and Levy, E. K. (1975). Laminar flow in a porous tube with suction, Trans. ASME, J. Heat Transfer, Vol. 2, pp. 66.

Raithby, G. (1971). Laminar heat transfer in the thermal entrance region of circular tubes and two-dimensional rectangular ducts with wall suction and injection. Int. J. Heat Mass Transfer 14, 223-243.

Regirer, S.A. (1960). On the approximate theory of the flow of a viscous incompressible liquid in a tube with permeable walls. Sobiet Phys. Tech. Phys., USSR 5, 602-605

Reynolds, O. (1895), On the dynamical theory of imcompressible viscous fluids and the determination of the criterion, Philosophical Transactions of the Royal Society of London, Series A, Vol. 186, p. 123.

Ruff, J. F., and Gelhar, L.W. (1970), "porous boundary effects in turbulent shear flow, "Report No. 126, Ralph M. Parsons Laboratory for Water Resources and Hydrodynamics, Massachusetts Institute of Technology, Cambridge, MA.

SAS user's guide: statistics (1985). SAS Institute Inc., Cary, N.C.

Schildknecht, M., Miller, J., A., and Meier, G. E. A. (1979), The influence of suction on the structure of turbulence in fully developed pipe flow, Journal of Fluid Mechanics, Vol. 90, 67-107.

Sieveka, E. H. (1966), Reverse osmosis pilot plants, in U. Merten (Ed.), Desalination by reverse osmosis, The M.I.T Press, Cambridge, MA, Chap. 7.

Silver, R. S. and Wallis, (1965), An general theory of surface condensers. Proc. Instn. Mech. Engrs, Lond., pp. 336-339.

Singh, R., and Laurence, R.L. (1979). Influence of slip velocity at a membrane surface on

ultrafiltration performance 2. Tube flow system. Int. J. Heat Nass Transfer 12, 731-737.

Sovran, G., and Klomp, E. (1967), Experimentally determined optimum geometries for rectillinear diffusers with rectangular, conical or annular cross section, Fluid Mechanics of Internall Flow, pp. 243-249.

Swamee P., K., & Jain A., K. (1976), J Hydraulic Div Am Soc Civil Eng, Vol. 102, 657-667

Taylor, G. (1956). Fluid flow in regions bounded by porous surfaces, Proc. of the Royal Society, London, Vol. 234, pp. 456-475

Tennekes, H. and Lumley, J. L. (1983), A first course in turbulence, MIT Press, Cambridge, MA.

Terrill, R.M., (1964). Laminar flow in a uniformly porous channel, Aeronaut, Q., Vol. 15, pp. 299-310.

Terrill, R.M., (1982). An exact solutuon for flow in a porous pipe. Journal of Appl. Math. Phys. Vol. 33, 547-552

Terrill, R.M., (1983). Laminar flow in a porous tube. Trans. ASMR: Journal of Fluids Engr. Vol. 105, 303-307.

Terrill, R.M., (1984). A note on laminar flow through a porous pipe with slip. IMA Journal Appl. Math. 33, 169-174.

Terrill, R.M., (1986). Fluid flow in a region bounded by a porous cylindrical pipe. Phys. Fluids 29(3), 625-627

Terrill, R.M., and Thomas, P.W. (1969). On laminar flow through a uniformly porous pipe. Appl. Sci. Res. 21, 37-67.

Townsend, A. A. (1956), The structure of Turbulent flow, Cambridge University Press

Urbina, J. L. (1976). "Head loss characteristics of trickle irrigation hose with emitters," thesis presented to the Utah State University, in partial fulfillment of the requirements for the degree of Master of Science.

Venkatesan R., Das S. K. and Biswas M. N. (1990). Friction factors for small diameter transparent PVC. Indian Jounal of Tec hnology,Vol. 28, .549-552

von Bernuth R., D., Wilson T., J. (1989), Friction factors for small diameter plastic pipes, Journal of Hydraulic Eng., Vol. 115, 183-191.

Wageman, W. E., and Guevara, F. A. (1960), Fluid flow through a porous channel, Physics of Fluids, vol. 3, 1960, pp. 878-881.

Wallis, G.B. (1965-6), A simple theory for longitudinal pressure drop in the presence

of lateral condensation, Proc. Instn Mech. Engrs 180, 27-35

Weast, R.C. (1981). CRC Handbook of Chemistry and physics, 62nd ed. CRC Press, Boca Raton, Florida.

Weissberg, H. L. and Berehman, A. S. (1955). Velocity and pressure distribution in turbulent pipe flow with uniform wall suction. Heat Transfer Fluid Nech. Inst., Univ. Calif., Los Angeles 14, 1-30

Weissberg, H.L. (1959). Laminar flow in the entrance region of a porous pipe. Physics of Fluids 2(5), 510-516.

White, F.M. (1962). Laminar flow in a uniformly porous tube. AME: J. Appl. Mech. 29, 201-204.

Williams, F. A. (1968). Linearized analysis of constant-property duct flows, Journal of Fluid Mechanics, Vol. 34, pp. 241-261

Wilcox., D. C. (1993), Turbulence Modeling for CFD, DCW Industries, Inc., La Canada.

Yakhot V., Orszag S. A., Thangam S., Gatski T. B. and Spezial C. G., (1992), Development of turbulece models for shear flows by double expansion technique, Physics of Fluids, A 4 (7), pp. 1510-1520.

Yuan, S.W. , and Finkelstin, A.B. (1956). Laminar pipe flow with injection and

suction through a porous wall. Trans. ASME 78, 719-724.

Zagni, A. F. E., and Smith, K. V. H. (1976), "Channel flow over permeable beds of graded spheres, "Journal of the Hydraulics Division, ASCE, Vol. 102, No. HY2,. 207-222

Appendices

Appendix A

Experimental Data

Table A.1- Experimental data for L/D= 26.6 and inlet Reynolds number Re_{axi} = 38318

Experiment Number	Measured Porous Volume Collected (mL)	Measured Porous Collection Time (sec)	Measured Outlet Volume Collected (mL)	Measured Outlet Collection Time (sec)	Measured Head Difference (cm H_2o)	Rotameter Reading	Inlet pressure (psi)	Average Temperature (°C)	Inlet Axial Reynolds Number $Re_{axi.}$	Radial Reynolds Number Re_w	Outlet/Inlet Average Velocity U_2/U_1	Dimensionless Pressure Drop $(p_o-p_i)/1/2\rho v_1^2$
1	1420	78.28	4030	13.44	30.895	5.0	9.50	24.0	39333.6	21.08	0.943	-0.323
2	1810	78.50	4042	13.68	26.885	5.0	13.00	24.0	38923.3	26.79	0.928	-0.260
3	2320	75.22	3770	13.55	17.42	5.0	15.75	24.0	38350.4	36.66	0.900	-0.100
4	2560	61.56	4106	14.66	8.535	5.0	18.50	24.0	38773.1	48.32	0.871	0.105
5	3280	65.45	4110	15.65	-0.625	5.0	23.25	24.0	38223.2	59.57	0.840	0.300
6	3170	48.00	4023	15.75	-14.455	5.0	28.50	25.0	38105.5	76.73	0.795	0.606
7	3810	46.81	4022	16.91	-26.55	5.0	34.00	25.0	37583.1	94.57	0.745	0.897
8	4020	44.64	3780	16.32	-31.35	5.0	36.00	25.0	38654.6	107.04	0.720	1.000
9	3630	35.22	3930	17.98	-39.68	5.0	39.50	25.0	38512.3	122.50	0.680	1.201
10	3720	33.13	3940	18.60	-45.975	5.0	41.50	25.0	38733.8	133.46	0.654	1.336

Table A.2- Experimental data for $L/D = 26.6$ and inlet Reynolds number $Re_{axi.} = 30731$

Experiment Number	Measured Porous Volume Collected (mL)	Measured Porous Collection Time (sec)	Measured Outlet Volume Collected (mL)	Measured Outlet Collection Time (sec)	Measured Head Difference (cm H_2o)	Rotameter Reading	Inlet pressure (psi)	Average Temperature (°C)	Inlet Axial Reynolds Number $Re_{axi.}$	Radial Reynolds Number Re_w	Outlet/Inlet Average Velocity U_2/U_1	Dimensionless Pressure Drop $(p_o-p_i)/1/2\rho v_1^2$
1	695	76.12	3870	16.66	-25.125	4.0	7.50	23.0	29450.3	10.37	0.962	-0.536
2	980	66.72	3740	15.41	-22.345	4.0	11.00	24.0	31656.8	17.07	0.943	-0.389
3	1360	64.34	3990	16.94	-16.14	4.0	15.00	24.0	31191.7	24.56	0.918	-0.221
4	1900	62.37	3980	17.79	-9.78	4.0	20.00	24.0	30546.4	35.39	0.880	-0.037
5	2510	64.66	3920	17.97	-3.025	4.0	24.00	23.0	29963.1	44.07	0.849	0.191
6	2880	62.37	3780	18.10	0.14	4.0	27.50	24.0	30270.2	53.65	0.819	0.297
7	3210	54.16	4066	20.32	8.685	4.0	31.50	25.0	31329.4	70.45	0.771	0.589
8	3160	49.11	3990	20.45	14.64	4.0	34.60	25.0	31226.4	76.48	0.752	0.803
9	3130	43.25	3640	19.54	18.615	4.0	37.33	25.0	31038.1	86.02	0.720	0.951
10	3580	45.12	4074	22.81	19.47	4.0	40.00	25.0	30870.9	94.31	0.692	0.989

Table A.3- Experimental data for L/D= 26.6 and inlet Reynolds number $Re_{axl.}$ = 22693												
Experiment Number	Measured Porous Volume Collected (mL)	Measured Porous Collection Time (sec)	Measured Outlet Volume Collected (mL)	Measured Outlet Collection Time (sec)	Measured Head Difference (cm H_2o)	Rotameter Reading	Inlet pressure (psi)	Average Temperature (°C)	Inlet Axial Reynolds Number $Re_{axl.}$	Radial Reynolds Number Re_w	Outlet/Inlet Average Velocity U_2/U_1	Dimensionless Pressure Drop $(p_o-p_i)/1/2\rho v_1^2$
1	350	95.38	4000	21.62	-17.52	3.0	5.25	24.0	23881.9	4.26	0.981	-0.606
2	530	79.79	3900	21.41	-15.36	3.0	8.00	23.0	22973.5	7.54	0.965	-0.535
3	660	67.43	3920	21.91	-13.535	3.0	10.50	24.0	23250.8	11.37	0.948	-0.462
4	1680	79.00	3920	23.35	-5.675	3.0	17.50	24.0	22848.5	24.71	0.888	-0.043
5	1960	77.62	4060	24.81	-3.305	3.0	20.00	25.0	23222.4	30.01	0.866	0.095
6	1670	48.47	3580	23.19	1.46	3.0	25.50	24.0	22479.8	40.03	0.818	0.388
7	2320	66.94	4000	25.97	1.46	3.0	25.50	24.0	22462.1	40.27	0.816	0.388
8	2940	68.65	3840	26.34	6.235	3.0	30.00	24.0	22312.7	49.76	0.773	0.699
9	3080	59.03	3850	28.22	8.485	3.0	34.50	23.0	21685.2	59.24	0.723	0.852
10	3400	51.78	4000	32.04	15.03	3.0	39.50	24.0	22297.6	76.29	0.655	1.280

Table A.4- Experimental data for L/D= 26.6 and inlet Reynolds number Re_{axi} = 15222												
Experiment Number	Measured Porous Volume Collected (mL)	Measured Porous Collection Time (sec)	Measured Outlet Volume Collected (mL)	Measured Outlet Collection Time (sec)	Measured Head Difference (cm H_2o)	Rotameter Reading	Inlet pressure (psi)	Average Temperature (°C)	Inlet Axial Reynolds Number Re_{axi}	Radial Reynolds Number Re_w	Outlet/Inlet Average Velocity U_2/U_1	Dimensionless Pressure Drop $(p_o-p_i)/1/2\rho v_1^2$
1	180	153.44	3940	31.69	-10.48	2.0	3.50	24.0	16136.8	1.36	0.991	-0.848
2	224	87.97	3980	32.19	-8.925	2.0	5.50	24.0	15942.9	2.96	0.980	-0.725
3	760	100.56	3910	32.94	-6.115	2.0	10.00	24.0	15586.4	8.78	0.940	-0.459
4	1200	81.87	3890	34.43	-2.34	2.0	15.50	24.0	15491.4	17.03	0.885	-0.002
5	2102	97.34	4000	38.44	-0.105	2.0	20.50	24.0	15085.8	25.09	0.828	0.283
6	2188	80.38	3880	39.19	1.395	2.0	24.50	24.0	15050.1	31.63	0.784	0.492
7	2440	78.00	3790	39.78	2.835	2.0	26.70	24.0	15039.3	36.35	0.753	0.695
8	2820	75.00	3880	43.84	4.695	2.0	30.50	24.0	14908.4	43.69	0.702	0.972
9	2810	55.97	3720	48.06	7.185	2.0	36.00	24.0	14989.7	58.33	0.607	1.324
10	3370	57.62	3980	57.53	9.28	2.0	39.50	24.0	14942.8	67.95	0.542	1.641

Table A.5- Experimental data for $L/D = 26.6$ and inlet Reynolds number $Re_{axi} = 9997$

Experiment Number	Measured Porous Volume Collected (mL)	Measured Porous Collection Time (sec)	Measured Outlet Volume Collected (mL)	Measured Outlet Collection Time (sec)	Measured Head Difference (cm H_2o)	Rotameter Reading	Inlet pressure (psi)	Average Temperature (°C)	Inlet Axial Reynolds Number Re_{axi}	Radial Reynolds Number Re_w	Outlet/Inlet Average Velocity U_2/U_1	Dimensionless Pressure Drop $(p_o-p_i)/1/2\rho v_i^2$
1	250	320.45	4090	52.54	-4.115	1.3	3.86	24.0	10071.3	0.34	0.990	-0.852
2	1250	220.65	4030	53.48	-2.586	1.3	8.60	24.0	10060.3	2.47	0.930	-0.460
3	2150	200.85	3975	55.52	-1.285	1.3	13.04	24.0	10055.9	4.68	0.870	-0.090
4	2690	170.65	4050	60.21	-0.13	1.3	17.13	24.0	10037.9	6.89	0.810	0.254
5	3490	160.44	3935	63.54	1.09	1.3	21.51	24.0	10028.1	9.50	0.740	0.630
6	4190	155.87	3570	62.45	2.015	1.3	24.89	24.0	10015.0	11.74	0.680	0.923
7	3130	90.46	3760	75.45	3.27	1.3	29.37	24.0	9996.8	15.11	0.590	1.328
8	3470	87.22	3570	79.66	3.995	1.3	31.98	24.0	9983.3	17.38	0.530	1.567
9	3900	86.89	3395	85.24	4.645	1.3	34.23	24.0	9970.4	19.61	0.470	1.784
10	4150	80.22	3020	91.25	5.395	1.3	36.75	24.0	9956.6	22.60	0.390	2.037
11	3655	62.45	2905	110.54	6.025	1.3	38.69	24.0	9934.1	25.56	0.310	2.255
12	3385	53.21	3615	170.56	6.415	1.3	39.77	24.0	9924.0	27.79	0.250	2.389

Table A.6- Experimental data for L/D= 26.6 and inlet Reynolds number $Re_{axi.}$ = 7558

Experiment Number	Measured Porous Volume Collected (mL)	Measured Porous Collection Time (sec)	Measured Outlet Volume Collected (mL)	Measured Outlet Collection Time (sec)	Measured Head Difference (cm H_2o)	Rotameter Reading	Inlet pressure (psi)	Average Temperature (°C)	Inlet Axial Reynolds Number $Re_{axi.}$	Radial Reynolds Number Re_w	Outlet/Inlet Average Velocity U_2/U_1	Dimensionless Pressure Drop $(p_o-p_i)/1/2\rho v_1^2$
1	5	160.68	3560	57.97	-2.94	1.0	2.25	24.0	8036.6	0.04	0.999	-0.953
2	222	193.41	3600	59.69	-2.42	1.0	4.00	24.0	7861.5	1.33	0.981	-0.811
3	690	178.57	3540	61.10	-1.91	1.0	7.75	24.0	7705.1	4.49	0.937	-0.645
4	860	108.28	3650	67.34	-1.025	1.0	12.00	24.0	7617.6	9.23	0.872	-0.235
5	1315	110.55	3160	70.63	-0.14	1.0	15.75	25.0	7027.4	14.14	0.790	0.201
6	1980	109.53	3040	68.78	0.755	1.0	20.00	24.0	7484.0	21.00	0.710	0.707
7	2670	93.97	3410	98.41	1.77	1.0	26.50	25.0	7668.9	33.77	0.549	1.273
8	2620	70.22	2440	95.78	2.645	1.0	32.00	25.0	7579.4	44.35	0.406	1.816
9	2275	58.53	2630	127.09	3.185	1.0	35.50	25.0	7161.4	46.20	0.347	2.380
10	2855	64.55	2850	143.22	3.39	1.0	35.75	25.0	7708.3	52.57	0.310	2.200
11	2920	59.22	1385	99.45	3.61	1.0	38.25	25.0	7580.9	58.61	0.220	2.404
12	2940	52.78	590	76.57	3.79	1.0	40.50	25.0	7584.9	66.21	0.122	2.515
13	2660	47.71	490	70.28	3.64	1.0	40.50	25.0	7503.3	66.27	0.111	2.472

Table A.7- Experimental data for L/D= 26.6 and inlet Reynolds number Re_{axi} = 5495												
Experiment Number	Measured Porous Volume Collected (mL)	Measured Porous Collection Time (sec)	Measured Outlet Volume Collected (mL)	Measured Outlet Collection Time (sec)	Measured Head Difference (cm H_2o)	Rotameter Reading	Inlet pressure (psi)	Average Temperature (°C)	Inlet Axial Reynolds Number $Re_{axi.}$	Radial Reynolds Number Re_w	Outlet/Inlet Average Velocity U_2/U_1	Dimensionless Pressure Drop $(p_o-p_i)/1/2\rho v_1^2$
1	105	240.15	2990	70.21	-1.245	0.73	3.30	24.0	5544.8	0.19	0.990	-0.829
2	915	230.21	3450	85.66	-0.655	0.73	7.15	24.0	5534.2	1.74	0.910	-0.328
3	1510	210.54	3280	87.22	-0.22	0.73	10.33	24.0	5520.9	3.13	0.840	0.077
4	1960	180.45	3430	99.65	0.22	0.73	13.74	24.0	5521.5	4.74	0.760	0.506
5	2335	150.24	3340	110.55	0.695	0.73	17.68	24.0	5524.8	6.79	0.660	0.984
6	2910	140.66	3060	120.87	1.13	0.73	21.60	24.0	5512.1	9.04	0.550	1.437
7	3255	130.89	3090	145.96	1.43	0.73	24.49	24.0	5489.4	10.86	0.460	1.765
8	3270	120.45	2840	150.52	1.565	0.73	25.96	24.0	5474.3	11.86	0.410	1.920
9	3495	110.85	2650	180.44	1.795	0.73	28.43	24.0	5478.6	13.77	0.318	2.167
10	3190	90.85	2115	190.68	1.935	0.73	30.29	24.0	5463.9	15.34	0.240	2.334
11	3450	88.82	1560	210.85	2.05	0.73	31.97	24.0	5456.8	16.97	0.160	2.470
12	2995	69.25	735	240.28	2.15	0.73	33.65	24.0	5453.9	18.89	0.066	2.588

Table A.8- Experimental data for L/D= 26.6 and inlet Reynolds number Re_{axi} = 3671												
Experiment Number	Measured Porous Volume Collected (mL)	Measured Porous Collection Time (sec)	Measured Outlet Volume Collected (mL)	Measured Outlet Collection Time (sec)	Measured Head Difference (cm H_2o)	Rotameter Reading	Inlet pressure (psi)	Average Temperature (°C)	Inlet Axial Reynolds Number $Re_{axi.}$	Radial Reynolds Number Re_w	Outlet/Inlet Average Velocity U_2/U_1	Dimensionless Pressure Drop $(p_o-p_i)/1/2\rho v_1^2$
1	40	247.91	2360	82.00	-0.74	0.5	2.00	25.0	3890.4	0.19	0.994	-1.081
2	230	124.07	2030	75.28	-0.61	0.5	5.00	25.0	3738.7	2.20	0.936	-1.000
3	430	130.22	1920	80.22	-0.32	0.5	6.50	26.0	3576.9	4.01	0.879	-0.499
4	645	110.79	1970	85.75	-0.085	0.5	9.75	25.0	3640.1	6.92	0.798	0.089
5	860	109.12	1830	90.33	0.05	0.5	11.25	26.0	3617.8	9.58	0.720	0.402
6	1140	103.43	1560	85.66	0.225	0.5	14.50	25.0	3639.0	13.10	0.623	0.811
7	1250	93.55	1660	105.44	0.3	0.5	16.25	26.0	3688.9	16.24	0.541	1.000
8	1610	94.66	1410	115.19	0.49	0.5	18.50	25.0	3606.7	20.22	0.418	1.471
9	1680	84.34	940	102.84	0.65	0.5	21.00	26.0	3646.7	24.21	0.315	1.919
10	2780	120.44	720	110.44	0.7	0.5	23.25	26.0	3700.0	28.06	0.220	2.004
11	2460	95.22	495	140.56	0.72	0.5	25.00	26.0	3659.1	31.40	0.120	2.102
12	1940	69.56	184	123.56	0.755	0.5	26.50	26.0	3653.6	33.90	0.051	2.208

Table A.9- Experimental data for L/D= 53.2 and inlet Reynolds number $Re_{axi.}$ = 38318												
Experiment Number	Measured Porous Volume Collected (mL)	Measured Porous Collection Time (sec)	Measured Outlet Volume Collected (mL)	Measured Outlet Collection Time (sec)	Measured Head Difference (cm H_2o)	Rotameter Reading	Inlet pressure (psi)	Average Temperature (°C)	Inlet Axial Reynolds Number $Re_{axi.}$	Radial Reynolds Number Re_w	Outlet/Inlet Average Velocity U_2/U_1	Dimensionless Pressure Drop $(p_o-p_i)/1/2\rho v_1^2$
1	3280	81.65	4205	15.31	-44.265	5.0	8.50	25.0	39559.5	23.60	0.872	-0.605
2	3240	71.41	3920	14.35	-36.615	5.0	10.50	24.0	39249.1	26.36	0.858	-0.459
3	3530	59.34	3840	14.93	-17.785	5.0	13.50	24.0	38642.2	34.56	0.812	-0.110
4	3740	47.68	4114	17.13	-2.35	5.0	17.00	24.0	38529.9	45.57	0.754	0.201
5	3580	39.41	3830	16.81	9.535	5.0	19.50	24.0	38334.8	52.77	0.715	0.452
6	3420	34.75	4036	18.44	15.085	5.0	22.00	24.0	37989.3	57.17	0.690	0.579
7	3910	36.12	3640	17.32	22.885	5.0	23.75	24.0	38010.7	62.89	0.660	0.750
8	4070	32.88	3890	19.90	33.445	5.0	27.00	24.0	37923.0	71.91	0.612	0.990
9	4060	29.54	3890	21.36	44.635	5.0	29.75	24.0	37815.6	79.84	0.570	1.250
10	3900	25.81	3980	23.53	51.055	5.0	32.50	24.0	37768.0	87.78	0.528	1.403

Table A.10- Experimental data for L/D= 53.2 and inlet Reynolds number Re_{axi} = 30731

Experiment Number	Measured Porous Volume Collected (mL)	Measured Porous Collection Time (sec)	Measured Outlet Volume Collected (mL)	Measured Outlet Collection Time (sec)	Measured Head Difference (cm H_2o)	Rotameter Reading	Inlet pressure (psi)	Average Temperature (°C)	Inlet Axial Reynolds Number Re_{axi}	Radial Reynolds Number Re_w	Outlet/Inlet Average Velocity U_2/U_1	Dimensionless Pressure Drop $(p_o-p_i)/1/2\rho v_1^2$
1	1660	98.25	3970	16.90	-44.87	4.0	7.50	24.0	31433.8	9.82	0.933	-1.066
2	1660	90.06	3840	16.31	-44.025	4.0	8.50	24.0	31538.0	10.71	0.927	-1.041
3	2042	84.25	3940	17.06	-36.1	4.0	10.00	24.0	31502.3	14.08	0.905	-0.820
4	2440	67.38	3840	17.63	-24.61	4.0	13.50	24.0	30995.8	21.04	0.857	-0.515
5	2620	52.50	3850	18.65	-12.72	4.0	17.00	24.0	31000.1	28.99	0.805	-0.146
6	3770	69.41	3980	19.87	-9.955	4.0	18.50	24.0	30691.0	31.55	0.787	-0.066
7	3630	53.97	4052	21.66	0.71	4.0	21.50	24.0	30478.6	39.07	0.736	0.284
8	3120	41.90	3690	20.44	5.565	4.0	23.50	24.0	30452.3	43.26	0.708	0.449
9	3330	37.53	3960	23.72	14.765	4.0	27.00	24.0	30370.2	51.55	0.653	0.768
10	3500	35.37	3980	25.12	20.775	4.0	28.50	24.0	30510.1	57.49	0.616	0.969
11	3410	31.22	3580	24.41	26.925	4.0	30.00	24.0	30271.2	63.45	0.573	1.196

Table A.11- Experimental data for L/D= 53.2 and inlet Reynolds number Re_{axi} = 22693												
Experiment Number	Measured Porous Volume Collected (mL)	Measured Porous Collection Time (sec)	Measured Outlet Volume Collected (mL)	Measured Outlet Collection Time (sec)	Measured Head Difference (cm H_2o)	Rotameter Reading	Inlet pressure (psi)	Average Temperature (°C)	Inlet Axial Reynolds Number Re_{axi}	Radial Reynolds Number Re_w	Outlet/Inlet Average Velocity U_2/U_1	Dimensionless Pressure Drop $(p_o-p_i)/1/2\rho v_i^2$
1	740	89.50	3600	19.91	-29.885	3.0	5.50	24.0	23889.2	4.80	0.956	-1.234
2	890	83.66	3680	20.66	-28.345	3.0	6.50	24.0	23694.6	6.18	0.944	-1.195
3	1580	84.28	3480	20.44	-20.98	3.0	9.50	24.0	23378.3	10.89	0.901	-0.873
4	2010	75.38	3500	21.65	-15.49	3.0	12.50	24.0	23048.4	15.49	0.858	-0.615
5	2680	71.32	3620	23.69	-6.38	3.0	16.00	24.0	23078.1	21.83	0.803	-0.102
6	2940	64.56	3680	25.63	-2.28	3.0	18.50	24.0	22796.2	26.46	0.759	0.128
7	3100	57.88	3760	27.81	0.765	3.0	20.50	24.0	22662.6	31.11	0.716	0.307
8	2980	47.06	3940	31.16	4.455	3.0	23.50	24.0	22663.0	36.79	0.666	0.531
9	3370	44.84	3440	30.12	10.265	3.0	26.50	24.0	22509.9	43.66	0.603	0.899
10	3280	37.85	3440	33.16	16.92	3.0	28.50	24.0	22568.7	50.34	0.545	1.315

Table A.12- Experimental data for L/D= 53.2 and inlet Reynolds number $Re_{axi.}$ = 15222

Experiment Number	Measured Porous Volume Collected (mL)	Measured Porous Collection Time (sec)	Measured Outlet Volume Collected (mL)	Measured Outlet Collection Time (sec)	Measured Head Difference (cm H_2o)	Rotameter Reading	Inlet pressure (psi)	Average Temperature (°C)	Inlet Axial Reynolds Number $Re_{axi.}$	Radial Reynolds Number Re_w	Outlet/Inlet Average Velocity U_2/U_1	Dimensionless Pressure Drop $(p_o-p_i)/1/2\rho v_1^2$
1	310	137.19	3640	29.66	-16.505	2.0	3.50	24.0	16070.1	1.31	0.982	-1.505
2	450	90.56	3530	29.16	-15.035	2.0	5.25	24.0	15951.2	2.89	0.961	-1.413
3	665	92.75	3690	31.13	-14.03	2.0	6.50	24.0	15779.4	4.17	0.943	-1.357
4	910	82.94	3440	29.88	-11.835	2.0	8.50	24.0	15665.1	6.37	0.913	-1.147
5	1240	88.94	3760	33.63	-10.855	2.0	10.00	24.0	15523.2	8.10	0.889	-1.069
6	1550	81.10	3660	34.22	-8.565	2.0	12.50	24.0	15428.7	11.10	0.848	-0.817
7	1970	81.03	3670	36.03	-6.38	2.0	14.75	24.0	15342.7	14.12	0.807	-0.561
8	2320	79.09	3940	40.81	-4.255	2.0	16.50	24.0	15240.6	17.04	0.767	-0.300
9	2920	84.00	3400	37.13	-2.77	2.0	18.50	24.0	15227.8	20.19	0.725	-0.110
10	2620	62.97	3500	41.34	0.085	2.0	21.00	24.0	15145.8	24.17	0.670	0.270
11	2980	57.25	3540	47.87	3.34	2.0	23.50	24.0	15047.9	30.24	0.587	0.717
12	3080	51.15	3300	49.84	5.65	2.0	25.50	24.0	15050.8	34.98	0.524	1.038
13	3200	45.68	3280	58.30	8.115	2.0	28.00	24.0	14982.8	40.70	0.445	1.398
14	3120	38.22	2760	61.16	10.27	2.0	30.00	24.0	14995.7	47.42	0.356	1.704

Table A.13- Experimental data for L/D= 53.2 and inlet Reynolds number $Re_{axi.}$ = 9997

Experiment Number	Measured Porous Volume Collected (mL)	Measured Porous Collection Time (sec)	Measured Outlet Volume Collected (mL)	Measured Outlet Collection Time (sec)	Measured Head Difference (cm H_2o)	Rotameter Reading	Inlet pressure (psi)	Average Temperature (°C)	Inlet Axial Reynolds Number $Re_{axi.}$	Radial Reynolds Number Re_w	Outlet/Inlet Average Velocity U_2/U_1	Dimensionless Pressure Drop $(p_o-p_i)/1/2\rho v_1^2$
1	240	310.45	3725	48.23	-7.515	1.3	3.18	24.0	10067.9	0.34	0.990	-1.764
2	1570	280.45	3835	51.66	-5.655	1.3	5.90	24.0	10059.3	2.45	0.930	-1.329
3	2875	235.88	3925	56.88	-3.64	1.3	9.29	24.0	10052.0	5.32	0.850	-0.796
4	3800	201.45	3950	62.58	-1.89	1.3	12.41	24.0	10036.0	8.24	0.770	-0.303
5	3715	155.34	3765	64.33	-0.715	1.3	14.59	24.0	10029.3	10.45	0.710	0.042
6	3495	120.85	3540	65.87	0.355	1.3	16.61	24.0	10005.6	12.63	0.650	0.363
7	3750	110.33	3495	71.45	1.33	1.3	18.49	24.0	9993.3	14.85	0.590	0.662
8	4060	99.63	3745	88.25	2.475	1.3	20.76	24.0	9982.4	17.80	0.510	1.020
9	3915	82.32	3325	92.82	3.485	1.3	22.77	24.0	9969.9	20.77	0.430	1.342
10	3750	70.25	3625	120.58	4.235	1.3	24.31	24.0	9952.1	23.32	0.360	1.587
11	4045	68.21	3650	150.65	4.885	1.3	25.65	24.0	9941.8	25.90	0.290	1.800
12	3630	55.68	3500	190.58	5.425	1.3	26.79	24.0	9928.4	28.48	0.220	1.981

Table A.14- Experimental data for L/D= 53.2 and inlet Reynolds number $Re_{axi.}$ = 7558

Experiment Number	Measured Porous Volume Collected (mL)	Measured Porous Collection Time (sec)	Measured Outlet Volume Collected (mL)	Measured Outlet Collection Time (sec)	Measured Head Difference (cm H_2o)	Rotameter Reading	Inlet pressure (psi)	Average Temperature (°C)	Inlet Axial Reynolds Number $Re_{axi.}$	Radial Reynolds Number Re_w	Outlet/Inlet Average Velocity U_2/U_1	Dimensionless Pressure Drop $(p_o-p_i)/1/2\rho v_1^2$
1	223	328.88	3340	54.31	-4.875	1.0	3.00	24.0	8042.5	0.39	0.989	-1.787
2	500	257.03	2880	47.66	-4.42	1.0	3.50	24.0	8019.8	1.13	0.969	-1.626
3	825	246.34	3310	56.32	-4.125	1.0	4.50	24.0	7909.8	1.95	0.946	-1.580
4	1300	255.59	2840	49.62	-3.665	1.0	5.50	24.0	7873.9	2.95	0.918	-1.413
5	1640	214.88	2860	52.34	-3.11	1.0	7.50	24.0	7774.0	4.43	0.877	-1.227
6	2450	212.04	2810	55.19	-2.26	1.0	9.50	24.0	7727.1	6.71	0.815	-0.855
7	2860	156.19	3010	68.60	-0.84	1.0	12.50	24.0	7610.9	10.64	0.706	-0.183
8	3980	161.34	2750	73.47	0.22	1.0	15.25	24.0	7541.5	14.33	0.603	0.364
9	3970	129.37	2440	76.63	1.035	1.0	17.50	24.0	7553.3	17.83	0.509	0.799
10	3820	102.03	2610	99.37	2	1.0	20.50	24.0	7648.4	21.75	0.412	1.303
11	3450	77.69	1700	94.37	2.595	1.0	23.50	24.0	7454.7	25.80	0.289	1.704
12	3380	70.09	1050	75.75	2.825	1.0	24.50	24.0	7402.5	28.01	0.223	1.859
13	3140	60.03	690	67.75	3.08	1.0	26.00	24.0	7433.9	30.39	0.163	1.999

Table A.15- Experimental data for L/D= 53.2 and inlet Reynolds number $Re_{axi.}$ = 5495												
Experiment Number	Measured Porous Volume Collected (mL)	Measured Porous Collection Time (sec)	Measured Outlet Volume Collected (mL)	Measured Outlet Collection Time (sec)	Measured Head Difference (cm H_2o)	Rotameter Reading	Inlet pressure (psi)	Average Temperature (°C)	Inlet Axial Reynolds Number $Re_{axi.}$	Radial Reynolds Number Re_r	Outlet/Inlet Average Velocity U_2/U_1	Dimensionless Pressure Drop $(p_o-p_i)/1/2\rho v_1^2$
1	100	233.15	3360	79.54	-2.26	0.73	2.75	24.0	5538.5	0.19	0.990	-1.722
2	810	266.44	3180	78.65	-1.72	0.73	4.55	24.0	5532.9	1.33	0.930	-1.303
3	1695	201.22	3420	95.25	-0.825	0.73	7.98	24.0	5520.5	3.68	0.810	-0.523
4	2060	170.24	3625	110.85	-0.335	0.73	10.12	24.0	5528.1	5.29	0.730	-0.065
5	2540	160.85	3795	129.55	0.11	0.73	12.16	24.0	5523.6	6.90	0.650	0.362
6	2350	130.25	3565	131.75	0.36	0.73	13.38	24.0	5505.2	7.88	0.600	0.609
7	3315	146.75	3450	152.77	0.79	0.73	15.68	24.0	5480.0	9.87	0.500	1.048
8	3695	140.85	3065	161.47	1.085	0.73	17.40	24.0	5463.2	11.46	0.420	1.359
9	3735	130.45	3285	195.35	1.255	0.73	18.42	24.0	5479.1	12.51	0.370	1.530
10	3145	93.56	2385	201.85	1.555	0.73	20.50	24.0	5454.3	14.68	0.260	1.862
11	3160	84.65	1875	228.78	1.725	0.73	21.89	24.0	5451.9	16.31	0.180	2.049
12	3065	75.45	1485	295.44	1.85	0.73	23.01	24.0	5456.1	17.74	0.110	2.185

Table A.16- Experimental data for L/D= 53.2 and inlet Reynolds number $Re_{axi.}$ = 3671												
Experiment Number	Measured Porous Volume Collected (mL)	Measured Porous Collection Time (sec)	Measured Outlet Volume Collected (mL)	Measured Outlet Collection Time (sec)	Measured Head Difference (cm H_2o)	Rotameter Reading	Inlet pressure (psi)	Average Temperature (°C)	Inlet Axial Reynolds Number $Re_{axi.}$	Radial Reynolds Number Re_w	Outlet/Inlet Average Velocity U_2/U_1	Dimensionless Pressure Drop $(p_o-p_i)/1/2\rho v_1^2$
1	53	275.22	1840	67.88	-1.24	0.5	2.00	25.0	3669.6	0.11	0.993	-2.277
2	410	213.75	2035	76.29	-1.005	0.5	4.00	25.0	3741.5	1.14	0.933	-1.812
3	840	187.62	1310	53.50	-0.74	0.5	6.25	25.0	3725.0	2.66	0.845	-1.332
4	1770	216.34	1360	65.50	-0.36	0.5	9.00	25.0	3670.4	4.86	0.717	-0.567
5	3430	236.69	1250	86.97	0.115	0.5	13.00	25.0	3608.3	8.61	0.498	0.515
6	3420	198.75	1320	113.40	0.3	0.5	14.50	25.0	3591.0	10.23	0.404	0.971
7	3360	175.75	700	72.91	0.395	0.5	16.00	25.0	3561.3	11.36	0.334	1.227
8	3490	161.78	580	80.81	0.515	0.5	17.50	25.0	3552.8	12.82	0.250	1.544
9	3680	152.22	395	100.23	0.585	0.5	18.75	25.0	3465.4	14.37	0.140	1.805
10	3850	145.33	198	180.05	0.625	0.5	20.00	25.0	3392.0	15.74	0.040	1.997
11	2425	214.55	1362	77.12	-0.04	0.5	11.00	25.0	3644.2	6.72	0.610	0.153

Table A.17- Experimental data for L/D= 79.8 and inlet Reynolds number Re_{axi} = 38318												
Experiment Number	Measured Porous Volume Collected (mL)	Measured Porous Collection Time (sec)	Measured Outlet Volume Collected (mL)	Measured Outlet Collection Time (sec)	Measured Head Difference (cm H_2o)	Rotameter Reading	Inlet pressure (psi)	Average Temperature (°C)	Inlet Axial Reynolds Number $Re_{axi.}$	Radial Reynolds Number Re_w	Outlet/Inlet Average Velocity U_2/U_1	Dimensionless Pressure Drop $(p_o-p_i)/1/2\rho v_i^2$
1	3685	120.22	3988	14.45	-85.315	5.0	7.02	24.0	38377.3	13.39	0.900	-1.439
2	4305	95.50	3842	14.46	-65.965	5.0	10.20	24.0	38334.9	19.69	0.855	-1.093
3	3610	61.56	3860	15.45	-47.105	5.0	13.36	24.0	37655.8	25.61	0.810	-0.764
4	3665	50.25	3975	16.75	-31.795	5.0	16.49	24.0	37563.7	31.86	0.765	-0.450
5	4140	46.81	4062	17.85	-18.285	5.0	19.60	24.0	38005.6	38.63	0.720	-0.152
6	3650	36.13	4033	19.21	-4.915	5.0	22.68	25.0	38044.0	45.14	0.675	0.130
7	4055	35.12	3988	20.28	6.745	5.0	25.73	25.0	37997.2	51.59	0.630	0.397
8	4435	34.12	4095	22.35	17.505	5.0	28.75	25.0	37966.6	58.08	0.585	0.647
9	4120	28.13	4100	23.85	28.14	5.0	31.75	25.0	38444.7	65.45	0.540	0.882
10	3750	23.15	4040	25.45	37.79	5.0	34.72	25.0	38595.4	72.38	0.495	1.100
11	3755	21.15	3900	26.85	46.77	5.0	37.67	25.0	38721.3	79.33	0.450	1.303
12	3900	20.16	3713	28.21	55.12	5.0	40.59	25.0	38882.1	86.44	0.405	1.489

Table A.18- Experimental data for L/D= 79.8 and inlet Reynolds number Re_{axi} = 30731

Experiment Number	Measured Porous Volume Collected (mL)	Measured Porous Collection Time (sec)	Measured Outlet Volume Collected (mL)	Measured Outlet Collection Time (sec)	Measured Head Difference (cm H_2o)	Rotameter Reading	Inlet pressure (psi)	Average Temperature (°C)	Inlet Axial Reynolds Number Re_{axi}	Radial Reynolds Number Re_w	Outlet/Inlet Average Velocity U_2/U_1	Dimensionless Pressure Drop $(p_o-p_i)/1/2\rho v_1^2$
1	3950	160.22	4045	18.22	-55.175	4.0	10.13	24.0	30434.7	10.77	0.900	-1.518
2	3785	110.21	3855	17.22	-50.085	4.0	12.69	24.0	31582.5	15.00	0.867	-1.263
3	3875	90.45	3755	17.46	-40.77	4.0	15.13	24.0	31330.8	18.71	0.834	-1.017
4	4065	80.25	3765	18.45	-31.595	4.0	17.44	24.0	30773.4	22.13	0.801	-0.777
5	4145	70.46	4130	21.22	-23.86	4.0	19.64	24.0	30480.4	25.70	0.768	-0.547
6	3970	60.25	4300	23.52	-16.345	4.0	21.71	25.0	30479.5	29.44	0.735	-0.326
7	4180	55.46	3810	21.45	-10.485	4.0	23.66	25.0	30900.4	33.68	0.702	-0.113
8	3795	45.55	3965	23.55	-4.42	4.0	25.49	25.0	30651.6	37.23	0.669	0.093
9	3915	42.45	4005	24.85	1.21	4.0	27.19	25.0	30782.8	41.21	0.636	0.290
10	3975	39.45	3895	25.45	6.575	4.0	28.78	25.0	30765.2	45.02	0.603	0.478
11	3825	35.12	3875	26.85	11.565	4.0	30.24	25.0	30636.8	48.67	0.570	0.658
12	3945	33.54	3850	28.21	16.42	4.0	31.58	25.0	30689.8	52.56	0.537	0.830

Table A.19- Experimental data for L/D= 79.8 and inlet Reynolds number $Re_{axi.}$ = 22693

Experiment Number	Measured Porous Volume Collected (mL)	Measured Porous Collection Time (sec)	Measured Outlet Volume Collected (mL)	Measured Outlet Collection Time (sec)	Measured Head Difference (cm H_2o)	Rotameter Reading	Inlet pressure (psi)	Average Temperature (°C)	Inlet Axial Reynolds Number $Re_{axi.}$	Radial Reynolds Number Re_w	Outlet/Inlet Average Velocity U_2/U_1	Dimensionless Pressure Drop $(p_o-p_i)/1/2\rho v_1^2$
1	3495	180.22	4090	23.45	-34.69	3.0	10.55	24.0	23875.1	8.47	0.900	-1.555
2	3560	130.22	3745	22.87	-26.785	3.0	13.34	24.0	23327.5	11.94	0.857	-1.233
3	3955	110.58	3740	23.89	-20.915	3.0	16.02	24.0	23311.3	15.62	0.814	-0.924
4	3950	90.55	3800	25.88	-15.04	3.0	18.59	24.0	22952.7	19.05	0.771	-0.630
5	4225	80.45	3935	27.99	-10.32	3.0	21.05	24.0	23160.0	22.94	0.728	-0.348
6	3905	65.44	3875	29.88	-5.41	3.0	23.40	24.0	22617.8	26.06	0.685	-0.081
7	3885	57.22	3810	31.29	-1.25	3.0	25.65	24.0	22573.5	29.66	0.642	0.172
8	3815	50.22	3845	33.87	2.6	3.0	27.78	24.0	22483.2	33.18	0.599	0.412
9	4175	50.33	3715	35.78	5.97	3.0	29.81	24.0	22101.7	36.23	0.556	0.638
10	4185	45.22	3865	39.65	9.49	3.0	31.73	24.0	22431.2	40.42	0.513	0.851
11	4175	40.55	4065	44.54	13.1	3.0	33.53	24.0	22877.7	44.97	0.470	1.051
12	4260	38.55	3755	45.64	15.76	3.0	35.24	24.0	22664.0	48.27	0.427	1.235

Table A.20- Experimental data for $L/D = 79.8$ and inlet Reynolds number $Re_{axi} = 15222$

Experiment Number	Measured Porous Volume Collected (mL)	Measured Porous Collection Time (sec)	Measured Outlet Volume Collected (mL)	Measured Outlet Collection Time (sec)	Measured Head Difference (cm H_2o)	Rotameter Reading	Inlet pressure (psi)	Average Temperature (°C)	Inlet Axial Reynolds Number Re_{axi}	Radial Reynolds Number Re_w	Outlet/Inlet Average Velocity U_2/U_1	Dimensionless Pressure Drop $(p_o-p_i)/1/2\rho v_1^2$
1	2995	230.54	4120	35.22	-17.85	2.0	9.18	24.0	16098.2	5.67	0.900	-1.772
2	3940	200.54	3690	33.41	-14.05	2.0	12.15	24.0	15939.1	8.58	0.849	-1.405
3	3925	150.66	3800	36.89	-10.56	2.0	14.90	24.0	15687.8	11.38	0.798	-1.053
4	3940	120.78	3800	39.44	-7.66	2.0	17.44	24.0	15581.5	14.25	0.747	-0.720
5	3505	90.56	3590	40.54	-4.92	2.0	19.76	24.0	15300.4	16.91	0.696	-0.403
6	3180	70.45	3745	45.66	-2.59	2.0	21.86	24.0	15228.5	19.72	0.645	-0.102
7	3125	60.45	3990	52.78	-0.46	2.0	23.74	24.0	15195.9	22.58	0.594	0.181
8	3425	59.22	3840	55.89	1.49	2.0	25.41	24.0	15066.6	25.26	0.543	0.449
9	3775	58.45	3625	57.98	3.31	2.0	26.85	24.0	15101.4	28.21	0.492	0.700
10	4100	57.85	3350	59.88	4.95	2.0	28.09	24.0	15040.9	30.96	0.441	0.934
11	4210	53.87	3300	65.99	6.62	2.0	29.10	24.0	15179.0	34.14	0.390	1.152
12	3795	45.22	3035	70.55	7.89	2.0	29.89	24.0	15019.2	36.66	0.339	1.352

Table A.21- Experimental data for L/D= 79.8 and inlet Reynolds number Re_{axi} = 9997												
Experiment Number	Measured Porous Volume Collected (mL)	Measured Porous Collection Time (sec)	Measured Outlet Volume Collected (mL)	Measured Outlet Collection Time (sec)	Measured Head Difference (cm H_2o)	Rotameter Reading	Inlet pressure (psi)	Average Temperature (°C)	Inlet Axial Reynolds Number Re_{axi}	Radial Reynolds Number Re_w	Outlet/Inlet Average Velocity U_2/U_1	Dimensionless Pressure Drop $(p_o-p_i)/1/2\rho v_1^2$
1	1225	308.56	3870	51.22	-9.44	1.3	5.01	24.0	10084.2	1.73	0.950	-2.360
2	2565	264.56	3830	53.87	-7.245	1.3	8.04	24.0	10058.3	4.23	0.880	-1.832
3	3730	240.66	3660	55.45	-5.39	1.3	10.88	24.0	10028.8	6.77	0.810	-1.344
4	4035	188.56	3685	60.52	-3.77	1.3	13.51	24.0	10040.5	9.35	0.740	-0.883
5	3870	140.88	3725	66.85	-2.325	1.3	15.94	24.0	10085.8	12.00	0.670	-0.456
6	3675	110.85	3490	70.22	-0.97	1.3	18.17	24.0	9993.9	14.48	0.600	-0.060
7	3750	95.86	4080	92.56	0.21	1.3	20.21	24.0	9994.4	17.09	0.530	0.301
8	4020	89.75	3650	95.66	1.255	1.3	22.04	24.0	9930.7	19.56	0.460	0.631
9	3855	75.82	3580	110.22	2.205	1.3	23.67	24.0	9948.3	22.21	0.390	0.930
10	3930	69.27	3890	145.65	3.025	1.3	25.10	24.0	9939.7	24.78	0.320	1.195
11	3560	56.72	3250	155.29	3.745	1.3	26.33	24.0	9951.1	27.42	0.250	1.425
12	3715	54.22	3170	210.69	4.345	1.3	27.36	24.0	9920.9	29.93	0.180	1.628

Table A.22- Experimental data for L/D= 79.8 and inlet Reynolds number $Re_{inl.}$ = 7558

Experiment Number	Measured Porous Volume Collected (mL)	Measured Porous Collection Time (sec)	Measured Outlet Volume Collected (mL)	Measured Outlet Collection Time (sec)	Measured Head Difference (cm H_2o)	Rotameter Reading	Inlet pressure (psi)	Average Temperature (°C)	Inlet Axial Reynolds Number $Re_{axi.}$	Radial Reynolds Number Re_w	Outlet/Inlet Average Velocity U_2/U_1	Dimensionless Pressure Drop $(p_o-p_i)/1/2\rho v_1^2$
1	312	250.30	2770	45.22	-7.085	1.0	3.43	24.0	8043.0	0.54	0.980	-2.748
2	1390	220.35	2855	50.22	-5.285	1.0	6.21	24.0	7942.1	2.76	0.900	-2.142
3	2265	200.00	2760	53.45	-3.8	1.0	8.87	24.0	7808.9	4.95	0.820	-1.578
4	3282	200.21	2595	55.66	-2.605	1.0	11.40	24.0	7739.8	7.16	0.740	-1.054
5	2170	100.45	2510	60.78	-1.555	1.0	13.80	24.0	7668.5	9.44	0.657	-0.561
6	2405	90.25	2600	70.66	-0.685	1.0	16.07	24.0	7689.3	11.64	0.580	-0.119
7	2695	85.54	2685	85.22	0.105	1.0	18.22	24.0	7599.9	13.76	0.500	0.287
8	2990	84.25	2345	91.22	0.74	1.0	20.24	24.0	7350.8	15.50	0.420	0.654
9	2235	53.55	2270	105.65	1.39	1.0	22.14	24.0	7567.9	18.23	0.340	0.986
10	2795	59.45	1825	110.54	1.91	1.0	23.90	24.0	7581.4	20.54	0.260	1.271
11	2635	52.78	1430	130.58	2.15	1.0	25.54	24.0	7246.6	21.81	0.180	1.520
12	3350	58.56	1025	160.88	2.7	1.0	27.05	24.0	7551.4	24.99	0.100	1.730

Table A.23- Experimental data for L/D= 79.8 and inlet Reynolds number $Re_{axi.}$ = 5495												
Experiment Number	Measured Porous Volume Collected (mL)	Measured Porous Collection Time (sec)	Measured Outlet Volume Collected (mL)	Measured Outlet Collection Time (sec)	Measured Head Difference (cm H_2o)	Rotameter Reading	Inlet pressure (psi)	Average Temperature (°C)	Inlet Axial Reynolds Number $Re_{axi.}$	Radial Reynolds Number Re_w	Outlet/Inlet Average Velocity U_2/U_1	Dimensionless Pressure Drop $(p_o-p_i)/1/2\rho v_1^2$
1	105	245.18	3515	83.21	-2.255	0.73	2.75	24.0	5538.4	0.19	0.990	-1.718
2	780	255.87	3300	81.52	-1.715	0.73	4.55	24.0	5540.1	1.33	0.930	-1.294
3	1880	223.14	3475	96.85	-0.825	0.73	7.98	24.0	5517.5	3.68	0.810	-0.524
4	2315	191.21	3465	105.87	-0.33	0.73	10.12	24.0	5532.2	5.29	0.730	-0.060
5	2670	170.45	4100	139.85	0.11	0.73	12.16	24.0	5510.9	6.84	0.652	0.363
6	3530	195.65	3760	138.98	0.36	0.73	13.38	24.0	5504.6	7.88	0.600	0.610
7	3955	175.25	3585	158.78	0.79	0.73	15.68	24.0	5476.8	9.86	0.500	1.049
8	3635	138.54	3415	179.65	1.09	0.73	17.40	24.0	5467.0	11.46	0.420	1.363
9	3825	133.65	3360	199.87	1.26	0.73	18.42	24.0	5477.1	12.50	0.370	1.536
10	3325	98.78	2490	210.85	1.55	0.73	20.50	24.0	5459.1	14.70	0.260	1.854
11	3306	88.56	2420	295.45	1.72	0.73	21.89	24.0	5451.4	16.31	0.180	2.044
12	3245	79.85	1515	301.45	1.85	0.73	23.01	24.0	5457.9	17.75	0.110	2.184

Table A.25- Experimental data for L/D= 106.4 and inlet Reynolds number $Re_{axi.}$ = 38318												
Experiment Number	Measured Porous Volume Collected (mL)	Measured Porous Collection Time (sec)	Measured Outlet Volume Collected (mL)	Measured Outlet Collection Time (sec)	Measured Head Difference (cm H_2o)	Rotameter Reading	Inlet pressure (psi)	Average Temperature (°C)	Inlet Axial Reynolds Number $Re_{axi.}$	Radial Reynolds Number Re_w	Outlet/Inlet Average Velocity U_2/U_1	Dimensionless Pressure Drop $(p_o-p_i)/1/2\rho v_1^2$
1	4150	18.50	3880	42.13	55.3	5.0	35.50	24.0	37188.8	65.16	0.291	-1.518
2	4090	18.22	3740	39.68	55.9	5.0	36.50	24.0	37420.2	65.20	0.296	-1.520
3	4106	24.56	3930	26.12	25.44	5.0	30.50	23.0	36696.4	47.45	0.474	-0.805
4	3840	23.66	3780	24.35	22.605	5.0	31.50	23.0	36638.2	46.07	0.489	-0.746
5	3950	28.59	3940	21.91	3.105	5.0	28.50	24.0	37692.5	40.13	0.566	-0.300
6	3680	32.37	3770	18.25	-21.8	5.0	25.50	24.0	38126.2	33.02	0.645	0.242
7	3880	44.47	3920	17.00	-47.8	5.0	21.50	24.0	38089.0	25.34	0.725	0.796
8	3380	55.09	3960	15.56	-77.2	5.0	17.00	24.0	38197.3	17.82	0.806	1.391
9	2780	68.82	4052	14.53	-110.6	5.0	14.00	24.0	38901.9	11.73	0.873	1.978
10	2300	78.09	4014	13.78	-123.75	5.0	11.50	24.0	39381.3	8.56	0.908	2.147
11	2820	115.44	4116	14.06	-130.3	5.0	10.50	24.0	39080.5	7.10	0.923	2.296
12	2740	128.78	4058	13.63	-138.6	5.0	10.00	24.0	39380.2	6.18	0.933	2.407

Table A.26- Experimental data for L/D= 106.4 and inlet Reynolds number $Re_{axi.}$ = 30731												
Experiment Number	Measured Porous Volume Collected (mL)	Measured Porous Collection Time (sec)	Measured Outlet Volume Collected (mL)	Measured Outlet Collection Time (sec)	Measured Head Difference (cm H_2o)	Rotameter Reading	Inlet pressure (psi)	Average Temperature (°C)	Inlet Axial Reynolds Number $Re_{axi.}$	Radial Reynolds Number Re_w	Outlet/Inlet Average Velocity U_2/U_1	Dimensionless Pressure Drop $(p_o-p_i)/1/2\rho v_1^2$
1	3860	24.88	3520	34.53	22.205	4.0	38.50	24.0	30120.2	45.06	0.397	1.029
2	3620	31.34	3800	27.28	3.335	4.0	30.50	24.0	30123.8	33.55	0.547	0.352
3	3480	33.84	3530	23.46	-5.32	4.0	29.00	24.0	30005.3	29.87	0.594	0.047
4	3700	40.41	3680	22.22	-14.045	4.0	27.00	24.0	30548.6	26.60	0.644	-0.240
5	3420	47.44	3760	20.38	-28.965	4.0	23.00	24.0	30668.3	20.94	0.719	-0.727
6	3200	52.19	3880	19.94	-38.405	4.0	20.50	24.0	30722.9	17.81	0.760	-1.026
7	2920	69.53	3780	17.69	-59.6	4.0	16.50	24.0	30955.7	12.20	0.836	-1.665
8	2670	90.88	4033	17.78	-76	4.0	13.50	24.0	31262.4	8.53	0.885	-2.109
9	2400	110.54	4120	17.62	-86.5	4.0	11.50	24.0	31375.0	6.31	0.915	-2.385
10	1460	106.78	3900	16.22	-95.2	4.0	9.50	24.0	31432.7	3.97	0.946	-2.599
11	1280	130.68	3920	16.09	-101.1	4.0	7.50	24.0	31635.7	2.85	0.961	-2.690

Table A.27- Experimental data for L/D= 106.4 and inlet Reynolds number $Re_{axi.}$ = 22693												
Experiment Number	Measured Porous Volume Collected (mL)	Measured Porous Collection Time (sec)	Measured Outlet Volume Collected (mL)	Measured Outlet Collection Time (sec)	Measured Head Difference (cm H_2o)	Rotameter Reading	Inlet pressure (psi)	Average Temperature (°C)	Inlet Axial Reynolds Number $Re_{axi.}$	Radial Reynolds Number Re_w	Outlet/Inlet Average Velocity U_2/U_1	Dimensionless Pressure Drop $(p_o-p_i)/1/2\rho v_1^2$
1	3400	28.09	3400	49.25	14.29	3.0	37.50	23.0	21783.7	34.36	0.363	1.169
2	3650	33.45	3300	40.12	7.315	3.0	35.50	23.0	21978.9	30.97	0.430	0.700
3	3350	35.25	3570	38.00	4.13	3.0	33.00	23.0	21766.1	26.98	0.497	0.505
4	3110	36.22	3850	35.25	-2.27	3.0	30.75	23.0	22530.4	24.37	0.560	0.100
5	3440	48.72	3760	31.56	-8.73	3.0	27.50	23.0	22009.0	20.04	0.628	-0.308
6	3080	59.29	3760	27.16	-20.295	3.0	22.50	23.0	22255.9	14.75	0.727	-0.984
7	3050	77.93	3760	25.06	-28.53	3.0	19.00	23.0	22260.0	11.11	0.793	-1.458
8	2220	90.00	3260	21.56	-32.405	3.0	14.50	23.0	20912.5	7.00	0.860	-1.901
9	2047	120.63	3780	22.19	-43.875	3.0	12.00	23.0	22437.3	4.82	0.909	-2.245
10	1440	186.44	3820	20.84	-59.3	3.0	7.50	23.0	23302.4	2.19	0.960	-2.780
11	820	212.13	3560	19.04	-64.1	3.0	5.00	23.0	23648.8	1.10	0.980	-2.844

Table A.28- Experimental data for L/D= 106.4 and inlet Reynolds number Re_{axi} = 15222												
Experiment Number	Measured Porous Volume Collected (mL)	Measured Porous Collection Time (sec)	Measured Outlet Volume Collected (mL)	Measured Outlet Collection Time (sec)	Measured Head Difference (cm H_2o)	Rotameter Reading	Inlet pressure (psi)	Average Temperature (°C)	Inlet Axial Reynolds Number $Re_{axi.}$	Radial Reynolds Number Re_w	Outlet/Inlet Average Velocity U_2/U_1	Dimensionless Pressure Drop $(p_o-p_i)/1/2\rho v_1^2$
1	3640	44.34	2570	63.91	5.025	2.0	35.50	23.0	14046.7	23.30	0.329	1.019
2	3060	40.52	2920	60.45	3.095	2.0	33.25	23.0	14257.1	21.44	0.390	0.699
3	3730	56.21	3345	56.78	0.465	2.0	30.50	23.0	14472.1	18.84	0.470	0.300
4	3080	55.43	3710	52.45	-3.08	2.0	26.75	23.0	14665.5	15.77	0.560	-0.200
5	2940	64.63	3280	40.50	-5.825	2.0	22.00	23.0	14797.9	12.91	0.640	-0.557
6	2740	75.53	3470	38.38	-10.35	2.0	19.50	23.0	14892.1	10.30	0.714	-1.143
7	2620	90.68	3460	35.31	-13.64	2.0	17.25	23.0	14985.9	8.20	0.772	-1.540
8	2187	106.59	3540	33.63	-17.675	2.0	14.50	23.0	14956.3	5.82	0.837	-2.045
9	2090	179.13	3630	31.50	-22.84	2.0	10.50	23.0	15280.1	3.31	0.908	-2.523

Table A.29- Experimental data for L/D= 106.4 and inlet Reynolds number $Re_{axi.}$ = 9997

Experiment Number	Measured Porous Volume Collected (mL)	Measured Porous Collection Time (sec)	Measured Outlet Volume Collected (mL)	Measured Outlet Collection Time (sec)	Measured Head Difference (cm H_2o)	Rotameter Reading	Inlet pressure (psi)	Average Temperature (°C)	Inlet Axial Reynolds Number $Re_{axi.}$	Radial Reynolds Number Re_w	Outlet/Inlet Average Velocity U_2/U_1	Dimensionless Pressure Drop $(p_o-p_i)/1/2\rho v_1^2$
1	250	313.81	3855	48.89	-13.905	1.3	4.97	24.0	10102.5	0.35	0.990	-3.582
2	1520	269.81	3860	51.54	-11.595	1.3	7.52	24.0	10051.6	2.46	0.930	-3.076
3	3630	245.91	3570	53.12	-8.295	1.3	11.97	24.0	10048.6	6.45	0.820	-2.218
4	3995	193.81	3600	58.19	-6.45	1.3	14.65	24.0	10032.2	9.00	0.750	-1.709
5	3500	146.13	3785	64.52	-5.465	1.3	16.13	24.0	10011.3	10.46	0.710	-1.432
6	3270	116.10	3710	67.89	-4.335	1.3	17.94	24.0	9994.1	12.30	0.660	-1.105
7	3790	101.11	4135	90.23	-2.14	1.3	21.69	24.0	9980.4	16.37	0.550	-0.443
8	4275	95.00	3580	93.33	-0.585	1.3	24.56	24.0	9938.1	19.66	0.460	0.038
9	4070	81.07	3610	107.89	0.325	1.3	26.36	24.0	9947.1	21.93	0.400	0.327
10	4315	74.52	3730	143.32	1.535	1.3	28.92	24.0	9943.0	25.29	0.310	0.717
11	3970	61.97	3095	152.96	2.355	1.3	30.77	24.0	9962.5	27.98	0.240	0.982
12	4105	59.47	3160	208.36	2.955	1.3	32.27	24.0	9931.8	30.15	0.180	1.186

Table A.30- Experimental data for L/D= 106.4 and inlet Reynolds number Re_{axi} = 7558

Experiment Number	Measured Porous Volume Collected (mL)	Measured Porous Collection Time (sec)	Measured Outlet Volume Collected (mL)	Measured Outlet Collection Time (sec)	Measured Head Difference (cm H_2o)	Rotameter Reading	Inlet pressure (psi)	Average Temperature (°C)	Inlet Axial Reynolds Number Re_{axi}	Radial Reynolds Number Re_w	Outlet/Inlet Average Velocity U_2/U_1	Dimensionless Pressure Drop $(p_o-p_i)/1/2\rho v_i^2$
1	2740	46.50	340	76.34	2.09	1.0	30.00	23.0	7326.7	16.73	0.070	1.412
2	2980	55.25	460	52.25	1.7	1.0	28.50	23.0	7267.3	15.31	0.140	1.200
3	3190	66.78	1140	81.10	1.59	1.0	26.50	23.0	7181.6	13.56	0.227	1.157
4	2560	66.63	1990	85.69	0.31	1.0	23.25	23.0	7197.0	10.91	0.377	0.402
5	2465	80.29	2660	83.20	-1.14	1.0	20.25	23.0	7356.3	8.71	0.510	-0.401
6	2560	105.31	2990	79.57	-2.14	1.0	17.50	23.0	7305.2	6.90	0.607	-0.949
7	1820	116.19	3300	71.53	-4.06	1.0	13.50	23.0	7368.7	4.45	0.747	-1.919
8	2520	272.25	3110	59.34	-5.73	1.0	10.00	23.0	7439.0	2.63	0.850	-2.678
9	710	218.47	3270	55.50	-7.615	1.0	5.50	23.0	7675.5	0.92	0.948	-3.247
10	64	246.72	3230	53.00	-9.27	1.0	3.50	23.0	7689.8	0.07	0.996	-3.858

Table A.31- Experimental data for L/D= 106.4 and inlet Reynolds number Re_{axi} = 5495

Experiment Number	Measured Porous Volume Collected (mL)	Measured Porous Collection Time (sec)	Measured Outlet Volume Collected (mL)	Measured Outlet Collection Time (sec)	Measured Head Difference (cm H_2o)	Rotameter Reading	Inlet pressure (psi)	Average Temperature (°C)	Inlet Axial Reynolds Number Re_{axi}	Radial Reynolds Number Re_w	Outlet/Inlet Average Velocity U_2/U_1	Dimensionless Pressure Drop $(p_o-p_i)/1/2\rho v_1^2$
1	215	245.71	3690	87.20	-4.12	0.73	3.50	24.0	5553.5	0.38	0.980	-3.409
2	1095	279.00	3420	86.31	-3.395	0.73	4.50	24.0	5545.2	1.71	0.910	-2.836
3	1495	213.78	3785	102.91	-2.725	0.73	5.50	24.0	5530.4	3.05	0.840	-2.284
4	2180	182.80	3820	118.51	-1.84	0.73	6.47	24.0	5544.0	5.21	0.730	-1.490
5	2775	173.41	3905	137.21	-1.16	0.73	9.41	24.0	5501.8	6.99	0.640	-0.904
6	2750	142.81	3560	139.41	-0.71	0.73	11.55	24.0	5498.7	8.41	0.570	-0.479
7	3490	159.31	3660	160.43	-0.37	0.73	13.29	24.0	5460.1	9.57	0.510	-0.154
8	3870	153.41	3350	169.13	-0.01	0.73	15.21	24.0	5469.7	11.02	0.440	0.209
9	4330	143.01	3025	203.01	0.47	0.73	17.97	24.0	5451.8	13.23	0.330	0.705
10	3605	106.12	2375	209.51	0.77	0.73	19.79	24.0	5447.0	14.84	0.250	1.023
11	3665	97.21	1825	236.44	1.015	0.73	21.45	24.0	5443.6	16.47	0.170	1.288
12	3612	88.01	1380	303.10	1.205	0.73	22.77	24.0	5451.7	17.93	0.100	1.492

Table A.32- Experimental data for L/D= 106.4 and inlet Reynolds number $Re_{axi.}$ = 3671

Experiment Number	Measured Porous Volume Collected (mL)	Measured Porous Collection Time (sec)	Measured Outlet Volume Collected (mL)	Measured Outlet Collection Time (sec)	Measured Head Difference (cm H_2o)	Rotameter Reading	Inlet pressure (psi)	Average Temperature (°C)	Inlet Axial Reynolds Number $Re_{axi.}$	Radial Reynolds Number Re_w	Outlet/Inlet Average Velocity U_2/U_1	Dimensionless Pressure Drop $(p_o-p_i)/1/2\rho v_1^2$
1	3055	120.41	285	101.25	0.435	0.5	20.55	23.0	3307.1	7.20	0.100	1.405
2	2560	110.11	595	102.55	0.325	0.5	19.53	23.0	3414.8	6.60	0.200	1.045
3	2140	103.40	845	95.23	0.155	0.5	18.50	23.0	3482.6	5.87	0.300	0.597
4	3370	211.59	1140	86.72	-0.16	0.5	15.50	23.0	3448.0	4.52	0.452	-0.169
5	2920	210.22	1560	99.46	-0.415	0.5	14.50	23.0	3516.7	3.94	0.530	-0.748
6	2150	201.33	1880	103.44	-0.7	0.5	12.46	23.0	3451.1	3.03	0.630	-1.455
7	1965	250.45	2010	99.63	-0.98	0.5	10.50	23.0	3373.9	2.23	0.720	-2.202
8	1250	244.56	1860	85.33	-1.21	0.5	8.00	23.0	3274.3	1.45	0.810	-2.892
9	695	221.31	2010	87.33	-1.455	0.5	6.50	23.0	3208.5	0.89	0.880	-3.619
10	210	191.11	2270	85.04	-2.09	0.5	4.00	23.0	3474.7	0.31	0.960	-4.323

Table A.33- Experimental data for L/D= 159.6 and inlet Reynolds number $Re_{axi.}$ = 38318

Experiment Number	Measured Porous Volume Collected (mL)	Measured Porous Collection Time (sec)	Measured Outlet Volume Collected (mL)	Measured Outlet Collection Time (sec)	Measured Head Difference (cm H_2o)	Rotameter Reading	Inlet pressure (psi)	Average Temperature (°C)	Inlet Axial Reynolds Number $Re_{axi.}$	Radial Reynolds Number Re_w	Outlet/Inlet Average Velocity U_2/U_1	Dimensionless Pressure Drop $(p_o-p_i)/1/2\rho v_1^2$
1	4190	16.22	4220	65.36	42.885	5.0	26.74	24.0	38368.5	56.42	0.200	1.121
2	4420	18.54	4215	50.34	32.385	5.0	25.98	24.0	38321.6	52.07	0.260	0.894
3	4195	19.52	4070	40.25	19.755	5.0	25.07	24.0	37646.9	46.94	0.320	0.636
4	3905	19.99	4380	36.58	6.73	5.0	24.01	24.0	37597.6	42.66	0.380	0.346
5	3790	21.30	4270	30.54	-7.85	5.0	22.81	24.0	37991.6	38.86	0.440	0.026
6	3745	23.58	4000	25.21	-24.25	5.0	21.45	24.0	38050.5	34.69	0.500	-0.325
7	3740	26.88	3770	21.28	-42.18	5.0	19.95	24.0	38014.9	30.39	0.560	-0.708
8	3445	28.78	3930	20.12	-61.8	5.0	18.29	24.0	37989.6	26.14	0.620	-1.122
9	3215	31.66	4130	19.12	-85.37	5.0	16.49	24.0	38448.2	22.18	0.680	-1.568
10	3260	39.55	3940	16.78	-110.25	5.0	14.54	24.0	38597.3	18.00	0.740	-2.044
11	3165	49.99	3740	14.78	-137.7	5.0	12.44	24.0	38724.6	13.83	0.800	-2.552
12	3140	71.22	3935	14.52	-168.38	5.0	10.19	24.0	38869.5	9.63	0.860	-3.092

Table A.34- Experimental data for L/D= 159.6 and inlet Reynolds number $Re_{axi.}$ = 30731

Experiment Number	Measured Porous Volume Collected (mL)	Measured Porous Collection Time (sec)	Measured Outlet Volume Collected (mL)	Measured Outlet Collection Time (sec)	Measured Head Difference (cm H_2o)	Rotameter Reading	Inlet pressure (psi)	Average Temperature (°C)	Inlet Axial Reynolds Number $Re_{axi.}$	Radial Reynolds Number Re_w	Outlet/Inlet Average Velocity U_2/U_1	Dimensionless Pressure Drop $(p_o-p_i)/1/2\rho v_1^2$
1	3775	18.33	3685	71.55	24.39	4.0	30.46	24.0	30438.1	44.98	0.200	1.045
2	3985	20.33	3910	55.32	18.39	4.0	28.95	24.0	31593.6	42.81	0.265	0.788
3	4060	22.87	3745	43.22	9.425	4.0	27.38	24.0	31362.5	38.77	0.328	0.504
4	3920	24.89	4030	39.85	-0.365	4.0	25.72	24.0	30778.2	34.40	0.391	0.188
5	3745	26.87	4160	35.87	-10.72	4.0	23.95	24.0	30472.7	30.44	0.454	-0.163
6	3660	30.45	3930	30.54	-21.24	4.0	22.08	25.0	30479.9	26.85	0.517	-0.548
7	3745	35.45	3710	25.44	-34.28	4.0	20.11	25.0	30909.4	23.60	0.580	-0.965
8	3595	40.57	3800	23.78	-47.21	4.0	18.04	25.0	30661.6	19.80	0.643	-1.417
9	3665	50.22	3915	22.33	-62.52	4.0	15.87	25.0	30801.3	16.30	0.706	-1.902
10	3460	60.78	3645	19.22	-78.72	4.0	13.59	25.0	30770.5	12.72	0.769	-2.422
11	3105	75.88	3805	18.78	-95.79	4.0	11.22	25.0	30617.6	9.14	0.832	-2.978
12	3060	120.45	3865	17.87	-115.97	4.0	8.75	25.0	30681.2	5.68	0.895	-3.564

Table A.35- Experimental data for L/D= 159.6 and inlet Reynolds number Re_{axi} = 22693

Experiment Number	Measured Porous Volume Collected (mL)	Measured Porous Collection Time (sec)	Measured Outlet Volume Collected (mL)	Measured Outlet Collection Time (sec)	Measured Head Difference (cm H_2o)	Rotameter Reading	Inlet pressure (psi)	Average Temperature (°C)	Inlet Axial Reynolds Number $Re_{axi.}$	Radial Reynolds Number Re_w	Outlet/Inlet Average Velocity U_2/U_1	Dimensionless Pressure Drop $(p_o-p_i)/1/2\rho v_1^2$
1	3850	23.35	3775	104.22	12.905	3.0	27.25	24.0	23879.3	36.01	0.180	0.917
2	3840	25.87	3845	80.25	8.04	3.0	26.44	24.0	23341.8	32.42	0.244	0.665
3	3790	27.98	3935	65.22	3.2	3.0	25.46	24.0	23309.5	29.58	0.308	0.384
4	3730	30.87	3985	55.65	-2.15	3.0	24.30	24.0	22952.0	26.39	0.372	0.069
5	3680	33.69	3875	45.87	-8.11	3.0	22.97	24.0	23154.2	23.86	0.436	-0.276
6	3470	36.78	3795	40.22	-13.995	3.0	21.46	24.0	22615.0	20.60	0.500	-0.654
7	3480	42.54	3800	35.87	-20.75	3.0	19.78	24.0	22571.7	17.87	0.564	-1.063
8	3180	45.88	3655	31.22	-28.005	3.0	17.92	24.0	22494.0	15.14	0.628	-1.502
9	3125	55.68	3505	27.78	-34.865	3.0	15.89	24.0	22103.5	12.26	0.692	-1.974
10	4050	90.21	3595	25.87	-44.735	3.0	13.68	24.0	22422.9	9.80	0.756	-2.481
11	3215	95.88	3750	24.54	-56.65	3.0	11.30	24.0	22895.2	7.32	0.820	-3.012
12	2335	110.21	3855	23.88	-66.585	3.0	8.74	24.0	22662.1	4.63	0.884	-3.582

Table A.36- Experimental data for L/D= 159.6 and inlet Reynolds number $Re_{axi.}$ = 15222												
Experiment Number	Measured Porous Volume Collected (mL)	Measured Porous Collection Time (sec)	Measured Outlet Volume Collected (mL)	Measured Outlet Collection Time (sec)	Measured Head Difference (cm H_2o)	Rotameter Reading	Inlet pressure (psi)	Average Temperature (°C)	Inlet Axial Reynolds Number $Re_{axi.}$	Radial Reynolds Number Re_w	Outlet/Inlet Average Velocity U_2/U_1	Dimensionless Pressure Drop $(p_o-p_i)/1/2\rho v_1^2$
1	3975	35.33	3925	170.45	4.19	2.0	26.61	24.0	16108.8	24.57	0.170	0.710
2	3925	37.56	3835	130.22	2.425	2.0	25.43	24.0	15948.1	22.82	0.220	0.498
3	3750	40.22	3830	100.54	-0.18	2.0	23.74	24.0	15678.2	20.36	0.290	0.172
4	3820	45.89	3755	80.21	-2.965	2.0	22.01	24.0	15571.6	18.18	0.360	-0.188
5	3580	50.22	3945	70.45	-6.295	2.0	19.99	24.0	15296.6	15.57	0.440	-0.641
6	3725	60.78	3980	61.22	-9.785	2.0	18.05	24.0	15238.3	13.38	0.515	-1.103
7	3900	75.88	3990	53.95	-13.605	2.0	16.07	24.0	15192.9	11.22	0.590	-1.604
8	4050	90.78	3790	47.78	-16.155	2.0	14.72	24.0	15071.9	9.74	0.640	-1.960
9	3450	100.55	3760	42.21	-21.165	2.0	12.47	24.0	15102.3	7.49	0.722	-2.582
10	3390	120.45	3850	40.87	-24.095	2.0	11.13	24.0	15040.6	6.15	0.770	-2.965
11	2580	150.88	3945	37.54	-31.065	2.0	8.57	24.0	15174.1	3.73	0.860	-3.730
12	2305	240.25	3885	35.22	-35.155	2.0	6.83	24.0	15021.8	2.10	0.920	-4.262

Table A.37- Experimental data for L/D= 159.6 and inlet Reynolds number $Re_{axi.}$ = 9997												
Experiment Number	Measured Porous Volume Collected (mL)	Measured Porous Collection Time (sec)	Measured Outlet Volume Collected (mL)	Measured Outlet Collection Time (sec)	Measured Head Difference (cm H_2o)	Rotameter Reading	Inlet pressure (psi)	Average Temperature (°C)	Inlet Axial Reynolds Number $Re_{axi.}$	Radial Reynolds Number Re_w	Outlet/Inlet Average Velocity U_2/U_1	Dimensionless Pressure Drop $(p_o-p_i)/1/2\rho v_1^2$
1	1205	303.03	4365	57.80	-19.16	1.3	4.58	24.0	10115.1	1.74	0.950	-5.013
2	3125	259.03	4130	60.45	-15.075	1.3	7.07	24.0	10057.8	5.27	0.850	-4.085
3	4180	235.13	3905	62.03	-12.65	1.3	8.74	24.0	10018.4	7.77	0.780	-3.483
4	4005	183.03	3965	67.10	-11.08	1.3	9.89	24.0	10000.1	9.56	0.730	-3.070
5	3765	135.35	3970	73.43	-9.205	1.3	11.46	24.0	10054.9	12.15	0.660	-2.520
6	3620	105.32	3645	76.80	-7.06	1.3	13.18	24.0	9994.4	15.01	0.580	-1.937
7	3845	90.33	3925	99.14	-4.825	1.3	15.18	24.0	9979.2	18.59	0.482	-1.285
8	4120	84.22	3390	102.24	-3.235	1.3	16.69	24.0	9932.9	21.37	0.404	-0.817
9	3940	70.29	3080	116.80	-1.75	1.3	18.24	24.0	9940.6	24.48	0.320	-0.358
10	3955	63.74	3115	152.23	-0.615	1.3	19.50	24.0	9925.6	27.10	0.248	-0.005
11	3435	51.19	2550	161.87	0.2	1.3	20.46	24.0	9948.3	29.31	0.190	0.253
12	3670	48.69	1660	217.27	1.385	1.3	22.01	24.0	9939.3	32.92	0.092	0.632

Table A.38- Experimental data for L/D= 159.6 and inlet Reynolds number Re_{axi} = 7558												
Experiment Number	Measured Porous Volume Collected (mL)	Measured Porous Collection Time (sec)	Measured Outlet Volume Collected (mL)	Measured Outlet Collection Time (sec)	Measured Head Difference (cm H_2o)	Rotameter Reading	Inlet pressure (psi)	Average Temperature (°C)	Inlet Axial Reynolds Number Re_{axi}	Radial Reynolds Number Re_w	Outlet/Inlet Average Velocity U_2/U_1	Dimensionless Pressure Drop $(p_o-p_i)/1/2\rho v_1^2$
1	4075	64.25	600	180.23	0.885	1.0	19.26	24.0	8033.7	13.85	0.050	0.616
2	4095	70.66	1265	160.33	0.35	1.0	18.48	24.0	7937.0	12.66	0.120	0.360
3	4000	75.44	1700	145.89	-0.145	1.0	17.75	24.0	7808.3	11.58	0.180	0.113
4	3710	84.21	2785	140.55	-1.355	1.0	16.00	24.0	7742.3	9.62	0.310	-0.506
5	3785	95.65	3130	134.78	-1.945	1.0	15.12	24.0	7628.6	8.64	0.370	-0.832
6	3540	105.88	3570	120.45	-3.175	1.0	13.52	24.0	7695.7	7.30	0.470	-1.432
7	3555	130.45	3145	90.72	-4.28	1.0	11.97	24.0	7590.8	5.95	0.560	-2.033
8	3740	160.45	2220	60.85	-4.685	1.0	11.05	24.0	7352.7	5.09	0.610	-2.385
9	3380	190.78	2600	59.88	-6.545	1.0	9.12	24.0	7574.3	3.87	0.710	-3.149
10	2835	230.55	2825	58.52	-8.11	1.0	7.32	24.0	7568.4	2.69	0.797	-3.885
11	2710	336.58	2865	57.92	-8.565	1.0	5.95	24.0	7244.7	1.76	0.860	-4.432
12	615	350.22	3210	56.39	-11.89	1.0	3.42	24.0	7551.5	0.38	0.970	-5.481

Table A.41- Experimental data for L/D= 201.2 and inlet Reynolds number Re_{ai} = 38318												
Experiment Number	Measured Porous Volume Collected (mL)	Measured Porous Collection Time (sec)	Measured Outlet Volume Collected (mL)	Measured Outlet Collection Time (sec)	Measured Head Difference (cm H_2o)	Rotameter Reading	Inlet pressure (psi)	Average Temperature (°C)	Inlet Axial Reynolds Number Re_{ai}	Radial Reynolds Number Re_w	Outlet/Inlet Average Velocity U_2/U_1	Dimensionless Pressure Drop $(p_o-p_i)/1/2\rho v_1^2$
1	3510	11.37	820	61.44	46.3	5.0	17.50	23.0	38016.2	46.73	0.041	-1.118
2	3310	11.53	2132	58.78	36.43	5.0	17.00	23.0	38212.0	43.46	0.112	-0.905
3	3040	10.78	1970	49.81	34.9	5.0	17.00	23.0	38000.0	42.69	0.123	-0.883
4	3260	11.82	2450	49.47	30.86	5.0	16.50	23.0	38490.6	41.75	0.152	-0.782
5	3100	11.91	2720	46.66	24.565	5.0	16.50	23.0	37692.1	39.40	0.183	-0.679
6	3510	14.84	3100	37.41	8.205	5.0	15.50	23.0	37879.5	35.81	0.259	-0.337
7	3540	16.15	3180	31.66	-5.475	5.0	15.00	23.0	37957.2	33.18	0.314	-0.060
8	3200	16.28	3110	24.93	-26.49	5.0	14.00	23.0	38258.0	29.76	0.388	0.354
9	3370	19.41	3340	22.91	-48.5	5.0	12.75	23.0	38170.0	26.28	0.456	0.787
10	3240	20.62	3190	19.34	-69.8	5.0	12.00	23.0	38578.8	23.79	0.512	1.171
11	3320	24.22	3400	18.66	-92.35	5.0	11.00	23.0	38374.2	20.75	0.571	1.611
12	3560	30.59	3260	16.06	-120	5.0	10.00	23.0	38526.1	17.62	0.636	2.109
13	3180	29.72	3500	16.44	-132.9	5.0	9.50	23.0	38666.6	16.20	0.666	2.325
14	2860	30.00	3630	16.13	-150	5.0	9.00	23.0	38806.6	14.43	0.702	2.614
15	3130	35.50	3410	14.69	-162.6	5.0	8.50	23.0	38883.0	13.35	0.725	2.823
16	2980	36.22	3560	14.88	-173.7	5.0	8.50	23.0	39031.4	12.46	0.744	3.002

Table A.42- Experimental data for L/D= 201.2 and inlet Reynolds number $Re_{axi.}$ = 30731

Experiment Number	Measured Porous Volume Collected (mL)	Measured Porous Collection Time (sec)	Measured Outlet Volume Collected (mL)	Measured Outlet Collection Time (sec)	Measured Head Difference (cm H_2o)	Rotameter Reading	Inlet pressure (psi)	Average Temperature (°C)	Inlet Axial Reynolds Number $Re_{axi.}$	Radial Reynolds Number Re_{ω}	Outlet/Inlet Average Velocity U_2/U_1	Dimensionless Pressure Drop $(p_o-p_1)/1/2\rho v_1^2$
1	3600	14.04	0	0.00	30.065	4.0	18.50	22.0	29503.7	37.92	0.000	1.154
2	3380	13.81	790	71.47	27.02	4.0	17.75	23.0	30179.3	37.05	0.043	1.051
3	3470	15.00	1320	52.28	21.79	4.0	17.00	23.0	30321.8	35.02	0.098	0.870
4	3660	17.25	2196	49.31	13.28	4.0	16.00	23.0	30408.2	32.12	0.173	0.592
5	3500	18.25	3050	48.22	3.015	4.0	15.00	23.0	30285.4	29.03	0.248	0.266
6	3520	20.60	3180	37.53	-8.1	4.0	14.25	23.0	30413.9	25.87	0.331	-0.082
7	3320	20.97	2900	30.22	-20.295	4.0	13.50	23.0	30320.1	23.97	0.377	-0.468
8	3550	28.09	3820	29.13	-49.1	4.0	11.50	23.0	30897.0	19.13	0.509	-1.296
9	3320	34.19	3310	20.85	-79.6	4.0	9.50	23.0	30926.3	14.70	0.620	-2.168
10	3480	45.31	3470	19.59	-102	4.0	8.50	23.0	30826.6	11.63	0.698	-2.819
11	3460	54.53	3480	18.25	-119.4	4.0	7.50	23.0	31001.1	9.61	0.750	-3.256
12	3260	61.09	3720	18.44	-133.1	4.0	6.75	23.0	31246.0	8.08	0.791	-3.559

Table A.43- Experimental data for L/D= 201.2 and inlet Reynolds number Re_{axi} = 22693												
Experiment Number	Measured Porous Volume Collected (mL)	Measured Porous Collection Time (sec)	Measured Outlet Volume Collected (mL)	Measured Outlet Collection Time (sec)	Measured Head Difference (cm H_2o)	Rotameter Reading	Inlet pressure (psi)	Average Temperature (°C)	Inlet Axial Reynolds Number Re_{axi}	Radial Reynolds Number Re_w	Outlet/Inlet Average Velocity U_2/U_1	Dimensionless Pressure Drop $(p_o-p_i)/1/2\rho v_1^2$
1	3480	18.41	0	0.00	14.26	3.0	16.50	22.0	21847.1	27.95	0.000	1.013
2	3490	19.16	540	73.59	12.47	3.0	16.00	23.0	22445.7	27.57	0.039	0.899
3	3550	21.90	1940	72.25	6.385	3.0	14.75	23.0	22452.8	24.54	0.142	0.539
4	3300	24.00	3160	62.22	-3.965	3.0	13.00	23.0	22483.8	20.82	0.270	-0.058
5	3520	28.32	3210	50.12	-11.86	3.0	12.00	23.0	22559.9	18.82	0.340	-0.501
6	3290	28.94	3230	43.03	-17.93	3.0	10.75	23.0	22705.4	17.21	0.398	-0.822
7	3350	34.23	3730	41.22	-27.7	3.0	10.00	23.0	22722.1	14.82	0.480	-1.348
8	3200	40.22	3440	31.37	-41.4	3.0	9.00	23.0	22919.8	12.04	0.580	-2.037
9	3840	58.12	3840	31.32	-52.77	3.0	7.75	23.0	22986.6	10.00	0.650	-2.595
10	3010	59.15	3520	25.60	-68.6	3.0	7.00	23.0	23042.2	7.70	0.730	-3.377
11	2690	77.53	3400	22.04	-85.45	3.0	5.50	23.0	23329.6	5.25	0.816	-4.061
12	2950	100.62	3410	21.38	-91.7	3.0	5.00	23.0	23397.6	4.44	0.845	-4.312

Table A.44- Experimental data for L/D= 201.2 and inlet Reynolds number Re_{axi} = 15222												
Experiment Number	Measured Porous Volume Collected (mL)	Measured Porous Collection Time (sec)	Measured Outlet Volume Collected (mL)	Measured Outlet Collection Time (sec)	Measured Head Difference (cm H_2o)	Rotameter Reading	Inlet pressure (psi)	Average Temperature (°C)	Inlet Axial Reynolds Number $Re_{axi.}$	Radial Reynolds Number Re_w	Outlet/Inlet Average Velocity U_2/U_1	Dimensionless Pressure Drop $(p_o-p_i)/1/2\rho v_1^2$
1	3340	26.62	0	0.00	4.635	2.0	13.50	22.0	14614.6	18.55	0.000	0.772
2	3970	33.54	700	92.55	3.38	2.0	12.75	23.0	15048.8	17.92	0.060	0.599
3	3640	34.47	1900	90.12	-0.19	2.0	11.50	23.0	15199.4	15.99	0.166	0.142
4	3920	43.21	3000	85.21	-5.375	2.0	10.50	23.0	15162.2	13.73	0.280	-0.500
5	3380	43.50	2780	56.50	-10.645	2.0	9.50	23.0	15339.4	11.76	0.388	-1.110
6	3620	55.31	3470	57.42	-16.105	2.0	8.25	23.0	15299.1	9.91	0.480	-1.752
7	3210	61.31	3340	45.28	-23.34	2.0	7.00	23.0	15426.1	7.93	0.585	-2.531
8	2940	82.38	3470	38.37	-34.025	2.0	5.50	23.0	15571.5	5.40	0.717	-3.619
9	2990	138.91	3500	33.62	-44.7	2.0	4.50	23.0	15631.7	3.26	0.829	-4.690
10	1610	112.50	3470	30.97	-50.3	2.0	4.25	23.0	15756.8	2.17	0.887	-5.184
11	1830	144.21	3650	32.25	-51.65	2.0	3.50	23.0	15814.7	1.92	0.899	-5.211

Table A.45- Experimental data for L/D= 201.2 and inlet Reynolds number $Re_{axi.}$ = 9997

Experiment Number	Measured Porous Volume Collected (mL)	Measured Porous Collection Time (sec)	Measured Outlet Volume Collected (mL)	Measured Outlet Collection Time (sec)	Measured Head Difference (cm H_2o)	Rotameter Reading	Inlet pressure (psi)	Average Temperature (°C)	Inlet Axial Reynolds Number $Re_{axi.}$	Radial Reynolds Number Re_w	Outlet/Inlet Average Velocity U_2/U_1	Dimensionless Pressure Drop $(p_o-p_i)/1/2\rho v_1^2$
1	1855	298.22	4530	63.28	-23.78	1.3	2.78	24.0	10094.2	2.72	0.920	-6.091
2	3045	278.66	4430	65.93	-21.04	1.3	3.30	24.0	10067.7	4.77	0.860	-5.473
3	4100	185.62	3835	67.51	-15.65	1.3	4.50	24.0	10045.8	9.65	0.720	-4.152
4	4300	164.85	3840	72.58	-13.9	1.3	4.92	24.0	10023.0	11.39	0.670	-3.715
5	3325	110.58	3870	78.91	-12.28	1.3	5.35	24.0	10006.2	13.13	0.620	-3.298
6	3880	99.68	3335	82.28	-9.075	1.3	6.27	24.0	9987.9	17.00	0.510	-2.439
7	4005	89.56	3675	104.62	-7.29	1.3	6.86	24.0	10002.2	19.53	0.440	-1.938
8	4275	79.85	2840	107.72	-4.725	1.3	7.77	24.0	9961.0	23.38	0.330	-1.226
9	3870	65.44	2540	122.28	-3.31	1.3	8.34	24.0	9934.4	25.83	0.260	-0.822
10	3785	59.87	2650	157.71	-2.395	1.3	8.75	24.0	9930.1	27.61	0.210	-0.554
11	3465	48.55	1475	167.35	-0.775	1.3	9.56	24.0	9915.8	31.17	0.110	-0.072
12	3830	49.54	715	222.75	0.19	1.3	10.12	24.0	9935.5	33.77	0.040	0.221

Table A.46- Experimental data for L/D= 201.2 and inlet Reynolds number $Re_{axi.}$ = 7558

Experiment Number	Measured Porous Volume Collected (mL)	Measured Porous Collection Time (sec)	Measured Outlet Volume Collected (mL)	Measured Outlet Collection Time (sec)	Measured Head Difference (cm H_2o)	Rotameter Reading	Inlet pressure (psi)	Average Temperature (°C)	Inlet Axial Reynolds Number $Re_{axi.}$	Radial Reynolds Number Re_w	Outlet/Inlet Average Velocity U_2/U_1	Dimensionless Pressure Drop $(p_o-p_i)/1/2\rho v_1^2$
1	3540	57.68	0	0.00	0.18	1.0	9.00	22.0	7262.0	9.08	0.000	0.256
2	3690	68.23	730	99.41	-1.51	1.0	8.15	23.0	7468.9	8.19	0.120	-0.599
3	3530	72.75	1080	82.03	-1.91	1.0	7.50	23.0	7525.1	7.35	0.213	-0.778
4	3460	83.22	1730	88.43	-3.18	1.0	6.75	23.0	7488.8	6.29	0.320	-1.401
5	3050	82.69	1810	73.19	-4.23	1.0	6.00	23.0	7581.5	5.58	0.401	-1.846
6	3155	99.41	2070	70.56	-5.56	1.0	5.75	23.0	7527.3	4.80	0.480	-2.503
7	2370	88.21	2335	68.33	-6.925	1.0	5.00	23.0	7564.0	4.07	0.560	-3.087
8	2000	97.63	2880	70.31	-9.39	1.0	4.50	23.0	7645.6	3.10	0.667	-4.111
9	1980	146.32	2660	55.42	-11.61	1.0	3.50	23.0	7730.8	2.05	0.780	-4.901
10	1160	151.75	2930	54.72	-14.37	1.0	3.00	23.0	7734.3	1.16	0.875	-6.023
11	760	192.28	3220	55.84	-16.82	1.0	2.00	23.0	7911.8	0.60	0.936	-6.550
12	615	350.22	3210	56.39	-11.89	1.0	3.42	24.0	7551.5	0.38	0.970	-5.481

Table A.47- Experimental data for L/D= 201.2 and inlet Reynolds number Re_{axi} = 5495

Experiment Number	Measured Porous Volume Collected (mL)	Measured Porous Collection Time (sec)	Measured Outlet Volume Collected (mL)	Measured Outlet Collection Time (sec)	Measured Head Difference (cm H_2o)	Rotameter Reading	Inlet pressure (psi)	Average Temperature (°C)	Inlet Axial Reynolds Number Re_{axi}	Radial Reynolds Number Re_w	Outlet/Inlet Average Velocity U_2/U_1	Dimensionless Pressure Drop $(p_o-p_i)/1/2\rho v_i^2$
1	3485	81.25	110	84.25	0.39	0.73	6.31	24.0	5554.4	18.74	0.030	0.525
2	3185	79.33	355	89.25	0.125	0.73	6.03	24.0	5555.3	17.54	0.090	0.276
3	3350	89.66	1025	155.25	-0.175	0.73	5.75	24.0	5545.2	16.32	0.150	-0.003
4	3665	110.22	2025	192.80	-0.68	0.73	5.33	24.0	5534.7	14.52	0.240	-0.469
5	3365	115.40	3165	220.35	-1.25	0.73	4.92	24.0	5522.5	12.74	0.330	-0.993
6	3550	141.55	3830	210.87	-1.88	0.73	4.52	24.0	5505.1	10.95	0.420	-1.570
7	3385	154.56	4045	192.22	-2.42	0.73	4.21	24.0	5482.4	9.57	0.490	-2.071
8	2710	158.77	3850	150.45	-3.36	0.73	3.72	24.0	5471.7	7.46	0.600	-2.916
9	2555	166.89	3545	130.40	-3.73	0.73	3.55	24.0	5460.9	6.69	0.640	-3.255
10	2005	190.25	3485	110.25	-4.82	0.73	3.08	24.0	5446.6	4.60	0.750	-4.223
11	1415	210.55	3160	89.65	-5.84	0.73	2.69	24.0	5451.3	2.94	0.840	-5.085
12	705	240.98	3050	78.69	-6.96	0.73	2.32	24.0	5446.2	1.28	0.930	-6.029

Table A.48- Experimental data for L/D= 201.2 and inlet Reynolds number Re_{axi} = 3671												
Experiment Number	Measured Porous Volume Collected (mL)	Measured Porous Collection Time (sec)	Measured Outlet Volume Collected (mL)	Measured Outlet Collection Time (sec)	Measured Head Difference (cm H_2o)	Rotameter Reading	Inlet pressure (psi)	Average Temperature (°C)	Inlet Axial Reynolds Number Re_{axi}	Radial Reynolds Number Re_w	Outlet/Inlet Average Velocity U_2/U_1	Dimensionless Pressure Drop $(p_o-p_i)/1/2\rho v_1^2$
1	2600	90.25	0	0.00	0.485	0.5	5.25	22.0	3480.8	4.26	0.000	1.201
2	2420	88.53	340	195.23	0.38	0.5	5.00	23.0	3603.2	4.14	0.060	0.954
3	2255	89.63	680	165.23	0.095	0.5	4.70	23.0	3636.4	3.81	0.141	0.355
4	2210	95.55	960	155.65	-0.03	0.5	4.40	23.0	3648.5	3.50	0.211	0.102
5	2090	91.45	970	150.22	-0.18	0.5	4.40	23.0	3650.3	3.46	0.220	-0.199
6	2135	101.53	1350	165.45	-0.405	0.5	4.20	23.0	3641.5	3.18	0.280	-0.651
7	1810	97.77	1250	120.22	-0.63	0.5	3.90	23.0	3617.2	2.80	0.360	-1.108
8	1420	90.94	1090	83.78	-1.215	0.5	3.50	23.0	3596.6	2.36	0.455	-2.297
9	1485	121.22	1250	80.23	-1.545	0.5	3.30	23.0	3504.8	1.85	0.560	-3.108
10	1540	165.55	1545	85.65	-2.065	0.5	3.00	23.0	3455.8	1.41	0.660	-4.298
11	1140	157.31	1660	78.28	-2.64	0.5	3.00	23.0	3596.4	1.10	0.745	-5.096
12	710	155.55	1800	75.21	-3.52	0.5	2.60	23	3622.1	0.69	0.840	-6.677
13	380	143.69	1660	65.44	-3.975	0.5	2.50	23	3565.7	0.40	0.906	-7.782

Appendix B

Dimensionless Pressure Change and U_2/U_1 Relation

Table B.1- Dimensionless pressure change and U_2/U_1 relation for Re_{inn} =5495

L/D	Equation
206.4	$\frac{P_o - P_i}{\frac{1}{2}\rho U_1^2} = 0.639687 - 3.71814\left(\frac{U_2}{U_1}\right) - 3.69839\left(\frac{U_2}{U_1}\right)^2$
159.6	$\frac{P_o - P_i}{\frac{1}{2}\rho U_1^2} = 1.11359 - 2.94488\left(\frac{U_2}{U_1}\right) - 3.53938\left(\frac{U_2}{U_1}\right)^2$
106.4	$\frac{P_o - P_i}{\frac{1}{2}\rho U_1^2} = 1.71906 - 1.96587\left(\frac{U_2}{U_1}\right) - 3.33625\left(\frac{U_2}{U_1}\right)^2$
79.8	$\frac{P_o - P_i}{\frac{1}{2}\rho U_1^2} = 2.0218 - 1.47441\left(\frac{U_2}{U_1}\right) - 3.23469\left(\frac{U_2}{U_1}\right)^2$
53.2	$\frac{P_o - P_i}{\frac{1}{2}\rho U_1^2} = 2.32453 - 0.982939\left(\frac{U_2}{U_1}\right) - 3.13312\left(\frac{U_2}{U_1}\right)^2$
26.6	$\frac{P_o - P_i}{\frac{1}{2}\rho U_1^2} = 2.62726 - 0.491461\left(\frac{U_2}{U_1}\right) - 3.03157\left(\frac{U_2}{U_1}\right)^2$

Table B.2- Dimensionless pressure change and U_2/U_1 relation for $Re_{act.}$=7559

L/D	Equation
206.4	$\frac{P_o - P_i}{\frac{1}{2}\rho U_1^2} = 0.139094 - 3.71818\left(\frac{U_2}{U_1}\right) - 3.69835\left(\frac{U_2}{U_1}\right)^2$
159.6	$\frac{P_o - P_i}{\frac{1}{2}\rho U_1^2} = 0.775806 - 3.05001\left(\frac{U_2}{U_1}\right) - 3.49899\left(\frac{U_2}{U_1}\right)^2$
106.4	$\frac{P_o - P_i}{\frac{1}{2}\rho U_1^2} = 1.60575 - 2.08854\left(\frac{U_2}{U_1}\right) - 3.37773\left(\frac{U_2}{U_1}\right)^2$
79.8	$\frac{P_o - P_i}{\frac{1}{2}\rho U_1^2} = 1.93521 - 1.74714\left(\frac{U_2}{U_1}\right) - 3.09543\left(\frac{U_2}{U_1}\right)^2$
53.2	$\frac{P_o - P_i}{\frac{1}{2}\rho U_1^2} = 2.34364 - 1.68548\left(\frac{U_2}{U_1}\right) - 2.59647\left(\frac{U_2}{U_1}\right)^2$
26.6	$\frac{P_o - P_i}{\frac{1}{2}\rho U_1^2} = 2.65989 - 0.611614\left(\frac{U_2}{U_1}\right) - 3.05464\left(\frac{U_2}{U_1}\right)^2$

Table B.3- Dimensionless pressure change and U_2/U_1 relation for $Re_{ann.}$=9997

L/D	Equation
206.4	$\frac{P_o - P_i}{\frac{1}{2}\rho U_1^2} = 0.37215 - 3.63465\left(\frac{U_2}{U_1}\right) - 3.68072\left(\frac{U_2}{U_1}\right)^2$
159.6	$\frac{P_o - P_i}{\frac{1}{2}\rho U_1^2} = 0.928312 - 2.88258\left(\frac{U_2}{U_1}\right) - 3.55229\left(\frac{U_2}{U_1}\right)^2$
106.4	$\frac{P_o - P_i}{\frac{1}{2}\rho U_1^2} = 1.63887 - 1.92172\left(\frac{U_2}{U_1}\right) - 3.38818\left(\frac{U_2}{U_1}\right)^2$
79.8	$\frac{P_o - P_i}{\frac{1}{2}\rho U_1^2} = 1.99416 - 1.44129\left(\frac{U_2}{U_1}\right) - 3.30614\left(\frac{U_2}{U_1}\right)^2$
53.2	$\frac{P_o - P_i}{\frac{1}{2}\rho U_1^2} = 2.34944 - 0.960858\left(\frac{U_2}{U_1}\right) - 3.22409\left(\frac{U_2}{U_1}\right)^2$
26.6	$\frac{P_o - P_i}{\frac{1}{2}\rho U_1^2} = 2.70472 - 0.480423\left(\frac{U_2}{U_1}\right) - 3.14206\left(\frac{U_2}{U_1}\right)^2$

Table B.4- Dimensionless pressure change and U_2/U_1 relation for $Re_{ann.}$=15222

L/D	Equation
206.4	$\frac{P_o - P_i}{\frac{1}{2}\rho U_1^2} = 0.812929 - 3.67955\left(\frac{U_2}{U_1}\right) - 3.46205\left(\frac{U_2}{U_1}\right)^2$
159.6	$\frac{P_o - P_i}{\frac{1}{2}\rho U_1^2} = 1.30724 - 2.92974\left(\frac{U_2}{U_1}\right) - 2.39868\left(\frac{U_2}{U_1}\right)^2$
106.4	$\frac{P_o - P_i}{\frac{1}{2}\rho U_1^2} = 1.91194 - 1.73649\left(\frac{U_2}{U_1}\right) - 3.51181\left(\frac{U_2}{U_1}\right)^2$
79.8	$\frac{P_o - P_i}{\frac{1}{2}\rho U_1^2} = 2.2675 - 1.62314\left(\frac{U_2}{U_1}\right) - 3.18134\left(\frac{U_2}{U_1}\right)^2$
53.2	$\frac{P_o - P_i}{\frac{1}{2}\rho U_1^2} = 2.63698 - 1.72492\left(\frac{U_2}{U_1}\right) - 2.66623\left(\frac{U_2}{U_1}\right)^2$
26.6	$\frac{P_o - P_i}{\frac{1}{2}\rho U_1^2} = 2.88615 - 0.47011\left(\frac{U_2}{U_1}\right) - 3.27132\left(\frac{U_2}{U_1}\right)^2$

Table B.5- Dimensionless pressure change and U_2/U_1 relation for $Re_{act.}$=22693

L/D	Equation
206.4	$\frac{P_o - P_i}{\frac{1}{2}\rho U_1^2} = 1.03003 - 3.09765\left(\frac{U_2}{U_1}\right) - 3.86397\left(\frac{U_2}{U_1}\right)^2$
159.6	$\frac{P_o - P_i}{\frac{1}{2}\rho U_1^2} = 1.4525 - 2.28255\left(\frac{U_2}{U_1}\right) - 3.85956\left(\frac{U_2}{U_1}\right)^2$
106.4	$\frac{P_o - P_i}{\frac{1}{2}\rho U_1^2} = 1.95802 - 1.1101\left(\frac{U_2}{U_1}\right) - 3.93124\left(\frac{U_2}{U_1}\right)^2$
79.8	$\frac{P_o - P_i}{\frac{1}{2}\rho U_1^2} = 2.33688 - 1.0062\left(\frac{U_2}{U_1}\right) - 3.68547\left(\frac{U_2}{U_1}\right)^2$
53.2	$\frac{P_o - P_i}{\frac{1}{2}\rho U_1^2} = 2.61609 - 0.583251\left(\frac{U_2}{U_1}\right) - 3.63417\left(\frac{U_2}{U_1}\right)^2$
26.6	$\frac{P_o - P_i}{\frac{1}{2}\rho U_1^2} = 2.98635 - 0.326367\left(\frac{U_2}{U_1}\right) - 3.46154\left(\frac{U_2}{U_1}\right)^2$

Table B.6- Dimensionless pressure change and U_2/U_1 relation for $Re_{act.}$=30731

L/D	Equation
206.4	$\frac{P_o - P_i}{\frac{1}{2}\rho U_1^2} = 1.17174 - 2.59298\left(\frac{U_2}{U_1}\right) - 4.39065\left(\frac{U_2}{U_1}\right)^2$
159.6	$\frac{P_o - P_i}{\frac{1}{2}\rho U_1^2} = 1.61099 - 1.98043\left(\frac{U_2}{U_1}\right) - 4.2446\left(\frac{U_2}{U_1}\right)^2$
106.4	$\frac{P_o - P_i}{\frac{1}{2}\rho U_1^2} = 2.15681 - 1.09671\left(\frac{U_2}{U_1}\right) - 4.14663\left(\frac{U_2}{U_1}\right)^2$
79.8	$\frac{P_o - P_i}{\frac{1}{2}\rho U_1^2} = 2.46106 - 0.993374\left(\frac{U_2}{U_1}\right) - 3.80727\left(\frac{U_2}{U_1}\right)^2$
53.2	$\frac{P_o - P_i}{\frac{1}{2}\rho U_1^2} = 2.76758 - 0.71472\left(\frac{U_2}{U_1}\right) - 3.62563\left(\frac{U_2}{U_1}\right)^2$
26.6	$\frac{P_o - P_i}{\frac{1}{2}\rho U_1^2} = 3.0204 - 0.414085\left(\frac{U_2}{U_1}\right) - 3.44051\left(\frac{U_2}{U_1}\right)^2$

Table B.7- Dimensionless pressure change and U_2/U_1 relationfor $Re_{act.}$=38318

L/D	Equation
206.4	$\frac{P_o - P_i}{\frac{1}{2}\rho U_1^2} = 1.24622 - 2.4227\left(\frac{U_2}{U_1}\right) - 4.42664\left(\frac{U_2}{U_1}\right)^2$
159.6	$\frac{P_o - P_i}{\frac{1}{2}\rho U_1^2} = 1.65065 - 1.78497\left(\frac{U_2}{U_1}\right) - 4.33431\left(\frac{U_2}{U_1}\right)^2$
106.4	$\frac{P_o - P_i}{\frac{1}{2}\rho U_1^2} = 2.14599 - 0.848502\left(\frac{U_2}{U_1}\right) - 4.33773\left(\frac{U_2}{U_1}\right)^2$
79.8	$\frac{P_o - P_i}{\frac{1}{2}\rho U_1^2} = 2.45324 - 0.790473\left(\frac{U_2}{U_1}\right) - 3.92705\left(\frac{U_2}{U_1}\right)^2$
53.2	$\frac{P_o - P_i}{\frac{1}{2}\rho U_1^2} = 2.73508 - 0.512927\left(\frac{U_2}{U_1}\right) - 3.76067\left(\frac{U_2}{U_1}\right)^2$
26.6	$\frac{P_o - P_i}{\frac{1}{2}\rho U_1^2} = 2.99865 - 0.229146\left(\frac{U_2}{U_1}\right) - 3.53171\left(\frac{U_2}{U_1}\right)^2$

Appendix C

Dimensionless Pressure Change and L/D Relation

Table C.1- Dimensionless pressure change and L/D relation for $Re_{act.}$=5495

U_2/U_1	Equation	Coefficient of Determination
0.0	$\frac{P_o - P_i}{\frac{1}{2}\rho U_1^2} = -0.0113805\frac{L}{D} + 2.92992$	0.9996
0.1	$\frac{P_o - P_i}{\frac{1}{2}\rho U_1^2} = -0.0132662\frac{L}{D} + 2.90061$	0.9998
0.2	$\frac{P_o - P_i}{\frac{1}{2}\rho U_1^2} = -0.0152283\frac{L}{D} + 2.81269$	0.9997
0.3	$\frac{P_o - P_i}{\frac{1}{2}\rho U_1^2} = -0.0172667\frac{L}{D} + 2.66618$	0.9999
0.4	$\frac{P_o - P_i}{\frac{1}{2}\rho U_1^2} = -0.0193816\frac{L}{D} + 2.46106$	0.9998
0.5	$\frac{P_o - P_i}{\frac{1}{2}\rho U_1^2} = -0.0215727\frac{L}{D} + 2.19735$	0.9999
0.6	$\frac{P_o - P_i}{\frac{1}{2}\rho U_1^2} = -0.0238403\frac{L}{D} + 1.87504$	0.9997
0.7	$\frac{P_o - P_i}{\frac{1}{2}\rho U_1^2} = -0.0261841\frac{L}{D} + 1.49412$	0.9998
0.8	$\frac{P_o - P_i}{\frac{1}{2}\rho U_1^2} = -0.0286044\frac{L}{D} + 1.0546$	0.9999
0.9	$\frac{P_o - P_i}{\frac{1}{2}\rho U_1^2} = -0.031101\frac{L}{D} + 0.556482$	0.9997
1.0	$\frac{P_o - P_i}{\frac{1}{2}\rho U_1^2} = -0.033674\frac{L}{D} - 0.000232$	0.9997

Table C.2- Dimensionless pressure change and L/D relation for $Re_{ann.}$=7559

U_2/U_1	Equation	Coefficient of Determination
0.0	$\frac{P_o - P_i}{\frac{1}{2}\rho U_1^2} = -0.0145434\frac{L}{D} + 3.09593$	0.9985
0.1	$\frac{P_o - P_i}{\frac{1}{2}\rho U_1^2} = -0.0162284\frac{L}{D} + 3.02474$	0.9990
0.2	$\frac{P_o - P_i}{\frac{1}{2}\rho U_1^2} = -0.0180145\frac{L}{D} + 2.89972$	0.9990
0.3	$\frac{P_o - P_i}{\frac{1}{2}\rho U_1^2} = -0.0199019\frac{L}{D} + 2.72086$	0.9989
0.4	$\frac{P_o - P_i}{\frac{1}{2}\rho U_1^2} = -0.0218906\frac{L}{D} + 2.48819$	0.9990
0.5	$\frac{P_o - P_i}{\frac{1}{2}\rho U_1^2} = -0.0239805\frac{L}{D} + 2.20168$	0.9991
0.6	$\frac{P_o - P_i}{\frac{1}{2}\rho U_1^2} = -0.0261716\frac{L}{D} + 1.86134$	0.9993
0.7	$\frac{P_o - P_i}{\frac{1}{2}\rho U_1^2} = -0.028464\frac{L}{D} + 1.46718$	0.9996
0.8	$\frac{P_o - P_i}{\frac{1}{2}\rho U_1^2} = -0.0308577\frac{L}{D} + 1.01919$	0.9998
0.9	$\frac{P_o - P_i}{\frac{1}{2}\rho U_1^2} = -0.0333525\frac{L}{D} + 0.517372$	0.9999
1.0	$\frac{P_o - P_i}{\frac{1}{2}\rho U_1^2} = -0.0359487\frac{L}{D} - 0.038275$	0.9999

Table C.3- Dimensionless pressure change and L/D relation for $Re_{ann.}$=9997

U_2/U_1	Equation	Coefficient of Determination
0.0	$\frac{P_o - P_i}{\frac{1}{2}\rho U_1^2} = -0.0133559\frac{L}{D} + 3.05991$	0.9998
0.1	$\frac{P_o - P_i}{\frac{1}{2}\rho U_1^2} = -0.0151928\frac{L}{D} + 3.0293$	0.9999
0.2	$\frac{P_o - P_i}{\frac{1}{2}\rho U_1^2} = -0.0170914\frac{L}{D} + 2.93749$	0.9999
0.3	$\frac{P_o - P_i}{\frac{1}{2}\rho U_1^2} = -0.0190517\frac{L}{D} + 2.78447$	0.9997
0.4	$\frac{P_o - P_i}{\frac{1}{2}\rho U_1^2} = -0.0210736\frac{L}{D} + 2.57026$	0.9998
0.5	$\frac{P_o - P_i}{\frac{1}{2}\rho U_1^2} = -0.0231573\frac{L}{D} + 2.29485$	0.9998
0.6	$\frac{P_o - P_i}{\frac{1}{2}\rho U_1^2} = -0.0253026\frac{L}{D} + 1.95823$	0.9997
0.7	$\frac{P_o - P_i}{\frac{1}{2}\rho U_1^2} = -0.0275096\frac{L}{D} + 1.56042$	0.9998
0.8	$\frac{P_o - P_i}{\frac{1}{2}\rho U_1^2} = -0.0297783\frac{L}{D} + 1.1014$	0.9999
0.9	$\frac{P_o - P_i}{\frac{1}{2}\rho U_1^2} = -0.0321087\frac{L}{D} + 0.581183$	0.9997
1.0	$\frac{P_o - P_i}{\frac{1}{2}\rho U_1^2} = -0.0345008\frac{L}{D} - 0.000231$	0.9996

Table C.4- Dimensionless pressure change and L/D relation for $Re_{ann.}$=15222

U_2/U_1	Equation	Coefficient of Determination
0.0	$\frac{P_o - P_i}{\frac{1}{2}\rho U_1^2} = -0.0120453\frac{L}{D} + 3.22884$	0.9987
0.1	$\frac{P_o - P_i}{\frac{1}{2}\rho U_1^2} = -0.0137116\frac{L}{D} + 3.1677$	0.9999
0.2	$\frac{P_o - P_i}{\frac{1}{2}\rho U_1^2} = -0.0154323\frac{L}{D} + 3.04727$	0.9995
0.3	$\frac{P_o - P_i}{\frac{1}{2}\rho U_1^2} = -0.0172076\frac{L}{D} + 2.86758$	0.9987
0.4	$\frac{P_o - P_i}{\frac{1}{2}\rho U_1^2} = -0.0190374\frac{L}{D} + 2.62861$	0.9981
0.5	$\frac{P_o - P_i}{\frac{1}{2}\rho U_1^2} = -0.0209217\frac{L}{D} + 2.33036$	0.9980
0.6	$\frac{P_o - P_i}{\frac{1}{2}\rho U_1^2} = -0.0228606\frac{L}{D} + 1.97284$	0.9981
0.7	$\frac{P_o - P_i}{\frac{1}{2}\rho U_1^2} = -0.024854\frac{L}{D} + 1.55605$	0.9985
0.8	$\frac{P_o - P_i}{\frac{1}{2}\rho U_1^2} = -0.0269019\frac{L}{D} + 1.07997$	0.9990
0.9	$\frac{P_o - P_i}{\frac{1}{2}\rho U_1^2} = -0.0290044\frac{L}{D} + 0.544631$	0.9995
1.0	$\frac{P_o - P_i}{\frac{1}{2}\rho U_1^2} = -0.0311613\frac{L}{D} - .0499911$	0.9998

Table C.5- Dimensionless pressure change and L/D relation for Re_{∞} =22693

U_2/U_1	Equation	Coefficient of Determination
0.0	$\frac{P_o - P_i}{\frac{1}{2}\rho U_1^2} = -0.0110936\frac{L}{D} + 3.22227$	0.9954
0.1	$\frac{P_o - P_i}{\frac{1}{2}\rho U_1^2} = -0.0127165\frac{L}{D} + 3.21432$	0.9984
0.2	$\frac{P_o - P_i}{\frac{1}{2}\rho U_1^2} = -0.014383\frac{L}{D} + 3.13614$	0.9995
0.3	$\frac{P_o - P_i}{\frac{1}{2}\rho U_1^2} = -0.0160932\frac{L}{D} + 2.98774$	0.9999
0.4	$\frac{P_o - P_i}{\frac{1}{2}\rho U_1^2} = -0.0178471\frac{L}{D} + 2.76912$	0.9999
0.5	$\frac{P_o - P_i}{\frac{1}{2}\rho U_1^2} = -0.0196447\frac{L}{D} + 2.48027$	0.9998
0.6	$\frac{P_o - P_i}{\frac{1}{2}\rho U_1^2} = -0.0214859\frac{L}{D} + 2.12119$	0.9997
0.7	$\frac{P_o - P_i}{\frac{1}{2}\rho U_1^2} = -0.0233709\frac{L}{D} + 1.6919$	0.9997
0.8	$\frac{P_o - P_i}{\frac{1}{2}\rho U_1^2} = -0.0252995\frac{L}{D} + 1.19238$	0.9997
0.9	$\frac{P_o - P_i}{\frac{1}{2}\rho U_1^2} = -0.072718\frac{L}{D} + 0.622645$	0.9997
1.0	$\frac{P_o - P_i}{\frac{1}{2}\rho U_1^2} = -0.0292877\frac{L}{D} - -0.01732$	0.9998

Table C.6- Dimensionless pressure change and L/D relation for Re_{∞} =30731

U_2/U_1	Equation	Coefficient of Determination
0.0	$\frac{P_o - P_i}{\frac{1}{2}\rho U_1^2} = -0.0106629\frac{L}{D} + 3.31206$	0.9996
0.1	$\frac{P_o - P_i}{\frac{1}{2}\rho U_1^2} = -0.011956\frac{L}{D} + 3.27785$	0.9998
0.2	$\frac{P_o - P_i}{\frac{1}{2}\rho U_1^2} = -0.0133587\frac{L}{D} + 3.17625$	0.9997
0.3	$\frac{P_o - P_i}{\frac{1}{2}\rho U_1^2} = -0.0148711\frac{L}{D} + 3.00725$	0.9996
0.4	$\frac{P_o - P_i}{\frac{1}{2}\rho U_1^2} = -0.0164933\frac{L}{D} + 2.77087$	0.9995
0.5	$\frac{P_o - P_i}{\frac{1}{2}\rho U_1^2} = -0.0182252\frac{L}{D} + 2.4671$	0.9995
0.6	$\frac{P_o - P_i}{\frac{1}{2}\rho U_1^2} = -0.0200667\frac{L}{D} + 2.09594$	0.9996
0.7	$\frac{P_o - P_i}{\frac{1}{2}\rho U_1^2} = -0.0220181\frac{L}{D} + 1.65739$	0.9997
0.8	$\frac{P_o - P_i}{\frac{1}{2}\rho U_1^2} = -0.0240791\frac{L}{D} + 1.15145$	0.9998
0.9	$\frac{P_o - P_i}{\frac{1}{2}\rho U_1^2} = -0.0262498\frac{L}{D} + 0.578124$	0.9999
1.0	$\frac{P_o - P_i}{\frac{1}{2}\rho U_1^2} = -0.0285303\frac{L}{D} - 0.062586$	0.9999

Table C.7- Dimensionless pressure change and L/D relation for $Re_{act.}$=38318

U_2/U_1	Equation	Coefficient of Determination
0.0	$\frac{P_o - P_i}{\frac{1}{2}\rho U_1^2} = -0.0100675\frac{L}{D} + 3.25673$	0.9990
0.1	$\frac{P_o - P_i}{\frac{1}{2}\rho U_1^2} = -0.0113661\frac{L}{D} + 3.24206$	0.9999
0.2	$\frac{P_o - P_i}{\frac{1}{2}\rho U_1^2} = -0.0127669\frac{L}{D} + 3.15699$	0.9999
0.3	$\frac{P_o - P_i}{\frac{1}{2}\rho U_1^2} = -0.0142698\frac{L}{D} + 3.00154$	0.9999
0.4	$\frac{P_o - P_i}{\frac{1}{2}\rho U_1^2} = -0.0158749\frac{L}{D} + 2.7757$	0.9998
0.5	$\frac{P_o - P_i}{\frac{1}{2}\rho U_1^2} = -0.0175821\frac{L}{D} + 2.47948$	0.9998
0.6	$\frac{P_o - P_i}{\frac{1}{2}\rho U_1^2} = -0.0193916\frac{L}{D} + 2.11287$	0.9999
0.7	$\frac{P_o - P_i}{\frac{1}{2}\rho U_1^2} = -0.0213032\frac{L}{D} + 1.67587$	0.9999
0.8	$\frac{P_o - P_i}{\frac{1}{2}\rho U_1^2} = -0.023317\frac{L}{D} + 1.16849$	0.9999
0.9	$\frac{P_o - P_i}{\frac{1}{2}\rho U_1^2} = -0.0254329\frac{L}{D} + 0.590713$	0.9999
1.0	$\frac{P_o - P_i}{\frac{1}{2}\rho U_1^2} = -0.027651\frac{L}{D} - 0.0574416$	0.9981

Appendix D

Caparison between predicted values by Equation 7.10 and measured values of nondimension pressure change for different lengths and different inlet Reynolds numbers

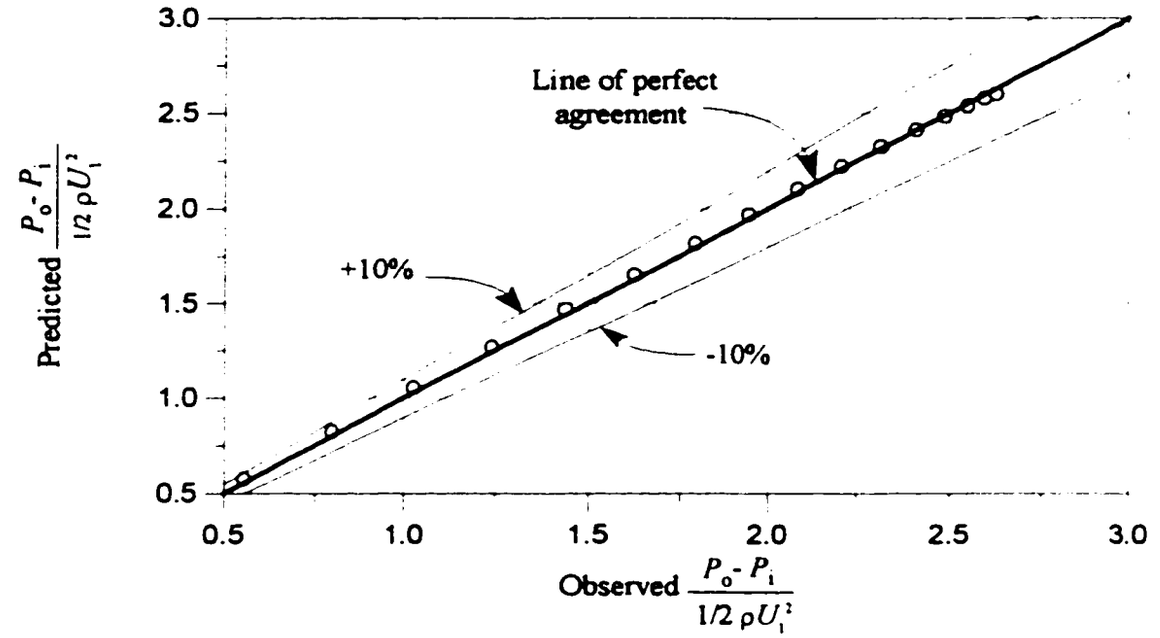

(a) Pressure gain

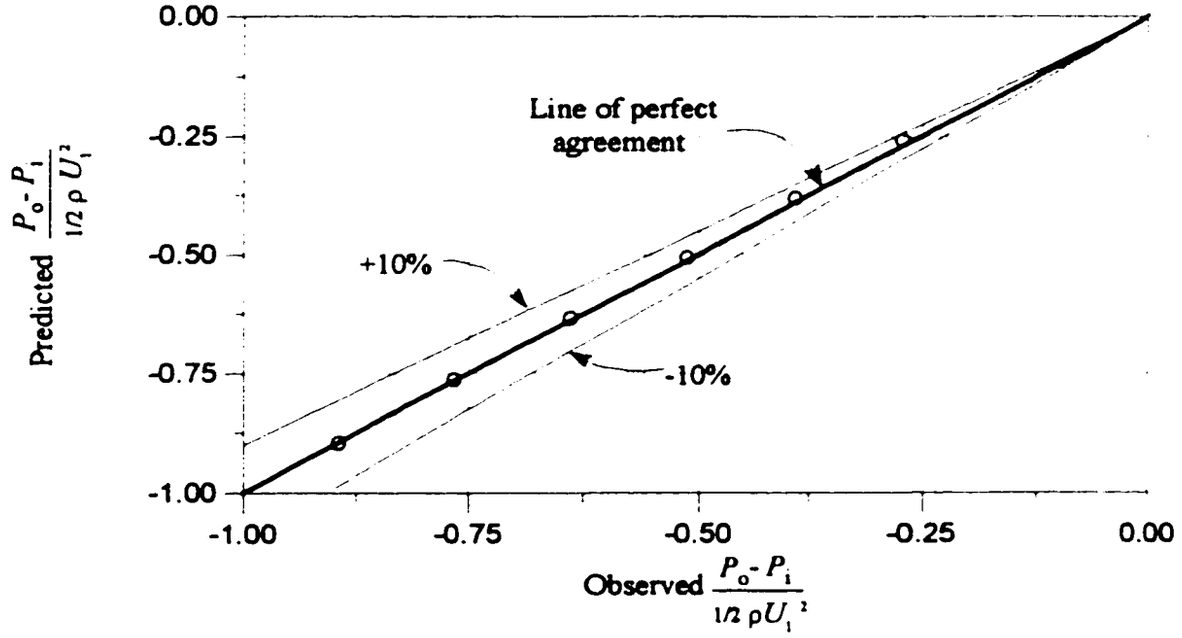

(b) Pressure drop

Figure D.1- Predicted vs. observed $\frac{P_o - P_i}{1/2\,\rho U_1^2}$ for L/D=26.6 and $Re_{axi.}$=5495

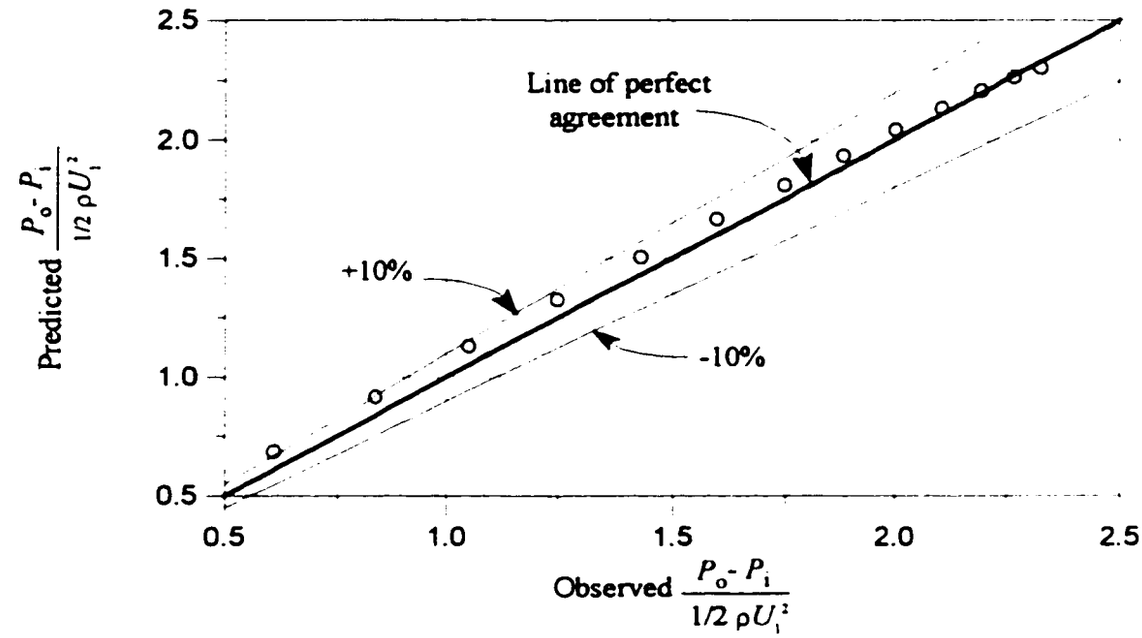

(a) Pressure gain

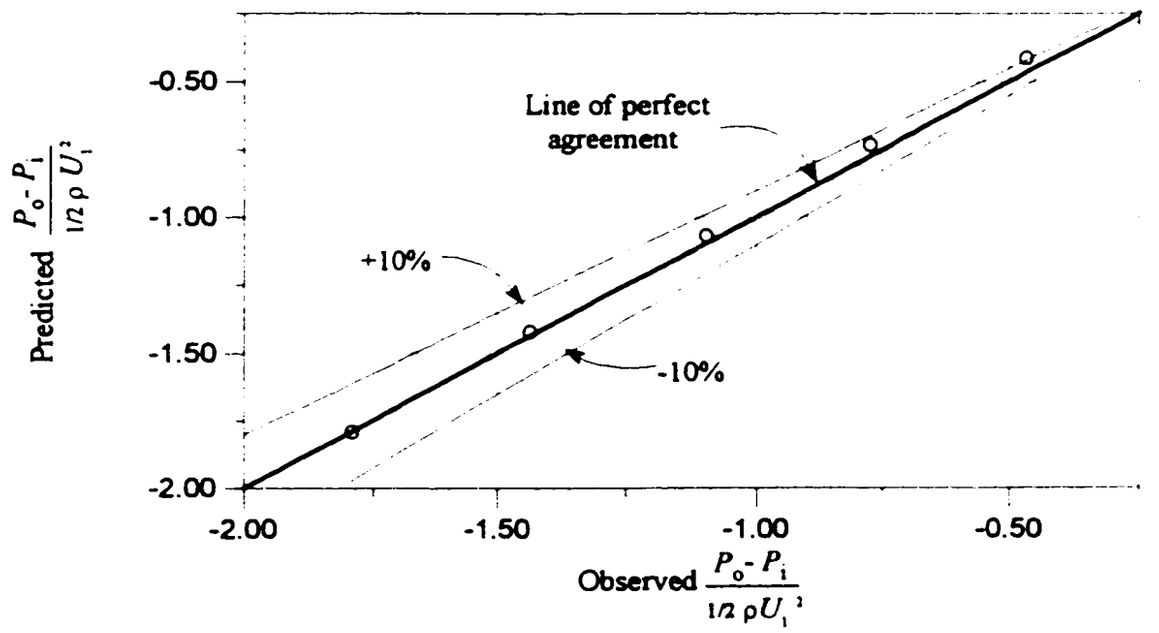

(b) Pressure drop

Figure D.2- Predicted vs. observed $\frac{P_o - P_i}{1/2\,\rho U_1^2}$ for L/D=53.2 and $Re_{axi.}$=5495

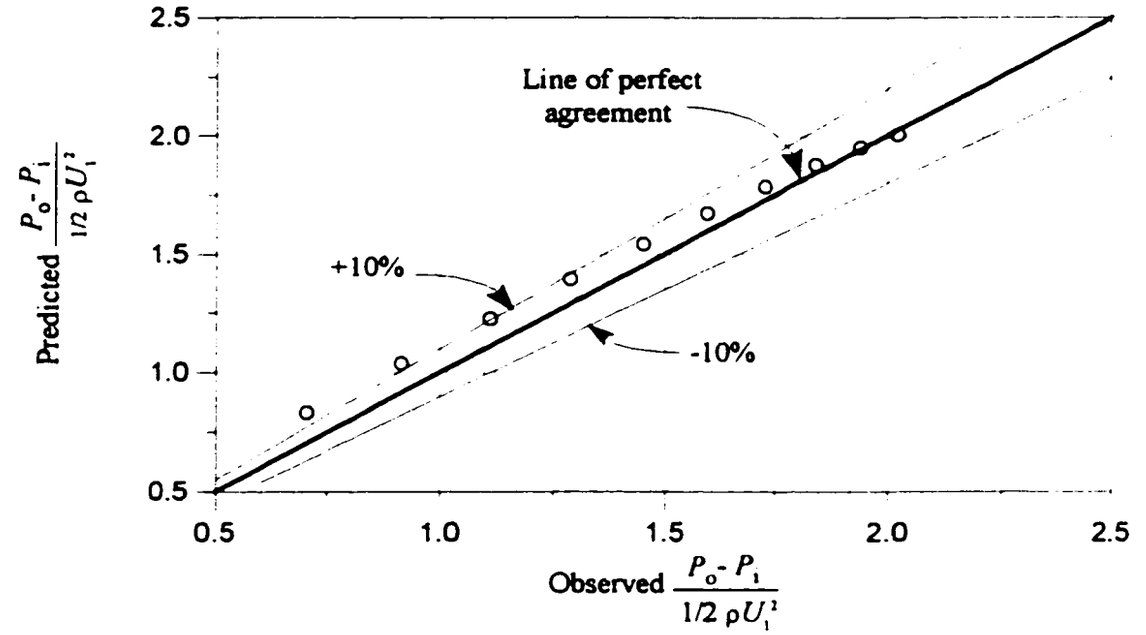

(a) Pressure gain

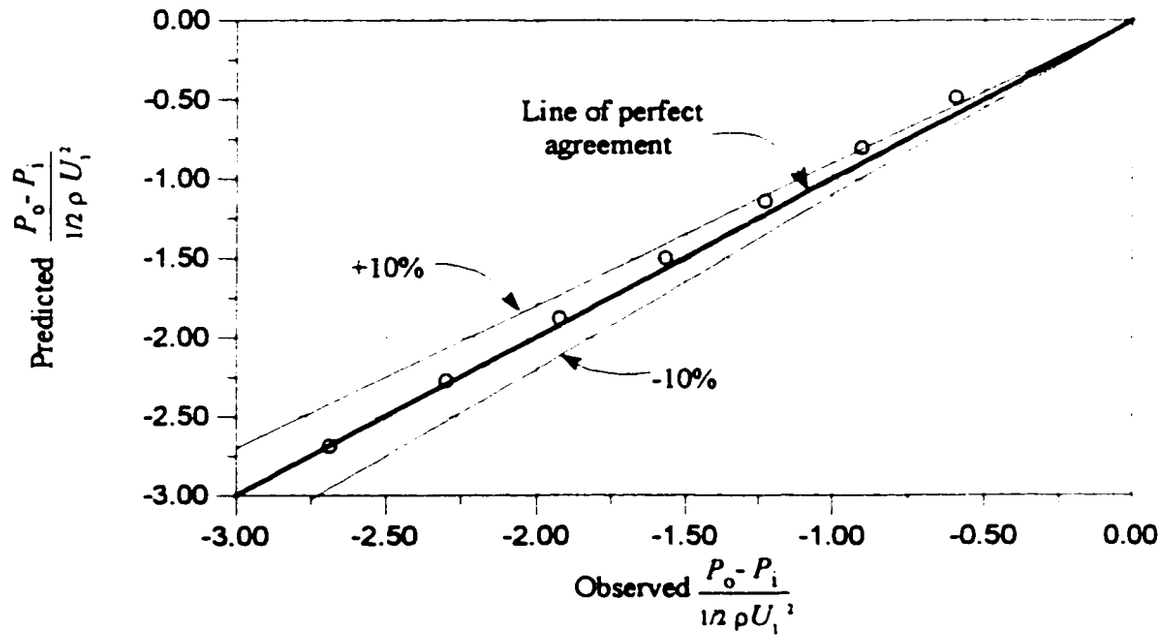

(b) Pressure drop

Figure D.3- Predicted vs. observed $\frac{P_o - P_i}{1/2\,\rho U_1^2}$ for L/D=79.8 and $Re_{axi.}$=5495

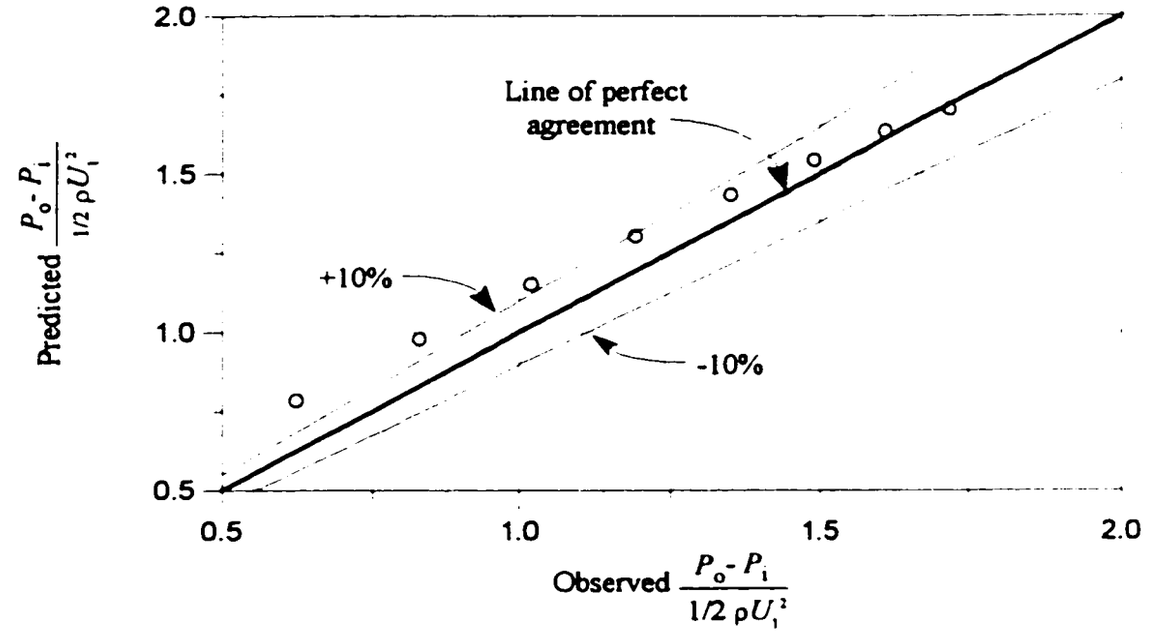

(a) Pressure gain

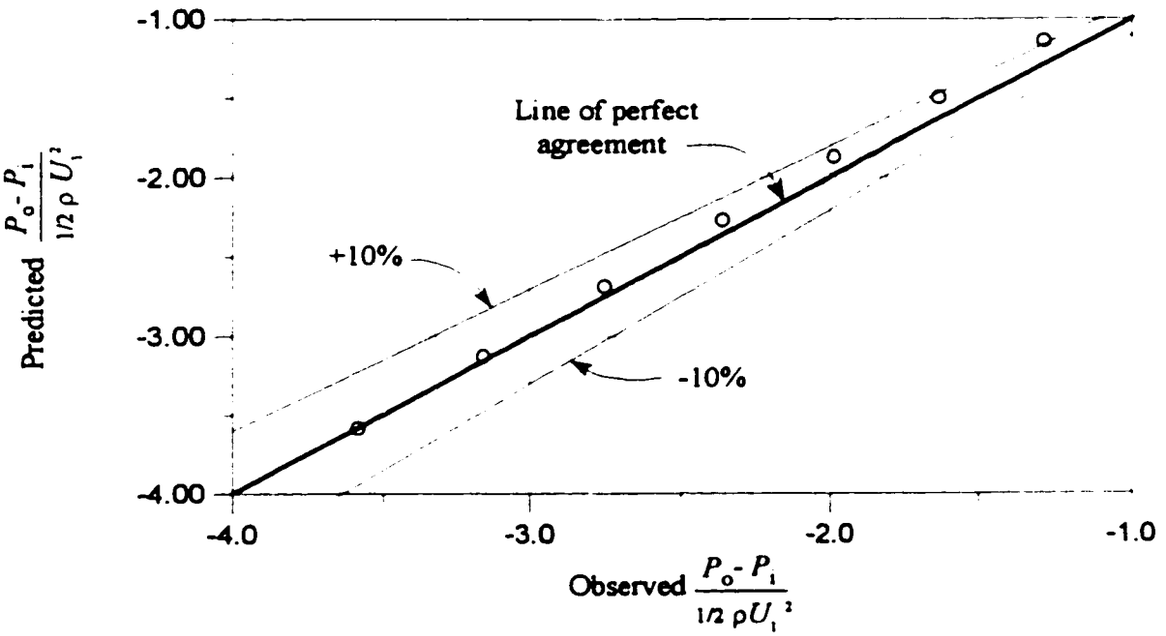

(b) Pressure drop

Figure D.4- Predicted vs. observed $\frac{P_o - P_i}{1/2\,\rho U_1^2}$ for L/D=106.4 and $Re_{axi.}$=5495

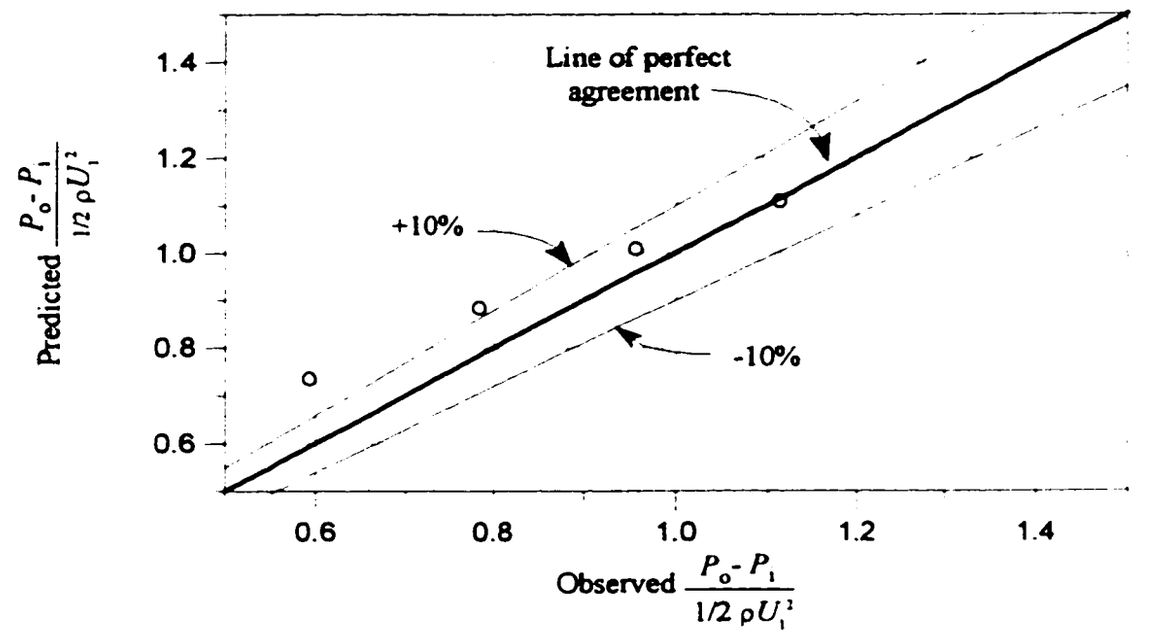

(a) Pressure gain

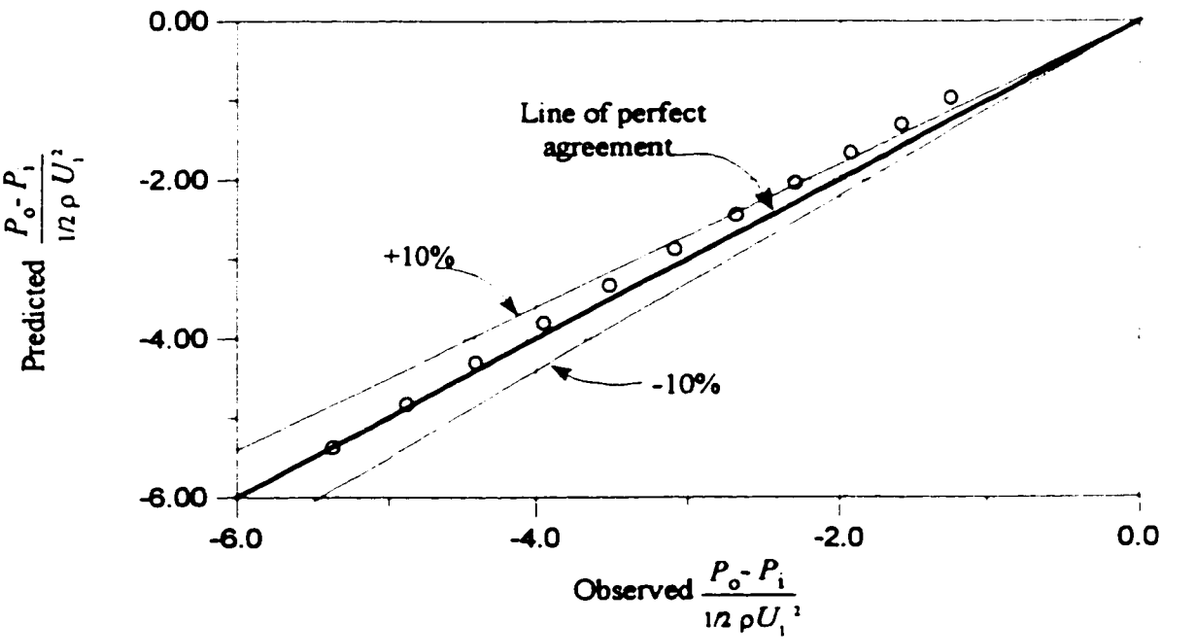

(b) Pressure drop

Figure D.5- Predicted vs. observed $\frac{P_o - P_i}{1/2\,\rho U_1^2}$ for L/D=159.6 and $Re_{axi.}$=5495

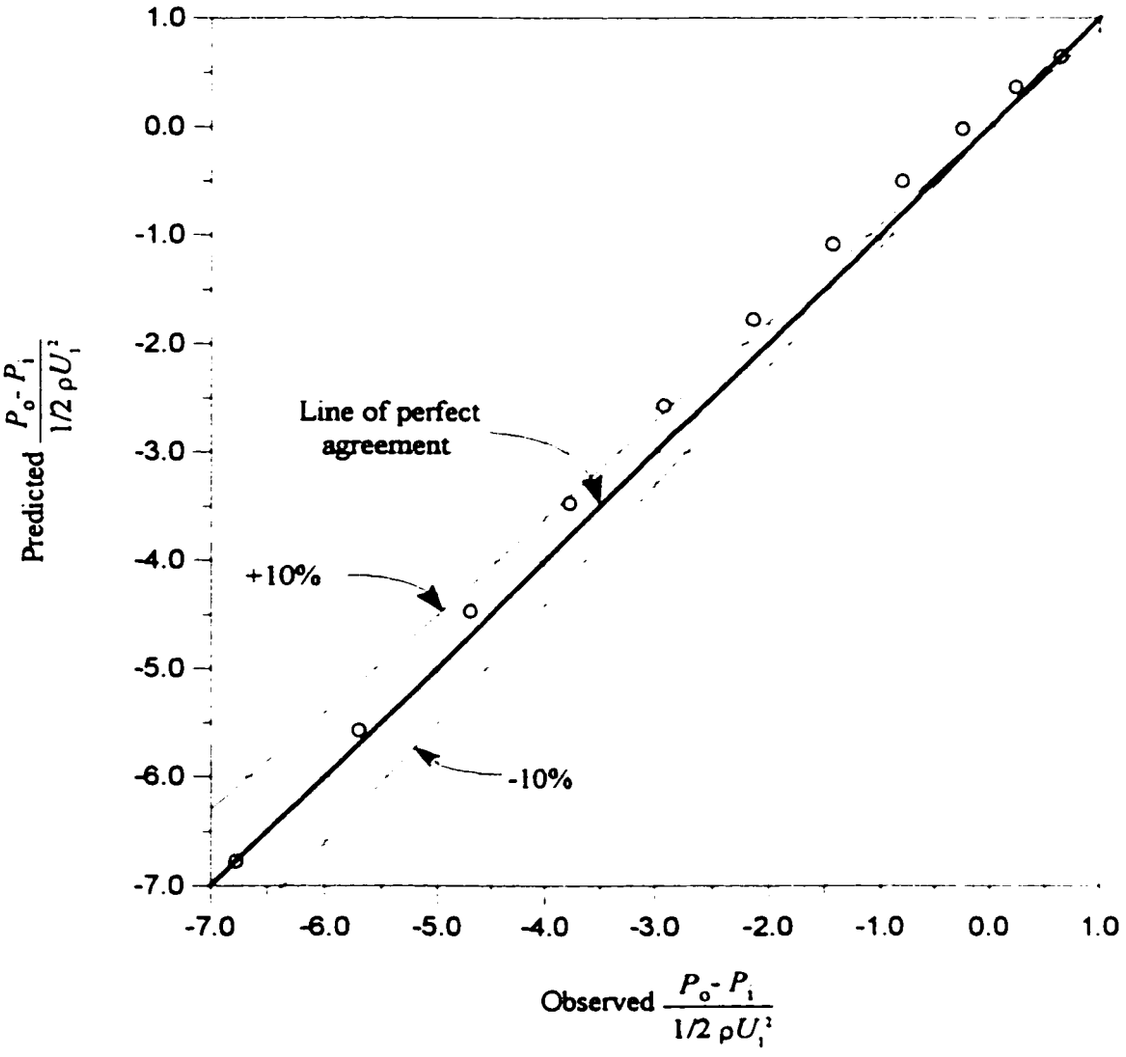

Figure D.6- Predicted vs. observed $\frac{P_o - P_i}{1/2\,\rho U_1^2}$ for L/D=206.6 and Re_{axi}=5495

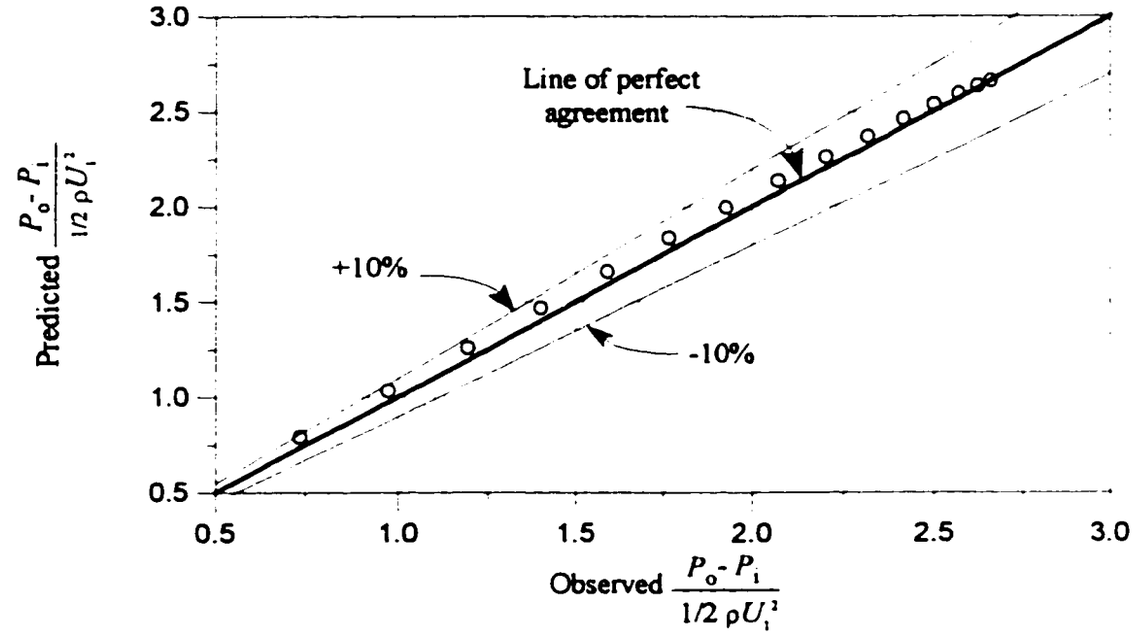

(a) Pressure gain

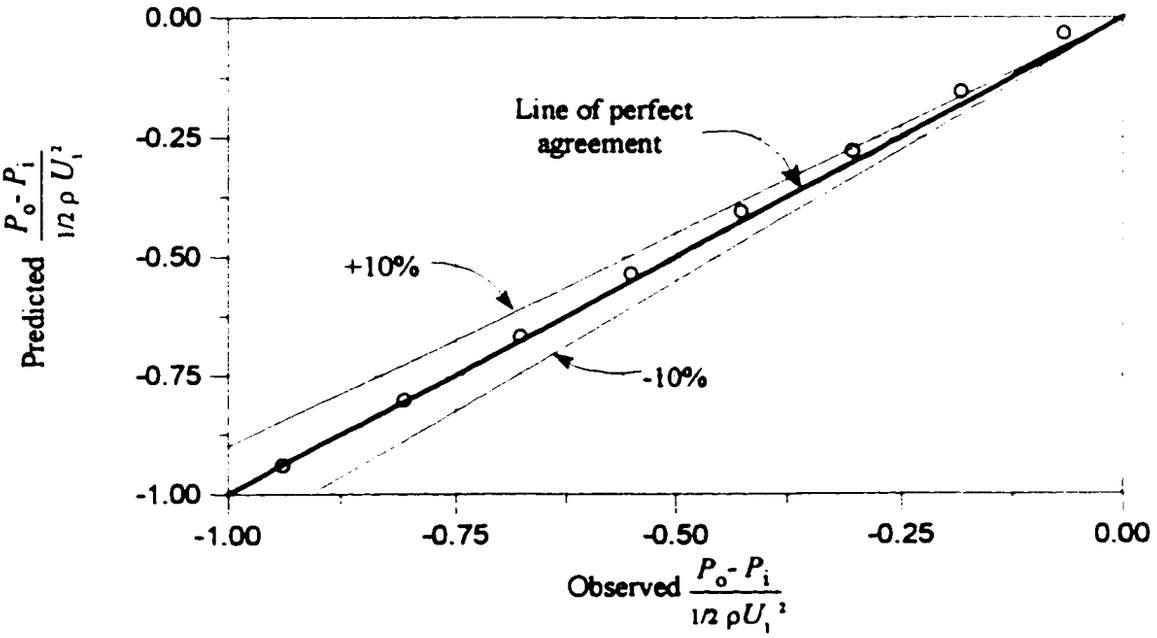

(b) Pressure drop

Figure D.7- Predicted vs. observed $\frac{P_o - P_i}{1/2\,\rho U_1^2}$ for L/D=26.6 and $Re_{axi.}$=7559

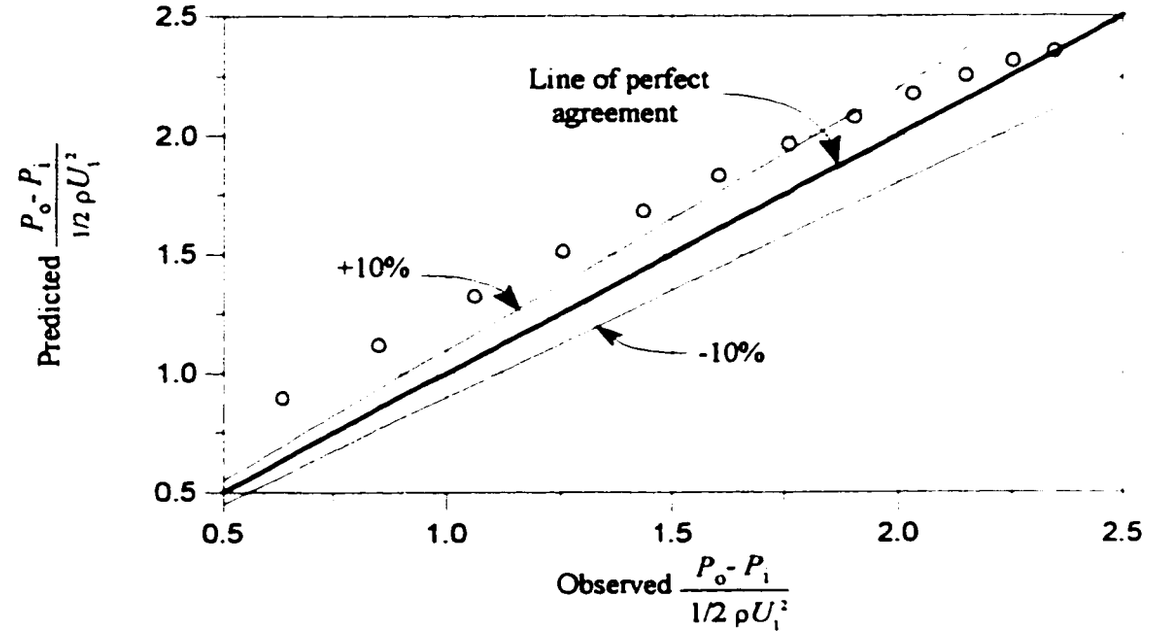

(a) Pressure gain

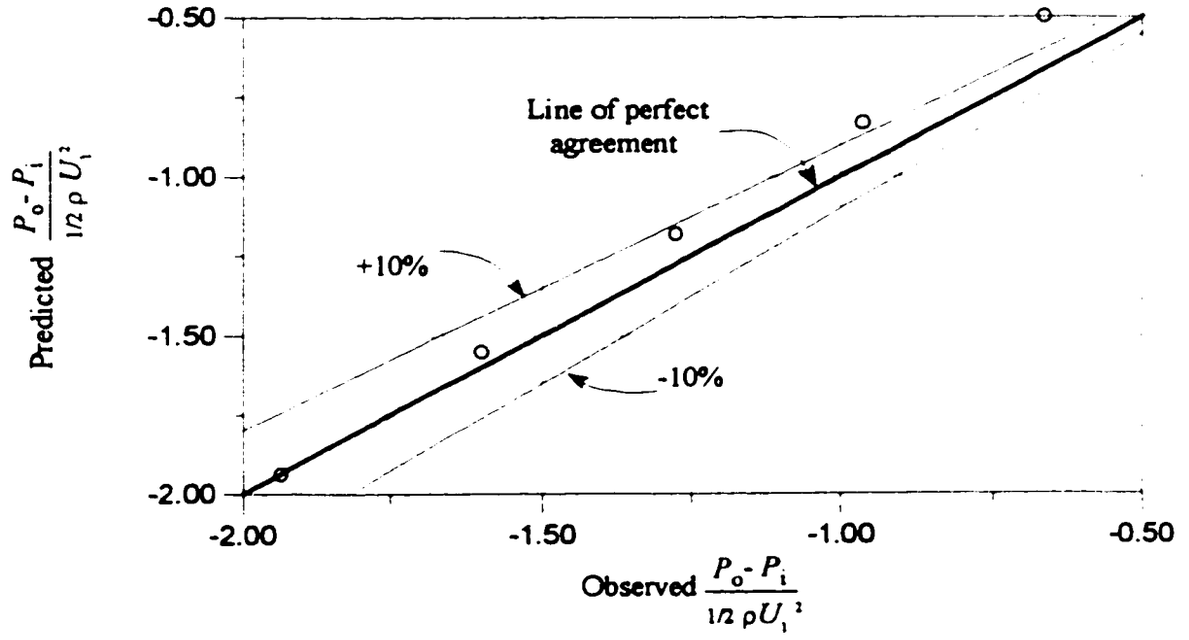

(b) Pressure drop

Figure D.8- Predicted vs. observed $\frac{P_o - P_i}{1/2\,\rho U_i^2}$ for L/D=53.2 and $Re_{axi.}$=7559

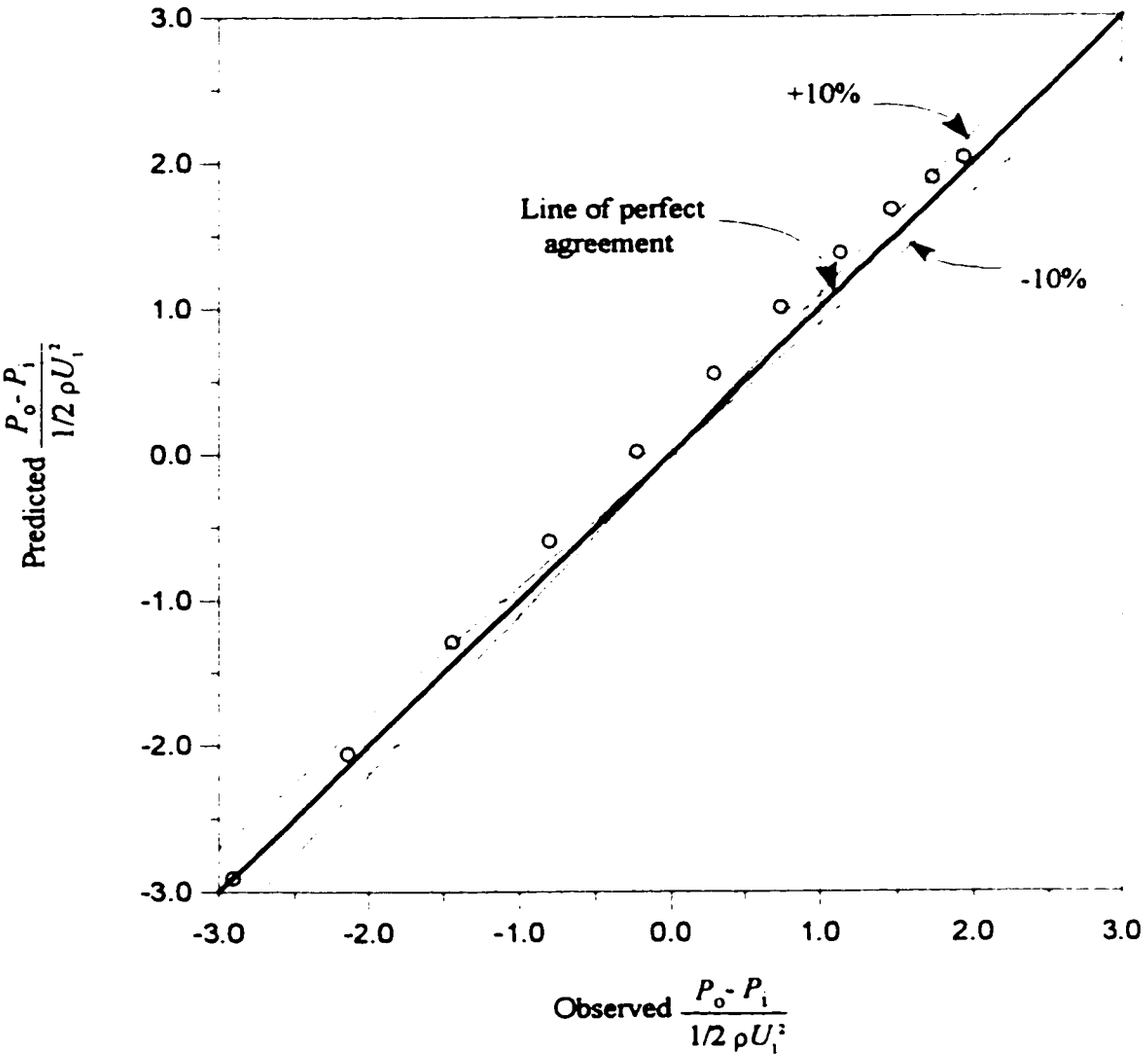

Figure D.9- Predicted vs. observed $\frac{P_o - P_i}{1/2\,\rho U_1^2}$ for L/D=79.8 and $Re_{axi.}$=7559

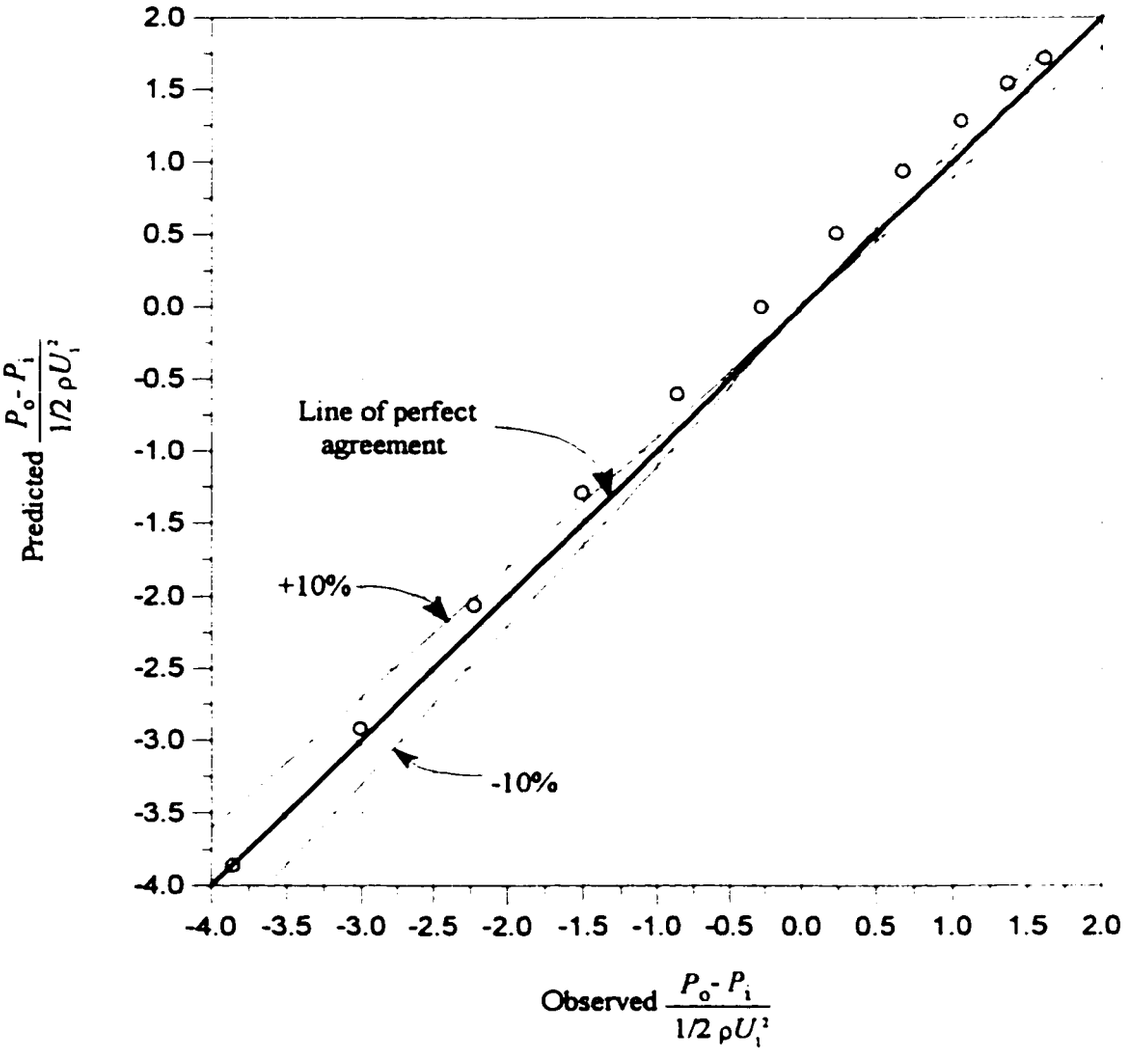

FigureD.10- Predicted vs. observed $\frac{P_o - P_i}{1/2\,\rho U_i^2}$ for L/D=106.4 and $Re_{axi.}$=7559

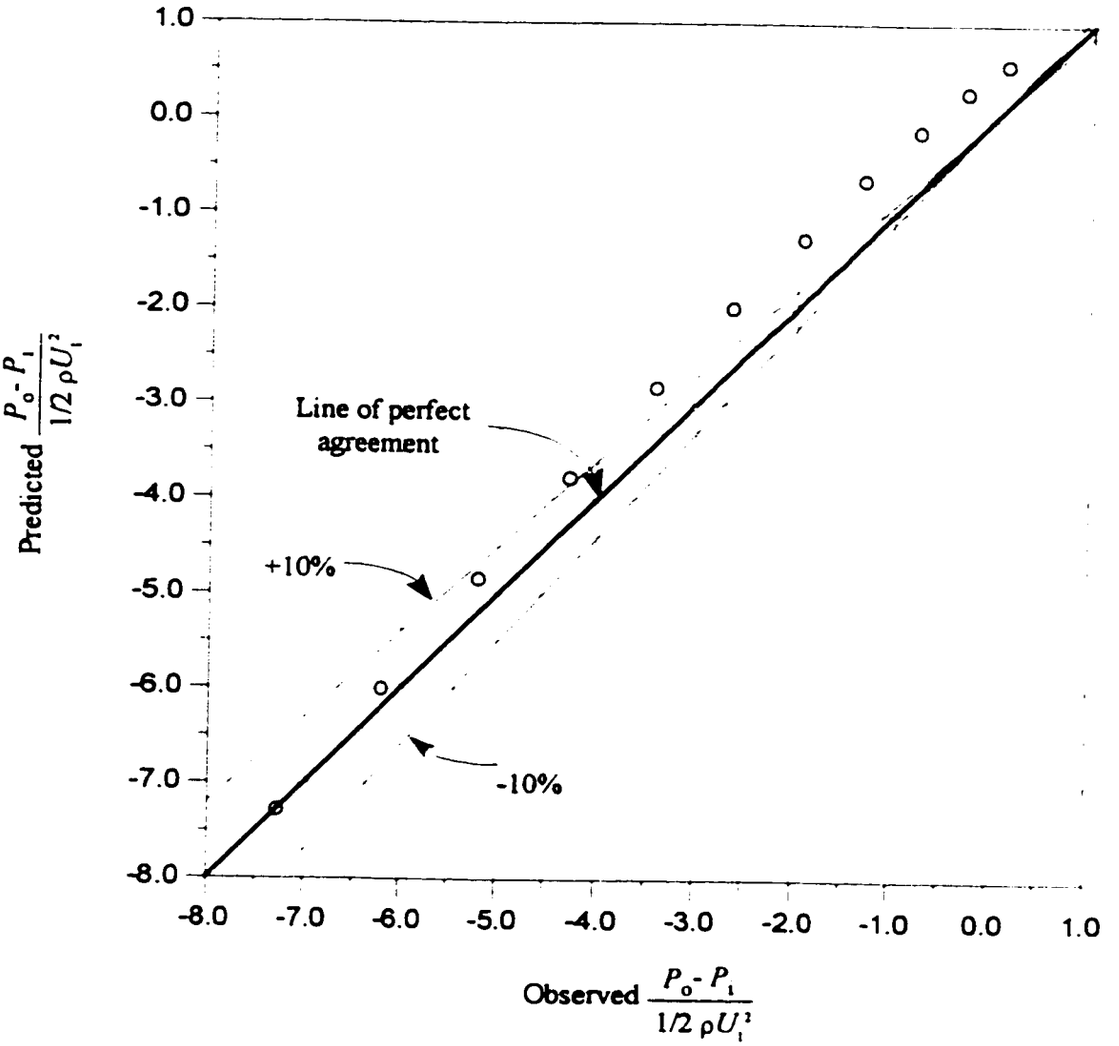

Figure D.11- Predicted vs. observed $\frac{P_o - P_i}{1/2\,\rho U_i^2}$ for L/D=159.6 and $Re_{axi.}$=7559

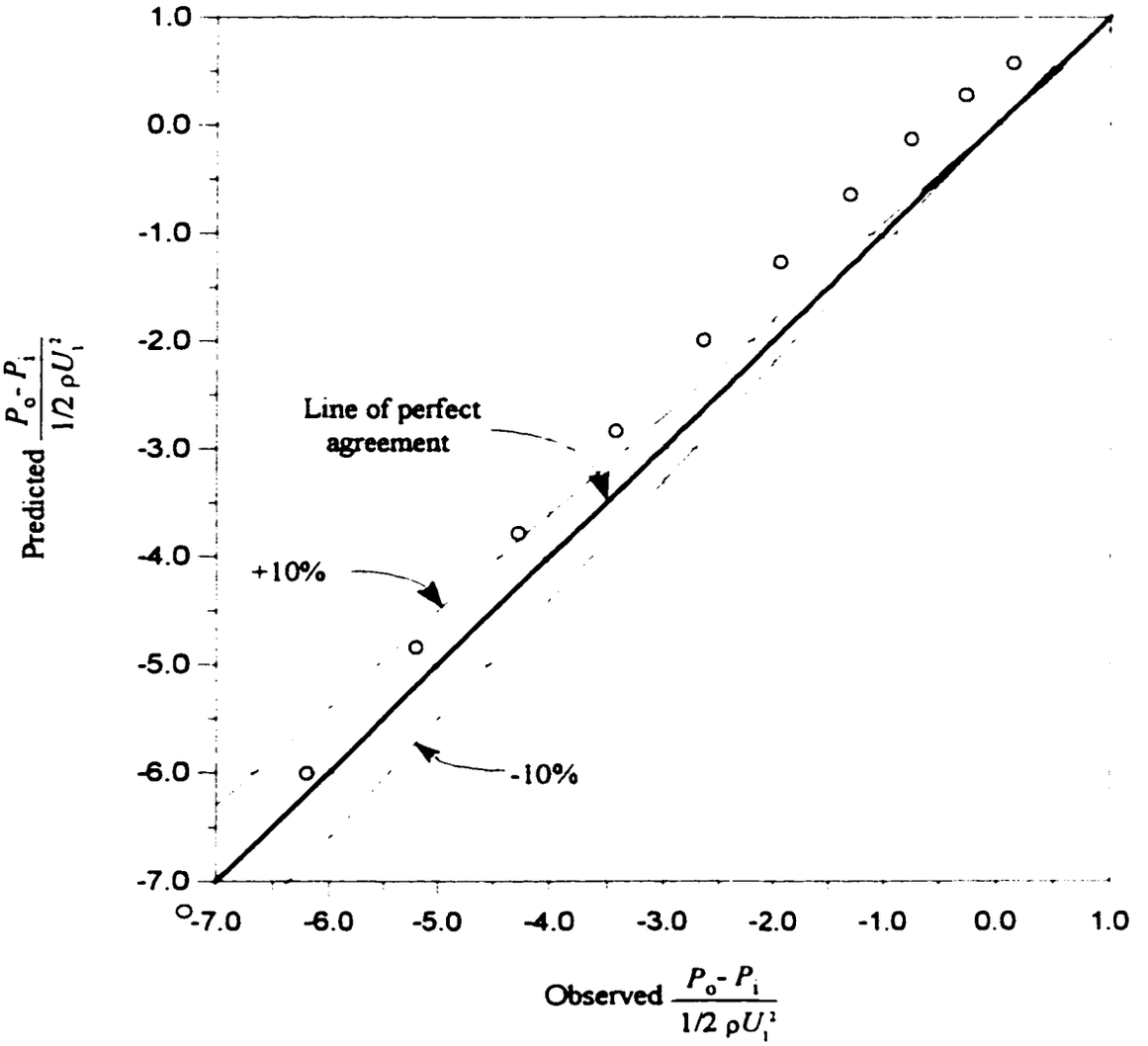

Figure D.12- Predicted vs. observed $\frac{P_o - P_i}{1/2\,\rho U_i^2}$ for L/D=206.6 and $Re_{axi.}$=7559

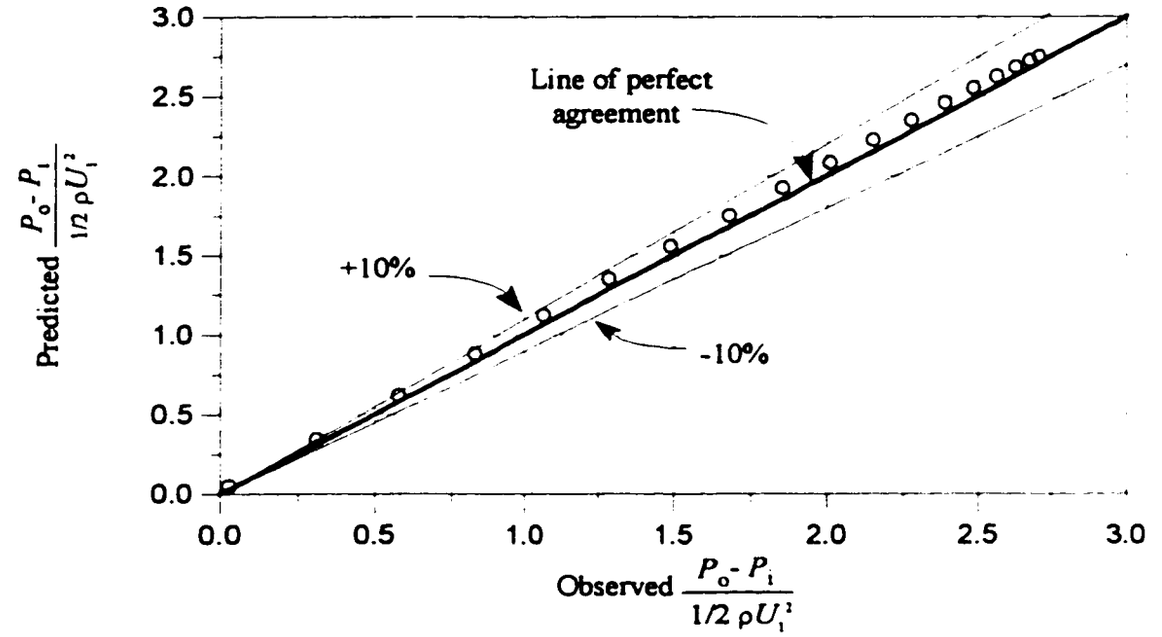

(a) Pressure gain

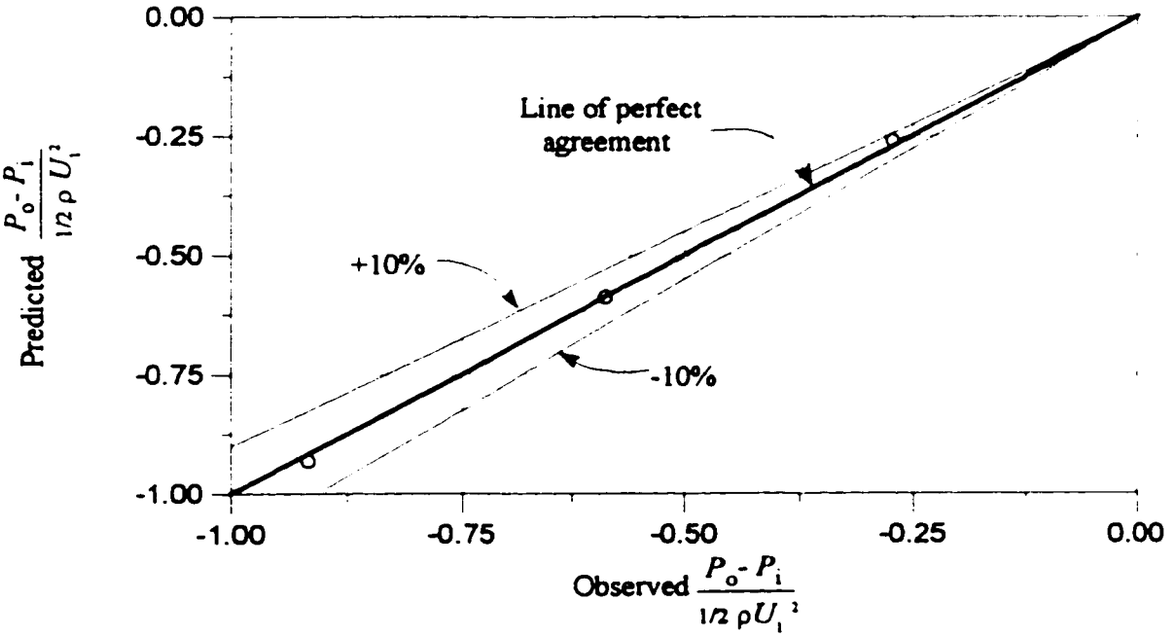

(b) Pressure drop

Figure D.13- Predicted vs. observed $\frac{P_o - P_i}{1/2\,\rho U_1^2}$ for L/D=26.6 and $Re_{axi.}$=9997

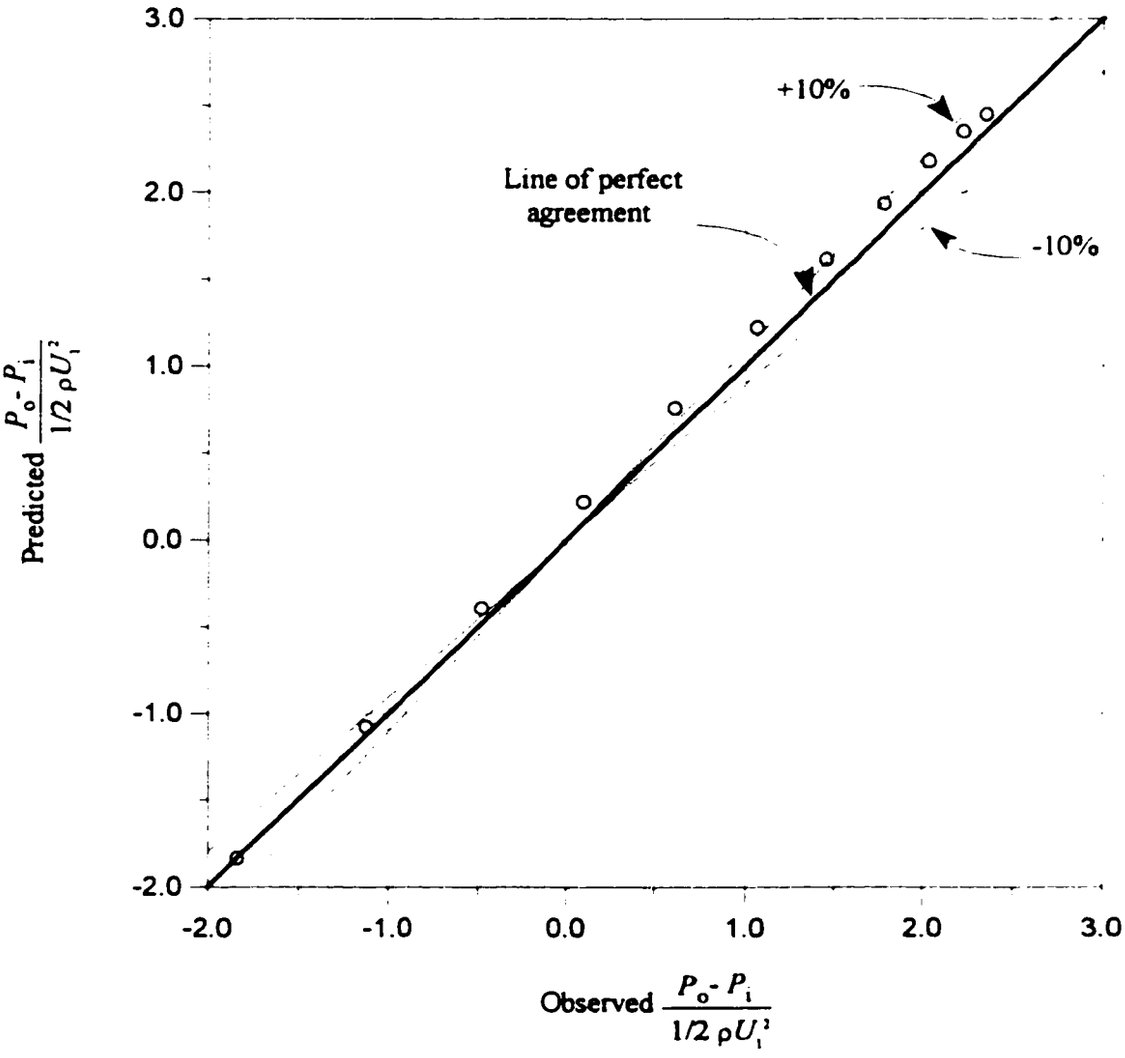

Figure D.14- Predicted vs. observed $\frac{P_o - P_i}{1/2\,\rho U_i^2}$ for L/D=53.2 and $Re_{axi.}$=9997

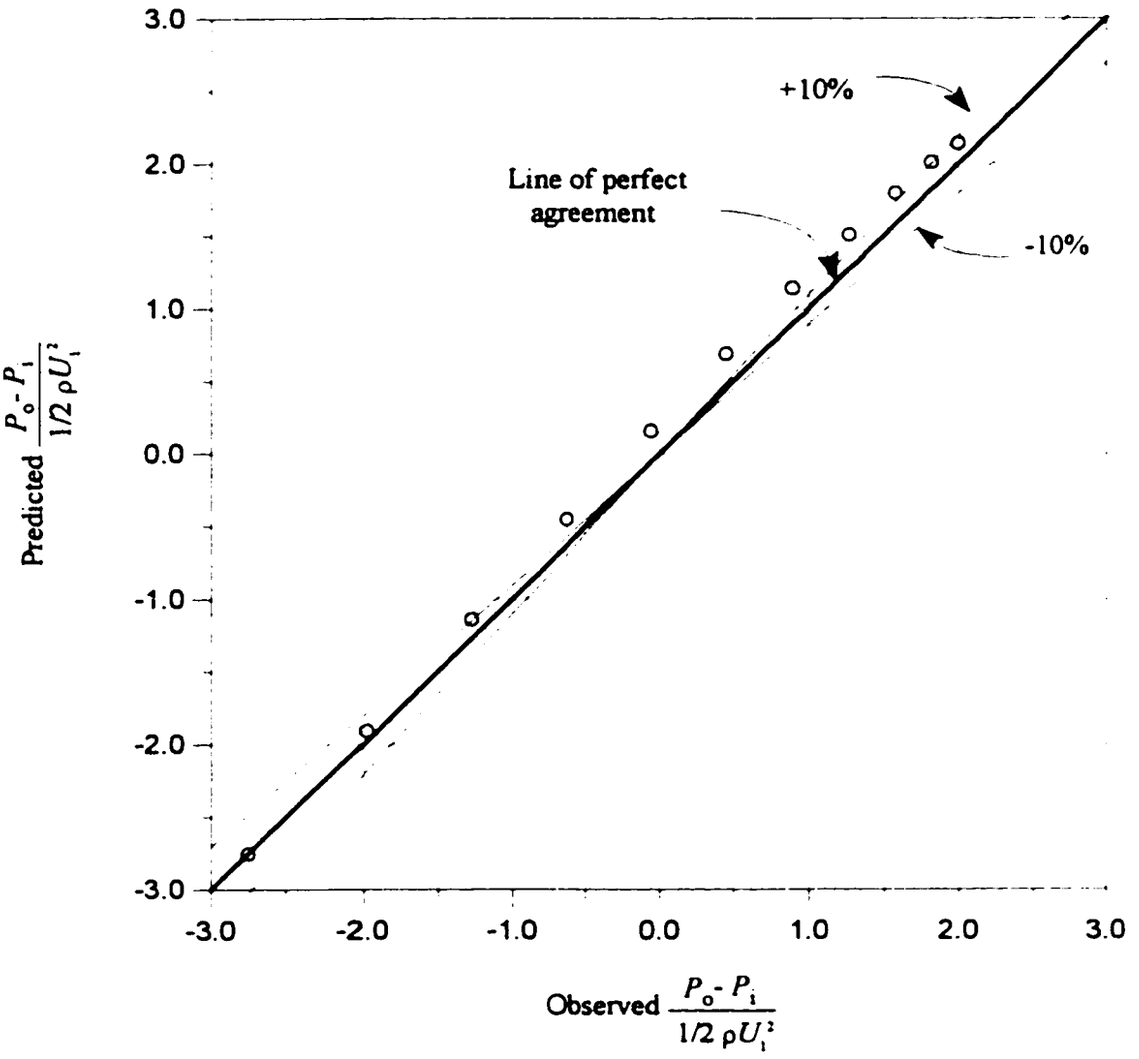

Figure D.15- Predicted vs. observed $\frac{P_o - P_i}{1/2\,\rho U_i^2}$ for L/D=79.6 and $Re_{axi.}$=9997

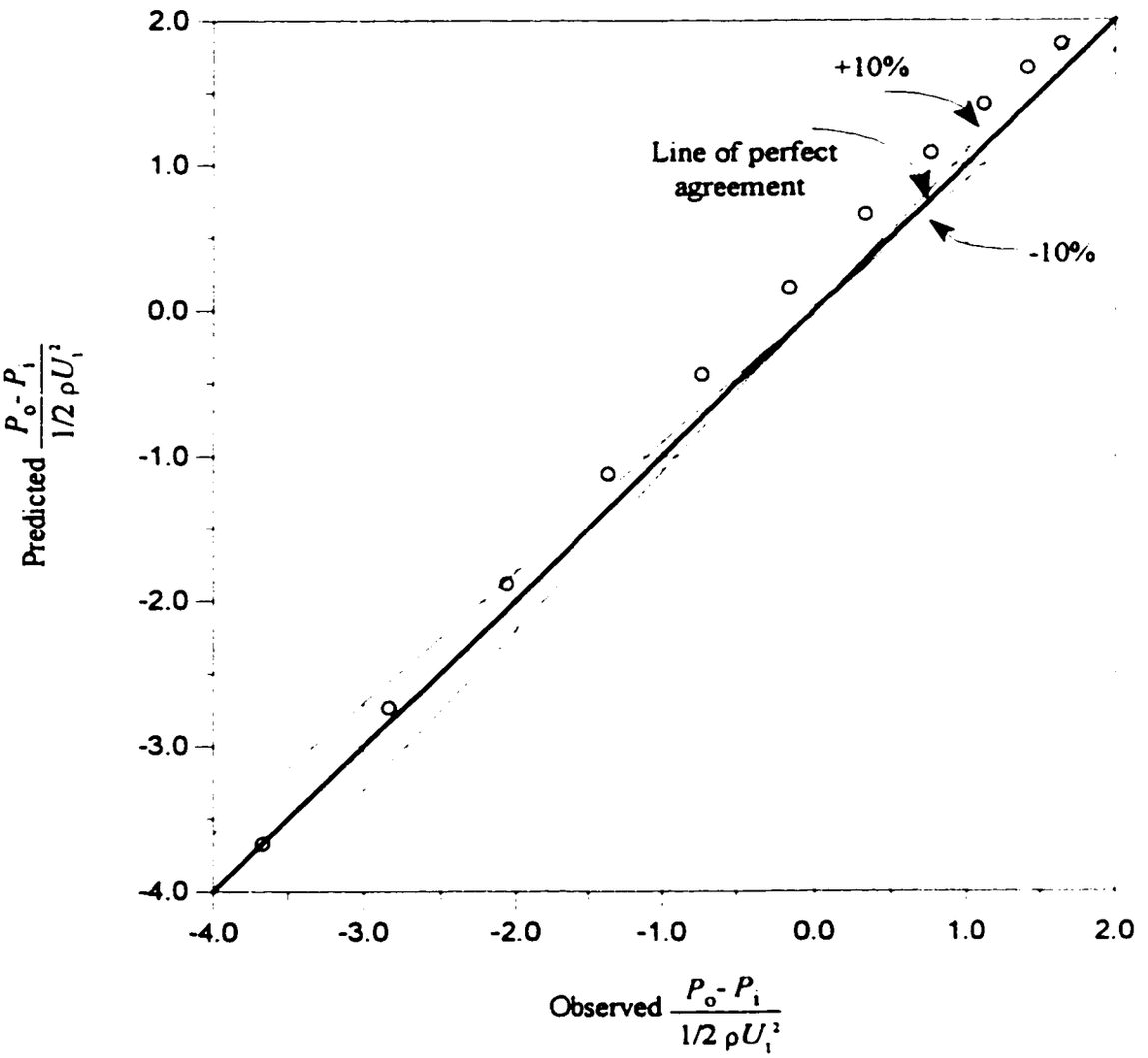

FigureD.16- Predicted vs. observed $\frac{P_o - P_i}{1/2\,\rho U_i^2}$ for L/D=106.4 and $Re_{axi.}$=9997

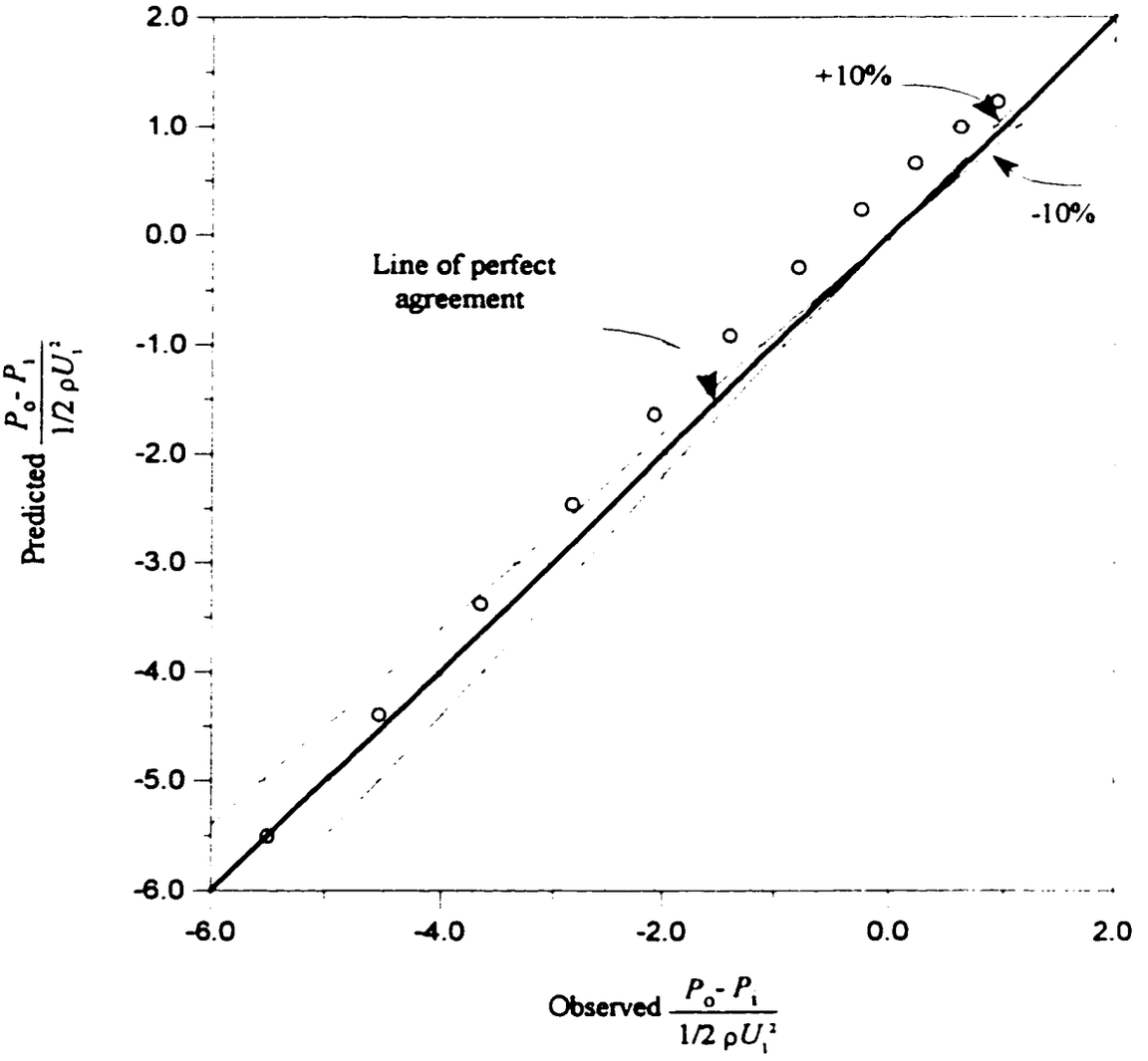

Figure D.17- Predicted vs. observed $\frac{P_o - P_i}{1/2\,\rho U_i^2}$ for L/D=159.6 and $Re_{axi.}$=9997

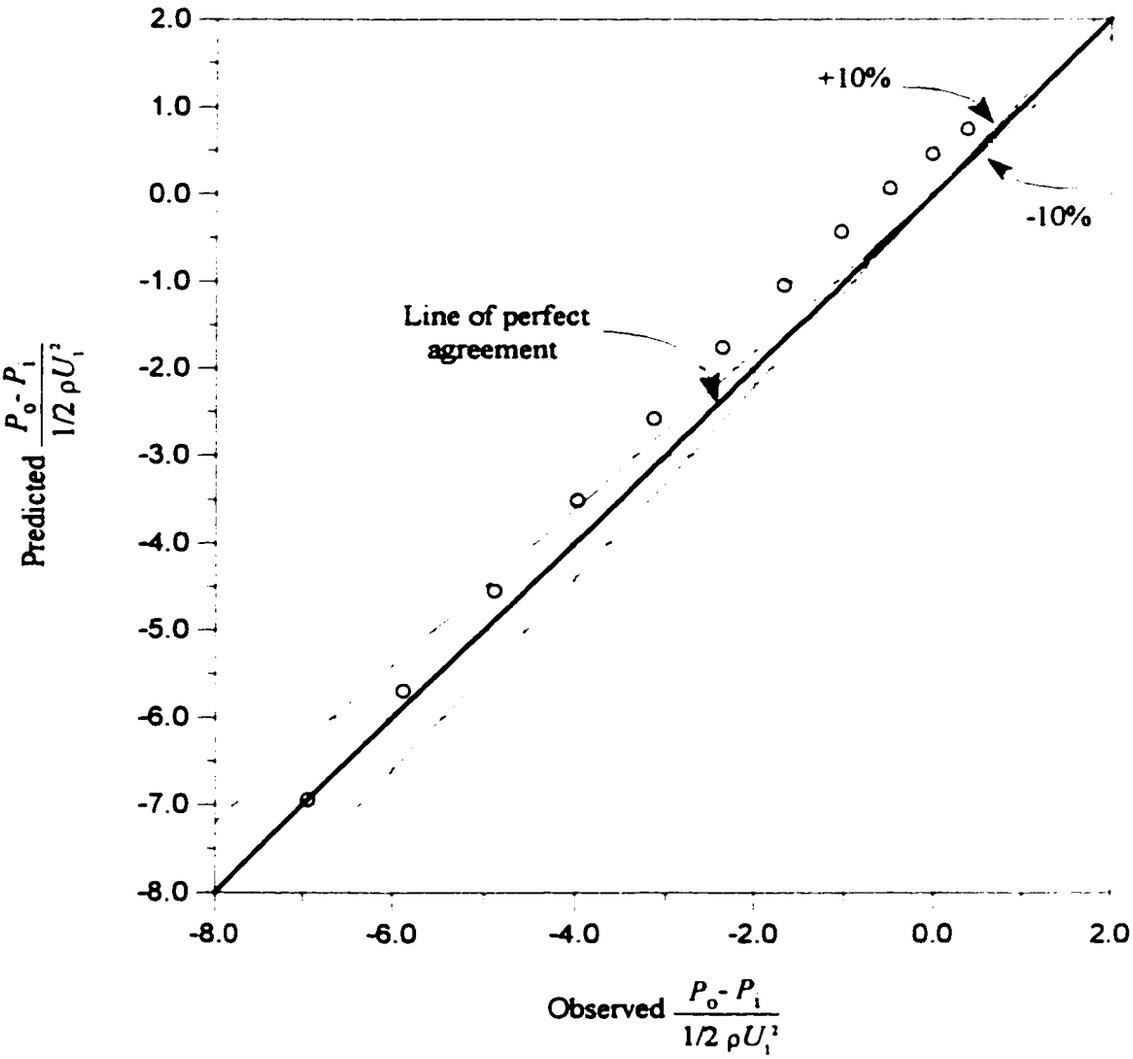

Figure D.18- Predicted vs. observed $\frac{P_o - P_i}{1/2\,\rho U_i^2}$ for L/D=201.24 and $Re_{axi.}$=9997

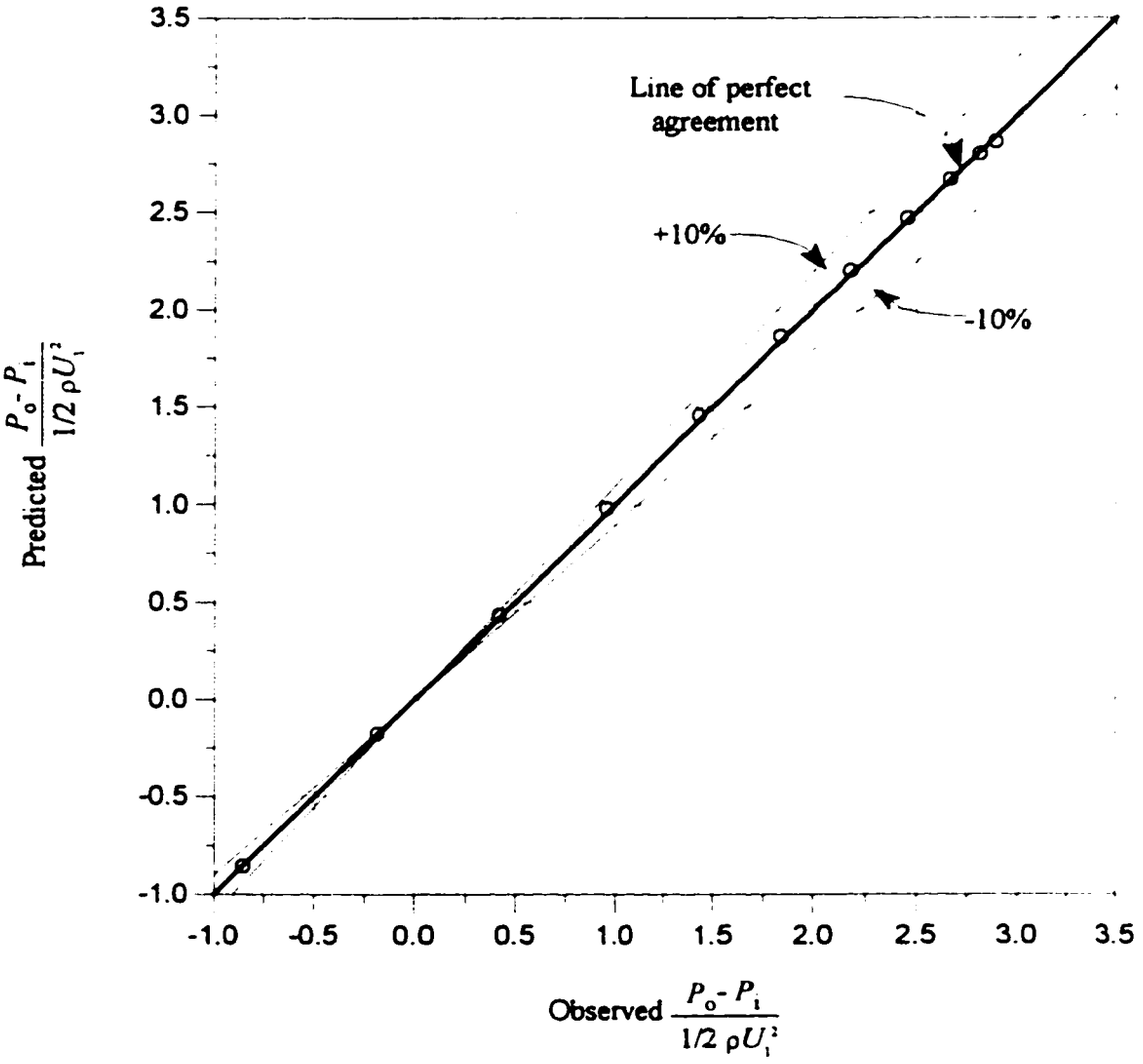

Figure D.19- Predicted vs. observed $\frac{P_o - P_i}{1/2\,\rho U_1^2}$ for L/D=26.6 and $Re_{axi.}$=15222

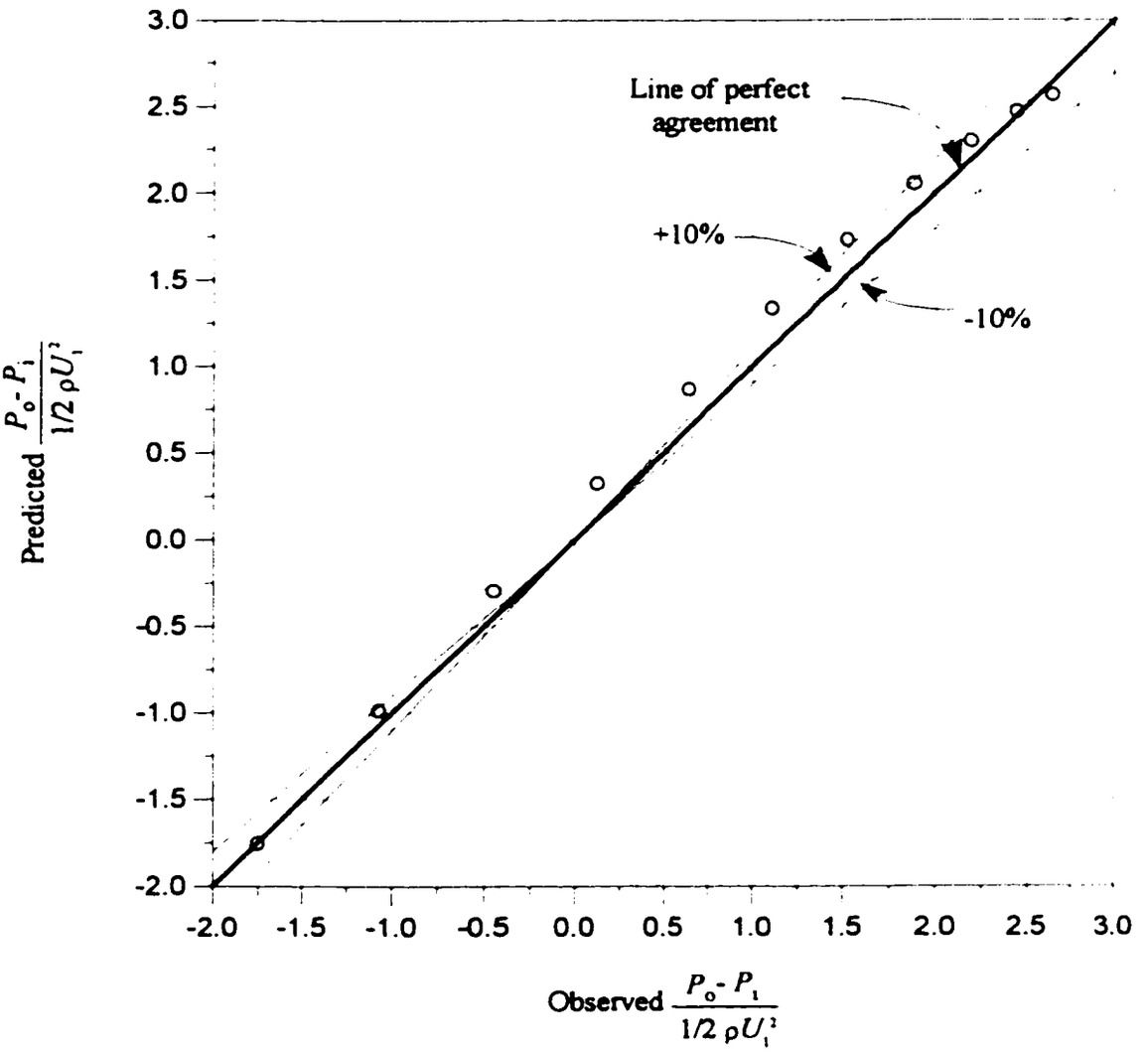

Figure D.20- Predicted vs. observed $\frac{P_o - P_i}{1/2\,\rho U_i^2}$ for L/D=53.2 and $Re_{axi.}$=15222

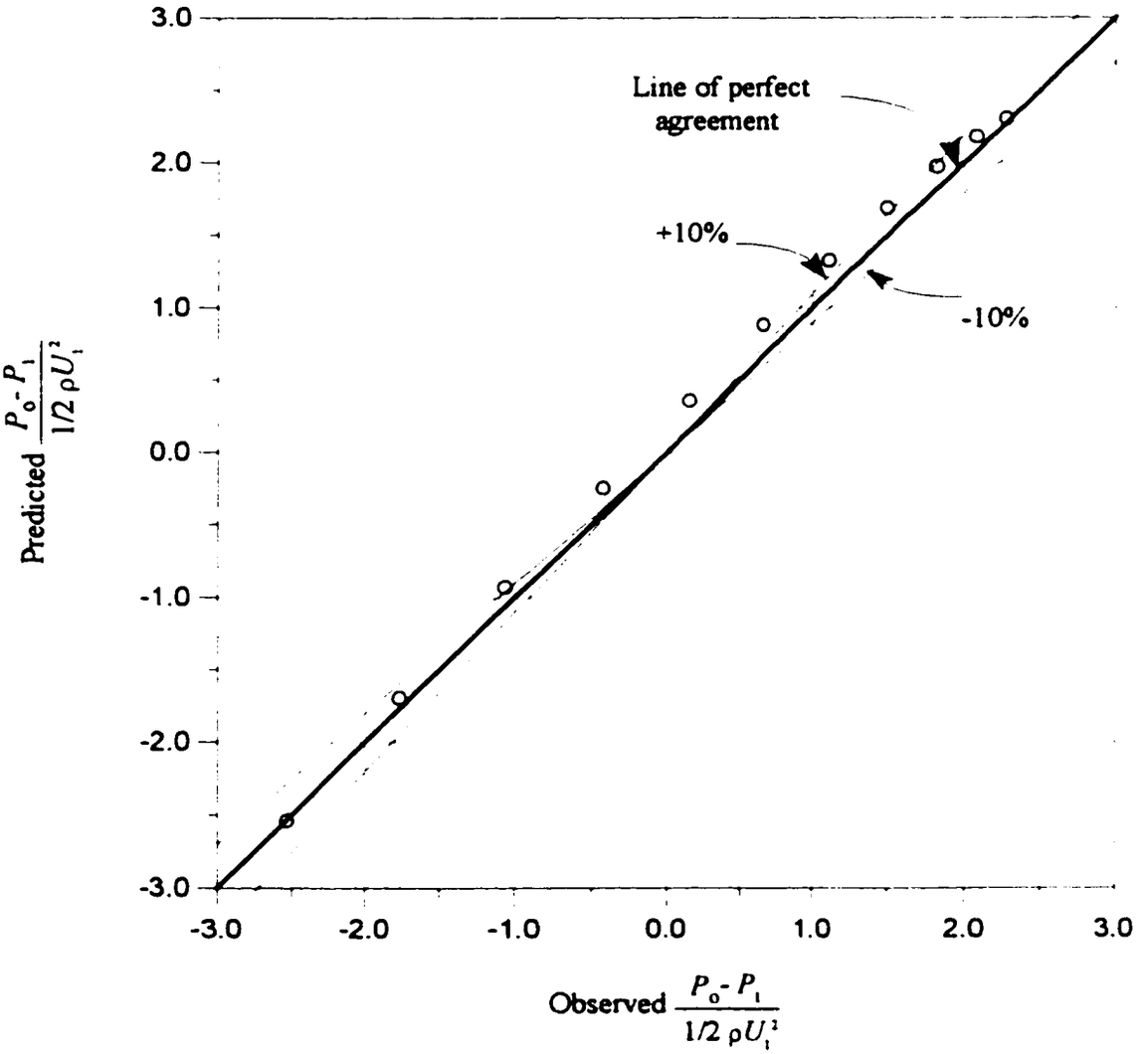

Figure D.21- Predicted vs. observed $\frac{P_o - P_i}{1/2\,\rho U_i^2}$ for L/D=79.8 and $Re_{axi.}$=15222

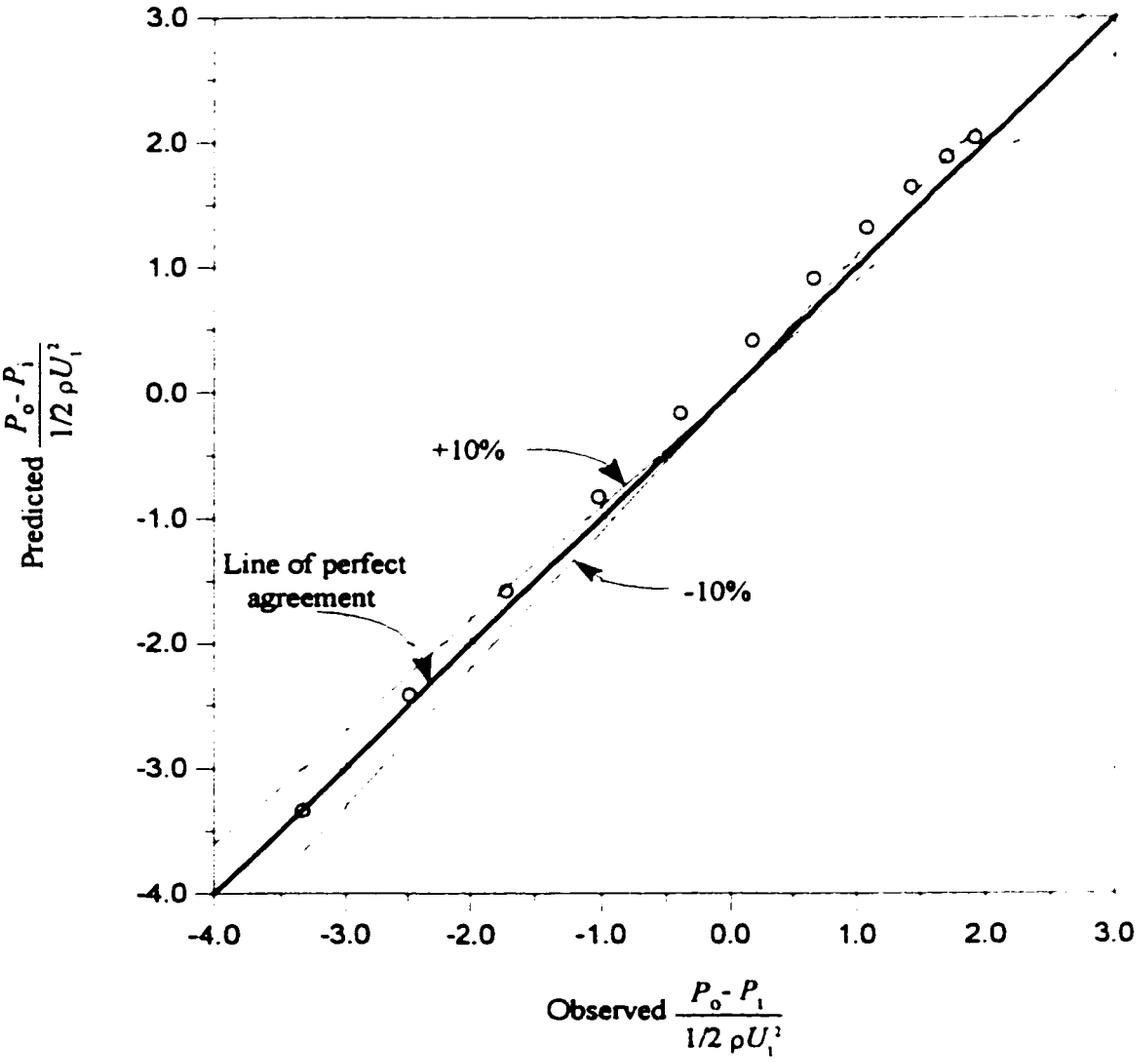

Figure D.22- Predicted vs. observed $\frac{P_o - P_i}{1/2\,\rho U_1^2}$ for L/D=106.4 and $Re_{axi.}$=15222

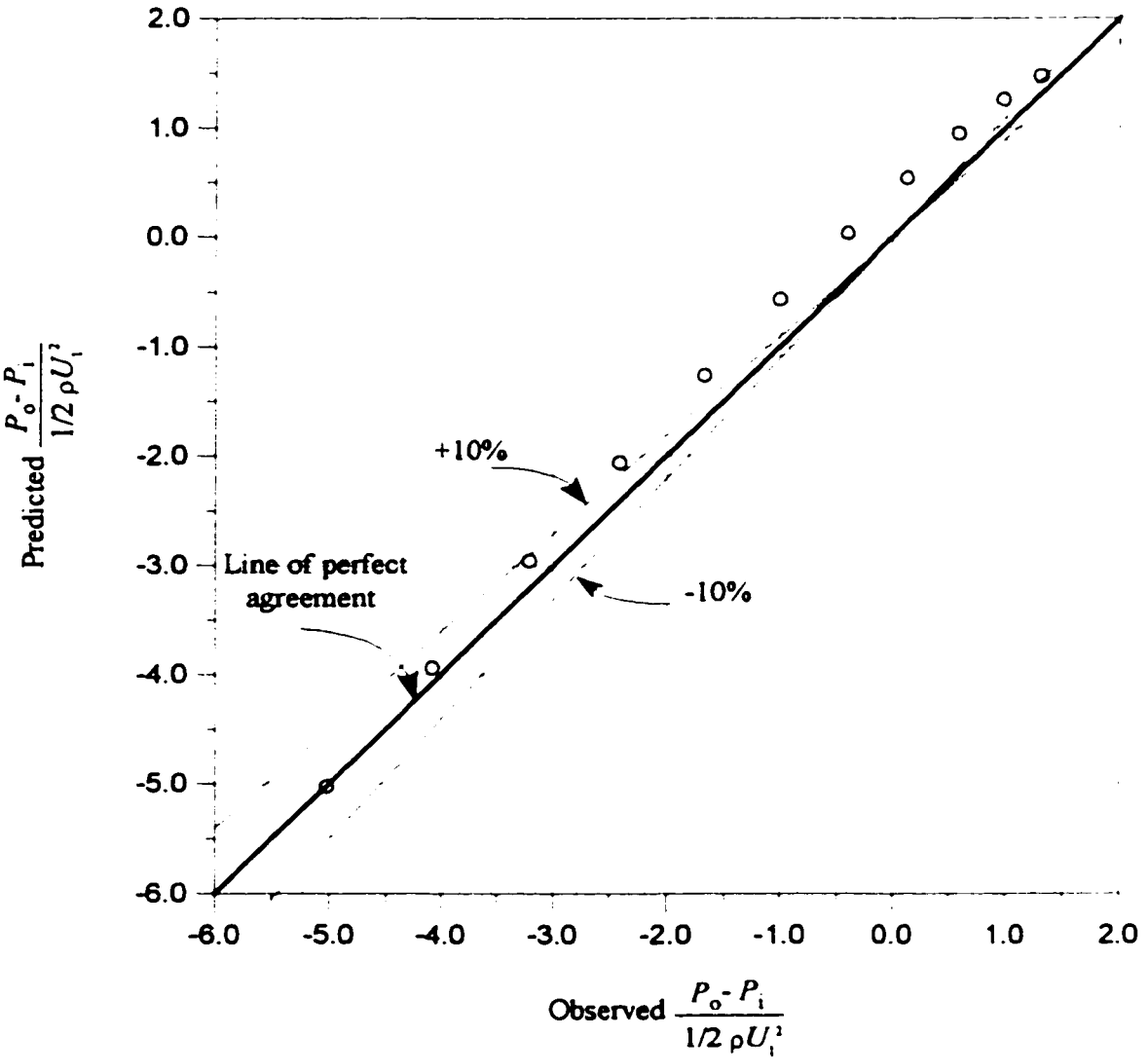

Figure D.23- Predicted vs. observed $\frac{P_o - P_i}{1/2\,\rho U_1^2}$ for L/D=159.6 and $Re_{axi.}$=15222

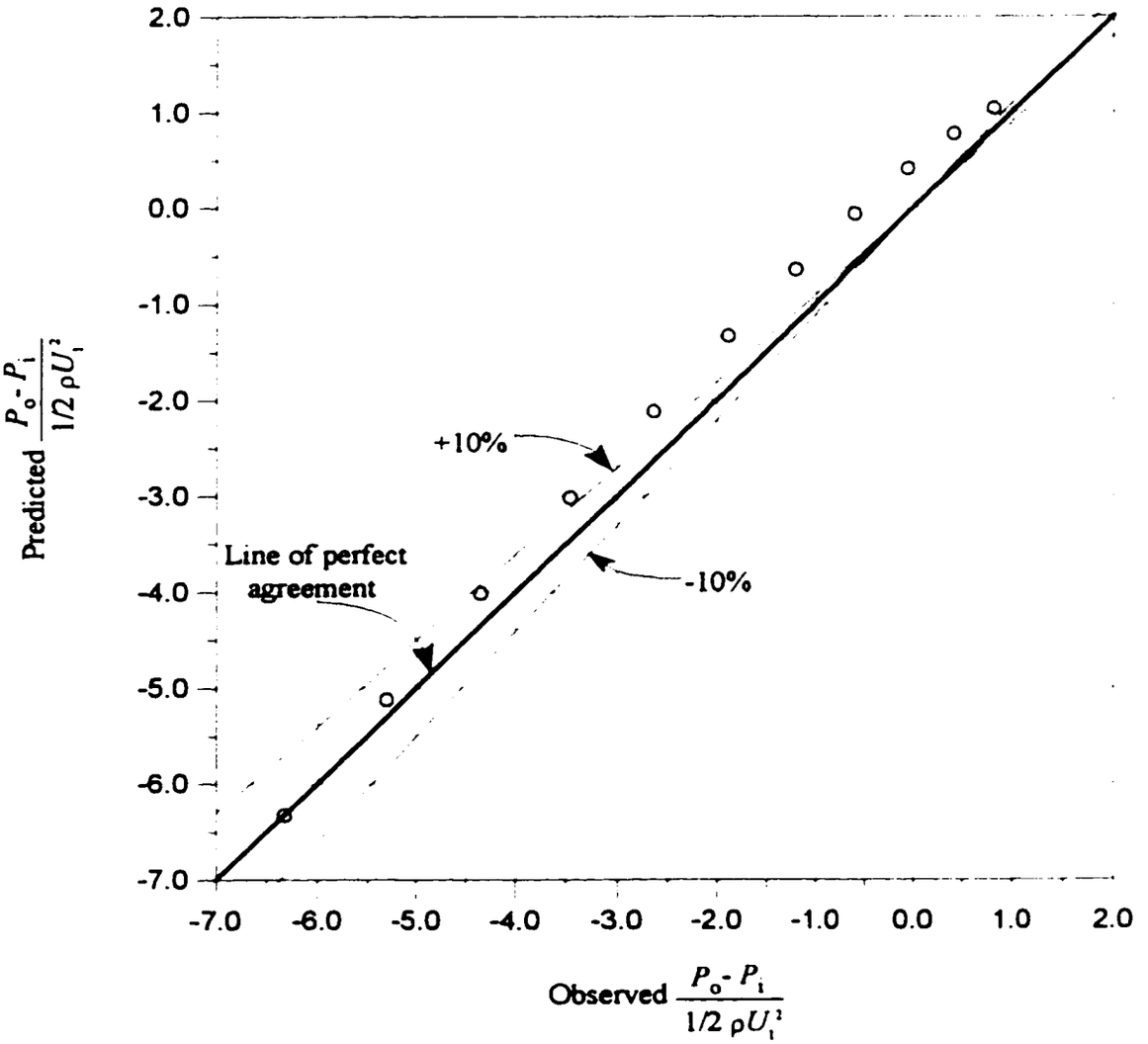

Figure D.24- Predicted vs. observed $\frac{P_o - P_i}{1/2\,\rho U_i^2}$ for L/D=206.6 and $Re_{axi.}$=15222

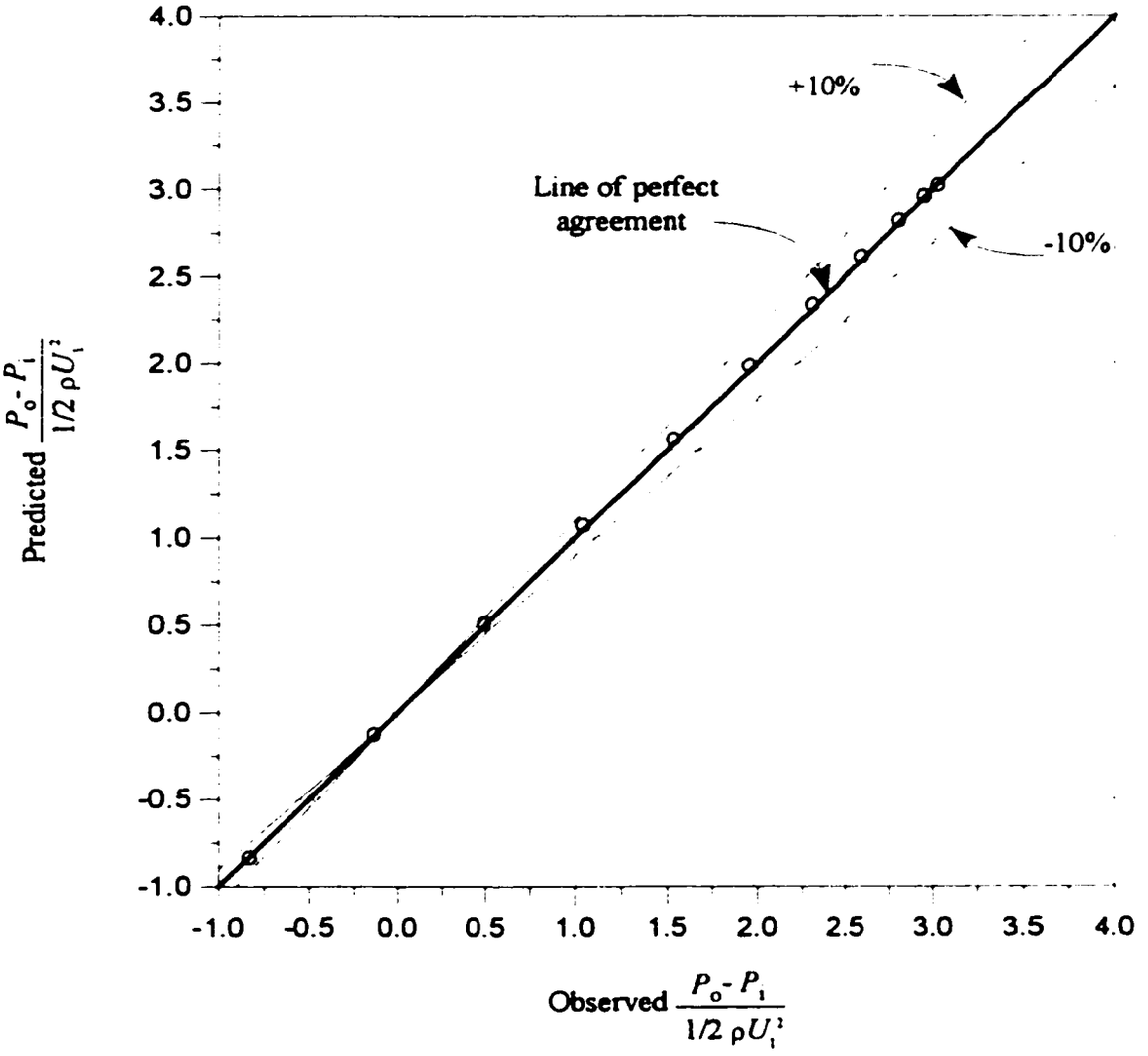

Figure D.25- Predicted vs. observed $\frac{P_o - P_i}{1/2\,\rho U_i^2}$ for L/D=26.6 and $Re_{axi.}$=30,731

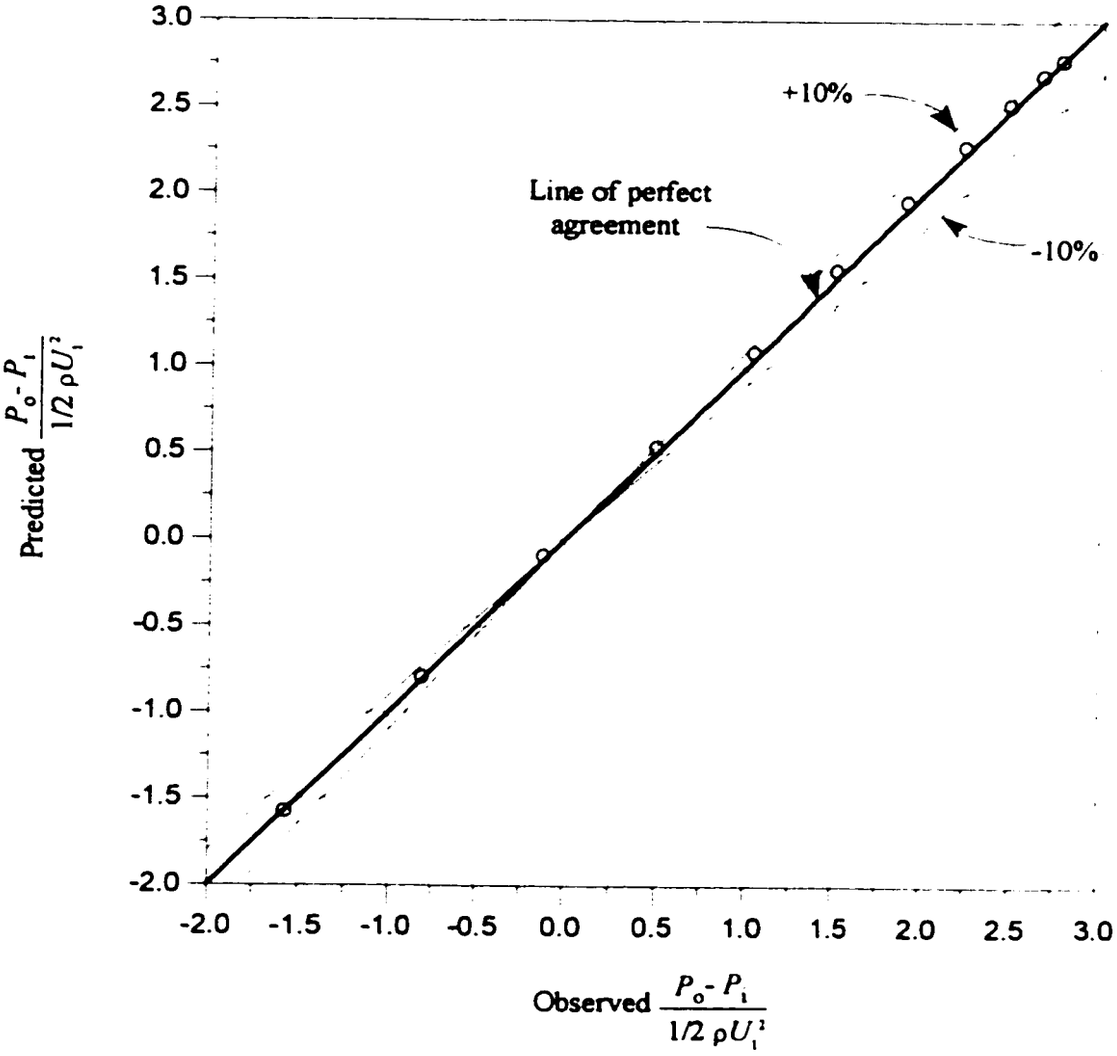

Figure D.26- Predicted vs. observed $\frac{P_o - P_i}{1/2\,\rho U_1^2}$ for L/D=53.2 and $Re_{axi.}$=30,731

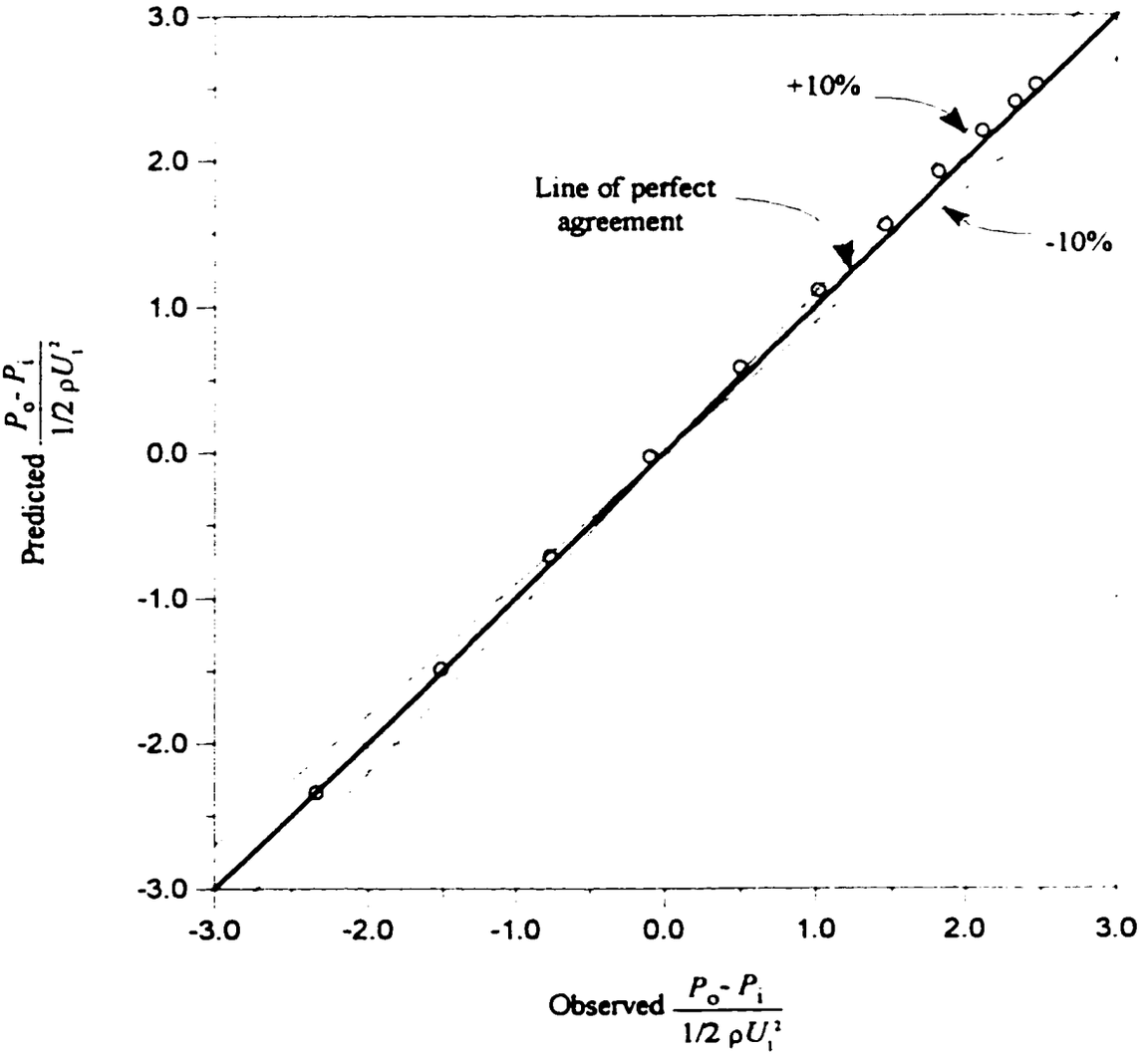

FigureD.27- Predicted vs. observed $\frac{P_o - P_i}{1/2\,\rho U_i^2}$ for L/D=79.8 and Re_{axi}=30,731

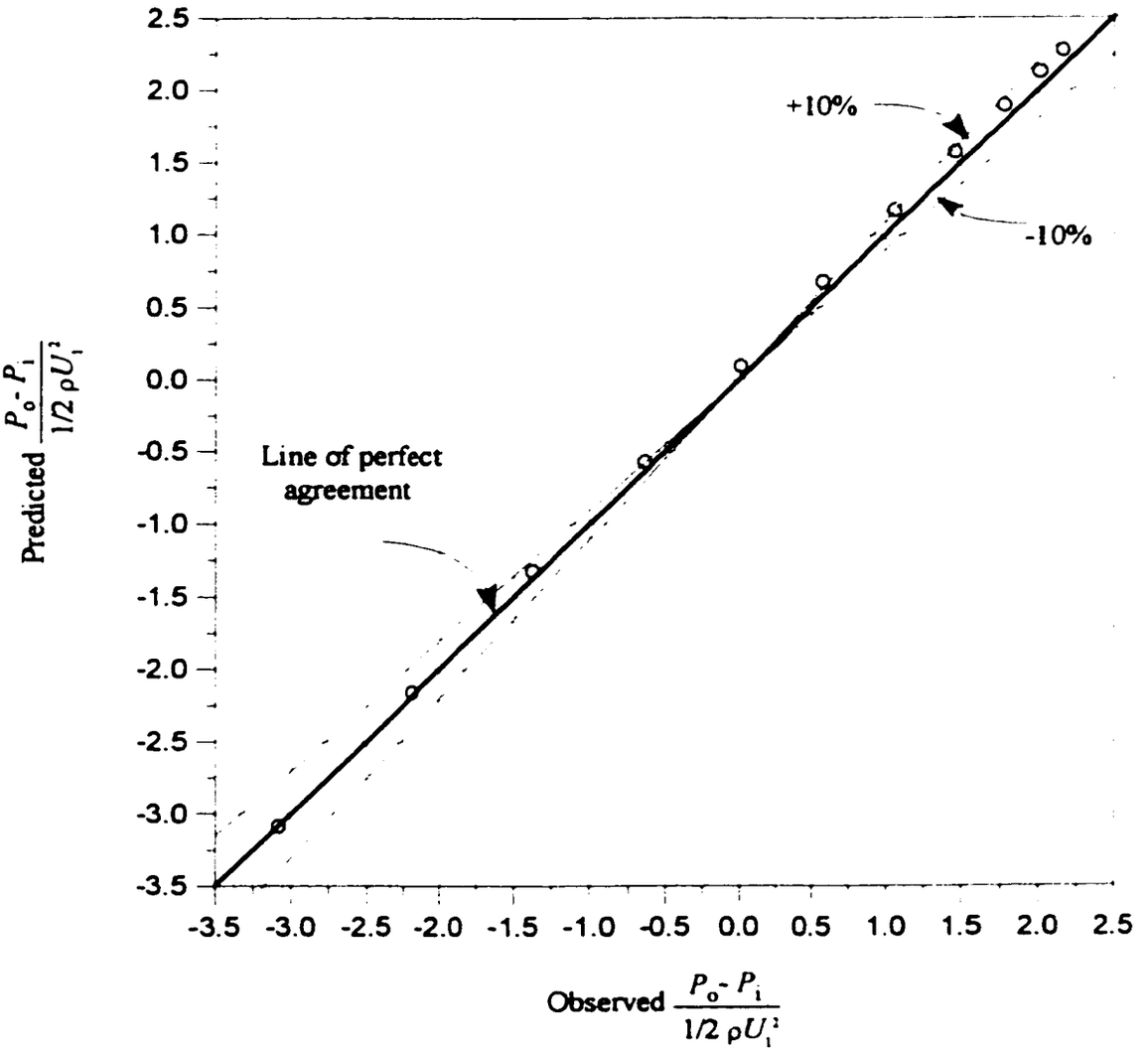

FigureD.28- Predicted vs. observed $\frac{P_o - P_i}{1/2\,\rho U_1^2}$ for L/D=106.4 and $Re_{axi.}$=30,731

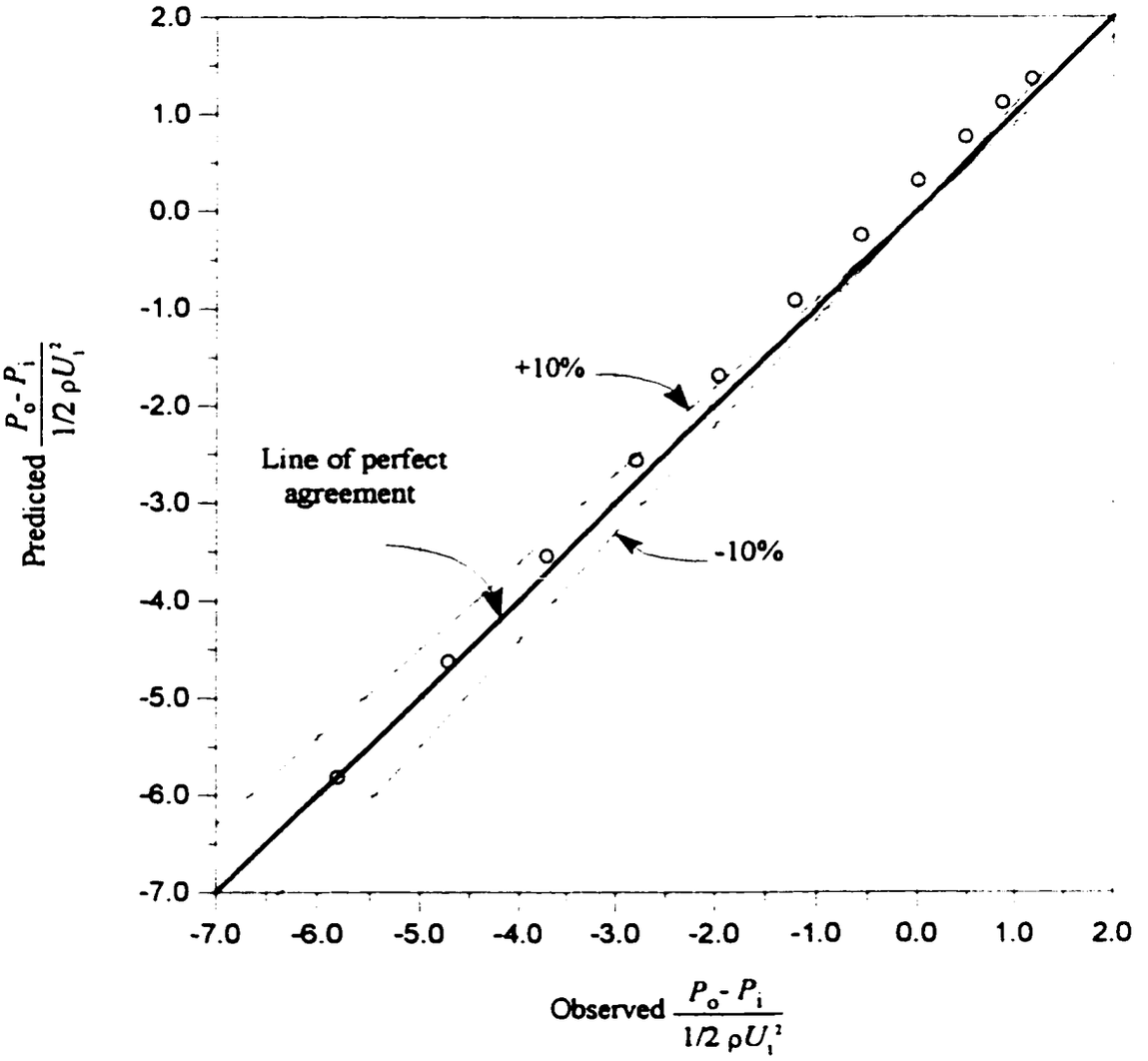

Figure D.29- Predicted vs. observed $\frac{P_o - P_i}{1/2\,\rho U_1^2}$ for L/D=159.6 and $Re_{axi.}$=30,731

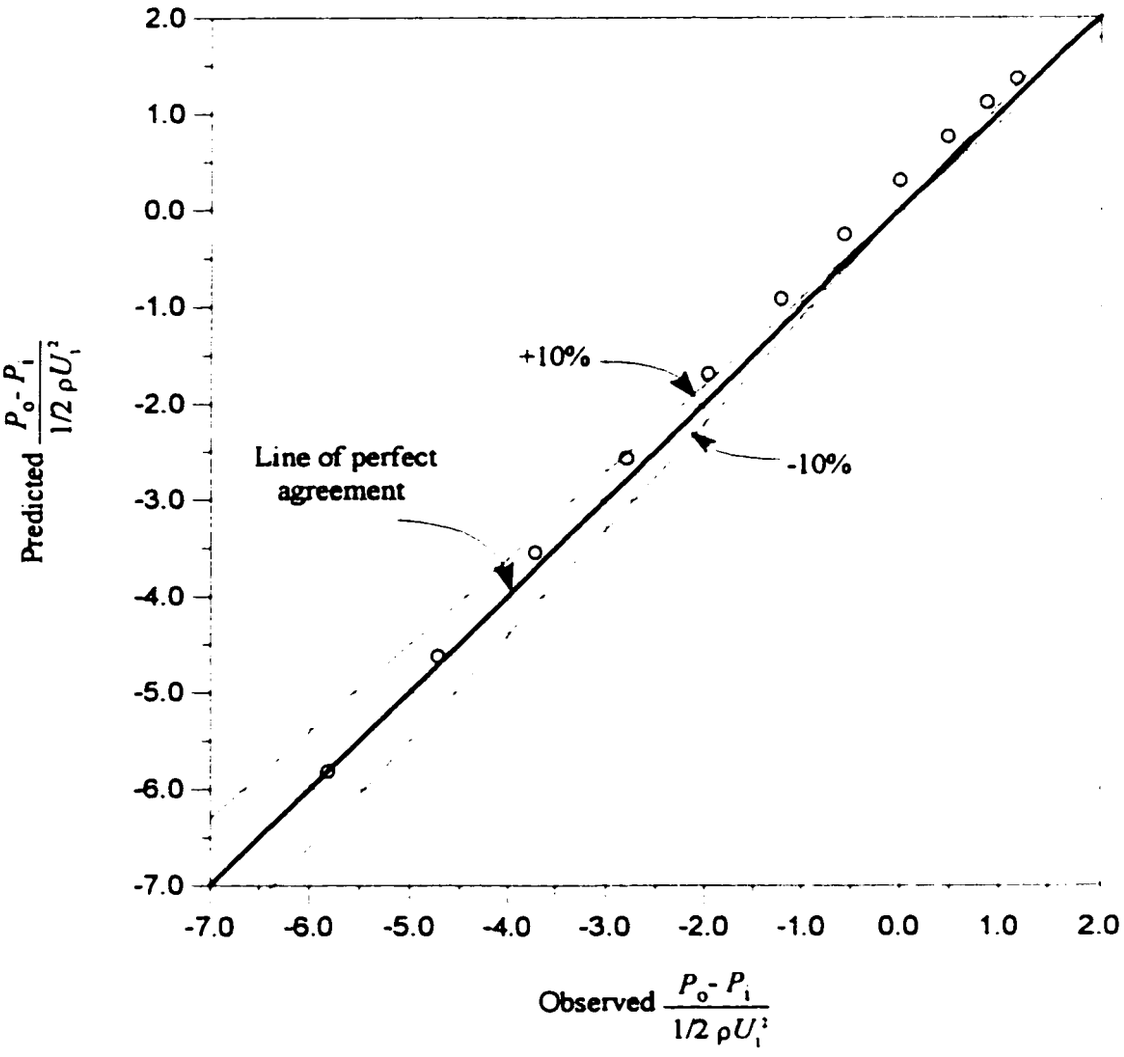

Figure D.30- Predicted vs. observed $\frac{P_o - P_i}{1/2\,\rho U_i^2}$ for L/D=206.6 and $Re_{axi.}$=30,731

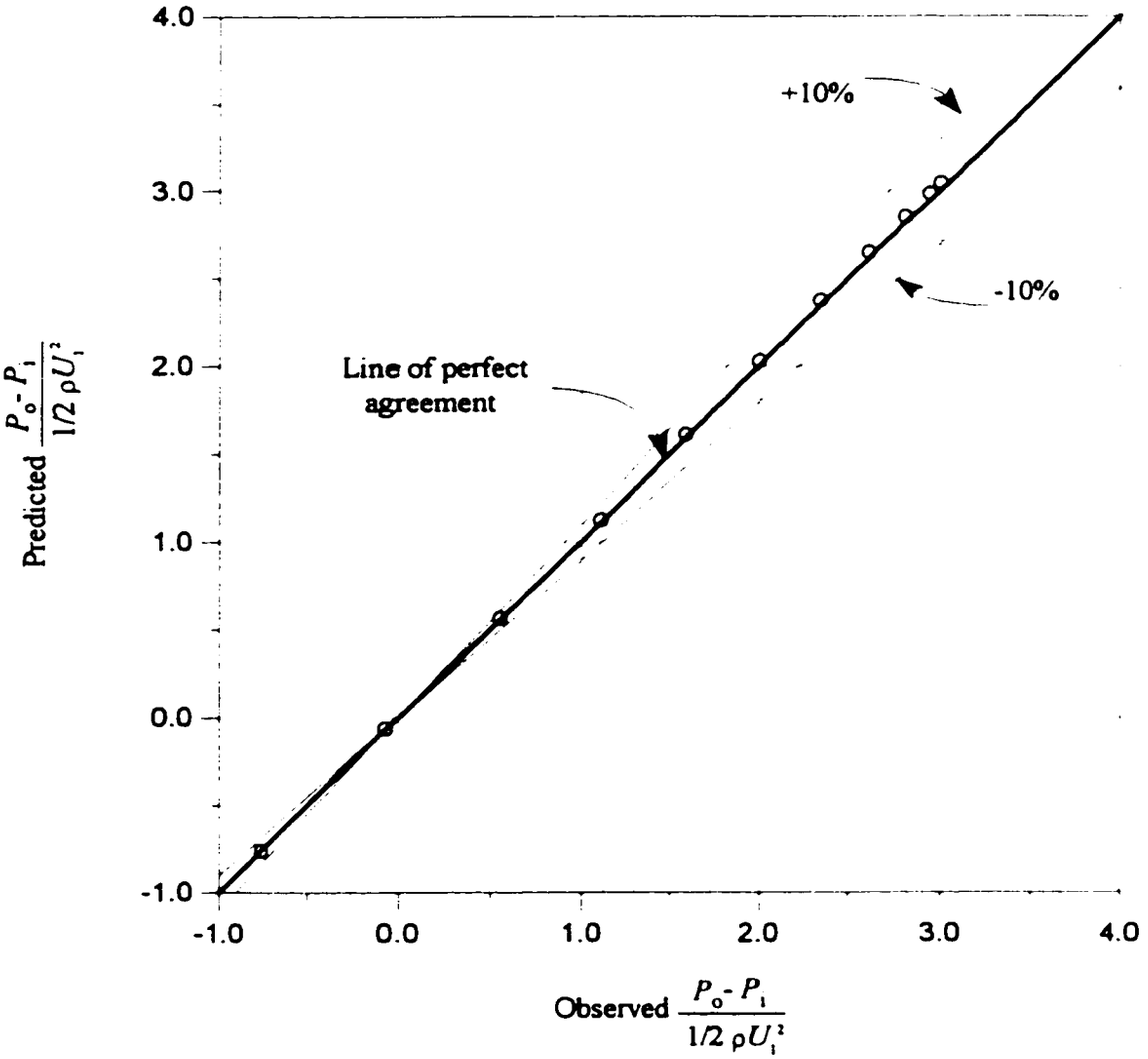

Figure D.31- Predicted vs. observed $\frac{P_o - P_i}{1/2\,\rho U_i^2}$ for L/D=26.6 and $Re_{axi.}$=38,318

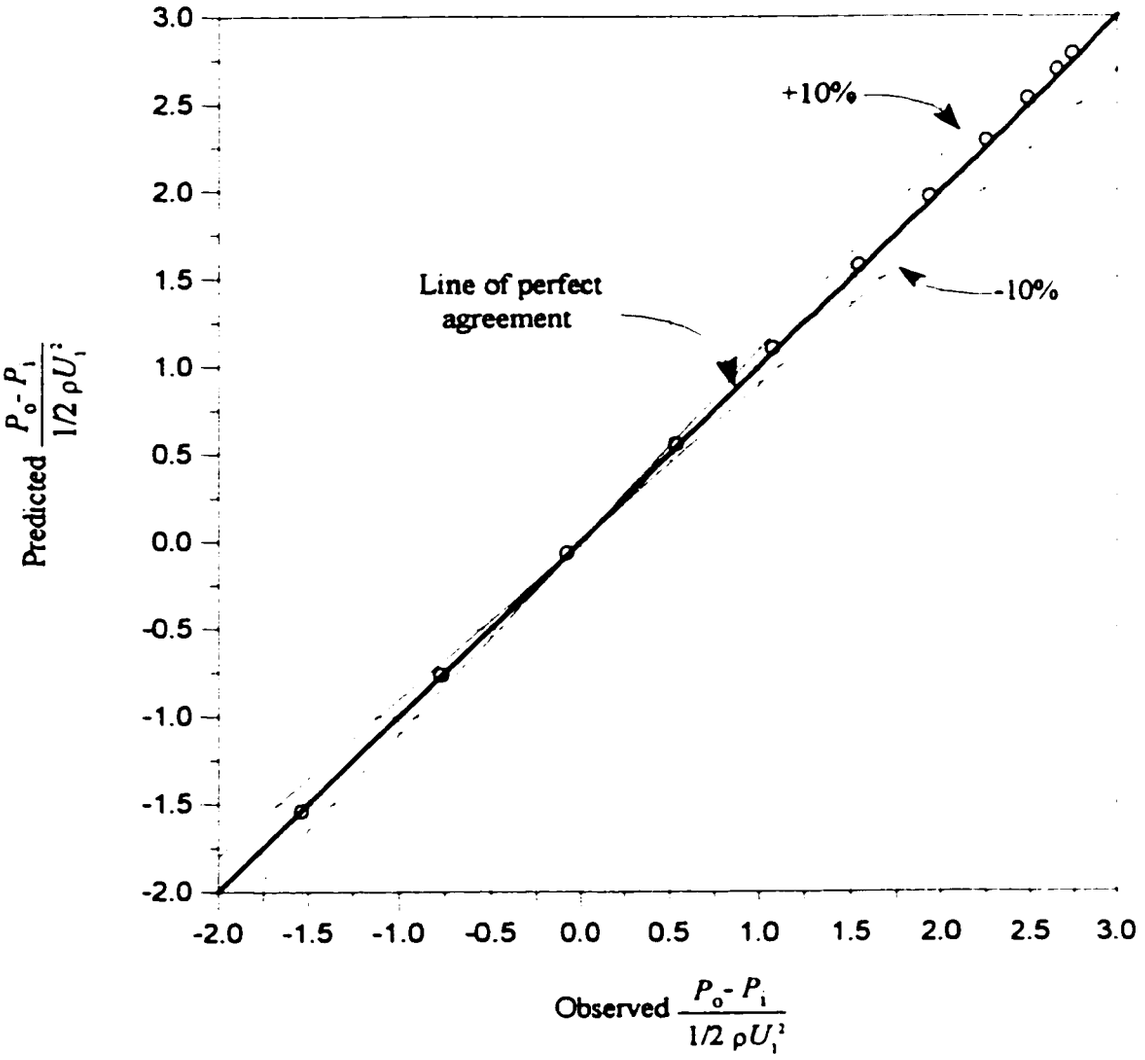

Figure D.32- Predicted vs. observed $\frac{P_o - P_i}{1/2\,\rho U_i^2}$ for L/D=53.2 and $Re_{axi.}$=38,318

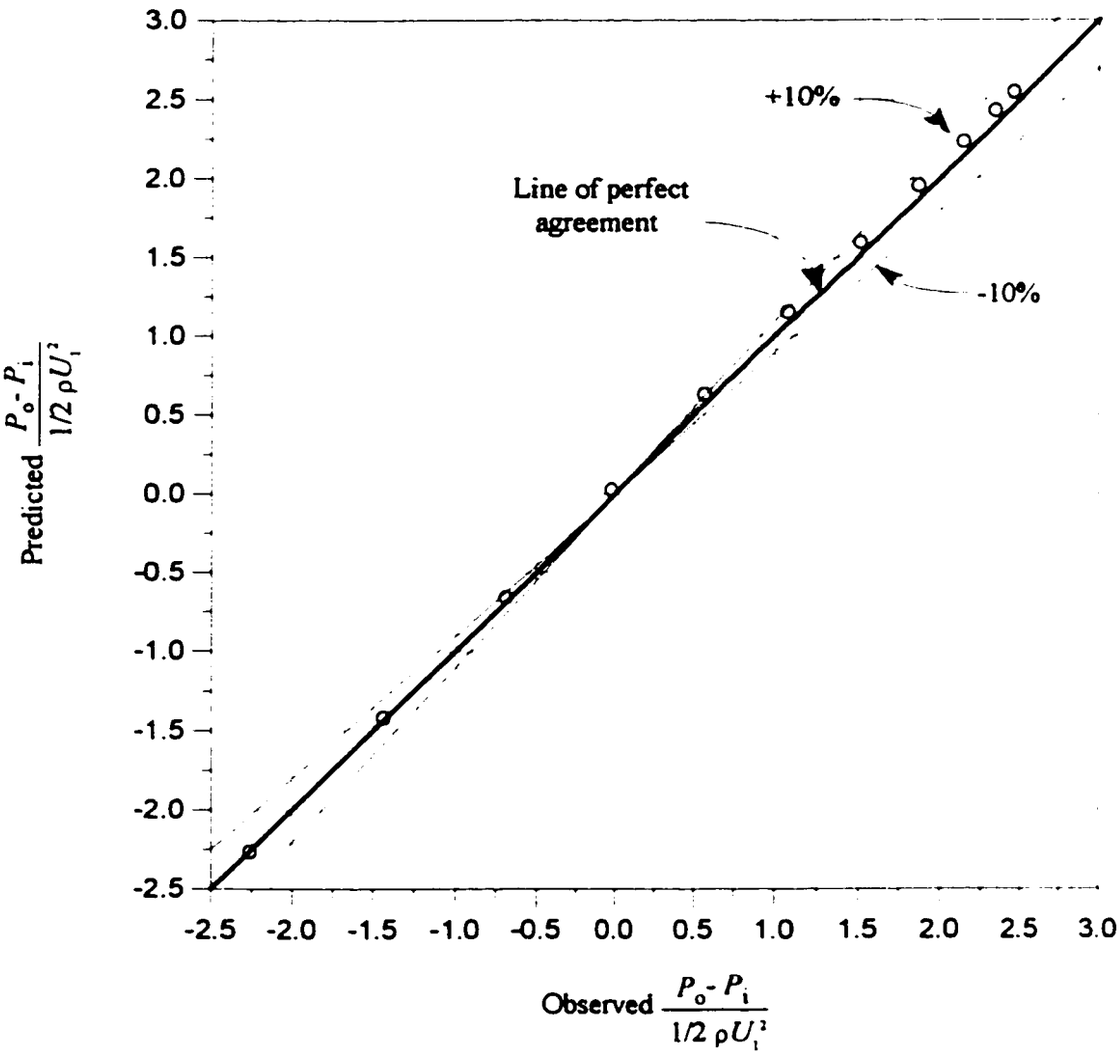

Figure D.33- Predicted vs. observed $\frac{P_o - P_i}{1/2\,\rho U_i^2}$ for L/D=79.8 and $Re_{axi.}$=38,318

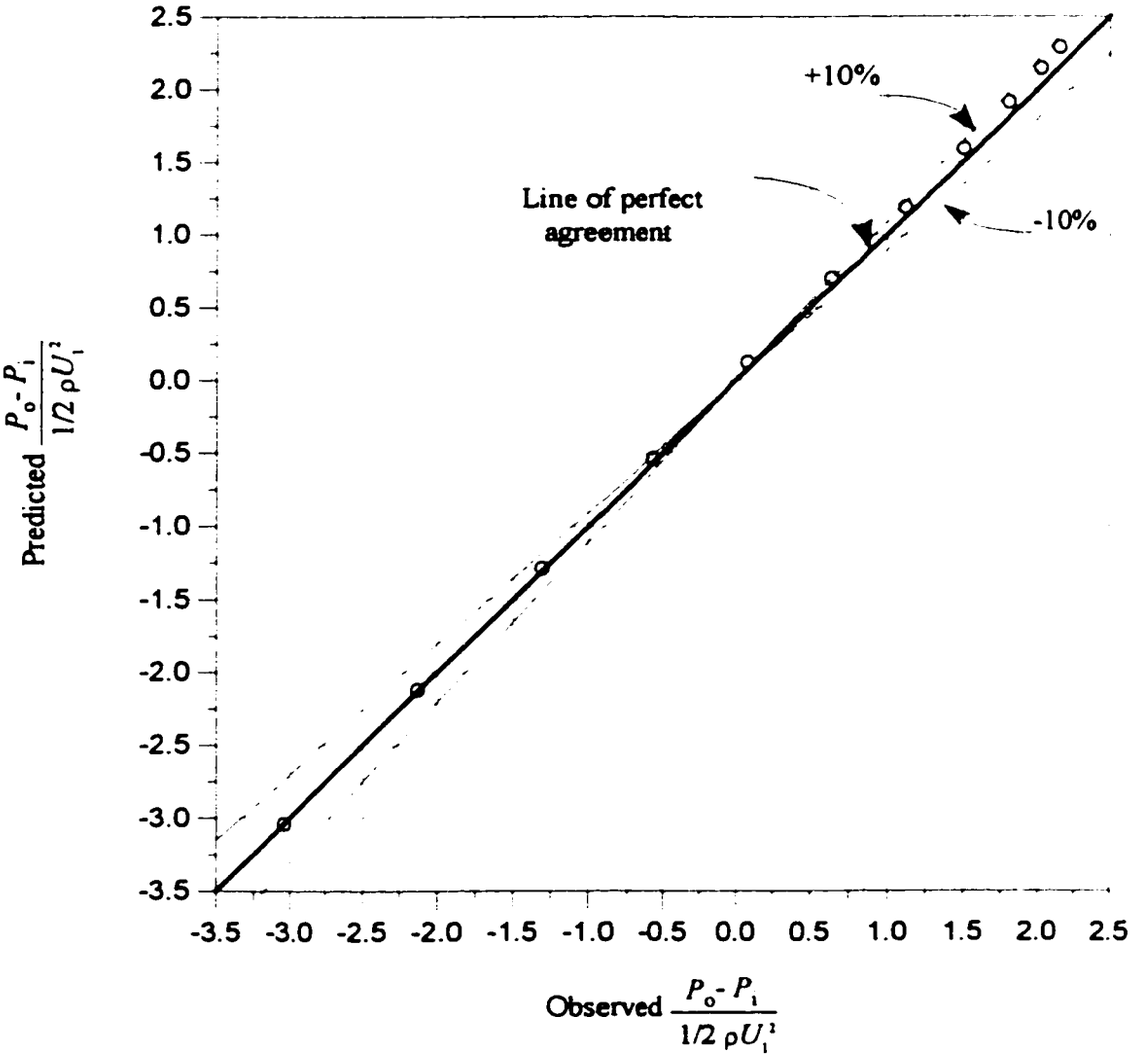

Figure D.34- Predicted vs. observed $\frac{P_o - P_i}{1/2\,\rho U_i^2}$ for L/D=106.4 and $Re_{axi.}$=38,318

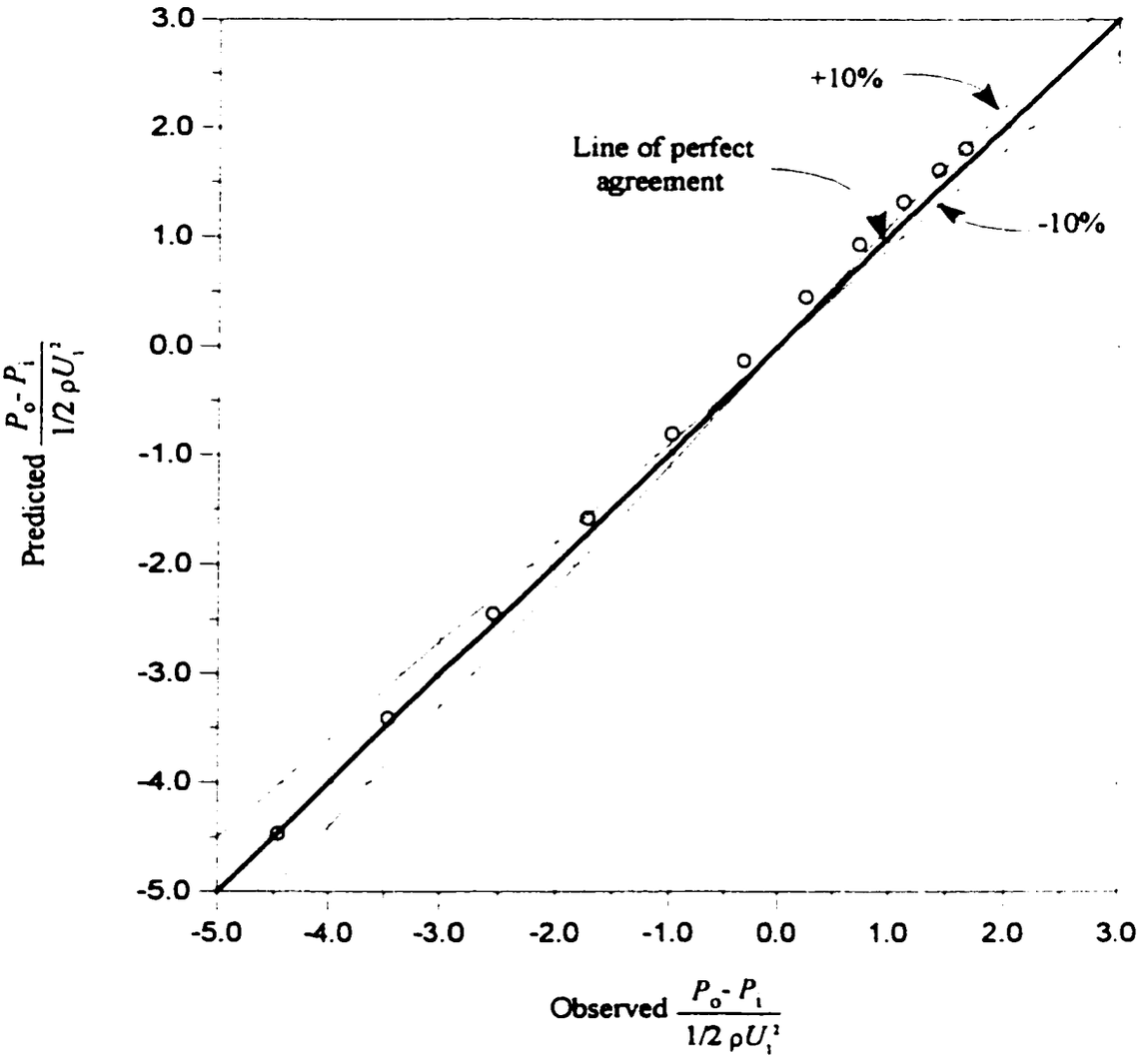

Figure D.35- Predicted vs. observed $\frac{P_o - P_i}{1/2\,\rho U_i^2}$ for L/D=159.6 and $Re_{axi.}$=38,318

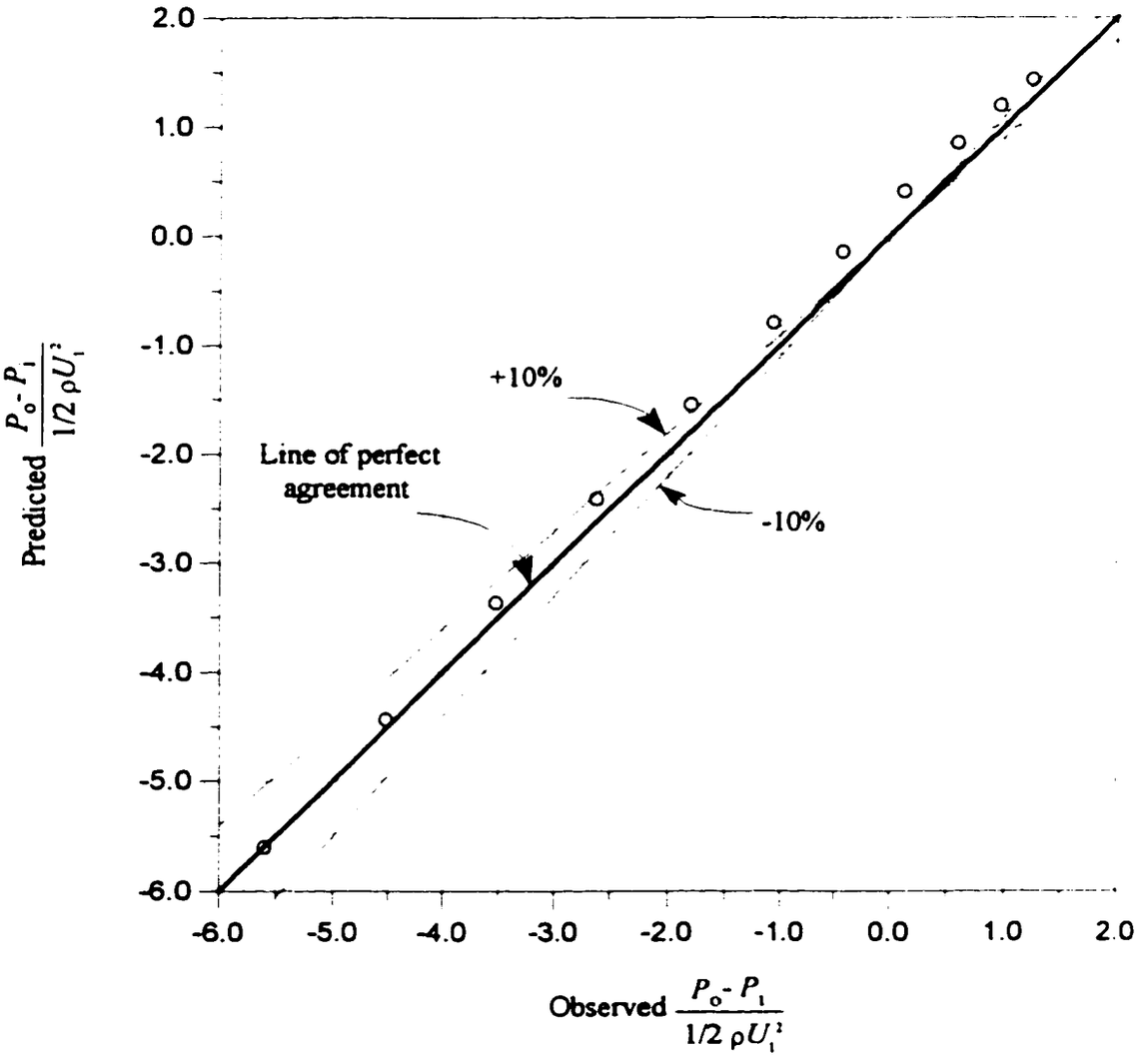

Figure D.36- Predicted vs. observed $\frac{P_o - P_i}{1/2\,\rho U_i^2}$ for L/D=206.6 and $Re_{axi.}$=38,318

Appendix E

Comparison between predicted values of pressure variation along porous tubing obtained by Equation 7.21 and measured values obtained by Aggarwal et al. (1972) and values obtained by numerical study

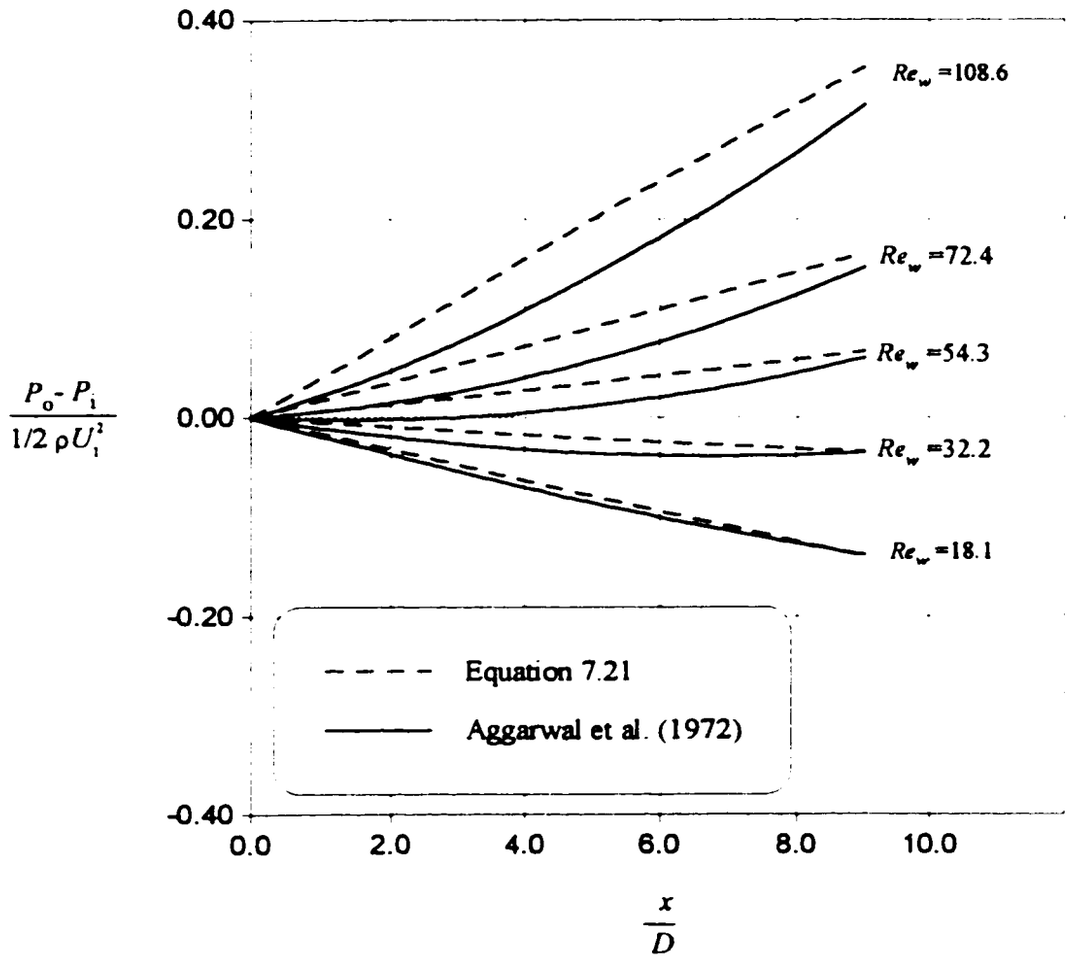

Figure E.1- Comparison between Equation 7.21 and Aggarwal et al. (1972) study for dimensionless pressure change $(P_o - P_i)/\frac{1}{2}\rho U_i^2$ along tubing for $Re_{axi.}$=21,710

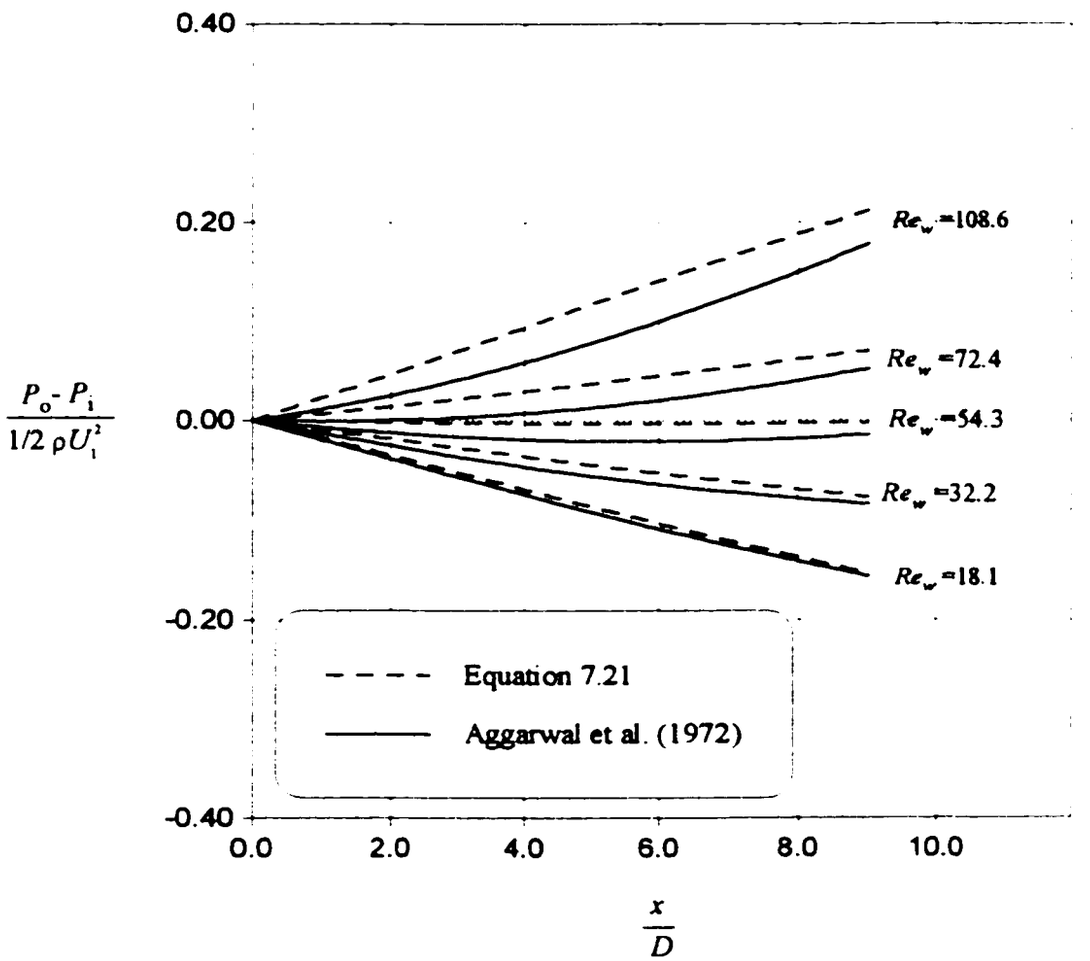

Figure E.2- Comparison between Equation 7.21 and Aggarwal et al. (1972) study for dimensionless pressure change $(P_o - P_i) / \frac{1}{2}\rho U_i^2$ along tubing for $Re_{axi.}$=29,980

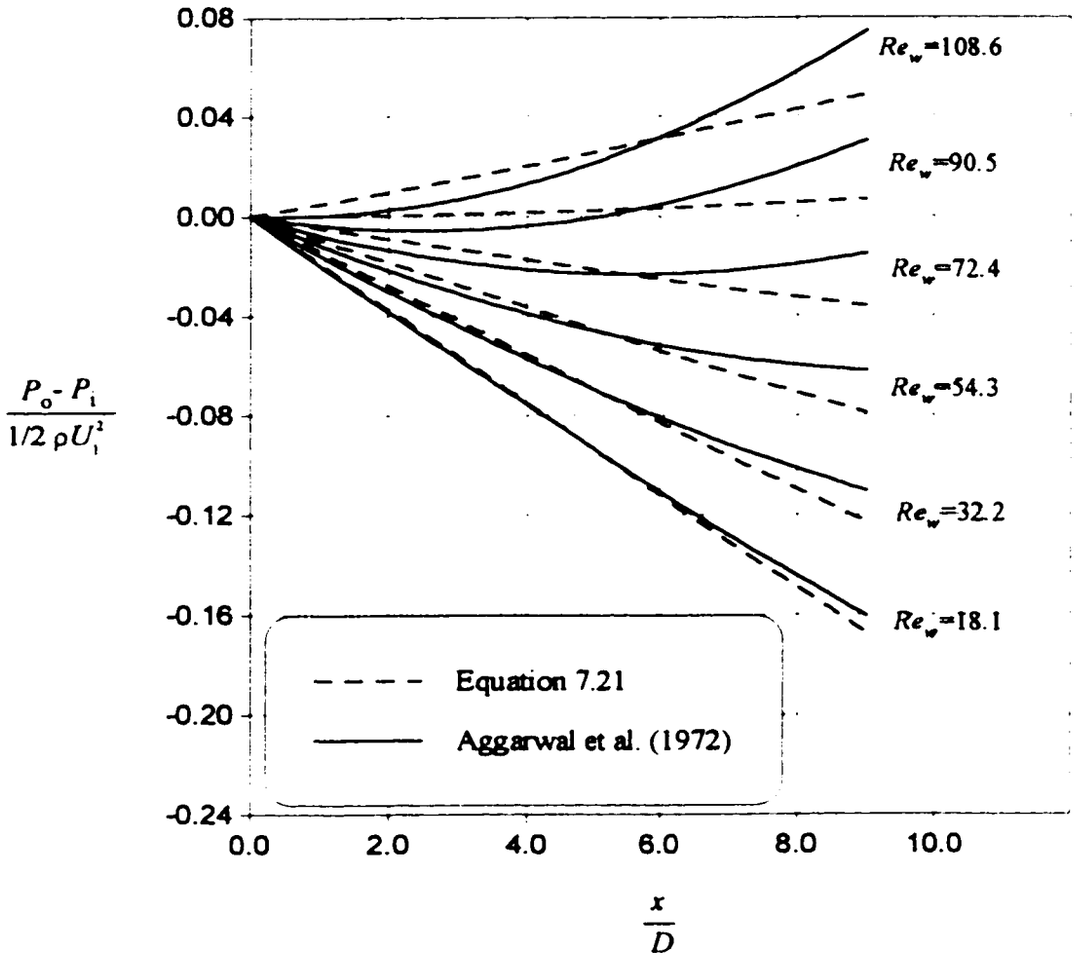

Figure E.3- Comparison between Equation 7.21 and Aggarwal et al. (1972) study for dimensionless pressure change $(P_o - P_i) / \frac{1}{2}\rho U_i^2$ along tubing for $Re_{axi.}$=52,120

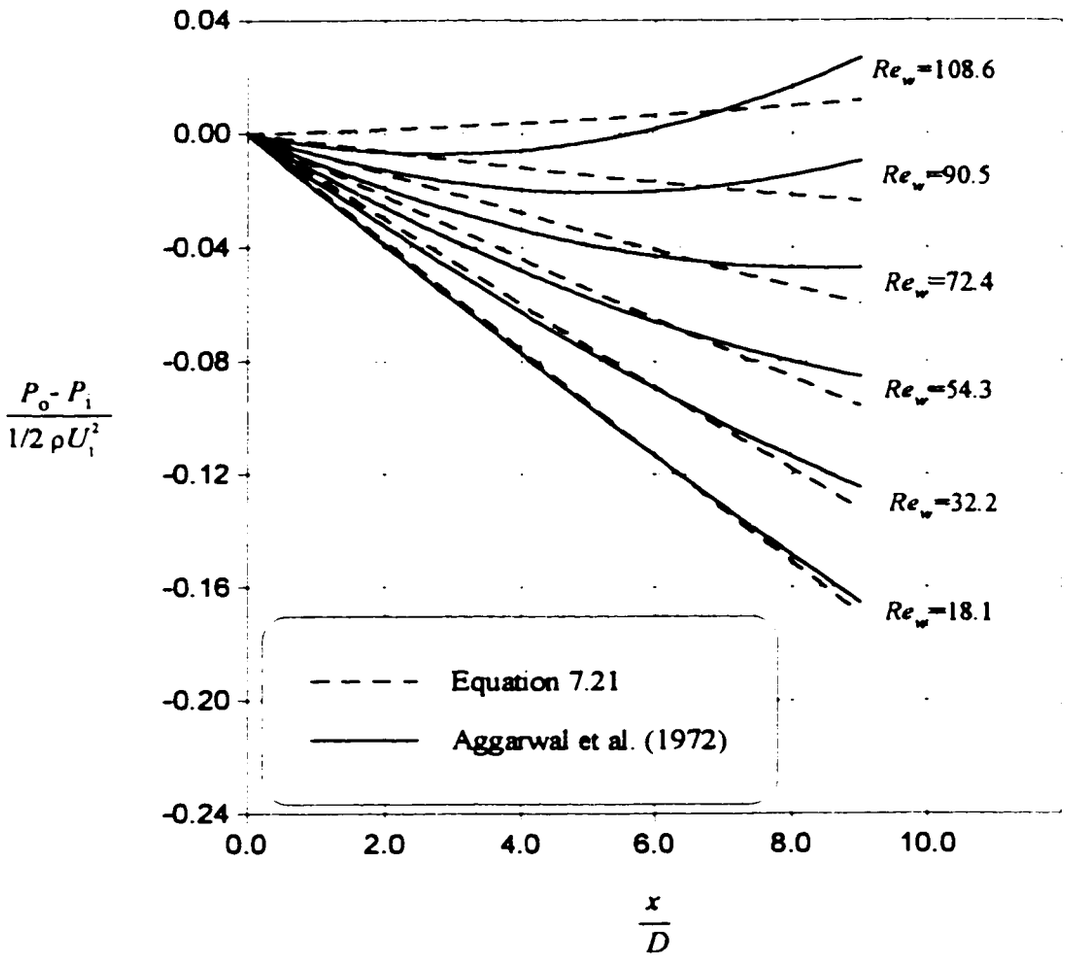

Figure E.4- Comparison between Equation 7.21 and Aggarwal et al. (1972) study for dimensionless pressure change $(P_o - P_i) / \frac{1}{2}\rho U_i^2$ along tubing for $Re_{axi.}$=62,550

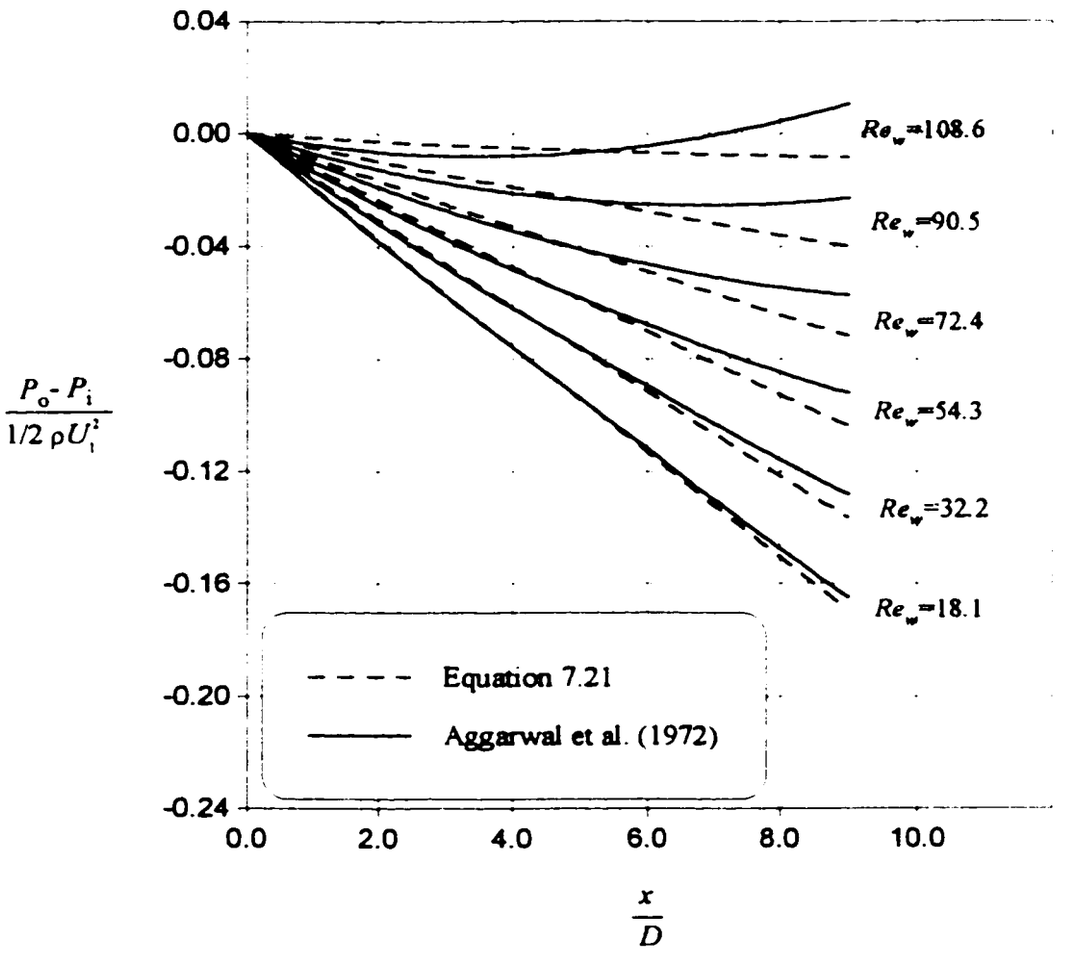

Figure E.5- Comparison between Equation 7.21 and Aggarwal et al. (1972) study for dimensionless pressure change $(P_o - P_i) / \frac{1}{2}\rho U_1^2$ along tubing for $Re_{axi.}$=70,670

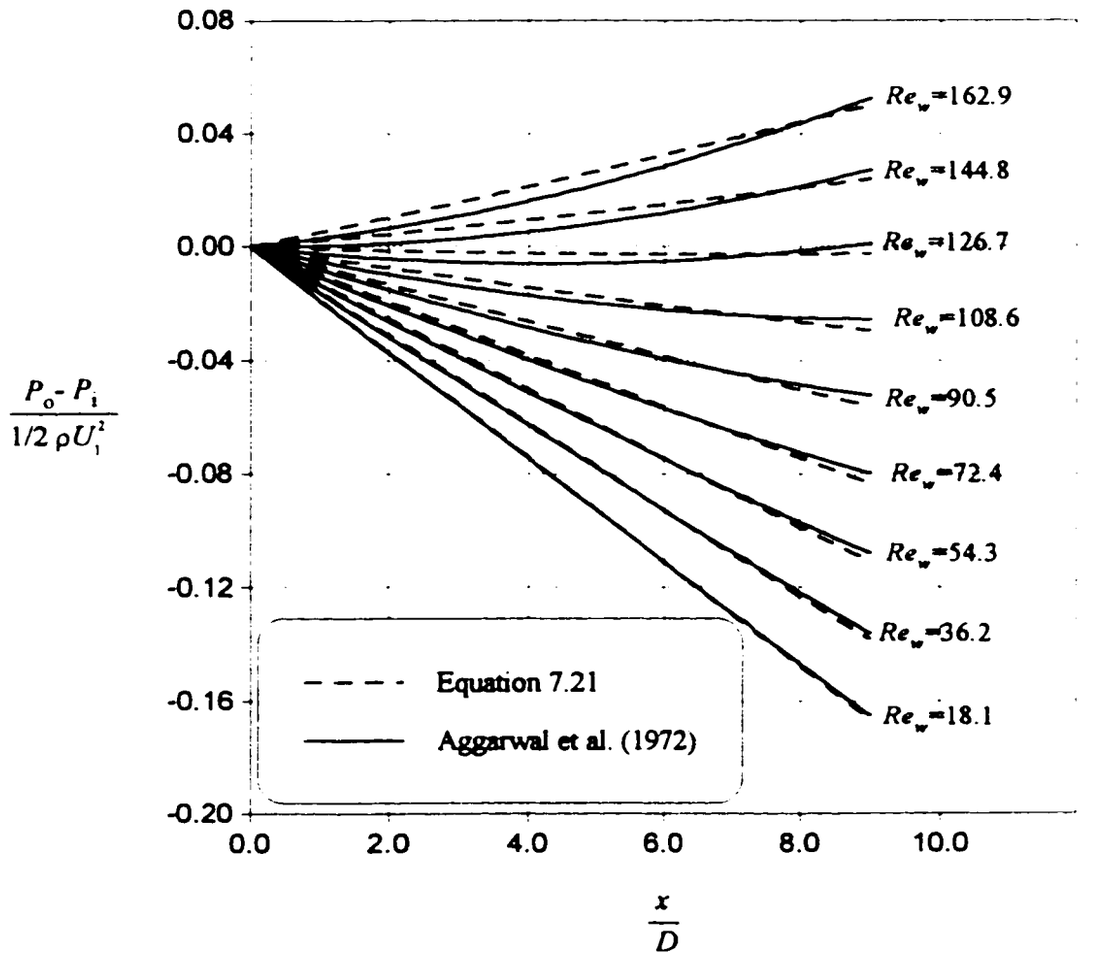

Figure E.6- Comparison between Equation 7.21 and Aggarwal et al. (1972) study for dimensionless pressure change $(P_o - P_i)/\frac{1}{2}\rho U_i^2$ along tubing for $Re_{axi.}$=83,280

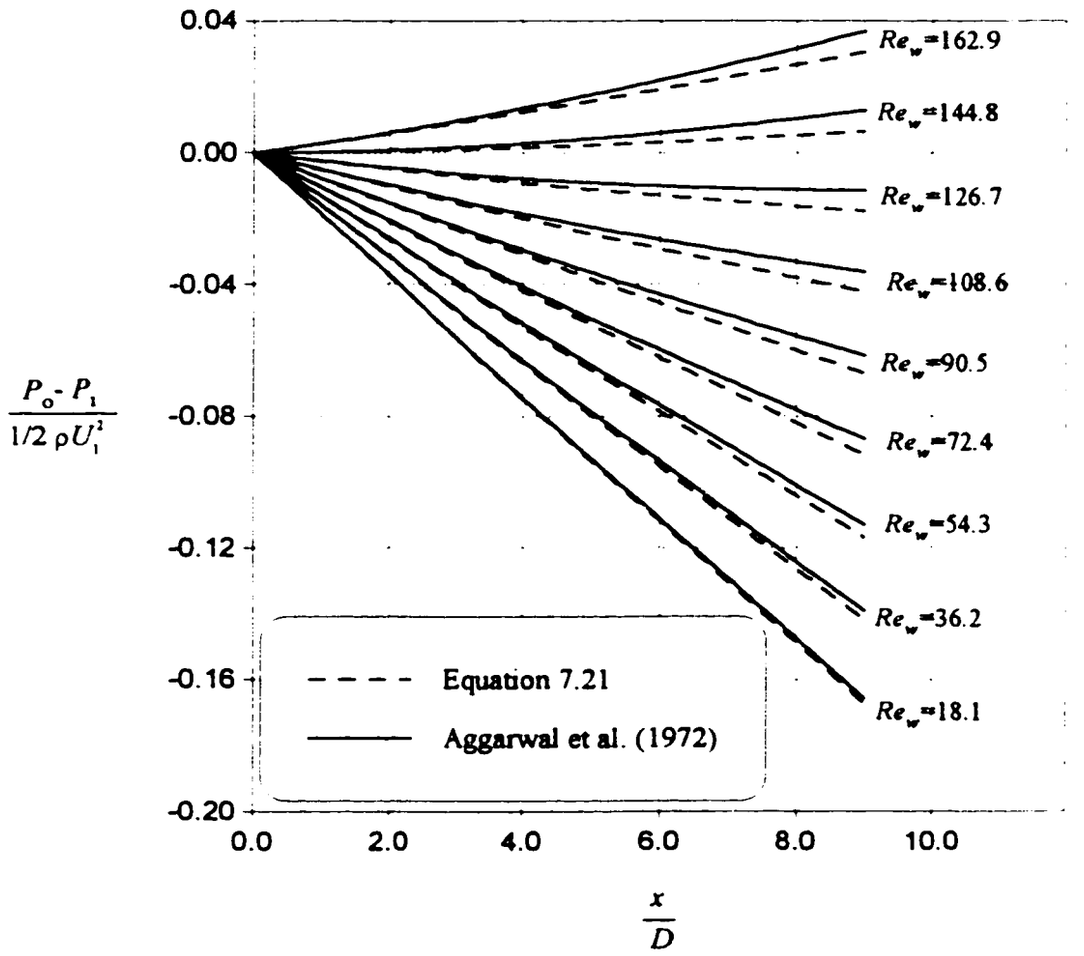

Figure E.7- Comparison between Equation 7.21 and Aggarwal et al. (1972) study for dimensionless pressure change $(P_o - P_i) / \frac{1}{2}\rho U_i^2$ along tubing for $Re_{axi.}$=91,420

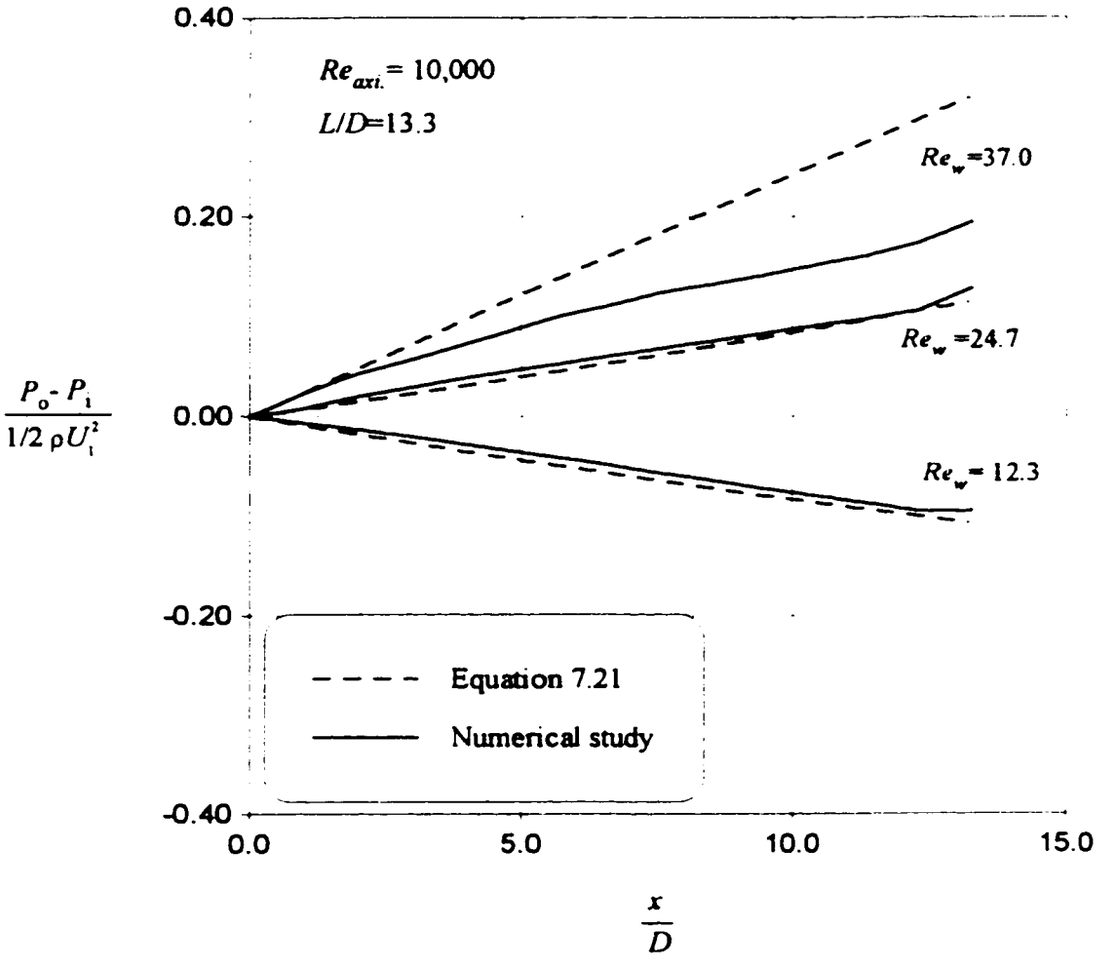

Figure E.8- Comparison between Equation 7.21 and numerical study for dimensionless axial pressure change $(P_o - P_i) / \frac{1}{2}\rho U_i^2$ along tubing for $Re_{axi.}$=10,000, L/D=13.3

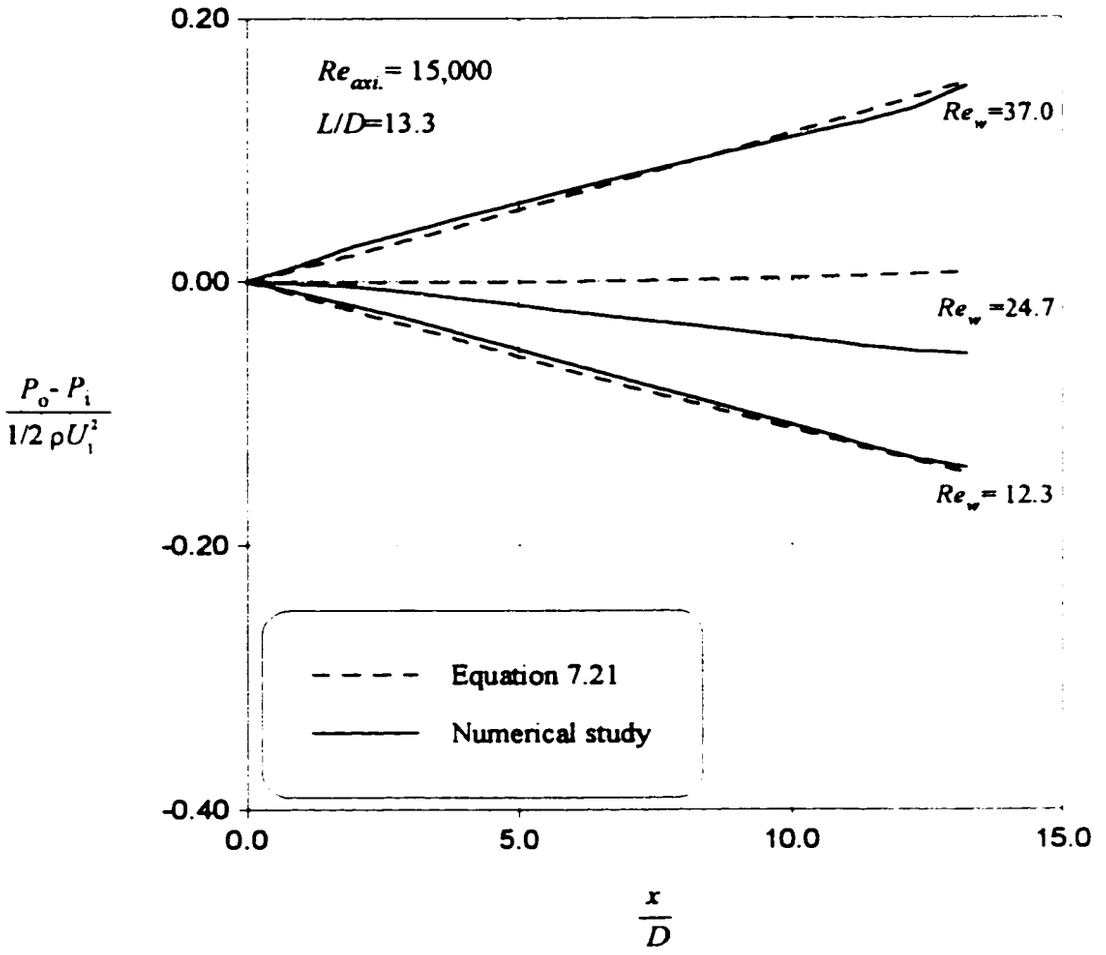

Figure E.9- Comparison between Equation 7.21 and numerical study for dimensionless axial pressure change $(P_o - P_i) / \frac{1}{2}\rho U_i^2$ along tubing for $Re_{axi.}$=15,000, L/D=13.3

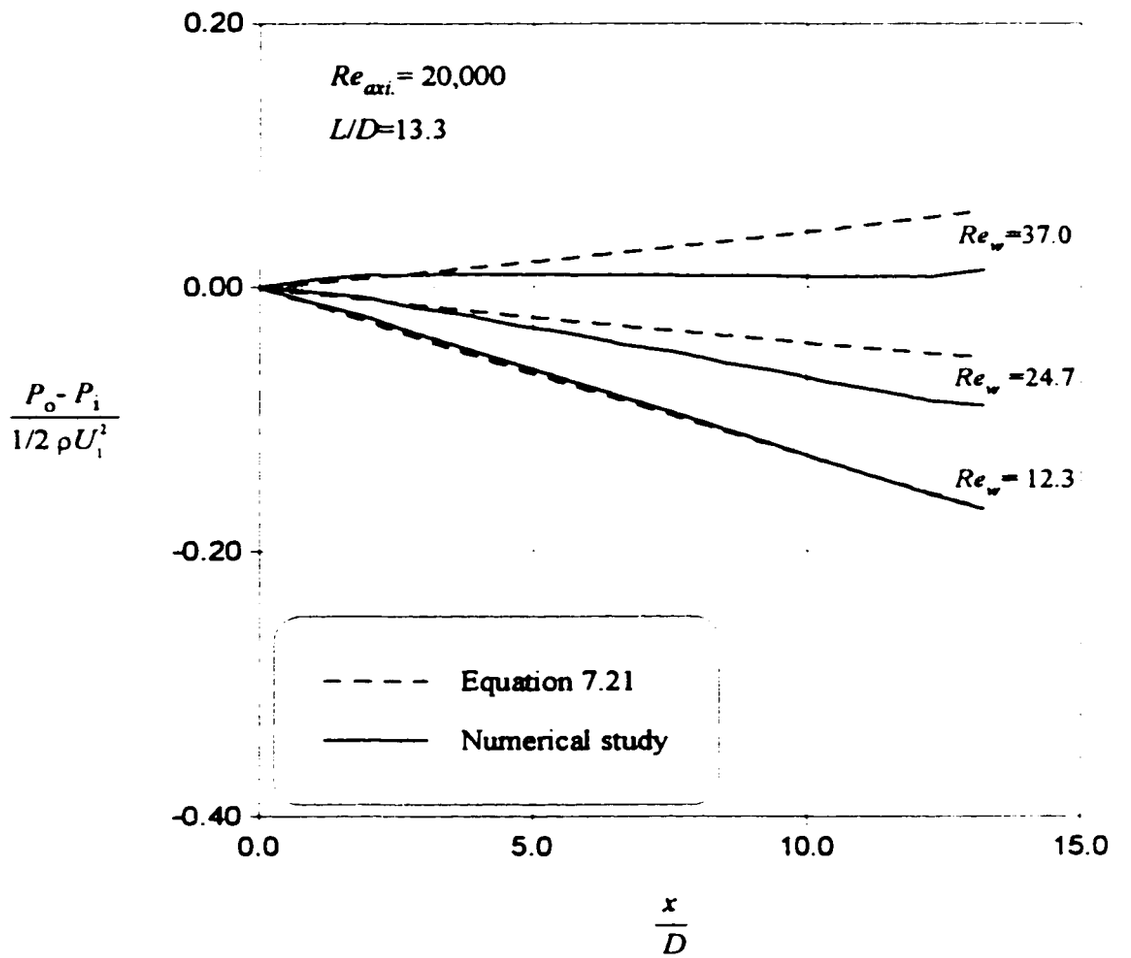

Figure E.10- Comparison between Equation 7.21 and numerical study for dimensionless axial pressure change $(P_o - P_i) / \frac{1}{2}\rho U_i^2$ along tubing for $Re_{axi.}$=20,000, L/D=13.3

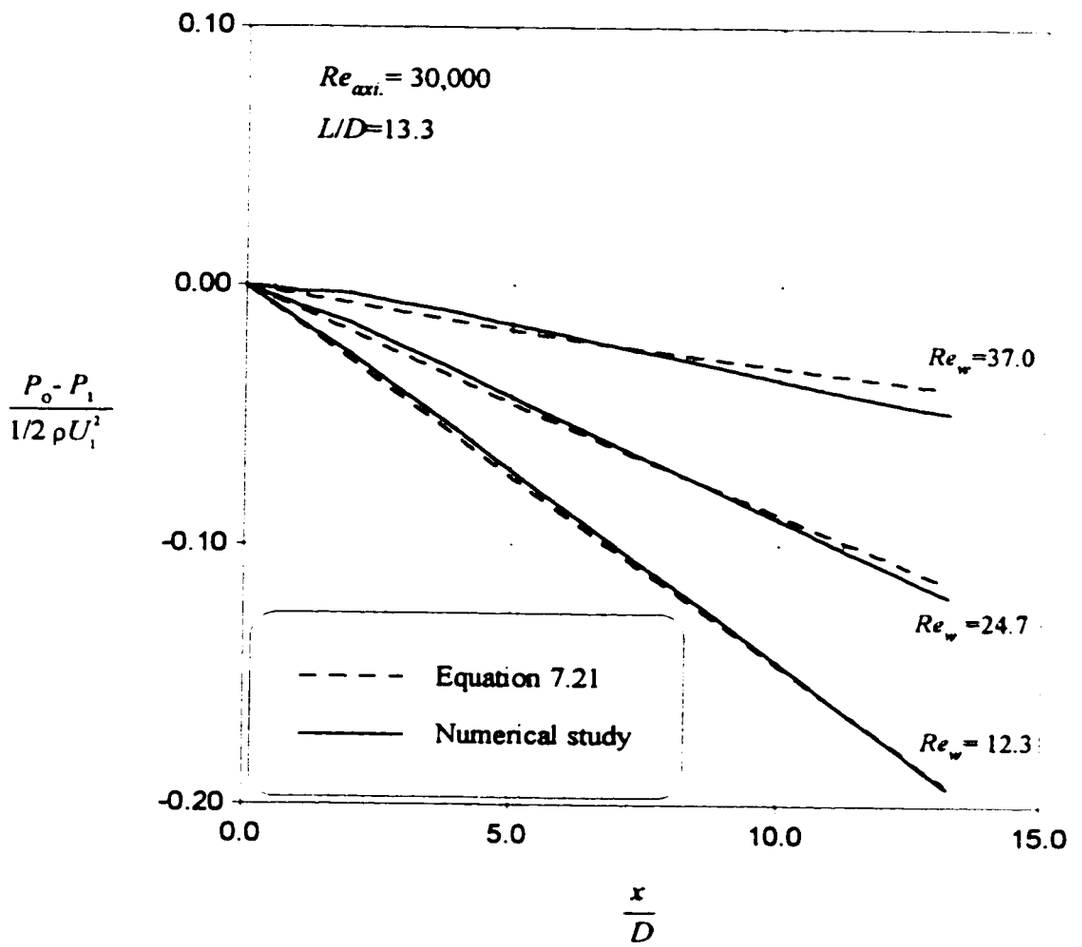

Figure E.11- Comparison between Equation 7.21 and numerical study for dimensionless axial pressure change $(P_o - P_i) / \frac{1}{2}\rho U_i^2$ along tubing for $Re_{axi.}$=30,000, L/D=13.3

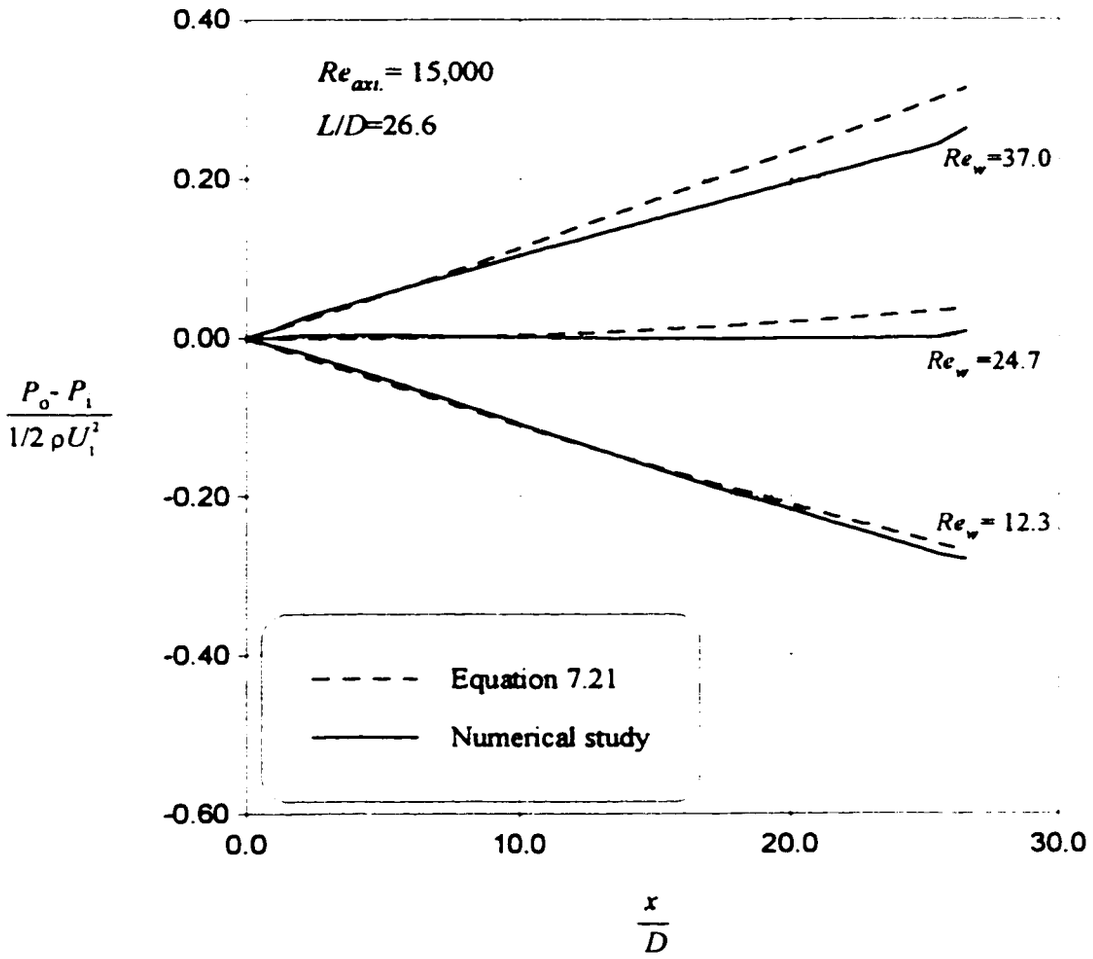

Figure E.12- Comparison between Equation 7.21 and numerical study for dimensionless axial pressure change $(P_o - P_i) / \frac{1}{2}\rho U_i^2$ along tubing for $Re_{axi.}$=15,000, L/D=26.6

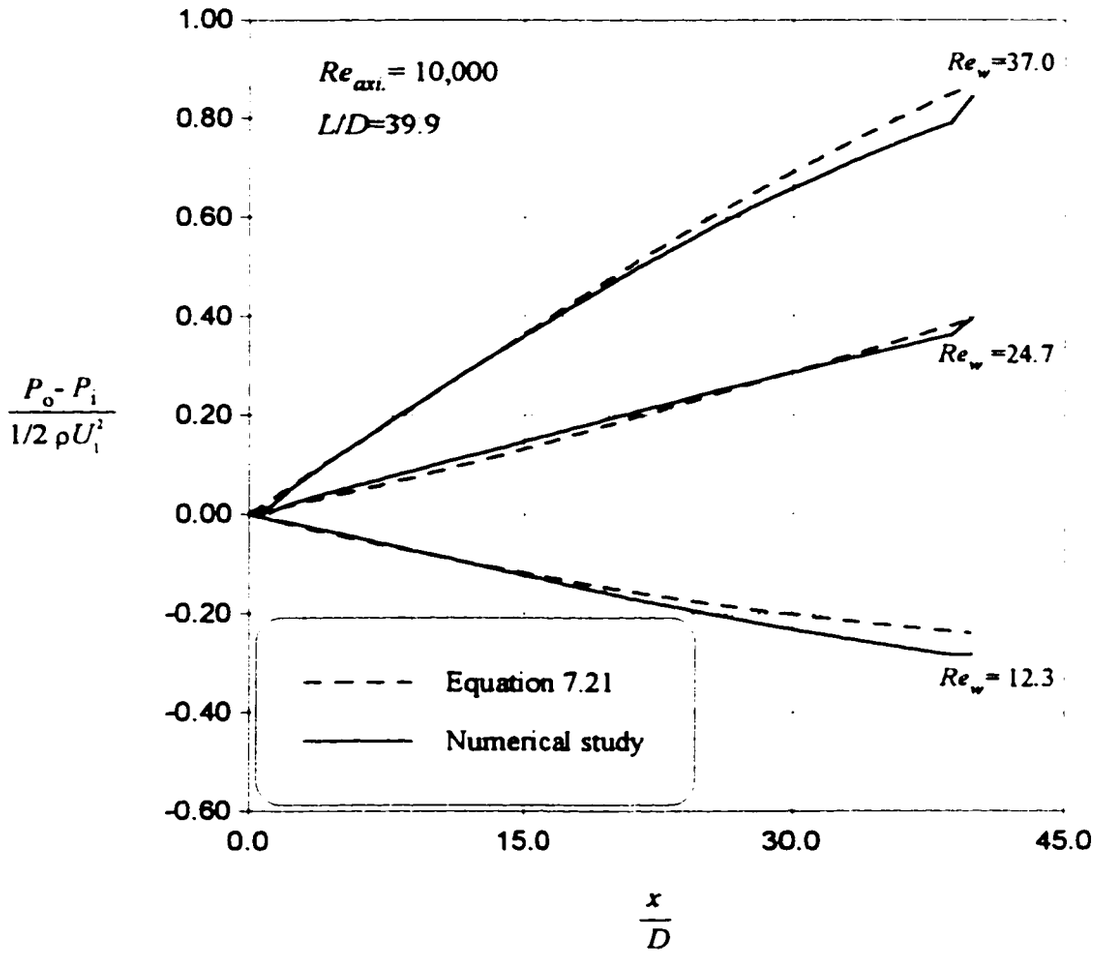

Figure E.13- Comparison between Equation 7.21 and numerical study for dimensionless axial pressure change $(P_o - P_i) / \frac{1}{2}\rho U_i^2$ along tubing for $Re_{axi.}$=10,000, L/D=39.9

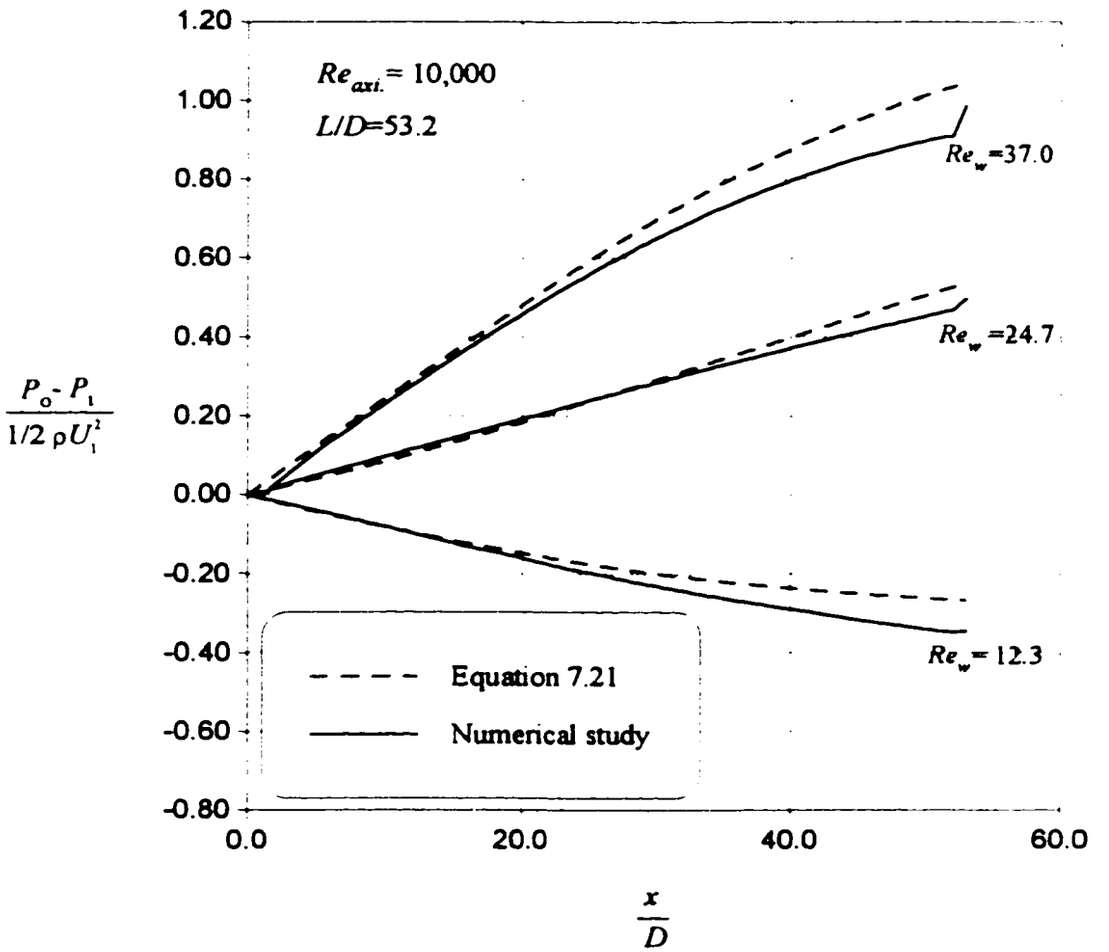

Figure E.14- Comparison between Equation 7.21 and numerical study for dimensionless axial pressure change $(P_o - P_i) / \frac{1}{2} \rho U_i^2$ along tubing for $Re_{axi.}$=10,000, L/D=53.2

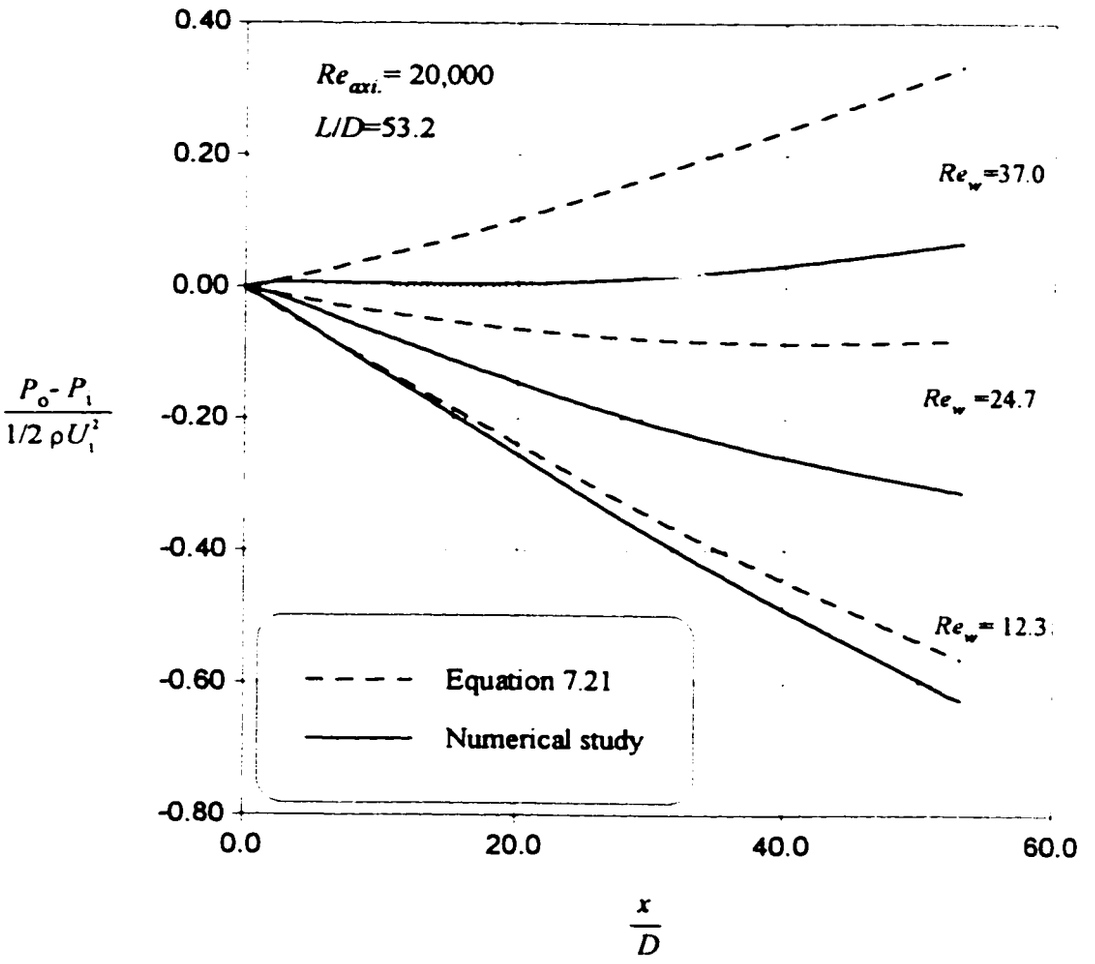

Figure E.15- Comparison between Equation 7.21 and numerical study for dimensionless axial pressure change $(P_o - P_i) / \frac{1}{2}\rho U_i^2$ along tubing for $Re_{axi.}$=20,000, L/D=53.2

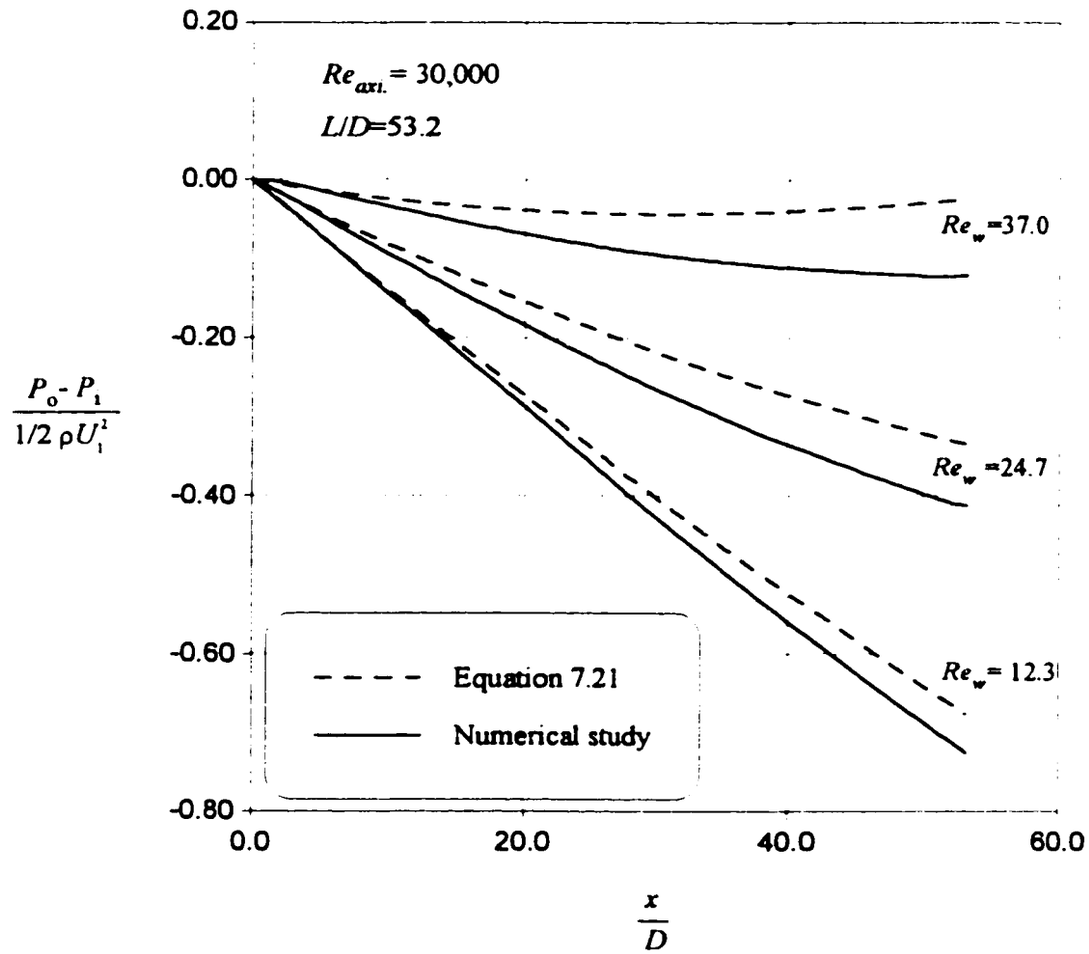

Figure E.16- Comparison between Equation 7.21 and numerical study for dimensionless axial pressure change $(P_o - P_i) / \frac{1}{2}\rho U_i^2$ along tubing for $Re_{axi.}$=30,000, L/D=53.2

IMAGE EVALUATION
TEST TARGET (QA-3)

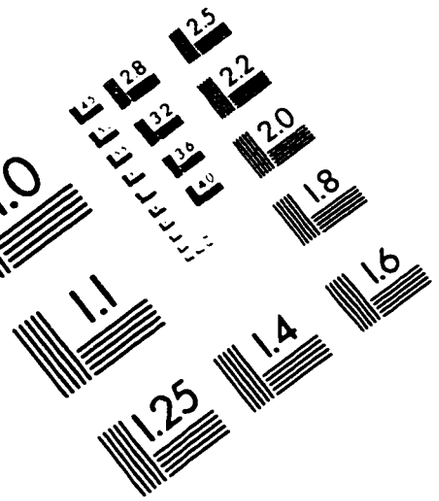

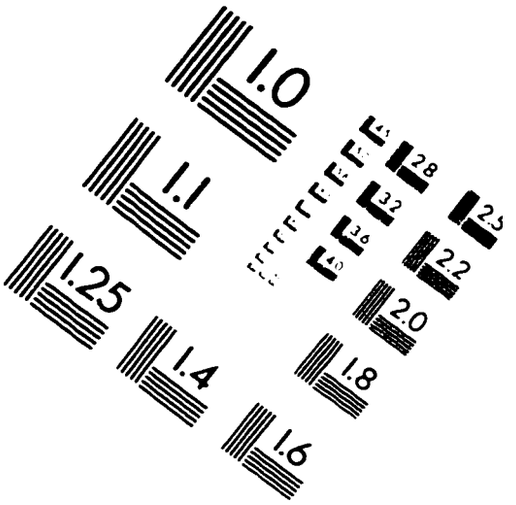

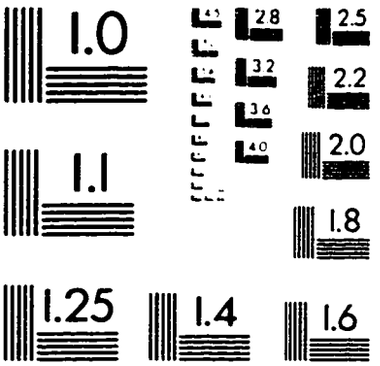

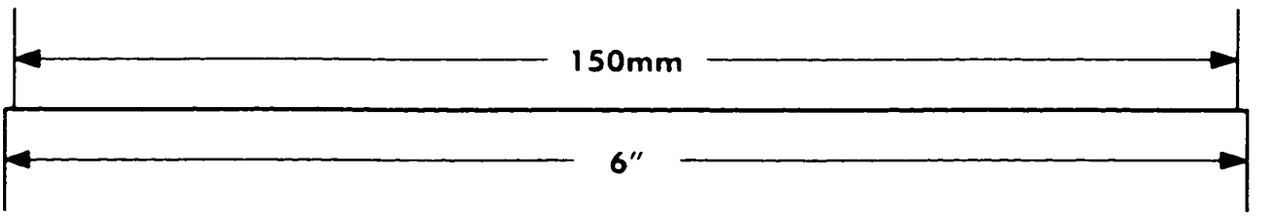

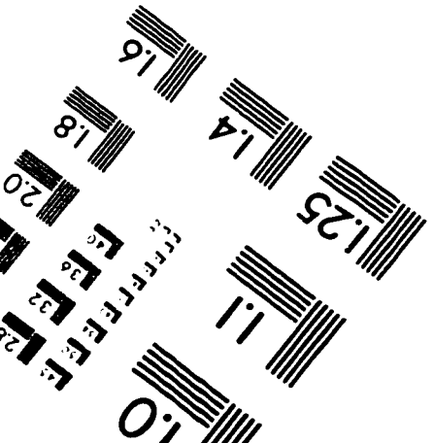

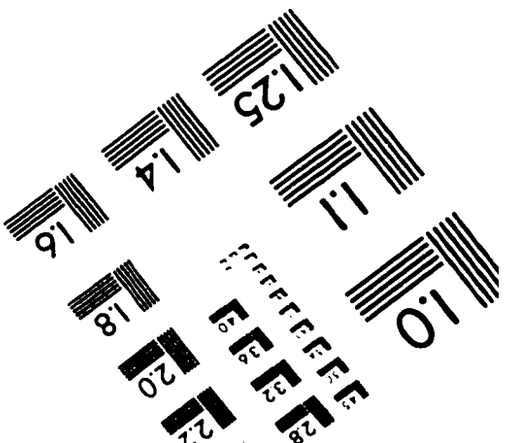

APPLIED IMAGE, Inc
1653 East Main Street
Rochester, NY 14609 USA
Phone: 716/482-0300
Fax: 716/288-5989